Improving mechanical interlock in concrete-to-concrete interfaces: A numerical study

Maria Koetsier

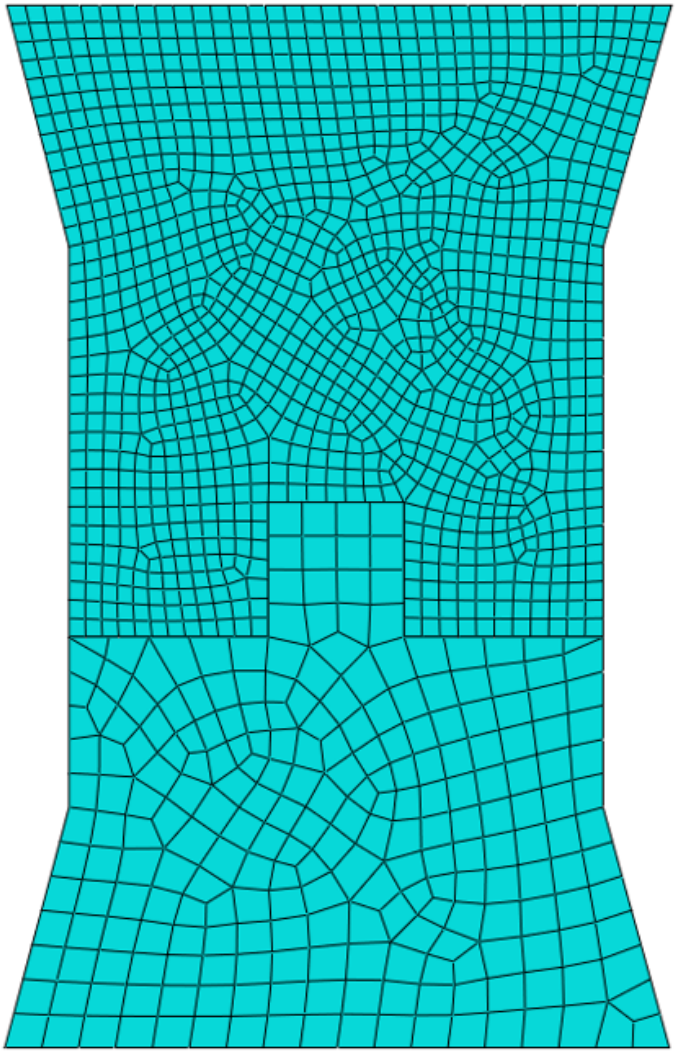

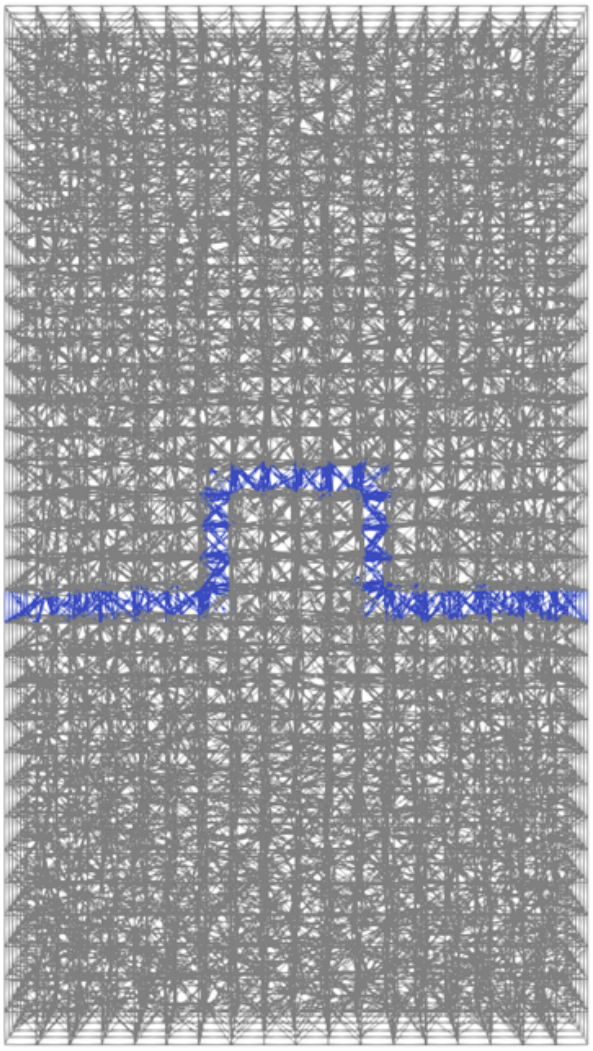

TU Delft

ADVIESBUREAU HAGEMAN

Improving mechanical interlock in concrete-to-concrete interfaces: A numerical study

A Master Thesis

by

Maria Koetsier

to obtain the degree of Master of Science
at the Delft University of Technology

Student number: 4827635
Project duration: November 1st, 2023 – December 12th, 2024
Thesis committee:
Dr. ir. M. Luković, Concrete Structures, TU Delft, Graduation Chair & Main Supervisor
Dr. M. Pavlović, Steel and Composite Structures, TU Delft, Secondary Supervisor
Dr. ir. D.A. Hordijk, Adviesbureau Hageman, Additional Supervisor

TU Delft

ADVIESBUREAU HAGEMAN

Abstract

Recent advancements at TU Delft have investigated the potential of geometrically enhanced profiles to improve the performance of concrete-to-concrete interfaces, with one study focusing on the tensile behavior of single-tab Strain Hardening Cementitious Composites (SHCC)-to-SHCC interfaces through experimental testing. SHCC, an advanced fiber-reinforced cement-based material, is known for its distributed cracking and strain-hardening capabilities, offering superior ductility and crack control compared to traditional concrete. Building on this foundation, this thesis models the tensile behavior of geometrically profiled SHCC-to-SHCC interfaces using a continuum smeared cracking model in Abaqus and a lattice discrete cracking model.

The research aims to assess the predictive capability of these numerical models in capturing the behavior of geometrically profiled SHCC-to-SHCC interfaces. It focuses on understanding how interface parameters, such as strength and geometric profiles, influence tensile performance, particularly in enhancing ductility, controlling fracture response, and shifting failure modes from brittle interface failure to ductile SHCC material failure.

To evaluate the ability of numerical models to represent the tensile behavior of geometrically profiled SHCC-to-SHCC interfaces and assess the benefits of geometric enhancements for improving tensile performance, a systematic methodology was adopted. This included an analytical analysis to identify underlying failure mechanisms and develop a simplified model for quantifying their force-displacement response. A continuum smeared cracking model in Abaqus was employed to replicate experimental behaviors and investigate the influence of interface parameters through a parametric study. Finally, a lattice model was implemented to capture fracture responses in detail, enabling an in-depth analysis of the effects of interface strength and interface geometry on strength, ductility and fracture response.

The numerical models provided insights into the tensile behavior of geometrically profiled SHCC-to-SHCC interfaces, revealing the influence of interface parameters and geometric characteristics on failure mechanisms. The continuum smeared cracking model demonstrated the ability to simulate various failure mechanisms by adjusting interface parameters, but it underestimated SHCC's strain-hardening behavior during local material-dominated failure due to the delayed introduction of damage. Conversely, the lattice discrete cracking model effectively captured distributed cracking patterns but exhibited overly brittle responses in interface-dominated failure mechanisms due to assumptions of brittle interface elements and the neglect of frictional resistance. Parametric studies confirmed that changing interface geometry and optimizing interface strength could shift failure modes from brittle, interface-dominated failure to ductile SHCC material-dominated failure.

This study highlights the capabilities and limitations of numerical models in optimizing the tensile behavior of geometrically profiled SHCC-to-SHCC interfaces. The continuum smeared cracking model in Abaqus identified critical parameters, such as tensile strength and fracture energy, influencing failure mechanisms. However, it underestimated SHCC hardening during tab failure due to delayed damage initiation, which should occur immediately after the elastic limit to accurately capture distributed cracking behavior.

The lattice discrete cracking model effectively simulated distributed cracking but exhibited overly brittle responses in interface-dominated failure mechanisms. This limitation stemmed from brittle interface assumptions and the omission of friction, resulting in a significant underestimation of displacement capacity.

Parametric studies using the analytical and lattice models revealed that modifying the interface geometry significantly reduces the interface strength required for ductile failure. For instance, the analytical model demonstrated that adjusting the geometry reduced the interface strength needed to transition from interface-dominated to material-dominated failure from 20% to 7%. In the lattice model, at low interface strengths (25%), a change in geometry of 1% enhanced SHCC damage by 3% to 6%. At

higher strengths (30%), interface-dominated failure mechanisms diminished, with full SHCC material activation observed beyond 150% strength, ensuring global rather than localized failure.

These findings confirm that optimizing interface strength and geometry enables the transition from brittle, interface-driven failure to ductile, material-driven failure. Nonetheless, the models' limitations must be addressed, particularly the insufficient representation of strength-geometry-friction interactions in the analytical model and the lack of interface ductility and friction in the lattice model. Despite these challenges, the results provide a valuable foundation for refining numerical models and guiding experimental validation to optimize SHCC-to-SHCC interfaces.

Preface

This master thesis marks the culmination of my Master of Science in Civil Engineering and my academic journey at TU Delft. The research presented herein focuses on enhancing mechanical interlock in concrete-to-concrete interfaces—an area that captivated me for its profound connection to innovation in concrete materials and structural engineering.

Conducted between November 1, 2023, and December 12, 2024, this work represents a combinatgion of theoretical exploration, numerical modeling, and analytical study. Beyond acquiring technical knowledge, this journey has been one of personal growth. It taught me the value of critical thinking, perseverance, and self-belief, pushing me to explore my boundaries both academically and personally.

I owe my deepest gratitude to my supervisors, whose expertise and encouragement were invaluable throughout this process. My heartfelt thanks go to Mladena Luković, whose unwavering academic and personal support inspired me to push forward and believe in my capabilities. Her enthusiasm and dedication were a constant source of motivation. I am also deeply grateful to Dick Hordijk for his guidance at Adviesbureau Hageman, his thoughtful feedback, and his ability to challenge me to think critically and refine my work. Lastly, I want to thank Marko Pavlovic for generously sharing his knowledge and for his steady support throughout this project.

Finally, I want to express my profound gratitude to my family and friends. Their unwavering encouragement, patience, and understanding were the pillars of strength I leaned on during this period. Their belief in me gave me the confidence and resolve to complete this journey.

I hope that this thesis serves as a valuable contribution to the field of concrete structures and inspires further inquiry into enhacing mechanical interlock in concrete-to-concrete interfaces.

Maria Koetsier
Delft, December 2024

Contents

Acronyms

CDP Concrete Damaged Plasticity. v, 38–41, 123

CZM Cohesive Zone Modeling. v, 38, 45, 47, 49, 123

DIC digital image correlation. 14, 63–65, 70, 71

FRC Fibre-Reinforced Concrete. 6

ITZ Interfacial Transition Zone. 23, 206

LVDT Linear variable differential transformer. 51, 63, 65, 70

NSC normal strength concrete. 6

SHCC Strain Hardening Cementitious Composites. ii, iii, v, 1, 3–15, 17, 20–39, 41, 45, 46, 59, 65, 69, 71, 73–75, 78–80, 82–86, 88–91, 93–97, 100, 103–105, 107–113, 115, 117–119, 121–124, 174, 210, 212–218, 221, 222, 224, 226

TU Delft Delft University of Technology. iv, 1

1 Introduction

1.1. Research context

Concrete-to-concrete interfaces are inherently weak and brittle, often making them the most vulnerable component in composite structural systems. In most cases, these interfaces are reinforced with steel bars crossing the joint to enhance their load-bearing capacity and displacement capacity. However, there are situations where minimizing or eliminating such reinforcement is necessary, such as when a thin layer of concrete is applied for structural strengthening or repair. In these cases, it becomes important to explore alternative methods for enhancing the interface's strength and toughness to ensure long-term performance and durability.

One promising approach involves the use of advanced fiber-reinforced cementitious composites, specifically Strain Hardening Cementitious Composites (SHCC), often referred to as "bendable concrete." Due to its strain-hardening behavior and ductile behavior under tensile loading, SHCC has been widely researched as a repair material for cracked reinforced concrete structures. Studies, such as those by Wagner [29], have shown that applying SHCC as a repair layer can reduce crack widths and enhance the durability of existing concrete structures. Building on this concept, research has also explored the interface properties of concrete-to-SHCC systems, aiming to understand and optimize their mechanical performance.

Notably, findings by Wagner, Bretschneider, and Slowik [30] reveal that increasing the surface roughness of concrete-to-SHCC interfaces significantly improves both ductility and load bearing capacity. This improvement arises from a greater portion of the interface area engaging with SHCC adherence, effectively shifting the failure mechanism from the weak and brittle interface to the more strong and ductile SHCC material. Inspired by these insights, this thesis focuses on further advancing this concept by combining geometrical interface roughness with the unique properties of SHCC. The goal is to enhance mechanical interlock in concrete-to-concrete interfaces using SHCC's ductile behavior to transition failure from weak and brittle interface failure to strong and ductile SHCC material failure. This shift has the potential to significantly enhance both the strength and deformation capacity of concrete-to-concrete interfaces, providing a robust solution for applications requiring unreinforced or minimally reinforced interfaces.

1.2. Research problem & objective

Research problem

Recently, research has emerged at TU Delft into the possibility to enhance the performance of concrete-to-concrete-like interfaces by using geometrically enhanced interface profiles. Studies have shown that surface roughness can enhance the ductility of interfaces between two cementitious composites [29], [28], [15]. As part of the research at TU Delft, in [15] the effect of different interfacial geometries of a conrete-to-concrete interface have been researched numerically by use of the lattice model. The

different geometrical shapes and the numerical results are shown in Figure 1.1. It can be seen that the smooth interface has a very brittle behavior, whereas the profiled interfaces behave more ductile.

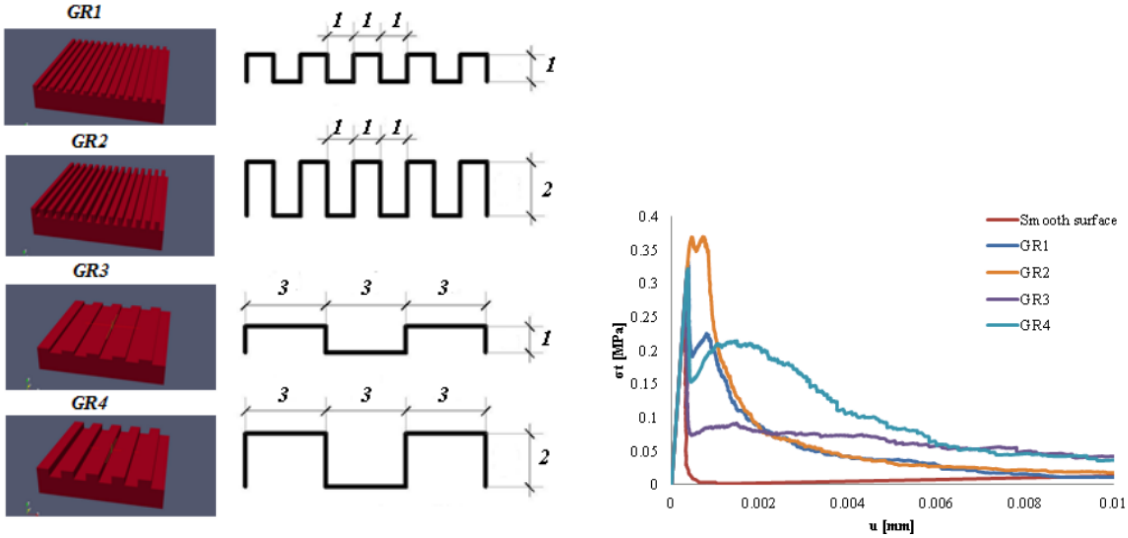

(a) Surface profiles for groove roughened surfaces [mm]. **(b)** Stress strain curves for the different surface profiles.

Figure 1.1: Design and results of profiled interfaces under direct tension test using numerical analysis [15].

More research on using geometrical enhancements to improve ductile behavior in interfaces is found in linear elastic materials. They have found their inspiration in nature where the concept of architectured sutured interfaces comes from. Literature review shows that connections in biologically evolved materials contain architectured interface connections. The important characteristic of these biological materials lies in their combination of strength and toughness, thereby imparting a disposition toward damage tolerance. These attributes are present in various biological interface connections, as illustrated in Figure 1.2. In these micro-structural configurations, the materials engage in interlocking through geometric alignment.

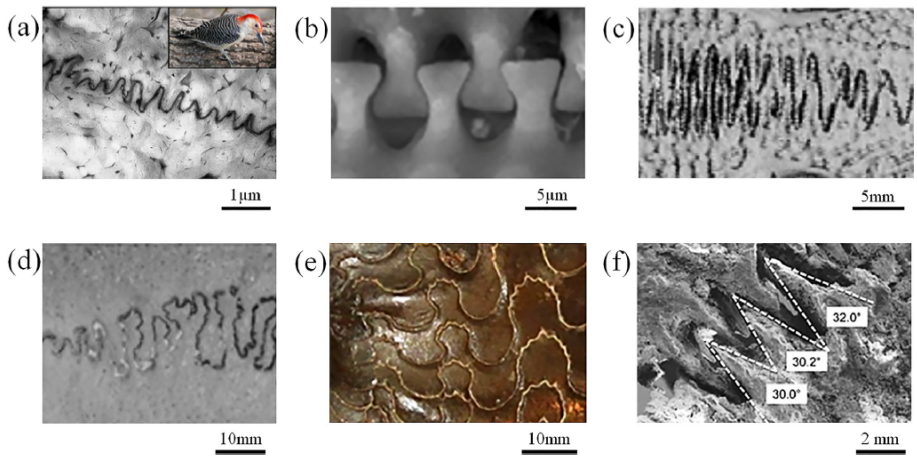

Figure 1.2: Examples of sutured interfaces in nature: (a) red-bellied woodpecker (Melanerpes carolinus) beak (adapted from [10]), (b) linking girdles of diatoms (adapted from [11]), (c) marine threespine stickleback (Gasterosteusaculeatus) (adapted from [27]), (d) Pan troglodytes cranial sutures (adapted from [6]), (e) Ammonite shell (Ceratitic ammonoid) with intricate suture lines [11] (f) osteoderms of a leatherback sea turtle shell (adapted from [17]).

Concrete materials are inherently brittle, characterized by a short linear elastic range before failure. In contrast, linear elastic brittle materials typically exhibit a much longer elastic range, emphasizing the

stark brittleness of concrete. This limitation raises the question of whether geometric enhancements, inspired by naturally optimized sutured interfaces, could similarly improve the mechanical performance of interfaces in cement-based materials. While concrete's elastic range remains short, introducing SHCC provides a promising alternative. Although SHCC does not significantly extend the elastic range, its strain-hardening behavior promotes distributed cracking, allowing the material to undergo significant plastic deformation before failure.

In concrete-to-SHCC interfaces, increased surface roughness has been shown to enhance ductility by shifting failure from the interface itself to within the SHCC material. Inspired by the strength and toughness of naturally occurring sutured interfaces, geometric profiling of SHCC-to-SHCC connections offers the potential to further improve ductile behavior. However, the effects of such geometric enhancements on concrete-to-concrete interface performance remain underexplored, particularly in the context of numerical modeling.

Given the limited research on modeling SHCC-to-SHCC interfaces with geometric profiles, this study aims to bridge this gap. The research will focus on developing numerical models capable of capturing the effects of interface geometry and material parameters on the tensile behavior of SHCC-to-SHCC interfaces. By exploring these interactions, the study seeks to advance understanding and optimization of geometrically enhanced interfaces.

Research objective

The objective of this research is to evaluate and enhance the predictive capabilities of numerical models in accurately simulating the tensile behavior of geometrically profiled SHCC-to-SHCC interfaces. By investigating the effects of interface strength and geometric profile characteristics on ductility and fracture response, the study aims to optimize interface performance and transition failure from brittle interface modes to ductile SHCC material failure.

1.3. Research questions

This research will answer the following main question:

How can an SHCC-to-SHCC interface be tailored—through adjustments to factors such as interface strength and geometry—to shift the failure mode from brittle interface failure to ductile material failure?

This main question will be answered by answering the following sub-questions:

1. Can the fracture behavior of the geometrically profiled SHCC-to-SHCC interface be predicted by the continuum smeared cracking model in Abaqus and which are the governing parameters influencing it?
2. Can the fracture behavior of the geometrically profiled SHCC-to-SHCC interface be predicted by the lattice discrete cracking model and which are the governing parameters influencing it?
3. How can the models be used to optimize the behavior of geometrically profiled SHCC-to-SHCC interfaces?

1.4. Research Scope

This research focuses on understanding the tensile behavior of geometrically profiled SHCC-to-SHCC interfaces under direct tension. The study investigates the effects of interface strength and tab geometry on fracture response and failure mechanisms, focusing exclusively on single straight tab designs adapted from prior research. The study does not consider cyclic or shear loading, alternative geometric profiles, or material properties beyond those of SHCC.

1.5. Research method

This study follows a structured approach, beginning with a comprehensive literature review and progressing through analytical and numerical modeling:

1. **Literature Review:** An exploration of current research on concrete-to-concrete and concrete-to-SHCC interfaces, with emphasis on geometrically profiled designs.
2. **Analytical Analysis:** A simplified analytical assessment is conducted to identify and understand the core mechanisms governing profiled interface behavior. The different failure mechanisms are identified and a simplified analytical model is developed to quantify the tensile response of the different failure mechanisms.
3. **Continuum Smeared Cracking Model:** Using Abaqus, a continuum smeared cracking model is developed, followed by a parametric study of the interface model parameters to refine the model and gain a deeper understanding in the workings of the interface model. Subsequently, the experimental behavior of geometrically enhanced interfaces from the literature is replicated.
4. **Lattice Model:** In an attempt to improve the prediction in fracture response, a lattice model is implemented to simulate the behavior of the different failure mechanisms of single straight tab profiled interfaces.
5. **Parametric Study:** To investigate the effect of interface parameters on the tensile response of the single straight tab interface, a parametric study is performed. The analytical model and the lattice model are used to assess the influence of interface strength and tab length on the tensile response of the connection.

1.6. Report Outline

The report is organized as follows:

1. **Introduction:** Introduces the project background, research problem, objectives, scope, and methodology, as well as the structure of the report.
2. **Literature Review:** Provides an overview of SHCC material properties and interface behavior in both profiled and non-profiled interfaces.
3. **Analytical Analysis:** Outlines a simplified analytical analysis to understanding mechanisms behind profiled interface behavior and provides a simplified analytical model and presents the analysis results and interpretations.
4. **Continuum Smeared Cracking Model:** Details the Abaqus-based smeared cracking model, including analysis results and interpretations.
5. **Lattice Model:** Explains the lattice model and presents the analysis results and interpretations.
6. **Discussion:** Compares the performance of the continuum smeared cracking model and the lattice discrete cracking model. Additionally a parametric study is performed using the anlaytical model and the lattice model on the influence of tab length and interface strength on the tensile response of the connection.
7. **Conclusions and Recommendations:** Summarizes findings and suggests directions for future research.

2

Literature review

In this literature review an introduction into the material properties of SHCC are given. Additionally the research performed on concrete-to-SHCC interfaces and on SHCC-to-SHCC interfaces is discussed.

2.1. Material and structural properties of SHCC

SHCC is not a conventional type of concrete, therefore in this section the basic material and structural properties of both materials will be discussed. First the general properties of SHCC will be discussed and then the fibre-cement interaction will be explained more thoroughly.

2.1.1. General properties

Over the past 50 years research has been conducted into the ability to create a concrete type which offers increased tensile ductility to overcome the brittle nature of concrete as a building material. Improving the tensile ductility of concrete will also improve the durability of reinforced concrete due to more dispersed and thus smaller crack formation. One of the materials which has been developed is Strain Hardening Cementitious Composites (SHCC). SHCC is named after their ability to resist increased tensile force after cracking over a long tensile deformation range [37]. The material forms multiple cracks with reduced crack width and spacing when subjected to tensile loads. To obtain this effect, only fine sand is used as aggregate material [12]. These narrow crack widths and spacings are induced by the crack-bridging effect of the fibres in the concrete. This principle is visualised in Figure 2.1, this principle is the same for synthetic fibres.

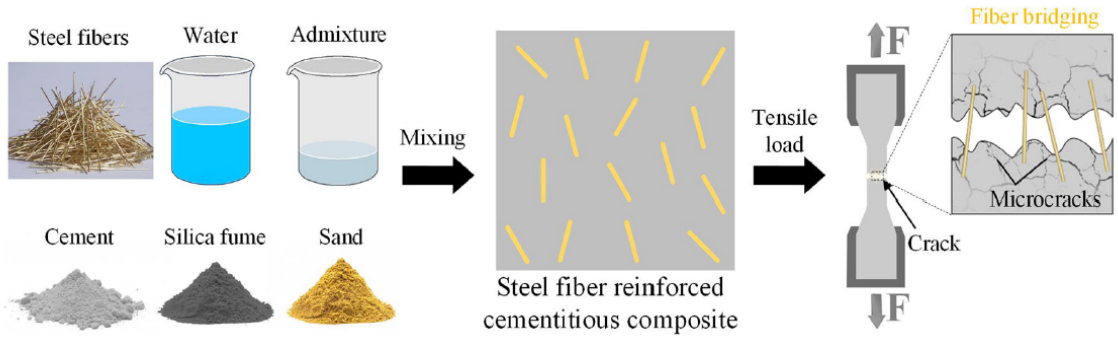

Figure 2.1: "Schematic diagram of the bridging effect of steel fiber at interface under tensile load. The stress transfers from cementitious matrix to steel fiber at interface, which retards the initiation and propagation of cracks in steel fibre reinforced cementitious composites." [36].

SHCC exhibit good crack width control over higher ranges of tensile deformation, this is due to the fact that in this material, the energy required to propagate the existing crack is higher than the required energy to create a new crack, this principle can be compared to the crack distributing effect

of conventional reinforcement, however, those cracks are bigger before a new crack is formed. This causes the existing cracks to have a more stabilised crack width at higher tensile loading, this is depicted in Figure 2.2. This figure shows the crack width development of polyvinyl alcohol fiber reinforced SHCC at the age of 28 days [31]. The crack width that was monitored was that of a single crack.

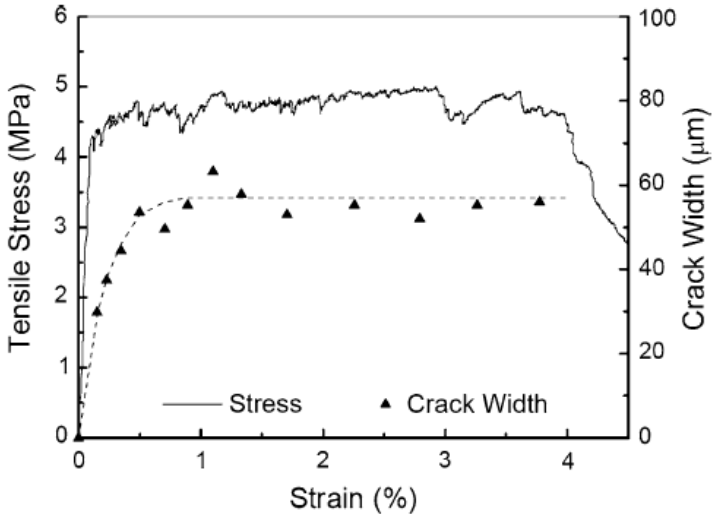

Figure 2.2: Direct tensile stress–strain response of SHCC showing that the crack width remains under 60 m until strain capacity is exhausted at 3.5%. [31].

The compressive strength and the tensile strength of SHCC are similar to that of normal strength concrete (NSC), however due to the properties of SHCC it has a 2-4 times as high resistance in flexure. The strain capacity of SHCC is where the material excels, there it has a 300-500 times higher tensile strain capacity than the typical tensile strain of 0.02% in NSC [22].

2.1.2. Fibre-cement interactions

In SHCC the fibres constitute a significant part of the material. In FRC a wide range of fibre types are used as reinforcement, such as steel, glass, carbon, kevlar, polypropylene, nylon or natural fibres, where polypropylene, nylon or natural fibres are so called low modulus fibres. It should be noted however that currently also synthetic fibres with high elasticity and high strength are developed.

For fibres to increase the strength of the composite material the fibres should have higher modulus of elasticity than the matrix itself. This is difficult to achieve with these low modulus fibres, however both theoretical and applied research shows that even concrete with low modulus fibres, considerable improvements can be obtained with respect to the strain capacity, toughness, impact resistance and crack control of the FRC composites [4]. The tensile or flexural strength is not increased with the use of these fibres, however, this is not always the objective of using fibres in a concrete mixture. The mechanical performance of a fibre reinforced cementitious composite is highly dependent on the interaction between the cementitious matrix and the fibre [36]. This interaction is based on three principles [4]:

1. physical and chemical adhesion (see Figure 2.3)
2. friction (see Figure 2.3)
3. mechanical anchorage (see Figure 2.4)

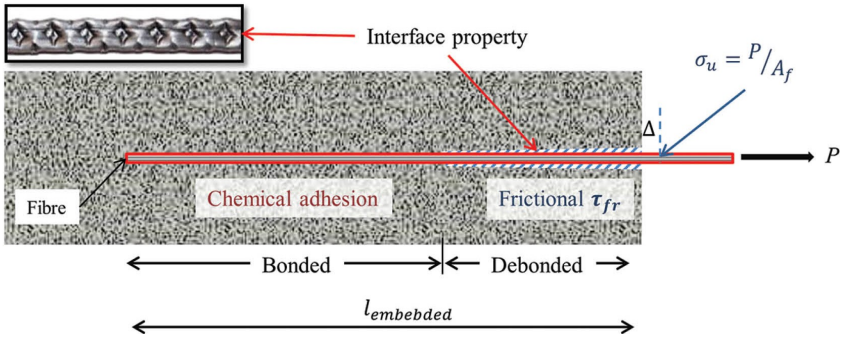

Figure 2.3: Fibre pull out mechanism [3]

The first two principles contribute little to the interaction of a fibre and the concrete mixture [4]. Only for fibres with a high surface area (very thin fibres in the range of diameter of 10 m) or in the case of advanced cementitious matrices with refined micro structure and very low porosity (water/binder ratio lower than 0.3) do these two principles contribute significantly to the interaction between the fibre and the concrete matrix [4].

In conventional concrete (water/binder ratio is 0.4 or higher) and fibres with a diameter in the range of 0.1 mm or bigger, then mechanical anchorage is needed for the interaction between the fibre and the concrete matrix [4]. Using corrugated or hooked fibres can increase the performance of the interface interaction. When Yoo and Kim examined the performance of hooked steel fibres compared with straight steel fibres it was found that the average bond for hooked fibres was approximately 4 times higher than the bond strength of straight fibres [35]. The pullout behavior and the mechanical anchorage of a steel fibre with different shapes is shown in Figure 2.4. It should be noted that fibres with geometrical deformations do induce a negative effect on the workability of the concrete mixture.

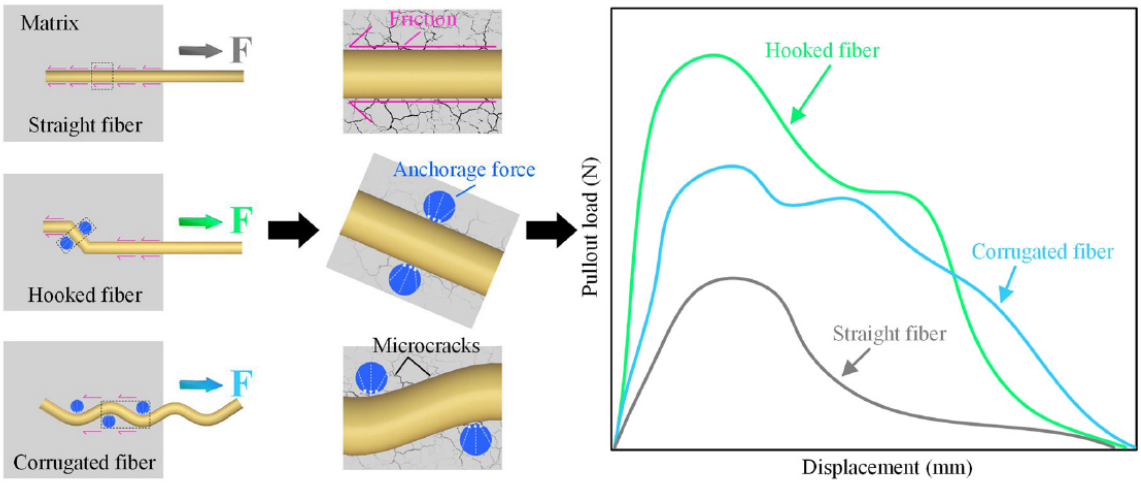

Figure 2.4: "Pullout behavior of steel fiber with various shapes from SFRCC matrix. For the straight steel fiber, the friction at interface is the main resistance from fiber pullout. For the hooked and corrugated steel fiber, the anchorage force at interface plays a critical role to resist fiber pullout." [36]

To determine the performance of a single fibre in a cement matrix the single fibre pull-out test is performed. This pull-out behavior can be divided in three stages, partial debonding (OA), complete debonding (AB) and interfacial debonding (BC) [5]. The last stage defines the nature of the frictional interface and is called the pull-out stage. Three main regimes which can occur are slip-softening, constant friction or slip-hardening [5]. This single fibre pull-out test with it's different stages and regimes is presented in Figure 2.5.

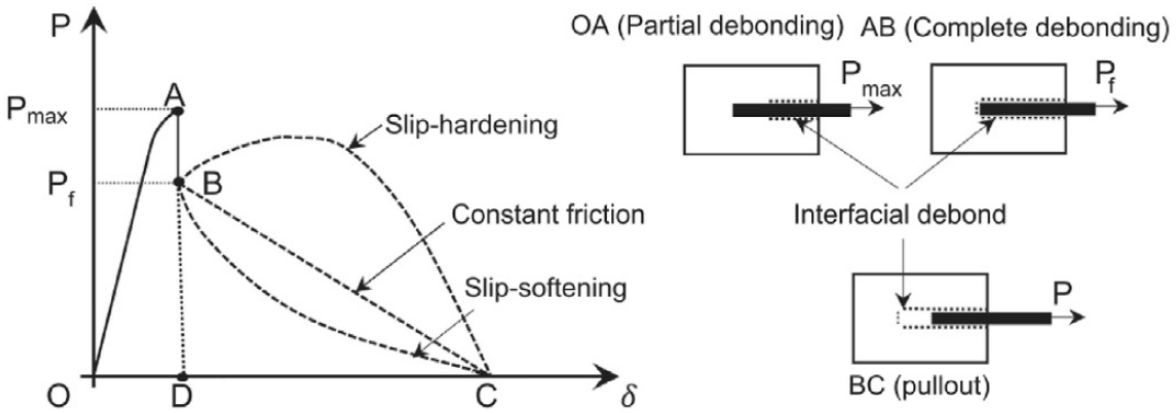

Figure 2.5: "Typical single fibre pull-out curve and pull-out mechanisms." [5]

2.2. Interface properties of a concrete-to-concrete and concrete-to-SHCC interface

In this section the interface characteristics of a concrete-to-concrete and concrete-to-SHCC interface are discussed. First the micro-structural characteristics are presented and thereafter the structural behavior of the interfaces are discussed.

2.2.1. Microstructural characteristics

A concrete-to-concrete interface is formed when fresh concrete is cast against an old concrete surface. These types of interfaces are present in construction, for example: between two different concrete elements, concrete overlays used for repair and strengthening of concrete members or composite members which consist partly of prefabricated concrete elements [18]. The interface between the new and the old concrete displays similar characteristics to that of an interface between an aggregate particle and cement paste, the interfacial transition zone (ITZ). These similar characteristics are attributed to the so called wall-effect, where small aggregate particles have a difficulty of packing closer to the surface of large particles. This similar effect is present in the interfacial zone between two concrete layers where small particles have a difficulty packing close to the interface.

Xie, Li, and Xiong [33] proposed a micro-structure model of the interfacial zone in a concrete-to-concrete interface . This model is shown in Figure 2.6. The first layer of this model is located at the surface of the old concrete and is called the penetration layer. The new concrete penetrates inside this layer and causes the layer to consist of mainly C-S-H and some amount of Aft (ettringite) or $CA(OH)_2$ (portlandite). This layer has no negative influence on the strength of the interface. The second layer of the interface is called the strongly-affected layer and is located at the boundary between the new concrete and old concrete. In this layer the predominant product phases are $CA(OH)_2$ and needle shaped Aft crystals. The layer is porous, contains large numbers of cracks and voids and is generally the weakest layer at the interface which determines the interfacial performance. The last layer is the third layer which is also called the weakly-affected layer. This layer is located inside of the new concrete and has a similar microstructure as the new concrete but contains less C-S-H. It's strength is better than that of the strongly-affected layer and it's thickness depends on the nature of the new concrete and the bonding agent.

The bonding mechanism of a concrete-to-SHCC interface is similar to that of a concrete-to-concrete interface [25]. Due to the fact that SHCC is more fluid and compact, the SHCC can fill pores and microcracks within the surface of the old concrete. This causes the interface structure of a concrete-to-SHCC interface to be more compact [25].

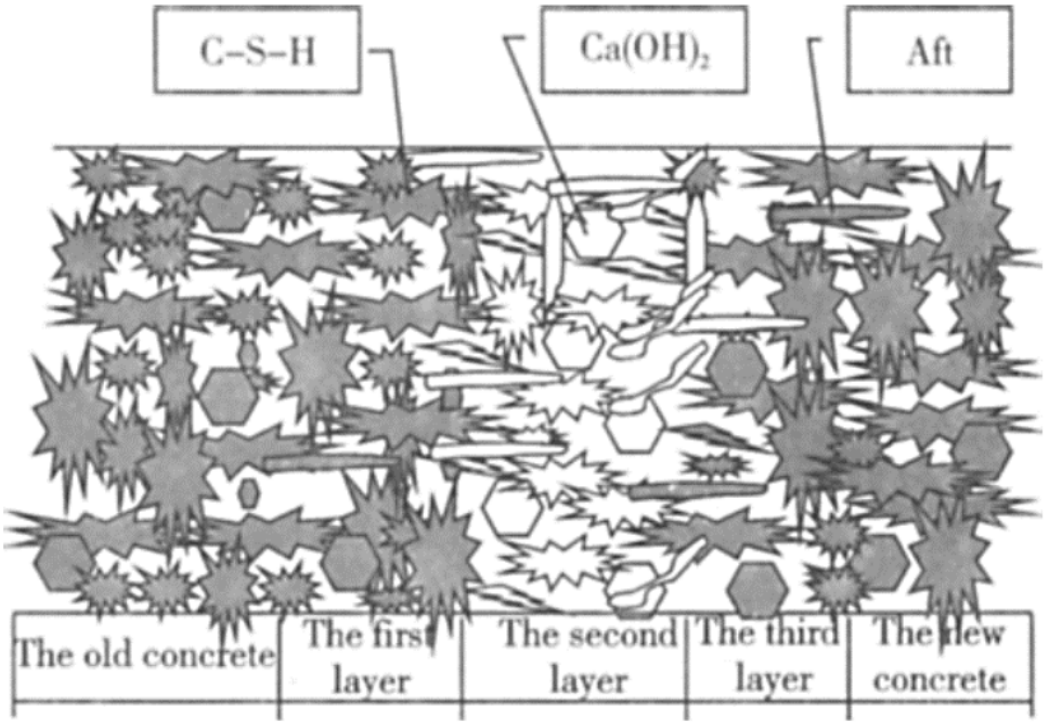

Figure 2.6: Micro-structure model of the interfacial zone in a concrete-to-concrete interface [33].

2.2.2. Mechanical behavior

The mechanical behavior of a concrete-to-concrete interface is defined by the adhesion force within the interface [18]. This adhesion force is defined by three types of bond between the old and the new substrate: a chemical bond which develops due to chemical reactions between the old and the new concrete, a mechanical bond which relates to mechanical interlocking due to the penetration of the new concrete inside of the roughness and porosity of the old concrete. and a physical bond associated with the Van der Waals and surface tension forces [18].

These bonding mechanisms are affected by the properties of the new and the old concrete, the surface properties (moisture content and roughness) of the interface and environmental conditions. Surface roughness is considered to be the major factor that contributes to bond strength [18].

Research has been performed on the effect of surface roughness or profiling on the interface behavior of concrete-to-concrete interfaces and of concrete-to-SHCC interfaces.

Numerical research has been performed by Luković et al. [15] to determine the effect of different types of surface roughness profiles on the behavior of a concrete-to-concrete interface. Four types of surface profiles for groove roughened surfaces have been used (see Figure 2.7a). These specimen have then been modelled in direct tension and the stress-displacement diagrams for these interfaces are shown in Figure 2.7b. It is noted that by increasing the depth of the groove, the ductility in a direct tension configuration is increased and that more energy is needed to break the interface [15].

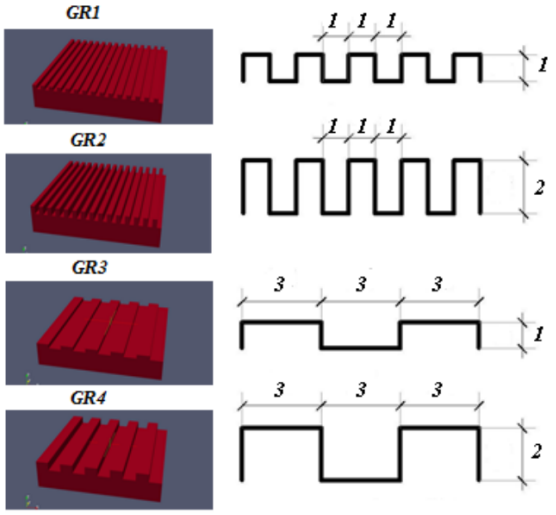

(a) Varied surface profiles for groove roughened surfaces [mm] [15].

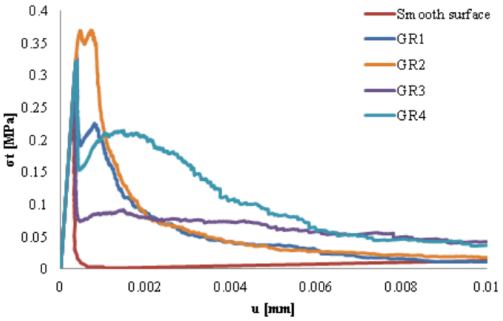

(b) Stress-displacement curve for varied roughness parameters [15].

Figure 2.7: Surface profiles and their stress-displacement curve for direct tension in a numerical model [15].

Wagner [29] performed experimental research to determine the effect of surface roughness on the behavior of a concrete-to-SHCC interface. The results from wedge splitting tests performed by Wagner are presented in Figure 2.8. It was shown that when a certain roughness threshold was not reached, the interfacial behavior was only attributed to bond failure. Whereas when this roughness threshold was reached, failure inside of the material itself may occur which leads to a more ductile behavior of the interface. In his research Wagner found that this roughness threshold lies around 0.29mm. From a certain roughness value the strength of the material determines the cracking within the interface and increasing the roughness further won't lead to further improvement of the interface behavior [29].

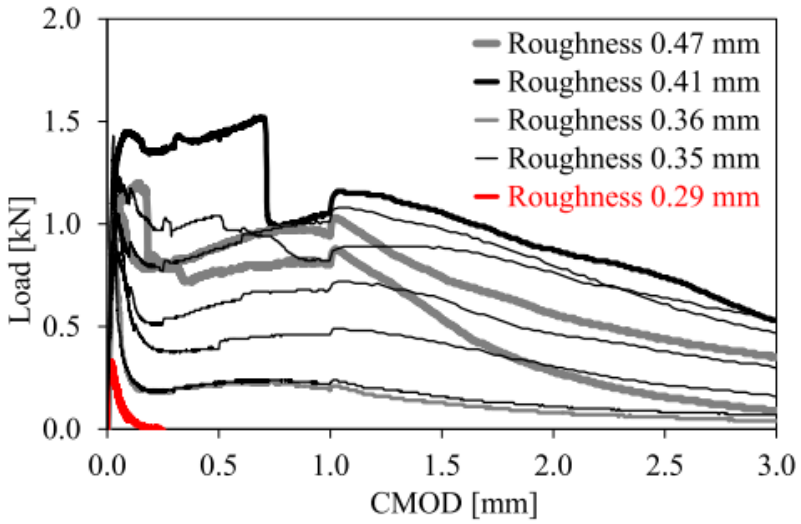

Figure 2.8: Load-displacement curves for the wedge splitting tests with a ligament length of 90 mm. [29].

Stander conducted an experimental investigation on the interface behavior of a concrete-to-SHCC interface employing various surface profiling techniques, as depicted in Figure 2.9. In addition to examining different profiling methods, Stander explored two distinct moistening approaches in accordance with the South African national standard. One method involved submerging the 'old' concrete in a

curing tank for 24 hours, followed by a drying period of 30-45 minutes before overlay casting [28]. Alternatively, the second method entailed air-drying the specimens for 24 hours, followed by a ten-minute moistening period and subsequent drying with a damp cloth before overlay casting [28].
Both of the curing methods have the goal to optimize the degree of saturation of the old concrete before casting the overlay.

The different roughening techniques used during this study were as follows [28]:

- Reference surface: mechanically untouched surface which means that the surface is as cast against the mould.
- Scrape surface: the surface is scraped with a sharp edged scraping plate to remove the weaker outer layer. This method only aimed at improving the chemical bond.
- Sandblast surface: roughening of the surface with sandblasting to improve chemical adhesion and to create mechanical interlocking on a meso-scale.
- Drill holes: drilling holes in the surface with a depth off about 5mm to increase the mechanical bond due to dowel effects.
- Precast grooves: precast grooves cannot be used for retrofitting but for new construction methods. Grooves are applied in the first element and fresh concrete is applied on top of the grooves.

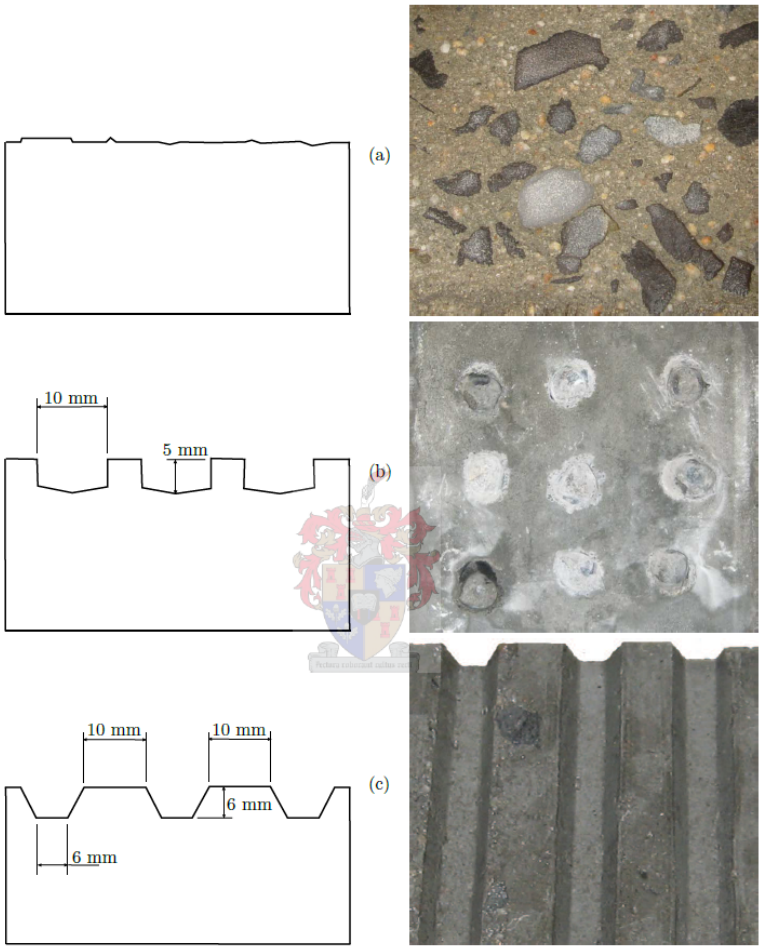

Figure 2.9: Illustrations of (a) sandblast, (b) drill holes and (c) groove roughened surfaces [28].

The results from the experimental program are summarized in Figure 2.10, where the specimen names are build up as: roughening technique - age (days) - moistening period (10 minutes or 24

hours). From the results it can be seen that the fracture energy is highest for sand blasted surfaces or surfaces with drill holes. For the interfaces with a sand blasted surface, secondary resistance is present after the initial fracture occurs [28]. This post-peak behavior is attributed to the fibres bridging a newly defined interface. Figure 2.11a shows the fibres bridging the newly defined interface. As can be seen from Figure 2.11b the fracture occurred in the SHCC material and not on the original interface. This is the same mechanism as described by Wagner [29].

SSPT	$f_{t,i}$ [MPa]	COV [%]	G_f^I [N/mm]
SB724	0.43	6.9	0.052
R1410	0.1	-	0.0065
S1410	0.6	13.2	0.11
S1424	0.625	2.2	0.06
SB1410	0.798	22.5	0.662
SB1424	0.835	16.1	0.46
DH1424	0.664	10.1	0.624
PG1424	0.71	29.0	0.079
R2810	0.087	0.21	0.077
R2824	-	-	-
SB2810	> 1.1	-	-
SB2824	> 0.919	-	-

Figure 2.10: Tensile parameter values obtained from experiments performed on the various surface profiling methods [28].

(a) Interfacial tensile test of a sandblasted specimen showing bridging fibres [28].

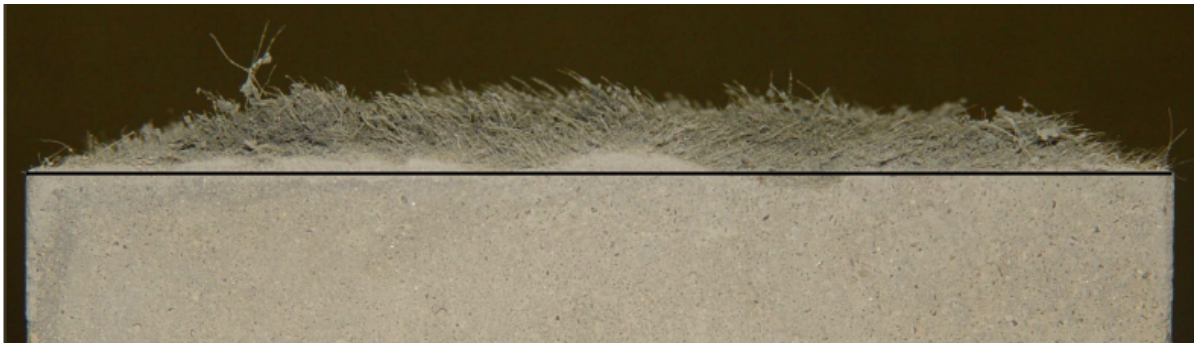

(b) The concrete part of a sandblasted interfacial tensile test, showing SHCC material on its fracture surface [28].

(c) Post-fractured surfaces for a sandblasted tensile specimen, showing SHCC on the left and concrete on the right [28].

Figure 2.11: Failure mechanism of a sandblasted tensile specimen, shwoing failure within the SHCC material [28].

2.3. SHCC-to-SHCC interface with a single straigth tab

In a recent experimental study performed at TU Delft, Papoulidou investigated the interface between two parts of SHCC. Drawing inspiration from nature, she explored the effect of geometrical enhancements on the tensile performance of the interface. Her research focused on an interface with a single tab (suture). For the tab two types of geometrical designs were used, both modeled after natural sutured interfaces (see Figure 1.2) [21]. The first design was a straight tab with varying width-to-height ratios. The second design, known as the bi-stable interlocking suture, was based on existing literature (see Figure 2.12).

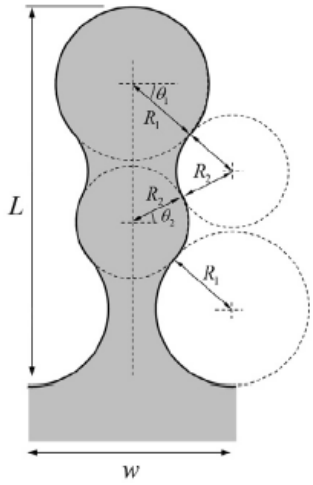

Figure 2.12: ”Shape of a bistable interlock tab. The profile of the tab consists of arcs of circles of radii R1 and R2 which blend according to angle θ1. Angle θ2 is dependent on R1, R2 and θ1.” [17]

Due to the fact that in this research the focus lies on the straight tab interface behavior, the results from[21] on the single straight tab interfaces are further discussed.

In her research, Papoulidou examined the interface conditions and geometrical shapes of the tabs. For the straight tabs, width-to-height ratios of 1.5, 1.0, and 0.5 were analyzed (see Figure 2.13). Two different interface treatments were employed: casting the elements against each other as is and casting the elements with the surface of the already hardened part lubricated to reduce the chemical bond formed at the interface.

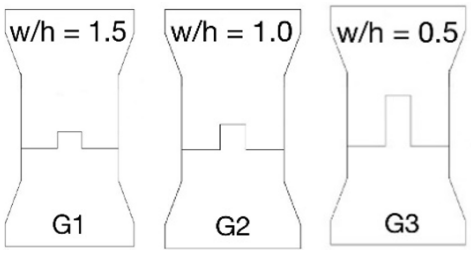

Figure 2.13: The three single straight tab interface specimen with width-to-height ratios of 1.5, 1.0 and 0.5 [21]

In this experimental research, three different types of failures can be identified. Each failure mechanism shows a different interplay between interface and SHCC material failure.

The first type of failure mechanism shows full interface failure with very limited SHCC material cracking. this failure mechanism was observed in the case of a lubricated specimen with a tab featuring a width-to-height ratio of 1.5, indicating that the tab's height is two-thirds of its width. The lubrication significantly reduced the interface strength by diminishing the chemical bonding, leading to premature failure at the interface.

The interface failure is particularly pronounced due to the minimal mechanical interaction within the SHCC material itself. As shown in Figure 2.14, the post-test specimen and the DIC images captured during the test clearly illustrate the process of interface failure. The corresponding force-displacement diagram highlights the low load-bearing capacity of this configuration. After the initial failure of the interface, most of the specimen's remaining load-bearing capacity is due to friction, resulting in relatively large displacements but at very low strength levels.

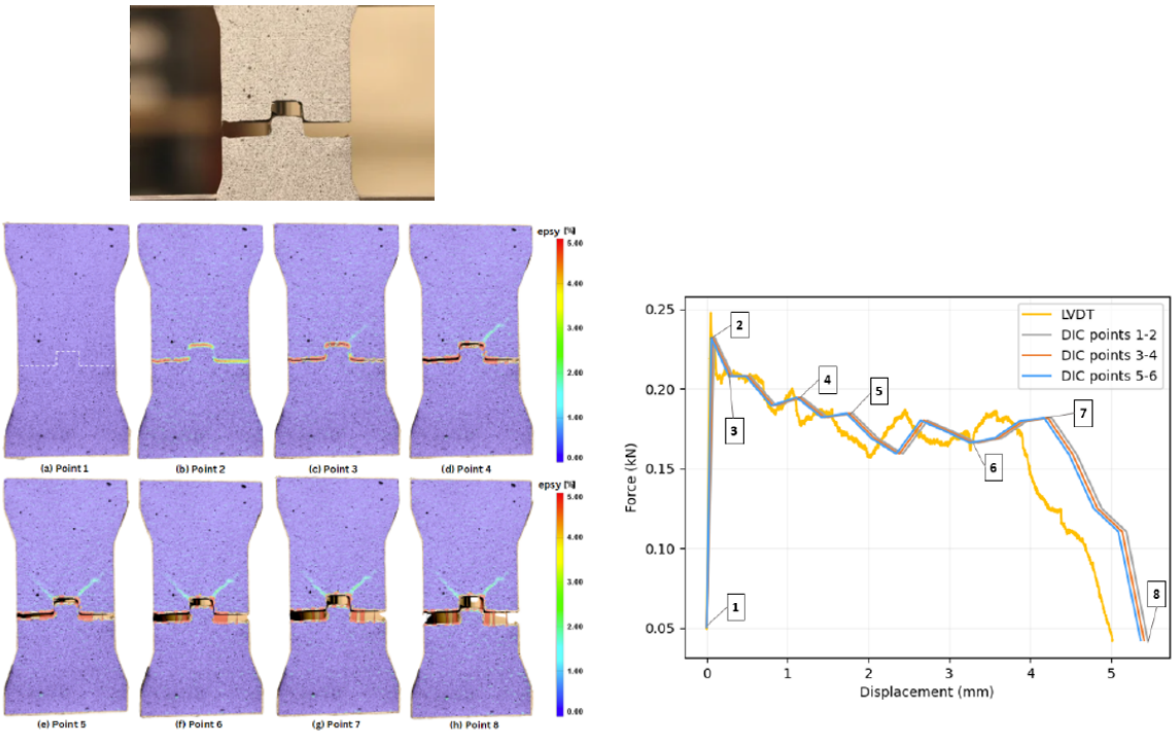

Figure 2.14: Delamination failure mechanism as was presented in the SLG12 specimen; width-over-height ratio of 1.5 and lubricated interface [21].

The second type of failure that is observed shows an interplay between interface failure and SHCC material failure. In this failure mechanism there is significant cracking inside the SHCC material inside the tab and in the material surrounding the tab but the governing failure crack going through only the interface.

This failure mode was observed in a cast-as-is specimen with a tab having a width-to-height ratio of 1.5, meaning that the tab's height is two-thirds of its width. The material in and surrounding the tab undergoes extensive cracking as the interface weakens, with visible fractures forming before the tab is fully pulled out.

In Figure 2.15, the progression of cracking in the tab and its surrounding material is evident. Additionally, the force-displacement diagram is presented, which clearly shows a higher load-bearing capacity compared to the previous failure mechanism. This increased capacity reflects the material's ability to sustain damage before failure, as opposed to the more weak and friction dominated failure observed in the previously shown failure mechanism. By the end of the analysis, the tab has detached from the surrounding material while remaining attached to the bottom part, confirming that the governing failure crack goes through only the interface.

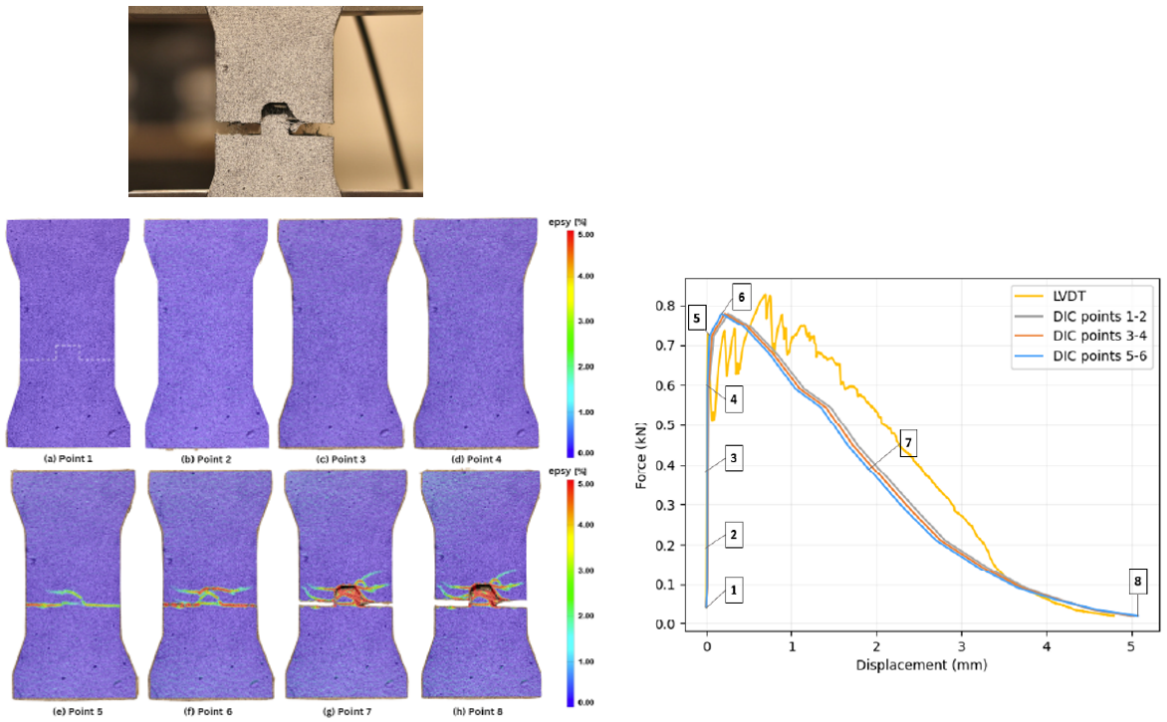

Figure 2.15: Pull-out failure mechanism as was presented in the SCG12 specimen; width-over-height ratio of 1.5 and cast-as-is interface [21].

The third failure mechanism observed in the experimental study is again an interplay between interface failure and material failure. However, in this failure mechanism the governing failure crack goes through both the interface and the SHCC material. It is observed that in this failure, extensive cracking within the material inside and surrounding the tab is present. Unlike the previous failure modes, here the interfaces along the tab can sustain greater forces than the tab itself, leading to failure of the SHCC material within the tab. The stress concentrations at the bottom of the tab, caused by sharp geometrical changes at the corners, play a critical role in this process, ultimately leading to the formation of a governing failure crack through the bottom horizontal interfaces and through the SHCC material at the bottom of the tab.

In this failure mode, the load-bearing capacity is governed by the strength of the SHCC material inside the tab, resulting in a higher capacity compared to the failure mechanisms where the governing failure crack goes through only the interface. This is because the tab material, rather than the interface, is the limiting factor. The increased load-bearing capacity makes this mechanism more resistant to failure, though it still eventually leads to separation.

In Figure 2.16, this mechanism is visually represented, including the post-test specimen and the corresponding force-displacement curve. The specimen shows that the tab has detached from the bottom part but remains attached to the top part through the interface.

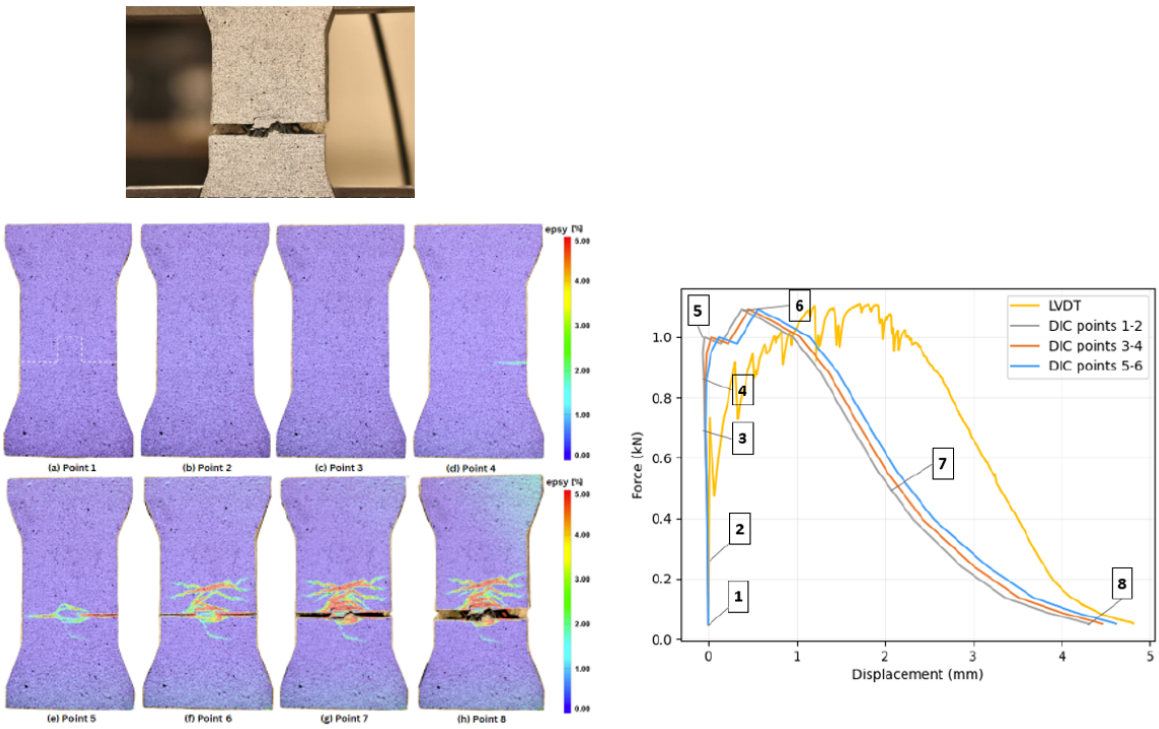

Figure 2.16: Tab failure mechanism as was presented in the SCG22 specimen; width-over-height ratio of 1.0 and cast-as-is interface [21].

3

Analytical analysis

As presented in chapter 2, the research on the interface behavior between two parts of SHCC is relatively limited. Some investigations have been conducted by Wagner and Stander on the interface behavior of concrete-to-SHCC interfaces. Additionally, a recent study by Papoulidou examined the behavior of geometrically enhanced SHCC-to-SHCC interfaces. These studies suggest that geometrically enhancing the interfaces between two SHCC parts can be very promising. Figure 3.1 illustrates the tensile behavior of a smooth concrete-to-SHCC interface, an interface with a 10.8mm high tab, and SHCC itself. The graph shows the superior performance of the connection with an interface with the tab compared to the smooth interface, which exhibits highly brittle behavior.

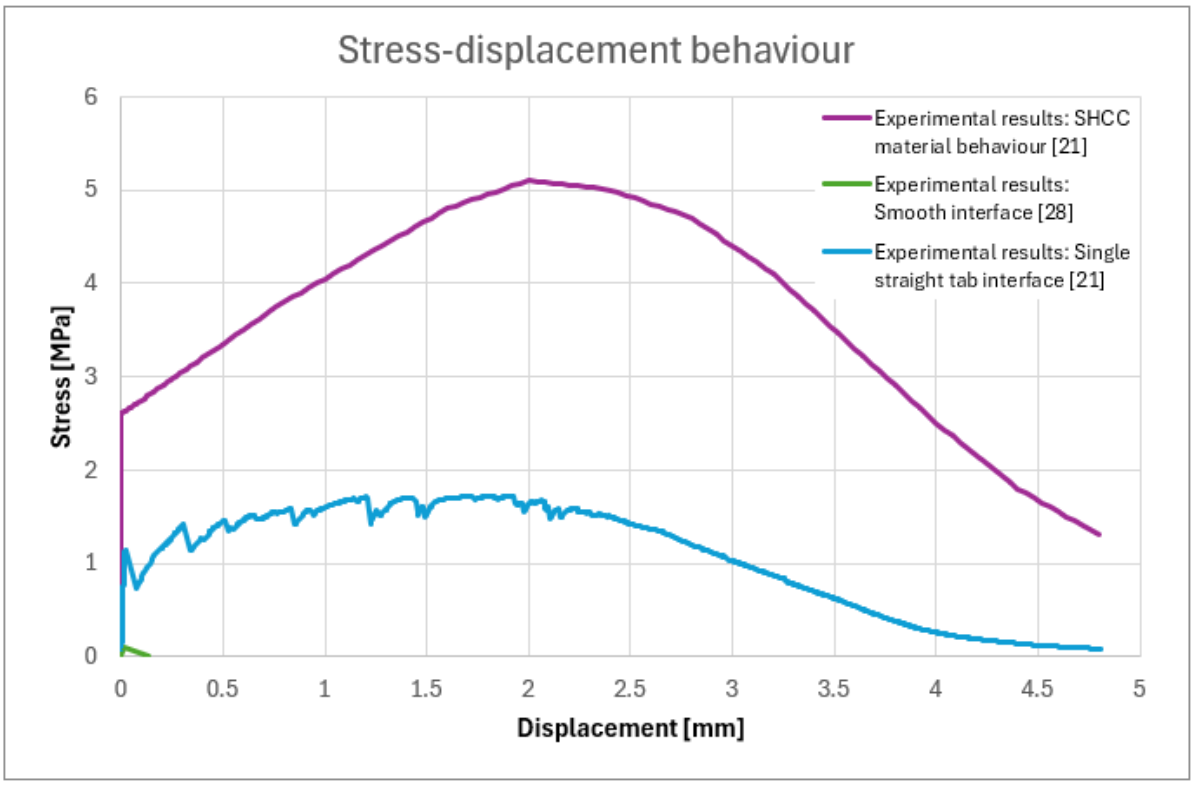

Figure 3.1: Tensile behavior of SHCC [21], a smooth concrete-to-SHCC interface [28] and an SHCC-to-SHCC interface with a single straight tab [21].

The current research aims to investigate the interface behavior of a geometrically enhanced interface using numerical analyses. To be able to understand the interface behavior and therefore the

numerical models, it is important to perform an analytical analysis of the interface behavior on a qualitative and quantative level. In this analytical analysis a simple interface scenario is chosen of a single tab interface in a similar configuration as experimentally investigated by Papoulidou [21].

The basic shape on which the analytical analysis will be base is presented in Figure 3.2. The analysis is performed in 3D where the width of the tab is defined as Ac, the height as Av and the thickness of the specimen is set at 15mm. On the sides of the tab the horizontal surface is defined as As, which is larger than Ac. First a qualitative analysis of the different mechanisms at play is performed after which a simplified quantitative analysis is performed.

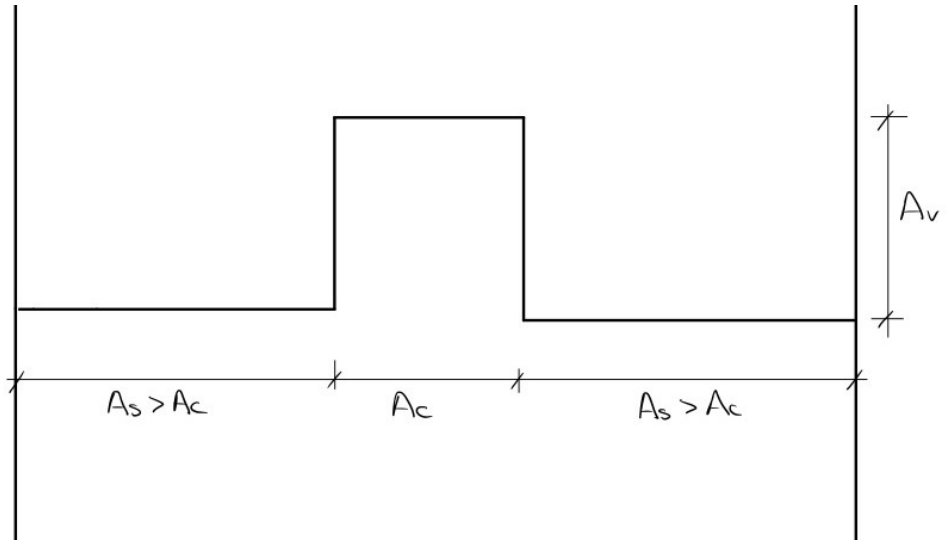

Figure 3.2: Shape of the basic interface for analytical analysis, with thickness 15mm.

3.1. Qualitative analysis

In this section the qualitative analytical analysis is performed. When a tensile force is applied to the interface this is taken up by stresses which are transferred through the interfaces (see Figure 3.3).

The force develops due to the interface between the new and the old concrete. The force develops within the specimen due to two acting stresses, the interface stress in the horizontal part of the interface (red) and the stresses which are transferred in the vertical part of the tab (green). In case this vertical interface is perfectly straight, pure shear stresses are transferred through this interface. However, if due to manufacturing imperfections this vertical interface is not perfectly straight but slightly inclined this interface can also transfer tensile or compressive stresses. These three scenarios are sketched in Figure 3.4.

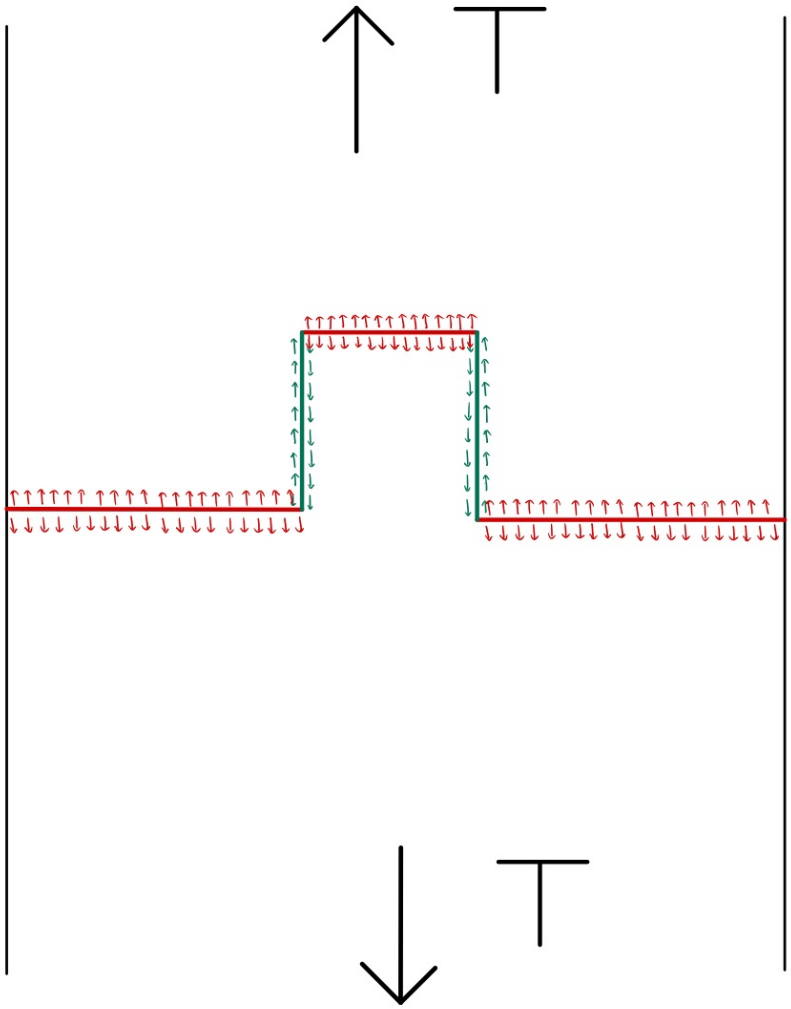

Figure 3.3: Tensile force T is transferred through the interface.

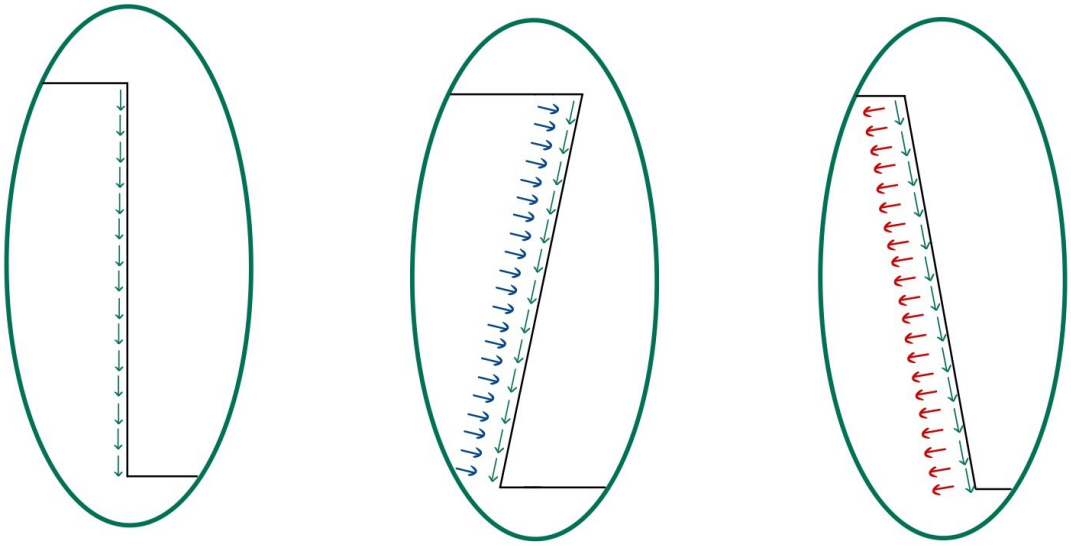

Figure 3.4: Stresses acting on the vertical part of the tab.

Assuming a perfectly vertical interface without any fabrication imperfection it can be said that when a tensile force is applied to the interface, several mechanisms are at play:

1. Traction-separation and shear-sliding relationship of the interface is not the same.
2. Distribution of shear stress in the vertical surface is not uniform
3. Stress concentrations occur around sharp corners.
4. Shear resistance of the vertical interface is build up out of cohesion and friction.
5. Fibres are crossing the interface and contribute to ductility.

   In this study, ”interface” specifically refers to the fracture surface along the interface. The influence of various mechanisms occurring at the fracture surface on the overall interface behavior is further detailed in this section.

Traction-separation and shear-sliding relationship of the interface is not the same.

From literature [28] it is found that the traction-separation behavior of an SHCC-to-concrete interface is much lower than the shear-sliding behavior of an SHCC-to-concrete interface. This is graphically sketched in Figure 3.5. From this sketch it is clear that the separation at maximum traction () is much lower than the sliding at maximum shear (). Same goes for the ultimate separation () and ultimate sliding (). For the interface this means that if the horizontal interface has reached it’s maximum peak stress and starts to damage with further separation, at the same value for the sliding the shear interface strength still increases.

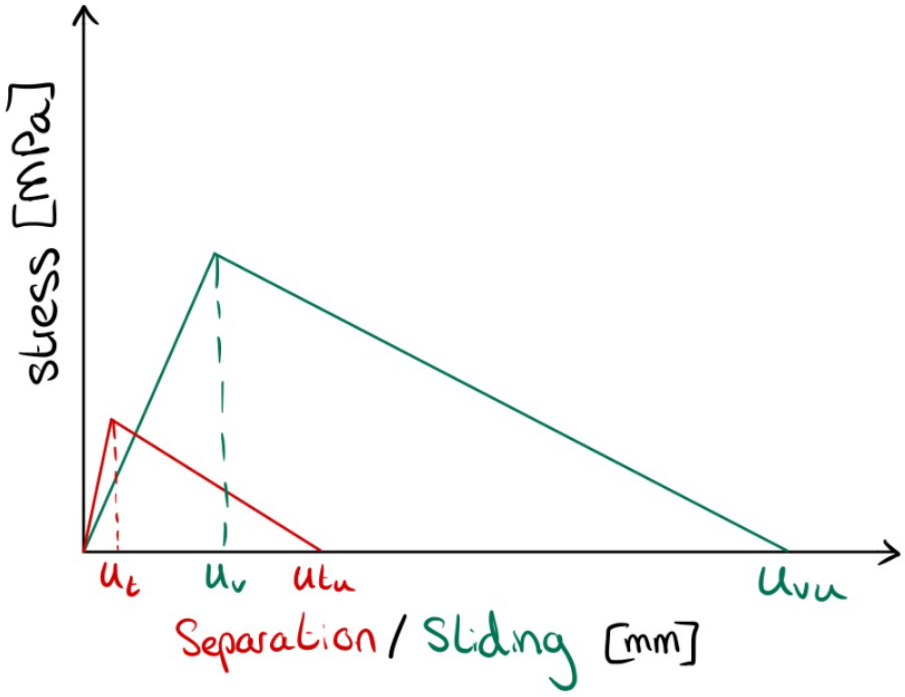

Figure 3.5: Graphical representation of the traction-separation (red) and shear-sliding (green) law of a concrete-to-concrete like interface.

Distribution of shear stress in the vertical surface is not uniform.

It can be theorized that the separation at the two bottom horizontal surfaces would be larger than at the top horizontal surface. This is due to the stiffer concrete on either side of the tab compared to the material inside the tab itself. The greater stiffness of the surrounding concrete causes the bottom horizontal surface to bear more stress than the top horizontal surface. As a result, the bottom interface undergoes more separation than the top, leading to greater displacement and sliding at the base of the vertical interface.

The increased sliding at the bottom of the tab causes the vertical interface to experience higher stresses in its lower section compared to the upper section. This uneven stress distribution leads to non-uniform shear stress along the vertical interface, with the bottom part carrying a larger portion of the load. As a result, damage is likely to initiate earlier at the bottom of the vertical interface, where the combination of higher shear stresses and increased sliding makes it more susceptible to failure.

While the top part of the interface also experiences separation and sliding, the stress levels are lower, causing damage to occur more slowly than at the bottom. However, it is important to note that damage will still progress at the top over time, though at a reduced rate. The central portion of the vertical interface, particularly toward the upper section, will remain undamaged for the longest period. This is because the stresses in this region are significantly smaller than those at the bottom, resulting in a more gradual accumulation of damage. Consequently, the middle portion, slightly closer to the top, experiences the least stress and is the last part of the vertical interface to be affected by the overall failure mechanism.

Stress concentrations occur around sharp corners.

Stress concentrations often arise from abrupt changes in a component's geometry, and in this case, they are predominantly located at the sharp corners of the tab in the interface. These corners are critical points where stress tends to concentrate within the SHCC material.

At these four corners, the nature of the geometry contributes to stress concentrations that are more

pronounced than in other areas of the material. It is anticipated that if material damage occurs, it will likely initiate in two primary locations: either in the surrounding material adjacent to the top corners or within the tab at the bottom corners.

Shear resistance of the vertical interface is build up out of cohesion and friction.

The shear behavior of the vertical interface plays a critical role in determining both its load-bearing capacity and deformation response, driven by a combination of cohesive and frictional mechanisms. Initially, when no compressive force is applied, the shear resistance of the interface relies solely on its cohesive properties, as illustrated in green in Figure 3.6. Under these conditions, the interface behaves in a linear elastic manner, with its shear capacity limited to what cohesion alone can support.

When a compressive force acts on the sliding surface, however, the resistance to shear increases significantly. This compressive force enhances the interface's stiffness and raises the maximum stress it can sustain within the elastic range. During this phase, while the interface remains cohesive, there is no true frictional sliding because no separate surfaces exist to slide against one another. Instead, the system's "sliding" behavior remains an elastic response, with the compressive force further reinforcing the interface's strength.

As the interface progresses beyond the linear elastic phase into a damage phase, cohesive properties start to degrade, eventually leading to the formation of distinct sliding surfaces. At this point, friction becomes active, contributing to the interface's overall shear resistance by supplementing the diminishing cohesive shear capacity. This frictional resistance continues to counter additional displacement as the interface deteriorates further, providing a secondary mechanism to resist sliding even as cohesive bonds weaken (see Figure 3.6).

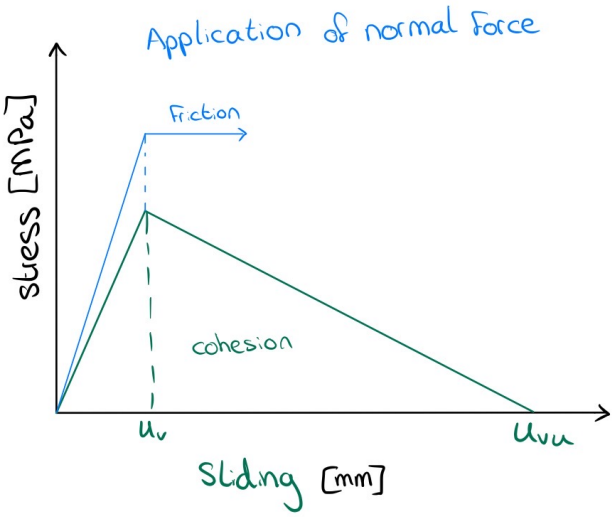

Figure 3.6: Graphical representation of the point from which friction is initiated in the shear-sliding law of the interface and of how the shear strength may increase due to an application of a compressive normal force.

Fibres are crossing the interface and contribute to ductility.

SHCC consists of mortar and polyethylene (PE) fibers, with the fibers contributing to its ductile properties. At the interface between two SHCC parts, these fibers play a crucial role in determining the failure mechanism. As stated before, in this study, "interface" specifically refers to the fracture surface along the interface.

From literature research conducted by Papoulidou [21], it has been observed that in designs featuring a single tab in the interface, a pull-out failure mechanism often results in fibers bridging the cracks along the interfaces.

The fiber bridging occurs due to the reduced material properties of the SHCC near the interface, a reduction which is attributed to the wall-effect caused by the 'old' SHCC. This wall-effect influences the alignment and distribution of fibers close to the interface, while an Interfacial Transition Zone (ITZ) forms at the boundary between the two SHCC layers.

It is important to note that whether fibers bridge cracks or not is highly dependent on the microstructure at the interface. For example, if the surface of the first-cast part is more porous, the second-cast layer can interlock more effectively with the existing SHCC, increasing the likelihood of the interface failing within the weaker SHCC material, leading to fiber bridging. However, if this surface has a very dense structure the second-cast layer cannot interlock as effectively and the likelihood of the interface failing within the weaker SHCC material is reduced. This micro structural variability can significantly influence the crack behavior and the overall performance of the interface.

3.2. Quantitative analysis

In this section the quantitative analytical analysis is performed.

The failure of a geometrically profiled SHCC-to-SHCC interface connection is influenced by a combination of interface failure and SHCC material failure. At one extreme, the interface can fail entirely without any cracking in the SHCC material, a scenario referred to as the **delamination failure mechanism** in this report. At the other extreme, the SHCC material can fail completely, behaving as though the interface were absent, which is defined as the **material failure mechanism**. Between these two extremes, a range of intermediate mechanisms emerges, reflecting varying interactions between interface damage and SHCC material cracking.

These intermediate failure mechanisms arise from the combined effects of interface and SHCC material failure, each contributing to the formation and propagation of the governing failure crack. In some cases, the failure crack is confined to the interface, while cracking in the SHCC material within and around the tab also occurs, characterizing a **pull-out failure mechanism** as defined in this report. In other cases, the failure crack propagates through both the interface and the SHCC material, forming what is referred to as a **tab failure mechanism**. This involves significant cracking within the SHCC material, particularly at the horizontal interfaces and the material beneath the tab.

At higher levels of interaction, the SHCC material across the entire specimen begins to crack, but the governing failure crack continues to involve both the interface and the material. This is defined as a **transitional failure mechanism**, which depends on the stress concentrations within the specimen, with the failure crack potentially forming at either the top or bottom interfaces. These various failure modes illustrate the complexity of the interplay between interface strength and SHCC material properties in determining the overall response of the connection.

For all of these five failure mechanisms, a sketch of their behavior is presented in Figure 3.7, where red indicates a damage in the interface and green indicates cracking in the SHCC material.

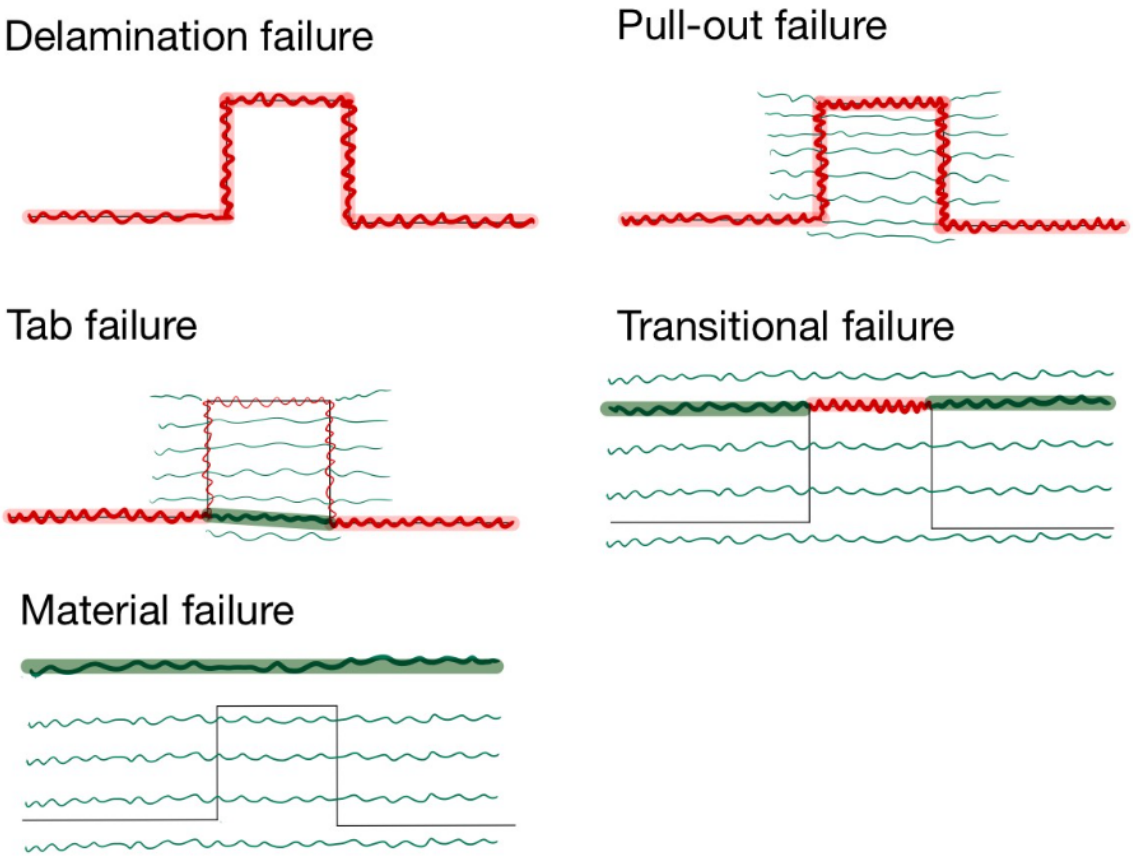

Figure 3.7: Graphical representation of the different failure mechanisms, where red represents cracking along the interface and green represents cracking in the material

An analytical analysis will be conducted for four of the five identified failure mechanisms to estimate the interface strengths required to activate different interface behaviors. The fifth failure mechanism, side failure, will be excluded from this analysis because stress concentrations cannot be accounted for, making it impossible to distinguish between the side failure mechanism and the material failure mechanism.

For each of the other four failure mechanisms a simplified calculation has been made to estimate their force-displacement response and required interface strength. Some model assumptions have been made to simplify these calculations;

- The material is homogeneous throughout the entire specimen;
- The interface properties are homogeneous throughout the entire interface;
- No stress concentrations are taken into account;
- The separation in the horizontal interfaces is equal to the slip in the vertical interface;
- The total displacement is a combination of separation (or slip) and cracking in the SHCC material;
- The stress inside the tab is constant over the height;
- No compressive normal force acts on the vertical interfaces, meaning there is no frictional interaction between the surfaces;
- Only the tensile and shear strengths of the interfaces can be modified. The tensile stiffness will remain unchanged as well as the maximum separation value of the traction-separation law. Also

for the shear interface behavior the stiffness will be kept constant as well as the maximum sliding (1.0 mm).

- The material properties of the SHCC material remain unchanged throughout the analyses.
- In case of a material failure mechanism, the specimen height is assumed to be 45 mm.

For each of the failure mechanisms the designs of the single straight tab interfaces from [21] are used for a width-over-height ratio of 1.5, 1.0 and 0.5 are used (see Figure 3.8).

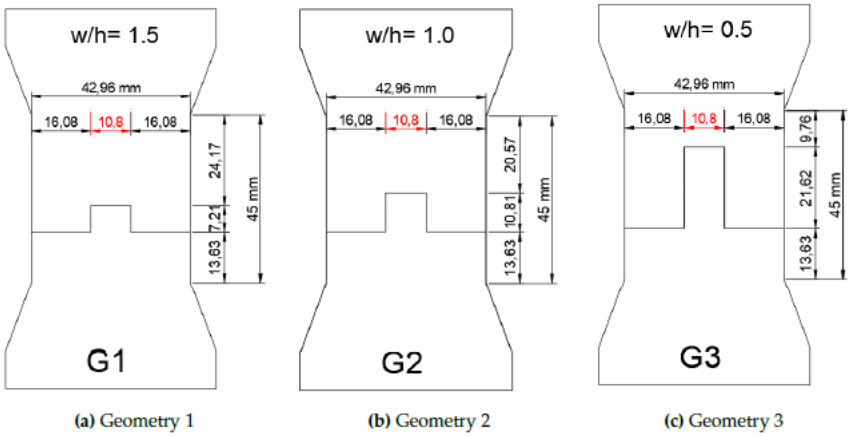

(a) Geometry 1 (b) Geometry 2 (c) Geometry 3

Figure 3.8: Design of the single straight tab specimen with a width-over-height ratio of 1.5, 1.0 and 0.5 and a thickness of 15mm [21].

To establish a basis for the traction-separation and shear-sliding laws, the experimental results from [28] are used. In Figure 3.9 the traction-separation and shear-sliding laws used for this analytical analysis are presented alongside the experimental results of the direct tension test and shear tests from [28].

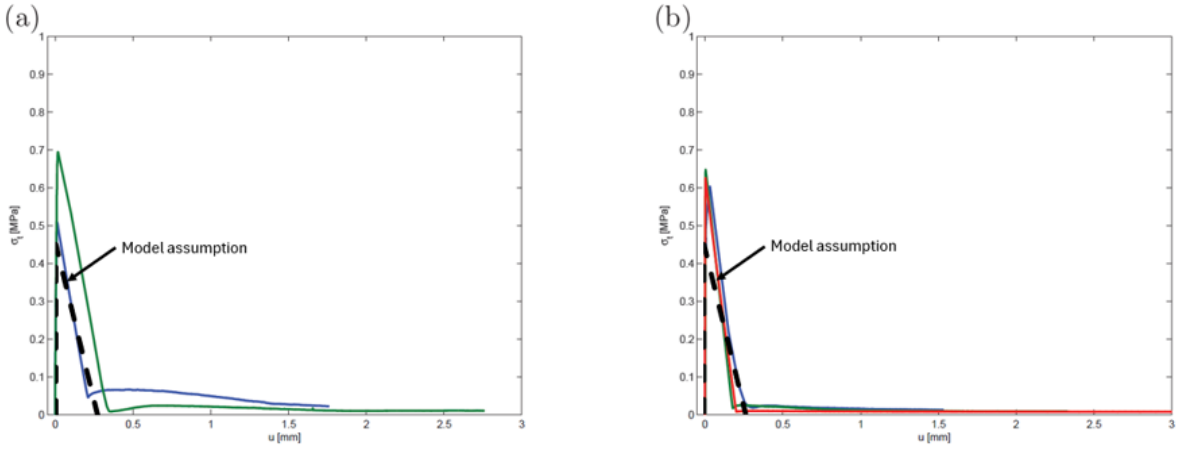

(a) Traction-separation law plotted against the experimental results from the direct tensile test for (a) S1410 and (b) S1424 specimens [28], with the black dotted line representing the traction-separation law.

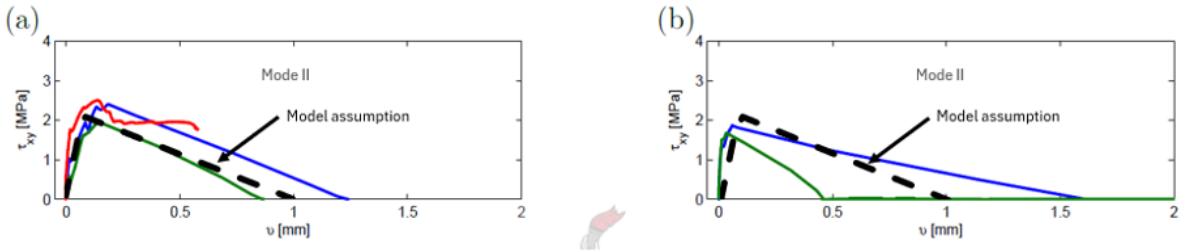

(b) Shear-sliding law plotted against the experimental results from the shear test for (a) S1410 and (b) S1424 specimens [28], with the black dotted line representing the shear-sliding law.

Figure 3.9: Traction-separation and shear-sliding law input for the analytical analysis, based on the experimental results from [28].

The stress-strain behavior of the SHCC material, experimentally determined through a direct tensile test on a dogbone specimen in [21], provides the basis for the material model. This behavior is divided into two phases: an initial phase characterized by distributed cracking throughout the specimen, and a subsequent phase where a dominant crack forms, which then continues to open. This transition occurs at a strain level of 4% (see Figure 3.10).

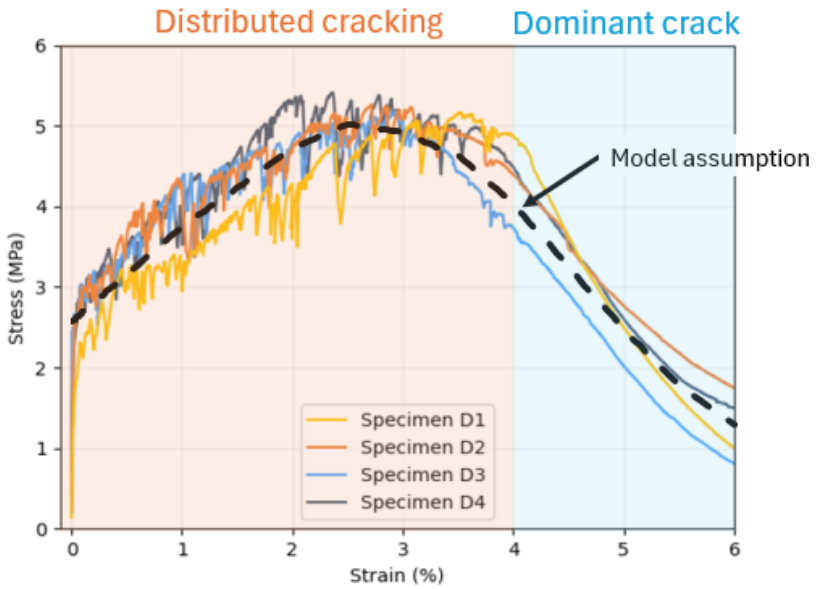

Figure 3.10: Stress-strain relationship with an initial distributed cracking phase until 4% strain and a subsequent phase where a dominant crack forms [21]. The black dotted line represents the assumed material model in this analytical model.

For the material behavior, the stress-strain relationship is utilized up to 4% strain to calculate displacement within the SHCC material. If cracking occurs within the tab or in the surrounding material, the stress-displacement response is directly derived from this stress-strain relationship up to 4% strain, as illustrated in Figure 3.10. In this phase, displacement is determined by multiplying the strain by the height of the tab.

Beyond the 4% strain threshold, the displacement recorded from dogbone tests in [21] is used to characterize the response once a dominant crack has formed. In cases where no dominant crack develops, the SHCC material's stress capacity remains constant, and further displacement is attributed not to additional material deformation but rather to other mechanisms at play. This approach allows for a clear delineation between the distributed cracking phase up to 4% strain and the dominant cracking phase beyond this point.

3.2.1. 1. Delamination

The first failure mechanism represents a delamination of the interface, resulting from a crack forming along the horizontal and vertical interfaces. The force-displacement behavior of this failure mechanism is a summation of the horizontal interface delamination and vertical interface delamination (see Figure 3.11).

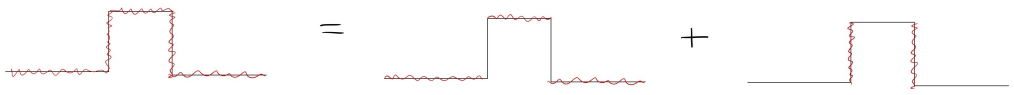

Figure 3.11: Different components of which the first failure mechanism is build up. The horizontal interface failure and the vertical interface failure.

In this failure mechanism, the SHCC material inside the tab or surrounding the tab is not activated, meaning that no cracking will occur in the material. This can only happen if the stress within the tab remains below the threshold of 2.6 MPa, ensuring that the SHCC material is not activated beyond its linear-elastic behavior. This condition can be verified by comparing the stress within the tab with the stress threshold for cracking within the SHCC (2.6 MPa).

The force within the specimen is composed of contributions from both the tensile and shear interfaces. The force absorbed within the tab is equal to the force carried by the shear interfaces on either side of the tab plus the tensile force transferred in the top horizontal interface. Consequently, the stress inside the tab is derived by dividing the force carried by these shear interfaces and the top horizontal interface by the tab's cross-sectional area.

Looking at the specimen design with a width-over-height ratio of 1.0, it can be seen that for the basis values of the interface design where the tensile interface strength equals 12% of material tensile strength (with $= 0.6$ MPa and $= 2.2$ MPa), the stress inside the tab is wihtin the distributed cracking stage of the SHCC material (see Figure 3.12a).

To ensure that the stress in the tab remains below the cracking threshold, the interface strength must be reduced to 6% of material strength (with $= 0.3$ MPa and $= 1.1$ MPa). This adjustment results in the stress within the tab falling within the linear elastic range of the SHCC material (see Figure 3.12b).

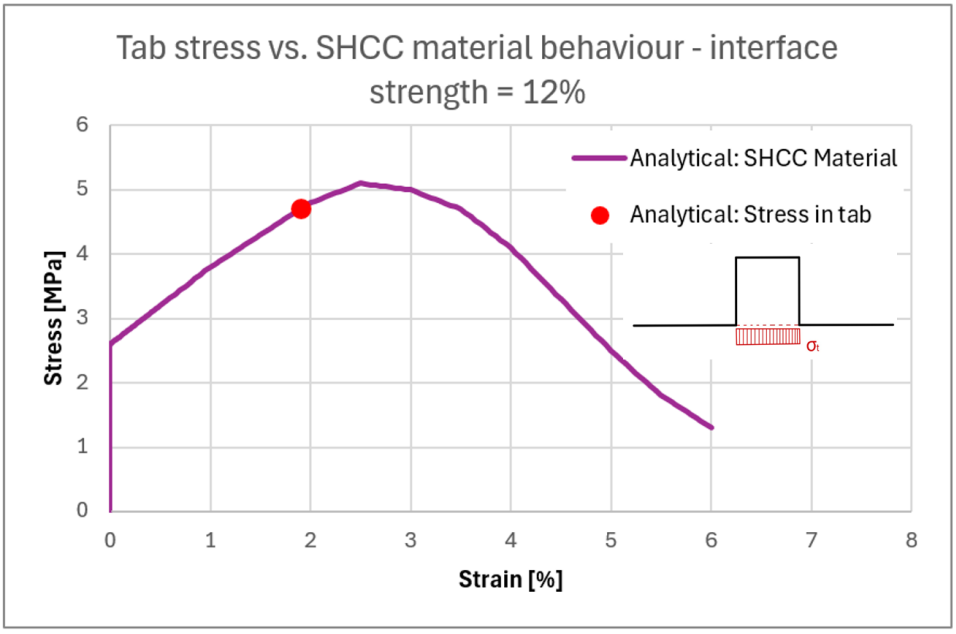

(a) Stress inside the tab for an interface strength of 12% of material strength.

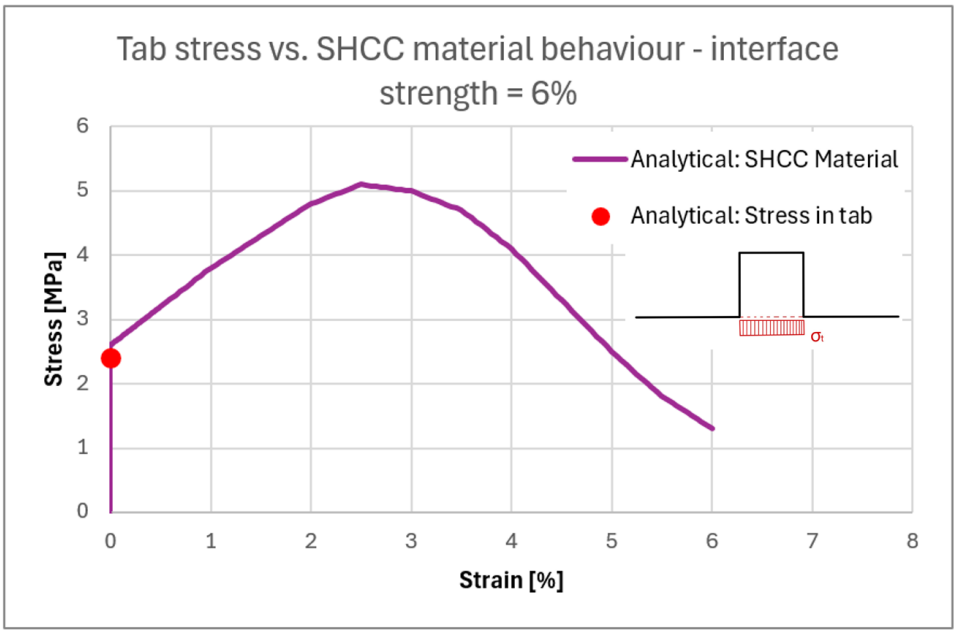

(b) Stress inside the tab for an interface strength of 6% of material strength.

Figure 3.12: Stress inside the tab with w/h = 1.0 due to shear stress transfer in the vertical interfaces and the tensile stress transfer in the top horizontal interface is compared to the SHCC cracking threshold and capacity limits for different values of interface strength.

The reduced interface properties lead to the occurrence of a delamination failure mechanism. The force-displacement behavior associated with this delamination is illustrated in Figure 3.13, which presents the overall force-displacement response of the interface. When comparing these results to the behavior of the SHCC material, it is evident that both the displacement capacity and the ultimate strength of the interface are significantly lower.

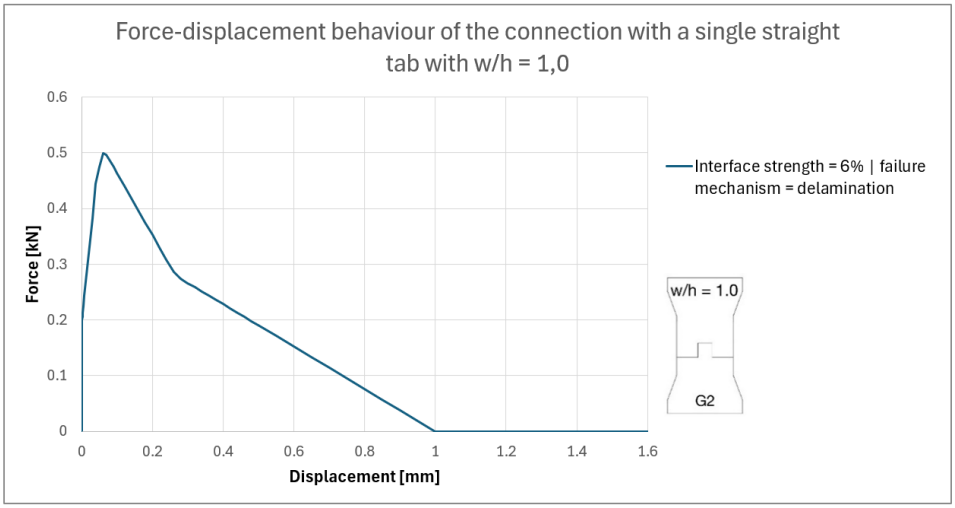

(a) Interface behavior of the interface with a tab with width-to-height ratio of 1.0 and a 6% interface strength.

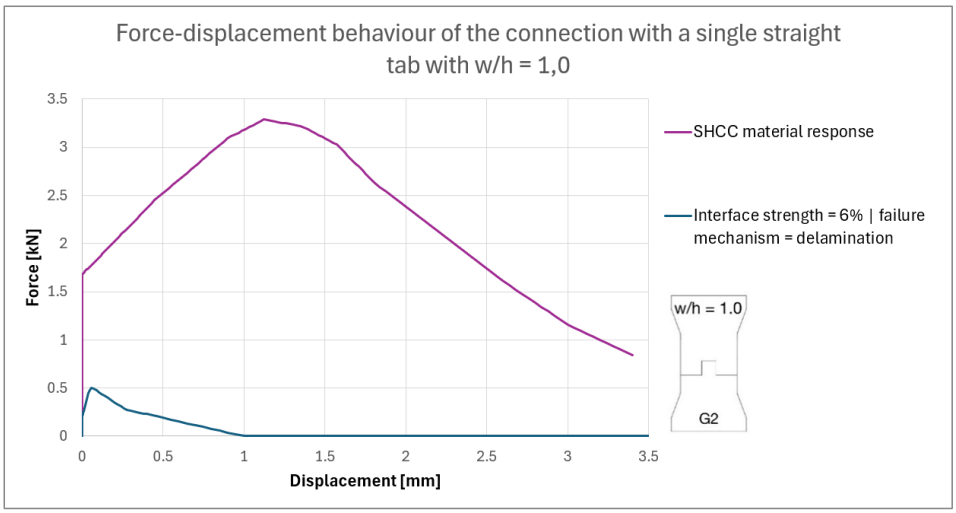

(b) Interface behavior of the interface with a tab with width-to-height ratio of 1.0 and a 6% interface strength including the SHCC material behavior.

Figure 3.13: Interface behavior of the interface with a tab with width-to-height ratio of 1.0 and a 6% interface strength: $= 0.3$ MPa and $= 1.1$ MPa.

For the interface designs featuring tabs with width-to-height ratios of 1.5, 1.0 and 0.5, the tensile interface strengths have been varied as a percentage of the tensile strength of the material while also varying the shear strength proportionally, ensuring that a delamination failure mechanism remains observable. The interface strengths for each tab design are summarized in Table 3.1 and are visually presented in Figure 3.14, indicating the stress range within which the delamination mechanism will still occur.

Specimen	w/h ratio	range of interface strength %	range of MPa	range of MPa
SCG1	1.5	0 - 9	0 - 0.45	0 - 1.65
SCG2	1.0	0 - 6	0 - 0.3	0 - 1.1
SCG3	0.5	0 - 3	0 - 0.15	0 - 0.55

Table 3.1: Interface properties for the delamination failure mechanism for different interface designs. represents the ultimate tensile strength and the ultimate shear strength of the interface.

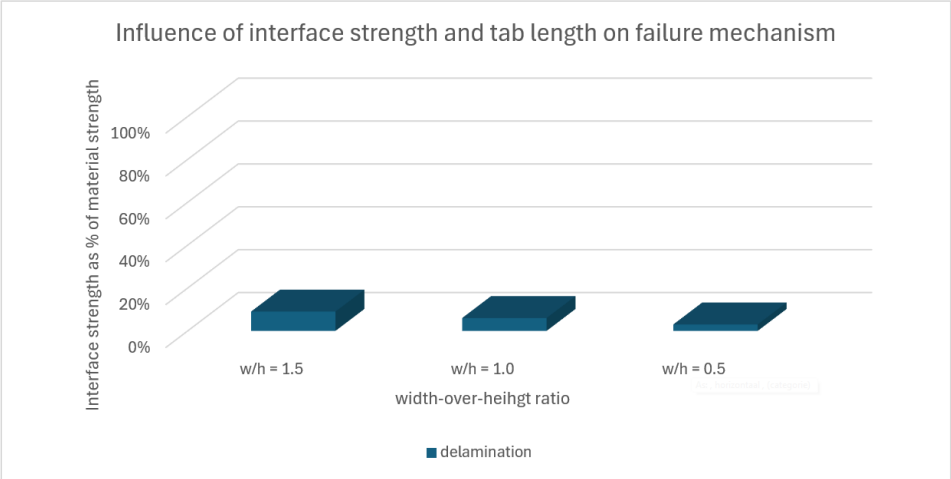

Figure 3.14: Range of interface strength at which a delamination failure occurs for different width-to-height ratios.

3.2.2. Pull-out

The second failure mechanism presents a pull-out mechanism of the interface. The mechanism is similar to the delamination mechanism, however, instead of no material activation, here the material inside the tab is activated. The force-displacement behavior in this failure mechanism is a summation of the horizontal interface behavior, vertical interface behavior and the cracking inside the SHCC material (see Figure 3.15). The displacement behavior in this type of failure mechanism is a result from both sliding behavior in the shear interface and crack opening inside the SHCC material inside the tab.

Figure 3.15: Different components of which the second failure mechanism is build up. The horizontal interface failure and the vertical interface activation in combination with material activation in and around the tab.

In this mechanism, the SHCC material both inside and surrounding the tab becomes activated, resulting in cracking within the material. However, this cracking does not ultimately lead to material failure; instead, the tab is pulled out. This behavior suggests that the stress within the tab must be within the distributed cracking range of the SHCC material while not exceeding the material capacity.

For the interface with a single straight tab that has a width-to-height ratio of 1.0, the pull-out mechanism is observed. In the case of the originally defined interface, the stress in the tab surpasses the cracking threshold of the SHCC material but remains below its maximum capacity (see Figure 3.12a). This indicates that the prevailing failure mechanism is indeed pull-out.

The load-bearing capacity is governed by the interface capacity; however, the displacement observed at specific loads results from a combination of interface separation or sliding and cracking within the SHCC material. The force-displacement behavior associated with this pull-out mechanism is illustrated in Figure 3.16, which presents the overall force-displacement response of the interface. For comparison, the force-displacement behavior of the delamination failure mechanism, observed at an interface strength of 6%, is also presented.

Furthermore, Figure 3.16b compares the force-displacement responses of these mechanisms to the behavior of the SHCC material. The pull-out mechanism at an interface strength of 12% demonstrates a significantly higher load-bearing capacity and greater displacement capacity than the delamination failure mechanism. However, both the load-bearing and displacement capacities remain substantially

lower than those of the SHCC material itself.

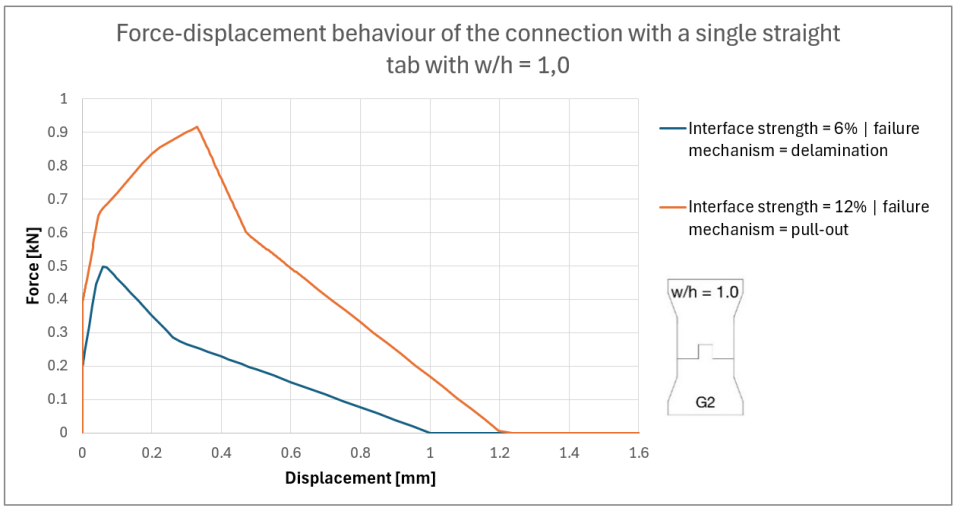

(a) Pull-out interface behavior of the interface with a tab with width-to-height ratio of 1.0 and a 12% interface strength.

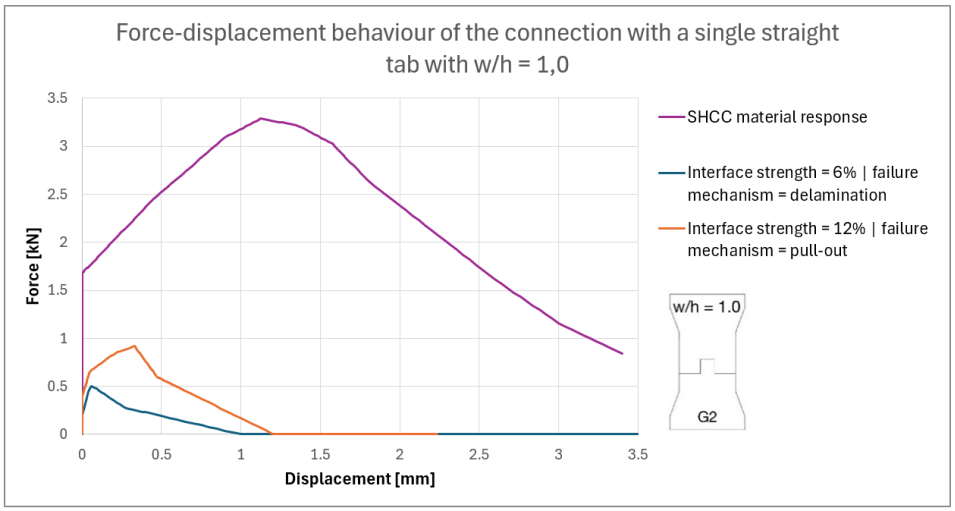

(b) Pull-out interface behavior of the interface with a tab with width-to-height ratio of 1.0 and a 12% interface strength including the SHCC material behavior.

Figure 3.16: Pull-out interface behavior of the interface with a tab with width-to-height ratio of 1.0 and a 12% interface strength: $= 0.6$ MPa and $= 2.2$ MPa.

For the interface designs featuring tabs with width-to-height ratios of 1.5, 1.0 and 0.5, the tensile interface strengths have been varied as a percentage of the tensile strength of the material while also varying the shear strength proportionally, ensuring that a pull-out failure mechanism remains observable. The interface strengths for each tab design are summarized in Table 3.2 and visualized in Figure 3.17, indicating the stress range within which the pull-out mechanism will still occur.

Specimen	w/h ratio	range of interface strength %	range of MPa	range of MPa
SCG1	1.5	9 - 19	0.48 - 0.99	1.76 - 3.63
SCG2	1.0	6 - 12	0.33 - 0.63	1.21 - 2.31
SCG3	0.5	4 - 6	0.18 - 0.33	0.66 - 1.21

Table 3.2: Range of interface properties for the pull-out failure mechanism for different interface designs. represents the ultimate tensile strength and the ultimate shear strength of the interface.

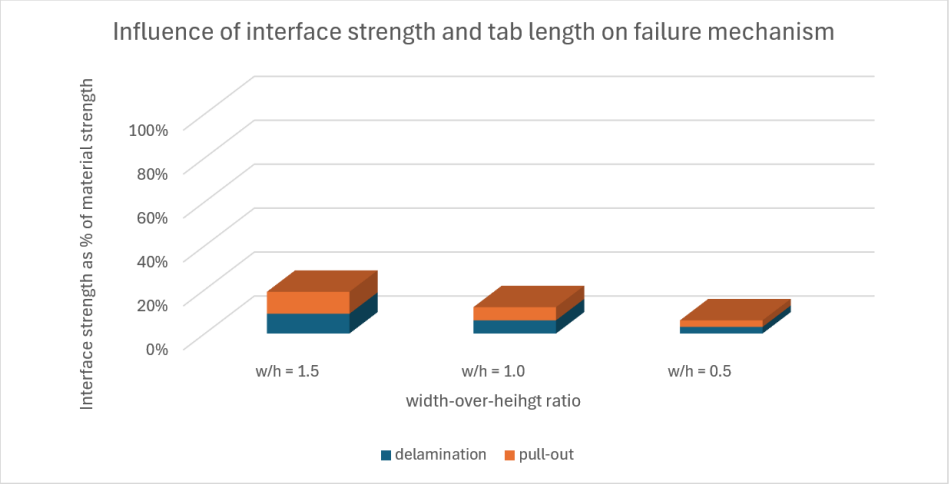

Figure 3.17: Range of interface strength at which either delamination or pull-out failure occurs for different width-to-height ratios.

3.2.3. Tab failure

The third failure mechanism is characterized as a tab failure mechanism. Its behavior is similar to that of the pull-out mechanism; however, rather than the tab being pulled out, the material inside the tab ultimately fails. The force-displacement behavior associated with this failure mechanism results from a combination of the responses of both the horizontal and vertical interfaces, along with the cracking behavior of the SHCC material (see Figure 3.18).

Once the stress in the tab exceeds the SHCC capacity of 5.1 MPa, the material behavior begins to dominate the overall response, causing the sliding of the vertical interfaces to cease. Eventually, a dominant crack forms within the tab, typically located at the bottom, where stress concentrations are highest.

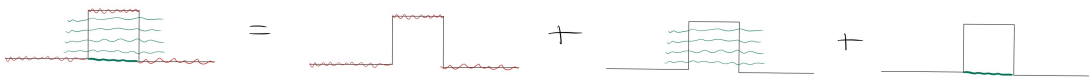

Figure 3.18: Different components of which the third failure mechanism is build up. The horizontal interface failure, the distributed cracking inside and on the sides of the tab and the dominant crack in the tab between the horizontal interfaces.

In this mechanism, the stress within the tab due to interface strength would exceed the material capacity of 5.1 MPa, meaning that the interface is stronger than the SHCC material at the bottom of the tab. This results in material failure rather than interface failure. The tab failure mechanism is observed in the interface with a single straight tab that has a width-to-height ratio of 1.0. As shown in Figure 3.19,

when the interface tensile strength is set to 14% of the material tensile strength, the stress in the tab surpasses 5.1 MPa due to stress transfer from the interface. This indicates that a tab failure will occur.

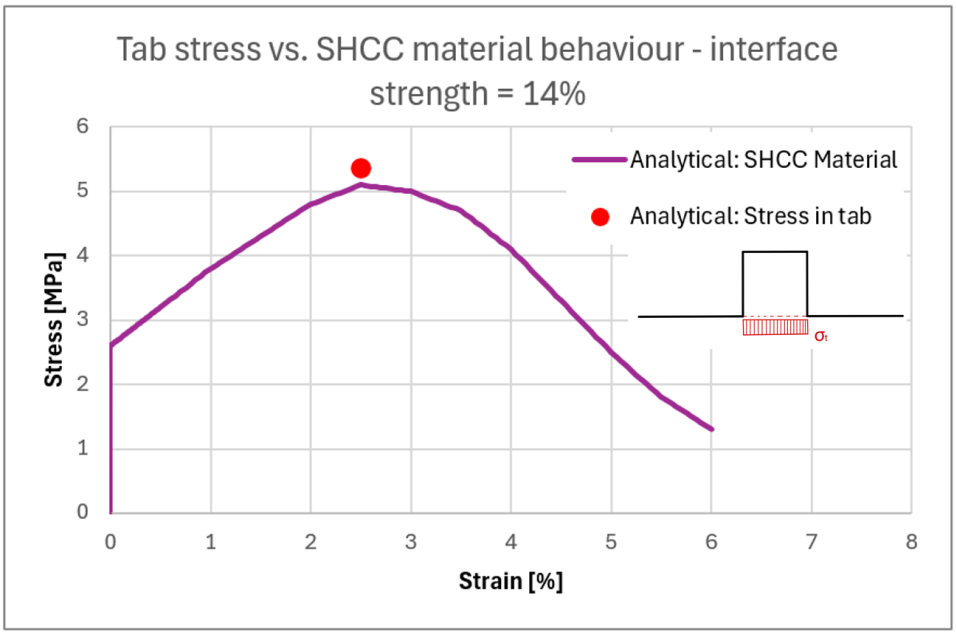

Figure 3.19: Stress inside the tab with w/h = 1.0 due to shear stress transfer in the vertical interfaces and the tensile stress transfer in the top horizontal interface is compared to the SHCC cracking threshold and capacity limits for a 14% interface strength.

In this failure mechanism, the load-bearing capacity is entirely governed by the material strength of the tab. Furthermore, the displacement behavior of the interface is influenced by the displacement characteristics of the SHCC material within the tab. The associated force-displacement behavior is illustrated in Figure 3.20, which presents the overall force-displacement response of the interface. Again, for comparison, the force-displacement behavior of the delamination and pull-out failure mechanism, observed at an interface strength of 6% and 12%, are also presented.

In **??**, the force-displacement responses of the tab failure mechanism at an interface strength of 14% are compared to those of the SHCC material. The tab failure mechanism exhibits a load-bearing capacity similar to that of the pull-out mechanism at an interface strength of 12%. However, its displacement capacity is significantly higher than that observed in both the pull-out and delamination failure mechanisms. Although the load-bearing capacity of the tab failure mechanism remains notably lower than that of the SHCC material, its displacement capacity approaches that of the SHCC material, albeit at a much lower strength.

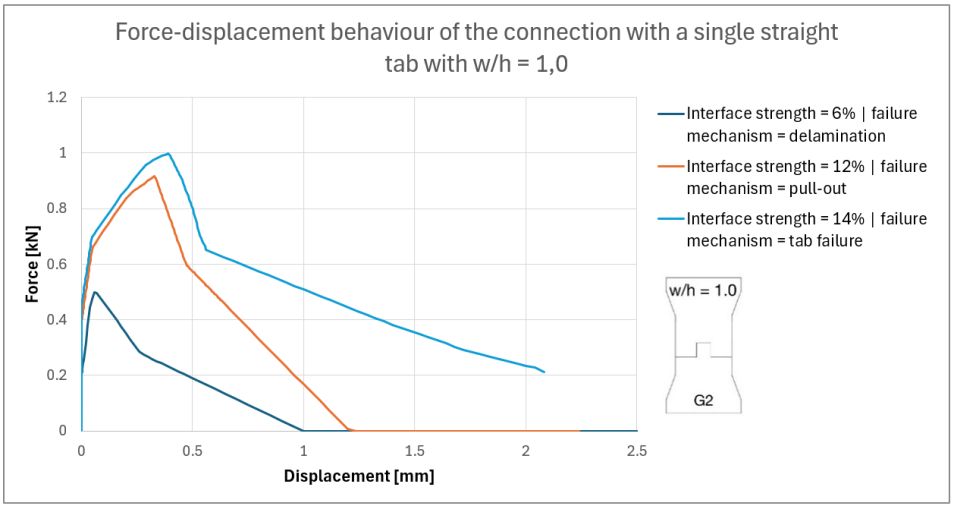

(a) Interface behavior of the interface with a tab with width-to-height ratio of 1.0 and a 14% interface strength.

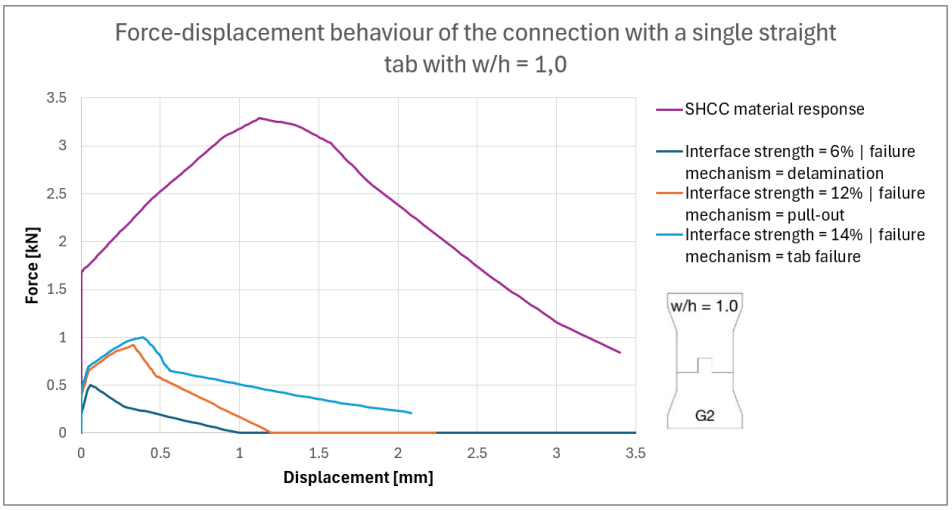

(b) Interface behavior of the interface with a tab with width-to-height ratio of 1.0 and a 14% interface strength including the SHCC material behavior.

Figure 3.20: Interface behavior of the interface with a tab with width-to-height ratio of 1.0 and a 14% interface strength: $= 0.69$ MPa and $= 2.53$ MPa

For the interface designs featuring tabs with width-to-height ratios of 1.5, 1.0 and 0.5, the tensile interface strengths have been varied as a percentage of the tensile strength of the material while also varying the shear strength proportionally, ensuring that a tab failure mechanism remains observable. The interface strengths for each tab design are summarized in Table 3.3 and visually presented in Figure 3.21, indicating the stress range within which the tab failure mechanism will occur.

Specimen	w/h ratio	range of interface strength %	range of MPa	range of MPa
SCG1	1.5	20 - 99	1.02 - 5.07	3.74 - 18.59
SCG2	1.0	13 - 99	0.66 - 5.07	2.42 - 18.59
SCG3	0.5	7 - 99	0.36 - 5.07	1.32 - 18.59

Table 3.3: Range of interface properties for the tab failure mechanism for different interface designs. represents the ultimate tensile strength and the ultimate shear strength of the interface.

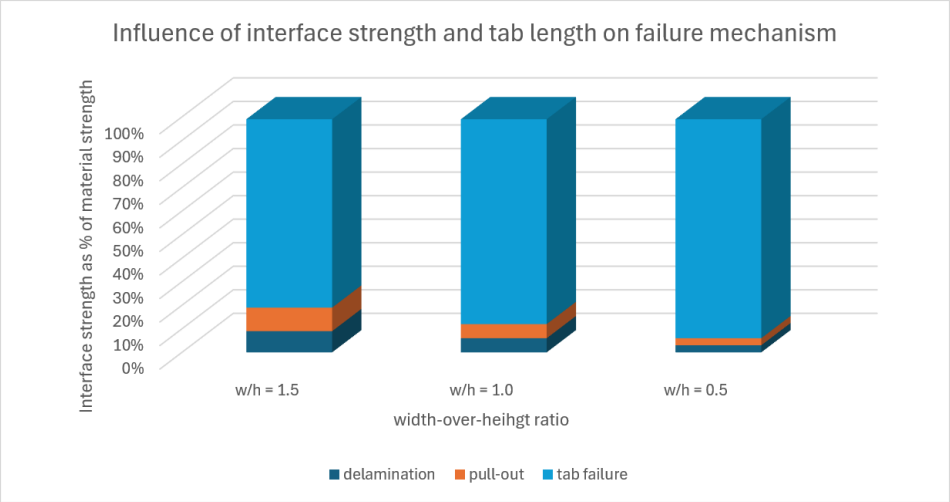

Figure 3.21: Range of interface strength at which delamination, pull-out or tab failure occurs for different width-to-height ratios.

From the bar plot in Figure 3.21, it is evident that even with a relatively short tab (w/h = 1.5), activating SHCC material behavior in pull-out or tab failure mechanisms is achievable at relatively low interface strengths—9% for pull-out failure and 20% for tab failure. Furthermore, increasing the tab length (w/h = 0.5) significantly reduces the required interface strength, with values dropping to 4% for pull-out failure and 7% for tab failure.

3.2.4. Material failure

The fourth failure mechanism is not strictly a failure of the interface but rather of the SHCC material itself. In this mechanism, no cracks form along the interface; instead, multiple cracks develop within the SHCC material, behaving as if the interface connection were absent. This principle is illustrated in Figure 3.22, where cracks are distributed throughout the specimen, eventually leading to the formation of a single dominant crack.

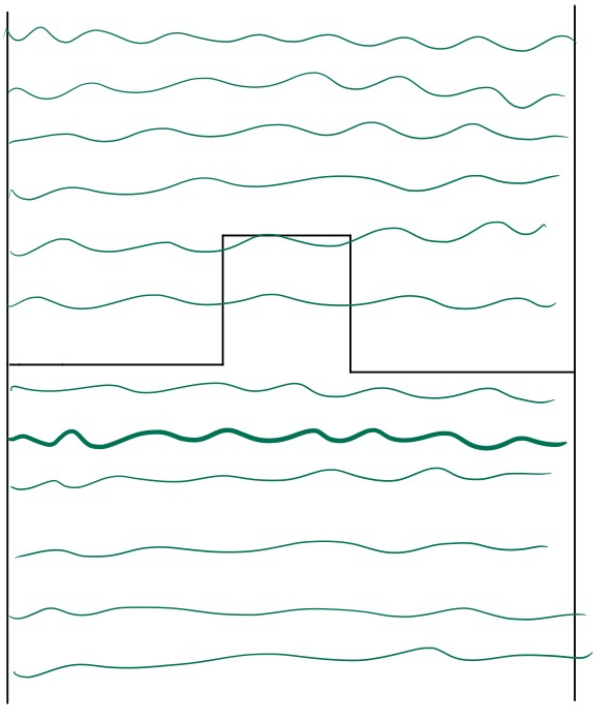

Figure 3.22: The fifth failure mechanism where cracks are spaced throughout the entire specimen in the SHCC material with finally one dominant crack forming.

For this failure mechanism to occur, the horizontal interface must be strong enough to prevent failure before the SHCC material becomes fully activated. This means that the tensile interface strength must be at least as high as the SHCC material strength, corresponding to an interface strength of 100% of material strength

In this scenario, where the SHCC material behaves as though the specimen were monolithic, the height of the activated material is equal to 45 mm. The force-displacement response is composed of two mechanisms: distributed cracking over the 45 mm height and the formation of the dominant crack. The force-displacement behavior of this failure mechanism is presented in Figure 3.23. The behavior remains the same for all three tab designs since the vertical interfaces have no significant influence on the overall specimen behavior.

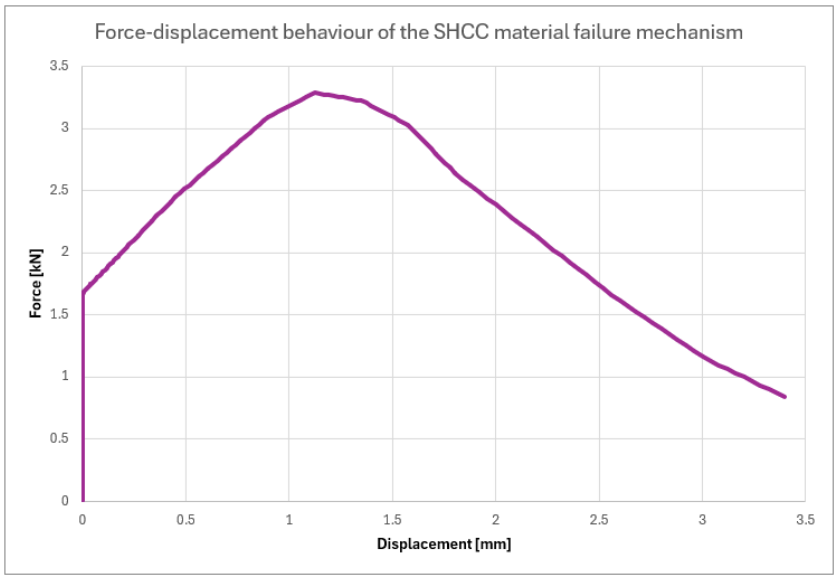

Figure 3.23: Force displacement behavior of the material failure mechanism, where the behavior is as if the specimen as a monolithic specimen.

3.2.5. Model discussion

The objective of this analytical model was to identify various potential failure mechanisms and quantify their force-displacement behavior for single straight tab interfaces with different width-to-height ratios. Additionally, the analysis aimed to investigate the influence of tab length and interface strength on the failure response of the SHCC-to-SHCC connection. In this subsection the workings of the analytical model will be discussed. The discussion of the results of the analysis will be perforemed in chapter 6.

By developing a simplified analytical model, it was possible to predict the force-displacement response across different interface strengths and geometries.

Nevertheless, the analytical model has limitations due to its simplified assumptions. Notably, the assumption of no stress concentrations restricts the model's ability to identify transitional failure mechanisms, particularly when high tensile interface strength causes the SHCC material adjacent to the tab to fail before a material failure mechanism occurs.

Additional limitations include the assumption of negligible friction, which can significantly influence the delamination and pull-out mechanisms. The model also assumes uniform stress distribution in the vertical interfaces, which does not reflect real-world conditions and can affect shear interface behavior. Lastly, the assumption that sliding and separation values of the interface remain constant when interface strength changes may overlook significant variations that could impact the overall behavior of the connection.

To address these limitations and gain a deeper understanding of the behavior of the single tab interface connection, a subsequent analysis has been conducted using a continuum smeared cracking model in Abaqus CAE. This analysis will be discussed in the next chapter, chapter 4.

4

Continuum smeared cracking model

This chapter focuses on modeling the interface behavior, as analytically reviewed in chapter 3, by employing a continuum smeared cracking model within the commercial software Abaqus/CAE. The primary objective is to gain a deeper understanding of the behavior of the single tab interface connection by investigating key interface parameters and evaluating the strengths and limitations of using the Concrete Damaged Plasticity (CDP) model for the material and the Cohesive Zone Modeling (CZM) for the SHCC-to-SHCC interface.

To achieve this objective, the following steps have been undertaken:

1. **Material Modeling:** The chapter begins by explaining the principles of modeling concrete, particularly SHCC, using the CDP model. The material is then modeled using this framework and validated against dogbone test results from Papoulidou [21].
2. **Interface Modeling Using Cohesive Zone Modeling (CZM):** The interface is modeled using the CZM approach. An initial interface model is developed based on preliminary numerical analyses of the experiments conducted in [28] and [21].
3. **Parametric Study:** A comprehensive parametric study is performed on the interface variables to assess their detailed effects on connection behavior. The parametric study is used to determine whether the different failure mechanisms identified in chapter 3 can be accurately modeled.
4. **Modeling Experimental Behavior:** The insights gained from the parametric study are applied to investigate the ability to model real experimental behavior using the continuum smeared cracking model in Abaqus. The interface parameters are optimized to match experimental results from [28] and [21], following these steps:
    - **Tensile Interface Properties:** After completing the parametric study, the tensile interface parameters are refined using the direct tensile test data from Stander [28].
    - **Shear Interface Properties:** Once the tensile interface parameters are optimized, the remaining interface parameters are adjusted based on experiments from [21].
    - **Model Verification:** Lastly, another interface experiment from [21] is analyzed, and the results are compared to the experimental data. This comparison serves to verify the combined effectiveness of the material and interface models, offering insights into whether the CDP and CZM models can accurately represent the behavior of an SHCC-to-SHCC interface.

4.1. Material Modelling

The first step in performing the numerical analysis was to model the SHCC material. In this section first the material model is presented and explained and then an analysis is performed of a dogbone tensile test. The result of this analysis is then compared to the result presented in [21].

4.1.1. Concrete Damaged Plasticity (CDP) Model

To model the behavior of Strain-Hardening Cementitious Composites (SHCC), the Concrete Damaged Plasticity (CDP) model in Abaqus was selected due to it's general capability for modeling concrete and other quasi-brittle materials [32]. Additionally the CDP model provides the possibility to use a user-defined tensile stress-strain or stress-displacement curve [32]. The CDP model encompasses three primary material definitions: elastic properties, plastic properties, and damage properties.

The **elastic properties** of the material, such as Young's modulus and Poisson's ratio, define the initial, undamaged stiffness of the SHCC. These properties are crucial for capturing the initial linear elastic response before any plastic deformation or damage occurs.

The **plastic properties** describe the irreversible deformations that the material undergoes beyond its elastic limit. These properties are governed by parameters such as the dilation angle, eccentricity, and the ratio *fb0/fc0*, which characterizes the relationship between the biaxial and uniaxial compressive yield stresses. Additionally, the parameter *K* represents the ratio between the Mises equivalent stress along the tensile and compressive meridians, typically set to 2/3 for concrete-like materials [2].

The **damage properties** account for the degradation of material stiffness due to tensile cracking and compressive crushing. In tension, the behavior and associated damage are defined using stress-displacement data, which reflect the material's progressive cracking under tensile loads. Conversely, the compressive behavior is characterized by stress-strain data, capturing the material's response under compressive loads. Notably, the model assumes that once tensile damage has occurred, the material cannot recover its stiffness under subsequent compressive loading.

An important aspect of the CDP model is the way it represents cracking. Instead of modeling cracks as discrete entities, the model employs a **smeared cracking approach**. This means that the cracks are distributed across the finite elements rather than being represented as distinct, localized discontinuities (see Figure 4.1). This approach simplifies the computational model by avoiding the complexities associated with tracking individual crack paths and allows for a more generalized representation of the material's damage and fracture behavior. In the smeared cracking model, the crack effects are averaged over the volume of the element, leading to a continuous degradation of stiffness as the tensile damage progresses.

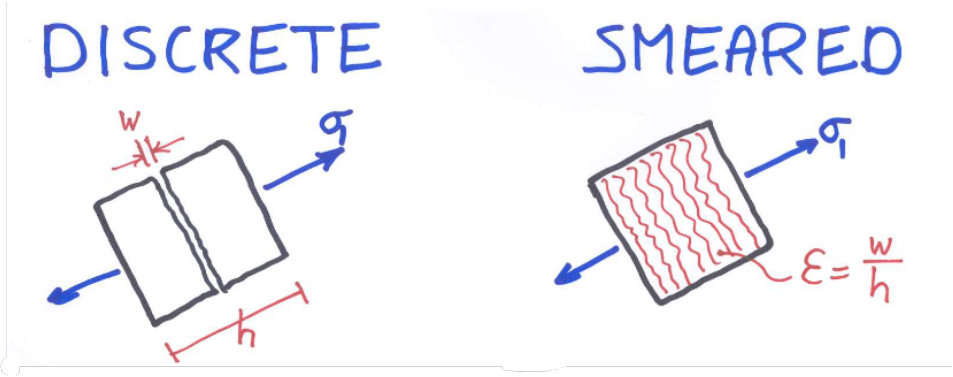

Figure 4.1: Principle of discrete cracking versus smeared cracking. [23]

The mass density used in the model is $2.4\ 10^{-7}$ N/mm^3 (equivalent to $2.4\ 10^{-10}$ kN/mm^3). Although this density is significantly lower than the actual value ($2.4\ \ 10^{-11}$ kN/mm^3), it was chosen to reduce inertial effects and ensure a stable numerical analysis.

The **yield condition** in the CDP model is influenced by the material's biaxial compressive behavior. This behavior is not highly significant for this study, as the focus is primarily on tensile behavior; however, it will still be briefly explained for the sake of completeness; The *fb0/fc0* ratio, is defined as the ratio between the initial equibiaxial and uniaxial compressive yield stress. The factor *K* represents

the ratio of the Mises equivalent stress along the tensile and compressive meridians.

For the plastic damage model, a **non-associated potential flow** is assumed. This means that the direction of plastic strain increment is not normal to the yield surface but is defined by a different potential function. In the CDP model in Abaqus, the plastic potential function is chosen as the Drucker-Prager hyperbolic function:

$$(_0 \tan)^2 + {}^2 - \tan = 0 \tag{4.1}$$

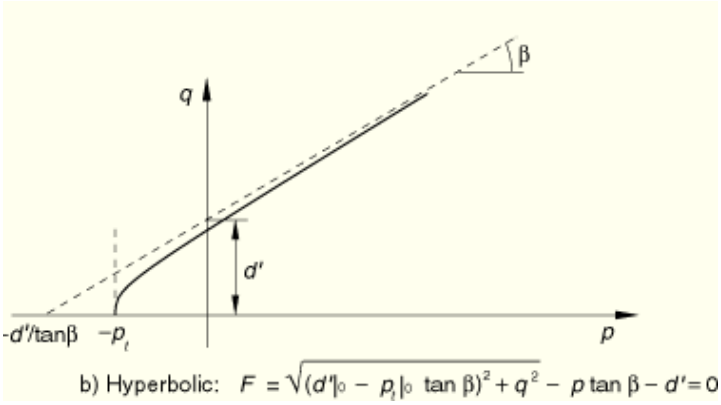

Figure 4.2: Hyperbolic yield criteria in the meridional plane, where is the Mises stress and the hydrostatic pressure [2].

In this function, the dilation angle (denoted as in Figure 4.2) represents the volumetric expansion of the material under confining pressure, and the eccentricity (denoted as $|-|$ in Figure 4.2) defines the rate at which the function approaches the asymptote, indicating that the flow potential tends to a straight line as the eccentricity approaches zero.

To address the convergence difficulties typically encountered in implicit analysis involving materials with softening behavior, a **viscoplastic regularization** of the constitutive equations is implemented. This approach helps to stabilize the numerical solution by permitting stresses to exceed the yield surface slightly, which is particularly useful in the softening regime. Using a small value for the viscosity parameter (relative to the characteristic time increment) generally improves the convergence rate without significantly compromising the accuracy of the results [2].

The values for the basic material properties used in this study are presented in Table 4.1.

Material Definition	**Parameter**	**Value**	**Unit**
General property	Density	$2.4\ 10^{-7}$	N/mm^3
Elastic property	Young's modulus	32,000	MPa
Elastic property	Poisson's ratio	0.2	-
Plastic property	Dilation angle	35	degrees
Plastic property	Eccentricity	0.1	-
Plastic property	fb0/fc0	1.16	-
Plastic property	K	0.6667	-
Plastic property	Viscosity Parameter	0.0001	-

Table 4.1: Material properties for the Concrete Damaged Plasticity model in Abaqus analysis.

When modeling Strain-Hardening Cementitious Composites (SHCC) using the Concrete Damaged Plasticity (CDP) model, it is crucial to account for the mesh sensitivity inherent in the model. The CDP model, similar to many other constitutive models with softening behavior, exhibits sensitivity to the size and distribution of the finite element mesh. This sensitivity can lead to variations in the predicted material behavior, making it essential to carefully consider and address mesh-related issues during the modeling process.

In this study, two different mesh sizes—3 mm and 1.5 mm—were employed to evaluate the influence of mesh sensitivity on the simulation results. For each mesh size, the dogbone test from [21] was replicated, and the material model was optimized to closely match the experimental results. A hexagonal mesh configuration was used, and 3D stress elements from the Abaqus Explicit element library were selected, with a linear geometric order.

For the finer 1.5 mm mesh, enhanced hourglass control was implemented to mitigate potential numerical issues. Hourglassing is a common problem in reduced integration elements, where zero-energy deformation modes, known as hourglass modes, can occur. These modes do not contribute to actual stress or strain, leading to mesh distortion and potentially inaccurate results. The enhanced hourglass control method in Abaqus addresses this issue, but it can also significantly influence the material's stiffness response [1]. Therefore, the dogbone specimen tests were performed with this enhanced hourglass control method to ensure accurate and reliable results.

The material input for tensile behavior in the Abaqus analyses is defined using stress-displacement data for a single crack. To ensure the accuracy of these input parameters, validation tests were performed to replicate the tensile behavior observed in the experimental study performed by Papoulidou [21]. These validation tests are essential to confirm that the chosen stress-displacement data for different mesh sizes accurately represents the material's response under tensile loading.

To validate the tensile behavior of the material models, a uniaxial tensile test on a dogbone specimen was simulated, following the experimental setup used by Papoulidou [21]. The dogbone specimens in the experimental study had a cross-section of 13 mm by 30 mm and a gauge length of 80mm, and both the test setup and its corresponding numerical model are depicted in Figure 4.3.

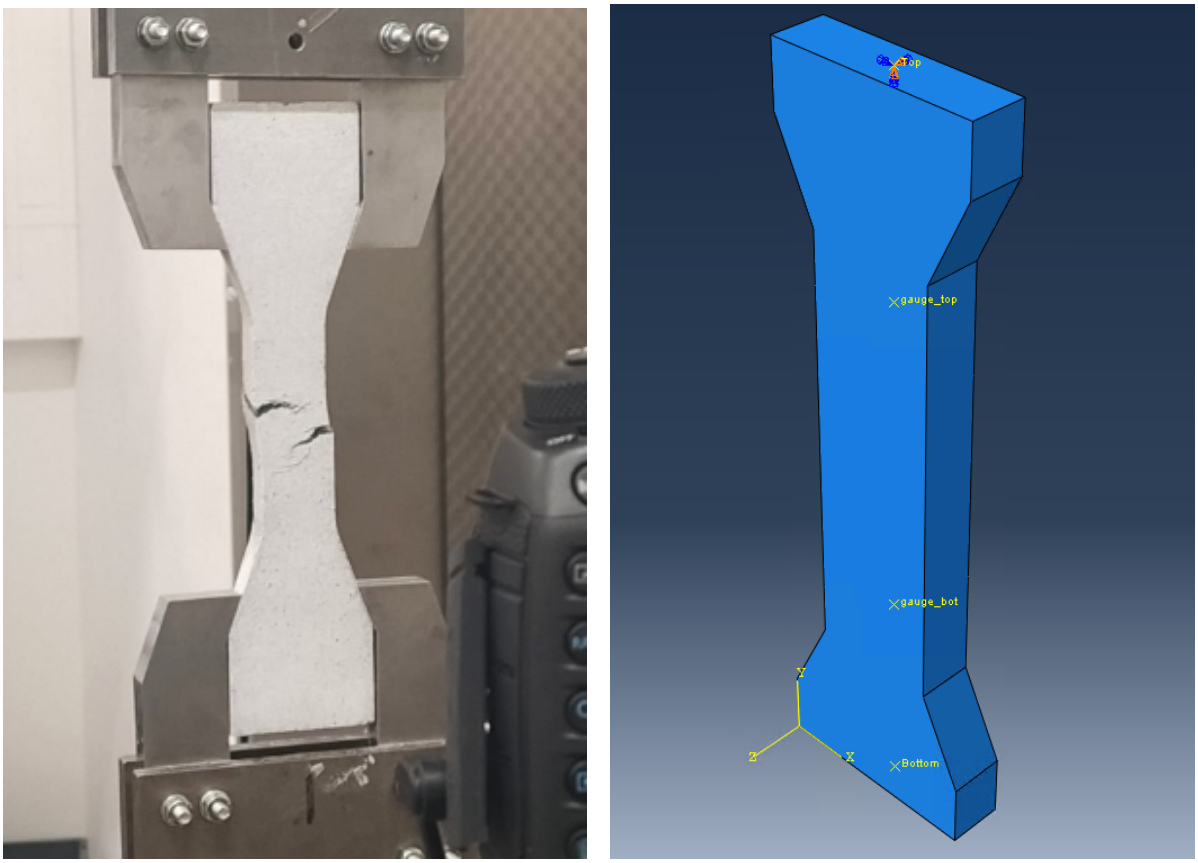

(a) Dogbone specimens tensile test setup [21]. **(b)** Dogbone specimen modeled in Abaqus.

Figure 4.3: Dogbone specimen tensile test setup [21] and it's modeled equivalent in Abaqus.

The simulations were carried out using two different mesh sizes: 3 mm and 1.5 mm. For each mesh size, the stress-displacement data for a single crack were defined and used as input for the material behavior under tension (see Figure 4.4). These data values were determined by the author through a trial-and-error reverse engineering process to ensure that the dogbone tensile test results closely matched the experimental findings reported in [21].

Additionally, Figure 4.4 presents the tensile damage parameter, which is defined as 1 minus the ratio of the tensile stress at a specific displacement to the maximum tensile stress reached in the material up to that point . This definition is further illustrated in Figure 4.4a).

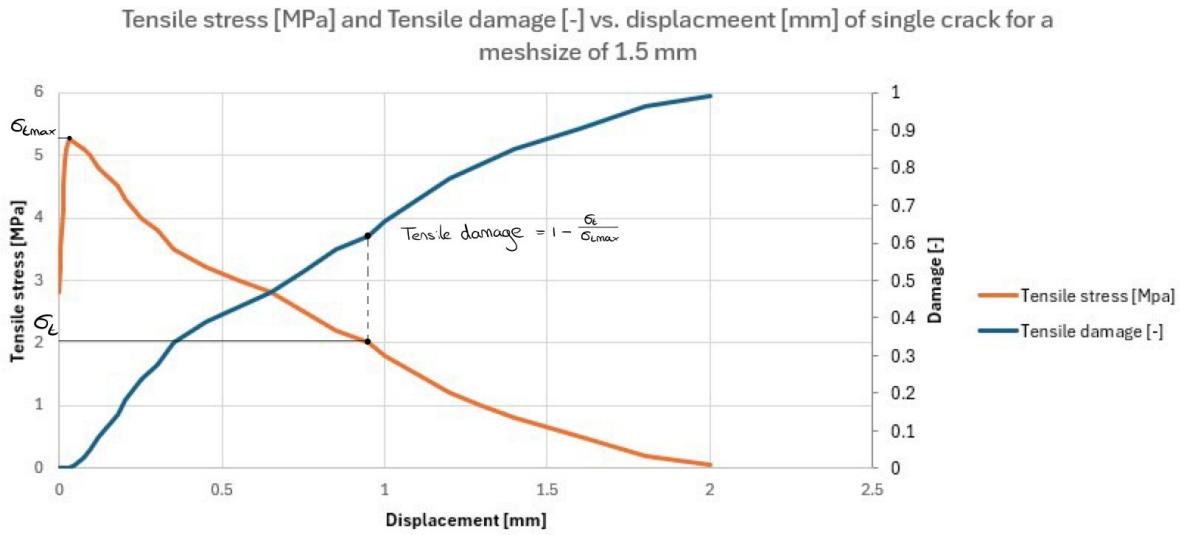

(a) Stress-displacement and Damage-displacement behavior of the material model for elements with a mesh size of 1.5 mm and enhanced hourglass control.

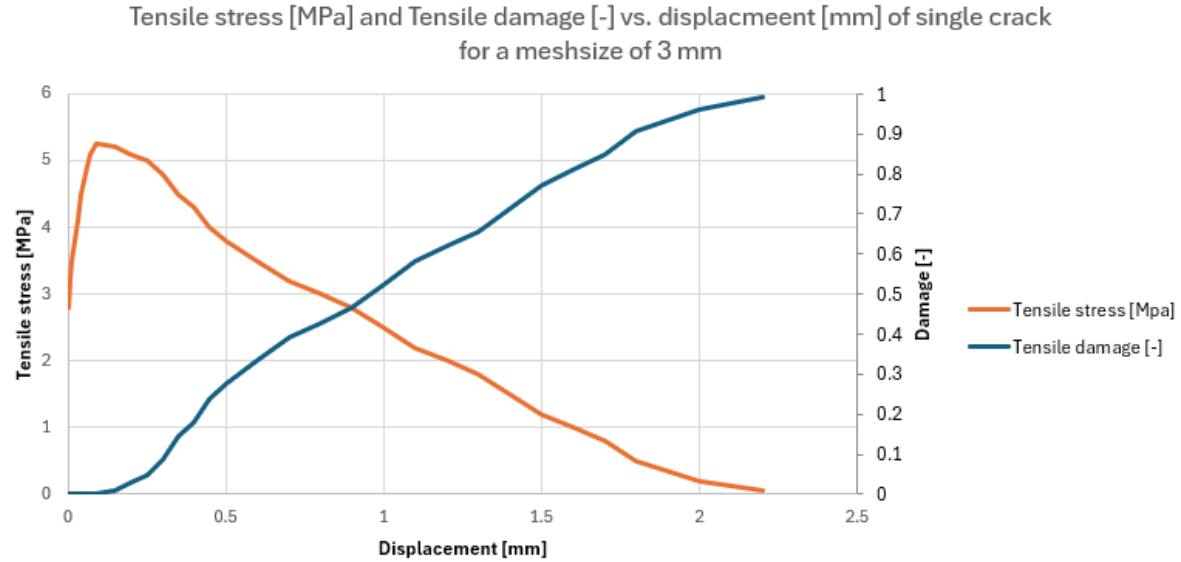

(b) Stress-displacement and Damage-displacement behavior of the material model for elements with a mesh size of 3 mm.

Figure 4.4: Stress-displacement and Damage-displacement behavior of the material model for elements with different meshes.

The results from these simulations were compared to the experimental data to directly evaluate the model's accuracy in replicating the tensile behavior observed in physical tests. The numerical outcomes of the current material models, plotted alongside the experimental results (shown in red), are presented in Figure 4.5 and Figure 4.6. This comparison allows for a direct evaluation of the model's accuracy in replicating the tensile behavior observed in the physical tests.

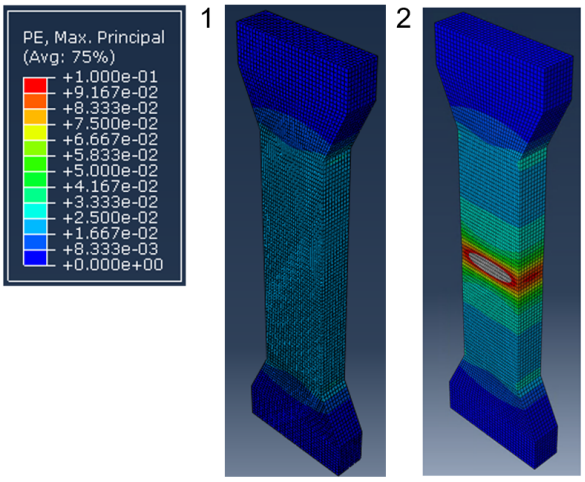

(a) Localisation of the failure crack in the dogbone specimen test analysis.

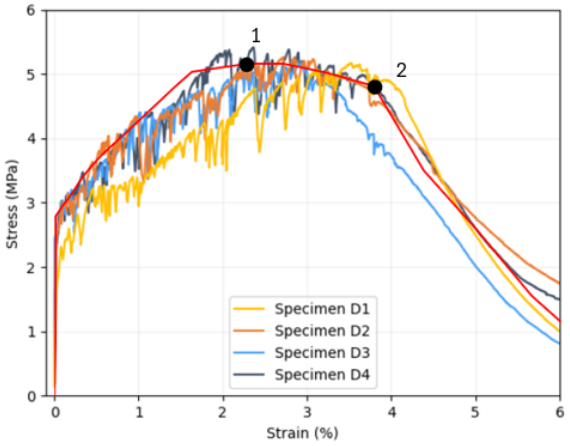

(b) Force-displacement behavior of the dogbone specimen test analysis from abaqus

Figure 4.5: Results from the dogbone specimen test analysis with elements with a mesh size of 1.5 mm and enhanced hourglass control.

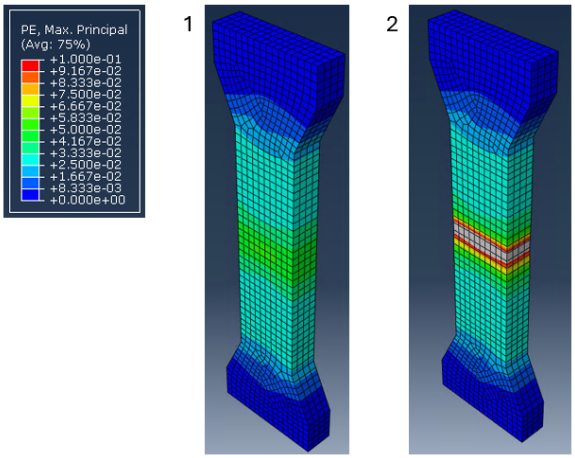

(a) Localisation of the failure crack in the dogbone specimen test with elements with a mesh size of 1.5 mm and enhanced hourglass control.

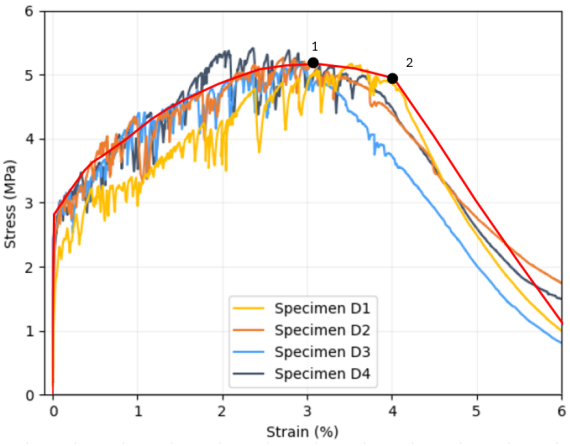

(b) Localisation of the failure crack in the dogbone specimen test with elements with a mesh size of 3 mm.

Figure 4.6: Results from the dogbone specimen test analysis with elements with a mesh size of 3 mm and enhanced hourglass control.

As shown in Figure 5.4a, the dogbone specimen in this experiment failed in tension due to the formation of two separate cracks [21]. In contrast, [21] also presents two additional specimens after failure (see Figure 4.7), where failure occurred along a single crack. This variation arises from the inherent heterogeneity of the material and possible imperfections in the specimens, which leads to slightly different failure patterns in each experiment. The numerical results from the Abaqus analyses, however, exhibit a single-crack failure pattern due to the assumption of homogeneous material properties throughout the specimen.

Figure 4.7: SHCC dogbone specimens after the tensile test [21].

4.2. Interface Modeling Using Cohesive Zone Modeling

To model the interface behavior between two SHCC components, a surface-based Cohesive Zone Modeling (CZM) approach is utilized. The CZM is a well-established method for analyzing fracture problems in bimaterial interfaces [20]. For concrete-to-concrete-like interfaces, direct extraction of material properties is not feasible due to their infinitesimal thickness. As a result, macroscopic material properties are not directly applicable, requiring the use of concepts derived from fracture mechanics. Following the guidelines of the Abaqus manual [2], a traction-separation-based cohesive zone model is adopted for this purpose. This model can be implemented using either interface elements or surface-based cohesive zone modeling. Given that the crack path within the interface is predefined and to minimize computational effort, the surface-based cohesive zone model governed by a traction-separation constitutive law is chosen.

The interaction is defined by designating a TopSurf (slave surface) and a BotSurf (master surface), thereby establishing cohesive contact between them. It is important to note that in the Abaqus software, both the tensile and shear behaviors are modeled using a traction-separation constitutive framework. However, for clarity in this report, the tensile constitutive model is referred to as the ”traction-separation law,” while the shear constitutive model is referred to as the ”shear-sliding law.”

The interaction behavior between the surfaces is defined through several key properties: tangential behavior, normal behavior, cohesive behavior, and damage behavior. For the damage behavior the damage initiation, damage evolution and damage stabilization are important aspects.

At the beginning of this master thesis, preliminary numerical analyses were conducted using Abaqus to gain familiarity with the finite element model. These initial analyses helped establish preliminary values for critical parameters related to tangential, normal, cohesive, and damage behavior. With these initial values a parametric study has been performed which is further discussed in section 4.3. After this parametric study, the interface parameters have been optimized such that the interface model presents the experimental results from [28] and [21] best. To fully understand the parameters used in the cohesive zone model and thus also this numerical model a detailed explanation of the different interface behaviors is provided below.

Normal behavior

For the normal behavior of the interface, the ”Pressure-overclosure” condition is modeled using the ”Hard” contact formulation. In Abaqus, ”Pressure-overclosure” describes how the normal contact pressure between two surfaces behaves as they come into contact and are subsequently compressed.

The ”Hard” contact model assumes that, once contact is established, the surfaces are rigid and non-deformable, preventing any further penetration or compression. This ensures that the interface resists additional deformation beyond the initial contact state, effectively treating the surfaces as perfectly impenetrable under compressive forces. Further detailed information about the cohesive normal behavior is given later in this section.

Cohesive behavior: stiffness coefficients

The cohesive behavior between the interacting surfaces is defined through specific stiffness coefficients, including the normal stiffness coefficient and the shear stiffness coefficients and . The stiffness coefficients are uncoupled, meaning that the normal and shear stiffness operate independently of each other, allowing for a clear distinction between the different modes of interaction at the interface.

Theoretically the interface stiffness coefficients are defined as the interface material stiffness divided by the true physical initial thickness of the interface [2]. To properly define the interface stiffness coefficients, the true interface thickness should ideally be determined, allowing the stiffness coefficients to be calculated based on that thickness. The stiffness values of the interface material could be assumed to be the same as those of the SHCC, which would typically be the preferred method for defining these coefficients.

As will be explained further in this chapter, due to the low values of interface strength and high values of material stiffness of the SHCC material this theoretical approach will prove to not be feasible in the current numerical study.

Damage initiation

Damage initiation in the pure tensile or pure shear mode is defined by the normal contact stress and the shear contact stress at which the linear-elastic range of the interface response ends. This means that the damage initiation starts when the elastic range ends. In the Abaqus model, the normal tensile stress is represented as , and for the shear stress, a distinction is made between shear in the first direction and the second direction . In this study, only shear in the first direction is of importance. However, due to the 3D nature of the model, shear properties for both shear directions must be defined. Therefore, equal values will be assigned to both shear directions.

Damage Evolution

The damage evolution of the interface is defined by the plastic range of the traction-separation and shear-sliding law of the constitutive model. The default traction-separation and shear-sliding law in Abaqus is presented by a bi-linear model. However, it is also possible to define a user-defined constitutive model. For both methods different parameters are defined. Both methods and their parameters will be briefly explained here.

Bi-linear traction-separation and shear-sliding law:

For the bi-linear constitutive model an energy-based approach is utilized to model how damage propagates in the interface. This method takes into account the fracture energy necessary to advance a crack for each fracture mode—opening (Mode I), sliding (Mode II), and tearing (Mode III). While only Mode I and Mode II are pertinent to the current study, Mode III has also been included for the model’s completeness.

In this study, a linear softening law is assumed, meaning that the traction-separation relationship decreases linearly from the peak traction to zero as separation displacement increases. The magnitude and slope of the linear softening region are determined by the fracture energy for each specific mode, which represents the area under the curve of the traction-separation or shear-sliding curve. This behavior is characterized by a gradual reduction in material stiffness, indicating a uniform decrease in the traction force corresponding to increasing displacement.

User-defined traction-separation and shear-sliding law:

The user-defined constitutive model utilizes a displacement-based approach to simulate damage prop-

agation within the interface. In this method, a traction-separation model and a shear-sliding model are manually defined, allowing for a more precise characterization of the interface's response. Damage variables are calculated for intermediate points along the curves of these models, capturing the evolution of damage as the loading conditions change.

By incorporating these damage values along with their corresponding displacement values—whether related to separation or sliding—Abaqus can effectively utilize this input to define the constitutive behavior of the interface.

Mixed-mode damage initiation and evolution

To define the damage initiation in the interface in case of a combined loading in tension and shear, the quadratic traction criterion, as recommended by [8], is utilized. This criterion determines when damage begins by assessing the quadratic interaction function involving the nominal stress ratios. Damage is considered to initiate when this function reaches a value of one. The criterion is mathematically expressed as:

$$\cdot\square^2 + \cdot\square^2 + \cdot\square^2 = 1 \tag{4.2}$$

where:

- is the normal contact stress in the pure normal mode,
- is the shear contact stress along the first shear direction,
- is the shear contact stress along the second shear direction,
- , , and are the corresponding maximum traction values.

The quadratic traction criterion assumes that damage factors are not activated under pure compression states and treats allowable shear stresses as independent of normal stress. However, this approach may not fully capture the behavior of concrete-to-concrete interfaces, where compressive normal stress can enhance shear strength [8]. This limitation could affect the results if the interface design involves compression. Nonetheless, for straight tabs, where no significant compressive normal stress is present, this criterion is still applicable.

For cases involving combined loading in tension and shear, resulting in mixed-mode loading where multiple fracture modes interact, a linear relation between the different modes is used. In the case of the bi-linear constitutive models the Benzeggagh-Kenane (BK) model is utilized with a BK exponent of 1.0 to ensure this linear blending of the contributions from various fracture modes.

For reference, Figure 4.8 illustrates both a quadratic nominal stress criterion and a mixed-mode fracture criterion. It is important to note that, in contrast to the linear model used in this study, the example shown in the figure employs a non-linear relationship between the fracture modes.

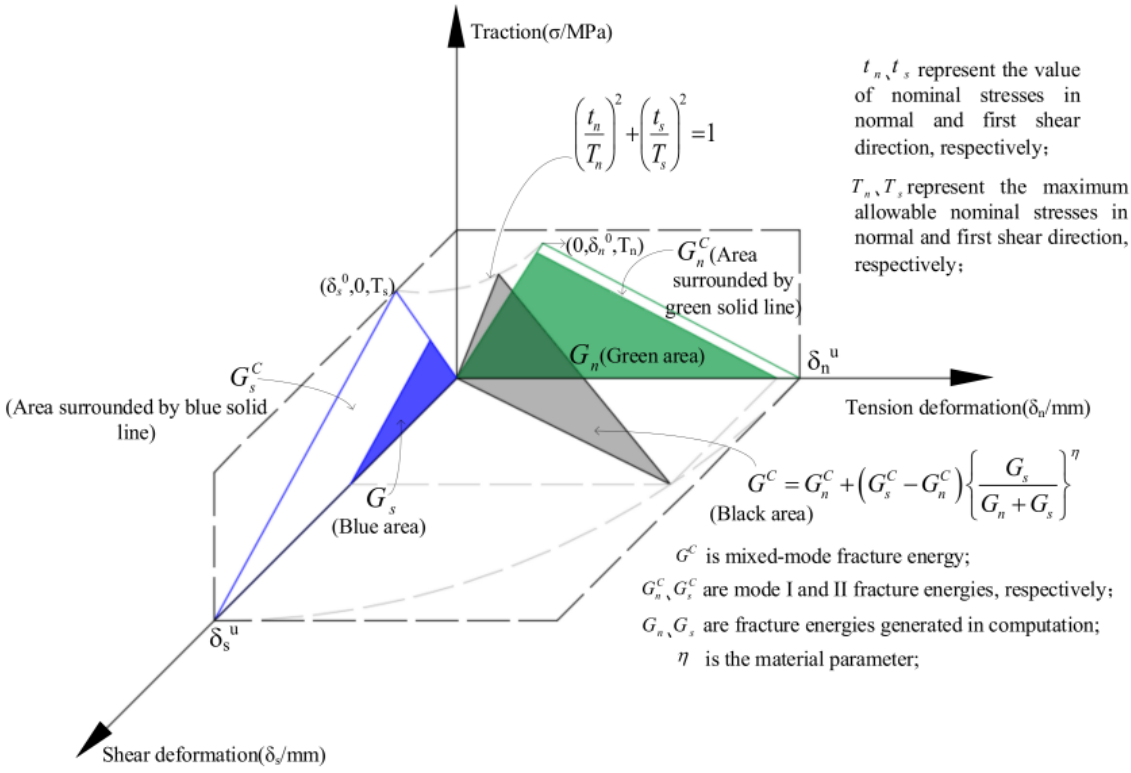

Figure 4.8: "The quadratic nominal stress criterion and mixed-mode fracture criterion."[34]

Interface damage variable

The damage variable CSDMG in Abaqus quantifies the degradation of the interface. For linear softening, CSDMG is calculated based on the stiffness degradation during the fracture process. As loading progresses, the effective traction decreases linearly from the peak traction $_0$ at the onset of damage (^{0}) to zero at complete failure ()). The damage variable increases from 0 at (^{0}) to 1 at (), indicating full degradation of the material stiffness. Abaqus calculates the CSDMG as follows:

$$= \frac{(- {}^0)}{(- {}^0)} \tag{4.3}$$

where refers to the maximum value of the effective separation attained during the loading history [1]. This approach ensures that the damage represents the stiffness material degradation as the crack propagates [24]. The definition behind the damage law as explained above is presented in Figure 4.9. The progression of the damage variable is presented in Figure 4.10. Additionally, for the tensile traction-separation law of the original interface used later in the parametric study, the damage evolution is illustrated in Figure 4.11. It is observed that, despite the relatively high traction, the damage parameter is already approaching a value of 1.0 at a separation of 0.05mm. This suggests that while the tensile interface damage remains a useful indicator for identifying the onset of interface damage in the subsequent parametric study, it is not a reliable measure of the remaining stress-transfer capacity. The exception occurs when the damage parameter reaches a value of 1.0, indicating that the interface is fully damaged and can no longer transfer any stresses.

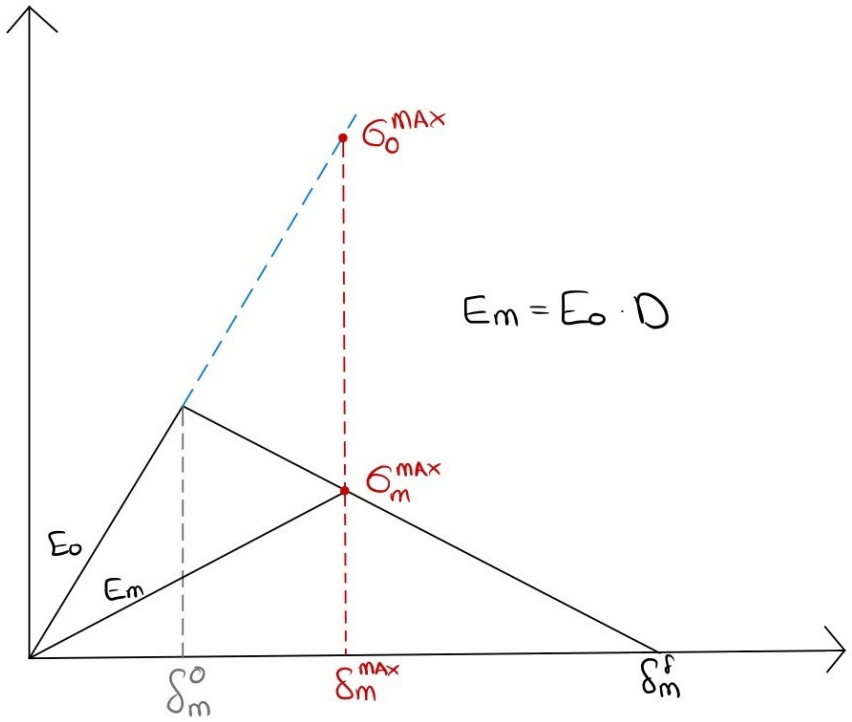

Figure 4.9: Definition of interface damage. Damage represents the magnitude of stiffness degradation.

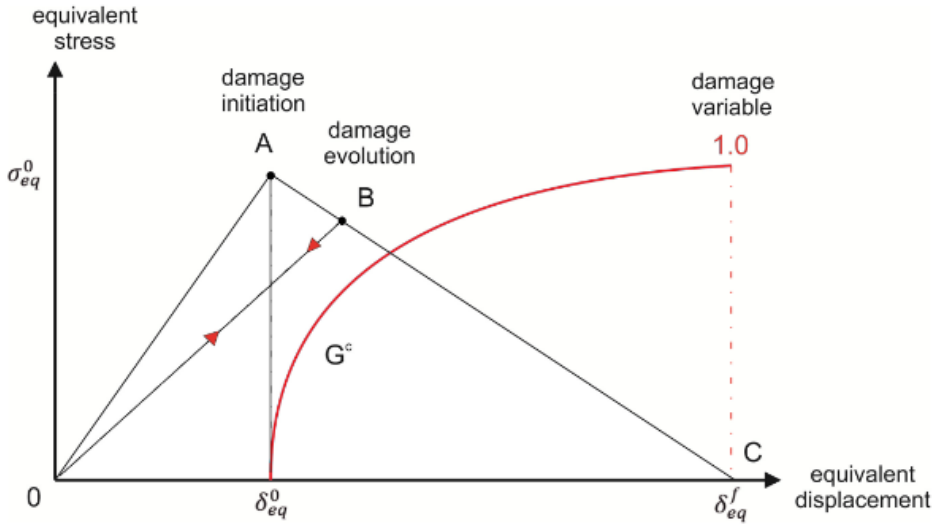

Figure 4.10: ”Traction-separation law-progressive failure analysis.” [24] Here ^{0} represents ^{0} and represents .

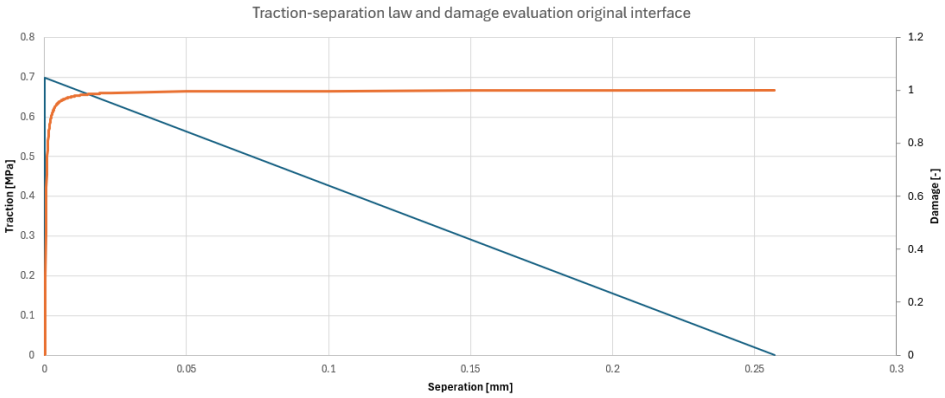

Figure 4.11: Traction-separation law-progressive failure analysis for the traction-separation law used in the original case of the parametric study in this thesis.

Damage stabilization

To enhance the stability of the damage model, a small viscosity coefficient is introduced as part of the viscoplastic regularization. This technique allows for slight stress exceedances beyond the yield surface, effectively smoothing the damage evolution and mitigating convergence issues during the analysis. The application of this method, along with its benefits in terms of numerical stability, is further discussed in subsection 4.1.1.

Frictional behavior

In modeling the shear behavior of the interface, several key parameters have been defined to describe how shear forces and slip are managed between interacting surfaces. The shear behavior is characterized by two distinct stages.

Stage 1: Cohesion undamaged, friction inactive

In the first stage, cohesion is fully active, and no damage has occurred in the cohesive properties of the interface. At this point, the interface does not exhibit any frictional behavior; the shear stresses that develop are solely due to cohesive forces.

Stage 1: Cohesion damaged, friction active

In the second stage, some damage has occurred in the cohesive properties of the interface, although it may not yet be complete (i.e., damage is less than 100%). Once cohesion begins to degrade, frictional resistance is activated (see Figure 4.12, and the interface starts to resist further shear motion based on the defined frictional properties.

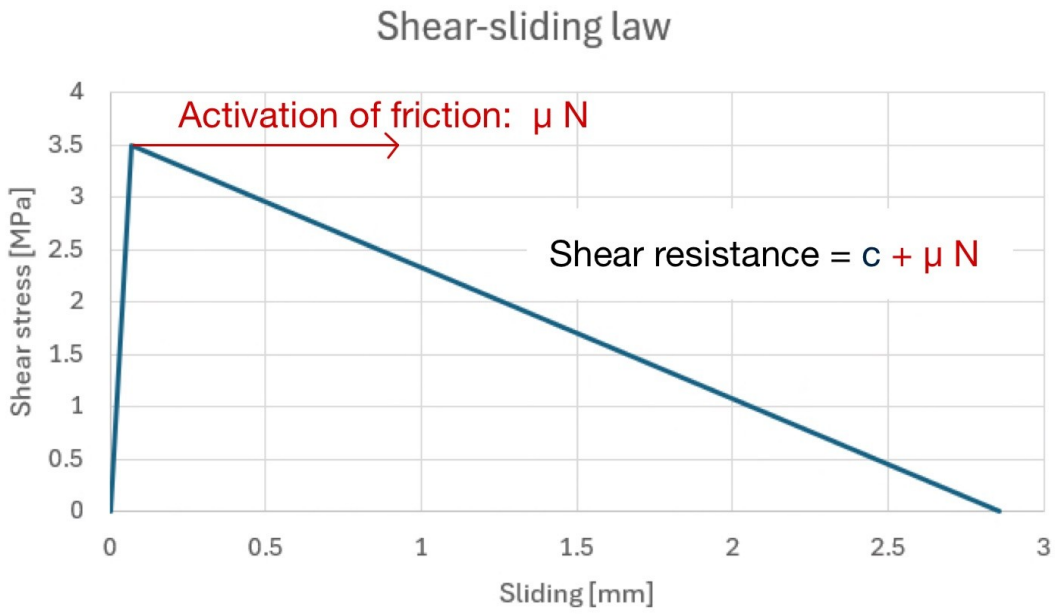

Figure 4.12: Effect of friction and cohesion on the shear resistance of the interface.

The input for friction in Abaqus is the friction coefficient, which determines the interface's capacity to withstand shear forces before sliding occurs solely due to friction. When examining the frictional behavior of the interface—distinct from its cohesive behavior-the shear stress limit is set to "No limit." This means that the interface does not impose an upper bound on shear stress, allowing shear stresses to theoretically increase indefinitely. This setting enables the transmission of substantial shear forces before failure occurs. Additionally, the elastic slip stiffness is set to "infinite," effectively preventing any slip between the surfaces under elastic conditions. While elastic behavior is allowed in the cohesive shear-sliding model, no elastic slip is associated with the frictional behavior.

4.3. Parametric study of the interface properties

In this research a parametric study has been done into the interface behavior of a single tab straight interface. For this parametric study the specimen design from Papoulidou [21] has been used for the straight tab interface with a width-over-height ratio of 1.0 (SCG2) (see Figure 4.13).

In the analysis the bottom part of the specimen is modeled using a meshsize of 3mm and the top part of the specimen is modelled using a meshsize of 1.5mm. All elements are hexagonal explicit elements with a linear geometric order. The different mesh sizes were chosen to reduce numerical issues during the analysis.

In the experimental analysis by Papoulidou [21], displacement was measured using an Linear variable differential transformer (LVDT) with an 80mm gauge length, whereas in this numerical analysis, the displacement was recorded over a 75mm length. This 5mm difference is noteworthy, especially if displacement extends throughout the entire specimen, as it could influence the overall measurement. However, since the displacement in this analysis is concentrated primarily around the interface, any discrepancy due to this variation would be limited to the linear-elastic deformation within that additional 5mm of concrete. Consequently, this difference should not significantly impact the comparison of results.

At the beginning of this master thesis, preliminary numerical analyses were conducted using Abaqus to gain familiarity with the finite element model. These initial analyses helped establish preliminary values for critical parameters related to tangential, normal, cohesive, and damage behavior. The de-

termined values, summarized in Table 4.2, were used to define the initial numerical model for the parametric study presented in the following section. In the table the values which have been changed throughout the parametric study are presented in red. For each of the parameters a much lower value and a much higher value have been used such that it is possible to see which effect this has in the extreme case. Only for the normal fracture energy just a much higher value has been used due to the already very low value of the initial normal fracture energy.

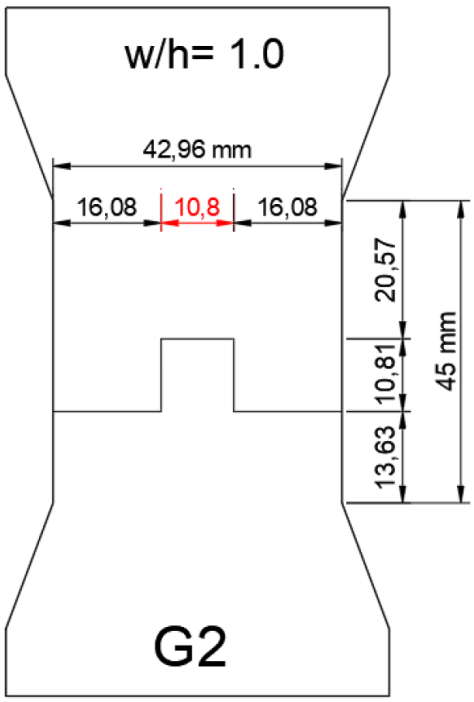

(a) Original design of the SCG2 specimen from [21].

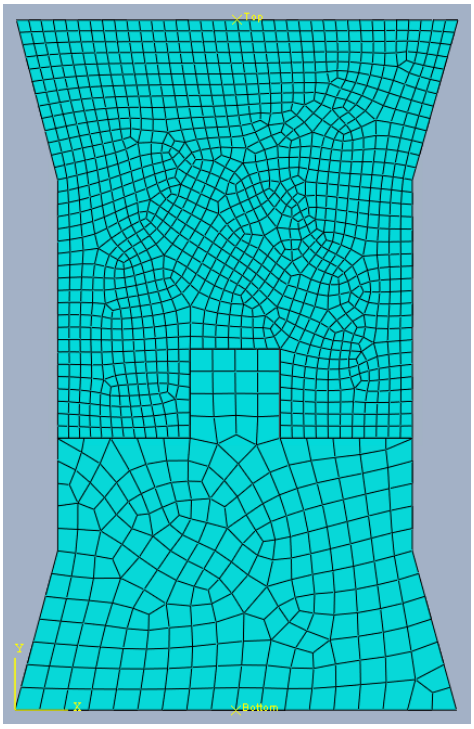

(b) Modelled equivalent of the SCG2 design in Abaqus.

Figure 4.13: Test specimen for the uniaxial tensile tests as modeled in Abaqus. The thickness of the specimen is 15 mm.

Contact Property	Parameter	Value	Unit
Tangential behavior	Friction coefficient	0.7	-
Tangential behavior	Shear stress limit	No limit	-
Tangential behavior	Elastic slip stiffness	Infinite (no slip)	-
Normal behavior	Pressure-overclosure	”Hard” Contact	-
Cohesive behavior	Knn (normal stiffness)	3000	MPa
Cohesive behavior	Kss (shear stiffness, 1st direction)	50	MPa
Cohesive behavior	Ktt (shear stiffness, 2nd direction)	50	MPa
Damage initiation	Normal contact stress ()	0.7	MPa
Damage initiation	Shear contact stress ()	3.5	MPa
Damage initiation	Shear contact stress ()	3.5	MPa
Damage evolution	Type	Energy	-
Damage evolution	Softening	Linear	-
Damage evolution	Mixed mode behavior	Benzeggagh-Kenane	-
Damage evolution	BK Exponent	1.0	-
Damage evolution	Normal Fracture Energy	0.09	N/mm
Damage evolution	1st Shear Fracture Energy	5	N/mm
Damage evolution	2nd Shear Fracture Energy	5	N/mm
Damage stabilization	Viscosity coefficient	0.0005	-

Table 4.2: Interface properties for the cohesive zone model in Abaqus analysis.

The objective of this parametric study is to explore the influence of each variable on the behavior of the SHCC-to-SHCC interface in detail. This study also aims to determine whether the different failure mechanisms identified in previous analyses can be accurately modeled, and to identify which parameters impact the occurrence of these mechanisms. Unlike the analytical approach, this study examines more than just variations in interface strength.

The full parametric study is presented in Appendix A, where each parameter is systematically varied to assess its specific effect on the mechanical response and failure mechanisms of the interface.

In this chapter, a detailed analysis is performed for the original interface configuration using the parameters specified in Table 4.2. Additionally, the chapter discusses the different failure mechanisms and identifies which parameters influence their occurrence.

Lastly, the implications of these findings are discussed, along with the limitations and their potential impact on the overall conclusions.

4.3.1. Original interface

The first step in the parametric study is investigating the behavior of the specimen with the interface parameters as defined in Table 4.2. In Figure 4.14 the force-displacement diagram of the analysis is shown, together with the locations of the different relevant steps. It can be seen that after step 35, the results become numerically unstable, therefore the choice has been made that in this analysis only steps 1-35 have been analysed.

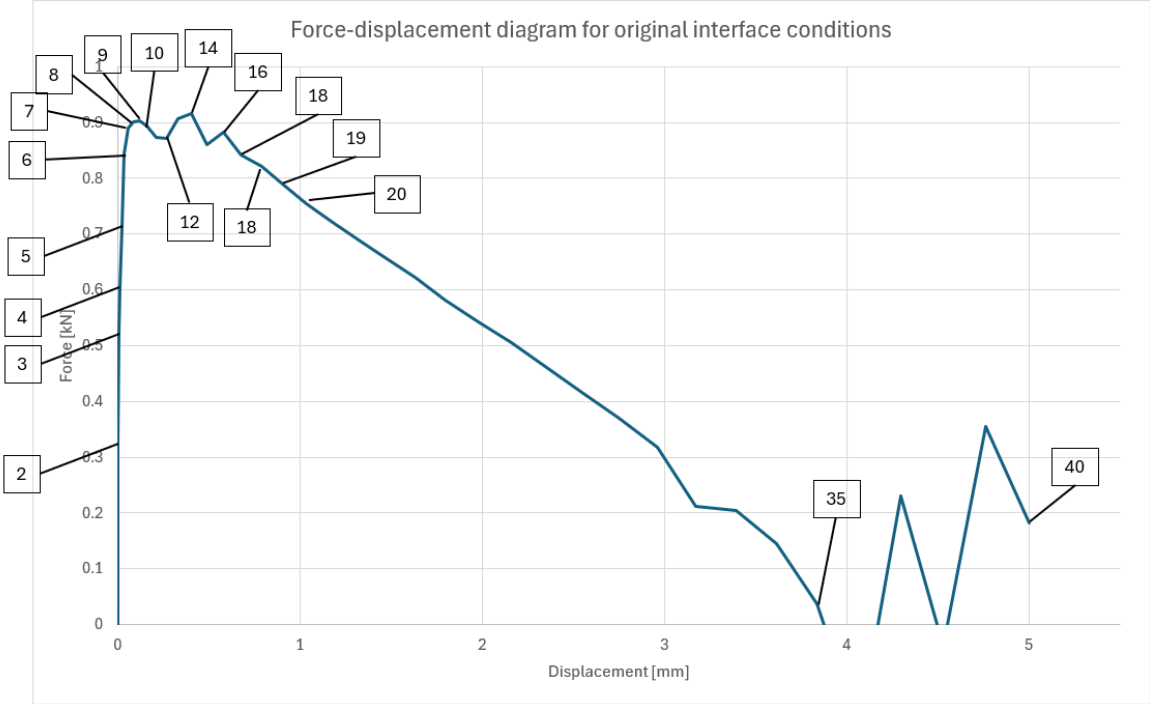

Figure 4.14: Force displacement diagram of the analysis with original interface conditions, with important steps identified for further analysis.

In Figure 4.15, the material's plastic strain throughout the analysis is presented. It can be seen from this output that the cracks start to form inside the tab at the bottom and at the top corners of the tab. When looking at the maximum principal stresses in the specimen at this stage, it can also be seen that the stresses are heavily concentrated around these areas (see Figure 4.16), complying with the locations of stress concentrations as defined in the analytical analysis. After this the plastic strain and thus the cracking behavior inside the material progresses mainly inside the tab at the bottom, additionally the plastic strain spreads out a bit further around the top corners and in the material underneath the tab. Even though the material sustains cracking around the interface, the material does not fail in tension. In the end the tab is pulled out (see step 35/40).

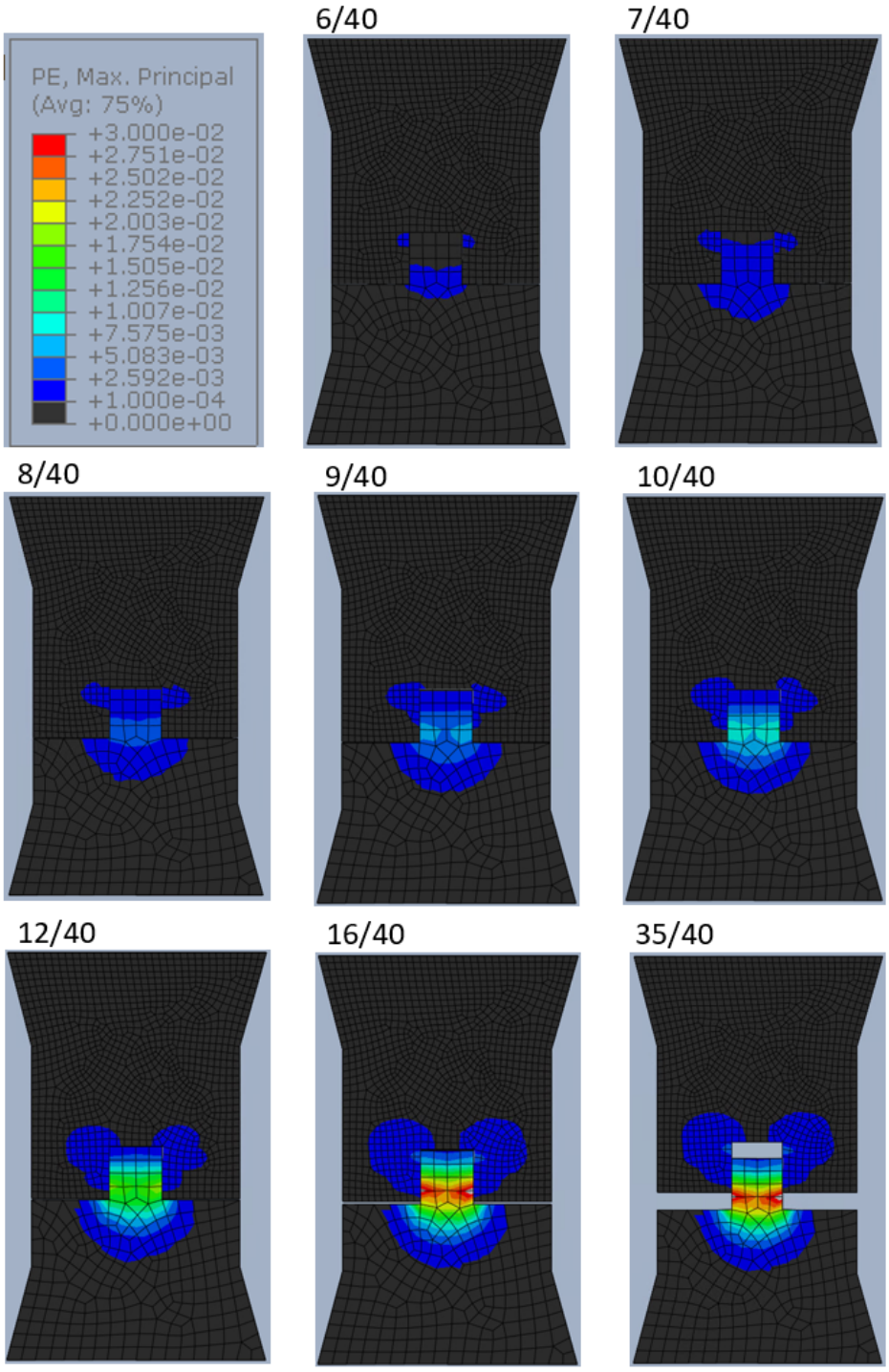

(a) Plastic strain values throughout the analysis with a color legend ranging from 0.0001 (0.01%) to 0.03 (3%).

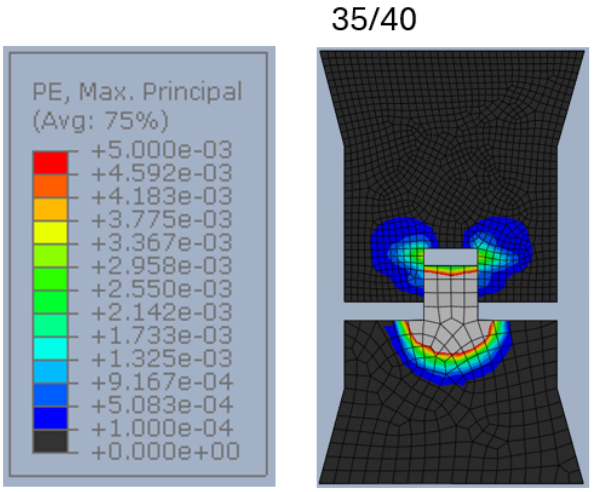

(b) Plastic strain values at step 35/40 with a color legend ranging from 0.0001 (0.01%) to 0.005 (0.5%).

Figure 4.15: Plastic strain values throughout the analysis of the specimen with original interface conditions.

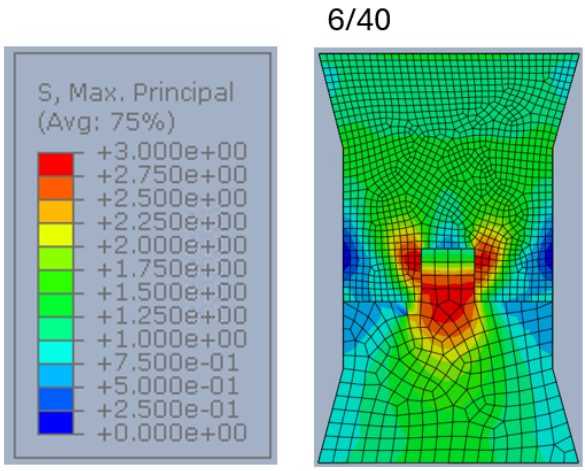

Figure 4.16: Maximum principal stress at step 6/40 of the specimen with original interface conditions.

The force which is applied at the top of the specimen is transferred through the interface between the top part of the specimen and the bottom part of the specimen. The failure mechanism has been identified as a pull-out failure. This means that the interface proves weaker than the material inside the tab. To further investigate this interface behavior, the interface damage evolution throughout the analysis is presented in Figure 4.17 for the interface under tensile loading and in Figure 4.18 for the interface under shear loading.

In the interface under tensile loading it is shown that the interface on top of the tab damages more heavily at the same step than the bottom surfaces of the interface. This is especially visible in step 3 and 4. Additionally it can be seen that the interface damage in tensile loading almost reaches a value of 1 before the vertical interface starts to damage.

For this vertical interface, the interface damage on one of the sides of the tab is investigated further (see Figure 4.18). The damage initially starts at the bottom of the tab, gradually develops towards the top, and eventually leaves only a small intact section in the middle, which is progressively compromised as well. It can be seen that the outer edges damage more quickly than the inner part, this indicates that for this interface design the thickness of the specimen, and especially the thickness of the tab, has a significant effect on the stress transfer mechanism in the vertical shear part of the tab.

The different distribution over the height of the tab can be attributed to the difference in slip values throughout the interface, which are shown for a few different steps in Figure 4.19.

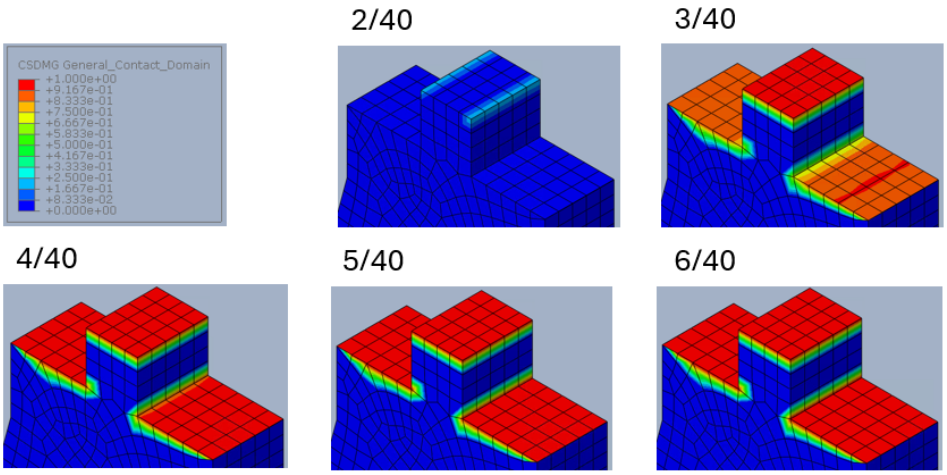

(a) Interface damage of the interface loaded in tension throughout the analysis with a color legend ranging from 0 (0%) to 1 (100%).

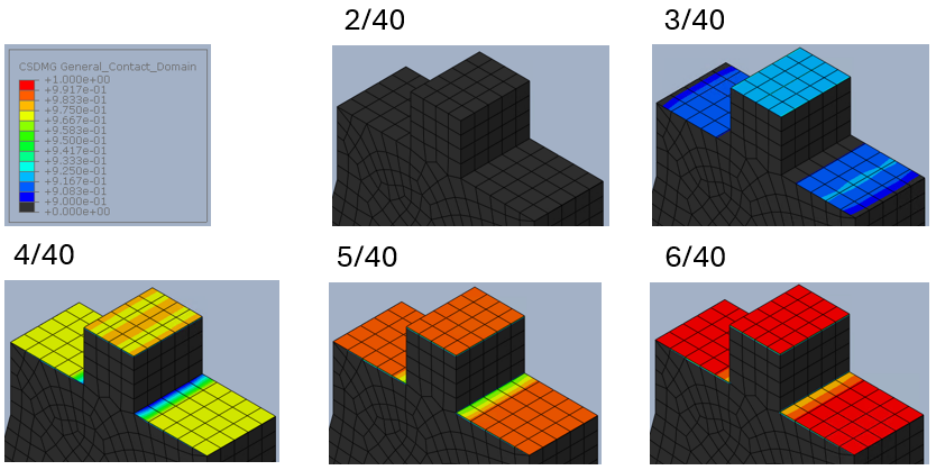

(b) Interface damage of the interface loaded in tension throughout the analysis with a color legend ranging from 0.9 (90%) to 1 (100%).

Figure 4.17: Interface damage of the interface loaded in tension throughout the analysis of the specimen with original interface conditions.

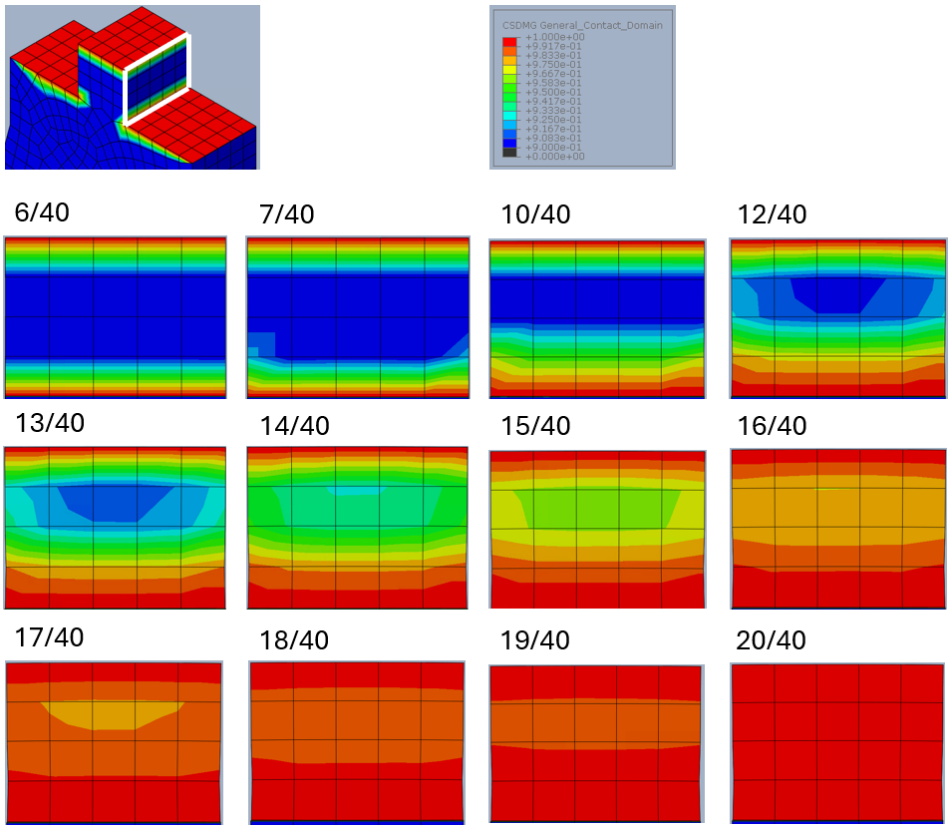

Figure 4.18: Interface damage of the interface loaded in shear throughout the analysis of the specimen with original interface conditions. Color legend ranges from 0 (0%) to 1 (100%).

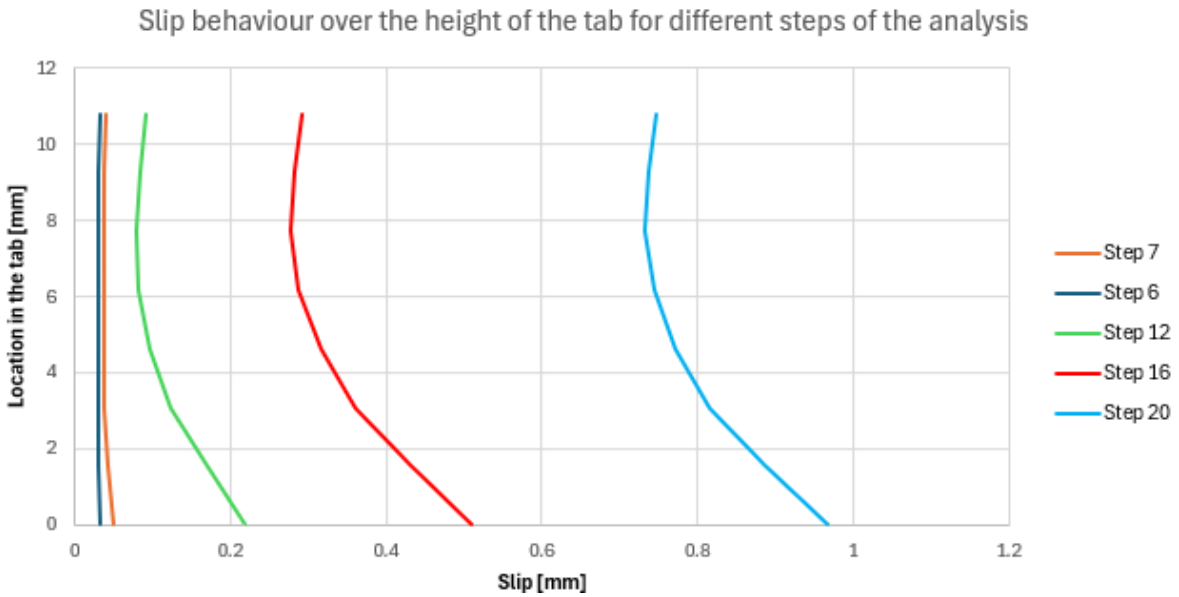

Figure 4.19: Slip over the height of the tab through different steps of the analysis.

Discussion: In the original configuration, the horizontal interface undergoes damage before the vertical interface, a sequence that aligns with the notable differences in stiffness and strength between the two interfaces. The shear stiffness of the interface is substantially lower than its tensile stiffness, and since the shear strength is also higher relative to the tensile strength, damage initiates at a lower

displacement in the tensile interface than in the shear interface. As a result, the horizontal interface sustains damage earlier than the vertical one.

The damage in the vertical interface does not develop uniformly, primarily due to the uneven slip behavior between the two surfaces. The slip distribution indicates that more slip occurs at the bottom of the tab, with a minimum in the middle and a slight increase towards the top. This suggests that the middle of the tab is most effective at transferring stresses, while the top and bottom are more susceptible to damage initiation.

This pattern of damage progression is visually represented in Figure 4.18, which illustrates the evolution of interface damage on the vertical surface throughout the analysis. Damage initially begins at the bottom of the tab, gradually progresses upward, and ultimately leaves only a small, intact section in the middle, which also becomes compromised over time.

Additionally, just before damage starts to manifest in the vertical interface (step 7/40), plastic strain begins to appear in the tab and at the top corners (step 6/7). This occurrence is attributed to the higher strain concentrations in these regions, exacerbated by stress concentrations at the tab corners. As shown in Figure 4.15, the plastic strain at the top corners and bottom of the tab continues to increase and spread throughout the specimen. Notably, while the plastic strain at the bottom of the tab increases significantly, it does not continue to grow between steps 16/40 and 35/40. Instead, the displacement of the top part of the specimen increases through a pull-out mechanism. This behavior indicates that, under the current interface configuration, the stresses transferred from the interface are insufficient to trigger a tab failure mechanism.

Using this originally defined interface behavior, the parametric study has been performed. The interface parameters are changed individually into a much lower and a much higher value to identify the influence of each parameter on the behavior of the interface connection. The parametric study showed that all five failure mechanisms which were identified in the analytical analysis can be predicted using different interface parameters. These different failure mechanisms and their modeled counterparts from the parametric study are further detailed in Appendix B.

4.4. Comparison to experimental results

After the parametric study had been performed, the insights from this parametric study on the influence of each interface parameter is used to refine the interface model for better alignment with experimental results. The improvement process is implemented in three stages:

1. **Tensile Interface Properties:** The tensile interface properties are calibrated based on a direct tensile test of a concrete-to-SHCC interface reported by [28], where SHCC served as the substrate material.
2. **Shear Interface Properties:** The shear properties of the interface are further optimized to accurately represent an experimental test from [21], involving a single tab with a width-to-height ratio of 1.5.
3. **Model Verification:** Finally, with the redefined interface properties, the model is verified using a test with a different geometry—a width-to-height ratio of 1.0—also from [21].

It is essential to note that during the optimization process, the material model itself remains constant; only the interface model is modified.

4.4.1. Tensile Interface Properties.

The first step in defining an effective interface model is to establish the tensile interface variables that play a critical role in the uniaxial tensile test. This test, originally performed by Stander [28], was conducted on a horizontal scraped surface interface. Importantly, Stander also investigated the effect of moistening time on the first part of the specimen before casting the second part, leading to the development of two distinct specimen types for the scraped surface treatment: one with a 14-day curing time and a 10-minute moistening period (S1410), and another with a 14-day curing time and a 24-hour

moistening period (S1424).

To accurately capture the tensile behavior of the interface under a mode I tensile load, a bi-linear constitutive model is used. Key parameters in this constitutive model, such as the normal stiffness (Knn), the maximum normal contact stress (), and the normal fracture energy play an important role.

To properly define the normal interface stiffness coefficient, the interface material stiffness should be divided by the physical thickness of the interface. However, as will be explained in detail in subsection 4.4.2, a user-defined shear-sliding law will be employed to model the shear behavior of the interface. This approach presents a numerical challenge when very high stiffness coefficient values are combined with relatively low interface strengths. Such a combination leads to instability in the numerical model, as the large stiffness values create abrupt changes in the force-displacement response, making it difficult to obtain reliable results.

To avoid this issue, the tensile interface stiffness will be set to a more manageable value of 400 MPa/mm. This lower stiffness allows for a smoother and more stable simulation of the interface behavior.

The values for the tensile strength () and the normal fracture energy were derived from the uniaxial tensile tests conducted by Stander, and the corresponding test setup was recreated in Abaqus for numerical analysis. The original test design is illustrated in Figure 4.20a, while the modeled equivalent in Abaqus is shown in Figure 4.20b.

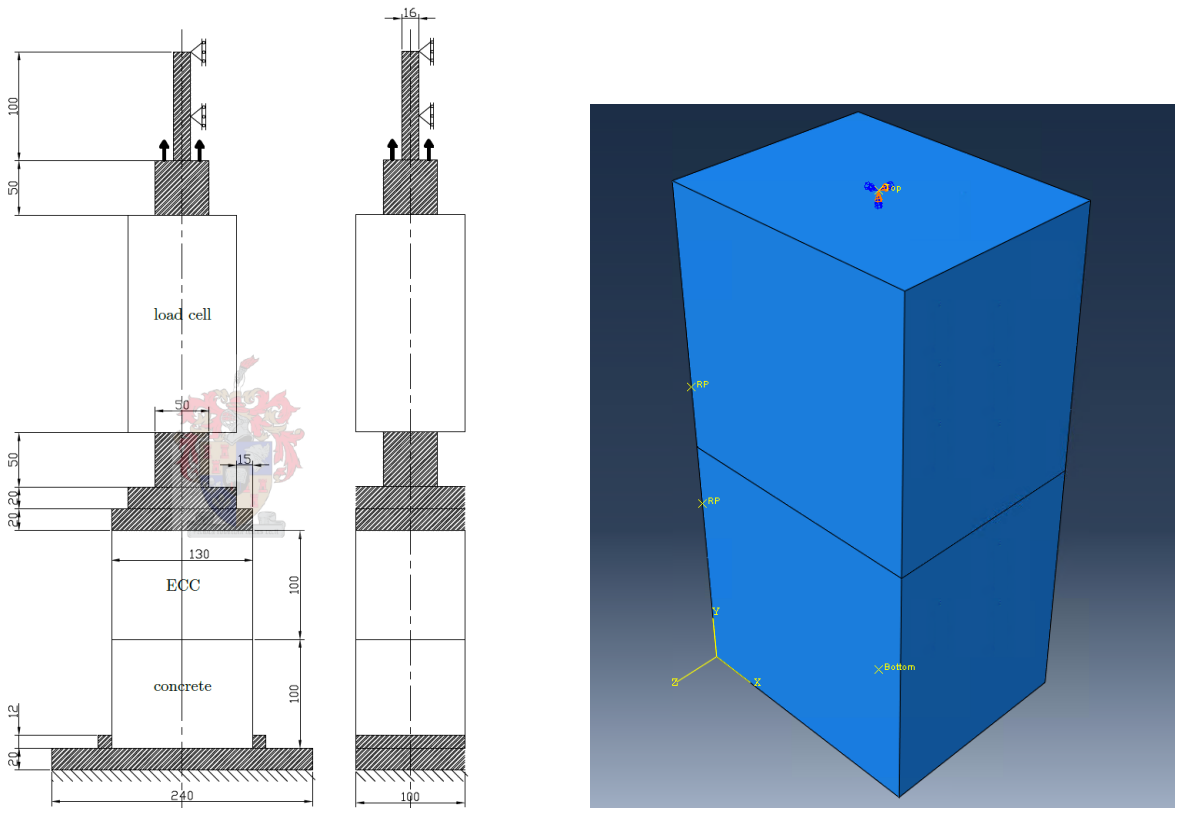

(a) Tensile test setup design [28].

(b) Tensile test specimen modeled in Abaqus.

Figure 4.20: Tensile test setup as designed for experimental analysis [28] and its modeled equivalent in Abaqus.

In determining the initial estimates for these interface variables, average values from both the S1410 and S1424 specimens were used. The experimental results for these tensile tests, as reported by Stander, are depicted in Figure 4.21. These results served as the basis for selecting the initial values for the interface parameters in the numerical model. Subsequent tuning of these parameters was performed to ensure that the numerical results closely matched the experimental outcomes. The tuned

parameters are summarized in Table 4.3, with the corresponding traction-separation law visually represented in Figure 4.22.

SSPT	$f_{t,i}$ [MPa]	COV [%]	G_f^I [N/mm]
SB724	0.43	6.9	0.052
R1410	0.1	-	0.0065
S1410	0.6	13.2	0.11
S1424	0.625	2.2	0.06
SB1410	0.798	22.5	0.662
SB1424	0.835	16.1	0.46
DH1424	0.664	10.1	0.624
PG1424	0.71	29.0	0.079
R2810	0.087	0.21	0.077
R2824	-	-	-
SB2810	> 1.1	-	-
SB2824	> 0.919	-	-

Figure 4.21: Tensile parameter values obtained from experiments performed on the various substrate surface preparation techniques [28].

Contact Property	**Parameter**	**Value**	**Unit**
Cohesive behavior	Knn (normal stiffness)	400	MPa
Damage initiation	Normal contact stress ()	0.7	MPa
Damage evolution	Normal Fracture Energy	0.1	N/mm

Table 4.3: Interface properties for the cohesive zone model in Abaqus analysis determined using the experimental results from [28].

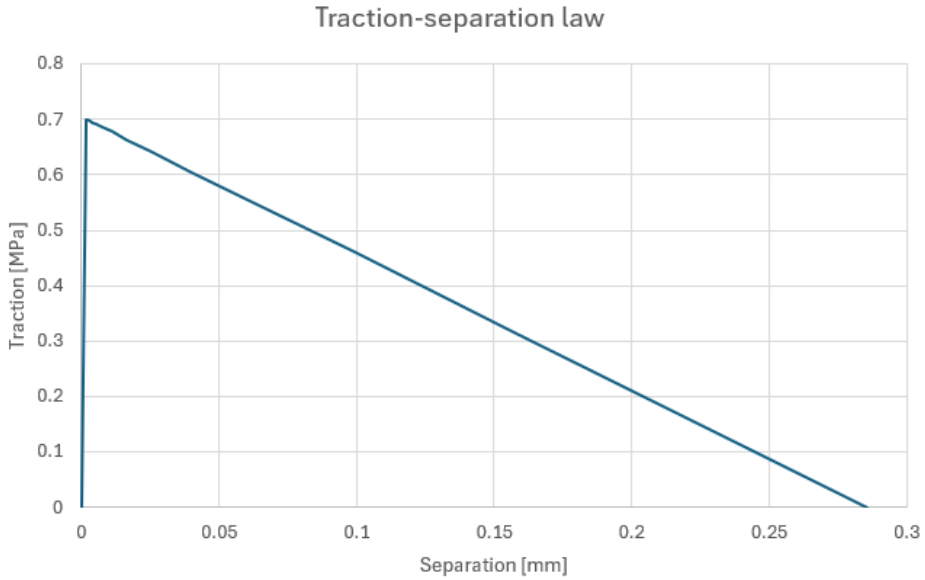

Figure 4.22: Traction-separation law for the tensile interface variables matching the experimental results.

The results for the scraped surface specimens (S1410 and S1424) are shown in Figure 4.23, with the black dotted line representing the numerical analysis conducted in Abaqus. The close alignment between the numerical and experimental results demonstrates that the tensile properties of the interface model have been accurately verified. It is worth noting that the average maximum tensile stress over the entire interface area (approximately 0.57 MPa) is slightly lower than the maximum tensile stress defined in the interface properties (0.7 MPa).

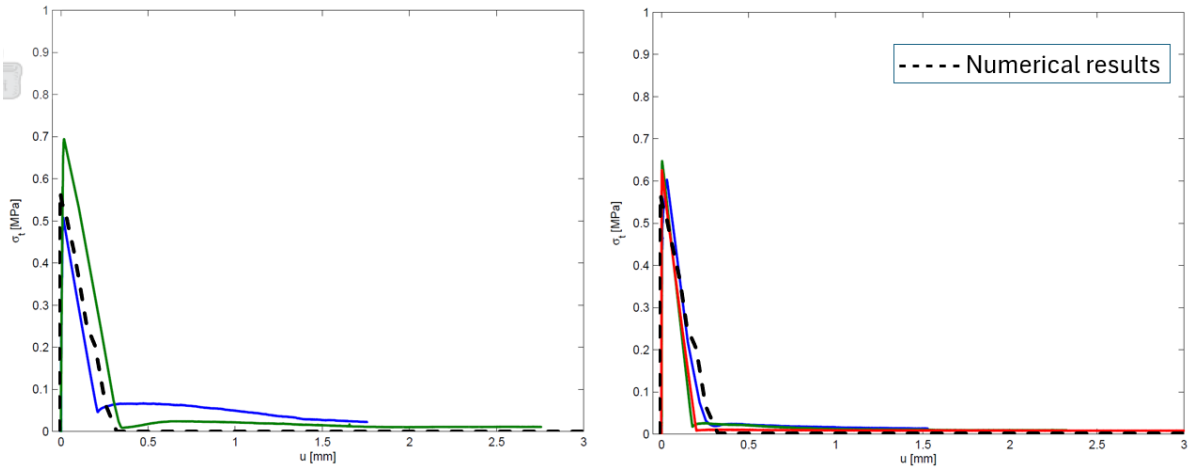

Figure 4.23: Tensile stress plotted against vertical displacement for (a) S1410 and (b) S1424 specimens [28], with the black dotted line representing the numerical result.

4.4.2. Shear Interface Properties

The second step in defining an effective interface model is to define the left-over parameters. These left-over parameters all play a role in the shear interface behavior and are as follows:

1. Friction Coefficient
2. Shear-sliding law

The first parameter to define is the friction coefficient. For this parameter, the value given by the PCI's Design Handbook [9] is used. PCI's Design Handbook says the concrete-to-concrete friction co-

efficient for dry conditions is 0.80 [9].

Tri-linear shear-sliding law

In contrast to the bi-linear shear-sliding law which has been used in the parameter study earlier in this chapter, for the tuning of the shear interface parameters a user-defined tri-linear shear-sliding law has been defined. This has been chosen such that even with lower shear strengths a high deformation capacity of the interface at the initial stage of the shear-sliding law can be reached.

For defining the input for the tri-linear shear-sliding law, the experimental research performed by Papoulidou [21] is used. In that research, Papoulidou [21] combined a horizontal and vertical interface by using a single tab in the interface. In this part of defining the interface variables, the straight tab interface with a width-over-height ratio of 1.5 (SCG1) (see Figure 4.24) has been used. In the experimental analysis, three different failure mechanisms were identified in the three tested specimen with a width-to-height ratio of 1.5. In one of the specimen, the failure mechanism clearly shows in plane bending due to specimen imperfections, therefore this specimen result is not used in this analysis. Another specimen shows very big discrepancies between the Linear variable differential transformer (LVDT) and digital image correlation (DIC) data, which also indicates a possible problem with specimen imperfections. Therefore, for the optimization of the shear interface properties, the specimen is used which represents the most stable results (see Figure 4.25).

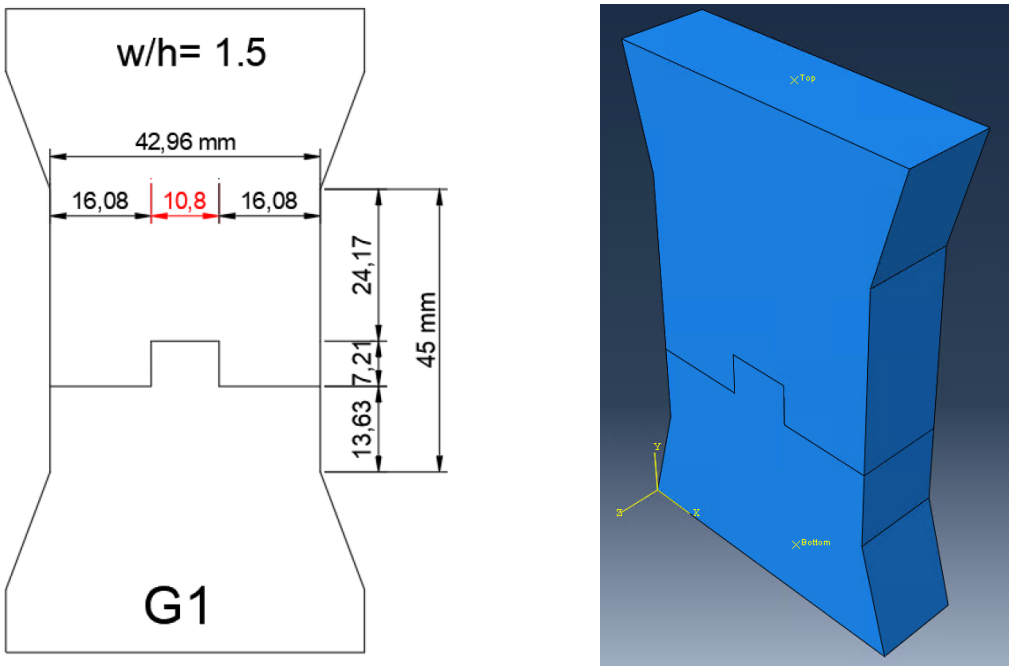

(a) Original design of the SCG1 specimen from [21].

(b) Modelled equivalent of the SCG1 design in abaqus.

Figure 4.24: Test specimen for the uniaxial tensile tests as modeled in Abaqus.

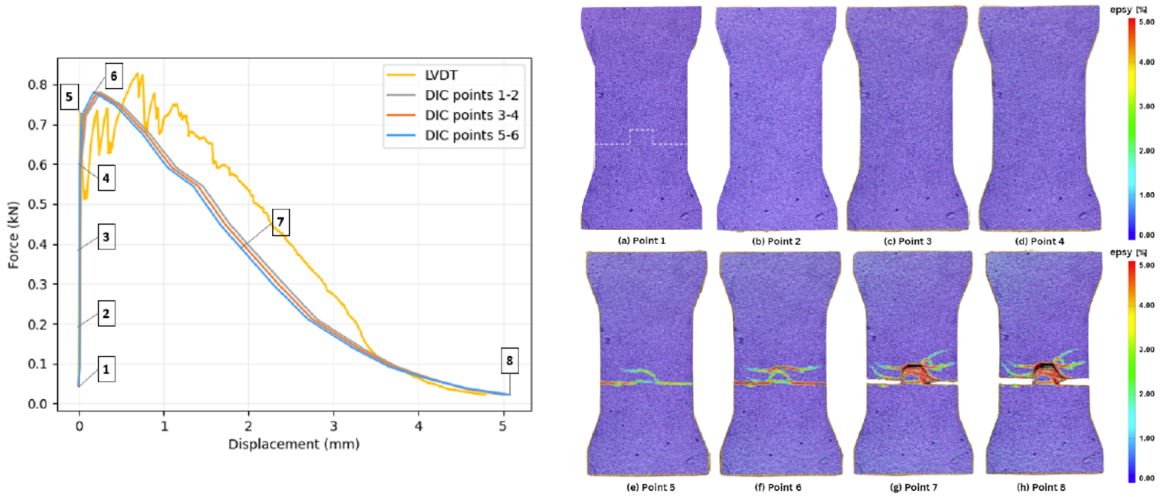

Figure 4.25: Results from the uniaxial tensile test of the the SCG1 specimen from [21], with left the force-displacement diagram and right the strain contours from the DIC analysis.

The shear sliding law was calibrated to closely align the force-displacement results of the numerical direct tensile test with those of the experimental direct tensile test described in [21].

The shear stiffness coefficient is calculated from the tensile stiffness, defined in the previous section, using the relationship between shear and tensile stiffness (see equation below). This ensures that the interaction between the normal and shear components remains balanced while avoiding numerical difficulties.

$$= \frac{}{2\ (1+\ )} = \frac{400}{2\ (1+0.2)} = 166.667/ \tag{4.4}$$

where E represents the tensile stiffness and represents the Poisson's ratio which is equal to 0.2 for concrete.

The final form of this user-defined shear sliding law is illustrated in Figure 4.26. By fine-tuning this constitutive law, it ensures that the model accurately captures the force-displacement response observed in the experiment.

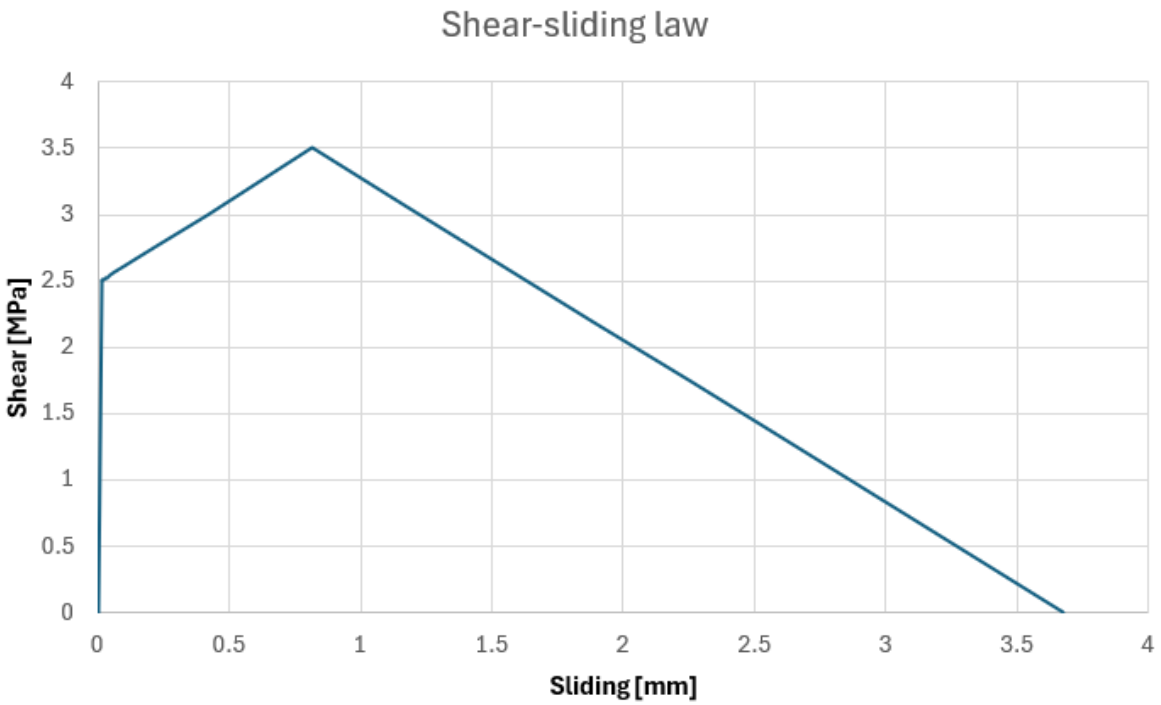

Figure 4.26: The user-defined shear-sliding law with a maximum shear contact stress of 2.5 MPa and a bridging shear contact stress of 3.5 MPa and a total fracture energy of 7.5 N/mm.

The results obtained for the SCG1 specimen, which employs this custom-defined shear sliding law in combination with the traction-separation law outlined in the previous section, are displayed in Figure 4.27. In this figure, specific stages from the experimental analysis are aligned with corresponding stages in the numerical analysis, offering a direct comparison between the two. At these stages the plastic strain distributions from the numerical analysis are shown to facilitate comparison with the DIC results from [21], which are also presented in the same figure.

In the force-displacement graph, the numerical analysis shows an initial peak at around 0.9 kN, which then drops to approximately 0.62 kN before the force rises again to about 0.8 kN and gradually declines to zero. Comparing this to the experimental data, we see that the prominent first peak observed in the numerical analysis is not reflected to the same extent in the experimental results. However, the second peak and subsequent force reduction closely match the experimental LVDT measurements, providing a similar post-peak trend. Toward the end of the simulation, some numerical instability appears, but the general trend still aligns well with experimental observations, reinforcing the model's reliability.

To compare the fracture pattern from the experimental analysis with the fracture pattern in the numerical analysis, the plastic strain distribution from the model is used. It can be seen that throughout stages 1 to 4, there is no plastic damage in the SHCC material in the numerical analysis, mirroring the absence of cracks in the experimental specimen at these stages. By stage 6, plastic damage begins to appear inside the tab and at the top corners in the surrounding material, a pattern also observed in the experimental specimen where cracks start to develop in the tab and two crack lines emerge at the tab's top corners in the surrounding material.

At stage 7, plastic strain in the numerical model intensifies, especially around the top corners of the tab and along its sides, mirroring the experimental specimen where cracks propagate along the tab's sides and adjacent areas near the top corners. By stage 8, plastic strain continues to increase at the top and sides of the tab in the numerical model. However, the experimental results show only minimal crack progression between stages 7 and 8, indicating a slight discrepancy in crack development timing between the numerical and experimental analyses. Furthermore, while the experimental specimen displays significant cracking in the material surrounding the tab, plastic strain remains comparatively low in this area within the numerical model, particularly on the left side of the tab.

Overall, the results from the force-displacement diagram and the distribution of damage in the specimen show a strong correlation between the numerical and experimental outcomes, indicating the model's ability to accurately replicate physical behavior of the SCG1 specimen.

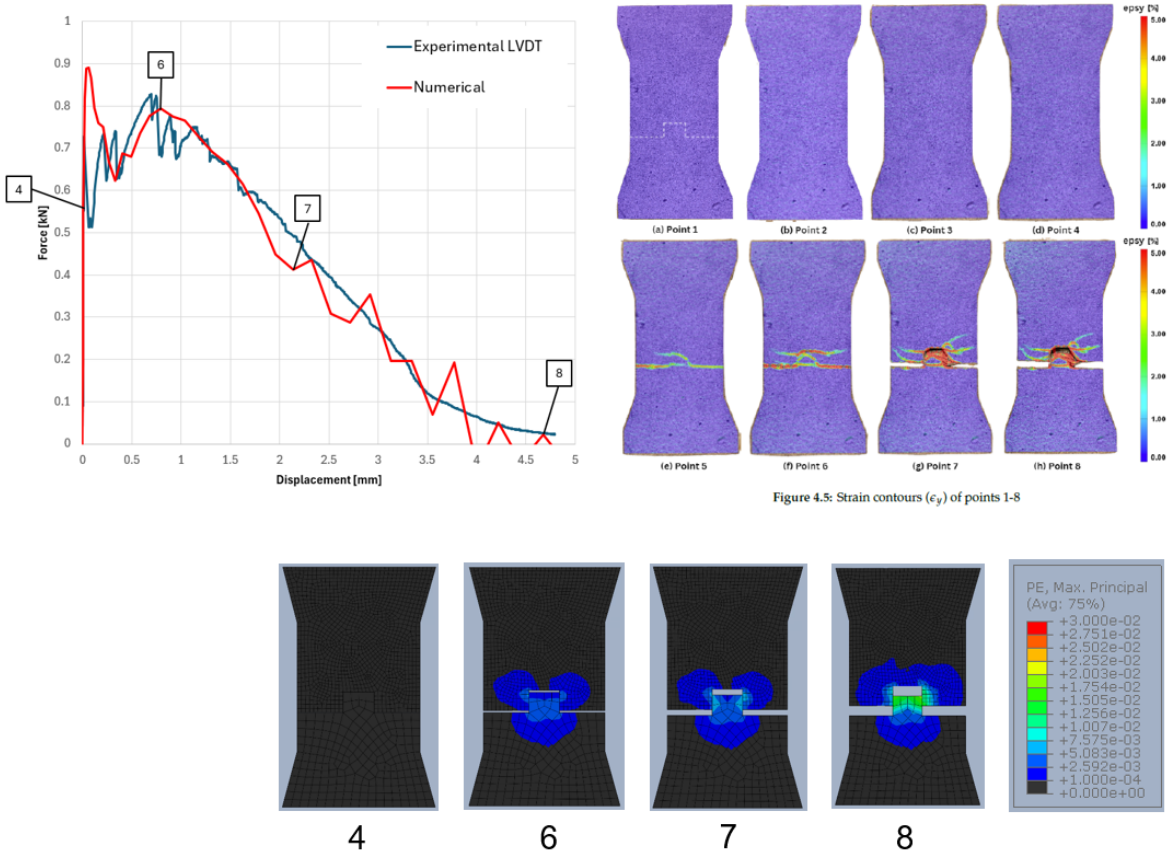

Figure 4.5: Strain contours (ϵ_y) of points 1-8

Figure 4.27: Results from the analysis of specimen SCG1 with the tri-linear shear-sliding law and the optimized traction-separation compared to the experimental results from [21].

Comparison between bi-linear and tri-linear shear-sliding law

As reference to why a tri-linear shear-sliding law has been defined, the same analysis is performed but then with a bi-linear shear-sliding law. For this bi-linear shear-sliding law the same values for shear stiffness coefficient, maximum shear stress and fracture energy (total area under the curve) have been used. Both the bi-linear and tri-linear shear-sliding law are presented in Figure 4.28.

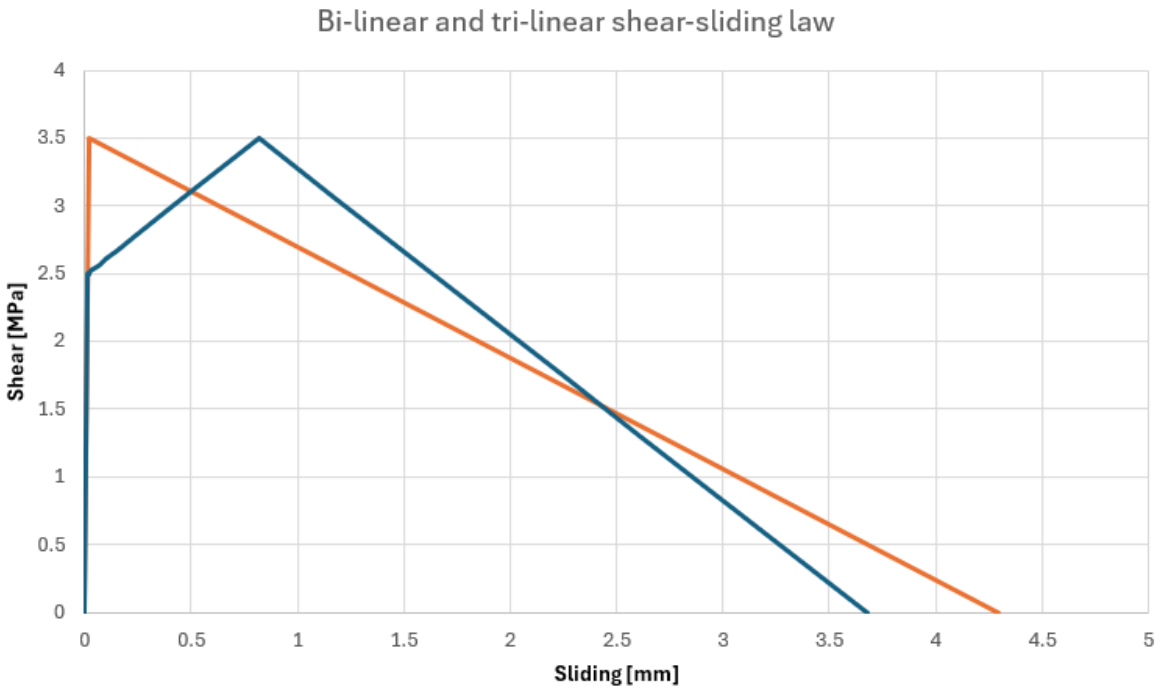

Figure 4.28: Bi-linear and tri-linear shear-sliding law input.

The results obtained from using the bi-linear shear-sliding law are presented in Figure 4.29.

In the force-displacement diagram, the initial peak force is consistent with that observed in the analysis utilizing the tri-linear shear-sliding law, indicating that the initial behavior of the interface remains largely unaffected by the change in shear-sliding law. However, differences in behavior become evident after this initial peak. Following the drop after the first peak, the force rapidly increases again, reaching approximately 0.77 kN, before dropping and continuing to decline until the end of the analysis. Notably, the total displacement capacity of the modeled interface is comparable to that of the tri-linear model. However, the second peak exhibits minimal hardening behavior, and the drop in force occurs significantly earlier in the analysis. The displacement capacity is obtained due to the more gradual slope of the force-displacement curve compared to the same slope in the tri-linear analysis.

Again to compare the fracture response, the plastic strain is used. There the earlier onset of interface damage is further reflected. At point 6, corresponding to the second peak, the plastic strain within the connection has nearly reached its maximum development, indicating that minimal additional stresses will be transferred, and little further material damage will occur. In contrast, at the same point in the tri-linear model, the plastic strain is not yet fully developed and will continue to evolve. This suggests that stresses will still be transferred after the second peak, leading to increased damage in the material within the tab.

When compared to the experimental results from [21], a similar trend is observed. At the peak force, not all cracks in the material have formed, and cracking continues beyond this point. Moreover, the hardening behavior seen in the tri-linear interface is also evident in the experimental results, reinforcing the consistency between the numerical model and empirical observations.

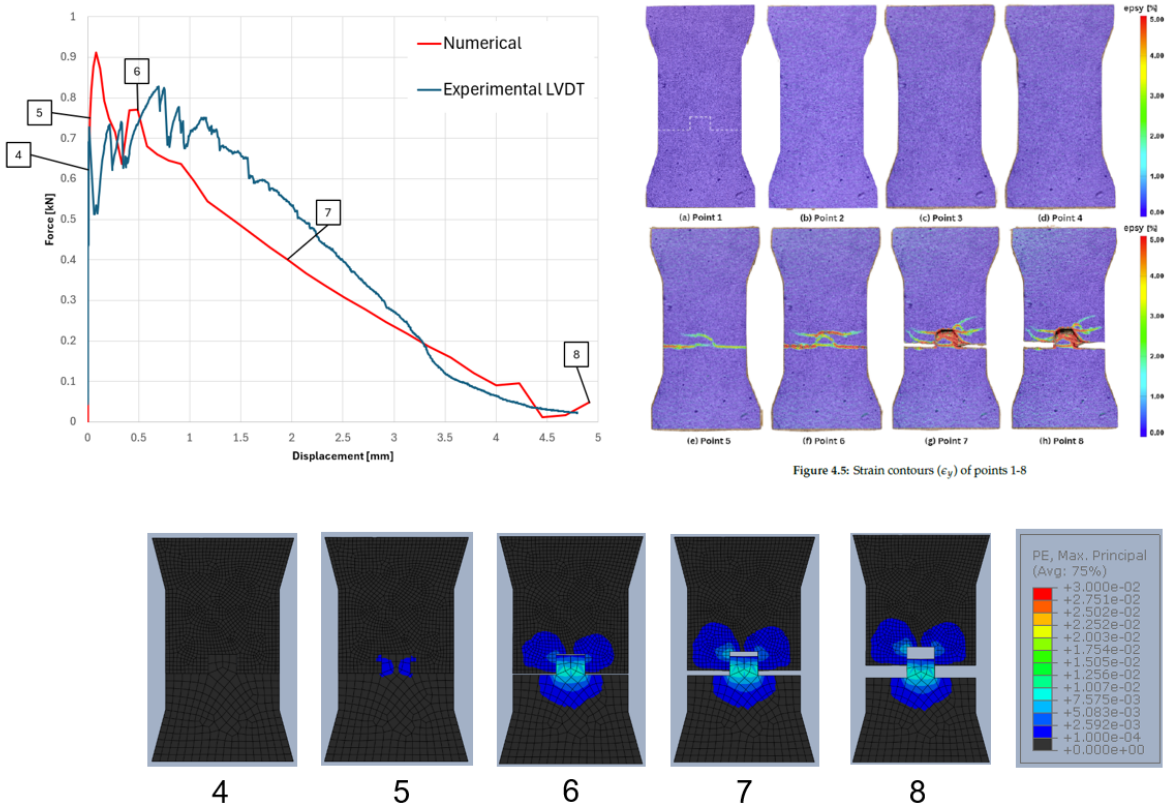

Figure 4.5: Strain contours (ϵ_y) of points 1-8

Figure 4.29: Results from the analysis of specimen SCG1 with the bi-linear shear-sliding law and the optimized traction-separation compared to the experimental results from [21].

Summary of interface parameter values Finally all the interface parameters as defined in the final interface model are summarized in Table 4.4. The softening and mixed-mode behavior are user-defined. Which means in Abaqus that they are part of the user-defined input. The mixed-mode behavior is linear, as discussed previously and the constitutive law is tri-linear.

Contact Property	Parameter	Value	Unit
Tangential behavior	Friction coefficient	0.8	-
Tangential behavior	Shear stress limit	No limit	-
Tangential behavior	Elastic slip stiffness	Infinite (no slip)	-
Normal behavior	Pressure-overclosure	”Hard” Contact	-
Cohesive behavior	Knn (normal stiffness)	400	MPa/mm
Cohesive behavior	Kss (shear stiffness, 1st direction)	166.667	MPa/mm
Cohesive behavior	Ktt (shear stiffness, 2nd direction)	166.667	MPa/mm
Damage initiation	Normal contact stress ()	0.7	MPa
Damage initiation	Shear contact stress ()	2.5	MPa
Damage initiation	Shear contact stress ()	2.5	MPa
Damage evolution	Type	Displacement	-
Damage evolution	Softening	User-defined (Tabular)	-
Damage evolution	Mixed mode behavior	User-defined (Tabular)	-
Damage evolution	Mode mix ratio	Energy	-
Damage stabilization	Viscosity coefficient	0.0005	-

Table 4.4: Interface properties for the cohesive zone model in Abaqus analysis.

4.4.3. Model Verification

The final step in evaluating the performance of the continuum smeared cracking model in Abaqus for modeling an SHCC-to-SHCC interface with geometric enhancements is to verify if, in cases where tab failure occurs experimentally, the numerical analysis accurately predicts both the failure mechanism and the post-peak behavior. To validate this, the SCG2 specimen—a single straight tab interface with a width-to-height ratio of 1.0, as used in the parametric study—was selected. In [21] three different specimen with a width-to-height ratio of 1.0 were tested experimentally. From the results, it is seen that one of the three specimen shows obvious bending cracks in the specimen. This indicates that during the experimental testing of this specimen in plane bending occurred due to possible specimen imperfections. Therefore just the two specimen that showed no in plane bending will be used to make a comparison between the numerical and experimental results. The experimental results from [21] of the SCG2 specimens are illustrated in Figure 4.30.

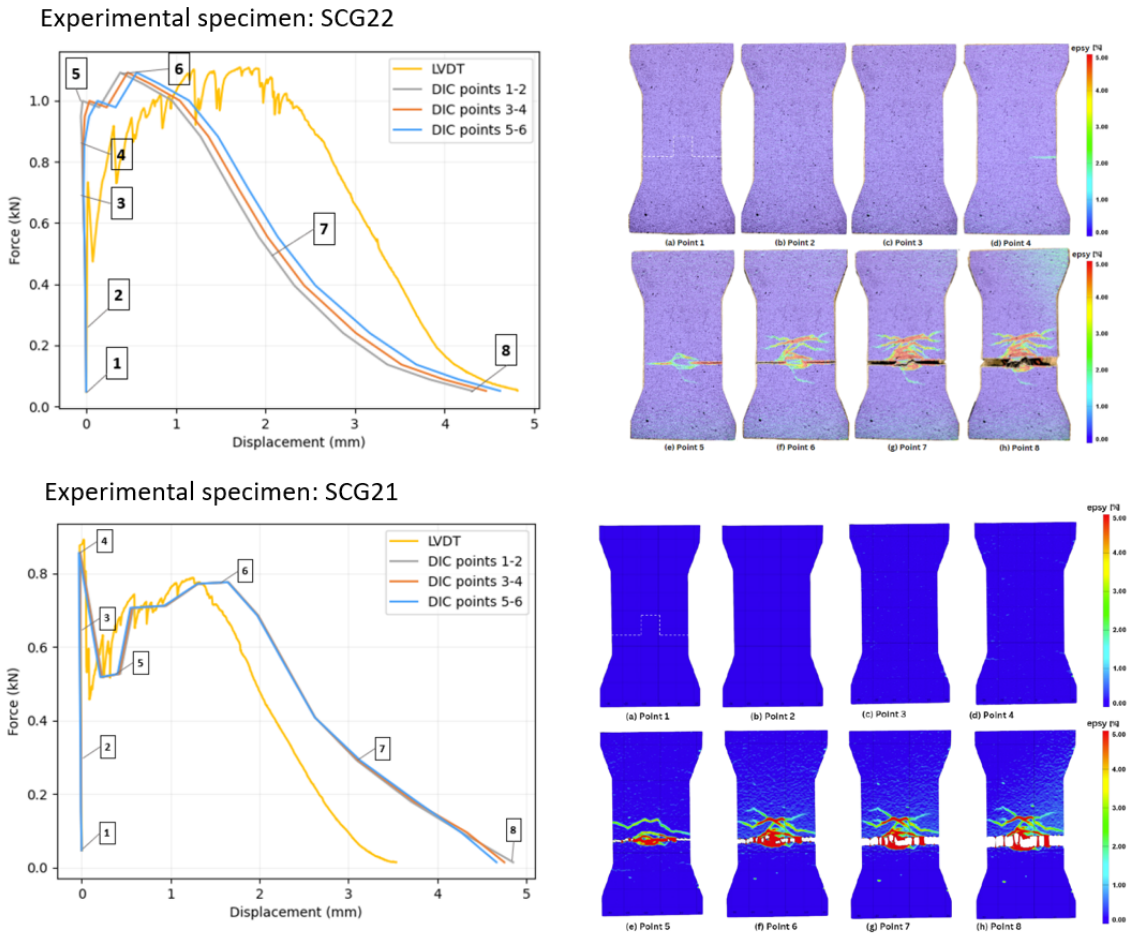

Figure 4.30: Results from the uniaxial tensile test of the the SCG22 and SCG21 specimens from [21], with left the force-displacement diagrams and right the strain contours from the DIC analyses.

As discussed in chapter 4, it is essential not only to confirm that the correct failure mechanism occurs but also to verify the material behavior within the tab in cases of tab failure. To enable this comparison, Figure 4.31 presents numerical results for the same specimen, with key stages from the numerical analysis. Plastic strain distributions from the numerical analysis are displayed alongside the fracture responses of both experimental specimens reported by Papoulidou in [21], providing visual comparison.

The results confirm that the experimental specimens and the numerical specimen all exhibit a tab failure mechanism, validating that the numerical model can accurately predict the failure mode for a single tab with a width-to-height ratio of 1.0.

For the comparison of the force-displacement behavior between the two experimental specimens and the numerical model, the LVDT data of the experimental specimens was utilized (see Figure 4.31). The experimental results reveal considerable differences between the two specimens.

In the SCG21 specimen, a peak force of approximately 0.9 kN is observed at the start of the analysis. This is followed by a force drop and subsequent hardening behavior, during which the force rises again to almost 0.8 kN. In contrast, the SCG22 specimen does not exhibit this initial peak force. Instead, it displays immediate hardening behavior, culminating in a peak force of approximately 1.1 kN. Despite these differences, both specimens show a similar trend in force decline and displacement toward the end of the analysis, corresponding to the formation of a dominant crack. However, SCG21 exhibits a shorter hardening phase, and due to its lower peak force, its ultimate displacement capacity is clearly lower than that of SCG22.

These variations suggest that the experimental results are subject to significant scatter, highlighting

variability in the behavior of the interface connection. Nonetheless, the DIC results show similar cracking behavior for both specimens, with distributed cracking observed in the SHCC material both within and around the tab. This distributed cracking is reflected in the force-displacement behavior of both specimens as a phase of material hardening. Although the ultimate load-bearing and displacement capacities differ, the underlying damage mechanisms and behavior types are consistent.

When comparing the fracture patterns of the experimental specimens to the plastic strain distribution in the numerical model from Abaqus, similarities in cracking progression are evident. Both experimental specimens exhibit cracking initiating at the bottom of the tab, which aligns with the numerical results. Additionally, significant cracking occurs both inside the tab and in the surrounding material. However, in the numerical model, eventhough the plastic strain surrounding the tab covers a similar area as in the experimental specimens, its magnitude is significantly low.

Notable differences in force-displacement behavior are also observed. While the numerical model's peak force aligns closely with that of the SCG22 specimen, the experimental specimens display pronounced material hardening attributed to distributed cracking. This hardening delays the formation of the dominant crack until substantial displacement has occurred (approximately 2.25 mm for SCG22 and 1.3 mm for SCG21). In contrast, the numerical model exhibits minimal hardening, leading to a much lower displacement capacity before dominant crack formation (around 0.5 mm). Despite this, once the dominant crack forms, the force-displacement behavior of all cases becomes comparable.

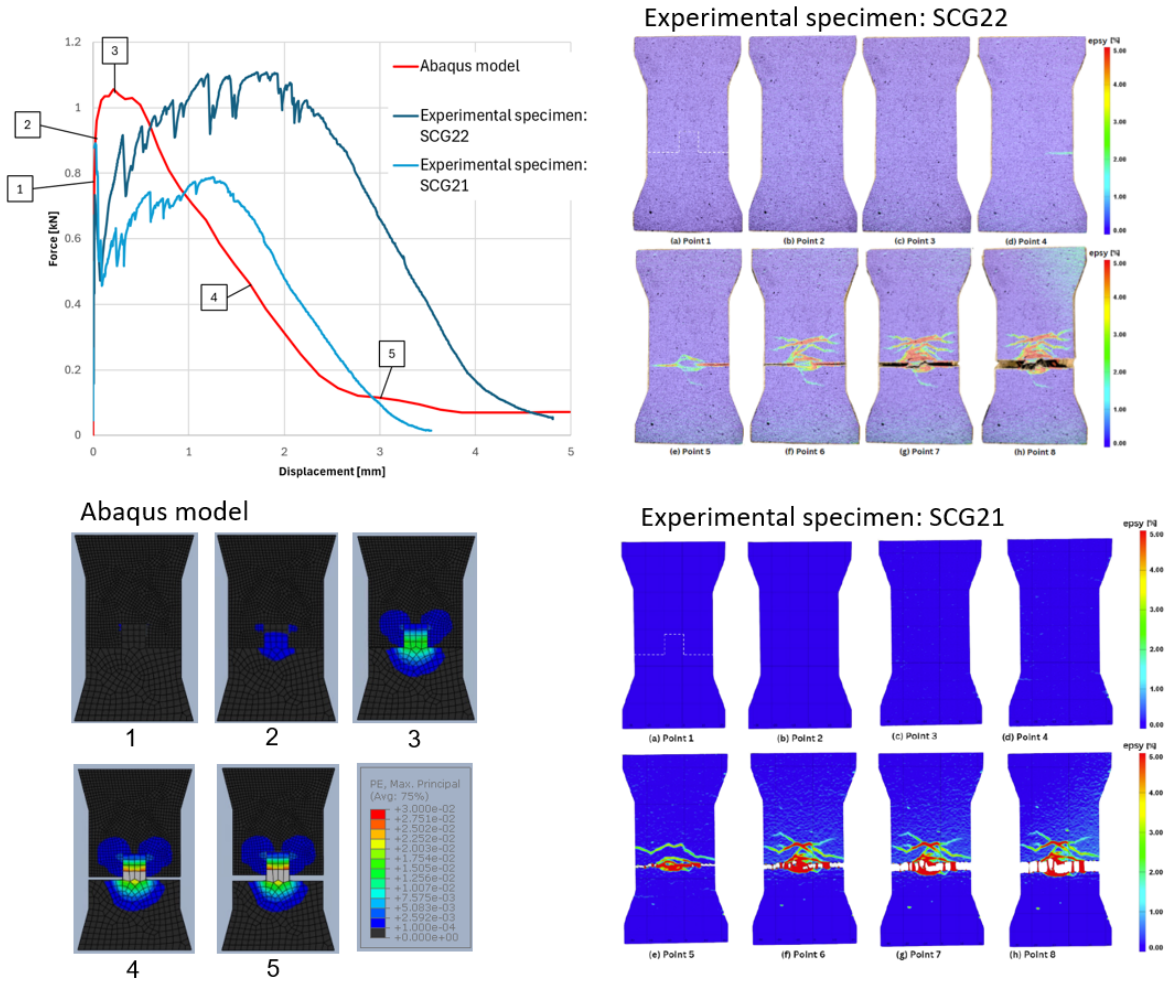

Figure 4.31: Results from the analysis of specimen SCG2 with the material and interface model determined in this research compared to the experimental results from [21].

4.5. Discussion

The objective of the study in this chapter was to use the continuum smeared cracking model in Abaqus to gain a deeper understanding of the behavior of a single-tab interface connection. Achieving this understanding required exploring how the interface is modeled within Abaqus and determining the influence of each parameter on the connection's performance. To this end, a parametric study was conducted to assess the impact of various interface parameters. Results from the parametric study demonstrated that the continuum smeared cracking model could replicate the failure mechanisms identified in the analytical analysis by adjusting interface parameters.

With these insights into model behavior and parameter influence, the interface model was optimized to closely align with one of the experimental pull-out results for a single-tab interface with a width-to-height ratio of 1.5. In the optimized case, the numerical model successfully replicated the fracture response pattern observed experimentally, and the force-displacement behavior demonstrated a strong correlation with the experimental data.

The optimized model was then applied to a single-tab interface with a width-to-height ratio of 1.0, where the tab failure mechanism was effectively captured. However, significant discrepancies were noted between the experimental and numerical force-displacement responses.

For both specimen designs, the Abaqus model results are compared to the experimental data from [21] in Figure 4.32. This figure presents the force-displacement behavior of the numerical model alongside the experimental specimens and includes the fracture patterns observed at the end of the analyses. For the specimen design with a width-to-height ratio of 1.5, the estimated force-displacement behavior of the numerical model closely matches the experimental results of SCG11, which was used for optimization. The numerical results also resemble the behavior of the SCG13 specimen, although notable scatter is observed between these two experimental specimens. Despite the scatter, the ultimate displacement capacity is similar for both experimental specimens.

The SCG13 specimen exhibits a pull-out failure mechanism, accompanied by cracking and localized failure at the top corners of the tab, with a slightly higher load-bearing capacity compared to SCG11. Both experimental specimens demonstrate distinct hardening behavior, leading to substantial displacement capacity before the dominant crack forms. This principle of distributed cracking and subsequent hardening is also evident in the Abaqus model results, indicating a consistent representation of the pull-out failure mechanism.

For the specimen design with a width-to-height ratio of 1.0, the experimental results, discussed in the previous section, reveal a tab failure mechanism with comparable fracture responses. However, significant scatter is observed in the force-displacement behavior of the experimental specimens. Despite this variability, both specimens exhibit pronounced hardening behavior, which allows for substantial displacement before the dominant failure crack develops (approximately 2.25 mm for SCG22 and 1.3 mm for SCG21). In contrast, the numerical model shows a different response, with minimal hardening behavior and the dominant crack forming after only about 0.5 mm of displacement.

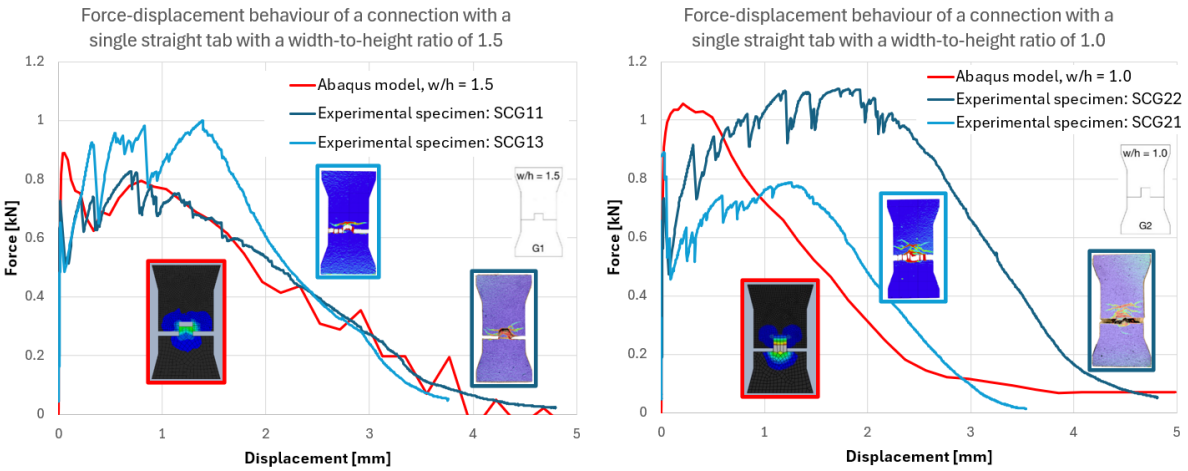

Figure 4.32: Results from the Abaqus numerical model compared to the experimental results from [21] for both specimens with a width-to-height ratio of 1.5 and 1.0.

These discrepancies between the model's predictions for pull-out and tab failure mechanisms can be attributed to differences in how displacement capacity is generated. In the pull-out mechanism, the predicted displacement is a result from the shear-sliding behavior of the interface model and the distributed cracking inside the SHCC material model. In contrast, the tab failure mechanism mainly derives its displacement capacity from the SHCC material model, which appears to underestimate the displacement capacity of the SHCC material seen in the experimental results. This suggests that the numerical model underrepresents the distributed cracking behavior of the SHCC material and that in the pull-out failure mechanism, the model overestimates the contribution of interface behavior on the hardening behavior in the specimen.

The underestimation of distributed cracking in the material model, despite the dogbone tensile test models closely matching experimental results, highlights a critical issue with the balance between plasticity and damage in the concrete damaged plasticity material model. In Abaqus, plasticity spreads deformation across a larger volume, resulting in smeared behavior that does not inherently drive crack formation. In contrast, damage introduces strain softening, localizing deformation and promoting discrete crack formation. The current model only initiates damage after the stress in the stress-displacement curve of a single crack begins to decline. However, in reality, the hardening behavior in SHCC material arises from distributed cracking, meaning that damage should be introduced immediately after the elastic limit is reached. This suggests that the damage-plasticity balance in the current material model is inadequately defined. To address this, further research is needed to refine the relationship between the damage parameter and the actual behavior of SHCC material.

Another limitation lies in the extensive number of parameters required to define the interface model in Abaqus. While these numerous input parameters theoretically enable precise modeling, the current study faced challenges due to limited knowledge of the individual mechanisms governing interface behavior. Despite efforts to derive reliable parameter values, this lack of understanding rendered the model somewhat of a "black box."

To mitigate this black-box nature, future research should focus on systematically investigating the properties of SHCC-to-SHCC interfaces. This could include step-by-step experimental studies of tensile and shear interface behavior, with iterative updates to the numerical model based on experimental findings. Such an approach would provide a clearer understanding of interface mechanisms and improve the reliability of the modeling process.

In conclusion, the challenges in accurately modeling the relationship between damage parameters and SHCC material behavior, coupled with the current knowledge gap around SHCC-to-SHCC interface behavior, resulted in a transition to a different modeling approach. In this research, the lattice

discrete cracking model was adopted, where material behavior is defined purely by damage rather than a combination of plasticity and damage. This model offers a more focused approach to capturing the distributed cracking behavior characteristic of SHCC materials.

5

Lattice model

This chapter focuses on modeling the interface behavior, using the lattice model. The primary objective in the chapter is to examine the influencing parameters and evaluate the strengths and limitations of using the lattice model for both the material and the interface modelling.

The investigation follows these steps to assess the potential for modeling the SHCC-to-SHCC interface behavior with the lattice model:

1. **Theoretical background:** First the theoretical background and workings of the lattice model will be presented.
2. **Material modelling:** The principle of modelling SHCC with the lattice model will be explained. Afterwards two types of SHCC materials will be discussed which will be used in the lattice analysis.
3. **Interface modeling:** The principle of how the interface is modelled using the lattice model will be explained and the different interface strengths that have been chosen will be discussed.

5.1. Theoretical background

This section provides a theoretical background on the lattice model, a discrete modeling approach distinct from the continuum model used in the Abaqus analysis. In the lattice model, the material is represented as a network of beam elements, each exhibiting linear elastic behavior. At each loading step, the most critical element, defined as the one where the stress reaches its strength, is removed or modified from the mesh [13][7]. This iterative removal of elements imparts a non-linear behavior to the model.

The lattice model

The beam elements can have varying properties to represent different components within the concrete mix, such as aggregates, mortar, and the interfacial transition zone (see Figure 5.1a). However, instead of discretely modeling the concrete or SHCC with each element representing a different composite, this research utilizes a lattice model where the concrete or SHCC matrix is treated as a homogeneous material composed of a single type of element (see Figure 5.1b). Even when all beam elements have identical properties, their random distribution and element deletion or modification adds variability, allowing the model to capture the heterogeneous nature of concrete [7].

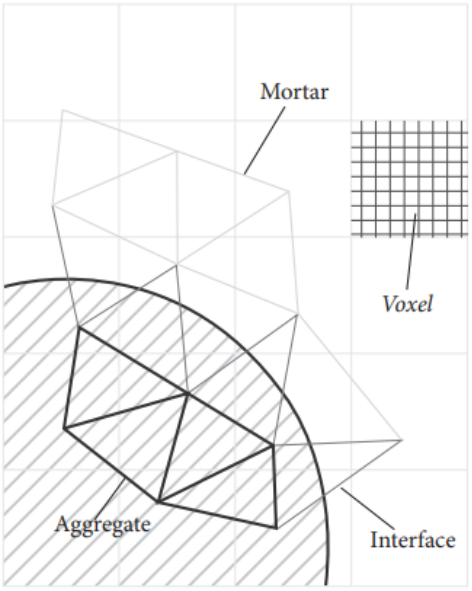

(a) "2D overlay procedure for generation of the lattice model in interface zone between aggregate and substrate mortar (ITZ)." [14]

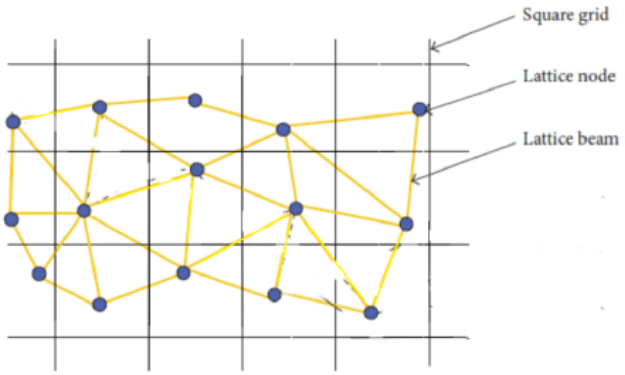

(b) Schematic presentation of homogeneous material lattice model [7].

Figure 5.1: Schematic presentation of the heterogeneous and homogeneous material modelling using the lattice model.

The procedure of generating the network for a 3D lattice is as follows [16][19][7]:

- A cubical grid is selected, where each cube is referred to as a voxel, representing the mesh size of the lattice.
- Within each voxel (of size), a smaller sub-voxel (of size) is placed (see Figure 5.2). Each node in the 3D system has six degrees of freedom.
- The four nearest nodes are connected by beam elements using Delaunay triangulation.
- For a hybrid specimen, the beams corresponding to the bottom and top parts are identified, and interface elements are created between the nodes of these parts (see Figure 5.2). Each element is assigned a unique tag, indicating whether it belongs to the top part, bottom part, or interface.
- Material properties are assigned to each element based on its tag and type.
- An element can fail in tension or compression when the stress exceeds its strength. For the fracture criterion, only axial forces are considered in calculating the stress within the beams. Elements at the boundaries are assigned a fracture criterion that prevents failure, minimizing boundary effects in the numerical analysis.

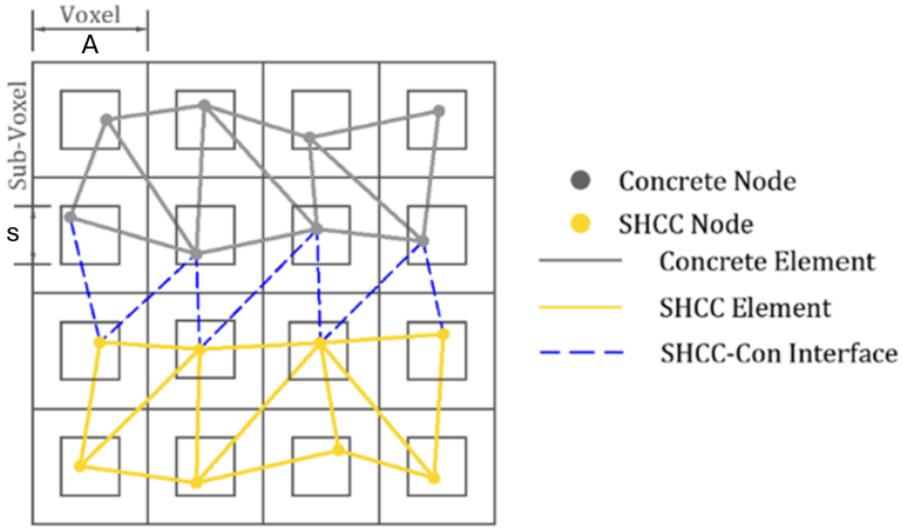

Figure 5.2: Procedure for generating the network for a hybrid lattice [19].

The analysis

After the specimen is discretized in beam elements and material properties are assigned to the elements, the global procedure of the lattice model is as follows [26]:

- Apply an initial load that is scaled proportionally.
- Perform a linear-elastic analysis to compute the principal stresses in the structure.
- Identify the most critical integration point, which is the point where the ratio of the stress level to the current material strength is the highest.
- Calculate the critical load multiplier, , for the critical integration point by dividing the current material strength by the stress level at that point.
- Adjust the reference load proportionally by the factor and reevaluate the stress-strain state of the structure.
- Modify the critical integration point by reducing its stiffness and strength in accordance with the specified constitutive model.
- Repeat this process iteratively until the damage has adequately propagated throughout the structure.

Element radius

Apart from the material property input an important parameter in the lattice model is the radius of the beam elements, which is strongly influenced by the mesh size used in the analysis. Before running an analysis it is of importance to define the radius of the elements.

To accurately define this radius, a calibration process is required. The calibration ensures that, under a direct tension test, the global structural stiffness matches the input material stiffness. An iterative procedure is developed for this purpose [7].

In the first step of the analysis, the displacement () and reaction force () are obtained. The global structural stiffness, , is then calculated using [7]:

$$= \frac{/}{/} \tag{5.1}$$

where is the cross-sectional area of the specimen and is the specimen's length. Based on the result of Equation 5.1, the calibrated lattice beam radius, , can be determined as [7]:

$$= \cdot \tag{5.2}$$

where is the initial lattice beam radius and is the local material Young's modulus.

5.2. Material modeling

This section focuses on modeling the SHCC material used in the lattice analyses. As outlined in the previous section, it is possible to modify an element's material properties once the stress within that element reaches its maximum strength. The material is defined through multiple segments, with each segment characterized by distinct values for the elastic modulus, shear modulus, tensile strength, and compressive strength. Previous studies have demonstrated that this segmentation method—where material properties are adjusted post-failure—effectively captures the ductile behavior of SHCC [7, 16].

In Figure 5.3 the principle of modeling a brittle material is shown on the left, whereas on the right, the method used to model the damage progression in the ductile SHCC material is illustrated.

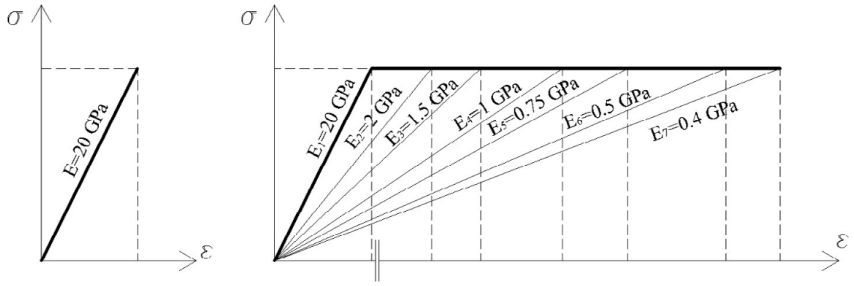

Figure 5.3: Using one segment to model the brittle behavior of the mortar material (left) and using multiple segments to model the ductile behavior of the SHCC (right) [16].

SHCC material model

The strain-hardening capacity of SHCC stems from its ability to form numerous fine cracks, closely spaced due to fiber bridging within the concrete matrix. This distributed cracking and the resulting narrow crack widths are essential for achieving enhanced ductility, which underscores the importance of accurately capturing cracking behavior when modeling SHCC with the lattice approach.

To model this ductile, strain-hardening response, a seven-segment material input model was developed, refined through trial and error to approximate the strain capacity and softening behavior observed experimentally in SHCC (as per [21]). The final input parameters used in the model are provided in Table 5.1.

Segment	E (MPa)	G (MPa)	ft (MPa)	fc (MPa)
1	32000	13333.333	4	86.5
2	1851.7	771.54	4	86.5
3	315.5	131.5	4	86.5
4	250	104.1667	4	86.5
5	150	62.5	4	86.5
6	73.3	30.5	4	86.5
7	25.5	10.6	4	86.5

Table 5.1: Material input of the SHCC material.

To assess the behavior of the SHCC material model, a direct tensile test using a dogbone specimen from the experimental setup described in [21] is simulated. To simulate this experimental setup, the straight part with a constant width of the dogbone specimen is replicated using the lattice model. The experimental specimen on which the simulation is based is shown in Figure 5.4a and the simulated test results are presented in Figure 5.4b.

The tensile dogbone test results for the SHCC material model indicate a steady increase in crack widths throughout the initial stages of the analysis with average crack widths reaching up to 0.2, up until the peak stress is reached at a strain of approximately 0.023 (2.3%). The maximum crack width escalates rapidly after the peak stress is reached at point 3. By point 4, a prominent crack has formed near the bottom of the specimen, reaching approximately 0.8 mm in width. At point 5, this crack expands further, and smaller, surrounding cracks start to close due to the redistribution and reduction of stress in adjacent elements. At this stage, the dominant crack widens beyond 1 mm, marking material failure.

The model exhibits pronounced softening behavior following the formation of the dominant crack, leading to notably larger crack widths, particularly in the dominant crack itself. The stress-strain relationship for the lattice SHCC material model aligns well with experimental SHCC results through the initial stages of the analysis (see Figure 5.5). Up until point 3, the model closely reflects experimental behavior. However, after reaching peak force at point 3, the model begins to diverge, displaying a softening trend that does not fully capture the exact softening behavior observed experimentally. This divergence is due to the fact that the lattice model inputs for SHCC cannot be directly derived from experimental data, necessitating a trial-and-error approach. This divergence will be a key consideration in the post-processing of interface specimen tests.

(a) Dogbone tensile test setup after testing from [21].

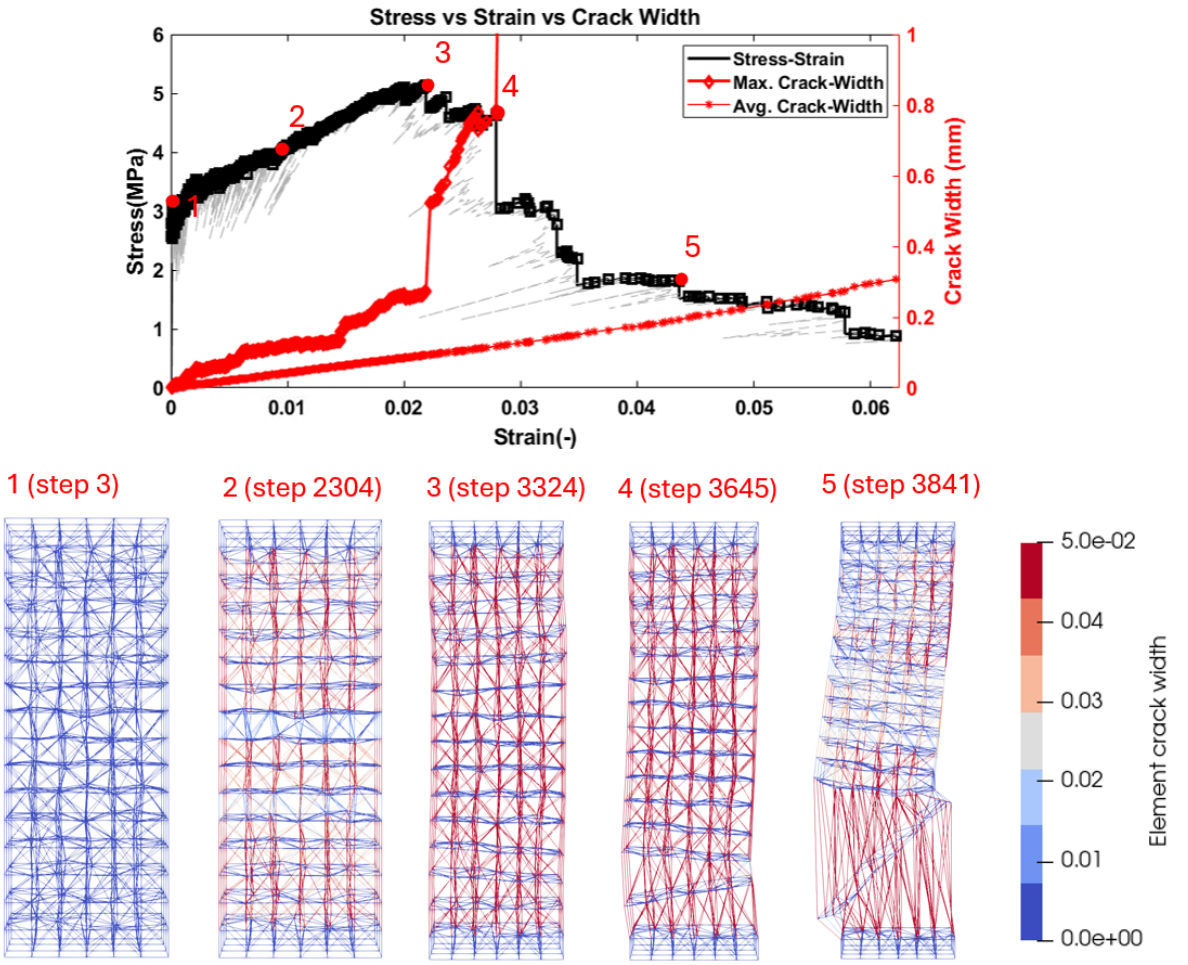

(b) Stress-strain relationship for the SHCC material including the crack width development at different stages of the tensile test with a scaling factor of 10.

Figure 5.4: Experimental test setup for the dogbone tensile test from [21] and the simulated results from the dogbone tensile test of the material model for the SHCC material.

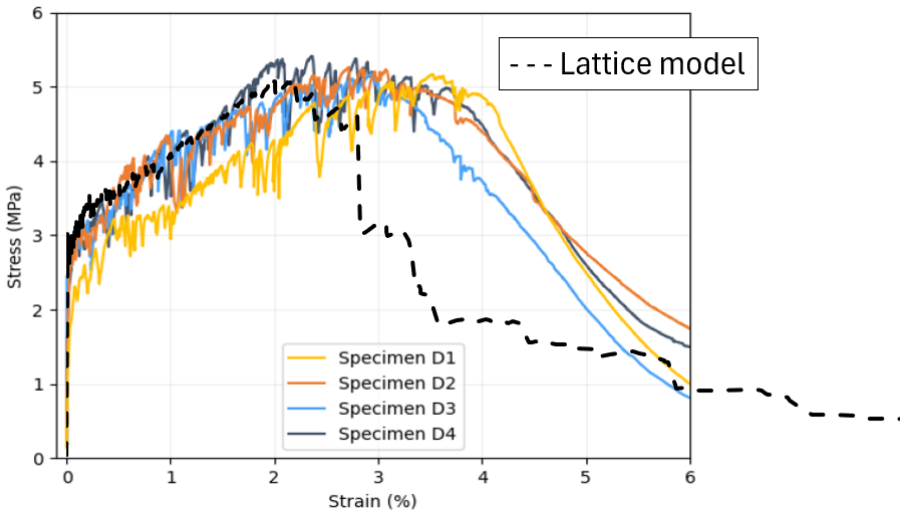

Figure 5.5: Stress-strain behavior of the SHCC material model in lattice and that of the experimental SHCC material from [21].

5.3. Interface modeling

After defining and testing the material model under direct tension, the next step is to incorporate an interface within the specimen and analyze the material's behavior. The design of the test sample and interface follows the work of Papoulidou [21]. The specimen dimensions are 45 mm in width, 15 mm in thickness, and 80 mm in height, with the 80 mm height chosen to match the gauge length used in the experimental study by Papoulidou [21]. The interface is located in the center of the specimen and contains a single straight tab. This tab has a width-to-height ratio of either 1.0 or 1.5 (see Figure 5.6).

In Papoulidou's design, the central portion of the specimen, where the width remains constant, is 45 mm in height. This geometry is recreated in the lattice model by assigning failure modes—either tension or compression—to the middle 45 mm section (highlighted in blue). The material at the top and bottom of the specimen is modeled as non-failing (shown in red), meaning that elements in these regions, once they reach their maximum stress, are not removed from the analysis and can continue to sustain stress throughout the simulation.

The interface in the lattice model is represented by white elements. Unlike the Abaqus model, where the interface was modeled as a surface, the interface in this numerical model has a finite thickness, providing more detailed insight into stress distribution across the interface.

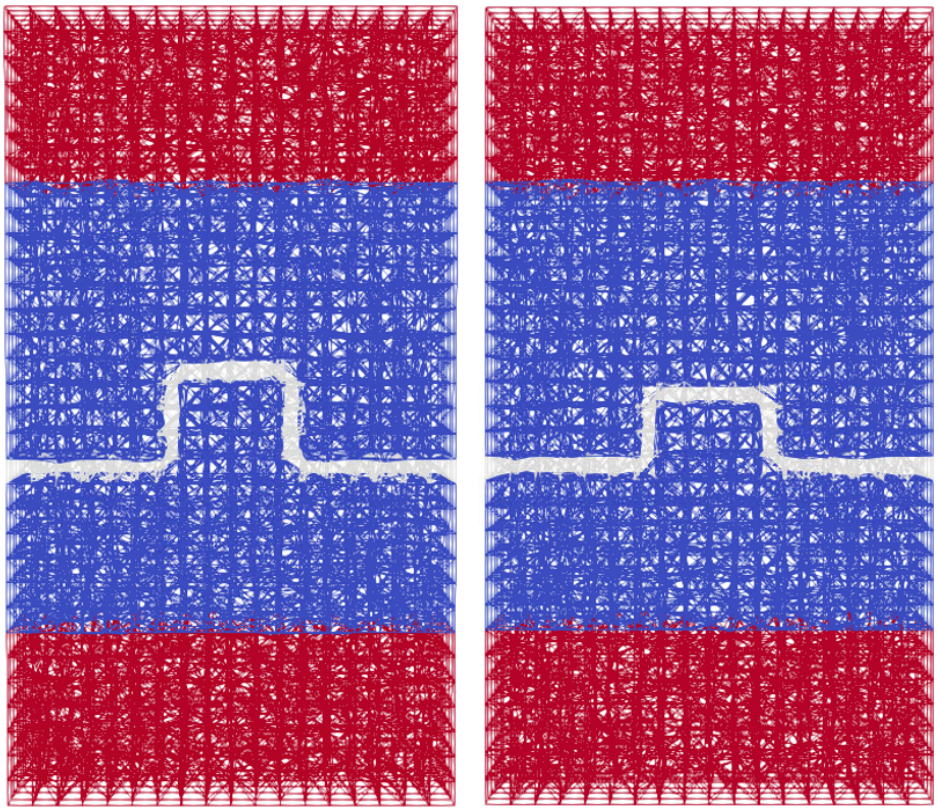

Figure 5.6: Lattice model for the tensile test specimen with a single straigth tab interface with a width-over-height ratio of 1.0 (left) and a widht-over-height ratio of 1.5 (right).

For the interface elements, a specific material input is required. The interface is modeled as a brittle material, represented by a single segment in the material definition. To ensure consistency between the interface and the bulk material, the Young's modulus and shear modulus of the interface are set to the same values as those used for the bulk material. This maintains stiffness continuity and encourages stress concentrations to form at the interface, allowing a realistic failure mechanism to develop.

The tensile and compressive strengths of the interface are varied across different analyses to inves-

tigate the influence of interface strength on the failure mechanism and the behavior of the connection under tension. These strengths are defined as a percentage of the values used for the bulk material. By adjusting the strength of the interface, the study aims to explore how the interface's capacity to withstand stress affects the overall structural performance, crack initiation, and the failure mode of the specimen under tensile loading.

5.4. Analysis

In the lattice model analysis, the material and interface model as discussed above are used to investigate the connections behavior. As mentioned, two different interface designs have been investigated in this analysis, SCG1 and SCG2, with width-to-height ratio of 1.5 and 1.0 respectively. First the interface strengths are varied such that the different failure mechanisms present themselves. In the analysis the interface strengths of 5, 10, 15, 20, 25, 30, 50, 75, 100, 150, 200, 300 and 500% are used to investigate the behavior and influence of different interface strengths. For each of the failure mechanisms, one specimen will be discussed in detail and further results can be found in Appendix C.

5.4.1. 1. Delamination

The initial failure mechanism observed is interface delamination, occurring when the interface elements fail before the SHCC material begins to crack. To achieve this delamination, the interface strength was adjusted as a percentage of the material strength, allowing delamination to precede material cracking. The interface strength values that result in a delamination failure mechanism are provided in Table 5.2.

Specimen	w/h ratio	interface strength %	tensile strength MPa	compressive strength MPa
SCG1	1.5	5, 10	0.2, 0.4	4.325, 8.65
SCG2	1.0	5	0.2	4.325

Table 5.2: Interface strengths that induce a delamination failure mechanism in the lattice analysis.

In this subsection, the SCG2 specimen with an interface strength of 5% is examined, highlighting a clear delamination failure mechanism as shown in the crack width distribution in Figure 5.7. The final damage state of the elements is also presented, where undamaged SHCC elements are displayed in grey, undamaged interface elements in pink, damaged interface elements in red, and SHCC elements color-coded from blue to red to indicate increasing damage levels.

The results reveal that cracks form exclusively along the interface, beginning at the horizontal interfaces with more pronounced crack widths on the outer sides of the bottom horizontal interfaces. These cracks then propagate to the vertical interfaces. At the end of the analysis, only the interface elements display damage, while the SHCC material elements remain intact.

The force-displacement graph further illustrates this delamination mechanism, showing two distinct peaks: the first peak corresponds to failure in the horizontal interfaces, while the second peak is associated with the vertical interfaces. This separation suggests that the tensile and shear interfaces do not work cohesively to sustain the load; rather, they operate independently. Consequently, most of the specimen's displacement capacity is attributed to shear interactions within the vertical interfaces.

The force-displacement behavior of the delamination failure mechanism is presented alongside the SHCC material behavior and the analytical delamination behavior in Figure 5.8. Comparing the force-displacement response of the delamination failure mechanism to that of the SHCC material without an interface reveals a substantially lower force and displacement capacity in the delamination response. The analytical force-displacement response, in contrast, exhibits both higher strength and significantly greater displacement capacity. This increased displacement capacity can be attributed to the softening behavior incorporated in the analytical model, as opposed to the brittle interface properties used in the lattice analysis. The reduction in force capacity in the delamination response is largely due to the independent functioning of the tensile and shear interfaces, which do not effectively work together to sustain force.

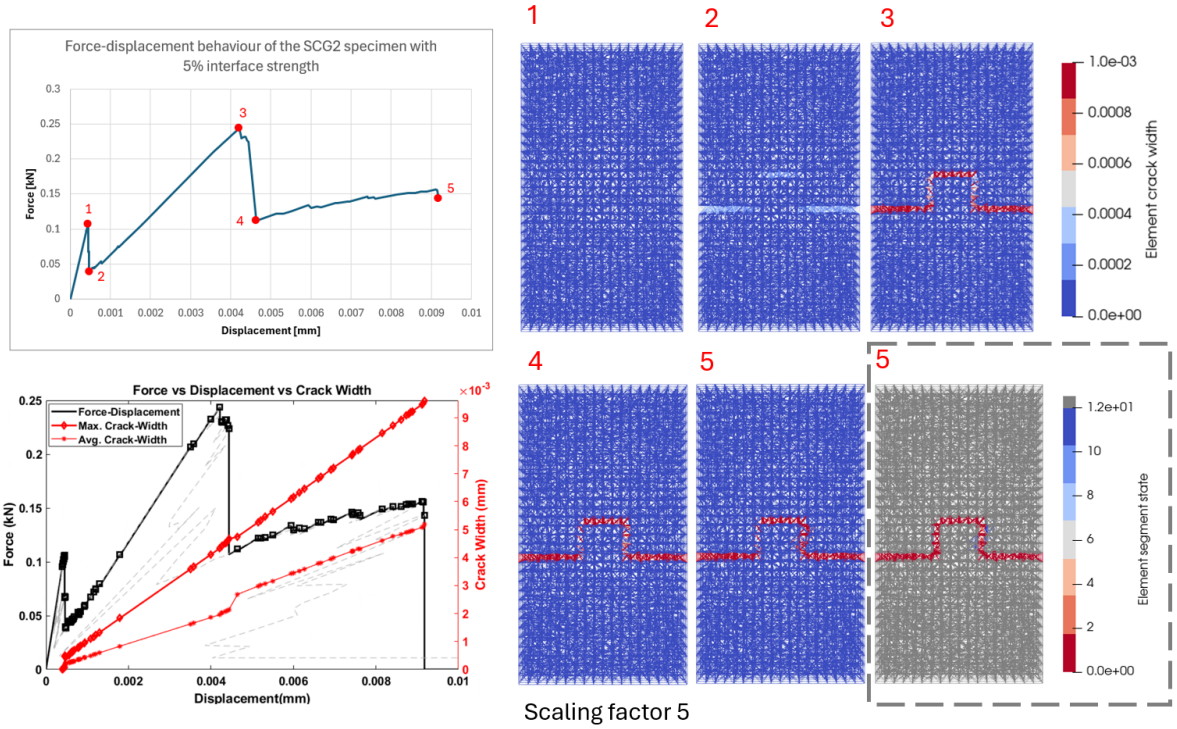

Figure 5.7: Delamination analysis results for the SCG2 specimen with 5% interface strength, showing force-displacement behavior, crack width distribution and progression during the analysis, and final element damage state.

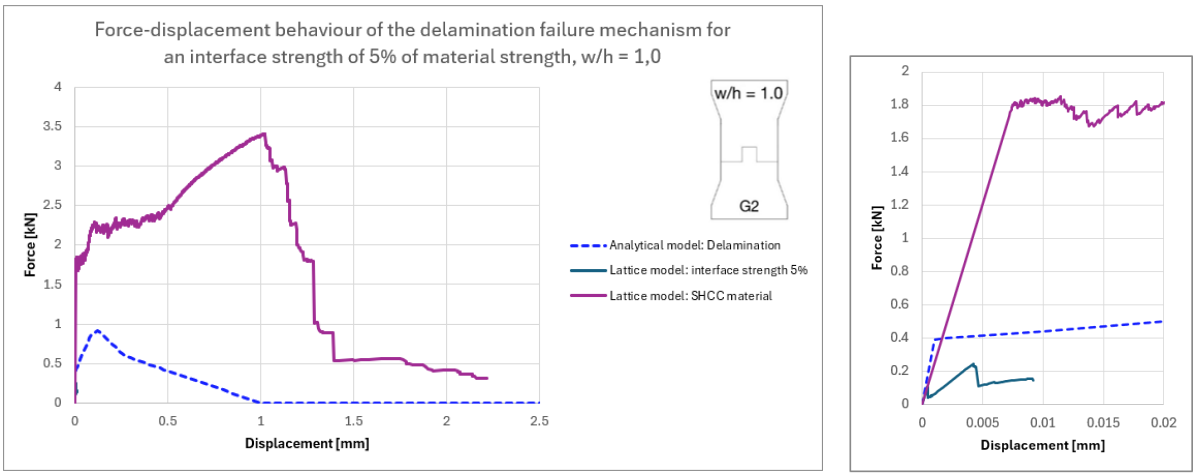

(a) Force-displacement response of the delamination failure mode from both lattice as analytical analysis vs. the material behavior of the SHCC material in the lattice model.

(b) Zoomed in force-displacement response.

Figure 5.8: Force-displacement response of the delamination failure mode from both lattice as analytical analysis vs. the material behavior of the SHCC material in the lattice model.

As noted in the literature review, the delamination failure mechanism was also observed in an experimental study conducted by Papoulidou. The fracture response shown in Figure 5.9 demonstrates a notable absence of cracking within the tab and the surrounding material, with one important exception. In the experimental study, two cracks developed at the top corners of the tab due to stress concentrations—an occurrence not observed in the lattice analysis.

To comparing the force-displacement behavior between the two cases it is important to note that the experimental result represents a delamination failure mechanism in a straight tab interface with

a width-to-height ratio of 1.5 and the lattice result represents a straight tab interface with a width-to-height ratio of 1.0. It is seen that the peak force which is reached, is similarly high in both, reflecting comparable ultimate resistance. However, the displacement capacity shows a pronounced difference: in the experimental study, displacement capacity reaches nearly 5 mm, while in the lattice analysis, the maximum displacement is around 0.01 mm. This large difference in displacement capacity is largely attributed to the role of friction in the experimental study [21], which contributes significantly to energy dissipation. In contrast, frictional effects are not modeled in the lattice analysis, resulting in a much more brittle delamination response.

Additionally, from the zoomed in force-displacement response in Figure 5.9c, it can be seen that the lattice model underestimates the interface stiffness measured in the SLG12 experimental specimen from [21].

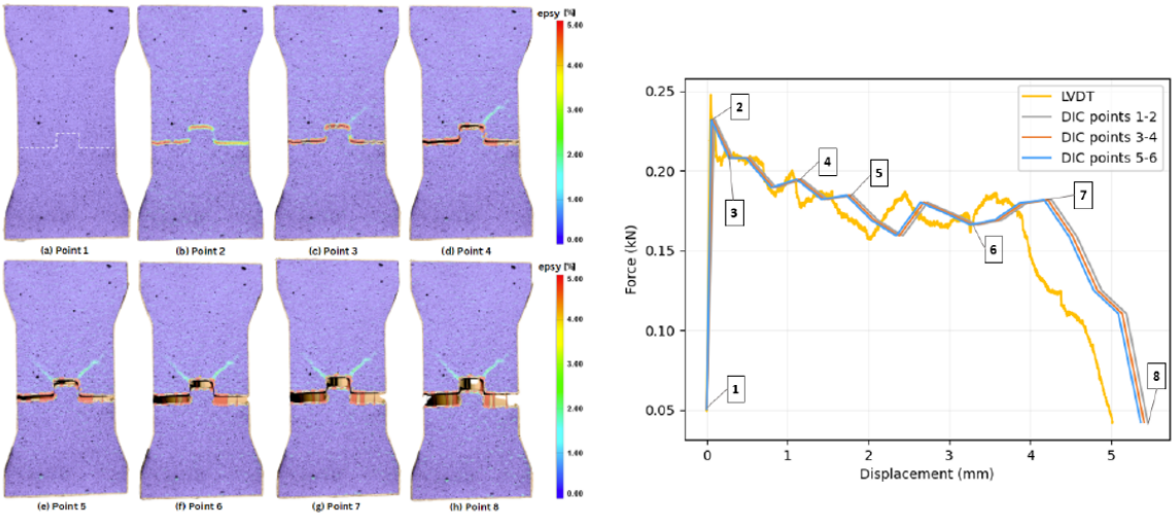

(a) Fracture response of the delamination failure mechanism as was presented in the experimental SLG12 specimen from [21].

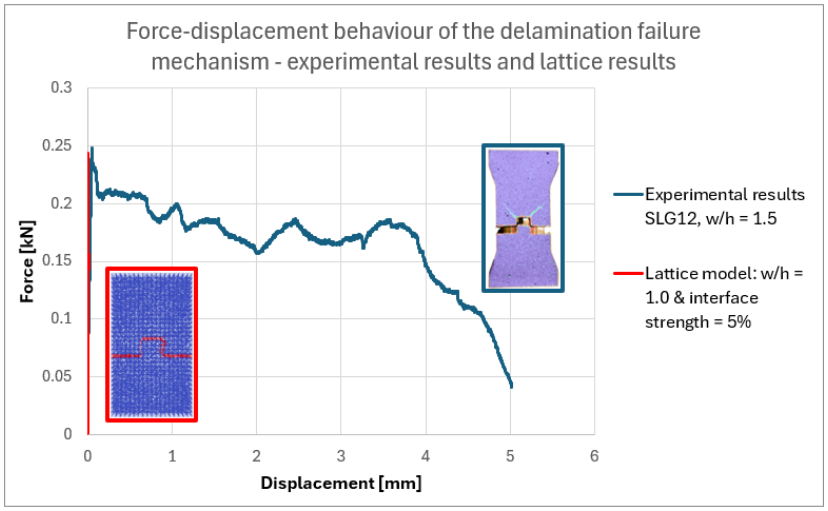

(b) Force-displacement response of the delamination failure mechanism for both the lattice model and the experimental analysis [21].

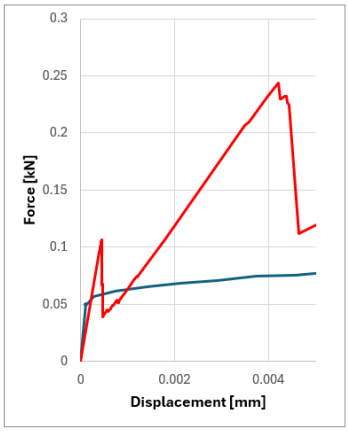

(c) Zoomed in force-displacement response.

Figure 5.9: Results from the experimental analysis of the delamination failure mechanism [21].

5.4.2. 2. Pull-out

The second failure mechanism observed is a pull-out mechanism, where the in the process of the tab being pulled-out the SHCC material starts cracking and damage in the material occurs. To achieve

this pull-out mechanism, the interface strength was adjusted as a percentage of the material strength, allowing the pull-out to happen after the material started cracking. The interface strength values that result in a pull-out failure mechanism are provided in Table 5.3.

Specimen	w/h ratio	interface strength %	tensile strength MPa	compressive strength MPa
SCG1	1.5	15, 20, 25	0.6, 0.8, 1.0	12.975, 17.3, 21.625
SCG2	1.0	10, 15, 20	0.4, 0.6, 0.8	8.65, 12.975, 17.3

Table 5.3: Interface strengths that induce a pull-out failure mechanism in the lattice analysis.

In this subsection, the SCG1 specimen with an interface strength of 25% is analyzed, demonstrating a distinct pull-out failure mechanism, as can be seen in Figure 5.10. The SHCC material within and around the tab shows progressive damage, with a crack forming inside the tab and propagating from the top horizontal interface into the surrounding material. When the force decreases from point 4 to point 5, the cracks within the tab and adjacent material begin to close. By the end of the analysis, the crack inside the tab remains partially open, yet the entire interface shows signs of damage. In contrast, the SHCC material within and around the tab is only in the early stages of damage.

The force-displacement behavior reveals an initial peak similar to that seen in the delamination case; however, with the increased interface strength, this peak force is also elevated. Following this peak, the shear interface primarily governs the connection's response, displaying notable displacement capacity. However, due to the brittle nature of the interface elements, the force-displacement curve exhibits abrupt drops, signaling progressive interface failure. The observed hardening in the force-displacement curve can be attributed to cracking within the SHCC material.

In Figure 5.11, the force-displacement behavior of the pull-out failure mechanism is compared with both the SHCC material behavior and the analytical pull-out response. Observing the lattice pull-out mechanism in relation to the SHCC material behavior reveals that while force and displacement capacities are still significantly lower than the material's full potential, they are markedly higher than those seen in the delamination failure mechanism. When comparing this behavior to the analytical response, a similar trend as in the delamination mechanism is evident: the lattice model shows a reduced displacement capacity due to the brittle nature of its interface elements. Additionally, the reduced force capacity results from the distinct, non-cohesive interaction between the tensile and shear interfaces within the lattice model.

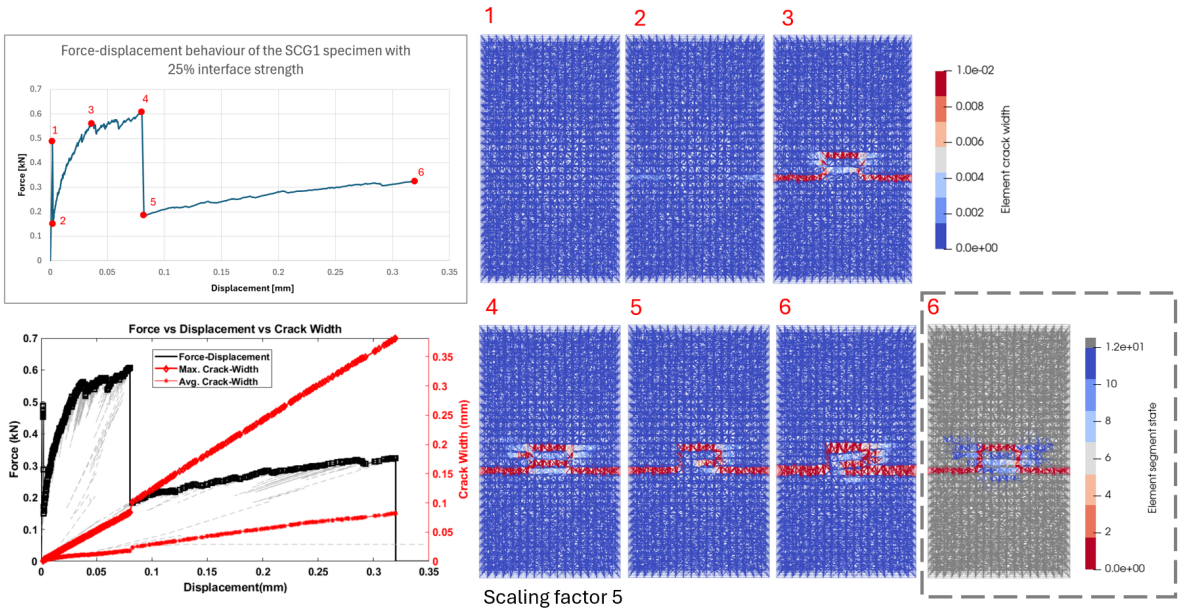

Figure 5.10: Pull-out analysis results for the SCG1 specimen with 25% interface strength, showing force-displacement behavior, crack width distribution and progression during the analysis, and final element damage state.

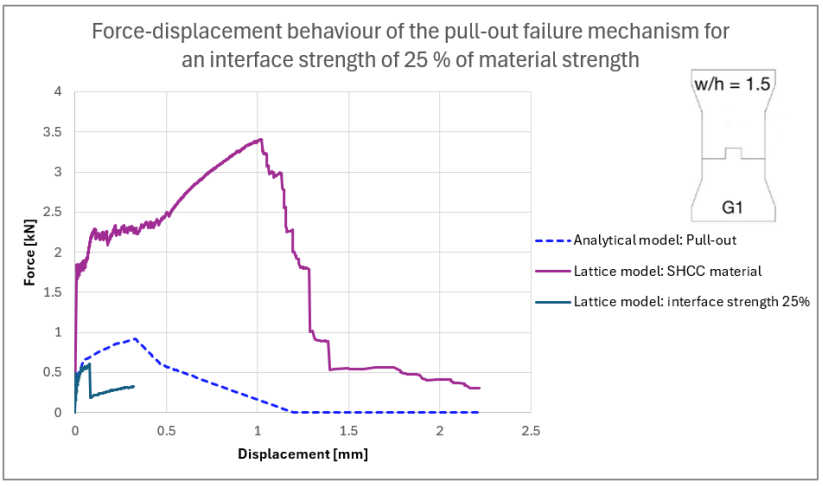

(a) Force-displacement response of the pull-out failure mode from both lattice as analytical analysis vs. the material behavior of the SHCC material in the lattice model.

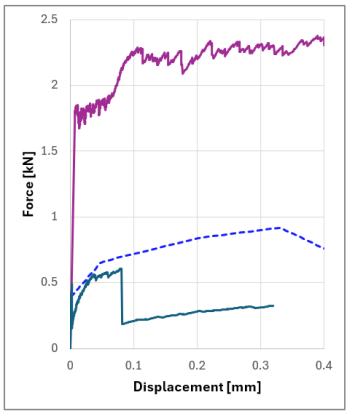

(b) Zoomed in force-displacement response.

Figure 5.11: Force-displacement response of the pull-out failure mode from both lattice as analytical analysis vs. the material behavior of the SHCC material in the lattice model.

The pull-out failure mechanism was similarly observed in the experimental study by [21]. The fracture response and corresponding force-displacement behavior for both the SCG11 and SCG13 specimens are presented in Figure 5.12. In the experimental response, cracks first develop along the bottom horizontal interface and within the tab itself. Subsequently, the top horizontal interface begins to crack, with the fracture extending into the material at the top corners of the tab. Additional cracks emerge along the sides of the tab and the tab is gradually pulled out. Where the tab in the SCG11 specimen remains fully intact and where the tab in the SCG13 specimen undergoes localized failure of the top corners of the tab.

In the lattice model, a similar pattern of fracture development is observed: cracking initiates at the bottom horizontal interface, followed by crack formation within the tab and along the top horizontal interface, with extensions into the material near the top corners. Side cracks around the tab expand,

as does the main crack within the tab, before the tab begins to pull out and the cracks in both the tab and surrounding material start to close. In the lattice model, the fracture response does not show the same localized failure in the top corners of the tab as seen in the SCG13 specimen, but represents more the SCG11 specimen behavior.

While the crack closure observed in the lattice model is not shown in the experimental results, the overall pattern and location of crack formation in the lattice model closely follow the experimental findings.

When examining the force-displacement behavior, notable differences emerge between the lattice model and the experimental results. The lattice model exhibits a lower peak force than observed in the experimental study. However, the most significant divergence lies in the displacement capacity: while the experimental specimen reaches a displacement of approximately 3.5-4 mm, the lattice model achieves only about 0.35 mm.

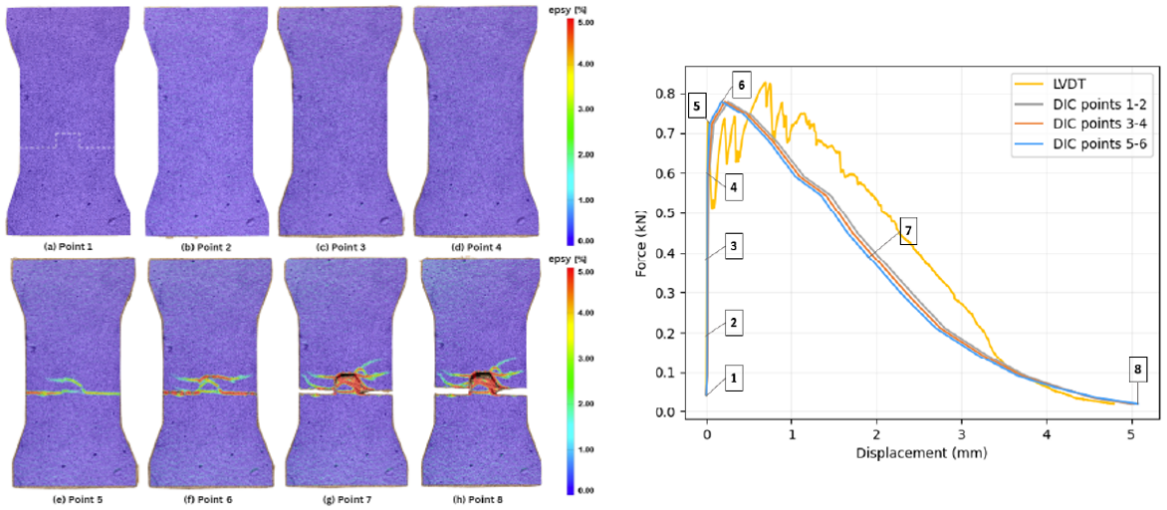

(a) Fracture response of the pull-out failure mechanism as was presented in the experimental SCG11 specimen from [21].

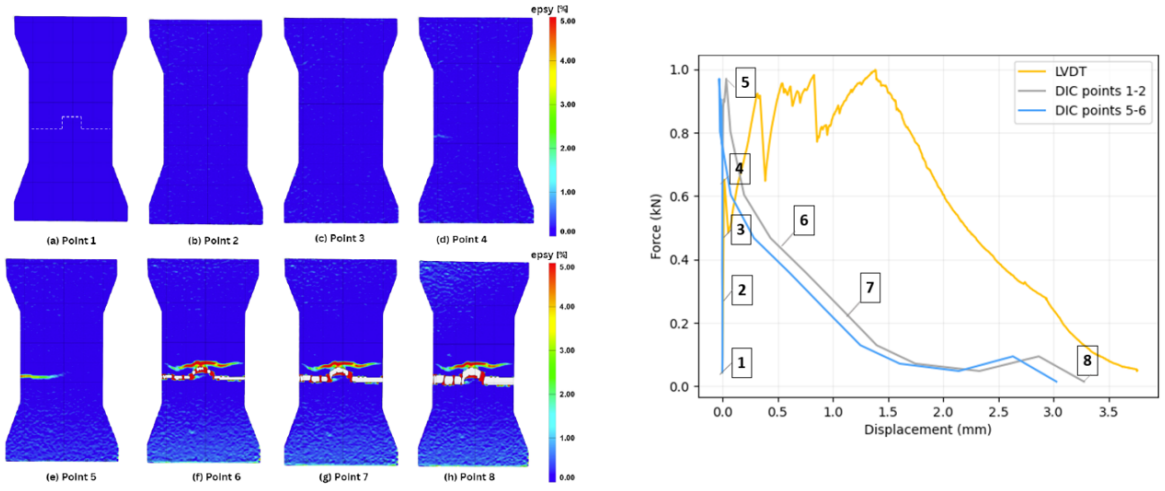

(b) Fracture response of the pull-out failure mechanism as was presented in the experimental SCG13 specimen from [21].

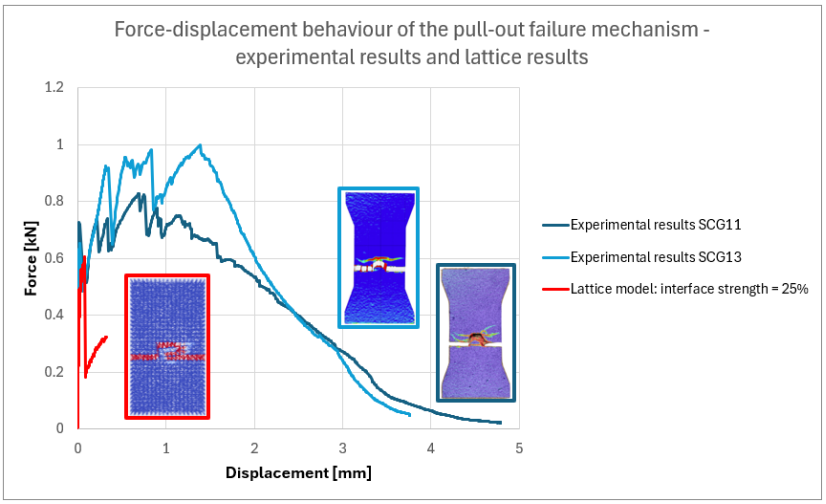

(c) Force-displacement response of the pull-out failure mechanism for both the lattice model and the experimental analysis [21]. For all three results, the cracking response at the end of the analysis is presented as well

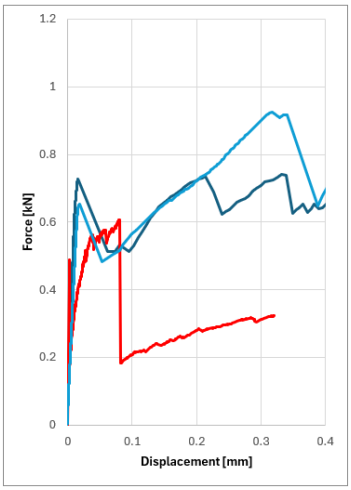

(d) Zoomed in force-displacement response.

Figure 5.12: Results from the experimental analysis of the pull-out failure mechanism of both SCG11 and SCG13 specimens from [21] compared to the lattice results for the pull-out failure mechanism with an interface strength of 25%.

The significant difference in displacement capacity can be attributed to the assumptions in the current lattice model, which presumes brittle behavior at the interface. In contrast, the experimental interface likely exhibits softening behavior and frictional effects, both of which enhance displacement capacity but are not accounted for in the lattice model. To explore the influence of ductility in the interface elements, an additional analysis was conducted using a specimen with a width-to-height ratio of 1.5 and an interface strength of 5% with ductile behavior. While this ductile interface was not optimized to replicate experimental results, it provides insight into how ductile interface behavior can affect the connection's performance. The findings from this analysis are shown in Figure 5.13.

The analysis indicates that the displacement capacity of the interface increases significantly, reaching an effective displacement of approximately 5 mm. Additionally, compared to the brittle interface specimen with an interface strength of 5% and a width-to-height ratio of 1.5, which exhibited a delamination failure mechanism, the specimen with ductile interface elements transitions to a pull-out failure mechanism, accompanied by considerable SHCC material damage.

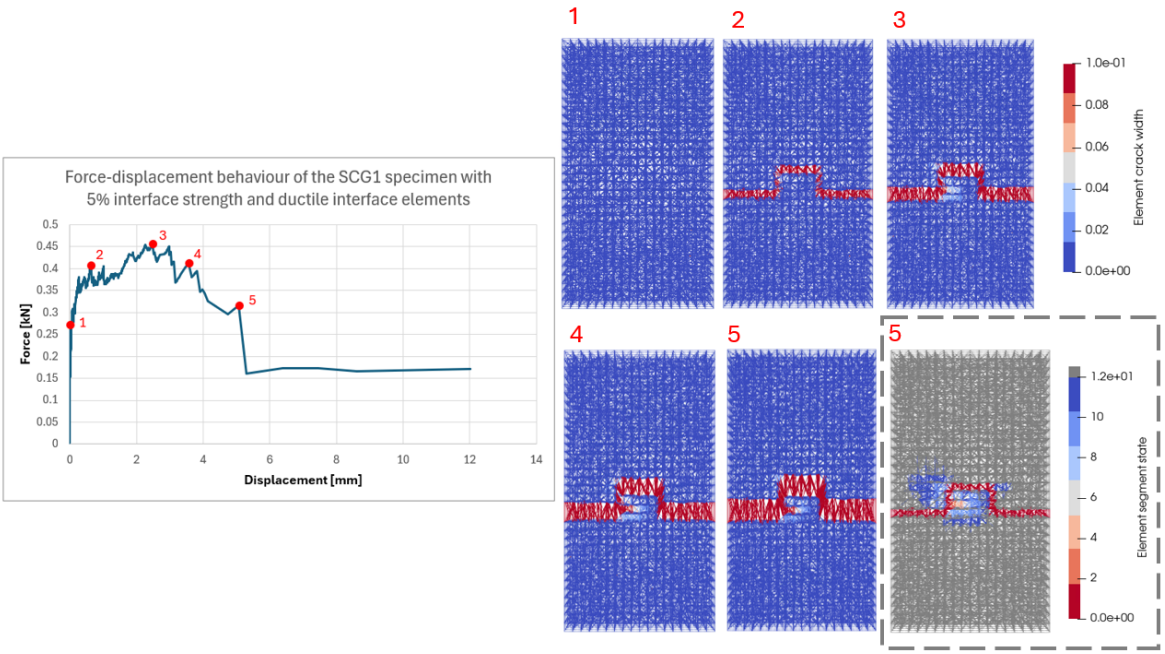

Figure 5.13: Analysis results of the SCG1 specimen with a 5% interface strength and ductile interface elements which presented a pull-out failure mechanism.

5.4.3. 3. Tab failure

The third observed failure mechanism is the tab failure mechanism. In this scenario, the SHCC material exhibits weaker properties than the interface, leading to cracking throughout the analysis. However, rather than a final crack forming through the interface, the dominant crack develops within the SHCC material of the tab. To facilitate this tab failure mechanism, the interface strength was adjusted as a percentage of the material strength, allowing the material inside the tab to fail without compromising the integrity of the entire specimen. The interface strength values that result in a tab failure mechanism are detailed in Table 5.4.

It is important to note that the 100% interface strength corresponds to the tensile strength input of the material, which is 4 MPa. However, during dogbone tensile tests, the tensile strength of the specimen reached approximately 5 MPa. This indicates that a 100% interface strength still falls below the material's tensile strength.

Specimen	w/h ratio	interface strength %	tensile strength MPa	compressive strength MPa
SCG1	1.5	30, 50, 75, 100	1.2, 2, 3, 4	25.95, 43.25, 64.875, 86.5
SCG2	1.0	25, 30, 50, 75, 100	1, 1.2, 2, 3, 4	21.63, 25.95, 43.25, 64.88, 86.5

Table 5.4: Interface strengths that induce a tab failure mechanism in the lattice analysis.

In this subsection, the SCG2 specimen with a 30% interface strength is analyzed, revealing a distinct tab failure mechanism, as can be seen in Figure 5.14. The crack width distribution indicates that cracks initiate at the horizontal interfaces and propagate into both the tab and the surrounding material. Multiple cracks form within the tab during the analysis, extending outward into the adjacent material. By the end of the analysis, a dominant crack emerges at the bottom of the tab, extending from the interface into the tab itself.

In the force-displacement behavior, an initial tensile peak appears similarly to the delamination and pull-out failure mechanisms. After this peak, the shear interface begins to govern the response, lead-

ing to an increase in force and a pronounced hardening effect, culminating in a second peak. Beyond this peak (point 6), cracks around the tab start to close (from point 6 to point 7), while the crack at the bottom of the tab continues to widen. This softening phase in the force-displacement curve is primarily due to the progression of the dominant crack at the base of the tab.

In Figure 5.15, the force-displacement behavior of various tab failure mechanisms across different interface strengths for specimens with a width-to-height ratio of 1.0 is presented, alongside the material behavior and the analytical tab failure response. Notably, the behavior across different interface strengths in the tab failure mechanism is quite similar. The only exception is the 100% interface strength, which shows an elevated initial peak force that quickly drops thereafter. When comparing tab failure behavior to the SHCC material's performance, it becomes evident that while the peak force remains lower than that of the material failure, it is still notably higher than in the pull-out failure. Additionally, the displacement capacity in tab failure is considerably greater than in pull-out failure and demonstrates a significant range relative to the SHCC material's behavior, even though it does not reach the full displacement capacity of the material.

Compared to the analytical force-displacement behavior, the lattice model demonstrates a similar overall trend, with one primary discrepancy: the displacement capacity and softening behavior following the formation of the dominant crack. Here, the displacement capacity is somewhat reduced compared to the analytical results, likely due to variations in the material definitions used for the SHCC material in both the lattice and analytical models

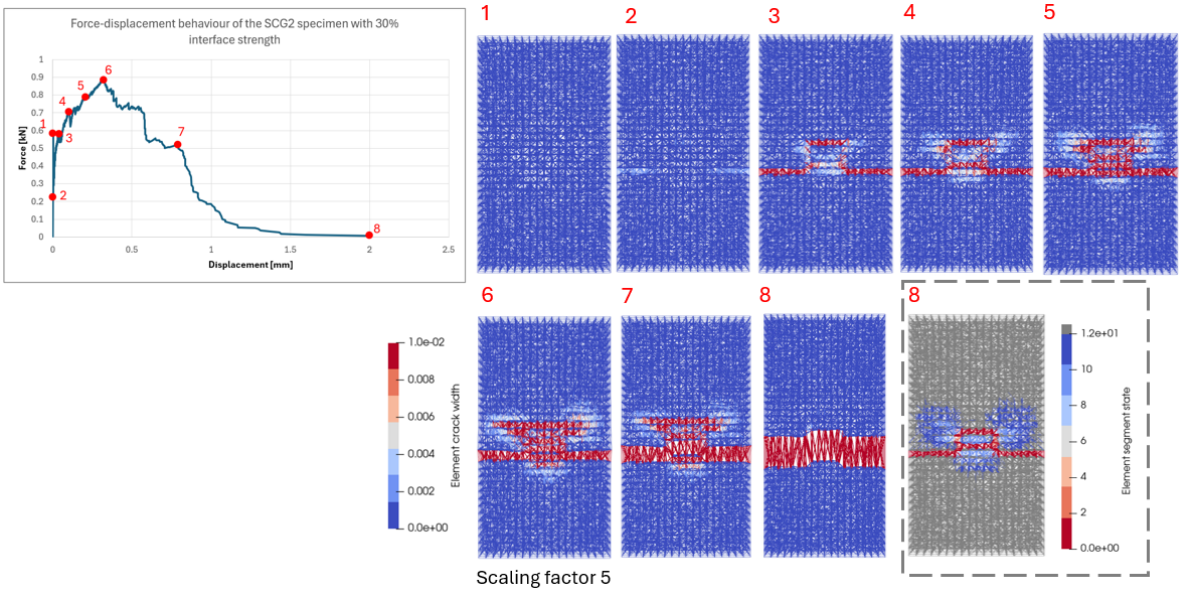

Figure 5.14: Tab failure analysis results for the SCG2 specimen with 30% interface strength, showing force-displacement behavior, crack width distribution and progression during the analysis, and final element damage state.

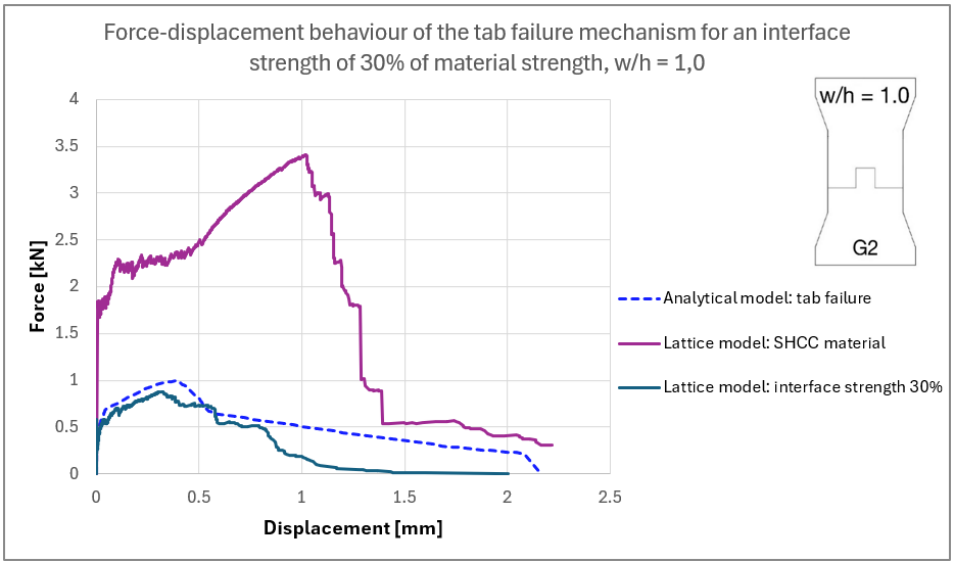

Figure 5.15: Force-displacement response of the tab failure mode vs. the material behavior of the SHCC material.

The tab failure mechanism is the final failure mode also observed in the experimental study by Papoulidou. The fracture response and force-displacement behavior of this failure mechanism in specimens SCG22 and SCG21 are presented in Figure 5.16. In the experimental responses, cracks initially form at the bottom horizontal interface, then propagate within the lower part of the tab and below it. Subsequently, a crack develops along the top horizontal interface, extending into the material near the top corners. Multiple cracks form within the tab and spread into the adjacent material. Eventually, a dominant crack emerges at the bottom of the tab, linking the cracks at the bottom horizontal interface, which ultimately expands, signifying specimen failure.

The lattice model's fracture response displays a similar crack pattern. Cracks appear at the bottom horizontal interfaces, followed by cracking at the tab's lower region and the top horizontal interface, where they extend into the material surrounding the top corners. Cracking occurs below the tab as well, with additional cracks forming within the tab and extending into the adjacent material. Ultimately, a dominant crack forms at the tab's bottom, connecting the cracks along the bottom horizontal interfaces, resulting in specimen failure. Similar to the pull-out mechanism, crack closure is illustrated in the lattice model, though this behavior is not evident in the experimental observations.

When comparing the force-displacement behavior between the experimental and lattice results, a similar shape is observed, though with notable differences. The peak force in the lattice model aligns with the peak force observed in the SCG21 specimen, which is significantly lower than the peak force in the SCG22 specimen, indicating large inherent scatter in the experimental results. The primary distinction between the lattice results and both experimental results lies in the displacement capacity. Although the fracture pattern and force-displacement curve shape are consistent, the lattice model underestimates the hardening response of the SHCC material, reflected in the reduced displacement capacity and the shortened hardening range in the force-displacement behavior.

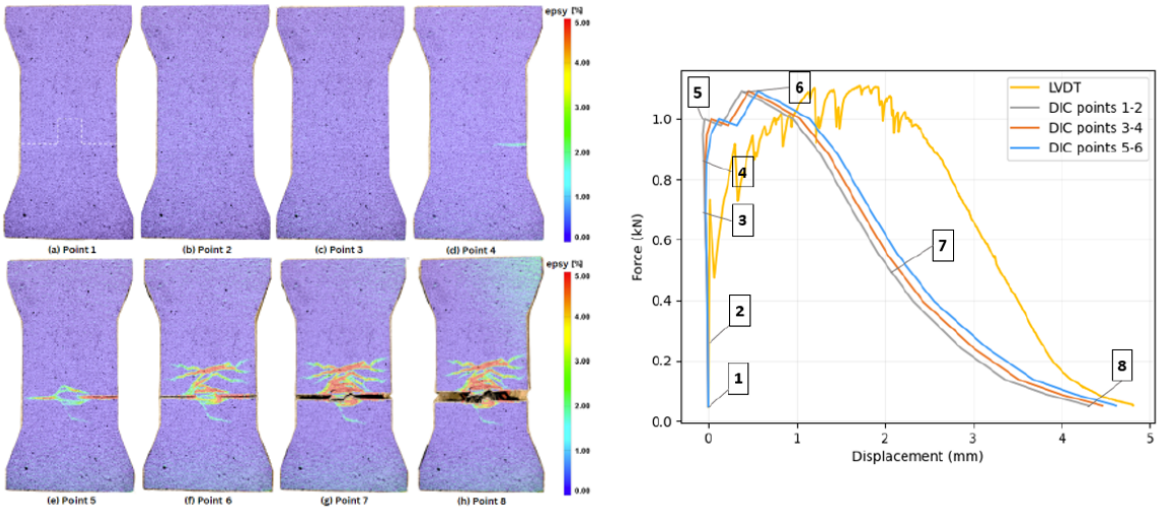

(a) Fracture response of the tab failure mechanism as was presented in the experimental SCG22 specimen from [21].

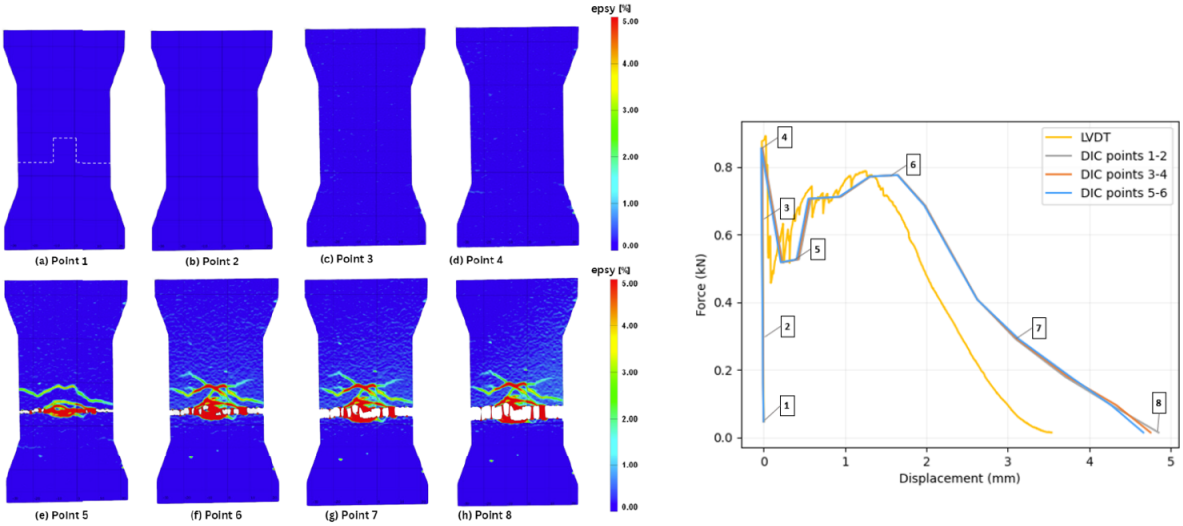

(b) Fracture response of the tab failure mechanism as was presented in the experimental SCG21 specimen from [21].

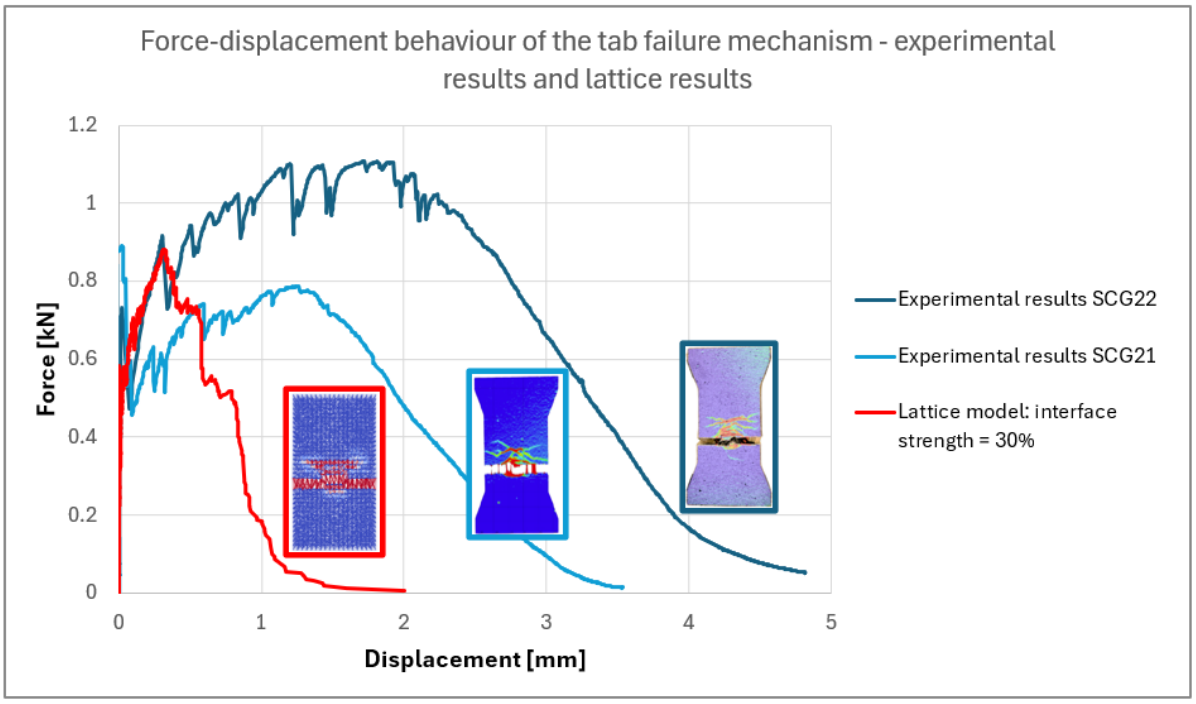

(c) Force-displacement response of the tab failure failure mechanism for both the lattice model and the experimental analysis [21]. For all three results, the cracking response at the end of the analysis is presented as well.

Figure 5.16: Results from the experimental analysis of the tab failure failure mechanism [21].

5.4.4. 4. Transitional failure

The fourth failure mechanism observed is the transitional failure mechanism. In this scenario, the SHCC material activates within the specimen, but the interface still plays an active role in the ultimate failure. Due to stress concentrations and the stiffness contrast between damaged SHCC elements and interface elements, cracks initiate at either the top corners of the tab or the bottom corners of the tab, forming a failure crack through both the interface and the SHCC material. This mechanism represents a transitional between local tab failure and global material failure. The values of the interface strength for which this transitional failure occurs are presented in Table 5.5.

Specimen	w/h ratio	interface strength %	tensile strength MPa	compressive strength MPa
SCG1	1.5	150, 200, 300	6, 8, 12	129.75, 173, 259.5
SCG2	1.0	150, 200, 300	6, 8, 12	129.75, 173, 259.5

Table 5.5: Interface strengths that induce a transitional failure mechanism between the tab failure and material failure mechanism in the lattice analysis.

In this subsection, the SCG2 specimen with an interface strength of 200% is examined, which exhibits the transitional failure mechanism with the dominant crack forming at the top horizontal surfac and in the SHCC material on the sides of the tab, as illustrated in Figure 5.17. The SHCC material displays significant cracking throughout the specimen, with the exception of the interface elements at the bottom horizontal interface, which remain intact. Additionally, the material above the top horizontal interface shows minimal cracking. At point 4, the opening of the top horizontal interface initiates cracking in the material at the top corners. As the analysis progresses, this crack extends further into the specimen. Damage assessment reveals that all material within the specimen is affected, with the least damage occurring in the material above and inside the tab, attributable to the relatively high interface strength and stiffness.

The force-displacement behavior indicates that after the initial linear-elastic stage, the force continues to increase, demonstrating distributed cracking throughout the specimen. A slight drop in force at point 3 corresponds to the formation of the dominant crack. The subsequent hardening and softening behavior beyond point 3 can be attributed to the growth of cracks along the sides of the top horizontal interface and the widening of the final dominant crack.

In Figure 5.18, the force-displacement behavior of the transitional failure mechanisms, as well as the force-displacement behavior of the SHCC material are shown for comparison. The graph illustrates that in each case, the initial force-displacement response closely mirrors the behavior of the SHCC material, following its distributed cracking pattern, as seen in the slight zig-zag curve. This distributed cracking is observed across all specimens, indicating the same general response early in the analysis.

The duration of this alignment with the SHCC material behavior depends on the interface strength; a stronger interface allows the specimen to follow the material's response pattern for a longer period. Consequently, all cases show relatively high peak forces and displacement capacities, approaching the material's peak force and displacement capacity.

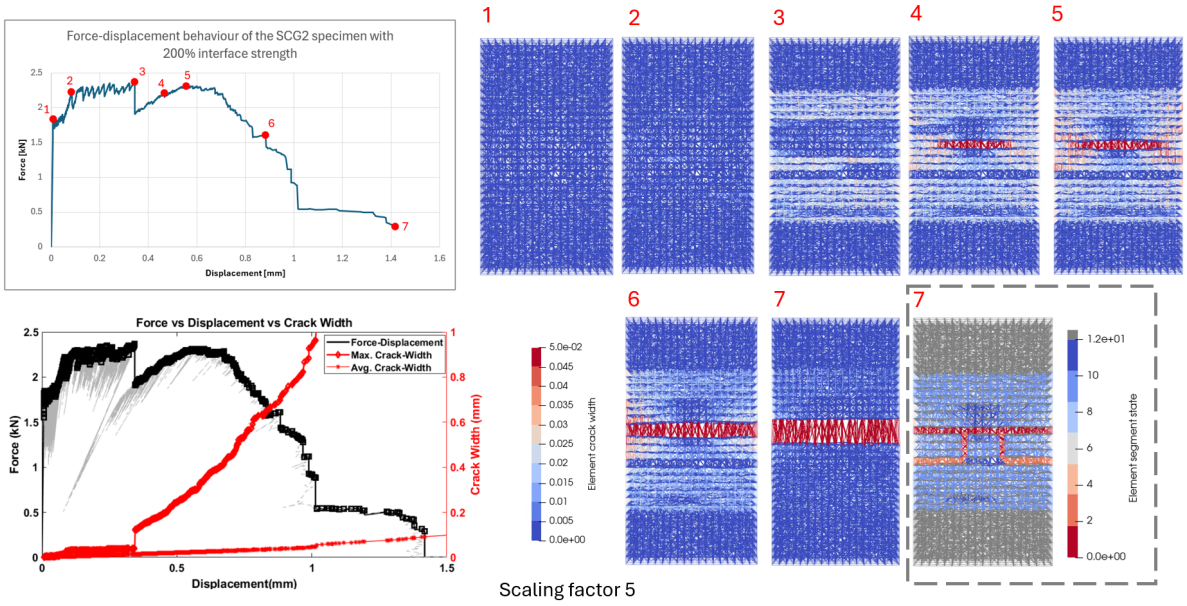

Figure 5.17: Side failure analysis results for the SCG2 specimen with 200% interface strength, showing force-displacement behavior, crack width distribution and progression during the analysis, and final element damage state.

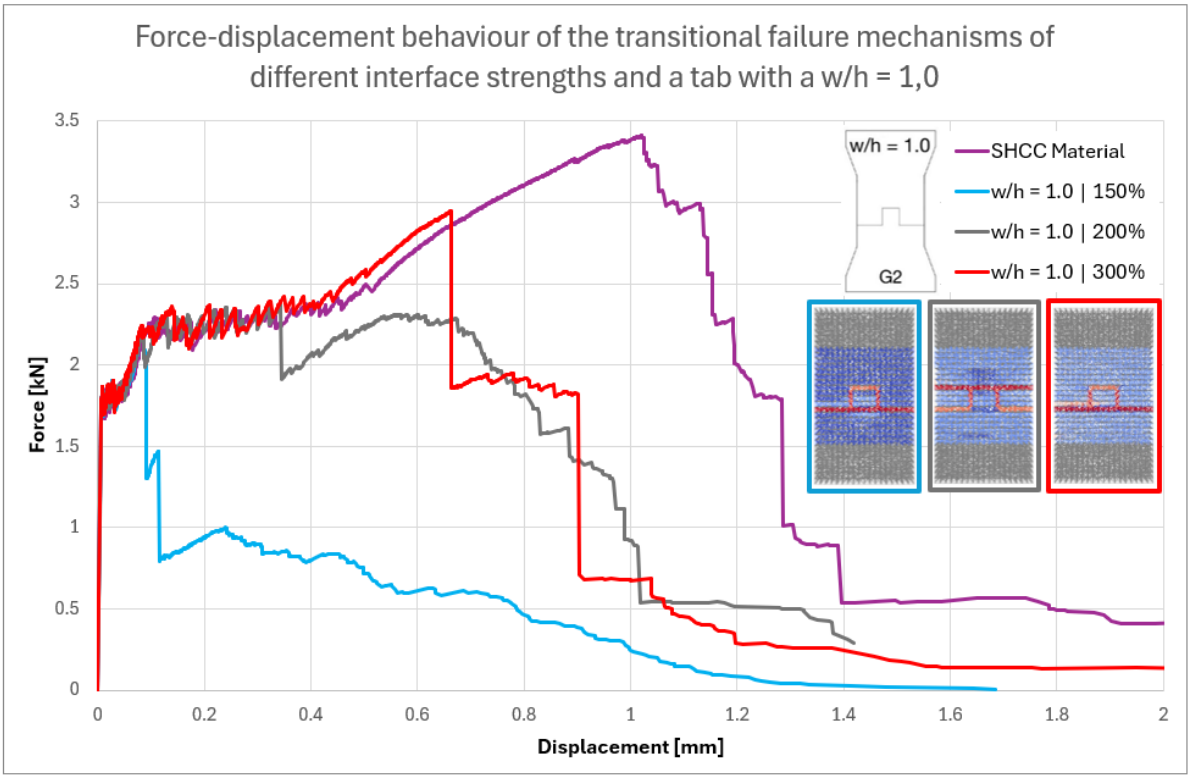

Figure 5.18: Force-displacement response of the transitional failure modes with interface strengths 150%, 200% and 300% vs. the material behavior of the SHCC material. For all three transitional failure modes, the damaged elements are shown. Where the undamaged interface elements are presented in pink, the damaged interface elements are presented in red and the damaged SHCC elements colour from blue to red indicating progressive damage.

5.4.5. 5. Material failure

The last failure mechanism is material failure, characterized by the activation of the entire specimen, leading to cracks forming throughout as if the interface were absent. To enable this type of failure mechanism, the interface strength must exceed the tensile strength of the material. Given the effects of stress concentrations and differences in stiffness, the interface strength needs to be significantly higher than the material's tensile strength to ensure that cracks propagate through the material rather than along the interface. For both interface designs, an interface strength of 500% induces a material failure mechanism (see Table 5.6).

Specimen	w/h ratio	interface strength %	tensile strength MPa	compressive strength MPa
SCG1	1.5	500	20	432.5
SCG2	1.0	500	20	432.5

Table 5.6: Interface strength that shows a material failure mechanism in the lattice analysis.

In this subsection, the SCG1 specimen with an interface strength of 500% is examined, highlighting a material failure mechanism. As shown in Figure 5.19, the dominant crack develops throughout the entire specimen rather than within the interface. The crack width distribution reveals that cracking initially occurs throughout the specimen, with delayed crack formation in the interface elements and in and around the tab, which is particularly visible at point 3. By point 4, cracks have also developed adjacent to and through the tab, and a dominant crack is forming. Notably, the horizontal interface elements remain free of cracking, as indicated by zero crack width. The element damage state further confirms that the horizontal interface elements are undamaged, while the vertical interface elements

display some damage due to cracks propagating through the tab.

In Figure 5.20, the force-displacement response of this analysis is compared with the SHCC material's response without an interface and with the analytical results of the material failure mechanism. The force-displacement behavior closely matches that of the SHCC material, with the only noticeable difference being a slightly compressed graph in the current analysis. This compression likely results from delayed cracking within and around the tab due to the influence of the surrounding interfaces, as well as the lack of damage in the interface elements.

When compared with the analytical results, the initial force-displacement response aligns well, but the softening behavior diverges between the models, as seen previously in the tab failure mechanism. This variation in softening behavior, also present in the SHCC material within the lattice model, can be attributed to differences in material representation rather than fundamental differences in physical behavior.

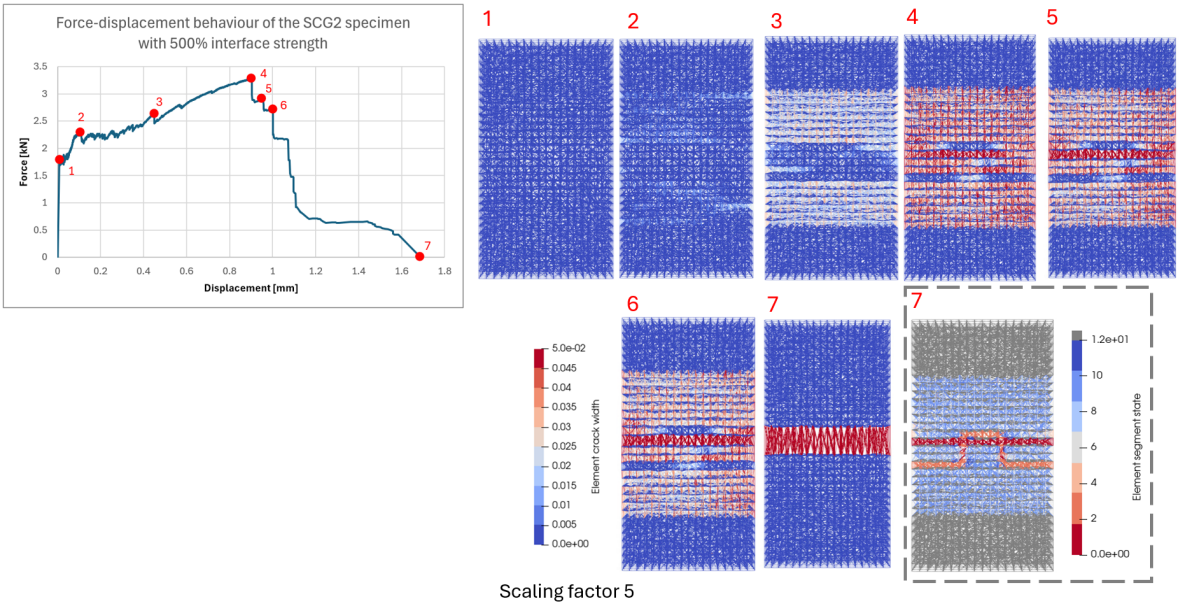

Figure 5.19: Material failure analysis results for the SCG2 specimen with 500% interface strength, showing force-displacement behavior, crack width distribution and progression during the analysis, and final element damage state.

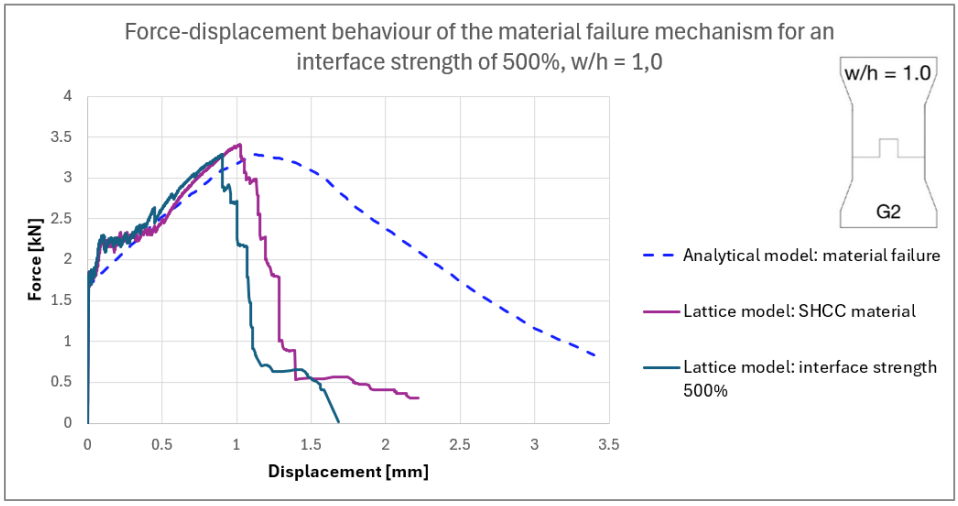

Figure 5.20: Force-displacement response of the material failure mode from both lattice as analytical analysis vs. the material behavior of the SHCC material in the lattice model.

6

Discussion

This chapter discusses the results obtained from the three models. First, the performance of the continuum smeared cracking model is compared with that of the lattice discrete cracking model. Following this, a parametric study is performed to examine the influence of interface strength and tab length on the tensile response of the connection, using both the analytical and lattice models.

6.1. Model performance comparison

In this section, the performance of the continuum smeared cracking model in Abaqus is compared with that of the lattice discrete cracking model. The models are evaluated based on their ability to predict the fracture development and force-displacement behavior for the pull-out and tab failure mechanisms.

6.1.1. Comparison of model results to experimental results.

Pull-out mechanism

Figure 6.1 compares the pull-out failure mechanism observed in the continuum smeared cracking model and the lattice discrete cracking model with experimental results from [21]. The continuum smeared cracking model closely matches the experimental force-displacement behavior, demonstrating good alignment. In contrast, the lattice discrete cracking model exhibits a highly brittle response, deviating significantly from experimental observations.

This discrepancy arises from the interface definitions in the two models. The continuum smeared cracking model incorporates a non-brittle interface with significant post-peak softening, which better captures the experimental behavior. Conversely, the lattice discrete cracking model currently employs brittle interface elements, leading to an abrupt failure response.

However, when examining the fracture response, the lattice model more accurately replicates the experimental fracture development. Cracking in the material surrounding the tab is better captured by the lattice model, suggesting it provides a closer representation of the experimental specimen's fracture behavior than the continuum smeared cracking model in Abaqus.

Additionally, despite the notable differences in the force-displacement response, both models have demonstrated the ability to accurately capture all the distinct failure mechanisms identified in the analytical analysis.

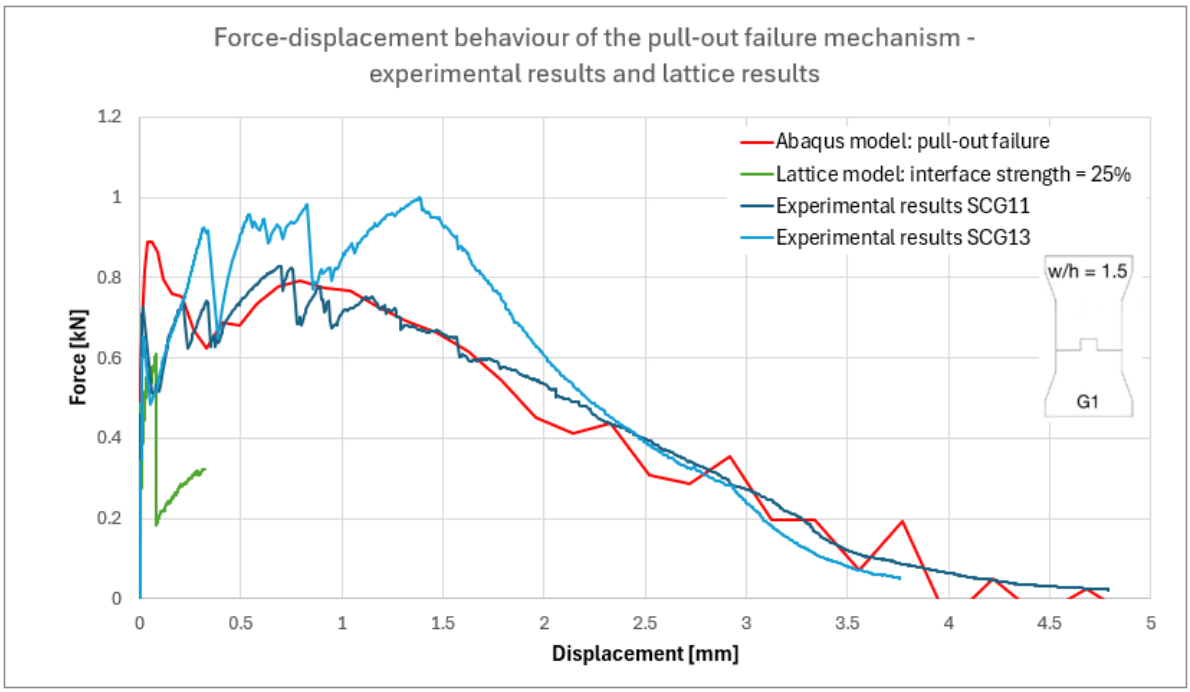

(a) Force-displacement response of the pull-out mechanism for the experimental specimens from [21], the continuum smeared cracking model in Abaqus and the lattice discrete cracking model.

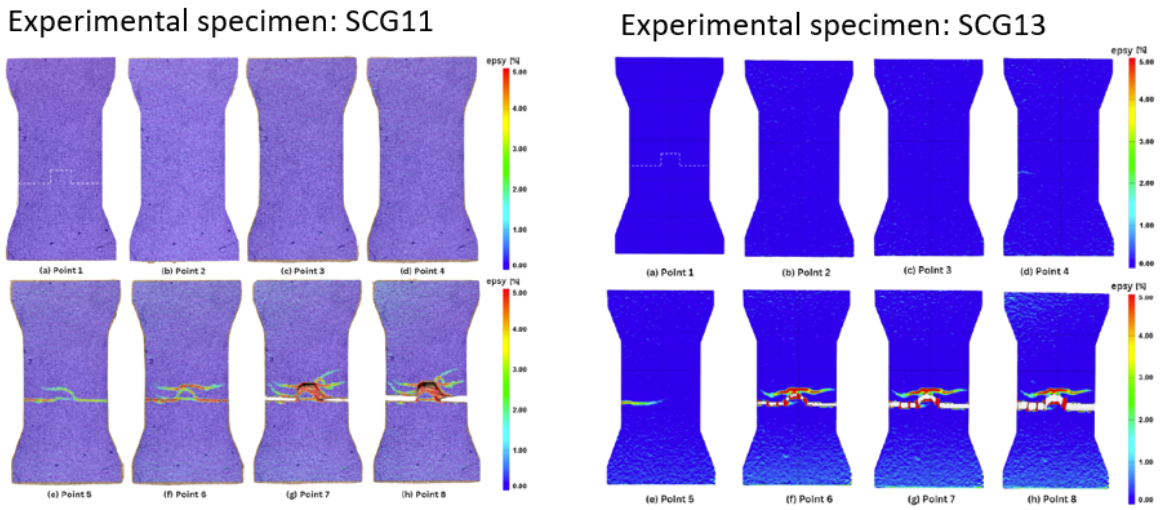

(b) Fracture response of the pull-out failure mechanism as was presented in the experimental SCG11 and SCG13 specimens from [21].

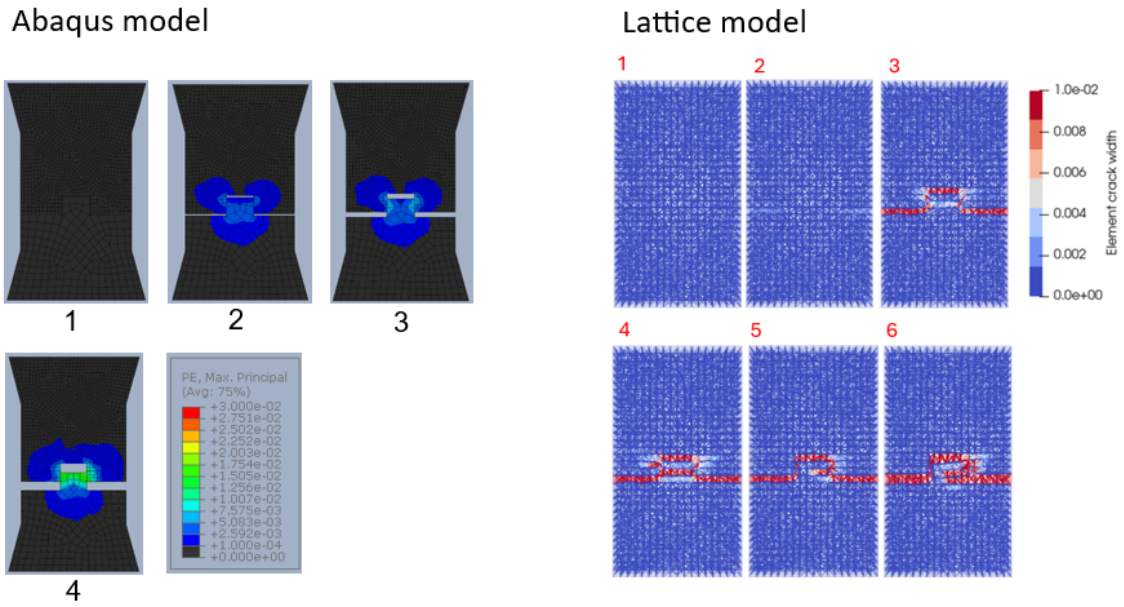

(c) Fracture response of the pull-out failure mechanism from both the continuum smeared cracking model in Abaqus and the lattice discrete cracking model.

Figure 6.1: Results from pull-out failure mechanism for the experimental specimens, the continuum smeared cracking model in Abaqus and the lattice discrete cracking model.

The potential for enhanced performance in the lattice model is illustrated in Figure 6.2, where a single straight-tab interface with a width-to-height ratio of 1.5 and an interface strength of 5% is analyzed using non-brittle interface elements. Although the interface parameters in this case have not been optimized, the results highlight that incorporating non-brittle interface elements enables the lattice model to replicate a non-brittle pull-out mechanism. This finding suggests that further refinement of the model could bring its predictions closer to experimental behavior.

Moreover, the results indicate that the interface strengths at which specific behaviors occur in the lattice model may currently be overestimated. In this case, a 5% interface strength with ductile interface elements produces a pull-out mechanism with substantial SHCC material damage. In contrast, the same interface strength with brittle interface elements results in a delamination failure mechanism. This discrepancy underscores the importance of improving the accurate representation of interface ductility to better align the model with physical observations.

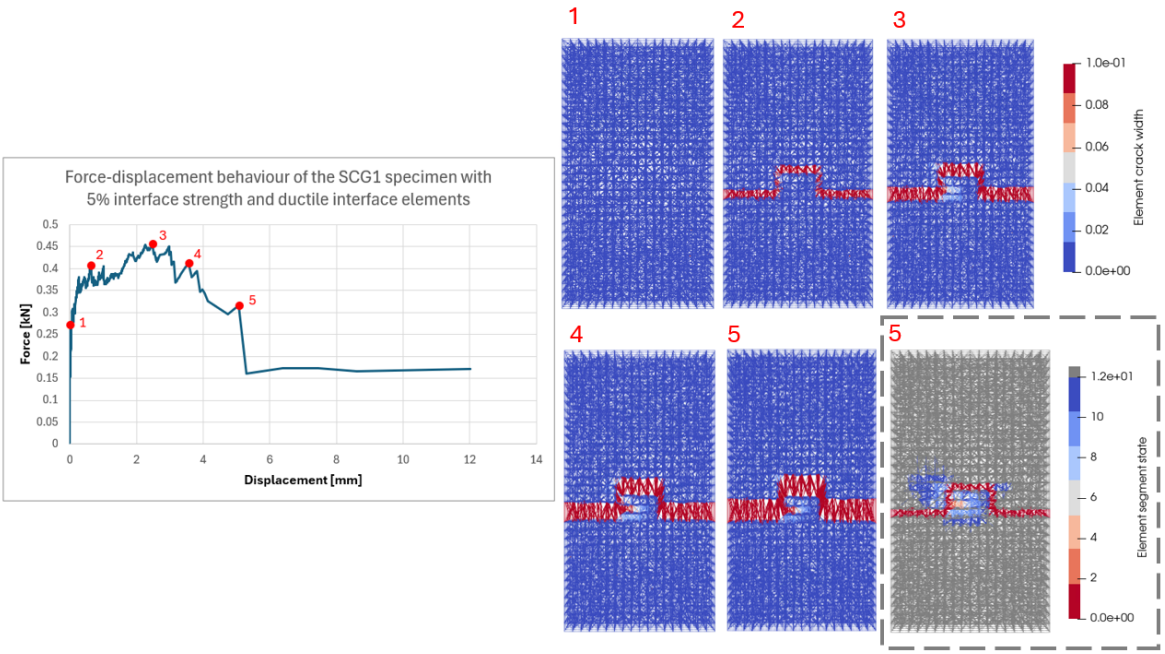

Figure 6.2: Analysis results of the SCG1 specimen with a 5% interface strength and ductile interface elements which presented a pull-out failure mechanism.

For the current models, the non-brittle interface in the smeared cracking model aligns more closely with experimental force-displacement behavior and is consistent with findings reported in the literature [28].

Tab failure mechanism

Figure 6.3 compares the tab failure mechanism observed in the continuum smeared cracking model and the lattice discrete cracking model with experimental results from [21]. Both models underestimate the displacement capacity and the extent of hardening behavior resulting from distributed cracking within the tab. However, the lattice model aligns more closely with the initial trend of the experimental hardening response, showing a gradual force increase over a broader range that reflects sustained hardening. In contrast, the Abaqus model exhibits a much stiffer initial response, followed by a rapid plateau in load-bearing capacity, failing to replicate the experimentally observed distributed hardening. While the displacement capacity at peak force is comparable between the two models, the marked difference in how hardening behavior is represented highlights the superior ability of the lattice model to capture the progression of distributed cracking within the tab.

Examining the fracture responses provides insight into these discrepancies. The lattice model accurately captures distributed cracking within the tab and its extension into the surrounding material, reflecting the experimental fracture behavior. Conversely, in the Abaqus model, significant plastic strain is confined within the tab, with only minimal strain observed in the surrounding material. This limited strain distribution indicates that the Abaqus model does not adequately predict the propagation of cracks from the tab into adjacent regions, contributing to its inability to represent the material's hardening response accurately.

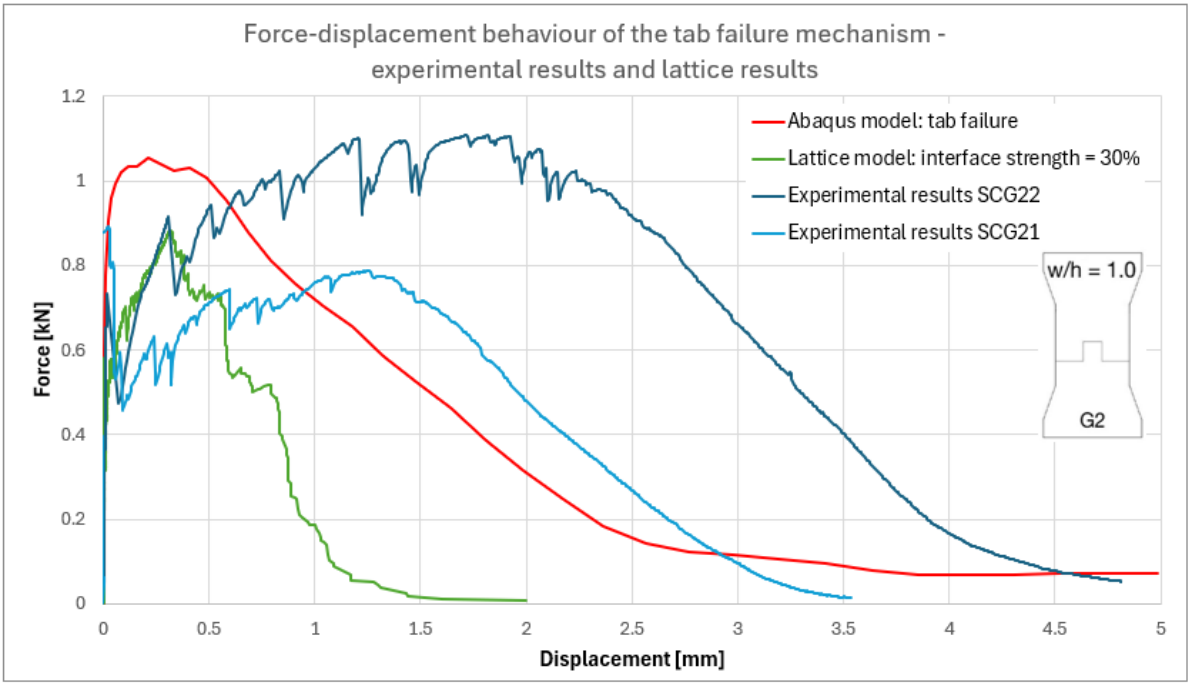

(a) Force-displacement response of the tab mechanism for the experimental specimens from [21], the continuum smeared cracking model in Abaqus and the lattice discrete cracking model.

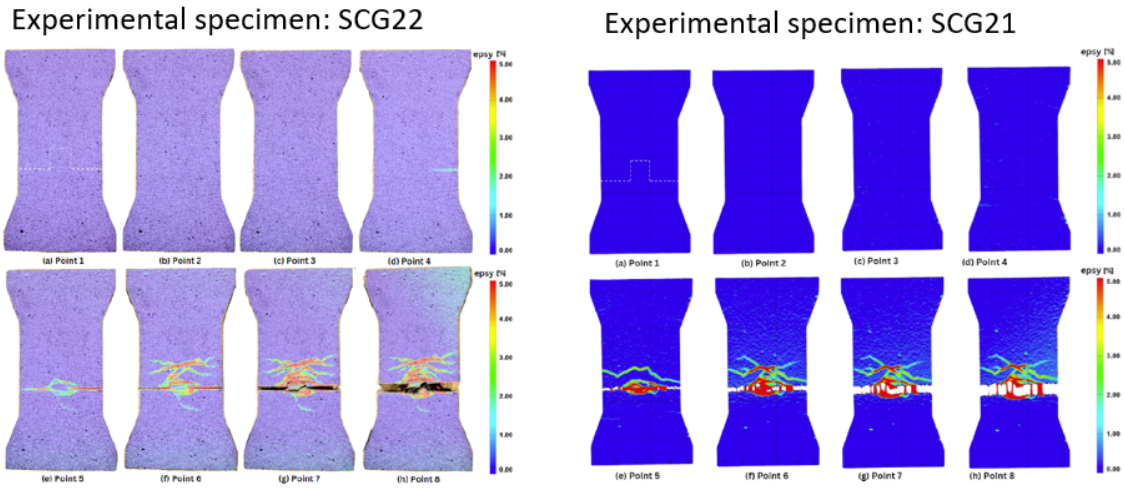

(b) Fracture response of the tab failure mechanism as was presented in the experimental SCG22 and SCG21 specimens from [21].

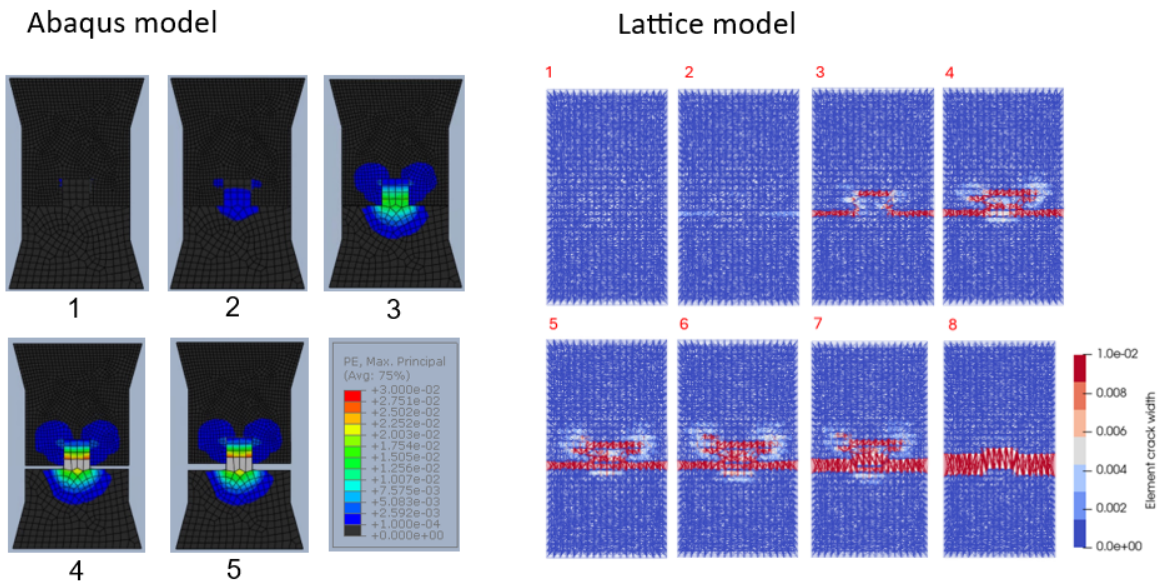

(c) Fracture response of the tab failure mechanism from both the continuum smeared cracking model in Abaqus and the lattice discrete cracking model.

Figure 6.3: Results from tab failure mechanism for the experimental specimens, the continuum smeared cracking model in Abaqus and the lattice discrete cracking model.

6.1.2. Comparison

The comparison of the two models in both the pull-out and tab failure mechanisms highlights distinct strengths and limitations. While the lattice model does not yet fully replicate the force-displacement behavior for either mechanism, it successfully captures the fracture response within the connection. In contrast, the continuum smeared cracking model, as implemented in this research, accurately reproduces the force-displacement behavior for the pull-out failure mechanism and demonstrates fracture patterns comparable to experimental results. However, comparing the extent of cracking in the experimental results to the magnitude of plastic strain in the SHCC material remains challenging.

For the tab failure mechanism, the continuum model does not accurately replicate the force-displacement behavior, and the fracture patterns observed experimentally differ significantly from the plastic strain development predicted by the model. The more accurate force-displacement representation for the pull-out mechanism in the continuum model can be attributed to differences in the governing failure mechanisms. In the pull-out mechanism, the observed hardening in the force-displacement curve arises primarily from the interface properties as defined in the Abaqus model. However, this derivation of hardening from the interface, rather than from the SHCC material itself, deviates from the actual mechanisms observed in experimental specimens.

Key Differences Between the Models

To compare the behavior of the two models effectively, it is essential to consider their underlying approaches to plasticity and damage. In the lattice model, plastic behavior is modeled exclusively through damage, defined as the degradation of element material properties once the element reaches its maximum stress. Conversely, in the continuum smeared cracking model, plastic behavior arises from a combination of plasticity and damage.

Damage development in the continuum model was defined to initiate when the stress in the single-crack stress-displacement relationship begins to decline. Before reaching this point, the material undergoes stress increase within the plastic range, without triggering damage. Only after the peak stress is reached and the stress begins to decrease does damage initiation occur.

Plasticity vs. Damage in Simulating Localized Cracking

A fundamental difference between modeling plastic behavior via plasticity and via damage lies in their ability to simulate localized cracking. Plasticity alone spreads deformation over a larger volume,

leading to smeared behavior that cannot inherently drive crack formation. In contrast, damage evolution introduces strain softening, concentrating deformation in localized zones and driving the formation of discrete cracks.

This distinction explains the continuum model's limitations in capturing localized hardening behavior at the interface. The material hardening behavior is primarily defined using plasticity, which is less suited to modeling highly localized phenomena. In the lattice model, however, damage governs the entire plastic behavior of the material, enabling it to more effectively capture this localized hardening response.

6.2. Parametric study

In this section the parametric study is performed to investigate the behavior of interface strength and tab length on the behavior of the interface connection. First the influence of interface strength and tab length on the tensile response is investigated using the analytical model, thereafter the influence of interface strength and tab length on the tensile response is investigated using the lattice model.

6.2.1. Analytical model

To examine the influence of interface strength and tab length on the tensile response of the interface connection, the peak force and absorbed energy (calculated as the area under the force-displacement curve) were analyzed and compared to those of the SHCC material without an interface. This comparison provides valuable insights into how variations in interface strength and tab length can shift the failure mechanism from brittle, interface-driven modes to a more ductile, material-driven response.

Influence of interface strength

In the analytical model, the interface strength was varied as a percentage of the material's tensile strength: 3%, 6%, 9%, 12%, 14%, and 100%. The corresponding force-displacement behavior is shown in Figure Figure 6.4, while Table Table 6.1 summarizes the failure modes, peak forces, and energy absorption (calculated as the area under the force-displacement curves) for each interface strength level.

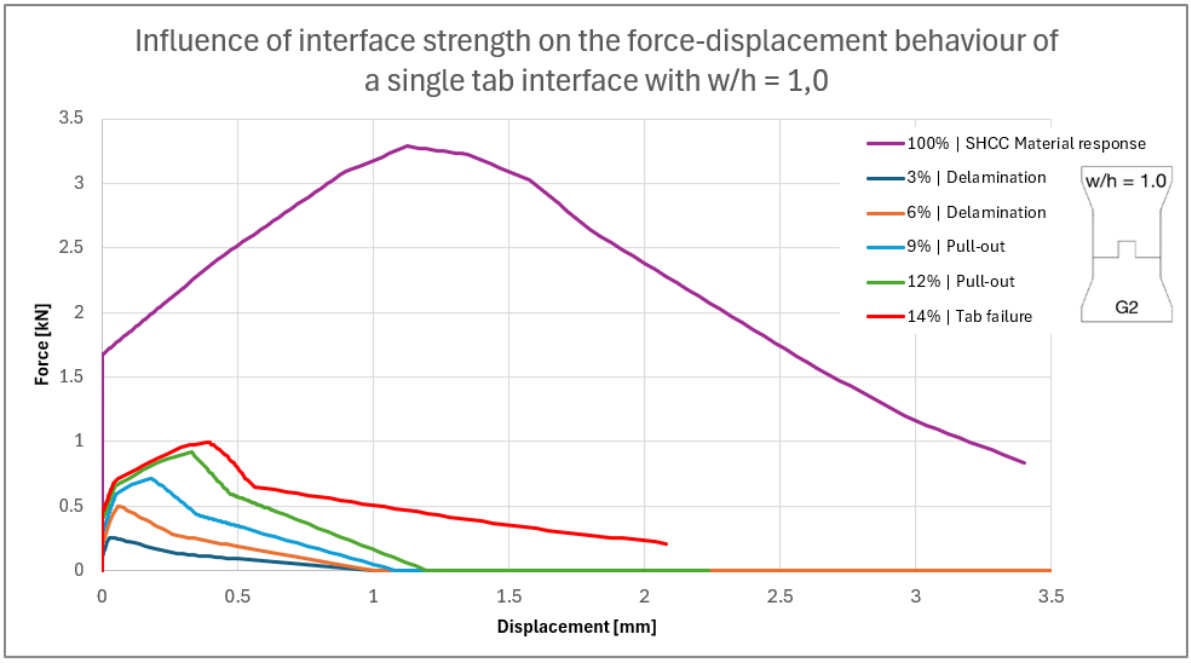

Figure 6.4: Influence of interface strength on the force-displacement behavior for an interface design with a width-to-height ratio of 1.0 in the analytical model.

As the interface strength increases, the peak force rises. In delamination failure modes, the dis-

placement capacity remains constant across different interface strengths. However, in pull-out failure modes, higher interface strength results in increased displacement capacity due to enhanced cracking within the tab. The tab failure mechanism demonstrates the highest displacement capacity among all failure modes. A critical transition occurs between 12% and 14% interface strength, where the failure mechanism shifts from pull-out failure to tab failure. While this transition does not significantly alter the peak force, it markedly increases energy absorption and ductility.

Interface strength	Failure mode	Peak Force [kN]	% of material	Energy [kN*mm]	% of material
3%	Delamination	0.260	8.2%	0.102	1.4
6%	Delamination	0.498	15.7	0.206	2.7
9%	Pull-out failure	0.744	23.5	0.385	5.1
12%	Pull-out failure	0.917	29.0	0.580	7.6
14%	Tab failure	0.972	30.7	1.238	16.2
100%	Material failure	3.165	100	7.621	100
No interface	Material failure	3.165	100	7.621	100

Table 6.1: Influence of interface strength on the presented failure mechanisms, peak force and energy absorption for an interface design with a width-to-height ratio of 1.0 in the analytical model.

The highest peak force and energy absorption are achieved at 100% interface strength, corresponding to material failure. Among the interface-dominated failure modes, the tab failure mechanism achieves approximately 31% of the material's peak strength and 16% of its energy absorption, highlighting its superior performance in energy dissipation compared to delamination and pull-out failure.

To further illustrate these trends, Figure Figure 6.5 presents the peak force, energy absorption, and failure mechanisms across varying interface strengths. This visualization clearly shows that the peak force steadily increases with interface strength, while energy absorption significantly rises when transitioning from interface-dominated failure modes (delamination and pull-out) to material-dominated failure (tab failure).

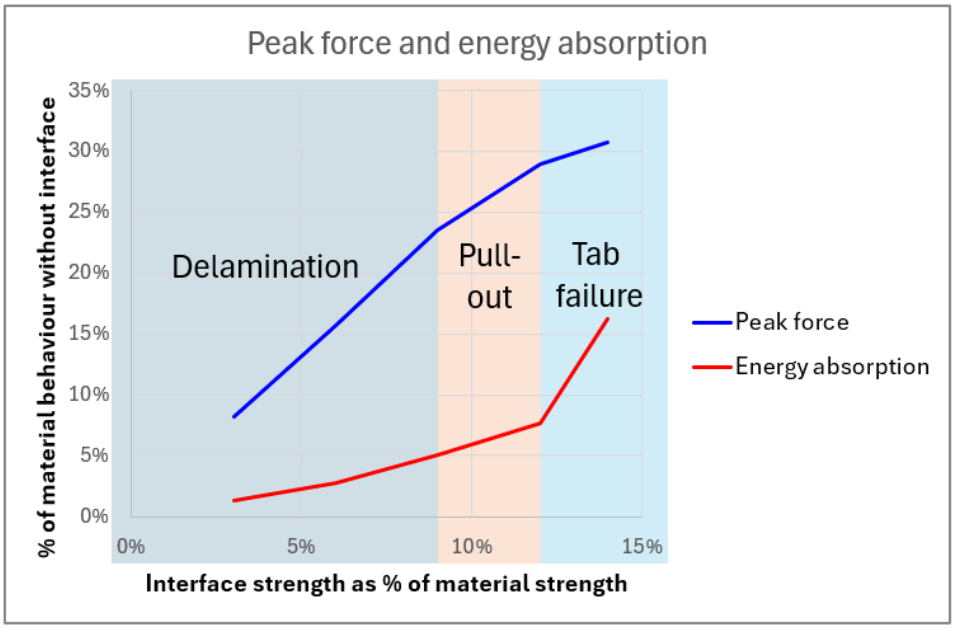

Figure 6.5: Influence of interface strength on the peak force, energy absorption values as a percentage of the peak force and energy absorption of the SHCC material without interface. Including the occurring failure mechanisms.

Influence of tab length

In the analytical model, three tab lengths with width-to-height (w/h) ratios of 1.5, 1.0, and 0.5 were used to investigate the influence of tab length on the tensile response. The interface strength was set to 12% of the material strength to isolate the effects of tab length. The force-displacement behavior for each tab length is shown in Figure 6.6, and Table 6.4 summarizes the corresponding failure modes, peak force, and energy absorption while Figure 6.7 visualizes those results.

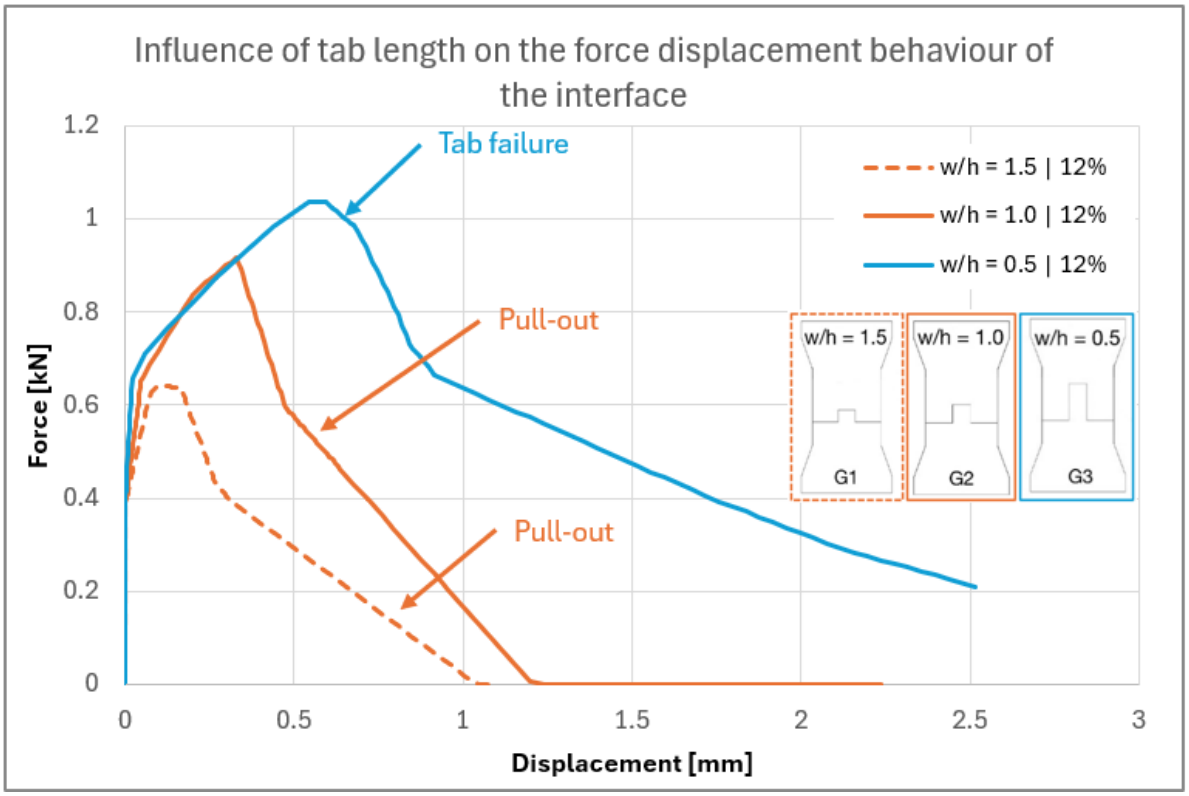

Figure 6.6: Influence of the tab length on the force-displacement behavior of an analytical analysis with an interface with 12% strength.

The force-displacement graphs reveal that, at this interface strength, increasing the tab length results in higher peak forces and greater displacement capacities. Additionally, the change in tab length can lead to different failure modes in the specimen, which in turn significantly impacts displacement capacity and energy absorption. For instance, shifting from pull-out failure in the specimen with a w/h ratio of 1.0 to tab failure in the specimen with a w/h ratio of 0.5 increases the peak force by approximately 13% and increases the absorbed energy by a substantial 153%.

w/h ratio	Failure mode	Peak Force [kN]	% of material	Energy [kN*mm]	% of material
1.5	Pull-out	0.641	20.3	0.3	3.9
1.0	Pull-out	0.917	29.0	0.580	7.6
0.5	Tab failure	1.038	32.8	1.466	19.2
No interface	Material failure	3.165	100	7.621	100

Table 6.2: Influence of tab length on the presented failure mechanisms, peak force and energy absorption for an interface design with a width-to-height ratio of 1.0 in the lattice discrete cracking model.

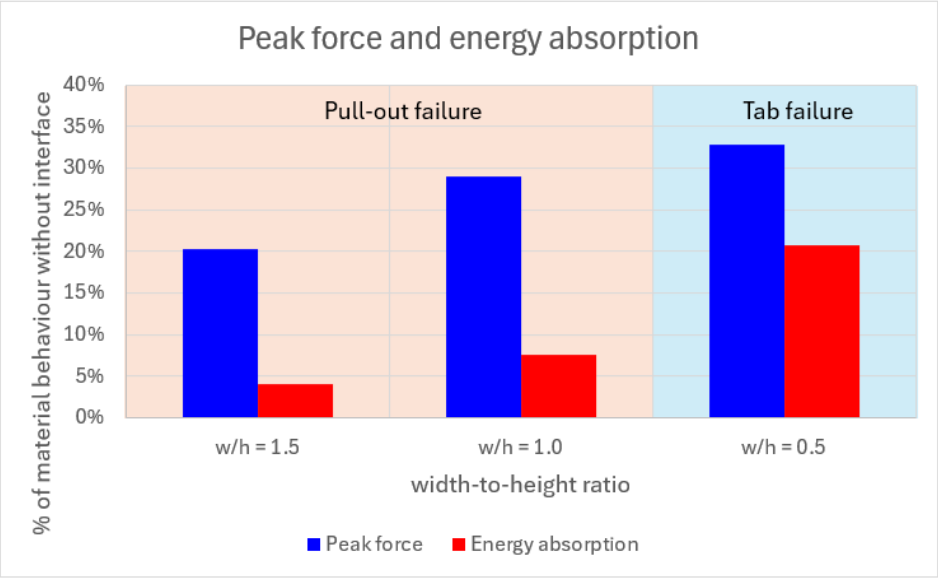

Figure 6.7: Influence of the tab length on peak force and energy absorption values as a percentage of the peak force and energy absorption of the SHCC material without interface for specimens with an interface strength of 12%. Including the occurring failure mechanisms.

Combined influence of interface strength and tab length

To examine the combined effect of tab length and interface strength, the force-displacement behaviors for interface strengths of 3%, 6%, 9%, 12%, and 14%, across varying tab lengths, are presented in Figure 6.8. The effects on failure mode, peak force, and energy absorption are summarized in Table 6.3.

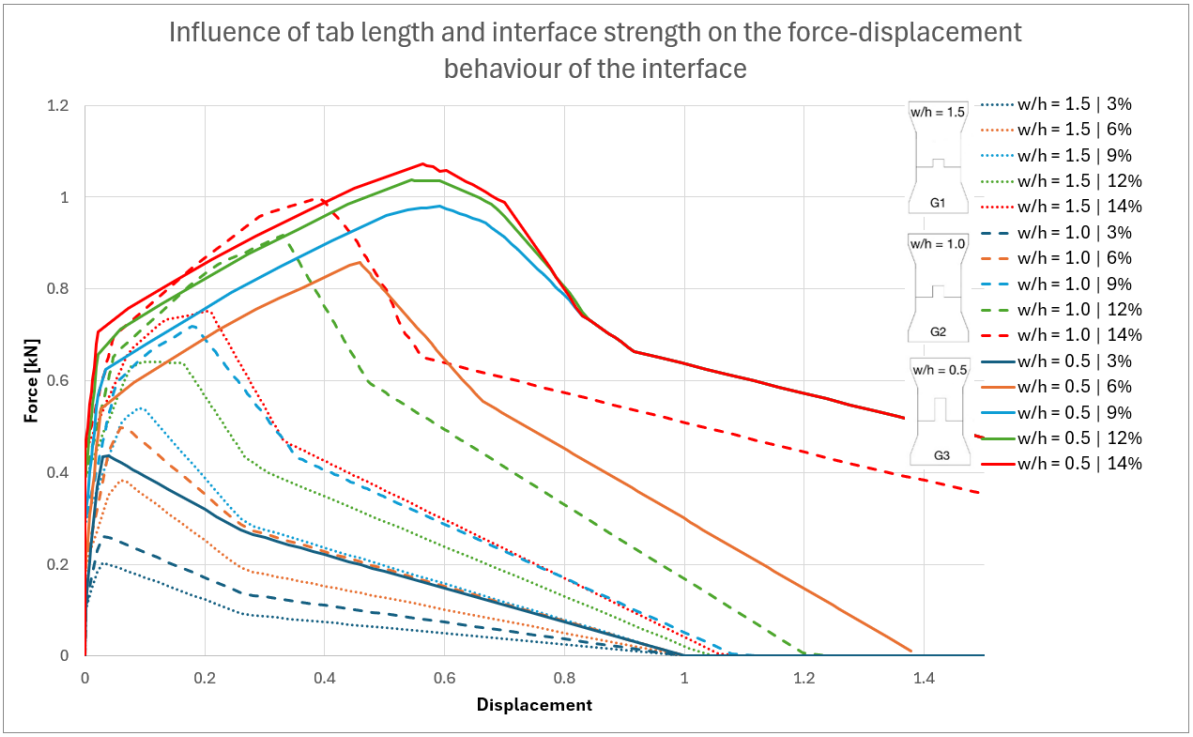

Figure 6.8: Influence of the tab length and interface strength on the force-displacement behavior of the connection in the analytical model.

As shown in Figure 6.8, increasing the tab length consistently enhances both the peak force and absorbed energy across all specimens. Notably, a specimen with a lower interface strength but a longer tab can exceed the load-bearing and displacement capacity of a specimen with a higher interface strength and a shorter tab. This trend is further detailed in Table 6.3 and Figure 6.9, which demonstrate that longer tabs can induce a tab failure mode even in specimens with weaker interfaces, whereas pull-out failure may still occur in specimens with stronger interfaces and shorter tabs.

Even with a relatively short tab (w/h = 1.5), activating SHCC material behavior in pull-out or tab failure mechanisms is achievable at relatively low interface strengths—9% for pull-out failure and 20% for tab failure. Increasing the tab length further (w/h = 0.5) significantly reduces the required interface strength, with values dropping to 4% for pull-out failure and 7% for tab failure. This observation aligns with the expectation that the stress transfer in the connection depends on the total area of the interface.

Interface strength	w/h ratio	Failure mode	Peak Force [kN]	% of material	Energy [kN*mm]	% of material
3%	1.5	Delamination	0.202	6.4	0.0726	1.0
	1.0	Delamination	0.260	8.2	0.102	1.3
	0.5	Delamination	0.436	13.8	0.192	2.5
6%	1.5	Delamination	0.383	12.1	0.146	1.9
	1.0	Delamination	0.489	15.7	0.206	2.7
	0.5	Pull-out	0.858	27.1	0.667	8.8
9%	1.5	Delamination	0.541	17.1	0.219	2.9
	1.0	Pull-out	0.744	23.5	0.385	5.1
	0.5	Tab failure	0.98	31.0	1.528	20.0
12%	1.5	Pull-out	0.641	20.3	0.313	4.1
	1.0	Pull-out	0.917	29.0	0.580	7.6
	0.5	Tab failure	1.038	32.8	1.598	20.7
14%	1.5	Pull-out	0.751	23.7	0.386	5.1
	1.0	Tab failure	0.972	30.7	1.238	16.2
	0.5	Tab failure	1.072	33.9	1.598	21.0
No interface	-	Material failure	3.165	100	7.621	100

Table 6.3: Influence of tab length and interface strength on the presented failure mechanisms, peak force and energy absorption in the analytical model.

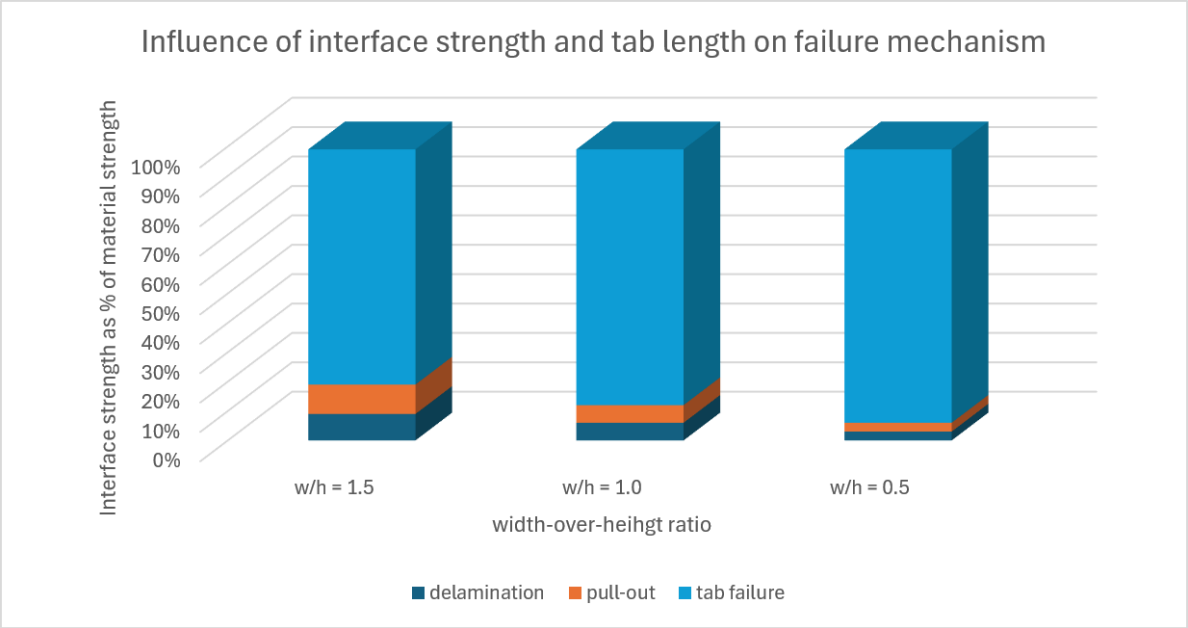

Figure 6.9: Influence of interface strength and tab length on the failure mechanism in the analytical model.

6.2.2. Lattice model

Similarly as in the parametric study in the analytical model, in the parametric study in the lattice model the influence of interface strength and tab length on the tensile response of the interface connection is examined. This is done by comparing the values of the peak force, absorbed energy (calculated as the area under the force-displacement curve) and the number of damaged SHCC elements in the analyses are compared to those of the SHCC material without an interface. This comparison provides valuable insights into how variations in interface strength and tab length can shift the failure mechanism from brittle, interface-driven modes to a more ductile, material-driven response.

Influence of interface strength

In the lattice model, a range of interface strengths was tested to evaluate their influence on the tensile behavior of the connection. The strengths examined extended from 5% to 500% of the material's tensile strength, specifically: 5%, 10%, 15%, 20%, 25%, 30%, 50%, 75%, 100%, 150%, 200%, 300% and 500%. Compared to the analytical model, the lattice model explored significantly higher interface strengths, continuing until full material failure was observed.

Figure 6.10 presents the force-displacement curves for these interface strengths. It is evident that the interface strength of 500% produces a behavior most similar to that of the SHCC material itself. The notably high interface strength required to achieve this similarity is largely due to the brittleness of the interface elements used in this research. As discussed in subsection 5.4.2, introducing ductility into the interface elements facilitates greater material activation at lower interface strengths. This suggests that incorporating some displacement capacity into the interface elements would reduce the interface strength needed to achieve full material activation.

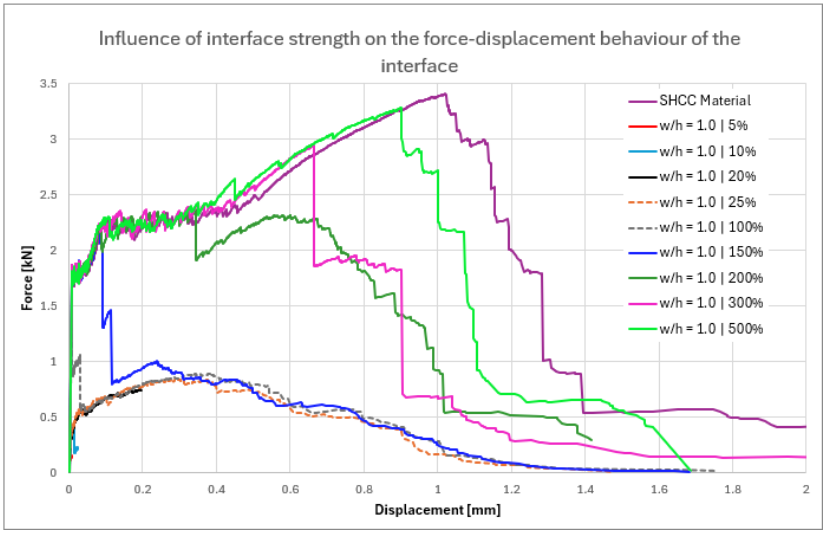

(a) Influence of interface strength on the force-displacement behavior for an interface design with a width-to-height ratio of 1.0 in the lattice discrete cracking model.

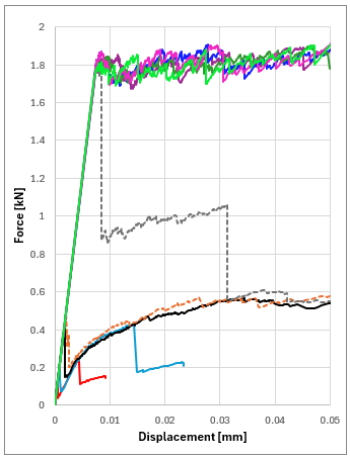

(b) Zoomed in force-displacement response.

Figure 6.10: Influence of interface strength on the force-displacement behavior for an interface design with a width-to-height ratio of 1.0 in the lattice discrete cracking model.

As detailed above, Figure 6.10 illustrates the force-displacement curves for various interface strengths. Additionally, Table 6.4 summarizes the corresponding failure modes, peak forces, energy absorption values, and the percentage of damaged SHCC elements, compared to the analysis of the specimen without an interface. Furthermore, Figure 6.11 visualizes the relationships between interface strength, damaged SHCC elements, peak force, and energy absorption.

From the force-displacement curves, it is evident that specimens with interface strengths of 5% and 10% exhibit significantly low displacement capacities and minimal energy absorption. However, even within the pull-out failure mechanism, a specimen with an interface strength of 20% demonstrates a substantial increase in both displacement capacity and energy absorption compared to the 10% specimen.

In failure modes dominated by delamination or pull-out with limited SHCC material damage, the absorbed energy and displacement capacity remain notably low. As the interface strength increases within the pull-out mechanism, a greater number of SHCC elements are activated, leading to enhanced displacement capacity and higher energy absorption. This highlights the critical role of interface strength in promoting more extensive material activation and improving the tensile response.

At moderate interface strengths (25%–100%), the failure mechanism transitions to tab failure. During this stage, peak force increases with interface strength, primarily due to the contribution of horizontal interface elements. However, energy absorption remains relatively constant at approximately 18%, and the percentage of damaged SHCC elements stabilizes around 30%. Figure 6.10 highlights that the force-displacement responses for specimens with 25% and 100% interface strengths are nearly identical beyond the peak force. While the peak force differs, reflecting the varying contributions of interface elements, the post-peak behavior follows the same trend.

As the interface strength increases further and transitions toward the material failure mechanism, the force-displacement response increasingly resembles the behavior of the original SHCC material. The range over which this alignment occurs expands with increasing interface strength, leading to slight increases in peak force and energy absorption. Once the transitional failure mechanism is reached at an interface strength of 150%, the percentage of damaged SHCC elements remains constant. This indicates that material activation at this stage is comparable to that observed in full material failure. However, because the elements in the transitional mechanism are not as extensively damaged as in the material failure mechanism, peak force and energy absorption continue to rise until full material failure is achieved.

Interface strength	Failure mode	Peak Force [kN]	% of material	Energy [kN*mm]	% of material	% of damaged SHCC elements
5%	Delamination	0.244	7	0.0013	0	1
10%	Pull-out	0.431	13	0.0061	0	3
15%	Pull-out	0.472	14	0.0368	1	10
20%	Pull-out	0.751	22	0.121	3	25
25%	Tab failure	0.839	25	0.626	16	28
30%	Tab failure	0.882	26	0.635	17	31
50%	Tab failure	1.002	29	0.673	18	31
75%	Tab failure	1.575	46	0.637	17	30
100%	Tab failure	1.825	54	0.705	18	36
150%	Transition failure	2.201	65	0.830	22	93
200%	Transition failure	2.368	69	2.215	58	93
300%	Transition failure	2.948	86	2.803	73	96
500%	Material failure	3.288	96	3.144	82	93
No interface	Material failure	3.409	100	3.818	100	100

Table 6.4: Influence of interface strength on the presented failure mechanisms, peak force and energy absorption for an interface design with a width-to-height ratio of 1.0 in the lattice discrete cracking model.

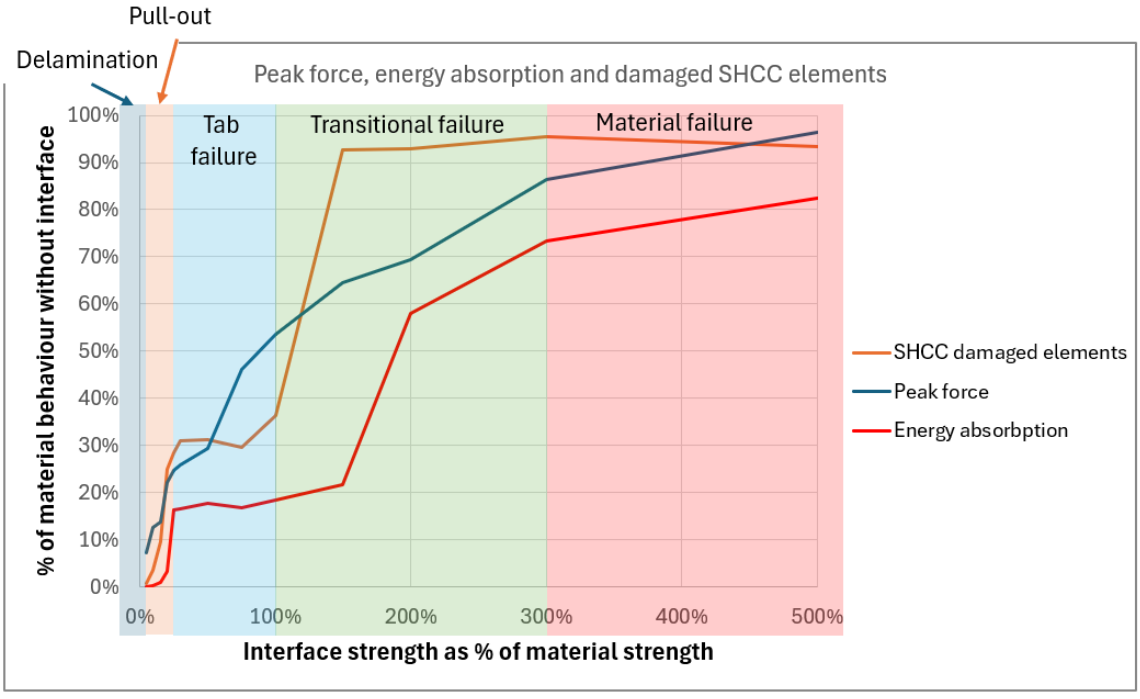

Figure 6.11: Influence of interface strength on peak force, absorbed energy and amount of damaged SHCC elements.

Influence of tab length

In the lattice model, the influence of tab length on the tensile behavior of the connection was analyzed using specimens with width-to-height (w/h) ratios of 1.5 and 1.0. An interface strength of 25% of the material's tensile strength was used to ensure that the effects of tab length could be isolated and directly compared. Figure 6.12, included below, illustrates the force-displacement behavior for the two tab lengths.

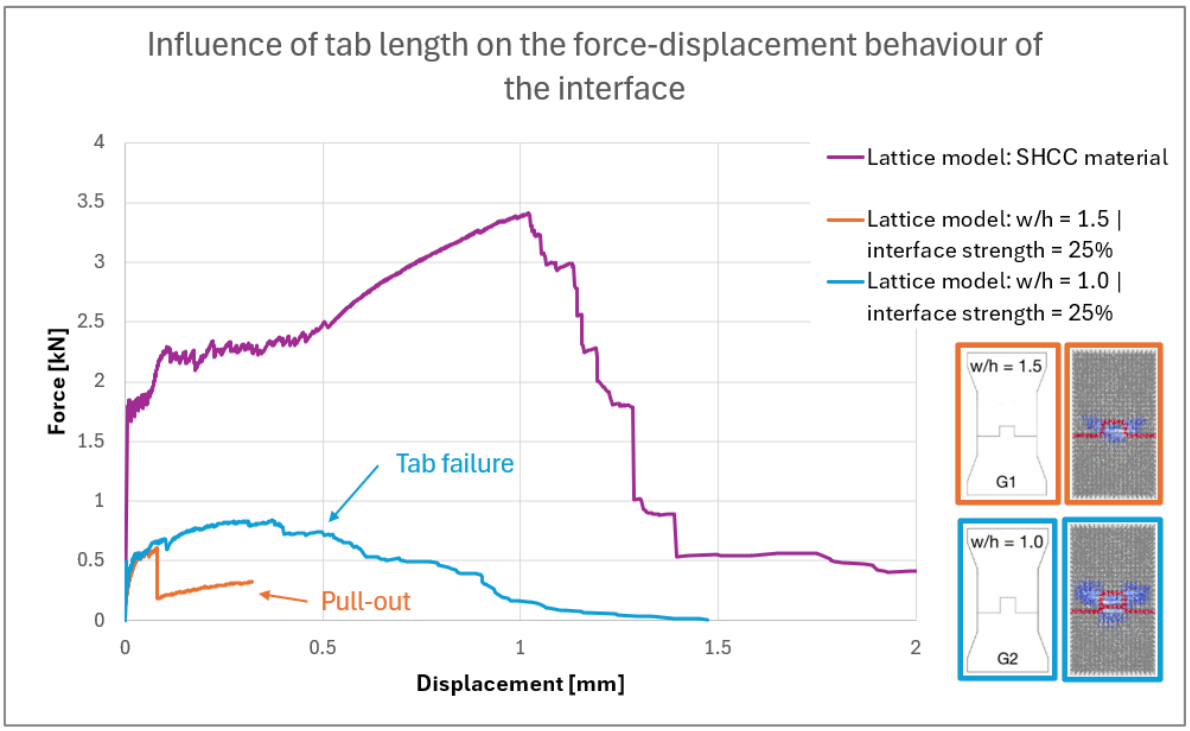

Figure 6.12: Influence of the tab length on the force-displacement behavior of a lattice analysis with an interface with 25% strength. For both specimens, the damaged elements are shown. Where the undamaged interface elements are presented in pink, the damaged interface elements are presented in red and the damaged SHCC elements colour from blue to red indicating progressive damage.

The graph clearly shows that increasing the tab length significantly improves both strength and displacement capacity. This improvement is primarily attributed to a change in failure mechanism. When the tab length is increased, the failure mode transitions from pull-out failure to tab failure, which allows more extensive activation of the SHCC material and a greater resistance to loading. This trend is supported by the data presented in Table 6.5, where the measured failure mechanisms, peak forces, and energy absorption values are summarized.

w/h ratio	Failure mode	Peak Force [kN]	% of material	Energy [kN*mm]	% of material	% of damaged SHCC elements
1.5	Pull-out	0.608	18	0.104	3	14
1.0	Tab failure	0.839	25	0.626	16	28
No interface	Material failure	3.409	100	3.818	100	100

Table 6.5: Influence of interface strength on the presented failure mechanisms, peak force and energy absorption for an interface design with a width-to-height ratio of 1.0 in the lattice discrete cracking model.

The relationship between tab length, peak force, energy absorption, and SHCC damage is visualized in Figure 6.13. This figure emphasizes the substantial improvements in energy absorption and

SHCC material activation when the tab length increases.

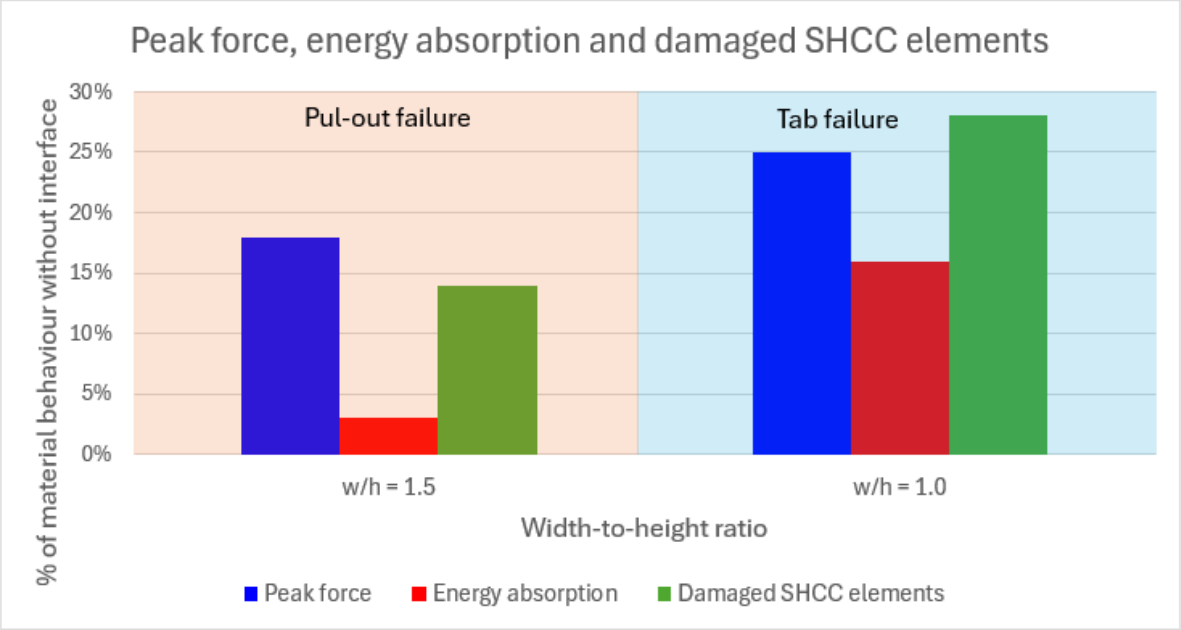

Figure 6.13: Influence of the tab length on peak force, energy absorption and amount of damaged SHCC elements as a percentage of the peak force and energy absorption of the SHCC material without interface for specimens with an interface strength of 25%. Including the occurring failure mechanisms.

The results demonstrate that while the peak force increases modestly with a longer tab (38%), the energy absorption rises dramatically, by 502%, reflecting a far greater ability of the connection to sustain deformation before failure. This is attributed to the shift in failure mechanism and the associated increase in SHCC material activation. Specifically, the percentage of damaged SHCC elements doubles when the tab length is increased from w/h = 1.5 to w/h = 1.0.

This increase in SHCC material activation can also be seen in Figure 6.12, where the damage in the specimen with w/h = 1.5 is limited to a smaller area, with less severe damage compared to the specimen with w/h = 1.0. The broader and more severe damage zone in the latter demonstrates the role of tab length in enhancing material engagement, resulting in a stronger and more ductile failure mode.

Combined influence of interface strength and tab length

To examine the combined effect of tab length and interface strength on the tensile response of the connection, force-displacement behaviors for interface strengths of 5%, 10%, 15%, 20%, 25%, 30%, 50%, 75%, 100%, 150%, 200%, 300% and 500% are analyzed. To improve clarity, interface strengths are divided into three groups: 5%-25% are presented in Figure 6.14, 30%-100% in Figure 6.15, and 150%-500% in Figure 6.16.

The effects of the different interface strengths and tab lengths on the failure mechanism, peak force, energy absorption and the amount of damaged SHCC elements are summarized in Table 6.6. For the different levels of interface strength, different observations are made.

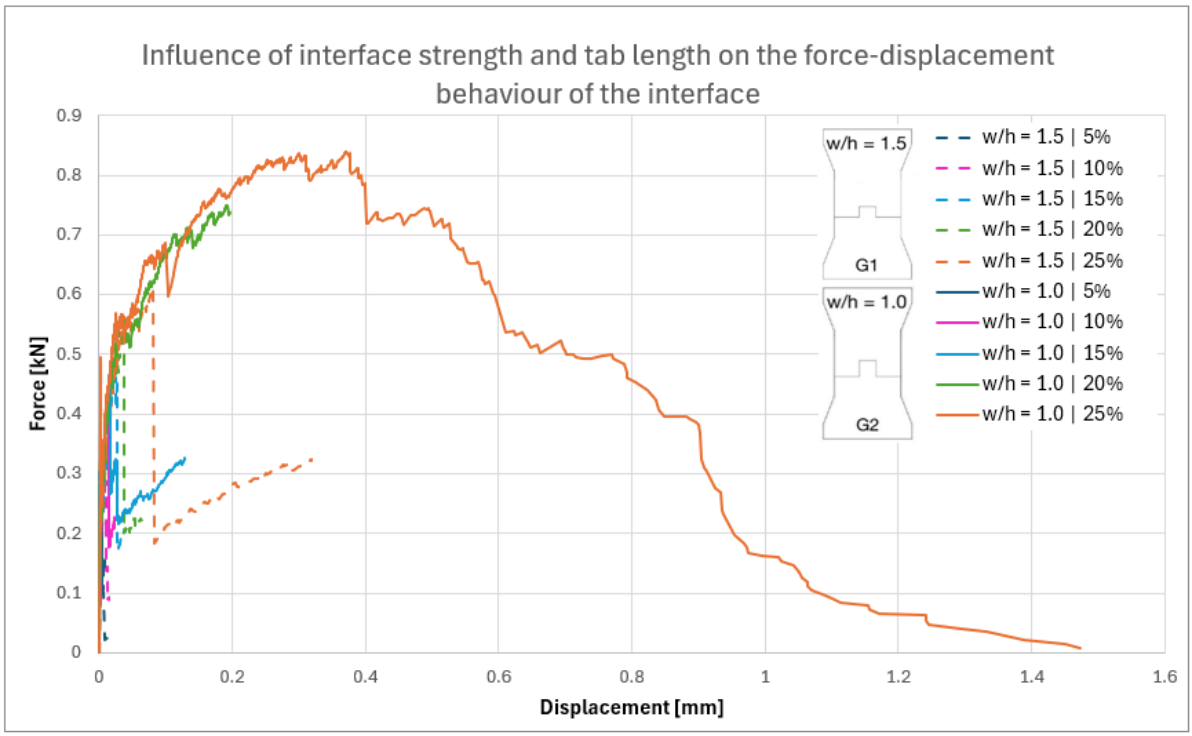

(a) Force-displacement behavior of the interface strengths 5%, 10%, 15%, 20% and 25%.

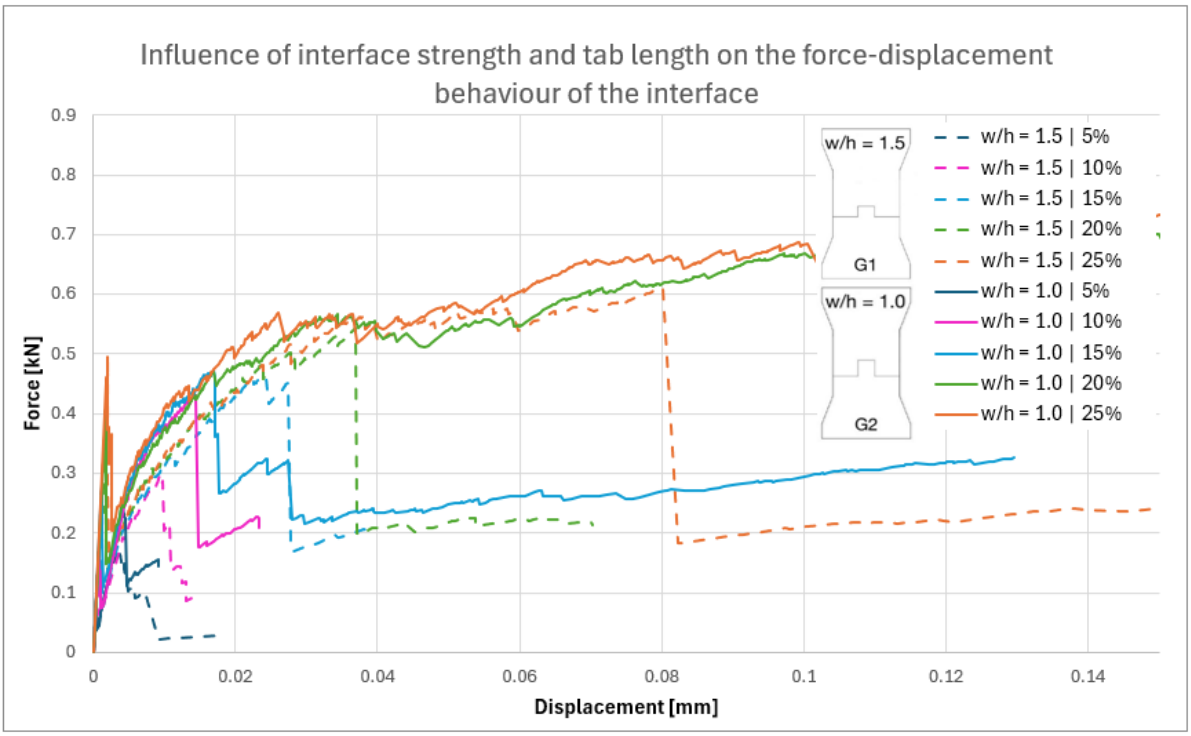

(b) Force displacement behavior of the interface strengths 5%, 10%, 15%, 20% and 25%, zoomed in on the first stages.

Figure 6.14: Influence of the tab length and interface strength on the force-displacement behavior of the connection in the lattice model for the interface strengths of 5%, 10%, 15%, 20% and 25%.

For the **lower interface strengths (5%-25%)**, different failure mechanisms emerge. At 5% and 10%, minor changes are observed in peak force and displacement capacity. However, at 15%-25%, more pronounced shifts occur. With 15% and 20% it is seen that a longer tab does not change the shape of the force-displacement graph, but it does significantly increase the displacement capacity. In

both cases, a pull-out mechanism dominates the behavior, where a longer tab increases the activated length of the SHCC material.

At 25%, a change in tab length also alters the failure mode: while the shorter tab results in a pull-out failure, the longer tab triggers a tab failure mechanism, leading to a notable increase in peak force and an especially significant boost in displacement capacity.

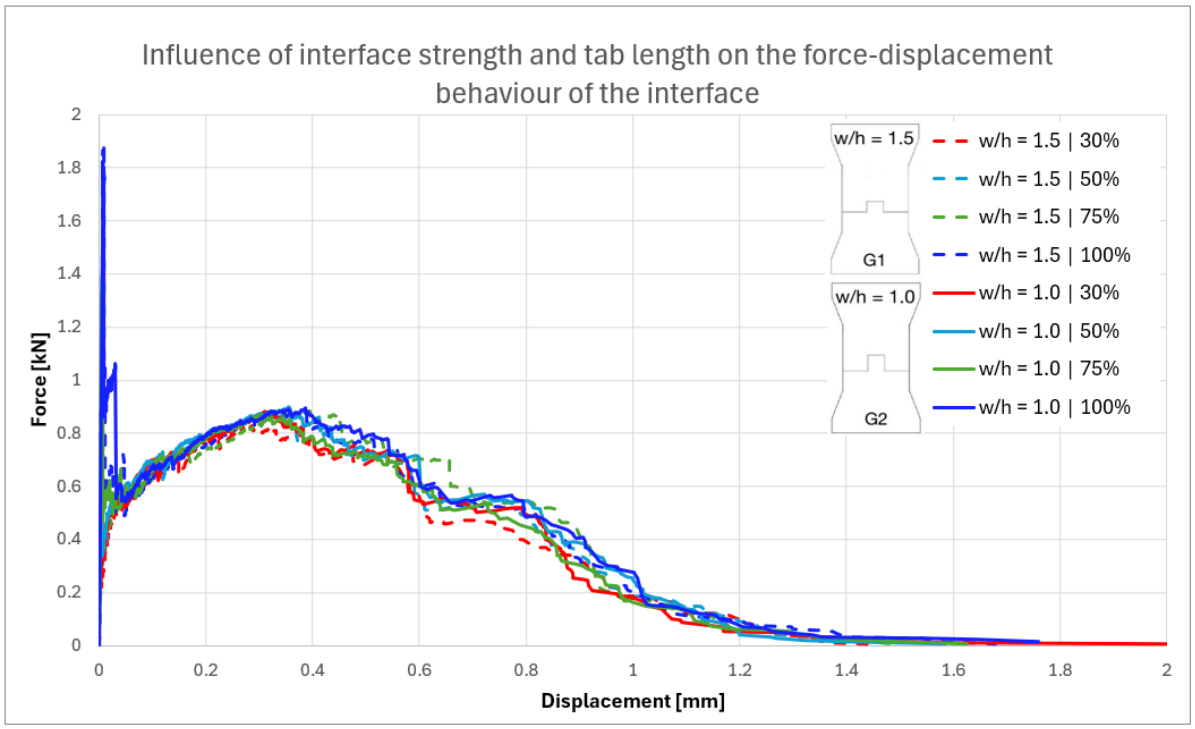

Figure 6.15: Influence of the tab length and interface strength on the force-displacement behavior of the connection in the lattice model for the interface strengths of 30%, 50%, 75% and 100%.

For **intermediate interface strengths (30%-100%)**, a tab failure mechanism is consistently observed across all cases. Here, variations in tab length have minimal effect on force-displacement behavior and peak force.

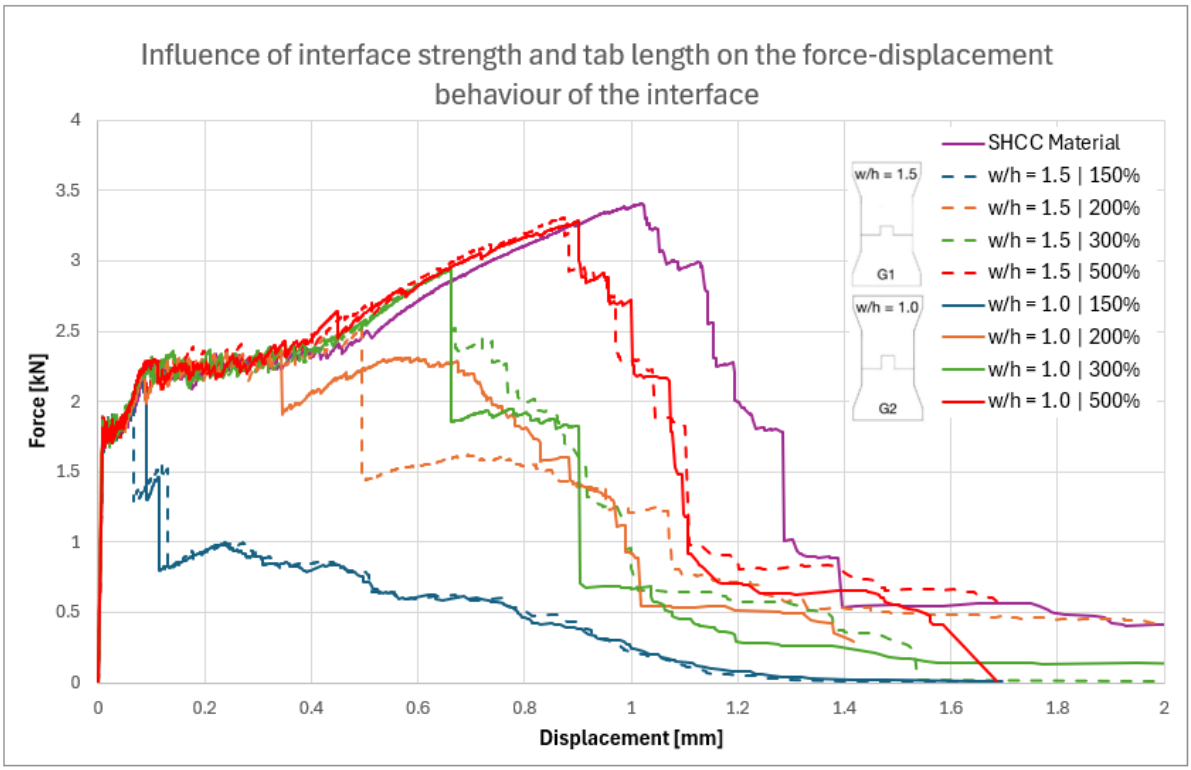

Figure 6.16: Influence of the tab length and interface strength on the force-displacement behavior of the connection in the lattice model for the interface strengths of 150%, 200%, 300% and 500%.

For **high interface strengths (150%-500%)**, the impact of tab length is generally limited. Only at 200% does the behavior vary significantly between tab lengths, primarily due to differences in stress concentration locations and interactions, rather than a shift in failure mode. This variability suggests that this response may not consistently recur with each tab length adjustment.

Interface strength	w/h ratio	Failure mode	Peak Force [kN]	% of material	Energy [kN*mm]	% of material	% of damaged SHCC elements
5%	1.5	Delamination	0.167	5	0.0011	0	0
	1.0	Delamination	0.244	7	0.0013	0	1
10%	1.5	Delamination	0.296	9	0.0026	0	1
	1.0	Pull-out	0.431	13	0.0061	0	3
15%	1.5	Pull-out	0.462	14	0.0113	0	5
	1.0	Pull-out	0.472	14	0.0368	1	10
20%	1.5	Pull-out	0.543	16	0.0218	1	8
	1.0	Pull-out	0.751	22	0.121	3	25
25%	1.5	Pull-out	0.608	18	0.104	3	14
	1.0	Tab failure	0.839	25	0.626	16	28
30%	1.5	Tab failure	0.827	24	0.605	16	31
	1.0	Tab failure	0.882	26	0.635	17	31
50%	1.5	Tab failure	0.927	27	0.649	17	33
	1.0	Tab failure	1.002	29	0.673	18	31
75%	1.5	Tab failure	1.518	45	0.673	18	34
	1.0	Tab failure	1.575	46	0.637	17	30
100%	1.5	Tab failure	1.874	55	0.673	18	38
	1.0	Tab failure	1.825	54	0.705	18	36
150%	1.5	Transition failure	1.959	57	0.826	22	92
	1.0	Transition failure	2.201	65	0.830	22	93
200%	1.5	Transition failure	2.531	74	3.230	85	99
	1.0	Transition failure	2.368	69	2.215	58	93
300%	1.5	Transition failure	2.957	87	2.48	65	94
	1.0	Transition failure	2.948	86	2.803	73	96
500%	1.5	Material failure	3.311	97	3.267	86	94
	1.0	Material failure	3.288	96	3.144	82	93
No interface	-	Material failure	3.409	100	3.818	100	100

Table 6.6: Influence of tab length and interface strength on the presented failure mechanisms, peak force and energy absorption in the lattice model.

Figure 6.11 illustrates the relationship between interface strength and three key parameters: damaged SHCC elements, peak force, and energy absorption for specimens with width-to-height (w/h) ratios of 1.5 and 1.0. The figure focuses on the range of interface strengths up to 50%, where the influence of tab length is most pronounced in the specimens with an interface strength up to 25%.

From the figure, it is clear that at interface strengths of 30% and above, the curves for both tab lengths align closely, indicating negligible influence of tab geometry in this range. However, at lower interface strengths (up to 25%), distinct differences emerge. The dashed lines, representing the shorter tab specimens, display behavior that resembles a delayed version of the solid lines corresponding to the

longer tab specimens. This suggests that while both configurations exhibit similar trends, the longer tab specimens activate SHCC material and reach higher performance levels at lower interface strengths than their shorter tab counterparts.

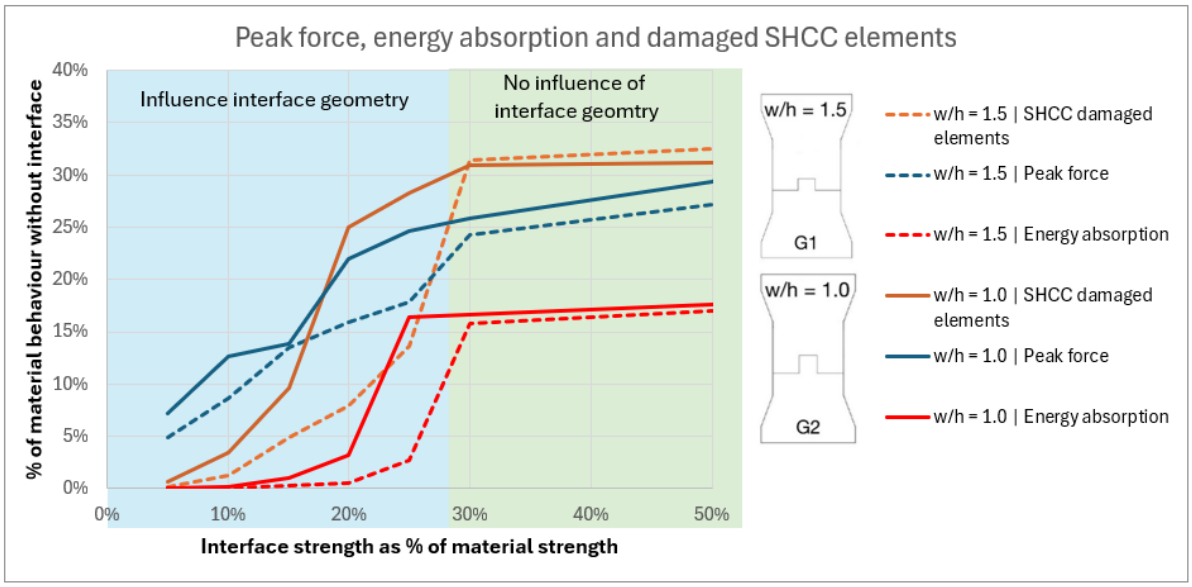

Figure 6.17: Influence of interface strength and tab length on peak force, absorbed energy and amount of damaged SHCC elements.

The number of damaged SHCC elements and failed interface elements provides a clear indication of whether failure in a specimen is dominated by brittle interface behavior or ductile SHCC material response. Figure 6.18 illustrates the percentage of damaged SHCC elements for various interface strengths and both width-to-height (w/h) ratios of the specimens.

From the figure, it is evident that for lower interface strengths (up to 25%), the geometry of the interface significantly influences the extent of SHCC material damage. Specifically, increasing the tab length with 1% results in an increase in SHCC damage of 3% to 6%. This suggests that at lower interface strengths, a longer tab activates more of the SHCC material during loading. In contrast, at higher interface strengths, the geometry has no observable influence on the SHCC damage.

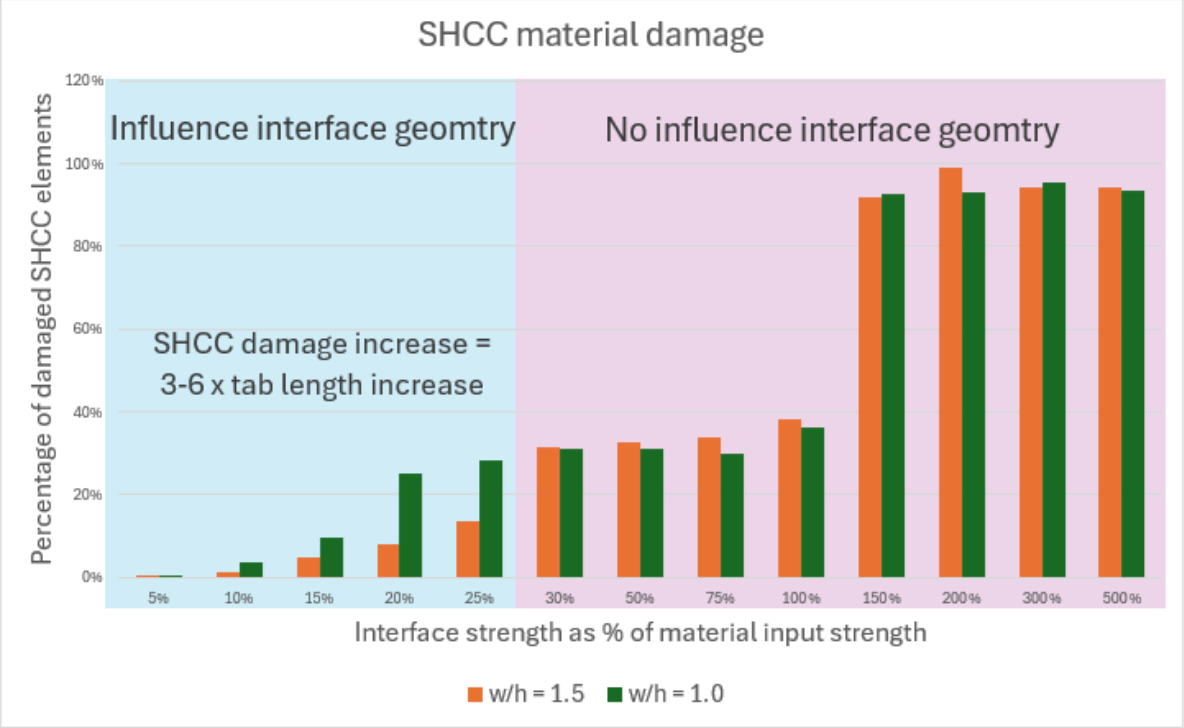

Figure 6.18: Influence of interface strength and tab length on the amount of damaged SHCC elements.

In Figure 6.19, the percentage of failed interface elements at the end of the analysis is presented. For interface strengths up to 20%, 100% of the interface elements fail, indicating an interface-dominated failure mechanism. At an interface strength of 25%, a divergence in failure behavior is observed: the shorter tab specimen experiences interface failure, while the longer tab specimen undergoes material-dominated failure.

Between interface strengths of 25% and 100%, coinciding with tab failure, the percentage of failed interface elements remains relatively constant, independent of strength or tab geometry. However, for higher strengths (150%-300%), the proportion of failed interface elements decreases significantly, coinciding with the transitional failure mechanism. This reduction indicates a shift from interface-dominated failure to a more distributed material response. At an interface strength of 500%, the number of failed interface elements becomes negligible, demonstrating that the interface no longer interferes with the specimen's behavior and material failure dominates.

These findings highlight the critical role of both interface strength and tab length in influencing the failure mechanism and material activation, particularly at lower interface strengths. The transition from brittle interface failure to ductile material failure is not only governed by strength but also by the geometric design of the interface.

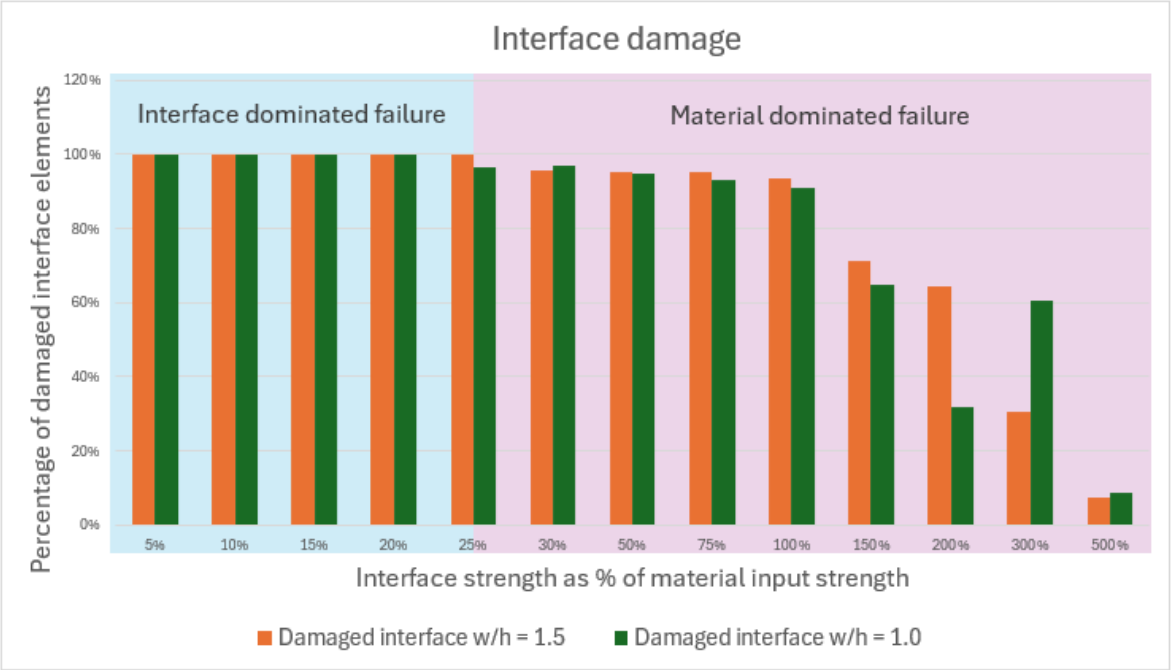

Figure 6.19: Influence of interface strength and tab length on the amount of damaged interface elements and subsequently on the activation of material driven failure instead of interface driven failure.

7

Conclusion and Recommendation

In this chapter, the conclusions of this research are drawn and recommendations will be made for future research.

7.1. Conclusions

This study aims to evaluate and enhance the predictive capabilities of numerical models in accurately simulating the tensile behavior of geometrically profiled SHCC-to-SHCC interfaces. By investigating the effects of interface stregnth and geometric profile characteristics on ductility and fracture response, this study aims to optimize interface performance and transition failure from brittle interface modes to ductile SHCC material failure. First the sub questions will be answered, which will then help answer the main research question.

Sub questions

1. Can the fracture behavior of the geometrically profiled SHCC-to-SHCC interface be predicted by the continuum smeared cracking model in Abaqus and which are the governing parameters influencing it?

The study demonstrated that the continuum smeared cracking model in Abaqus could activate various failure mechanisms by adjusting interface parameters. However, it significantly underestimated the hardening effect of SHCC material during the tab failure mechanism, where local SHCC material failure occurs. This highlights an issue with the balance between plasticity and damage in the current material model developed in this research. While plasticity spreads deformation across a larger volume, damage drives strain softening and localized crack formation. The current model only introduces damage after stress starts to decline in a single crack, yet SHCC's hardening behavior arises from distributed cracking, suggesting that damage should occur immediately after the elastic limit is reached. This underlines the need for further research to better define the damage-plasticity balance and improve the model's representation of SHCC material behavior, particularly its strain hardening, for more accurate predictions of interface performance.

2. Can the fracture behavior of the SHCC-to-SHCC interface be predicted by the lattice discrete cracking model and which are the governing parameters influencing it?

The lattice discrete cracking model effectively captured the distributed cracking patterns observed in experiments, offering a more realistic simulation of SHCC fracture behavior compared to the Abaqus smeared cracking model. This improvement is due to the lattice model's explicit treatment of plasticity through damage. However, it exhibited a more brittle failure response in interface-dominated failure mechanisms such as delamination and pull-out. It is shown that this brittleness stems from the assumption of brittle interface elements and the exclusion of friction, despite the real interface possessing softening capacity and frictional resistance.

In delamination failure, the lattice model significantly underestimated displacement capacity, predicting only 0.02 mm, compared to 1 mm from the analytical model, 3 mm from the Abaqus model, and up to 5 mm in experiments. For the pull-out mechanism, the lattice model's prediction of 0.35 mm was still lower than the analytical model's 1.25 mm and the Abaqus model's closer match to experimental results (both reaching approximately 4 mm). These discrepancies highlight the need for refining the lattice model to better represent the real interface behavior.

3. How can the models be used to optimize the behavior of geometrically profiled SHCC-to-SHCC interfaces?

The models provide valuable tools for investigating the influence of interface parameters on the behavior of geometrically profiled SHCC-to-SHCC interfaces. Insights gained from these studies can guide the optimization of interface behavior by tailoring parameters to achieve desired mechanical performance, such as enhanced ductility, controlled crack propagation, and improved energy dissipation.

The continuum smeared cracking model in Abaqus is effective in identifying critical interface parameters, such as tensile strength and fracture energy, which influence failure mechanisms. By systematically varying these parameters, the model provides insights into the impact of interface properties on different failure modes.

The lattice discrete cracking model excels in capturing distributed cracking behavior and offers a detailed understanding of how interface strength, geometry, and damage evolution affect fracture development. This model is particularly useful for exploring the influence of geometric parameters, such as tab length and width-to-height ratio, as well as frictional resistance, on the structural response of SHCC material.

Integrating findings from both models enables a comprehensive understanding of the interaction between material properties and geometric features, supporting the design of interfaces that maximize structural performance and ensure predictable failure mechanisms. However, it is important to acknowledge that while these models provide valuable insights, they are not yet sufficiently accurate to fully predict the real response of geometrically profiled SHCC-to-SHCC interfaces. The continuum smeared cracking model underestimates SHCC's hardening behavior during local failure due to its current insufficiently defined balance between plasticity and damage, failing to capture the material's distributed cracking behavior. The lattice model, while more realistic in representing distributed cracking, predicts overly brittle responses in delamination and pull-out mechanisms because of its current assumption of brittle interface elements and neglect of frictional resistance. This also results in an overestimation of interface strengths needed to induce certain SHCC material activation.

These limitations highlight the inherent challenges in modeling the complex behavior of geometrically profiled interfaces. Nonetheless, the insights gathered from these models are highly valuable for understanding and optimizing the behavior of SHCC-to-SHCC interfaces, reinforcing their potential as tools for advancing structural design in this area.

Main research question

The sub questions answered above, lead to a comprehensible answer to the main research question of this thesis.

How can an SHCC-to-SHCC interface be tailored—through adjustments to factors such as interface strength and geometry—to shift the failure mode from brittle interface failure to ductile material failure?

The parametric studies using both the analytical and lattice models demonstrate that it is indeed possible to shift the failure mode from brittle, interface-dominated failure to more ductile, material-dominated failure by optimizing interface strength and geometry.

The analytical model indicates that increasing the tab length consistently enhances both the peak force and absorbed energy, regardless of interface strength. Notably, a specimen with lower interface

strength but a longer tab can surpass the load-bearing and displacement capacity of a specimen with higher interface strength and a shorter tab. For interfaces with relatively short tabs (w/h = 1.5), activating SHCC material behavior requires interface strengths of 9% of the SHCC material strength for pull-out failure and 20% for tab failure. By increasing the tab length (w/h = 0.5), these requirements drop significantly to 4% and 7%, respectively, emphasizing the role of increased interface area in stress transfer.

The lattice model further highlights that tab length influences failure behavior primarily at lower interface strengths (≤25% of the SHCC material strength). Increasing the tab length by 1% enhances SHCC damage by 3–6%, promoting more distributed cracking. At interface strengths up to 20%, failure remains brittle and interface-dominated. At a strength of 25%, a divergence occurs: shorter tabs still result in interface failure, while longer tabs shift the behavior to material-dominated failure. Between 25% and 100% strength, while interface failure no longer dominates, the amount of SHCC damage remains relatively low (ca. 35%), and interface element failure remains high (ca. 95%). However, at higher interface strengths (150–300%), interface failure significantly decreases, and SHCC damage approaches levels seen in full material failure. At 500% strength, the interface no longer interferes with specimen behavior, and material failure fully dominates.

Both models underscore that the transition from brittle to ductile failure is governed not only by interface strength but also by the geometric design of the interface. However, these findings must be interpreted within the limitations and shortcomings of the respective models. The analytical model simplifies interface behavior and may not fully account for the complex interactions between strength and geometry. Similarly, the lattice model, while excelling in capturing distributed cracking, exhibits brittleness in certain failure mechanisms and overestimates the required interface strength for SHCC material activation due to its assumption of brittle interface elements and exclusion of friction. Despite these constraints, the results highlight the potential for tailoring interface design to achieve desired mechanical performance.

7.2. Recommendations

In this section, recommendations are provided for further research, focusing on enhancing the performance of the continuum smeared cracking model and the lattice discrete cracking model, as well as exploring methods to improve tensile connection performance through geometrically profiled interfaces.

To enhance the accuracy and effectiveness of the continuum smeared cracking model in Abaqus, the following recommendations are suggested:

- In the current model, the material properties of the SHCC material were derived through reverse engineering from a dogbone tensile test. A more precise approach would involve using experimental results from the specific behavior of a single crack in SHCC material. This targeted data could then serve as part of the material input.

  Additionally, as mentioned before, the balance between plasticity and damage in the current material model needs to be improved. Damage should be introduced immediately after the elastic limit is reached to account for the distributed cracking behavior in the SHCC material behavior. To be able to do this, research should be conducted into the relationship of the SHCC material behavior and the damage parameter defined in the Abaqus Concrete Damaged Plasticity model.

- Due to limited knowledge on the interface behavior of an SHCC-to-SHCC interface, several parameters for defining the Cohesive Zone Modeling (CZM) in this study remained uncertain. Currently, the interface properties were inferred through reverse engineering from experimental results of the sutured interface. However, this approach may have led to an overestimation of the hardening capacity of the interface. To address this, experimental studies should be conducted to examine the shear and tensile behavior of the SHCC interface, enabling the development of a more accurate and reliable interface model.

To improve the accuracy and effectiveness of the lattice discrete cracking model, the following recommendations are proposed:

- In the current research, matching the lattice model's output for a direct tensile test on a dogbone specimen with experimental results proved challenging. To enhance the lattice model's predictive performance, particularly in capturing the force-displacement behavior of the connection, more attention should be given to aligning the lattice model's material behavior with experimental observations. This alignment should go beyond force-displacement results alone; it is also essential to verify that the crack widths observed in experiments correspond to those calculated in the lattice model.
- Additionally, for simplicity, brittle interface properties were assumed in this study. However, it was shown that these brittle assumptions significantly influenced the force-displacement behavior of delamination and pull-out failure mechanisms. To improve agreement with experimental results and to more accurately represent real behavior, future research should incorporate interface elements with softening behavior. This adjustment would allow the model to better simulate the gradual degradation observed in actual SHCC interfaces.

For future research on enhancing the tensile behavior of interfaces through geometric profiling, the following recommendations are suggested:

- This study demonstrated that using geometrical profiling in the shape of a single straight tab can shift the failure mechanism from brittle interface failure to ductile SHCC material failure. Future research could explore specific tab design variations that promote favorable crack propagation patterns. For instance, a tapered or serrated tab design may encourage distributed cracking and improve overall tensile performance.
- The literature review on biologically occurring sutured interfaces revealed that, in natural interlocking structures, a thin protein layer often exists between two brittle materials, enhancing suture performance by allowing limited elastic deformation. Future research could investigate incorporating a similar thin, low-stiffness, elastic layer within an interlocking SHCC interface. This layer could provide additional linear elastic behavior that the SHCC material alone cannot offer, potentially improving the interface's capacity for energy absorption and deformation.

Bibliography

[1] *Abaqus Analysis User's Guide*. Dassault Systèmes Simulia Corp, 2016.

[2] *Abaqus Documentation Version 6.6*. Dassault Systèmes Simulia Corp, 2024.

[3] M. G. Alberti et al. "Recent advances in structural fibre-reinforced concrete focused on polyolefin-based macro-synthetic fibres." In: *Materiales de Construccion* 70 (337 Jan. 2020). ISSN: 19883226. DOI: 10.3989/mc.2020.12418.

[4] Arnon. Bentur and Sidney. Mindess. *Fibre reinforced cementitious composites*. Taylor Francis, 2007, p. 601. ISBN: 9780415250481.

[5] P. A. Bonnet-Masimbert et al. "Study of modifications on the chemical and mechanical compatibility between cement matrix and oil palm fibres." In: *Results in Engineering* 7 (Sept. 2020). ISSN: 25901230.

[6] James J. Cray, Mark P. Mooney, and Michael I. Siegel. "Timing of Ectocranial Suture Activity in Pan troglodytes as Related to Cranial Volume and Dental Eruption." In: 293.8 (Aug. 2010). DOI: 10.1002/AR.21167.

[7] Yue Dai. *Accelerated Corrosion Test Simulation: Lattice Model vs. Continuum Model*. Master's Thesis. 2018.

[8] Sławomir Dudziak, Wioletta Jackiewicz-Rek, and Zofia Kozyra. "On the calibration of a numerical model for concrete-to-concrete interface." In: *Materials* 14 (23 Dec. 2021). ISSN: 19961944. DOI: 10.3390/ma14237204.

[9] Prestressed Concrete Institute. *PCI Design Handbook: Precast and Prestressed Concrete*. Prestressed Concrete Institute, 1985. ISBN: 9780937040232. URL: https://books.google.nl/books?id=yLAM4tVS_7wC.

[10] Nayeon Lee et al. "Hierarchical multiscale structure-property relationships of the red-bellied woodpecker (Melanerpes carolinus) beak." In: 11.96 (July 2014). DOI: 10.1098/RSIF.2014.0274.

[11] Erica Lin et al. "3D printed, bio-inspired prototypes and analytical models for structured suture interfaces with geometrically-tuned deformation and failure behavior." In: 73 (Dec. 2014). DOI: 10.1016/J.JMPS.2014.08.011.

[12] M. Luković and D.A. Hordijk. *Literature review on new concrete types; A start on exploring their opportunities for Dutch infrastructure*. 2017.

[13] Mladena Luković, Erik Schlangen, and Guang Ye. "Combined experimental and numerical study of fracture behaviour of cement paste at the microlevel." In: *Cement and Concrete Research* 73 (2015), pp. 123–135. ISSN: 00088846. DOI: 10.1016/j.cemconres.2015.03.008.

[14] Mladena Luković et al. "Failure modes in concrete repair systems due to ongoing corrosion." In: *Advances in Materials Science and Engineering* 2017 (2017). ISSN: 16878442. DOI: 10.1155/2017/9649187.

[15] Mladena Luković et al. *IMPACT OF SURFACE ROUGHNESS ON THE DEBONDING MECHANISM IN CONCRETE REPAIRS MLADENA LUKOVIC*. 2013.

[16] Mladena Luković et al. "Tailoring strain-hardening cementitious composite repair systems through numerical experimentation." In: *Cement and Concrete Composites* 53 (2014), pp. 200–213. ISSN: 09589465. DOI: 10.1016/j.cemconcomp.2014.06.017.

[17] Mohammad Mirkhalaf and Francois Barthelat. "Design, 3D printing and testing of architectured materials with bistable interlocks." In: 11 (Feb. 2017). DOI: 10.1016/J.EML.2016.11.005.

[18] Fadhilah Muslim. "A Review on The Microstructure of Interfaces in Reinforced Concrete and Its Effect on The Bond Strength." In: *CSID Journal of Infrastructure Development* 3 (1 May 2020), p. 102. ISSN: 2407-4438. DOI: 10.32783/csid-jid.v3i1.105.

[19] Shozab Mustafa. *Lattice Modelling - TU Delft; Theory, Background and Application of Lattice Model*. 2022.

[20] V. Palmieri and L. De Lorenzis. “Multiscale modeling of concrete and of the FRP-concrete interface.” In: *Engineering Fracture Mechanics* 131 (Nov. 2014), pp. 150–175. ISSN: 00137944. DOI: 10.1016/j.engfracmech.2014.07.027.

[21] Sofia Papoulidou. *Tensile performance of bistable interlocks in sutured geometries*. Master’s Thesis. 2023.

[22] Suvash Chandra Paul and Adewumi John Babafemi. *A review of the mechanical and durability properties of strain hardening cement-based composite (SHCC)*. Jan. 2018. DOI: 10.1080/21650373.2017.1394236.

[23] Jan G. Rots, Rita Esposito, and Max Hendriks. *Smeared cracking model*. 2023.

[24] Patryk Rozylo. “Stability and failure of compressed thin-walled composite columns using experimental tests and advanced numerical damage models.” In: *International Journal for Numerical Methods in Engineering* 122 (18 Sept. 2021), pp. 5076–5099. ISSN: 10970207. DOI: 10.1002/nme.6757.

[25] Gao Shuling et al. “Experimental investigation of the interface bond properties between SHCc and concrete under sulfate attack.” In: *Construction and Building Materials* (2019).

[26] A. T. Slobbe, M. A.N. Hendriks, and J. G. Rots. “Sequentially linear analysis of shear critical reinforced concrete beams without shear reinforcement.” In: *Finite Elements in Analysis and Design* 50 (Mar. 2012), pp. 108–124. ISSN: 0168874X. DOI: 10.1016/j.finel.2011.09.002.

[27] Juha Song et al. “Quantitative microstructural studies of the armor of the marine threespine stickleback (Gasterosteus aculeatus).” In: 171.3 (Sept. 2010). DOI: 10.1016/J.JSB.2010.04.009.

[28] Heinrich Stander. *INTERFACIAL BOND PROPERTIES FOR ECC OVERLAY SYSTEMS*. 2007.

[29] Christian Wagner. “Dauerhaftigkeitsrelevante Eigenschaften von dehnungsverfestigenden zementgebundenen Reparaturschichten auf gerissenen Betonuntergründen.” PhD thesis. Technische Universität Dresden, 2016).

[30] Christian Wagner, Nick Bretschneider, and Volker Slowik. *CHARACTERIZATION OF THE INTERFACE BETWEEN STRAIN HARDENING CEMENTITIOUS REPAIR LAYERS AND CONCRETE SUBGRADE*. 2013. URL: www.htwk-leipzig.de.

[31] S. Wang and Victor Li. “Polyvinyl Alcohol Fiber Reinforced Engineered Cementitious Composites: Material Design and Performances.” In: (May 2005).

[32] Jiaying Wei et al. “Shear strengthening of reinforced concrete beams with high strength strain-hardening cementitious composites (HS-SHCC).” In: *Materials and Structures/Materiaux et Constructions* 53 (4 Aug. 2020). ISSN: 13595997. DOI: 10.1617/s11527-020-01537-1.

[33] Hui-cai Xie, Geng-ying Li, and Guang-jing Xiong. *Microstructure Model of the Interfacial Zone Between Fresh and Old Concrete*. 2002.

[34] Jingwei Ying and Jin Guo. “Fracture behaviour of real coarse aggregate distributed concrete under uniaxial compressive load based on cohesive zone model.” In: *Materials* 14 (15 Aug. 2021). ISSN: 19961944. DOI: 10.3390/ma14154314.

[35] Doo Yeol Yoo and Soonho Kim. “Comparative pullout behavior of half-hooked and commercial steel fibers embedded in UHPC under static and impact loads.” In: *Cement and Concrete Composites* 97 (Mar. 2019), pp. 89–106. ISSN: 09589465. DOI: 10.1016/j.cemconcomp.2018.12.023.

[36] Ao Zhou et al. *Interfacial technology for enhancement in steel fiber reinforced cementitious composite from nano to macroscale*. Jan. 2021. DOI: 10.1515/ntrev-2021-0037.

[37] Gideon P.A.G. van Zijl et al. “Durability of strain-hardening cement-based composites (SHCC).” In: *Materials and Structures/Materiaux et Constructions* 45 (10 Oct. 2012), pp. 1447–1463. ISSN: 13595997. DOI: 10.1617/s11527-012-9845-y.

A

Parametric study cohesive zone model

In this research a parametric study has been performed on the different interface parameters of the cohesive zone model in Abaqus. In this appendix the results from the parametric study are given, including an extensive summary per parameter and an overall discussion on the results of the parametric study.

The parameters and their starting values for this parametric study are presented in Table A.1. For each of the parameters presented in red a much lower value and a much higher value has been used such that it is possible to see which effect this has in the extreme case. Only for the normal fracture energy just a much higher value has been used due to the already very low value of the initial normal fracture energy.

Contact Property	Parameter	Value	Unit
Tangential behavior	Friction coefficient	0.7	-
Tangential behavior	Shear stress limit	No limit	-
Tangential behavior	Elastic slip stiffness	Infinite (no slip)	-
Normal behavior	Pressure-overclosure	”Hard” Contact	-
Cohesive behavior	Knn (normal stiffness)	3000	MPa
Cohesive behavior	Kss (shear stiffness, 1st direction)	50	MPa
Cohesive behavior	Ktt (shear stiffness, 2nd direction)	50	MPa
Damage initiation	Normal contact stress ()	0.7	MPa
Damage initiation	Shear contact stress ()	3.5	MPa
Damage initiation	Shear contact stress ()	3.5	MPa
Damage evolution	Type	Energy	-
Damage evolution	Softening	Linear	-
Damage evolution	Mixed mode behaviour	Benzeggagh-Kenane	-
Damage evolution	BK Exponent	1.0	-
Damage evolution	Normal Fracture Energy	0.09	N/mm
Damage evolution	1st Shear Fracture Energy	5	N/mm
Damage evolution	2nd Shear Fracture Energy	5	N/mm
Damage stabilization	Viscosity coefficient	0.0005	-

Table A.1: Interface properties for the cohesive zone model in Abaqus analysis.

A.1. Variable 1: Friction coefficient

Description: The friction coefficient is a critical parameter in this study as it quantifies the frictional resistance at the interface, expressed as a proportion of the normal (compressive) stresses. According to the cohesive model, frictional forces at the interface become significant only after the cohesive strength of the bond begins to degrade. Initially, when the cohesive stiffness is undamaged, the interface behavior is governed solely by the cohesive model, with any tangential slip being purely elastic and resisted by the cohesive strength [1].

As the cohesive bond begins to degrade, the friction model gradually activates, contributing increasingly to the shear stresses in the interface. The elastic stick stiffness of the friction model ramps up proportionally with the degradation of the cohesive stiffness. Prior to the ultimate failure of the cohesive bond, the interface shear stress results from a combination of the remaining cohesive strength and the growing contribution from frictional forces (see Figure A.1) [1]. Once the cohesive bond is fully degraded, the shear stress is entirely governed by the friction model.

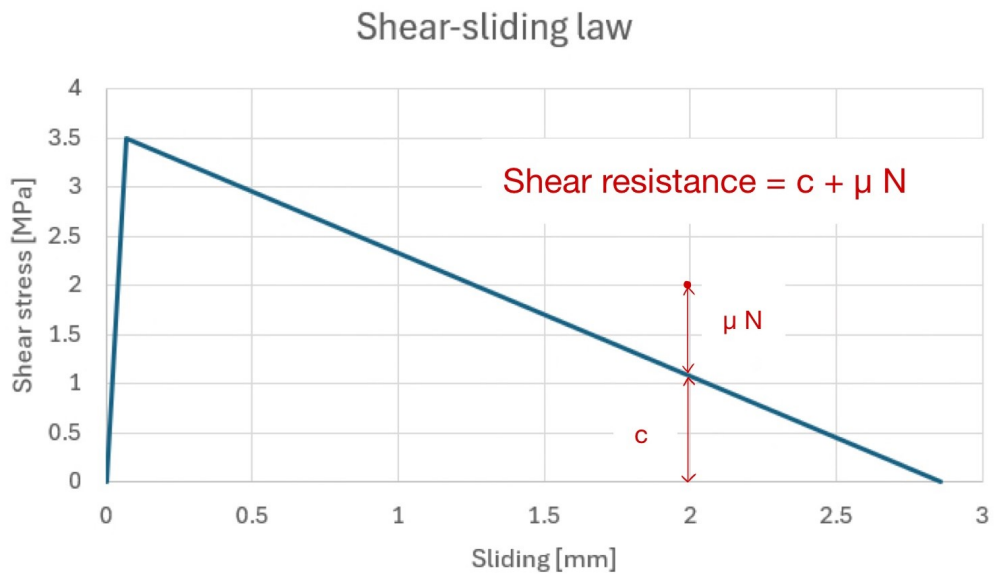

Figure A.1: Effect of friction and cohesion on the shear resistance of the interface.

For the original interface the cohesive shear force in the vertical interfaces has been calculated and presented next to the total force of the analysis (see Figure A.2). Due to the method of calculating this, the cohesive shear stress is only presented for the moment from which the entire vertical interface has sustained some level of damage. It can be seen that the interface takes up quite a bit more force than the shear interface takes up due to cohesion. At the beginning some stresses are still taken up by the horizontal interfaces as well, however after step 16/40 the horizontal interfaces are all fully damaged (interface damage reached a value of 1.0) and take up no further stresses. After this step the difference in force is due to the frictional stresses which develop in the vertical interface.

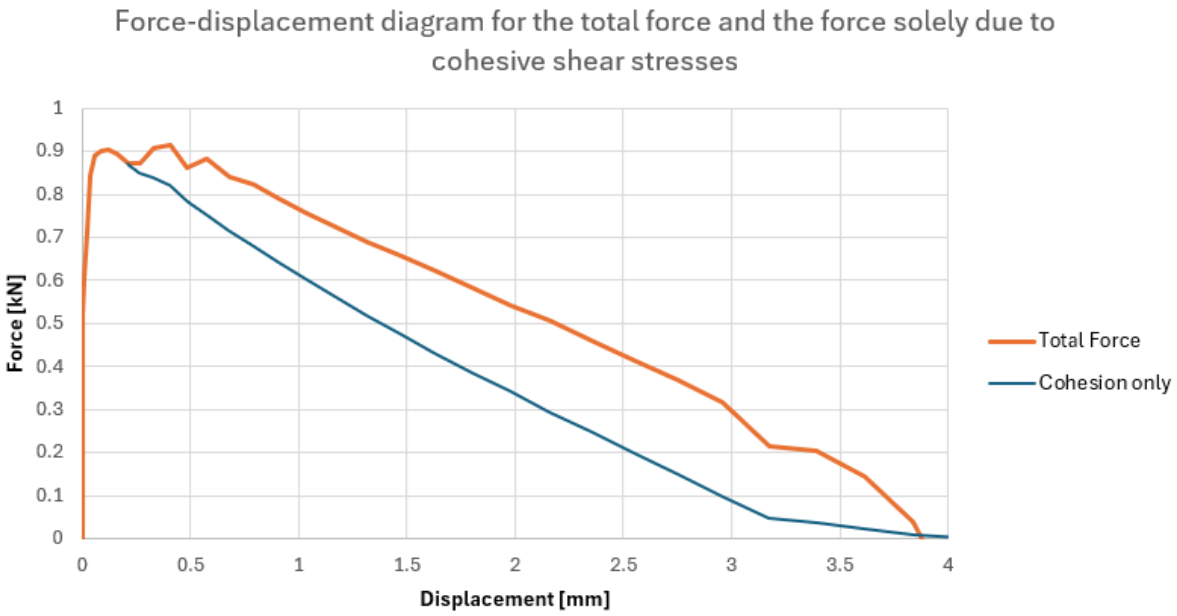

Figure A.2: Cohesive shear force contribution to total force in the SCG2 specimen and thus the effect of friction resistance of the interface.

For frictional stresses to develop, a compressive normal force must be present on the vertical interface. Upon examining the specimen's movement in the x-direction, it is observed that at both the

bottom and top of the tab—where slip is high—the material moves outward, away from the tab. In contrast, in the middle part of the tab, the material remains in contact with the interface (see Figure A.3). Furthermore, when analyzing the stresses in the x-direction, it is evident that compressive stresses are present in this contact area (see Figure A.4).

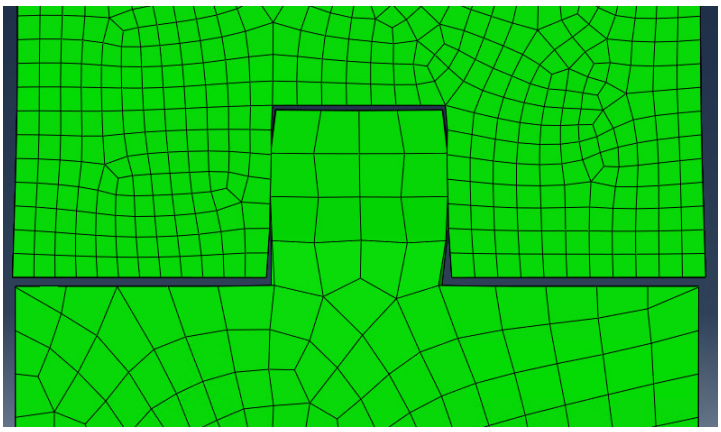

Figure A.3: Deformed shape of the SCG2 specimen in original interface conditions with the deformation in x-direction 30 times amplified at step 16/40.

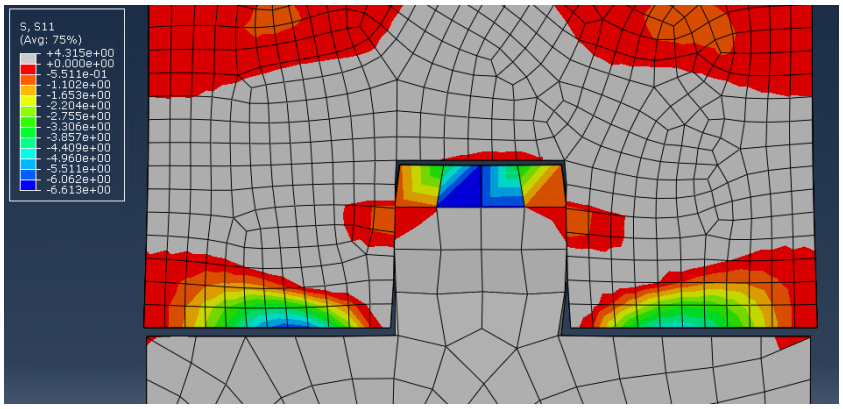

Figure A.4: Stresses in x-direction presented in the deformed shape of the SCG2 specimen in original interface conditions with the deformation in x-direction 30 times amplified at step 16/40. All the tensile stresses are presented in grey, whereas the compressive stresses are given according to the color legend.

This parametric study examines the influence of friction by comparing two extreme cases: a frictionless condition (coefficient = 0), representing a scenario where no frictional forces contribute to shear stresses, and a high-friction condition (coefficient = 10), where frictional forces significantly affect shear stress after the cohesive bond has been damaged. It is important to note that a friction coefficient of 10 is not physically realistic for concrete-to-concrete interfaces. However, this extreme value is chosen to ensure that the effect of friction is clearly observable and to understand its potential impact on the interface behavior.

Results: For both the frictionless interface and the interface with a friction coefficient of 10 the results of the analysis are presented below. First the results for the frictionless interface condition is shown and afterwards the results for the interface with a friction coefficient of 10 is shown.

A.1.1. Frictionless

In Figure A.5 the force-displacement diagram of the analysis is shown, together with the locations of the different relevant steps. It can be seen that after step 32, the results the force remains around a value of zero, therefore the choice has been made that in this analysis only steps 1-32 have been analysed.

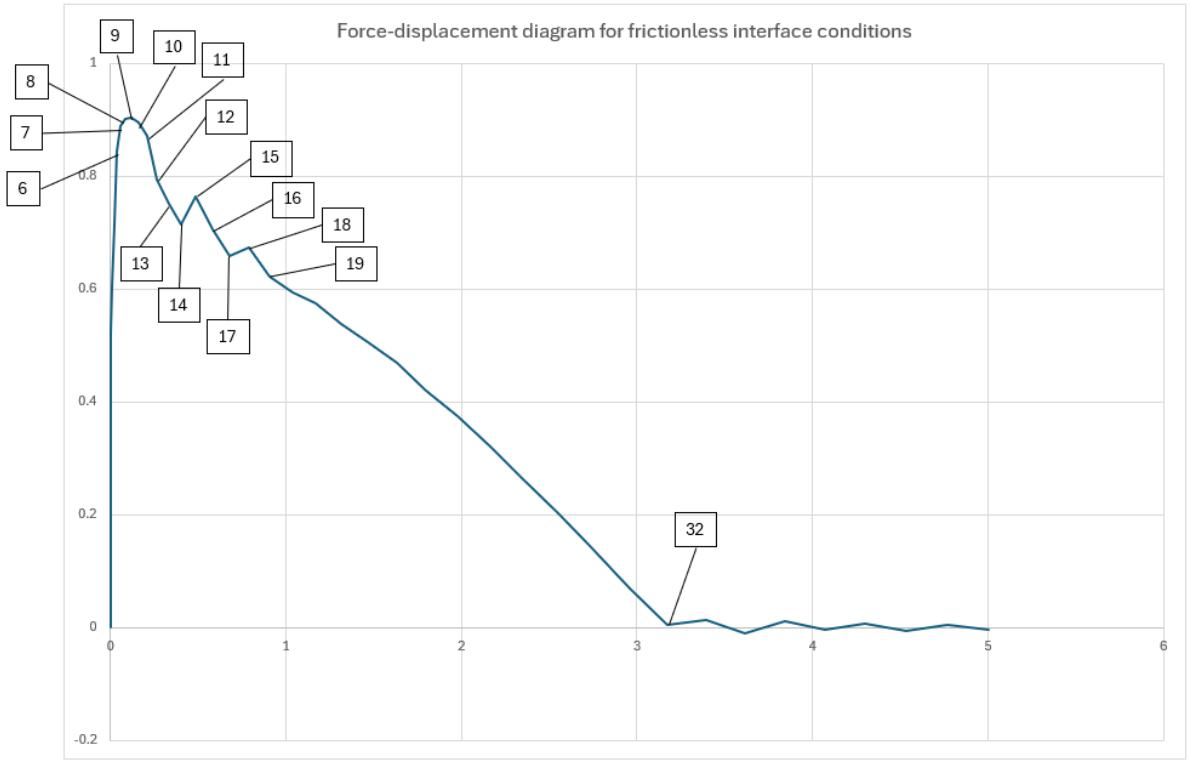

Figure A.5: Force displacement diagram of the analysis with frictionless interface conditions, with important steps identified for further analysis.

In Figure A.6 the plastic strain development in the frictionless specimen is shown throughout the analysis. The plastic strain develops up until step 12 after which the plastic strain does not increase further and the displacement of the top part of the specimen does not lead to higher plastic strains.

It can be seen that compared to the original interface the plastic strain development in the tab and surrounding material up until step 10 is almost, if not completely, identical to development of plastic strain in the original interface. For step 12 the plastic strain development in the original interface conditions is slightly higher than that in the frictionless specimen. Additionally, in the original interface the plastic strain development goes on to step 16 and reaches much higher values than in the case of the frictionless interface.

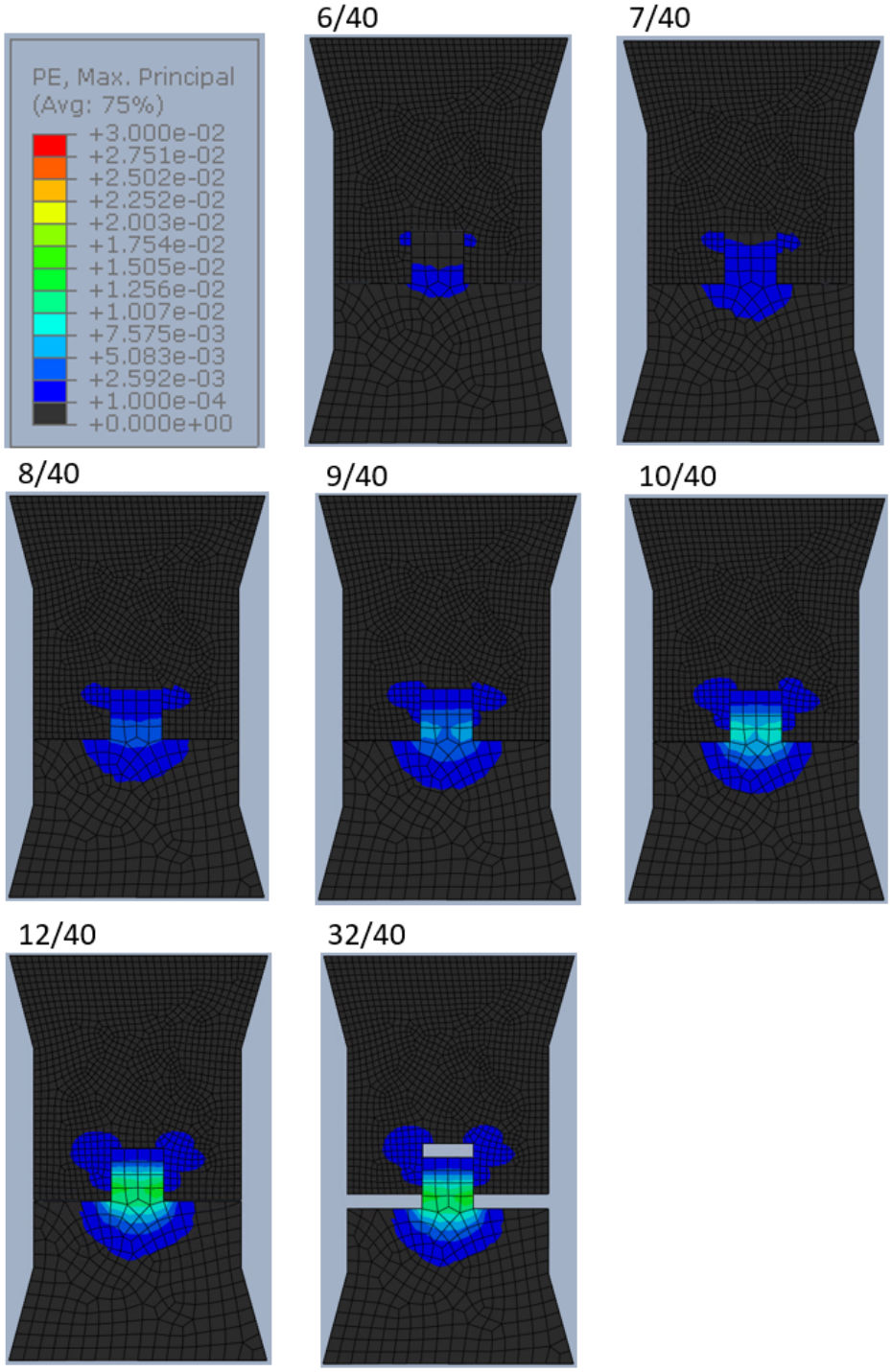

Figure A.6: Plastic strain values throughout the analysis with a color legend ranging from 0.0001 (0.01%) to 0.03 (3%).

The tensile interface damage development in the frictionless interface does not differ significantly from the original interface. For the interface damage in the vertical shear interfaces Figure A.7 shows the development of this shear interface damage throughout the analysis. It can be seen that the shear interface damage development is similar as in the original case up until step 10. After that it can be seen that the interface damage develops much quicker than in the original case.

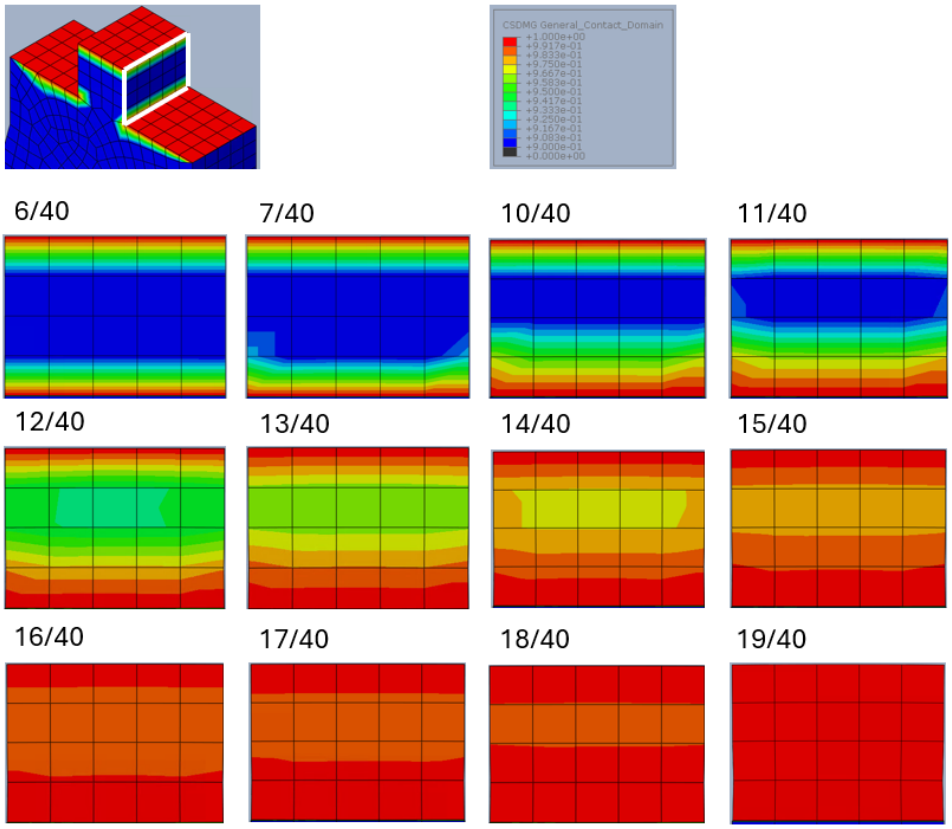

Figure A.7: Interface damage of the interface loaded in shear throughout the analysis of the specimen with frictionless interface conditions. Color legend ranges from 0 (0%) to 1 (100%).

Friction coefficient of 10

In Figure A.8 the force-displacement diagram of the analysis is shown, together with the locations of the different relevant steps. It can be seen that after step 30, the results the force remains around a value of zero, therefore the choice has been made that in this analysis only steps 1-30 have been analysed.

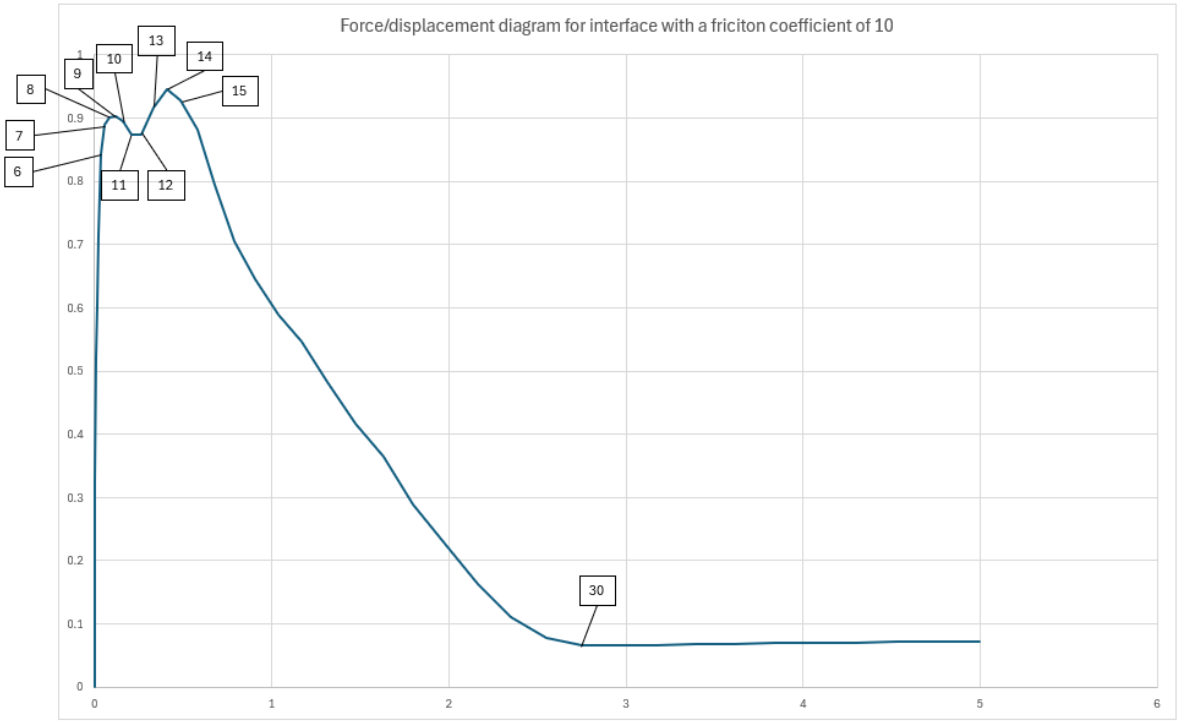

Figure A.8: Force displacement diagram of the analysis with an interface with a friction coefficient of 10, with important steps identified for further analysis.

In Figure A.9, the development of plastic strain in the specimen with a friction coefficient of 10 is shown throughout the analysis. It can be seen that compared to the original interface the plastic strain development in the tab and surrounding material up until step 12 is almost, if not completely, identical to development of plastic strain in the original interface. However, in the specimen with a friction coefficient of 10 the plastic strain quickly increases to higher values and the plastic strain continues to increase until the end of the analysis. On the other hand the for the original interface specimen the plastic strain develops much slower and only until step 16, after which the plastic strain does not increase.

In the specimen with a friction coefficient of 10, the plastic strain in the bottom of the tab exceeds the predefined color legend limit of 0.03 (3%) from step 15 onwards. To further illustrate the material behavior of the tab, the tensile damage parameter is presented in Figure A.10, which indicates that tensile damage is predominantly localized at the bottom of the tab, where material failure ultimately occurs, demonstrating a tab failure mechanism. It is important to note that tensile damage is a material property derived from the single-crack behavior. It is defined to remain zero until additional crack opening leads to a decrease in stress values, rather than an increase.

To provide a comprehensive view of the material damage, the final step (30/40) is displayed with a lower limit of 0.0001, revealing even the smallest damage areas, which are visible around the top corners of the tab and in the material surrounding the sides of the tab.

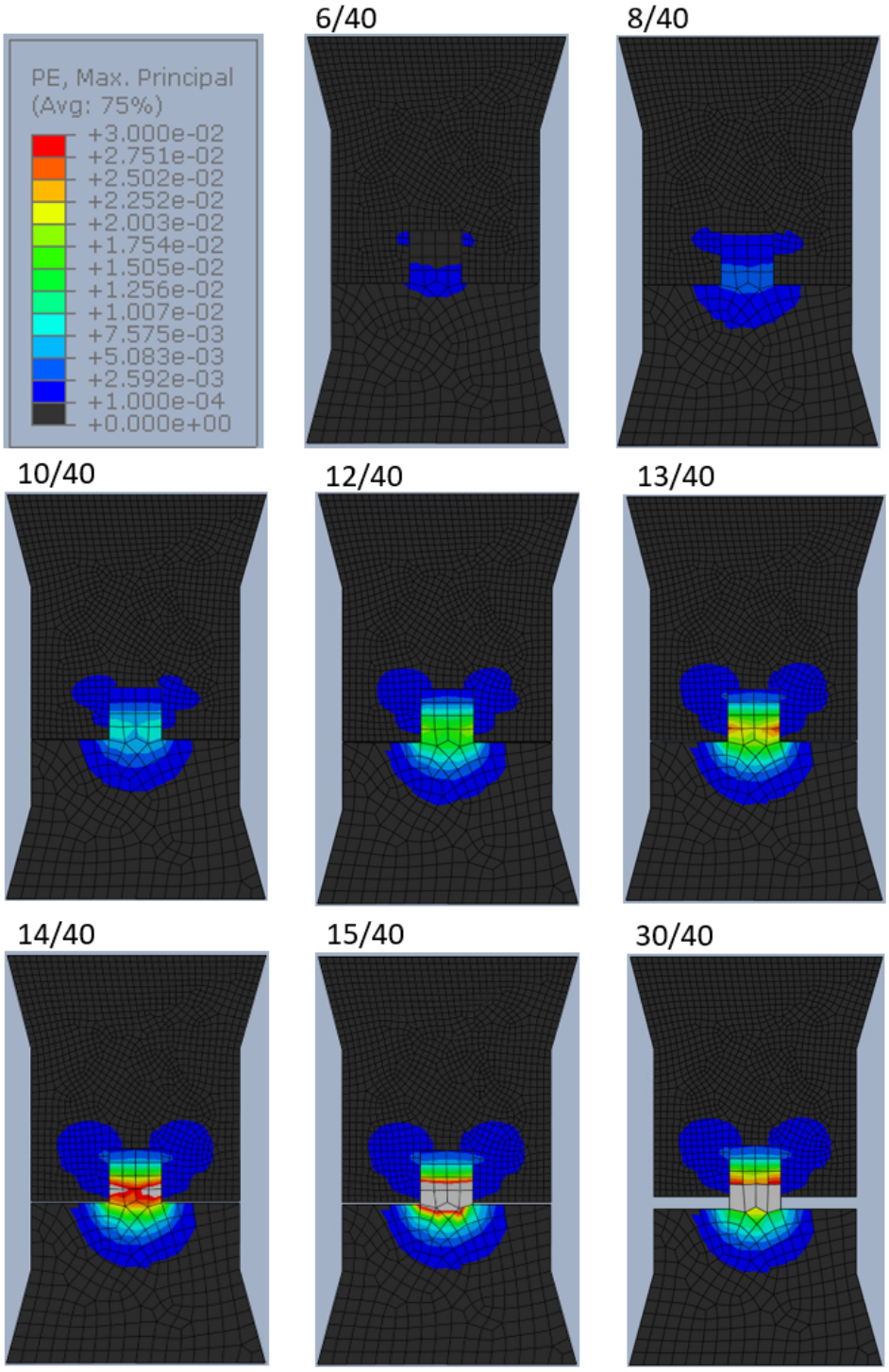

Figure A.9: Plastic strain values throughout the analysis with a color legend ranging from 0.0001 (0.01%) to 0.03 (3%).

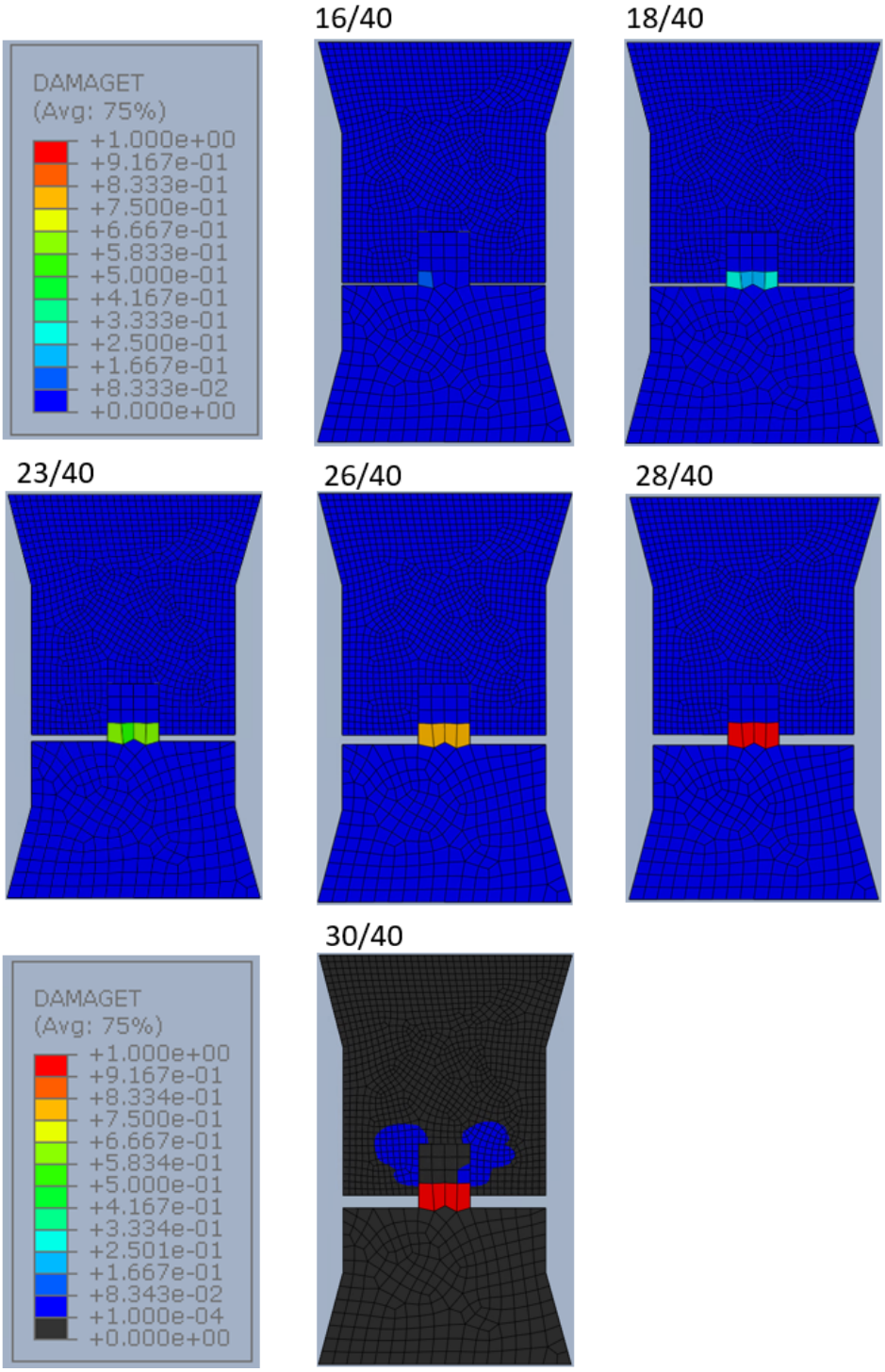

Figure A.10: Tensile damage values throughout the analysis with a color legend ranging from 0 (0%) to 1.0 (100%). Additionally for step 30 a color legend ranging from 0.0001 (0.01%) to 1.0 (100%) is used.

The tensile interface damage development in the interface with a friction coefficient of 10 does not differ significantly from the original interface. For the interface damage in the vertical shear interfaces Figure A.11 shows the development of this shear interface damage throughout the analysis. Again it can be seen that the shear interface damage development is the same as in the original case up until step 10. After that it can be seen that in this case, the interface damage develops quite a bit slower than in the original case. Additionally the shear interface damage stops progressing after step 14.

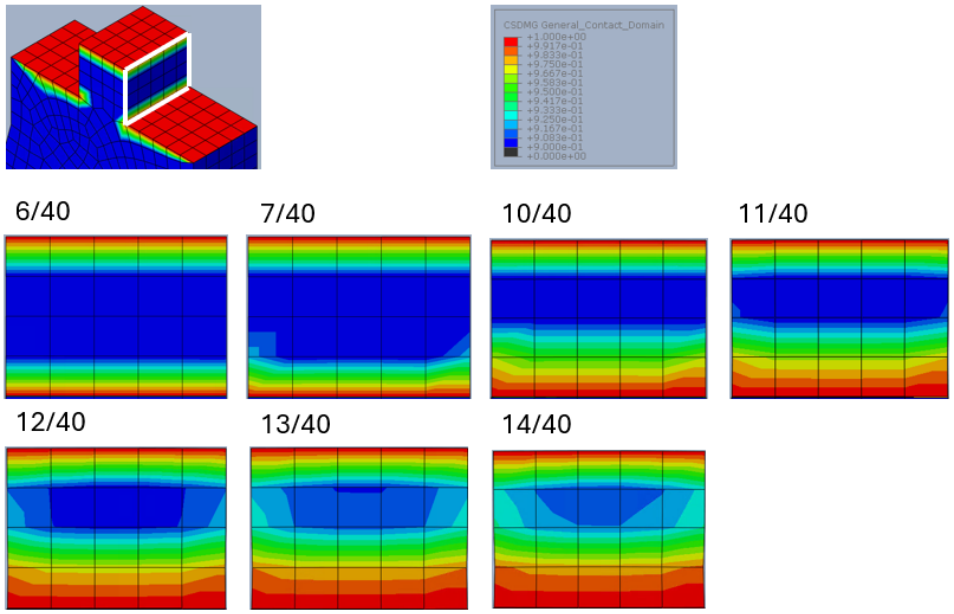

Figure A.11: Interface damage of the interface loaded in shear throughout the analysis of the specimen with a friction coefficient of 10. Color legend ranges from 0 (0%) to 1 (100%).

Lastly, the influence of the different values for the friction coefficients on the force-displacement behaviour is presented in Figure A.25. Additionally the same data is also presented as a stress-displacement diagram in Figure A.26

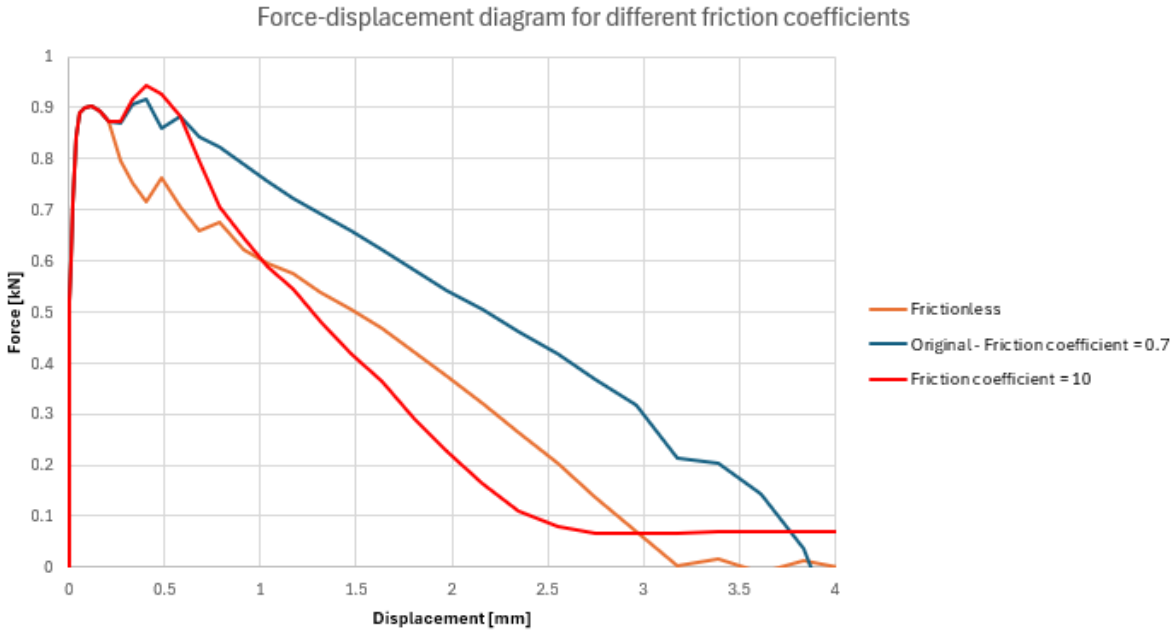

Figure A.12: Influence of the low and high values of friction on the force-displacement behaviour of the connection.

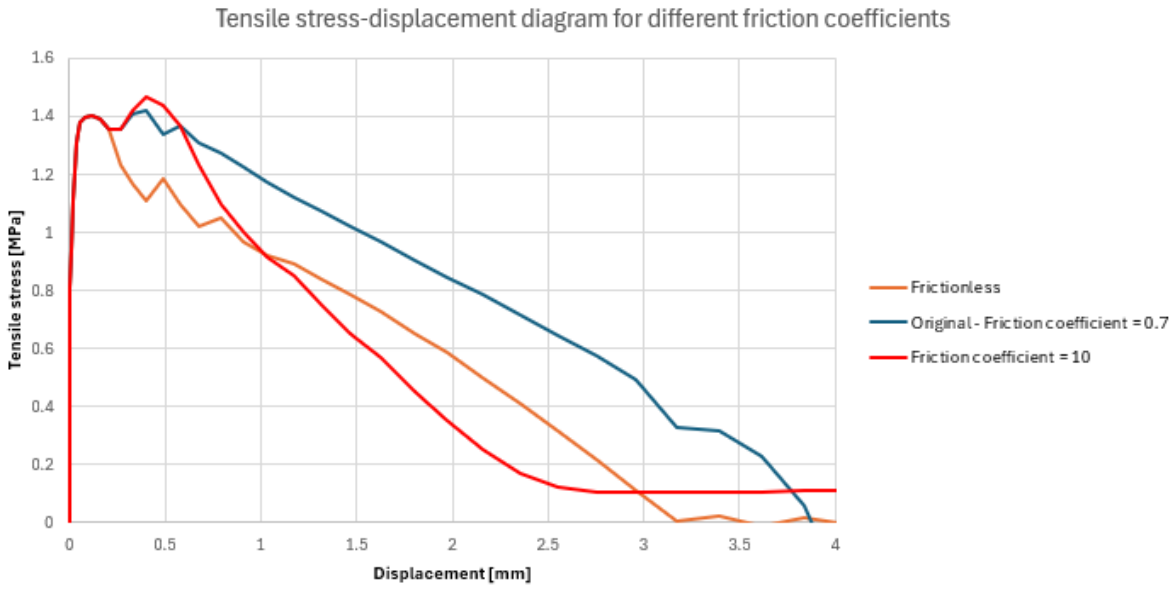

Figure A.13: Influence of the low and high values of friction on the tensile stress-displacement behaviour of the connection.

A.1.2. Discussion

The analysis of the interface behavior under varying friction coefficients reveals several important insights. First, it is important to note that changes in the friction coefficient do not influence the tensile interface behavior or the shear interface damage behavior up to step 10. This observation aligns with the force-displacement behavior, where no clear distinction can be made between the three different interface conditions up to the first peak. A zoomed-in version of the force-displacement diagram for the first 0.5 mm of displacement is shown in Figure A.14. Combined with the fact that plastic strain development is similar across all three specimens during the first 10 steps, this indicates that friction does not affect the initial specimen behavior. This finding is consistent with the expectation that friction becomes active only after damage begins to occur in the shear interface.

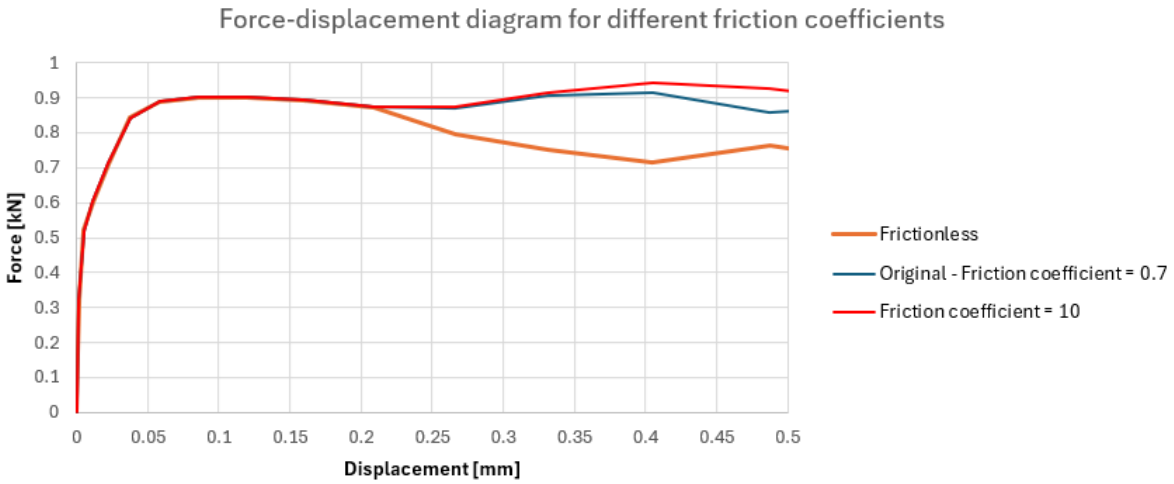

Figure A.14: Force-displacement diagram for different friction coefficients, zoomed in on the first 0.5mm of displacement.

After this initial state, however, notable differences emerge. In the case of a frictionless interface, the development of shear interface damage is significantly faster than in the original interface. This

rapid damage progression causes a drop in force after the first peak and results in the plastic strain reaching its maximum value by step 12. The failure mechanism observed after step 12 is a complete pull-out failure, without further material damage.

For a friction coefficient of 10, the force begins to increase again after the initial peak due to the slower progression of shear interface damage. This slower damage rate allows for further plastic strain development within the tab. The friction component absorbs a portion of the shear stresses that would otherwise be borne by the cohesive shear interface, leaving the latter partially undamaged. After step 14, the shear interface damage does not increase further. However, the material plastic strain in the tab continues to grow and becomes localized at the bottom. From step 16 onward, damage initiates at the bottom of the tab and continues to intensify until the end of the analysis, indicating a failure mechanism where the tab itself fails.

Interestingly, for both the frictionless and original conditions, the slope at which the force decreases with displacement after the initial post-peak drop is similar. This slope is also similar to the slope of the cohesive only shear force, shown in Figure A.2. This suggests that, as long as the interface presents a pull-out mechanism, the rate of force reduction is not influenced significantly by the friction coefficient but can mostly be attributed to the cohesive interface damage process in the vertical interface surfaces.

A.2. Knn (normal stiffness coefficient)

Description: The second variable in this parameter study is the normal stiffness coefficient. Theoretically this interface stiffness coefficient is defined as the interface material stiffness divided by the true physical initial thickness of the interface [2]. Practically, this stiffness coefficient defines the slope with which the tensile interface strength increases with displacement. In this study a value of 30 [MPa/mm] and 30000 [MPa/mm] are used (see Figure A.15).

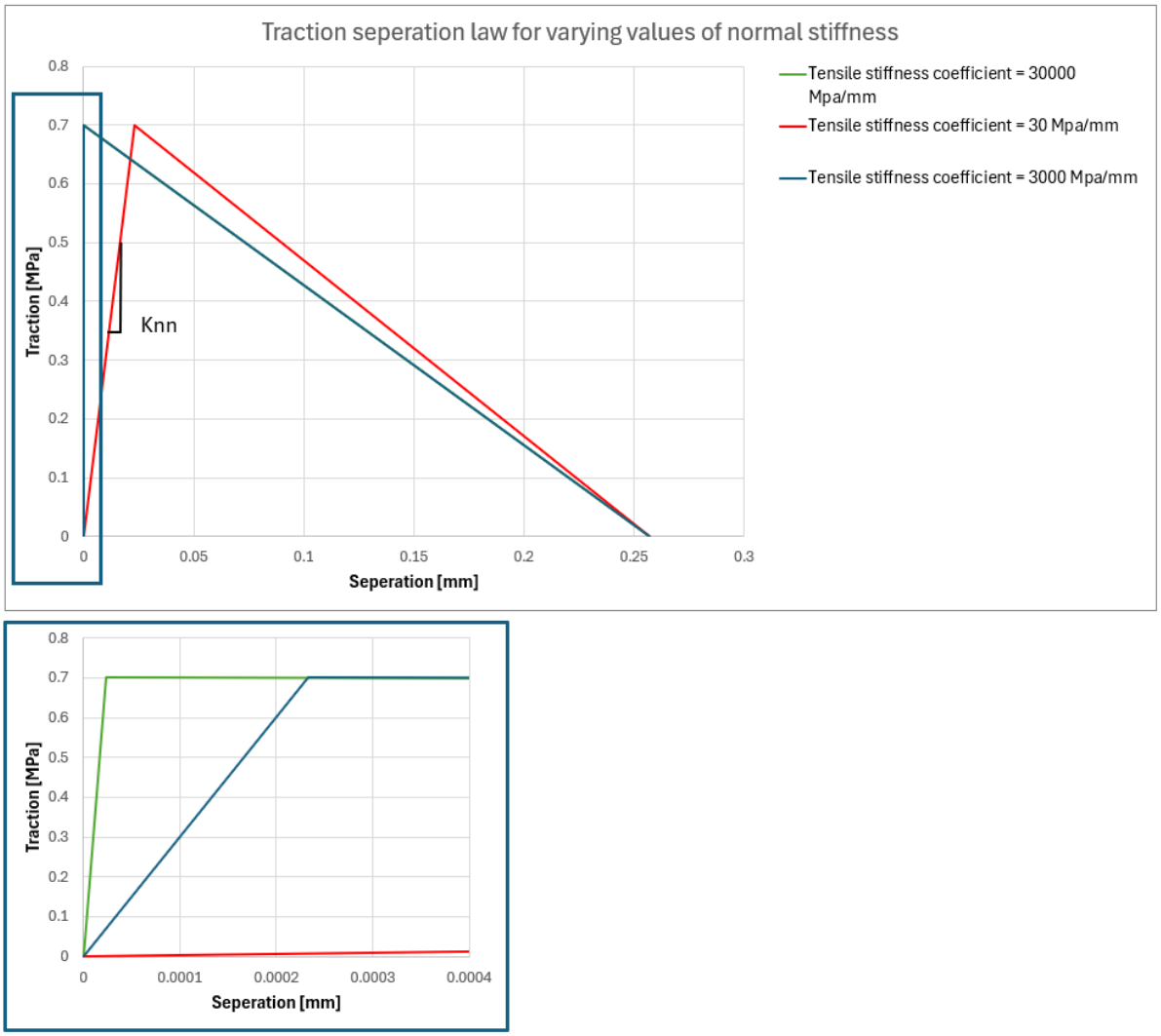

Figure A.15: Influence of the normal stiffness on the traction separation law of the interface's tensile behaviour

Results: For both the normal stiffness coefficients of 30 [MPa/mm] and 30000 [MPa/mm] the results of the analysis are presented below. First the results for the normal stiffness coefficient of 30 [MPa/mm] interface condition is shown and afterwards the results for the interface with a normal stiffness coefficient of 30000 [MPa/mm] is shown.

A.2.1. Knn = 30 [MPa/mm]

In Figure A.16 the force-displacement diagram of the analysis is shown, together with the locations of the different relevant steps. It can be seen that after step 30, the force remains around a value of zero, therefore the choice has been made that in this analysis only steps 1-30 have been analysed.

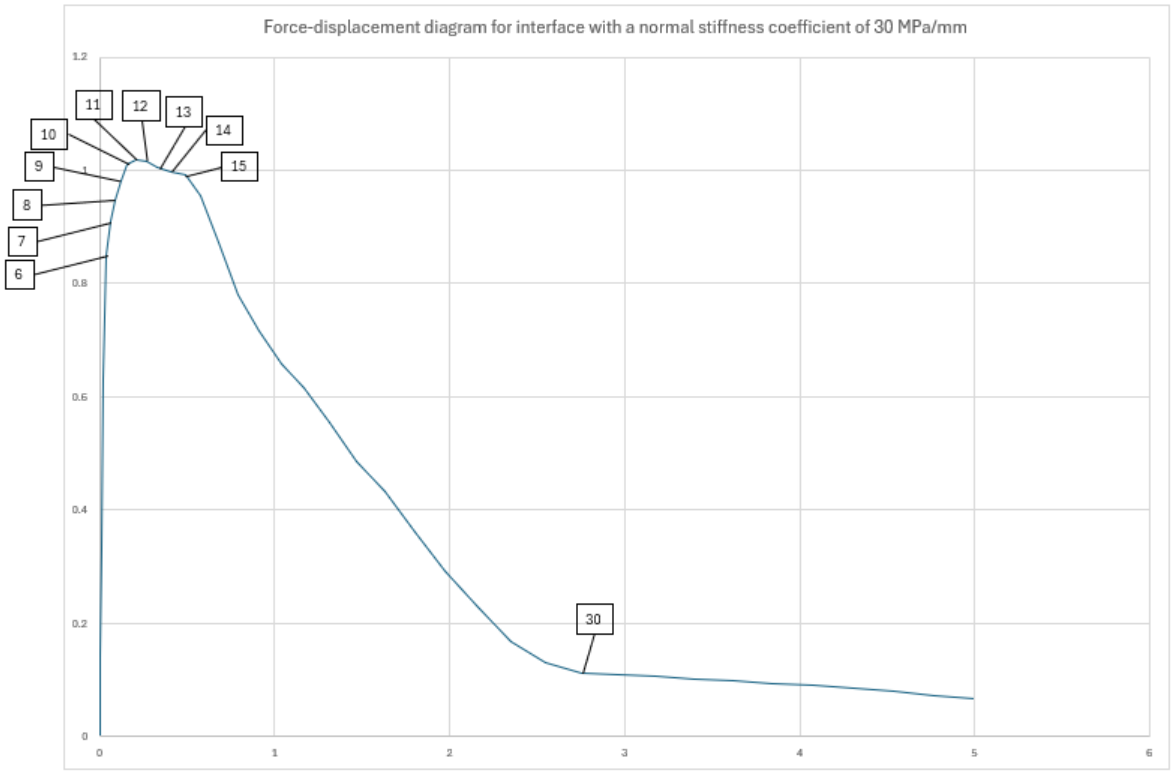

Figure A.16: Force displacement diagram of the analysis with an interface with a normal stiffness coefficient of 30 [MPa/mm], with important steps identified for further analysis.

In Figure A.17 the plastic strain development in the specimen with a normal stiffness coefficient of 30 MPa/mm is shown throughout the analysis. Compared to the original interface, the development of plastic strain in the tab and surrounding material remains almost identical up to step 8. However, by step 10, some differences become apparent. The strain at the bottom of the tab becomes slightly more localized, and a significantly larger amount of material around the top corners is activated in the case of the lower normal stiffness coefficient. In the specimen with a normal stiffness coefficient of 30 MPa/mm, plastic strain quickly rises to higher values and continues to increase until the end of the analysis. In contrast, for the original interface specimen, plastic strain develops more slowly and only up to step 16, after which no further increase is observed. Additionally, by the end of the analysis, a much larger region of material surrounding the corners and sides of the tab is activated in the specimen with the lower normal stiffness coefficient, and the plastic strain values in this region are significantly higher.

In the specimen with a normal stiffness coefficient of 30 MPa/mm, the plastic strain in the bottom of the tab exceeds the predefined color legend limit of 0.03 (3%) from step 15 onwards. To further illustrate the material behavior of the tab, the tensile damage parameter is presented in Figure A.18, which indicates that tensile damage is predominantly localized at the bottom of the tab, where material failure ultimately occurs, demonstrating a tab failure mechanism. It is important to note that tensile damage is a material property derived from the single-crack behavior. It is defined to remain zero until additional crack opening leads to a decrease in stress values, rather than an increase.

To provide a comprehensive view of the material damage, the final step (30/40) is displayed with a lower limit of 0.0001, revealing even the smallest damage areas, which are visible around the top corners of the tab and in the material surrounding the sides of the tab.

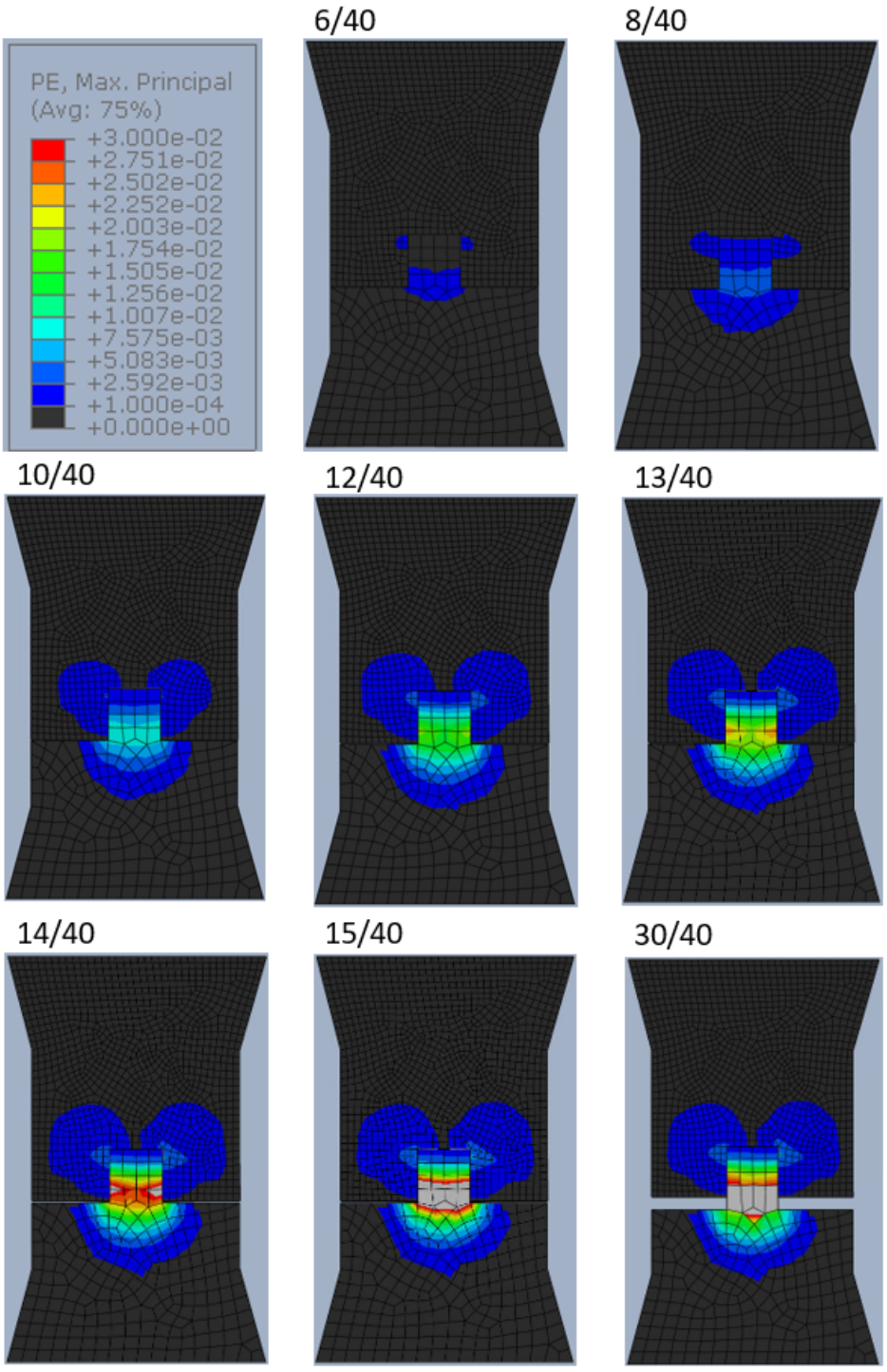

Figure A.17: Plastic strain values throughout the analysis with a color legend ranging from 0.0001 (0.01%) to 0.03 (3%).

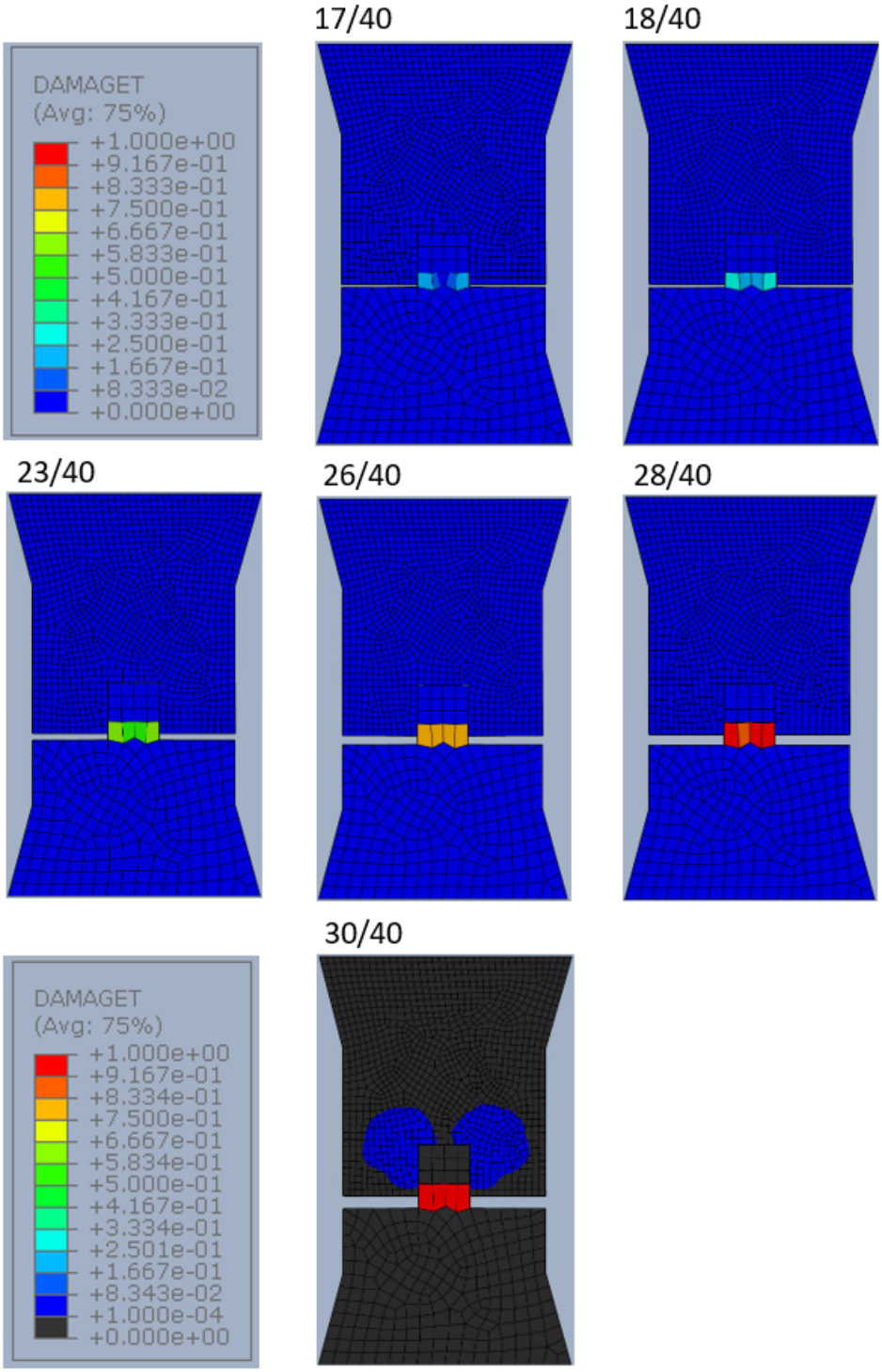

Figure A.18: Tensile damage values throughout the analysis with a color legend ranging from 0 (0%) to 1.0 (100%). Additionally for step 30 a color legend ranging from 0.0001 (0.01%) to 1.0 (100%) is used.

Changing the normal (tensile) stiffness coefficient, actively changes the tensile traction-separation law of the interface as shown in Figure A.15. Therefore it is important to look at the tensile interface behaviour. The interface damage development in the horizontal interfaces loaded in tension is shown in Figure A.19.

It can be seen that in contrast to the original interface, here the horizontal interface only starts to damage at step 6, whereas in the original interface at this step all three horizontal interfaces were

(almost) fully damaged already. The increase in damage in the interface increases at a much lower pace than it did in the original analysis. A big contrast to the original interface is that in the case of the low tensile stiffness coefficient the horizontal interfaces on the sides damage more quickly than the horizontal interface at the top of the tab. This is exactly contradictory to the shown damage pattern in the original interface. Additionally it can be seen that at step 15 the top horizontal interface is not fully damaged. After step 15 no further interface damage occurs in the horizontal interface at the top of the tab. Only some additional damage can be detected in the bottom horizontal surface at the attachment to the tab.

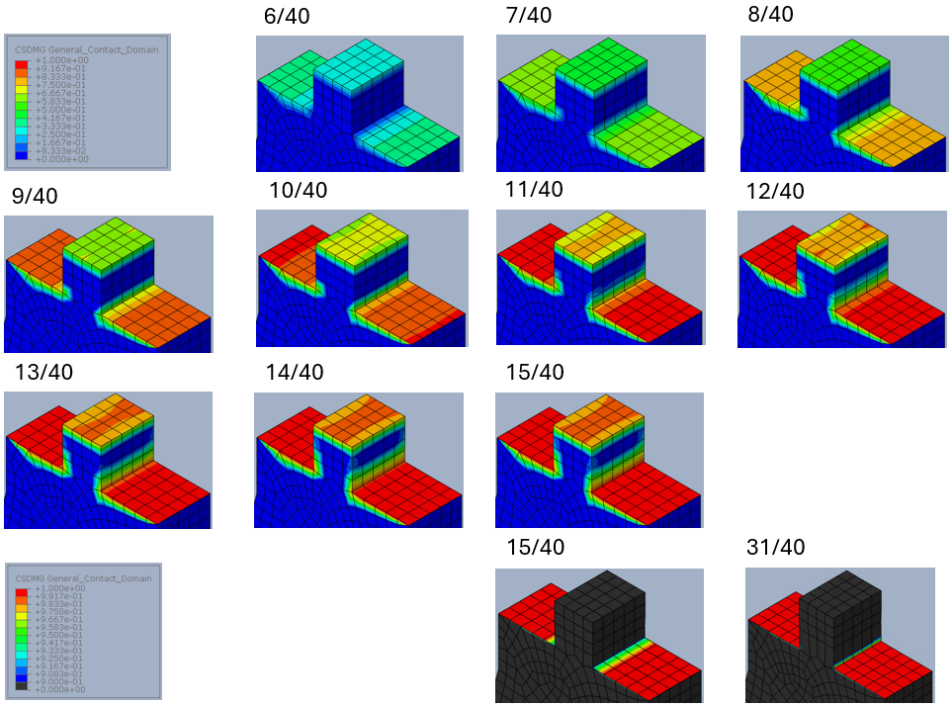

Figure A.19: Interface damage of the interface loaded in tension throughout the analysis of the specimen with a normal stiffness coefficient of 30 MPa/mm. Color legend ranges from 0 (0%) to 1 (100%).

For the vertical shear interface damage, Figure A.20 illustrates the progression of shear interface damage throughout the analysis. Due to the slower development of tensile interface damage, less influence is transferred from the tensile interface to the shear interface. It is also observed that the onset of shear interface damage begins at step 7, similar to the original interface. However, both the magnitude of the shear interface damage and the extent of the affected area are significantly lower at the start. Overall, the progression of shear interface damage is much slower compared to the original interface and halts entirely after step 15.

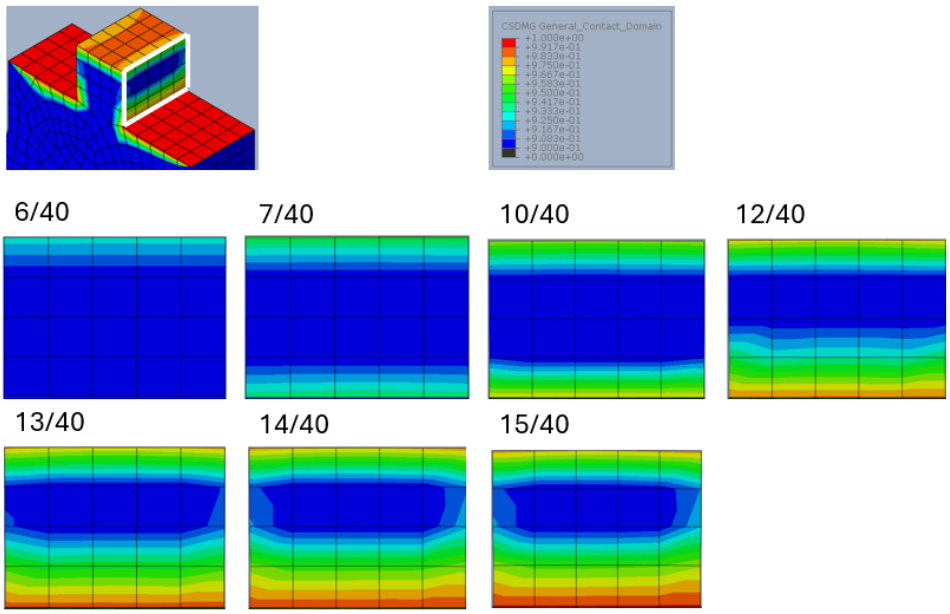

Figure A.20: Interface damage of the interface loaded in shear throughout the analysis of the specimen with a normal stiffness coefficient of 30 MPa/mm. Color legend ranges from 0 (0%) to 1 (100%).

Knn = 30000

In Figure A.21 the force-displacement diagram of the analysis is shown, together with the locations of the different relevant steps. It can be seen that after step 33, the results the force become slightly numerically unstable, therefore the choice has been made that in this analysis only steps 1-33 have been analysed.

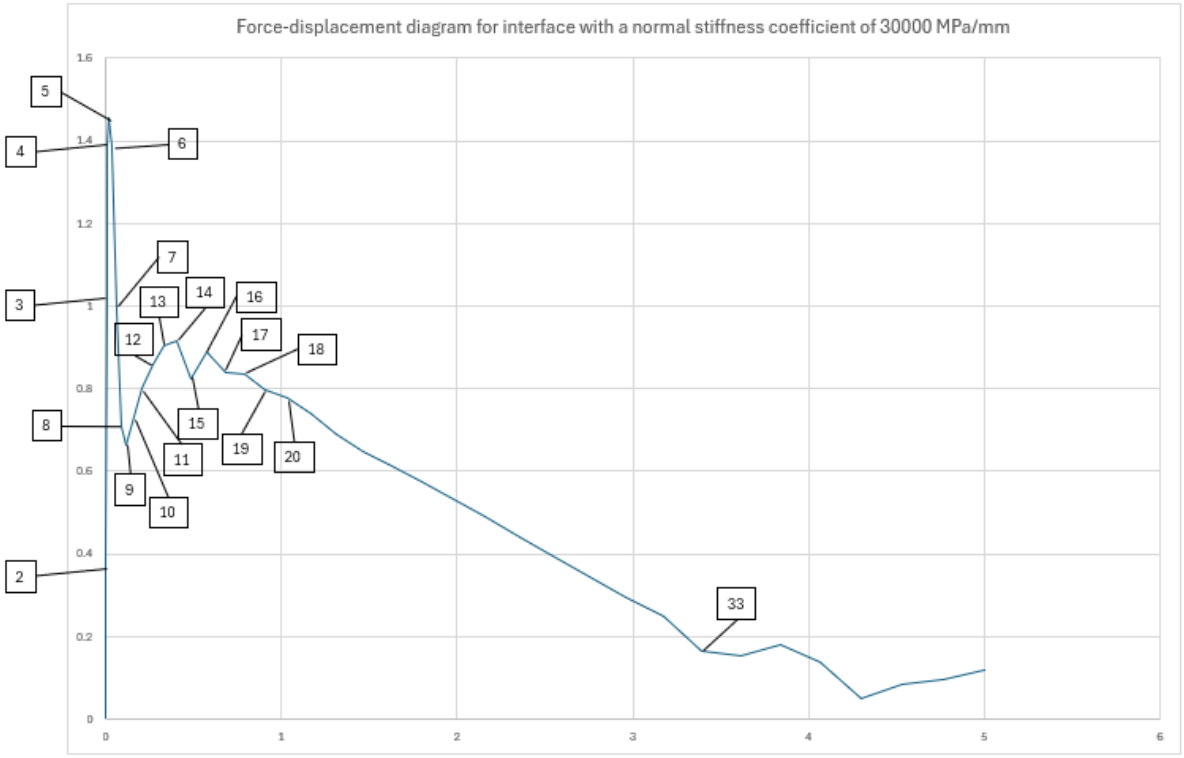

Figure A.21: Force displacement diagram of the analysis with an interface with a normal stiffness coefficient of 30000 [MPa/mm], with important steps identified for further analysis.

In Figure A.22, the development of plastic strain in the high tensile stiffness coefficient specimen is shown throughout the analysis. The first thing to note is that the first plastic strain which develops in this case is around the bottom horizontal interface, which is much different than for the original interface. After this the plastic strain develops in the material around the sides of the tab and at step 6 the plastic strain also develops at the bottom of the tab. In the analysis the plastic strain develops up until step 17, after which the plastic strain does not increase further and the displacement of the top part of the specimen does not lead to higher plastic strains. It can be seen that compared to the original interface the area of material which has been affected is much larger. Also the value of plastic strain in the material on the sides of the tab is higher than in the original interface. Lastly also the plastic strain inside the tab is higher than in the original interface.

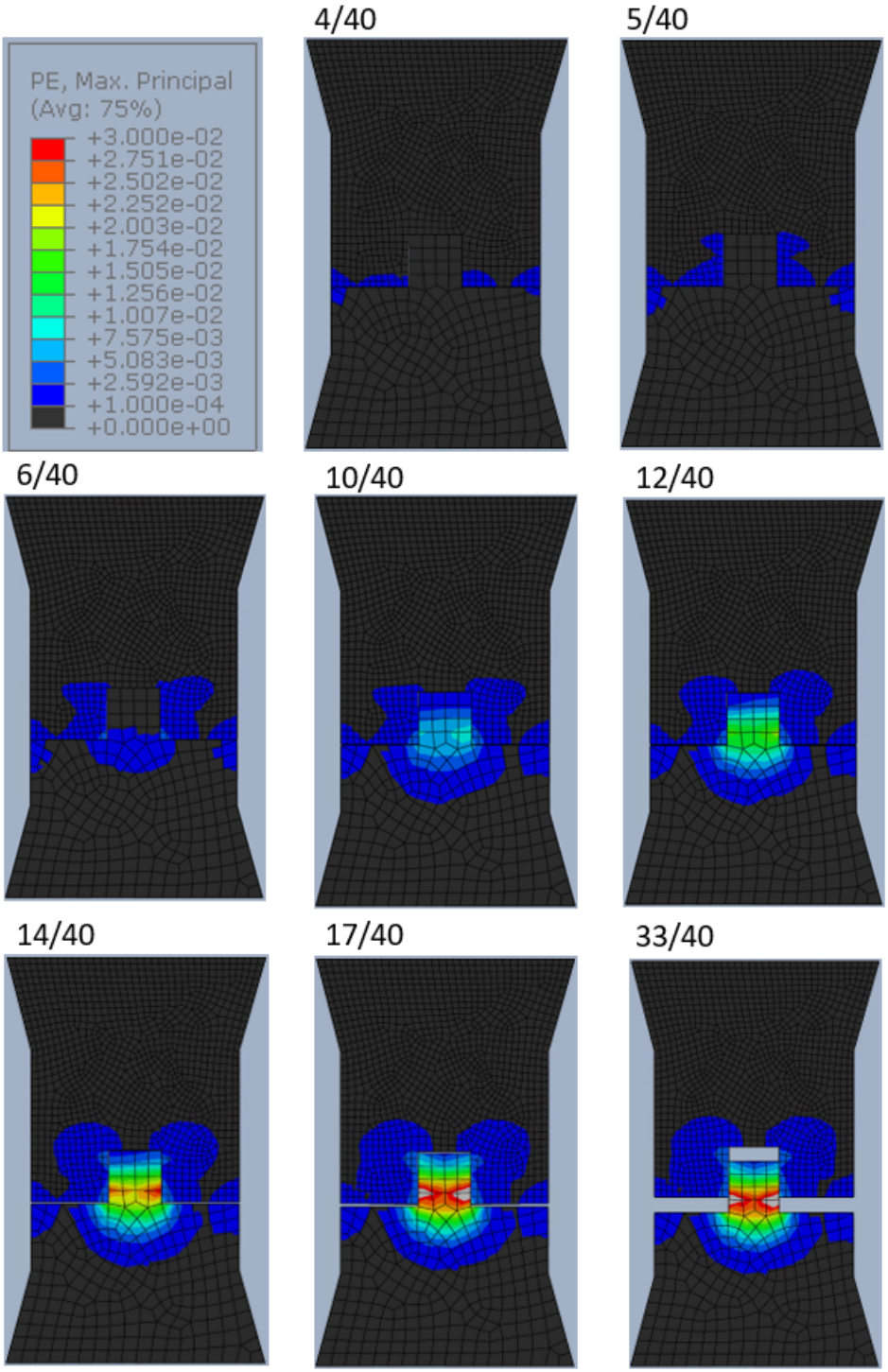

Figure A.22: Plastic strain values throughout the analysis with a color legend ranging from 0.0001 (0.01%) to 0.03 (3%).

Again it is important to look at the tensile interface behaviour due to the change to the tensile traction-separation law of the interface. The interface damage development in the horizontal interfaces loaded in tension is shown in Figure A.23. In this case with a high normal stiffness coefficient the horizontal interface at the top of the tab damages more quickly than the horizontal surfaces on the sides of the tab. This is different than in the case of the low normal stiffness coefficient but similar to the original interface behaviour. In general it can be said that the horizontal interface damages relatively quickly in comparison to the original interface.

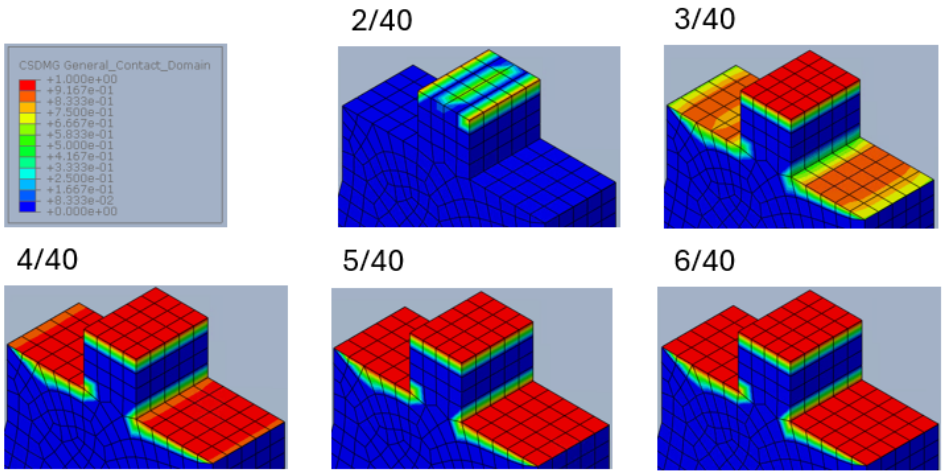

(a) Interface damage of the interface loaded in tension throughout the analysis with a color legend ranging from 0 (0%) to 1 (100%).

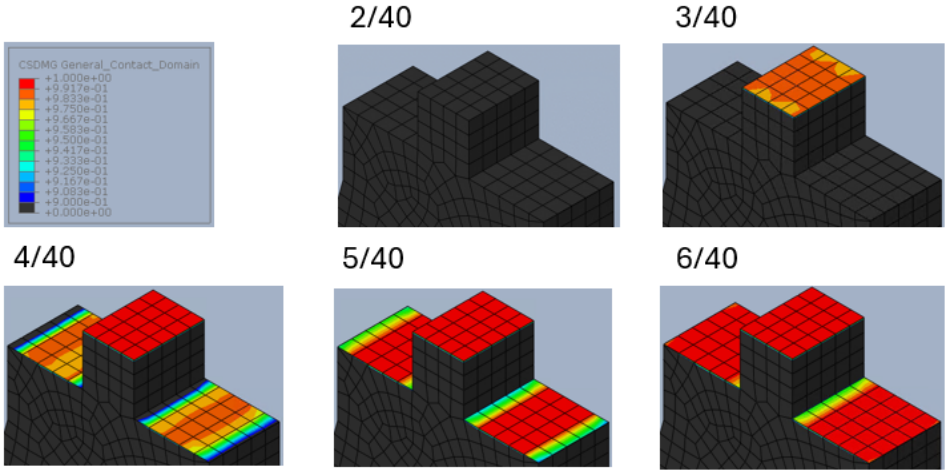

(b) Interface damage of the interface loaded in tension throughout the analysis with a color legend ranging from 0.9 (90%) to 1 (100%).

Figure A.23: Interface damage of the interface loaded in tension throughout the analysis of the specimen with a normal stiffness coefficient of 30000 MPa/mm.

For the interface damage in the vertical shear interfaces Figure A.24 shows the development of this shear interface damage throughout the analysis. Again it can be seen that the shear interface damage development is a bit different than in the original case. In step 7 no increase in shear interface damage can be seen, this starts at step 8. In general over all steps the shear interface damage develops a bit slower than in the original case. However both of the shear interfaces show a completely red (meaning damage between 99.17%-100%) interface.

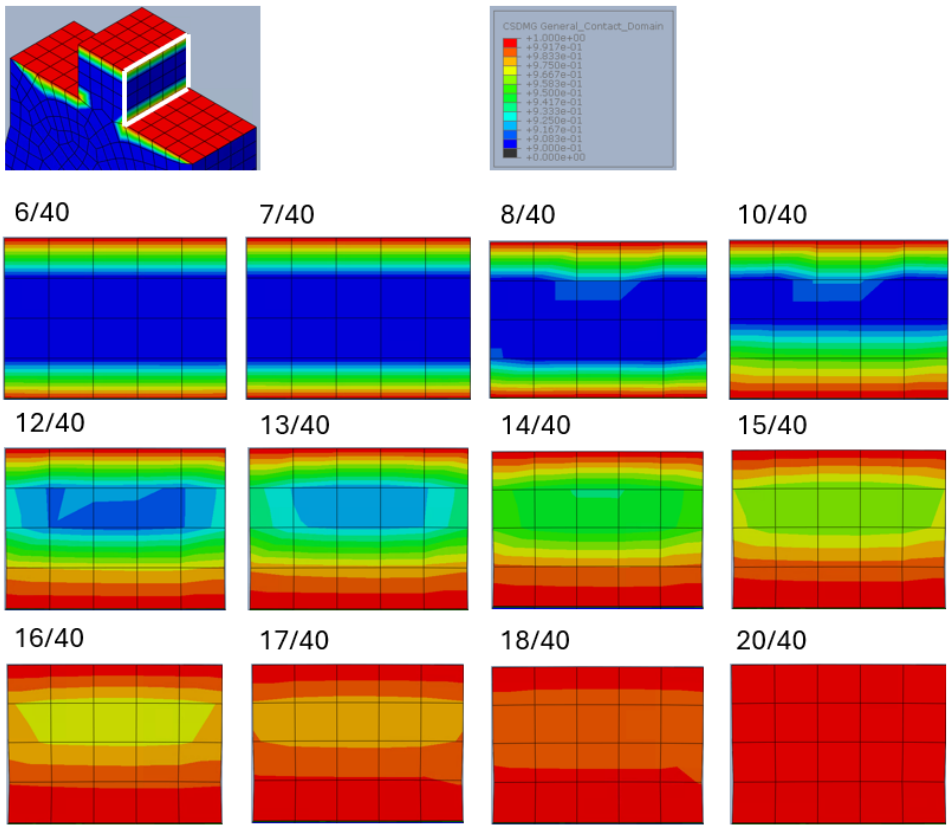

Figure A.24: Interface damage of the interface loaded in shear throughout the analysis of the specimen with a normal stiffness coefficient of 30000 MPa/mm. Color legend ranges from 0 (0%) to 1 (100%).

Lastly, the influence of the different values for the normal stiffness coefficients on the force-displacement behaviour is presented in Figure A.25. Additionally the same data is also presented as a stress-displacement diagram in Figure A.26

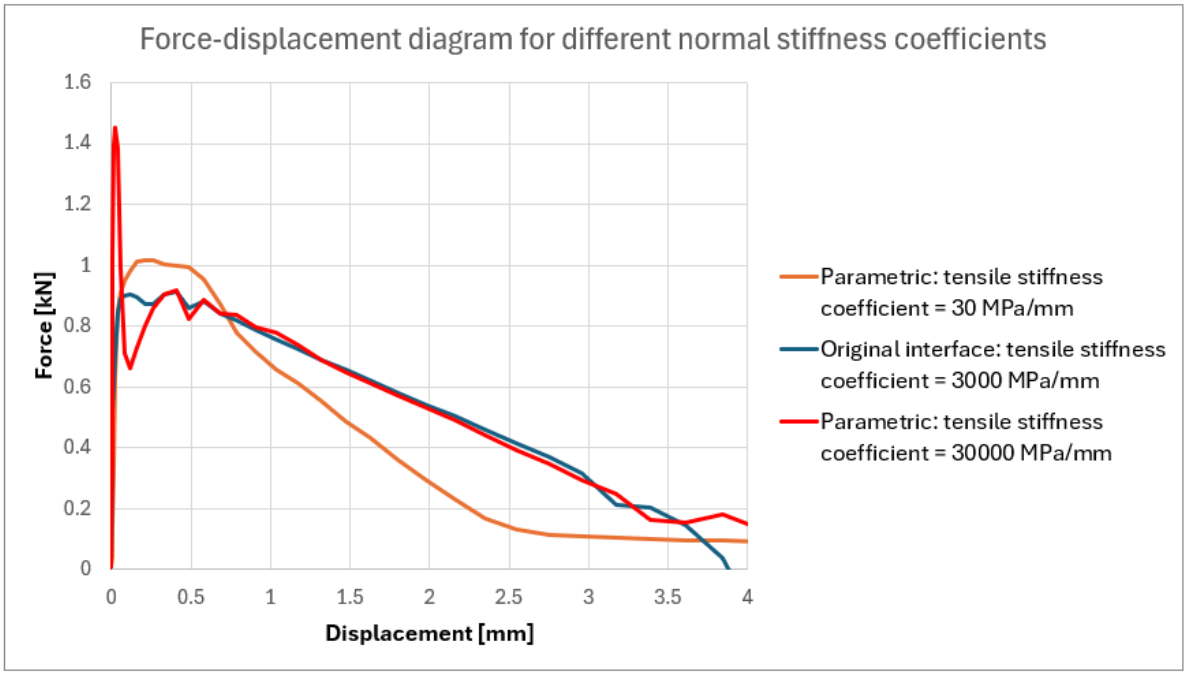

Figure A.25: Influence of the low and high values of normal stiffness coefficient on the force-displacement behaviour of the connection.

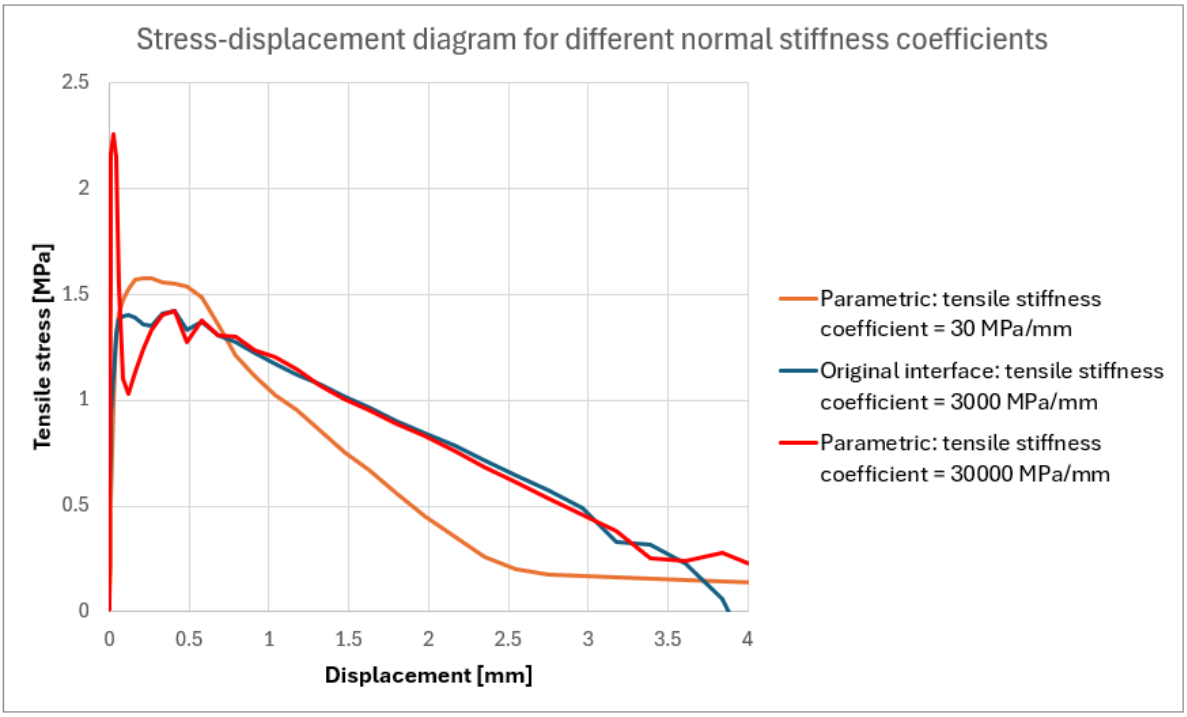

Figure A.26: Influence of the low and high values of normal stiffness coefficient on the tensile stress-displacement behaviour of the connection.

A.2.2. Discussion

The analysis of the interface behaviour under varying normal stiffness coefficients reveals several important insights. The main thing to note is that changing the tensile stiffness coefficient changes the way the horizontal (tensile) and vertical (shear) interfaces in the specimen work together.

The analysis of the specimen with a low normal stiffness coefficient provides several important insights into interface behavior. Initially, the tensile interface damage develops later and progresses more slowly compared to the original interface conditions. This slower progression means that the shear interface starts to experience damage before the tensile interface is fully compromised, which contrasts with the behavior observed in the original configuration. The closer similarity in stiffness between the horizontal and vertical interfaces causes stress to develop at a more synchronized rate across both surfaces. This results in a higher combined force that the interface can support before failure, surpassing the material's capacity in the tab and leading to tab failure.

In contrast, the specimen with a very high normal stiffness coefficient displays a different failure mechanism. The analysis shows that, from the start, the stress transferred through the horizontal interfaces is significantly high. By Step 4, plastic strain is already evident around the bottom horizontal interfaces, driven by high tensile stresses. The initial peak force in the force-displacement diagram is notably elevated in this case. Despite considerable damage to the tensile interface by Steps 3 and 4, the total reaction force continues to rise until Step 5.

Interestingly, a simplified calculation of the maximum force capacity of the horizontal interfaces—by multiplying the interface area by the tensile strength limit of 0.7 MPa—yields an upper force limit of around 0.45 kN. Given that the shear stiffness coefficient remains relatively low at 50 MPa, it would be unlikely for the peak force to exceed this calculated limit under realistic conditions. This discrepancy suggests that the significant peak force observed is likely a numerical artifact, arising from combining an unusually high stiffness with a low maximum tensile strength.

While plastic strain develops near the horizontal interfaces during this peak, these strain values should not be interpreted as accurate predictions of the physical response. However, the response of the shear interface during this loading can still be used meaningfully in the analysis. Overall, the results indicate that in cases of elevated tensile stiffness, the initial tensile peak will occur earlier in the force-displacement response, though the realistic peak force is likely closer to the calculated limit of approximately 0.45 kN. This provides a more reliable basis for assessing the specimen's response under these conditions.

Despite significant differences in tensile interface behavior and peak force between the high normal stiffness specimen and the original specimen, the shear interface degradation remains relatively similar. In both cases, the tensile stress in the horizontal interface and the shear stress in the vertical interface work effectively together only up to the initial peak. Beyond this peak, the horizontal interface becomes fully damaged, and the shear interface assumes the load. Notably, although the high normal stiffness specimen shows a higher initial peak force and activates more material, its post-peak behavior aligns closely with that of the original specimen. In both scenarios, the shear interface's strength is inadequate to sustain the stresses required for material failure in the tab, leading to a pull-out failure.

A.3. Kss and Ktt (shear stiffness coefficient, 1st and 2nd direction)

Description: The third variable in this parameter study is the shear stiffness coefficient. Theoretically this interface stiffness coefficient is defined as the interface material stiffness devided by the true physical initial thickness of the interface [2]. Practically this stiffness coefficient defines the slope with which the shear interface strength increases with displacement. In this study values of 5 [MPa/mm] and 3000 [MPa/mm] are used (see Figure A.27). For sake of completeness the shear stiffness coefficient in the first and second direction are changed in the same manner.

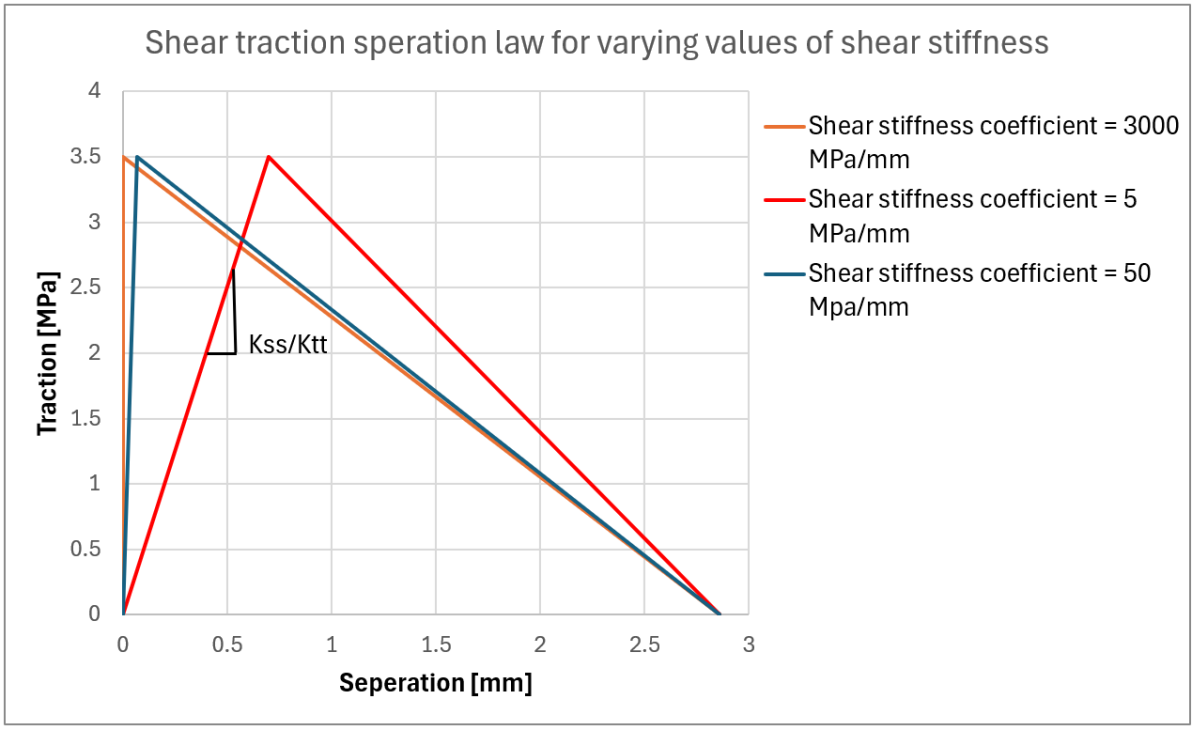

Figure A.27: Influence of the shear stiffness on the traction separation law of the interface's shear behaviour.

Results: For both the shear stiffness coefficients of 5 MPa/mm and 3000 MPa/mm the results of the the analysis are presented below. First the results for shear stiffness coefficient of 5 MPa/mm interface condition is shown and afterwards the results for the interface with a shear stiffness coefficient of 3000 MPa/mm.

A.3.1. Kss and Ktt = 5 MPa/mm

In Figure A.28 the force-displacement diagram of the analysis is shown, together with the locations of the different relevant steps. It can be seen that after step 31, the results become numerically unstable, therefore the choice has been made that in this analysis only steps 1-31 have been analysed.

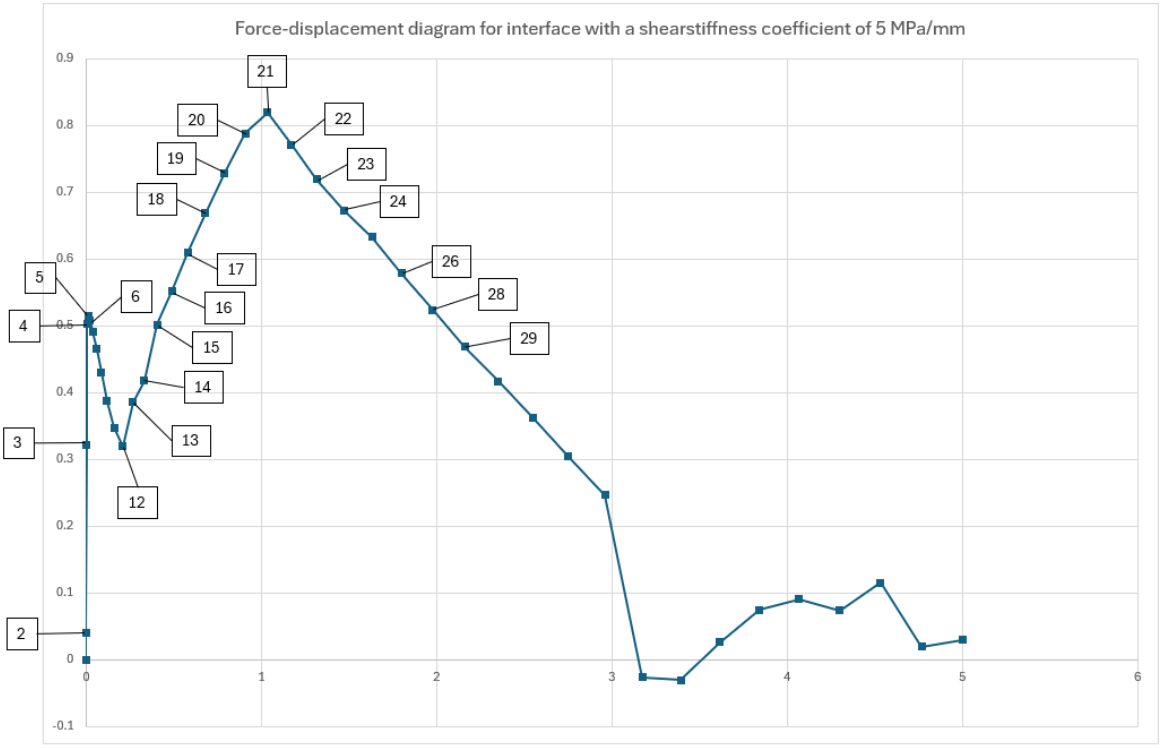

Figure A.28: Force displacement diagram of the analysis with an interface with a shear stiffness coefficient of 5 MPa/mm, with important steps identified for further analysis.

In Figure A.29 illustrates the plastic strain development in the specimen with a low interfacial shear stiffness coefficient throughout the analysis. In this scenario, plastic strain in the material begins to manifest at step 13/40, significantly later than in the original interface case. The plastic strain continues to develop up to step 21, after which it plateaus, and further displacement of the specimen's top part does not result in increased strain.

The rate of plastic strain development between steps 14 and 18 in this analysis is comparable to that observed in the original interface from steps 6 to 10. However, after step 18, the plastic strain in the specimen with the low shear stiffness coefficient remains notably lower and does not increase beyond step 21. In contrast, the original interface exhibits continued strain development up to step 16, reaching much higher values than the low shear stiffness coefficient case.

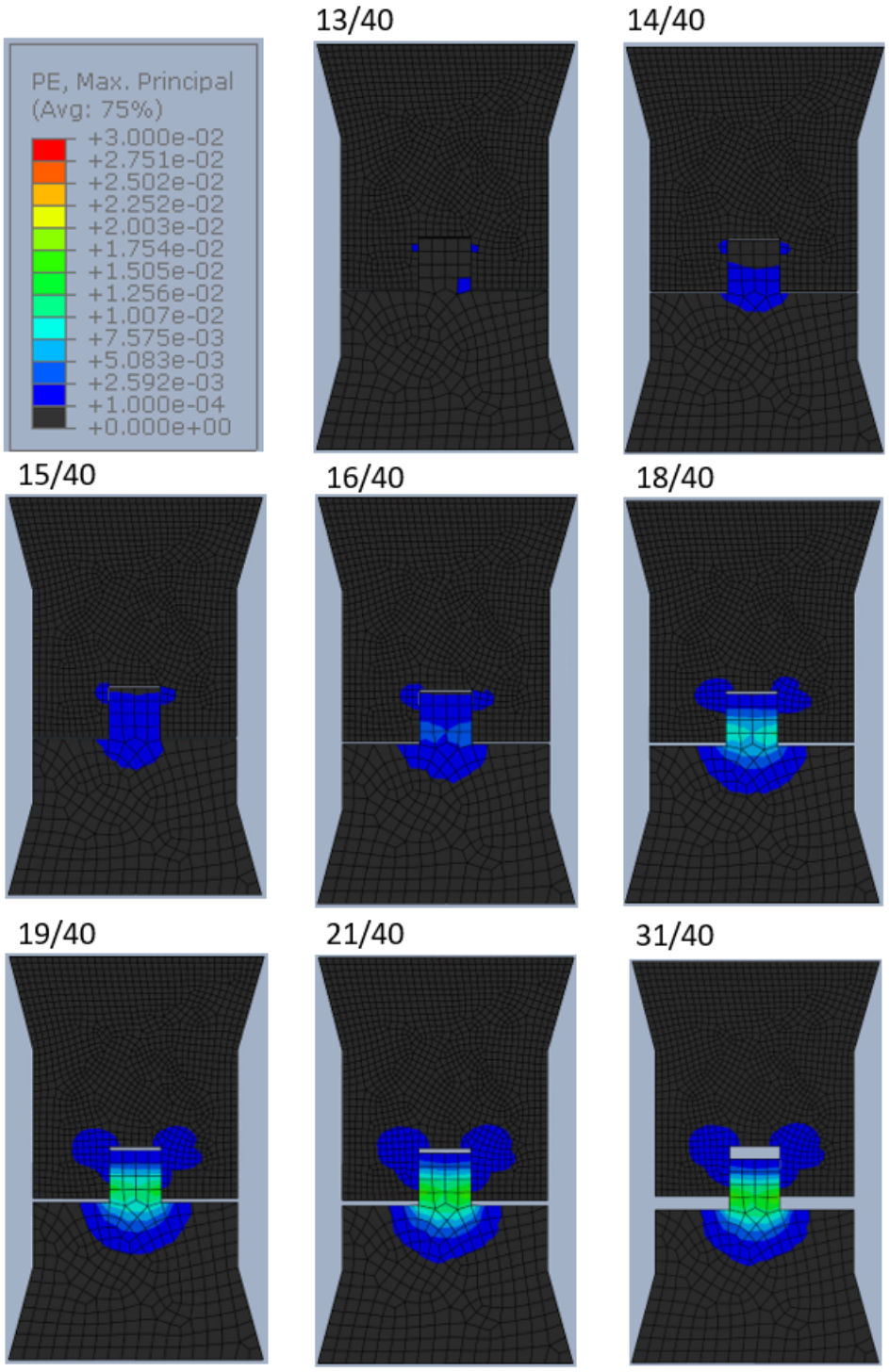

Figure A.29: Plastic strain values throughout the analysis with a color legend ranging from 0.0001 (0.01%) to 0.03 (3%).

Even though the shear stiffness coefficient changes the shear interface behaviour, it also changes the behaviour of the tensile interface in the specimen. The interface damage development in the horizontal interfaces loaded in tension is shown in Figure A.30. In this case with a very low shear stiffness coefficient the horizontal interface damages slightly more quickly than in the original case. However, the damage pattern stays constant, the top surface damages more quickly than the bottom two horizontal surfaces.

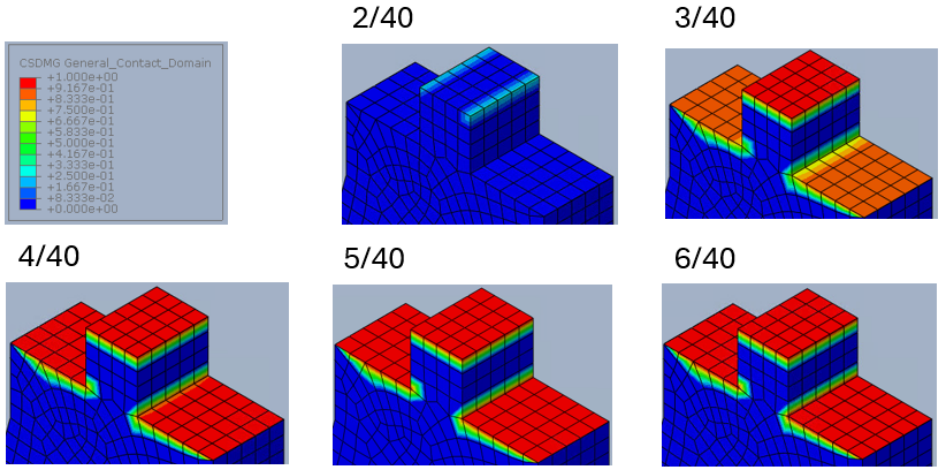

(a) Interface damage of the interface loaded in tension throughout the analysis with a color legend ranging from 0 (0%) to 1 (100%).

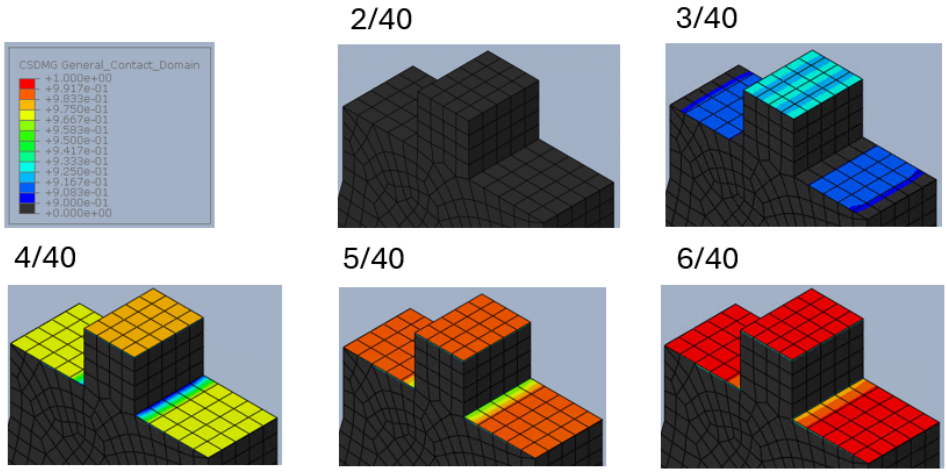

(b) Interface damage of the interface loaded in tension throughout the analysis with a color legend ranging from 0.9 (90%) to 1 (100%).

Figure A.30: Interface damage of the interface loaded in tension throughout the analysis of the specimen with a shear stiffness coefficient of 5 MPa/mm.

For the interface damage in the vertical shear interfaces Figure A.31 shows the development of this shear interface damage throughout the analysis. It can be seen that the shear interface damage development only starts at step 12, whereas in the original case the damage development starts in step 7. The damage development in the interface is more homogeneous over the width of the interface. is the same as in the original case up until step 10. After that it can be seen that the interface damage develops much quicker than in the original case.

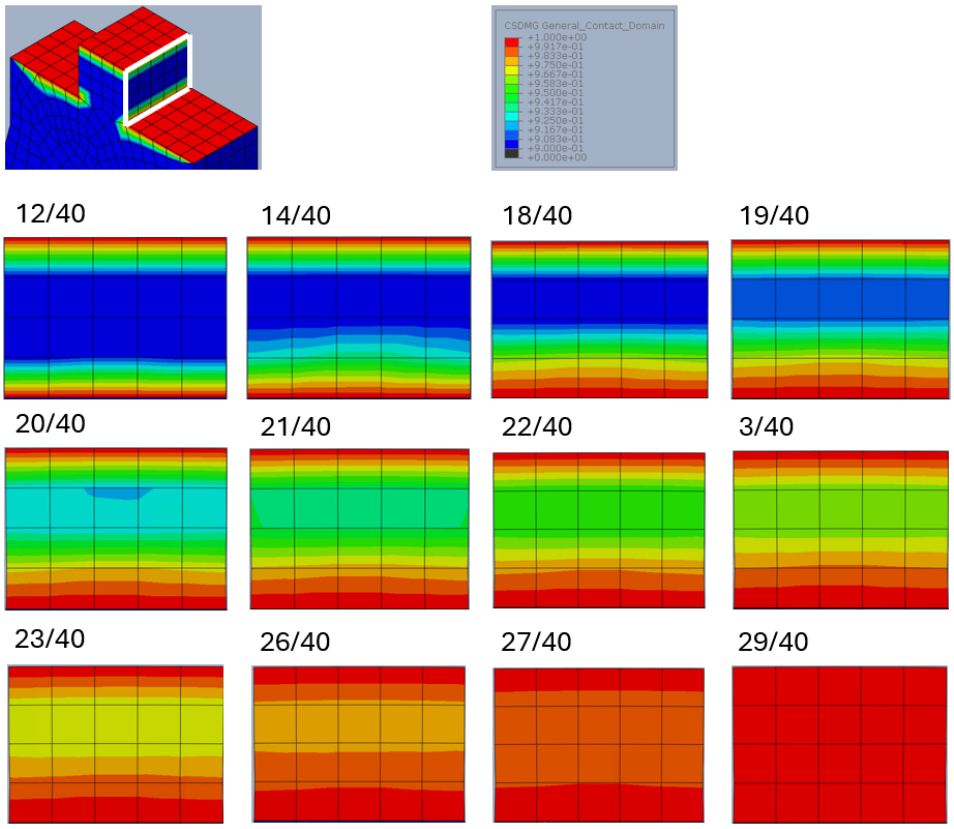

Figure A.31: Interface damage of the interface loaded in shear throughout the analysis of the specimen with frictionless interface conditions. Color legend ranges from 0 (0%) to 1 (100%).

A.3.2. Kss and Ktt = 3000

In Figure A.8 the force-displacement diagram of the analysis is shown, together with the locations of the different relevant steps. It can be seen that after step 30, the results the force remains around a value of zero, therefore the choice has been made that in this analysis only steps 1-30 have been analysed.

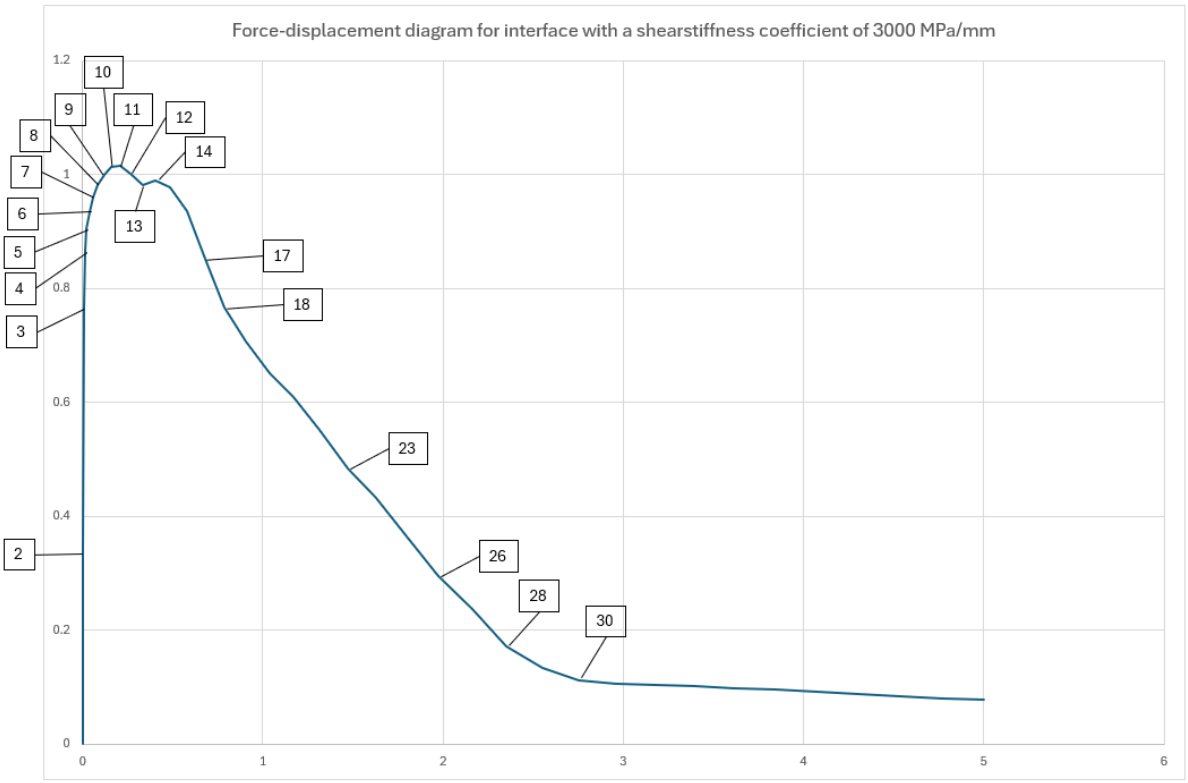

Figure A.32: Force displacement diagram of the analysis with an interface with a shear stiffness coefficient of 3000, with important steps identified for further analysis.

In Figure A.33, the development of plastic strain in specimen with an interfacial shear stiffness coefficient of 3000 MPa/mm is shown throughout the analysis. It can be seen that compared to the original interface the plastic strain development in all steps is much quicker in the case of the high shear stiffness coefficient. In this case it is also seen that plastic strain increases to higher values than in the original case and the plastic strain continues to increase until the end of the analysis. On the other hand the for the original interface specimen the plastic strain develops much slower and only until step 16, after which the plastic strain does not increase.

In the specimen with a shear stiffness coefficient of 3000 MPa/mm, the plastic strain in the bottom of the tab exceeds the predefined color legend limit of 0.03 (3%) from step 14 onwards. To further illustrate the material behavior of the tab, the tensile damage parameter is presented in Figure A.34, which indicates that tensile damage is predominantly localized at the bottom of the tab, where material failure ultimately occurs, demonstrating a tab failure mechanism. It is important to note that tensile damage is a material property derived from the single-crack behavior. It is defined to remain zero until additional crack opening leads to a decrease in stress values, rather than an increase.

To provide a comprehensive view of the material damage, the final step (30/40) is displayed with a lower limit of 0.0001, revealing even the smallest damage areas, which are visible around the top corners of the tab and in the material surrounding the sides of the upper part of the tab.

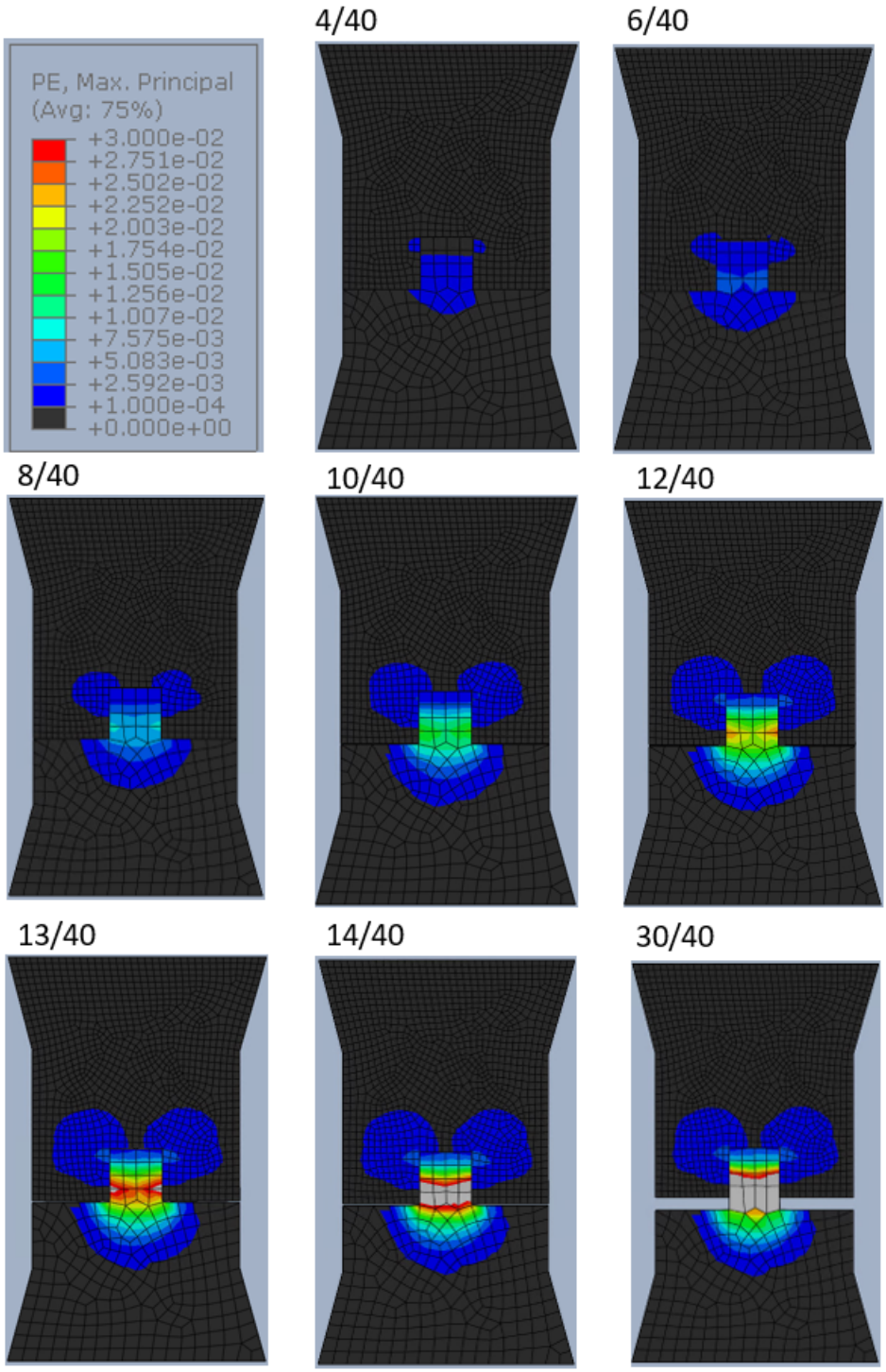

Figure A.33: Plastic strain values throughout the analysis with a color legend ranging from 0.0001 (0.01%) to 0.03 (3%).

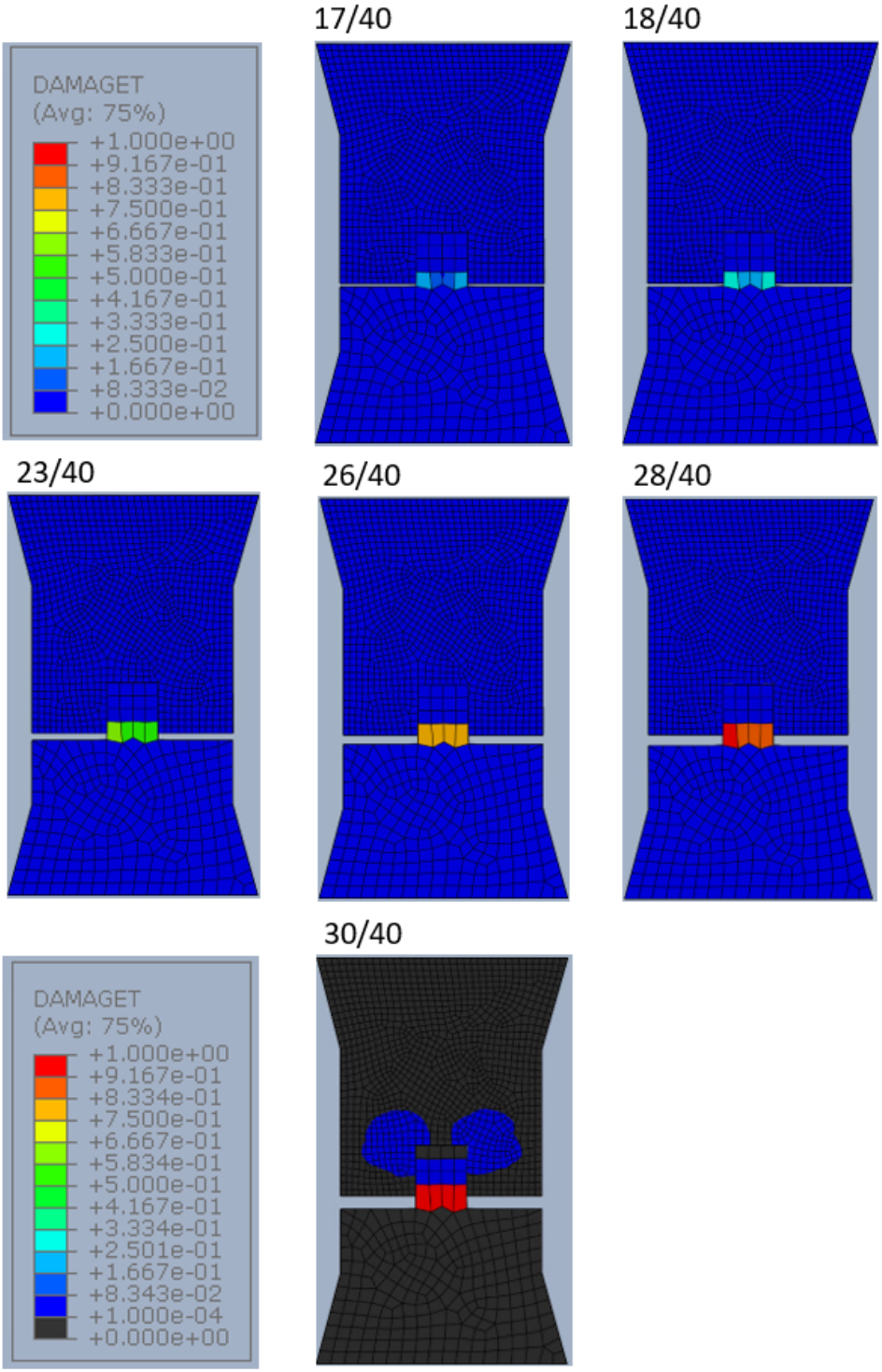

Figure A.34: Tensile damage values throughout the analysis with a color legend ranging from 0 (0%) to 1.0 (100%). Additionally for step 30 a color legend ranging from 0.0001 (0.01%) to 1.0 (100%) is used.

Although changes in the shear stiffness coefficient primarily affect the behavior of the shear interface, they also influence the tensile interface behavior. The damage development in the horizontal interfaces under tension is illustrated in Figure A.35. With a high shear stiffness coefficient, the damage in the bottom two horizontal interfaces progresses at nearly the same rate as in the original interface. However, a key difference is that the outer sections of the horizontal surfaces begin to damage before the areas closer to the tab. This is likely because, with a high shear stiffness coefficient, the material

on the sides of the tab moves significantly less at the same total displacement, contributing less to the damage in the horizontal interfaces.

Additionally, the horizontal interface at the top of the tab shows much slower damage progression compared to the original case. This can be attributed to the reduced sliding in the vertical interface, resulting in a much smaller opening at the top of the tab.

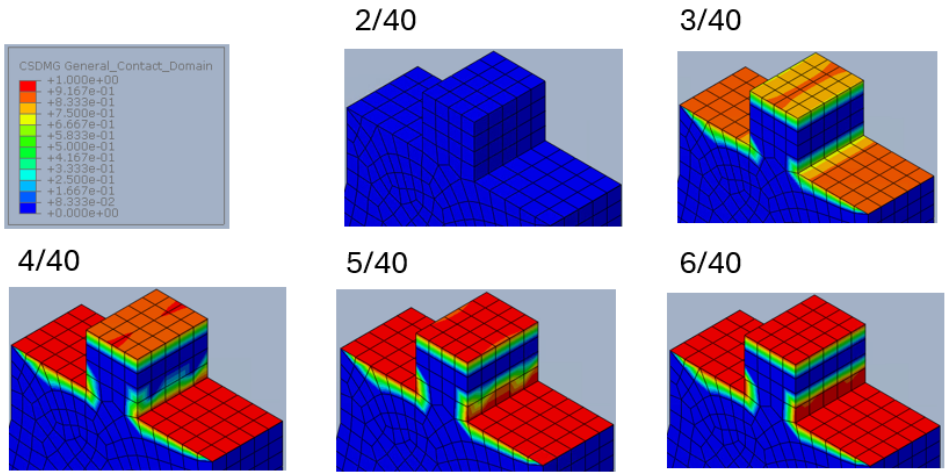

(a) Interface damage of the interface loaded in tension throughout the analysis with a color legend ranging from 0 (0%) to 1 (100%).

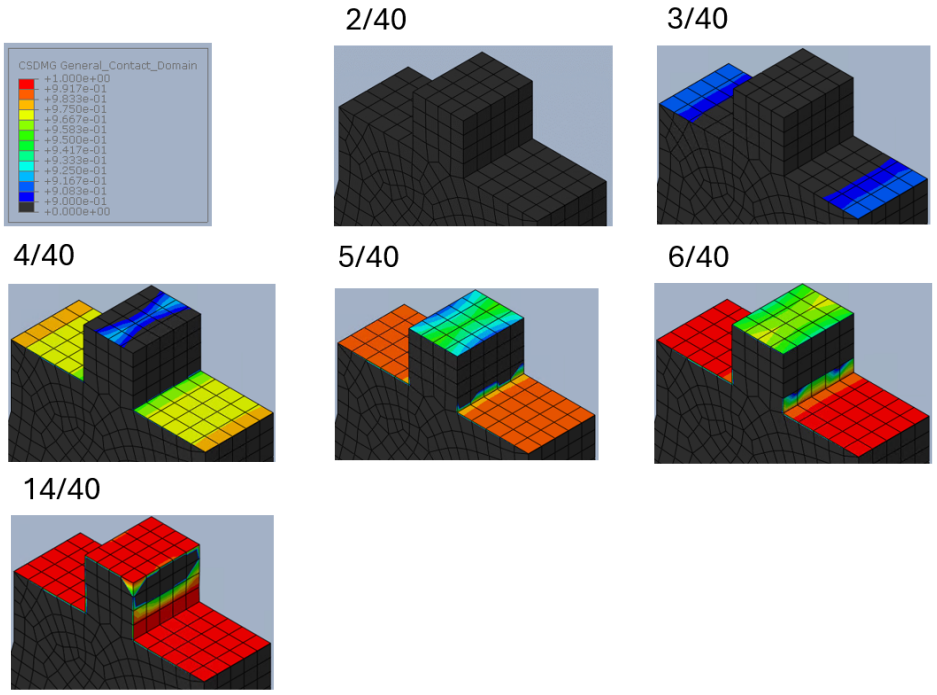

(b) Interface damage of the interface loaded in tension throughout the analysis with a color legend ranging from 0.9 (90%) to 1 (100%).

Figure A.35: Interface damage of the interface loaded in tension throughout the analysis of the specimen with a shear stiffness coefficient of 3000 MPa/mm.

For the interface damage in the vertical shear interfaces Figure A.36 shows the development of this shear interface damage throughout the analysis. In this case the shear interface damage starts to develop already in step 4 in comparison to step 7 in the original case. Where in the case of the low

shear stiffness coefficient the development of shear interface damage was mostly constant over the width of the tab, in the case of the high shear stiffness coefficient the shear interface damage develops more quickly on the outer sides of the tab width and remains intact only in a very small spot in the middle top of the sides of the tab. Additionally the shear interface damage stops progressing after step 14 due to the development of tab failure. Whereas in the original case the shear interface damages progresses throughout the entire analysis due to a pull-out failure mechanism.

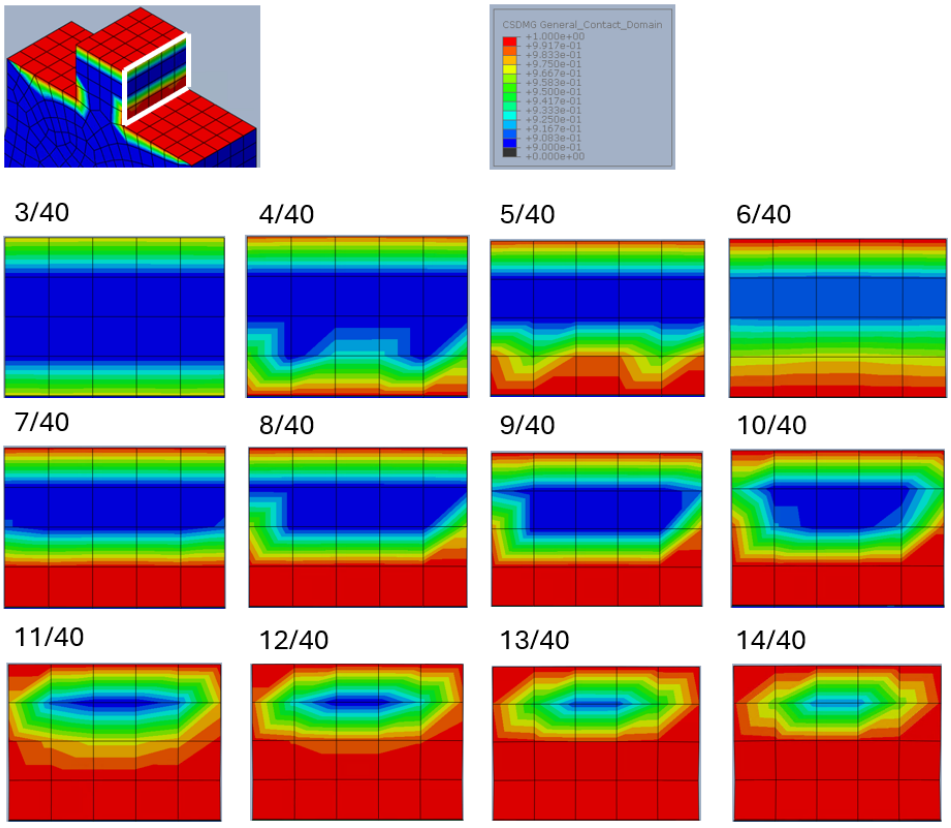

Figure A.36: Interface damage of the interface loaded in shear throughout the analysis of the specimen with a shear stiffness coefficient of 3000 MPa/mm. Color legend ranges from 0 (0%) to 1 (100%).

Lastly, the influence of the different values for the shear stiffness coefficients on the force-displacement behavior is presented in Figure A.37. Additionally the same data is also presented as a stress-displacement diagram in Figure A.38

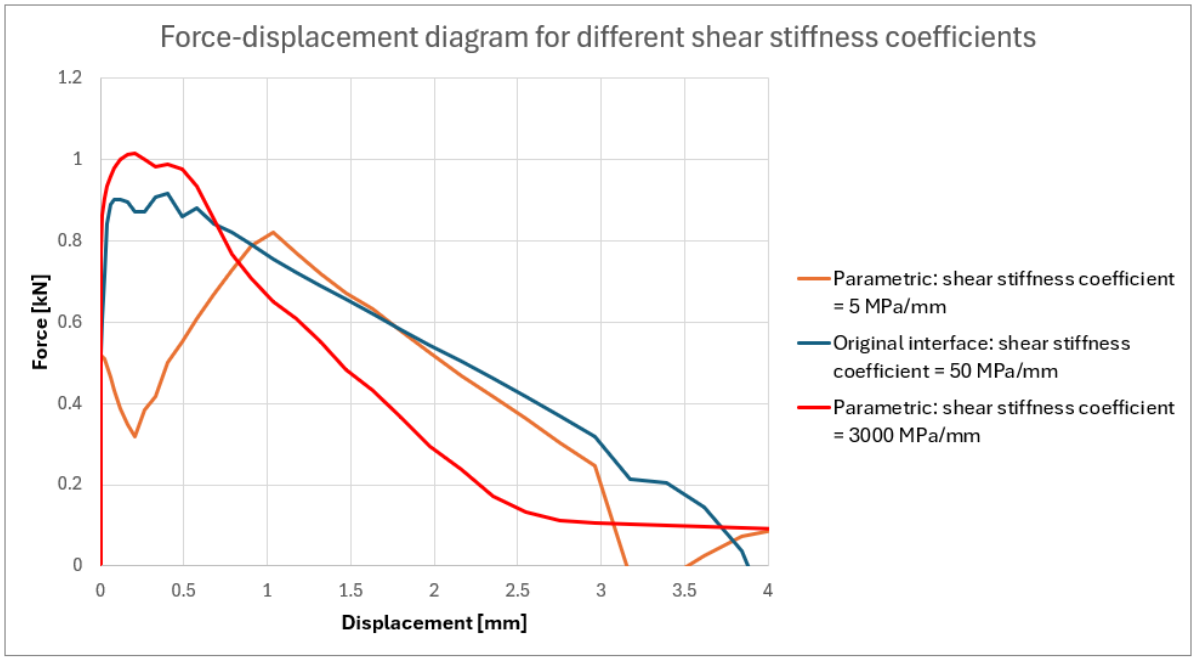

Figure A.37: Influence of the low and high values of the shear stiffness coefficients on the force-displacement behavior of the connection.

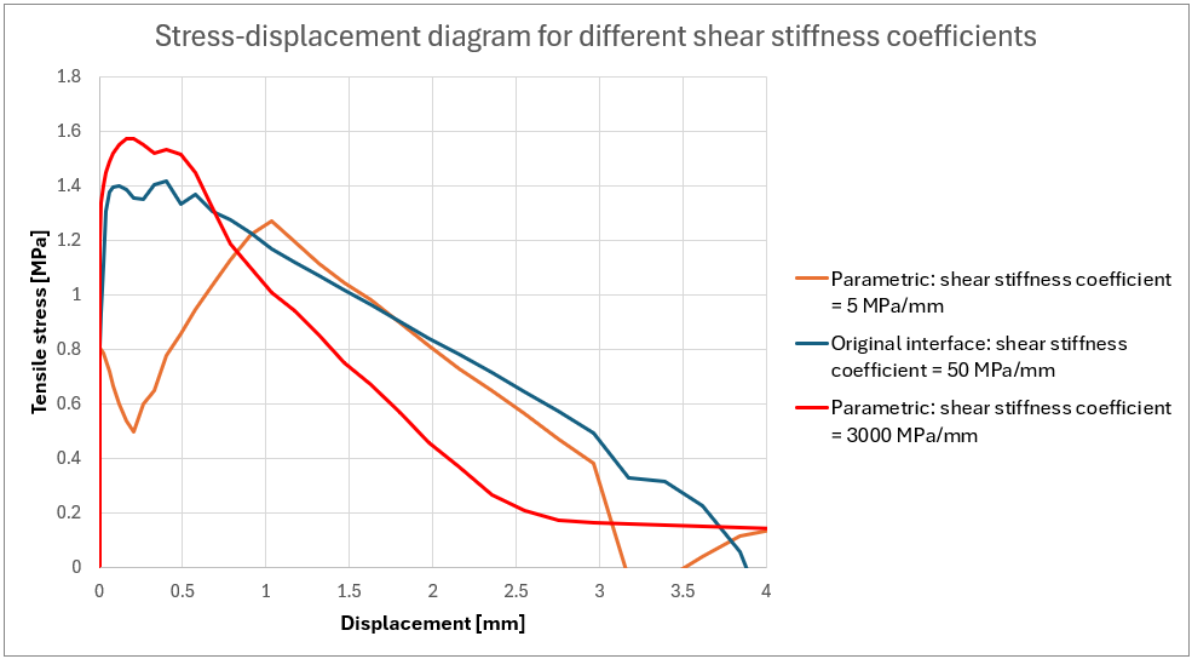

Figure A.38: Influence of the low and high values of the shear stiffness coefficients on the tensile stress-displacement behavior of the connection.

A.3.3. Discussion

The analysis of the interface behaviour under varying shear stiffness coefficients reveals several important insights. The main thing to note, similarly as with the normal stiffness coefficient, is that changing the shear stiffness coefficient changes the way the horizontal (tensile) and vertical (shear) interfaces in the specimen work together.

The analysis of the specimen with a low shear stiffness coefficient provides several important insights into interface behavior. Initially, the tensile interface damage develops slightly quicker than in the original interface conditions, primarily due to the limited shear contribution during the first steps of the analysis. At these early stages, the stresses in the interface are transferred almost exclusively through the tensile interface. This is evident in the force-displacement diagram, where a very low first peak force is observed, mainly attributed to the tensile interface contribution.

Following this initial peak, the force drops significantly before gradually increasing again at a much slower rate. This behavior can be explained by the low shear stiffness coefficient, which requires significant sliding in the vertical interfaces before the shear interface begins to contribute meaningfully to stress transfer. The onset of shear interface damage at step 12 coincides with the point where the force starts to rise again, indicating that the shear interface begins to take over the stress transfer from the tensile interface. This transition is also reflected in the plastic strain development, which begins only at step 13, compared to step 6 in the original case. While the rate of plastic strain development is quite similar between the original and low shear stiffness coefficient cases, the strain stops at a lower value for the low shear stiffness coefficient compared to the original case. After step 12, the shear interface damage is distributed quite evenly over the depth of the tab, suggesting that the depth of the tab does not significantly influence the shear stress distribution. The damage continues to increase throughout the analysis, eventually leading to a pull-out failure mechanism.

Interestingly, despite the considerable differences in the initial behavior, the rate at which the transferred force decreases with displacement is comparable between the case with the low shear stiffness coefficient and the original specimen. This observation highlights that, while the beginning of the connection behavior differs markedly, the post-peak response follows a similar pattern.

Important to note is that the force which is transferred through the interface keeps increasing up until step 21. However in the shear interface damage as presented in Figure A.31 the entire surface has sustained some level of damage by step 20. The author has not found a reason why this discrepancy exists in the damage and the transferred force. Because logically as soon as the entire surface has sustained some damage there is no area left for the stresses to further increase.

In the specimen with a very high shear stiffness coefficient, the progression of tensile interface damage is significantly affected. While the bottom two horizontal surfaces are not greatly influenced by the change, the top horizontal interface of the tab damages at a much slower rate than in the original specimen. This slower rate of damage can be attributed to the reduced sliding in the vertical interface, resulting in a much smaller opening at the top of the tab. Additionally, the plastic strain development, especially within the tab, progresses more rapidly than in the original case. Eventually, the plastic strain reaches a level where the material in the tab fails, leading to a different failure mechanism compared to both the original specimen and the specimen with a low shear stiffness coefficient. This outcome is likely due to the higher transferred stresses at the same sliding rate, which indicates that the shear interface transfers stresses more effectively.

When examining the shear interface damage, it becomes apparent that the outer sides of the shear interface on the tab are damaged more quickly than the central part. This damage pattern suggests a more pronounced effect of the tab's thickness on the overall performance of the interface.

A key difference between the high and low shear stiffness coefficients is the interaction between the tensile and shear interfaces. With a high shear stiffness coefficient, both interfaces are engaged simultaneously because less sliding is required for larger stresses to be transferred in the shear interface. This combined interaction allows for higher stresses to be transferred across the entire interface, enabling a tab failure to occur. As with the tensile stiffness coefficient, the shear stiffness coefficient influences how the horizontal and vertical interfaces work together. A higher shear stiffness coefficient leads to a more integrated interaction between the shear and tensile interfaces, whereas with a low shear stiffness coefficient, the behaviors of the two interfaces are more distinct and separate.

A.4. Normal contact stress ()

Description: The fourth variable in this parameter study is the maximum value for the normal contact stress. This maximum normal contact stress value defines the tensile strength of the interface. Changing the maximum normal contact stress without changing the fracture energy also influences the maximum separation of the interface as can be seen in Figure A.39. In this study values of 0.1 MPa as a low strength and 10 MPa as a high strength are used. It should be noted that for a concrete-to-concrete like interface without any adhesive the tensile strength of 10 MPa is physically not possible. However, this extreme value is chosen to ensure that the effect of a high tensile strength is clearly observable and to understand its potential impact on the interface behavior.

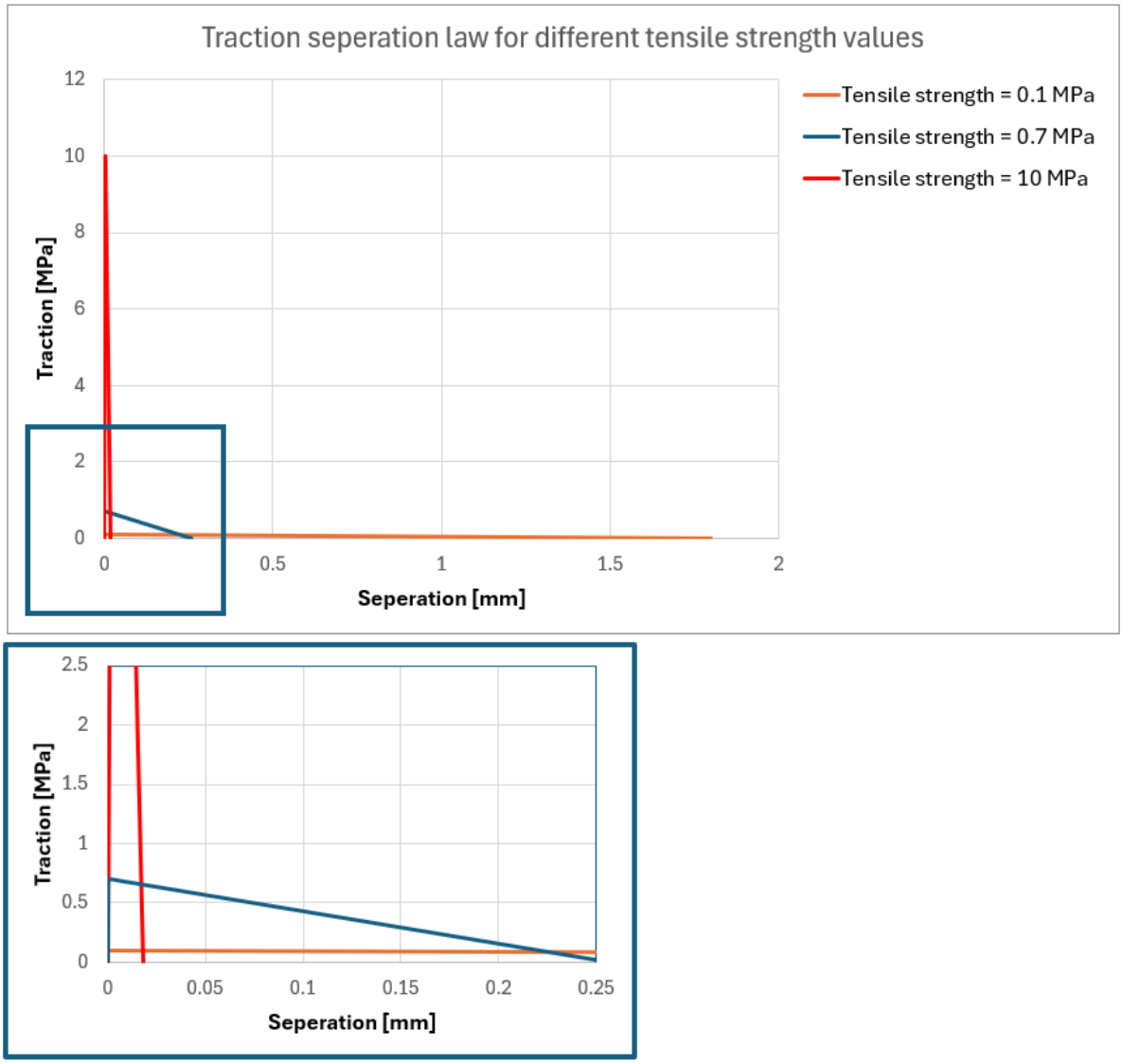

Figure A.39: Influence of the maximum normal contact stress on the traction separation law of the interface's tensile behaviour.

Result: For both the interfacial tensile strength values of 0.1 MPa and 10 MPa the results of the analysis are shown below. First the results for the tensile strength of 0.1 MPa will be discussed and then afterwards the results for the interface with a tensile strength of 10 MPa will be shown.

A.4.1. = 0.1 MPa

In Figure A.40 the force-displacement diagram of the analysis is shown, together with the locations of the different relevant steps. It can be seen that after step 32, the force remains around a value of zero.

Therefore the choice has been made that in this analysis only steps 1-32 have been analysed.

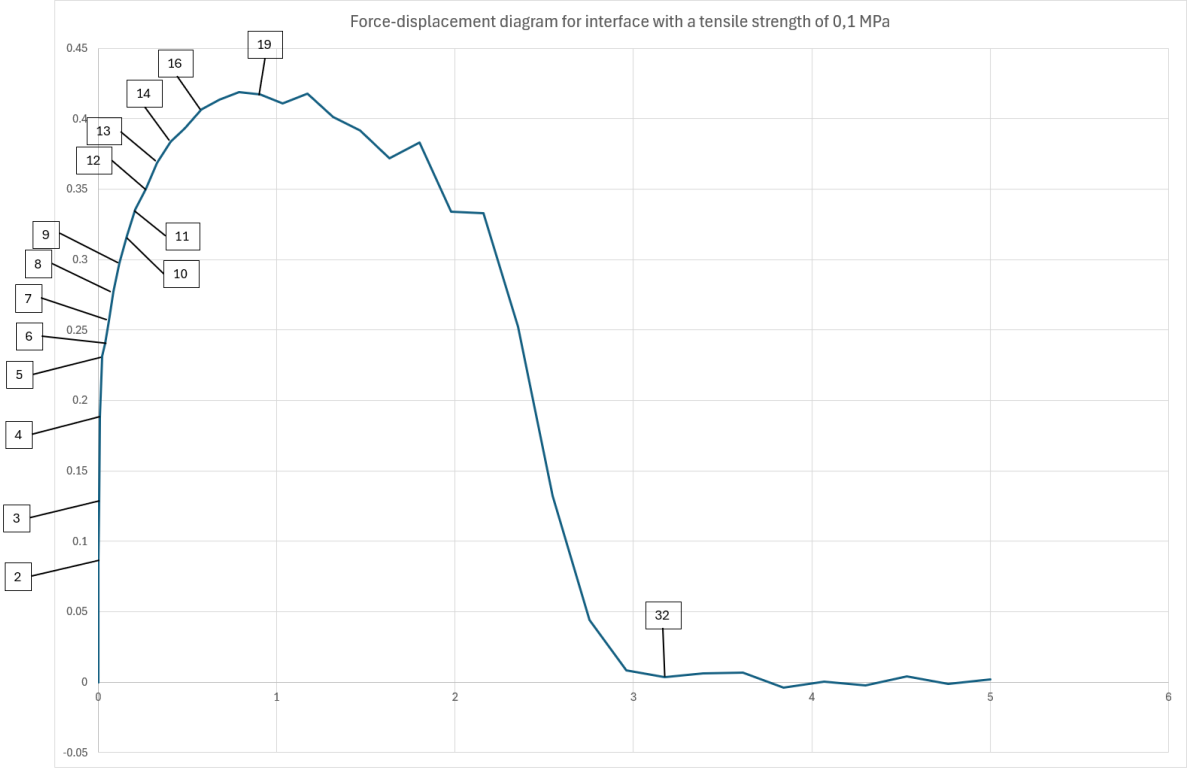

Figure A.40: Force displacement diagram of the analysis with an interface with a tensile strength of 0.1 MPa, with important steps identified for further analysis.

In Figure A.41 the plastic strain development in the specimen with an interfacial tensile strength of 0.1 MPa is shown throughout the analysis. It can be seen that only a very small part of the material around the top corners of the tab show some plastic strain. This plastic strain is very low and spans over a very small area which is almost negligible. Additionally this plastic strain starts developing only from step 16 until step 19. When looking at the force displacement graph this is exactly when the peak value of the tensile force is reached.

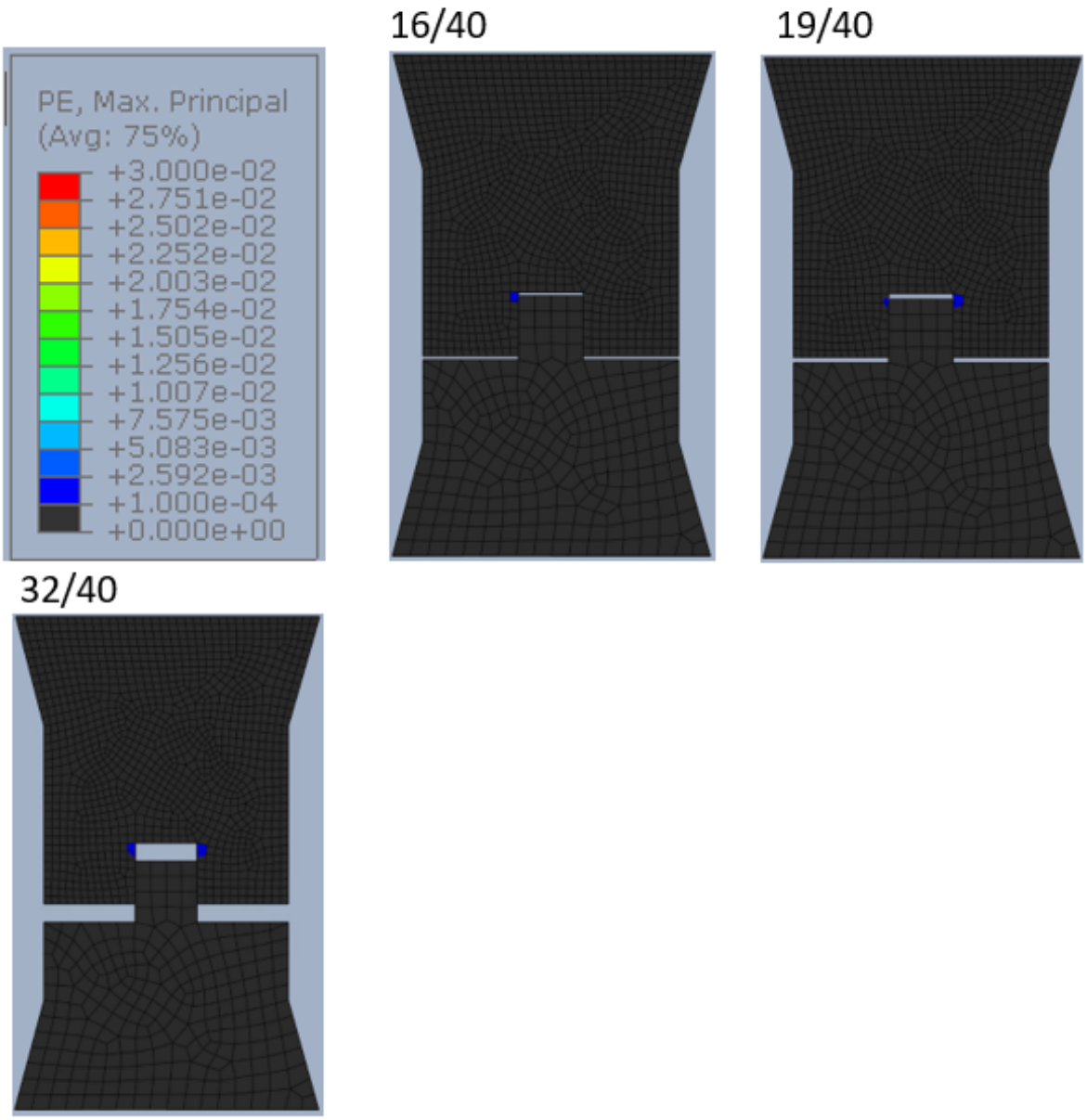

Figure A.41: Plastic strain values throughout the analysis with a color legend ranging from 0.0001 (0.01%) to 0.03 (3%).

Changing the tensile strength of the interface directly affects the tensile traction-separation law, making it essential to examine the tensile interface behavior throughout the analysis (see Figure A.42).

The progression of tensile interface damage indicates that the interface damages much more quickly than in the original case, which is expected given the reduced tensile strength. Additionally, when considering the shear interface damage (Figure A.43), the impact of the lower tensile strength becomes apparent. Compared to the original case, the shear interface damage begins much earlier—at step 4 instead of step 7. This earlier onset occurs because the shear interface must compensate for the reduced tensile strength sooner than in the original scenario. Furthermore, the overall progression of damage in the shear interface is much faster than in the original case.

There is also a notable difference in the spatial progression of interface damage. In the original specimen, damage initially occurs at the outer sides of the tab (in the depth direction) before spreading to the inner part. However, with the low tensile strength, damage begins at the inner part of the interface and only later affects the outer regions.

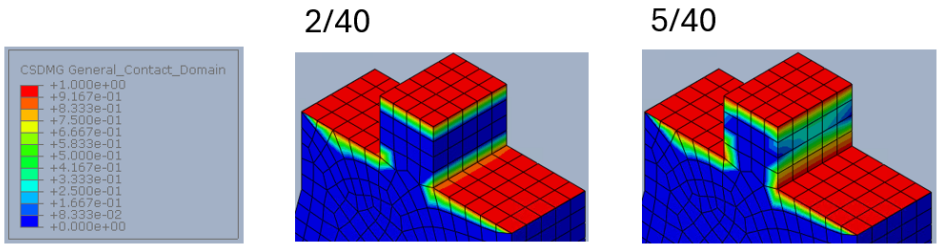

(a) Interface damage of the interface loaded in tension throughout the analysis with a color legend ranging from 0 (0%) to 1 (100%).

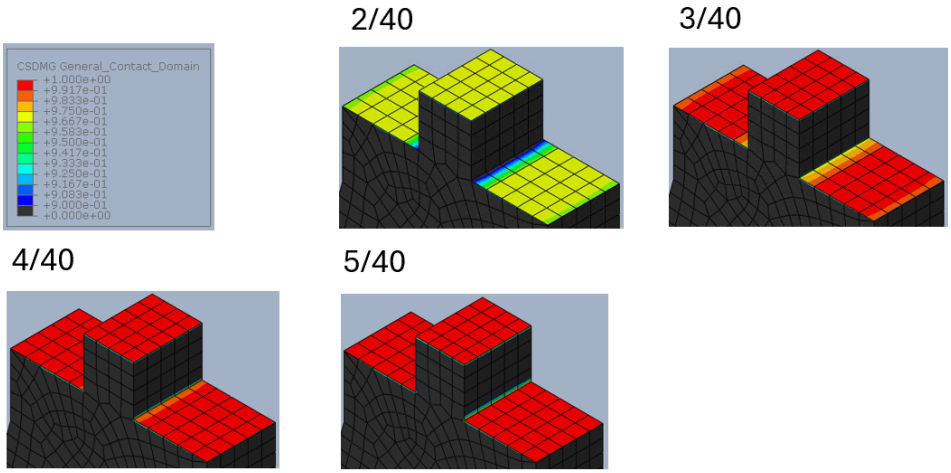

(b) Interface damage of the interface loaded in tension throughout the analysis with a color legend ranging from 0.9 (90%) to 1 (100%).

Figure A.42: Interface damage of the interface loaded in tension throughout the analysis of the specimen with a tensile strength of 0.1 MPa.

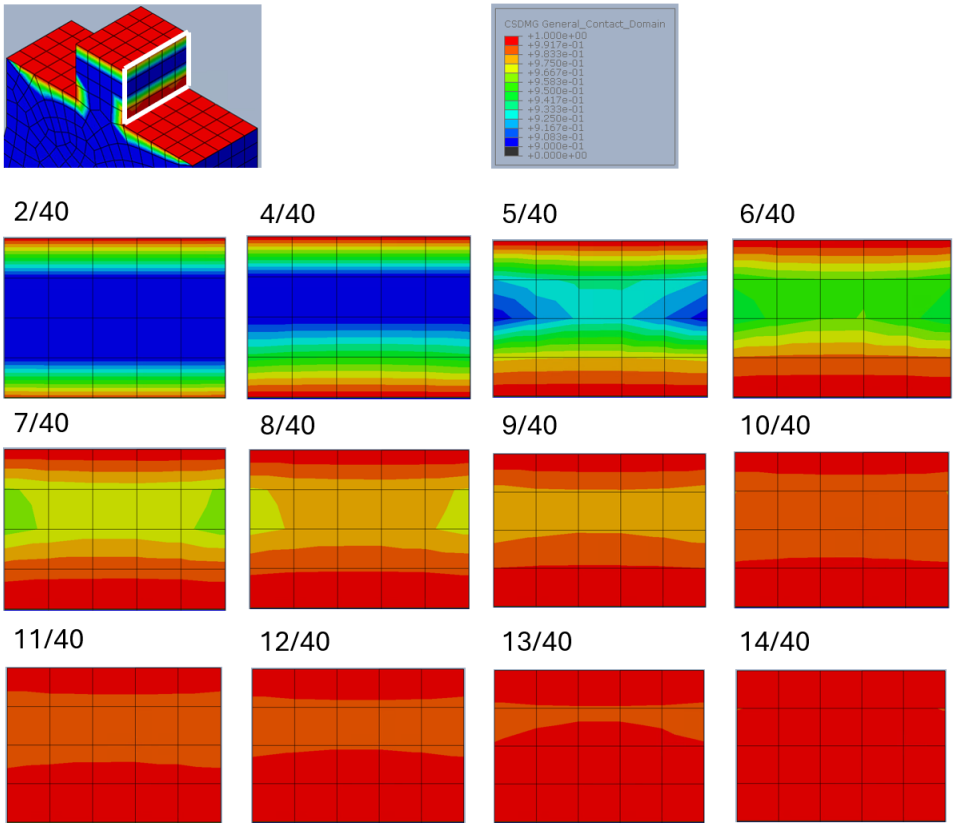

Figure A.43: Interface damage of the interface loaded in shear throughout the analysis of the specimen with a tensile strength of 0.1 MPa. Color legend ranges from 0 (0%) to 1 (100%).

A.4.2. = 10 MPa

In Figure A.44 the force-displacement diagram of the analysis is shown, together with the locations of the different relevant steps. In this analysis all 40 steps have been analysed.

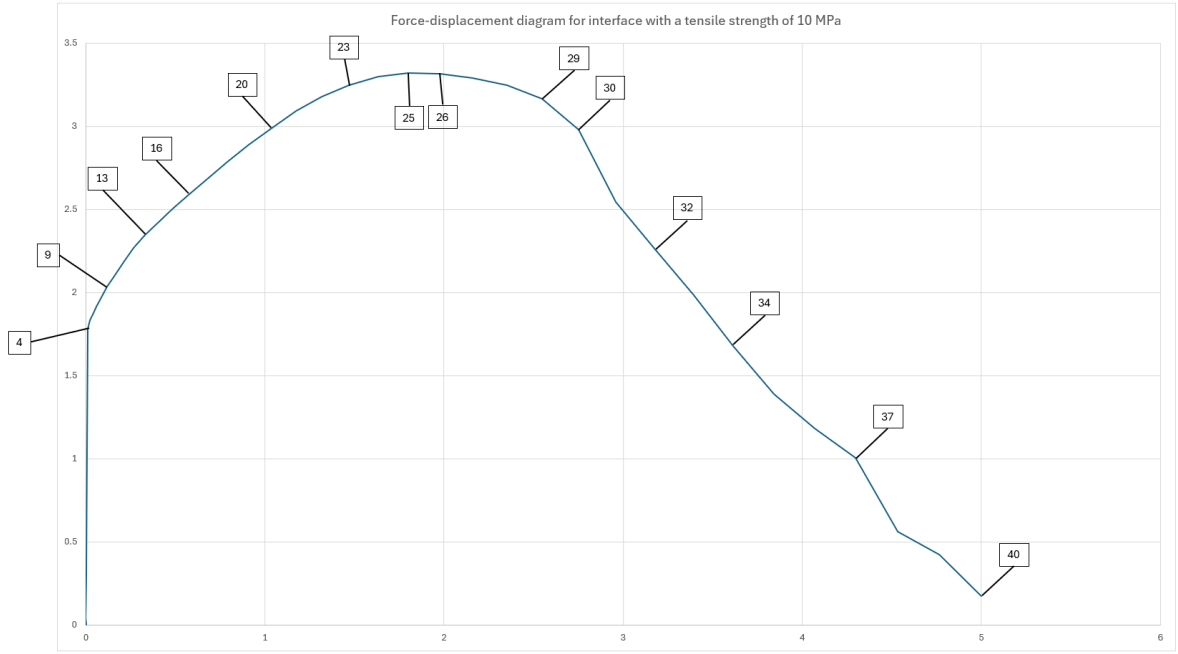

Figure A.44: Force displacement diagram of the analysis with an interface with a tensile strength of 10 MPa, with important steps identified for further analysis.

In Figure A.45, the development of plastic strain in the specimen with an interfacial tensile strength of 10 MPa is shown throughout the analysis. It is important to note that this tensile strength is higher than that of the material itself. The plastic strain begins to develop slightly earlier than in the original case and is initially distributed around the entire horizontal interface. Following this initial formation, the strain quickly spreads throughout the entire specimen, with all material regions activated by step 13.

As the analysis progresses, the plastic strain continues to increase across the specimen until around step 23, when it becomes more localized near the bottom of the interface. From step 23 onwards, the plastic strain exceeds the predefined color legend limit of 0.03 (3%). To further illustrate the material behavior, the tensile damage parameter is presented in **??**, which shows that tensile damage is predominantly concentrated around the material near the bottom horizontal interface.

To provide a comprehensive view of the damage progression, the final step (40/40) is displayed with a lower limit of 0.0001, revealing even minimal damage areas. It can be observed that almost the entire specimen, except for the lower part of the bottom section, exhibits damage. At this final step, it is also evident that the material ultimately fails in tension along the line of the bottom horizontal interface.

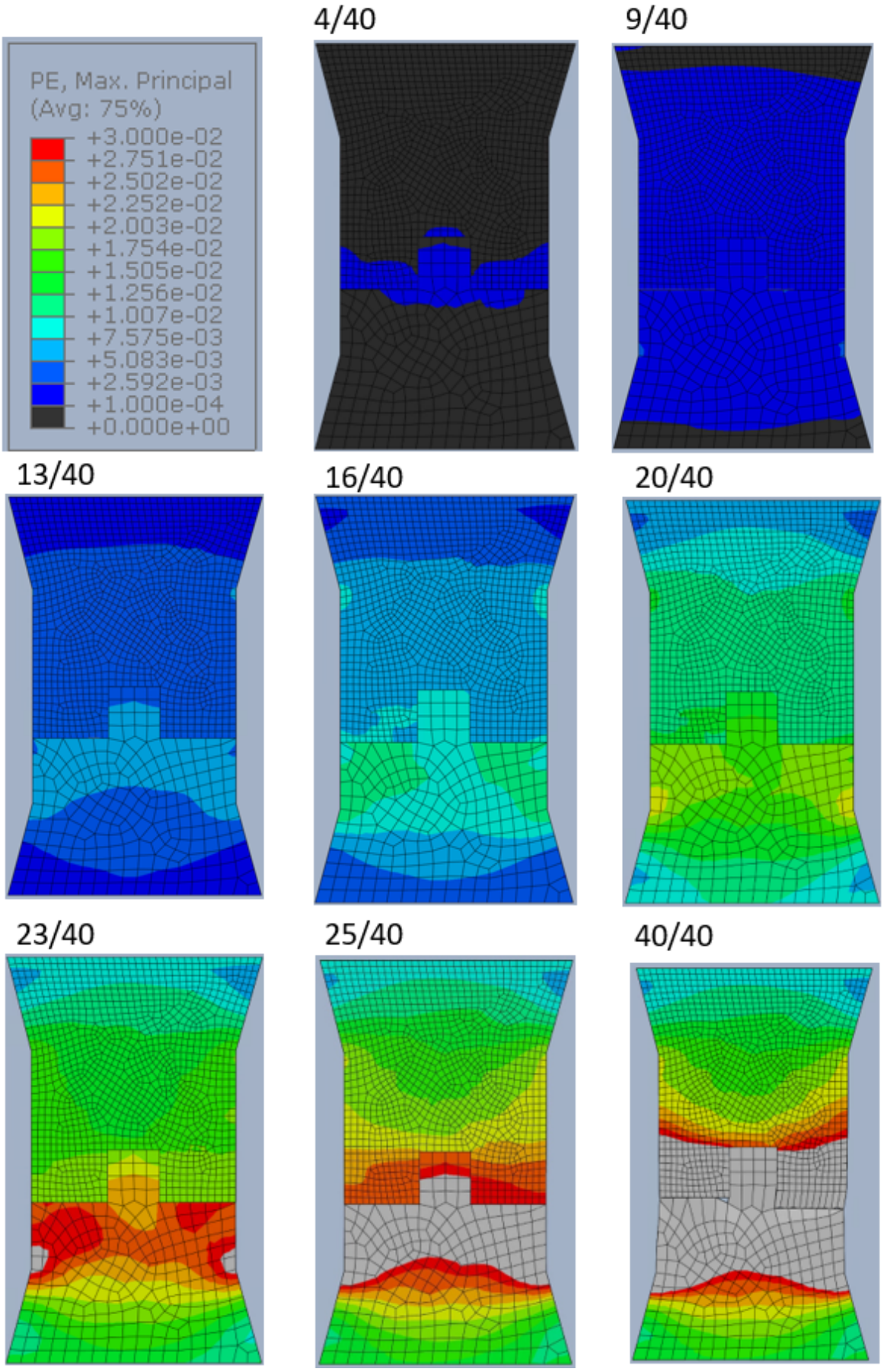

Figure A.45: Plastic strain values throughout the analysis with a color legend ranging from 0.0001 (0.01%) to 0.03 (3%).

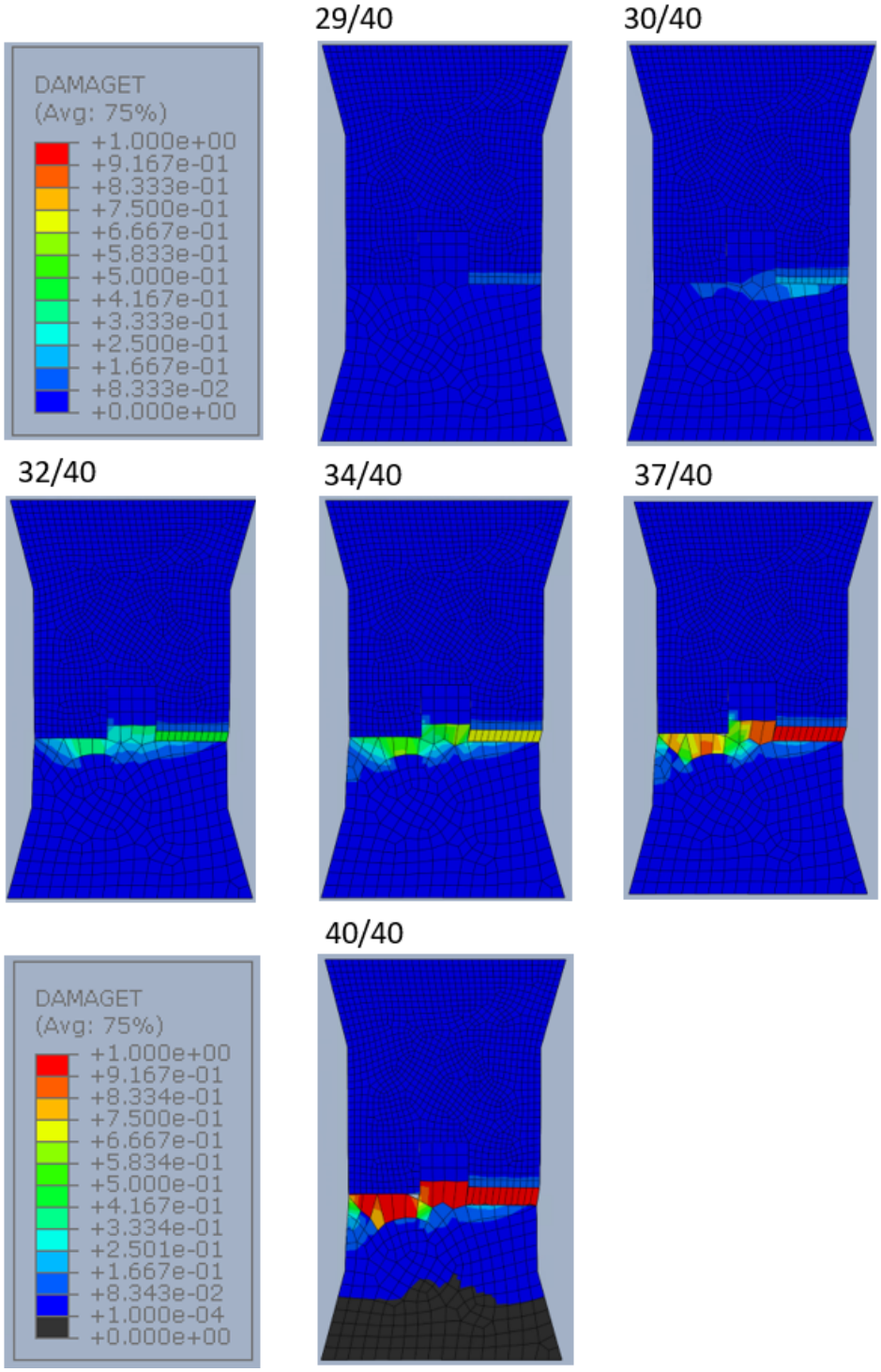

Figure A.46: Tensile damage values throughout the analysis with a color legend ranging from 0 (0%) to 1.0 (100%). Additionally for step 40 a color legend ranging from 0.0001 (0.01%) to 1.0 (100%) is used.

Observations of the tensile interface damage progression (see Figure A.47) are consistent with the patterns seen in the plastic strain and tensile damage, indicating that the specimen fails within the material itself rather than at the interface. This outcome is expected given the high interfacial tensile strength. Furthermore, the shear interface damage (see Figure A.48) shows that, due to the high tensile interface strength and the resulting lack of separation at this interface, there is minimal shear interface damage throughout the analysis, except at the top corners, likely due to localized stress

concentrations. The stiff behavior of the tensile interface prevents sufficient slip in the vertical interface, thereby inhibiting shear interface damage.

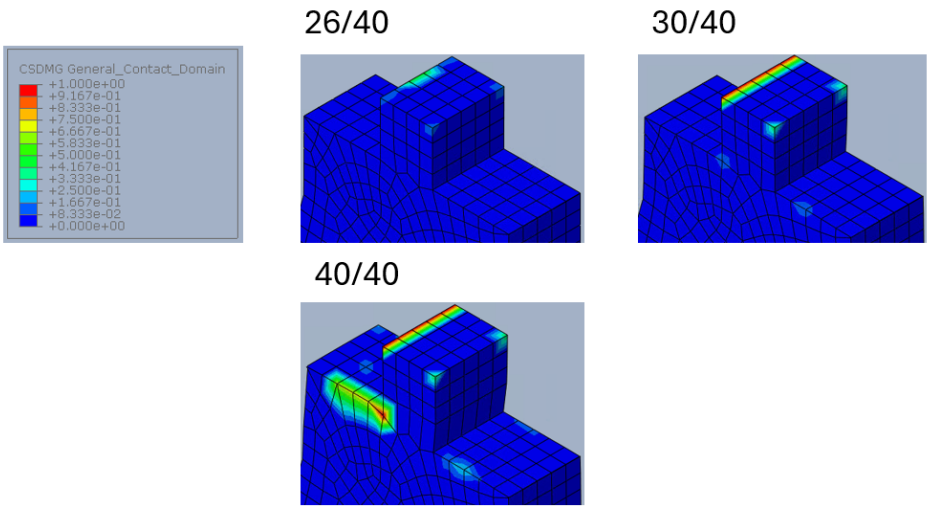

Figure A.47: Interface damage of the interface loaded in tension throughout the analysis of the specimen with a tensile strength of 10 MPa. with a color legend ranging from 0.9 (90%) to 1 (100%).

Figure A.48: Interface damage of the interface loaded in shear throughout the analysis of the specimen with a tensile strength of 10 MPa. Color legend ranges from 0 (0%) to 1 (100%).

Lastly, the influence of the different values for the friction coefficients on the force-displacement behaviour is presented in Figure A.49. Additionally the same data is also presented as a stress-displacement diagram in Figure A.50

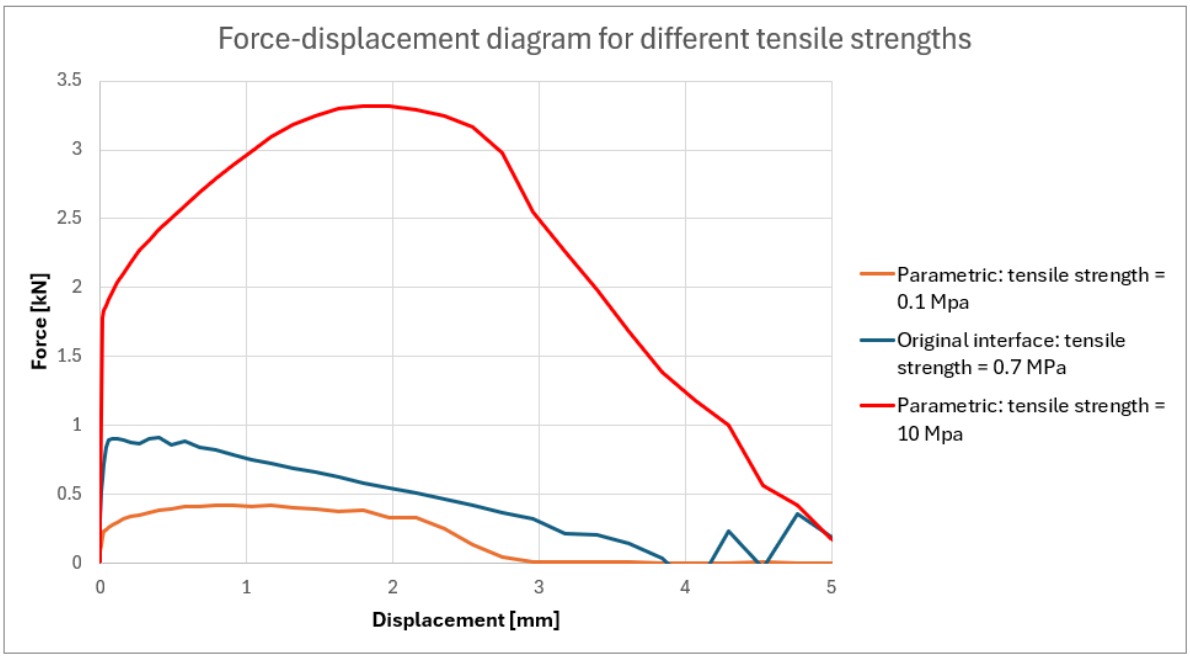

Figure A.49: Influence of the low and high values of the interfacial tensile strength on the force-displacement behaviour of the connection.

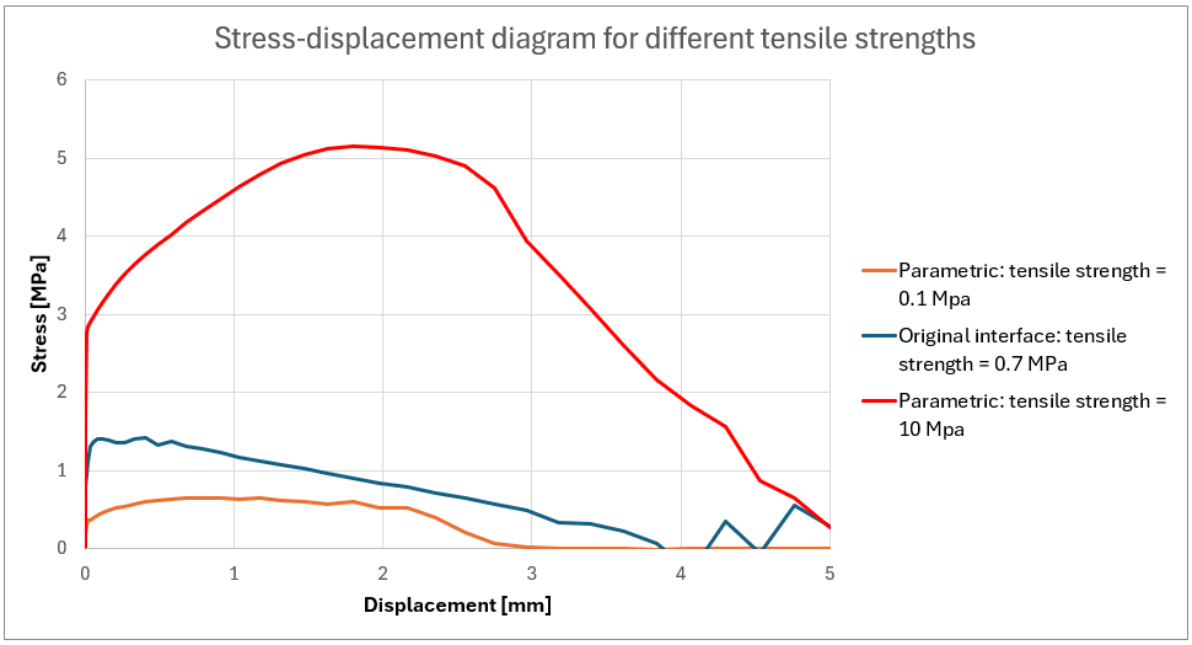

Figure A.50: Influence of the low and high values of the interfacial tensile strength on the stress-displacement behaviour of the connection.

A.4.3. Discussion

The influence of varying the maximum normal contact stress (tensile strength) on the interface behavior and failure mechanisms provides critical insights into the performance and structural integrity of the specimen.

The analysis of the specimen with an interfacial tensile strength of 0.1 MPa reveals significant differences in behavior compared to the original case. The plastic strain development indicates minimal

strain localized around the top corners of the tab, which is both small in magnitude and spatial extent. This suggests that a tensile strength of 0.1 MPa is insufficient to induce cracking in the tab. Additionally, it reveals that the current settings for the shear interface in the vertical surfaces alone are inadequate to cause cracking in the tab.

The progression of tensile interface damage is much more rapid compared to the original case, as expected due to the lower tensile strength. The interface damages quickly and does not contribute significantly to load-bearing capacity beyond the initial steps. This observation is further supported by the earlier onset of shear interface damage, which begins at step 4, in contrast to step 7 in the original case. The earlier damage in the shear interface is due to the rapid failure of the tensile interface, which forces the shear interface to take over the stress transfer prematurely. The shear interface damage then continues to progress throughout the entire analysis, ultimately leading to a pull-out failure mechanism, where the specimen is pulled out without cracking of the tab.

Additionally, the spatial progression of shear interface damage differs markedly from the original case. While the original specimen shows damage beginning at the outer sides of the tab (in the depth direction), in this case with lower tensile strength, damage initiates at the inner part of the interface and only later affects the outer regions.

Conversely, with a high tensile strength of 10 MPa, plastic strain is observed throughout the specimen, indicating substantial cracking. The failure mechanism is characterized by a clear crack propagating through the middle of the specimen around the interface but within the material itself. This is corroborated by the stress-displacement graph, which aligns very closely with the material behavior of the SHCC. For the high tensile strength condition, the interface does not significantly interfere with the specimen's behavior, effectively allowing the material properties to dominate the response. This suggests that the high tensile strength is sufficient to prevent interface failure, leading instead to material failure, which occurs internally rather than along the interface.

These observations highlight the crucial role of tensile strength in dictating the failure mechanisms and overall structural response of the specimen. Low tensile strength results in a significantly lower peak force, minimal to no material activation (plastic strain development) and a pull-out failure mechanism dominated by the shear interface after initial horizontal interface failure. In contrast, high tensile strength leads to material failure with extensive cracking and behavior governed by the material properties rather than the interface.

A.5. Shear contact stress (and)

Description: The fifth variable in this parameter study is the maximum value for the shear contact stress, where in this study no differentiation is made between the 1st and 2nd direction. This maximum shear contact stress defines the shear strength of the interface. Changing this maximum shear contact stress without changing the fracture energy, also influences the maximum separation of the interface, similarly as with the maximum normal contact stress. In this study the values of 0.5 MPa and 50 MPa are used as a low and high value of the maximum shear contact stress respectively. It should be noted that for a concrete-to-concrete-like interface without any adhesive a shear strength of 50 MPa is physically not possible. However, this extreme value is chosen to ensure that the effect of a high shear strength is clearly observable and to understand its potential impact on the interface behaviour.

For the value of 50 MPa, not changing the fracture energy leads to a physically impossible traction separation law (the displacement drops back to 0.2 mm after the maximum stress has been reached at a displacement of 1 mm), therefore there the fracture energy has been increased to 25 N/mm (see Figure A.51). The traction separation laws used for the different values of the maximum shear contact stress are presented in Figure A.52.

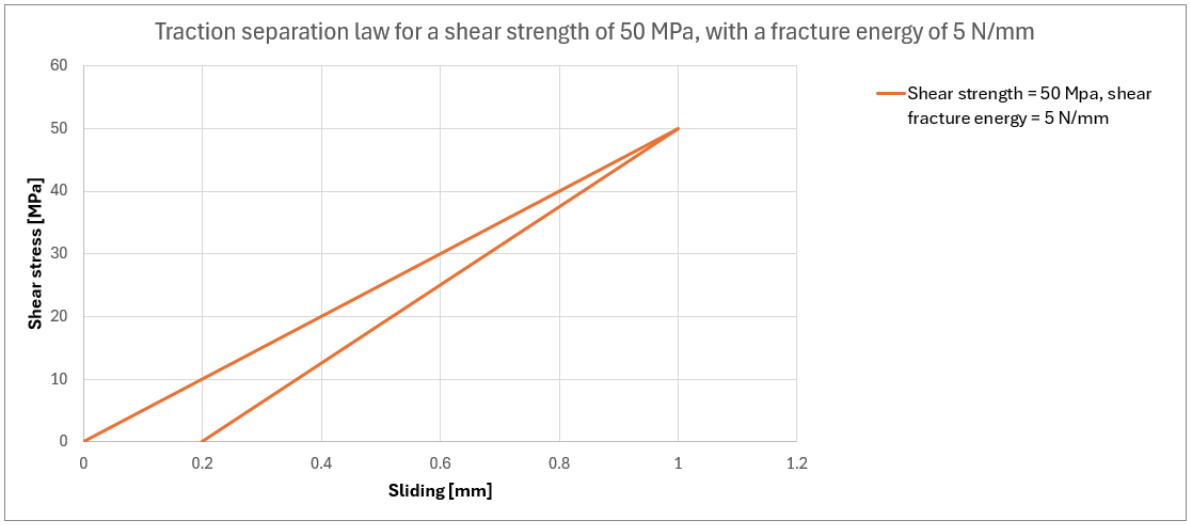

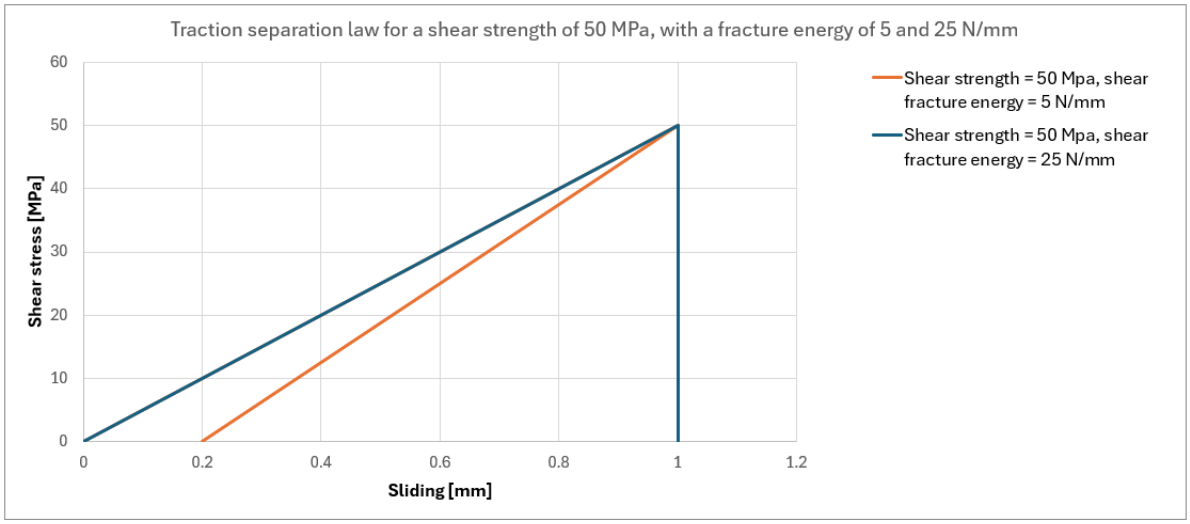

Figure A.51: Traction separation for a maximum shear contact stress of 50 MPa with a fracture energy of 5 N/mm and 25 N/mm.

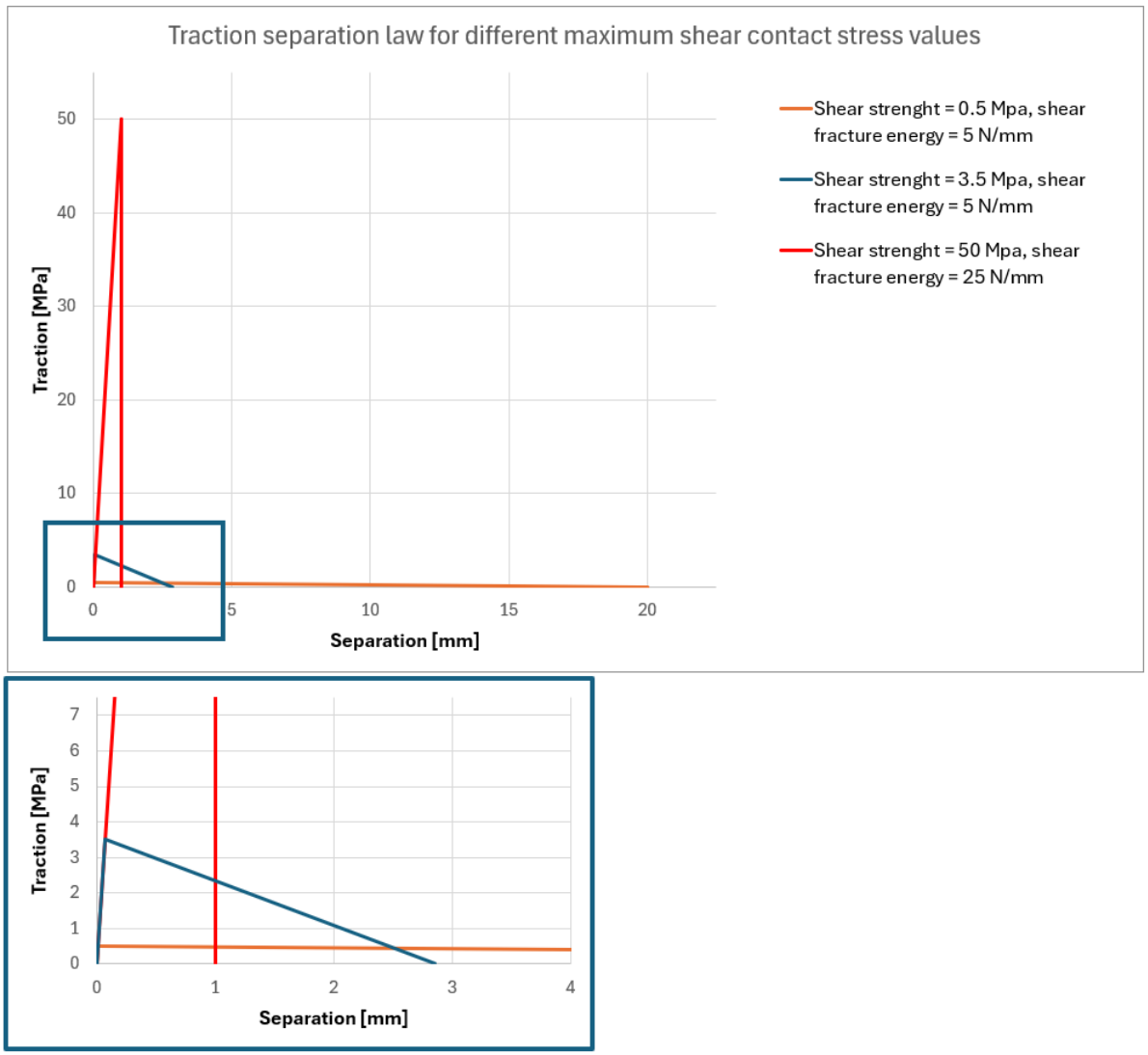

Figure A.52: Influence of the maximum shear contact stress on the traction separation law of the interface's shear behaviour.

Result: For both the interfacial shear strength values of 0.5 MPa and 50 MPa the results are shown below. First the results for the shear strength of 0.5 MPa will be discussed and then afterwards the results for the interface with a shear strength of 50 MPa.

A.5.1. / = 0.5 MPa

In Figure A.53 the force-displacement diagram of the analysis is shown, together with the locations of the different relevant steps. In the analysis all steps up until step 40 have been analysed.

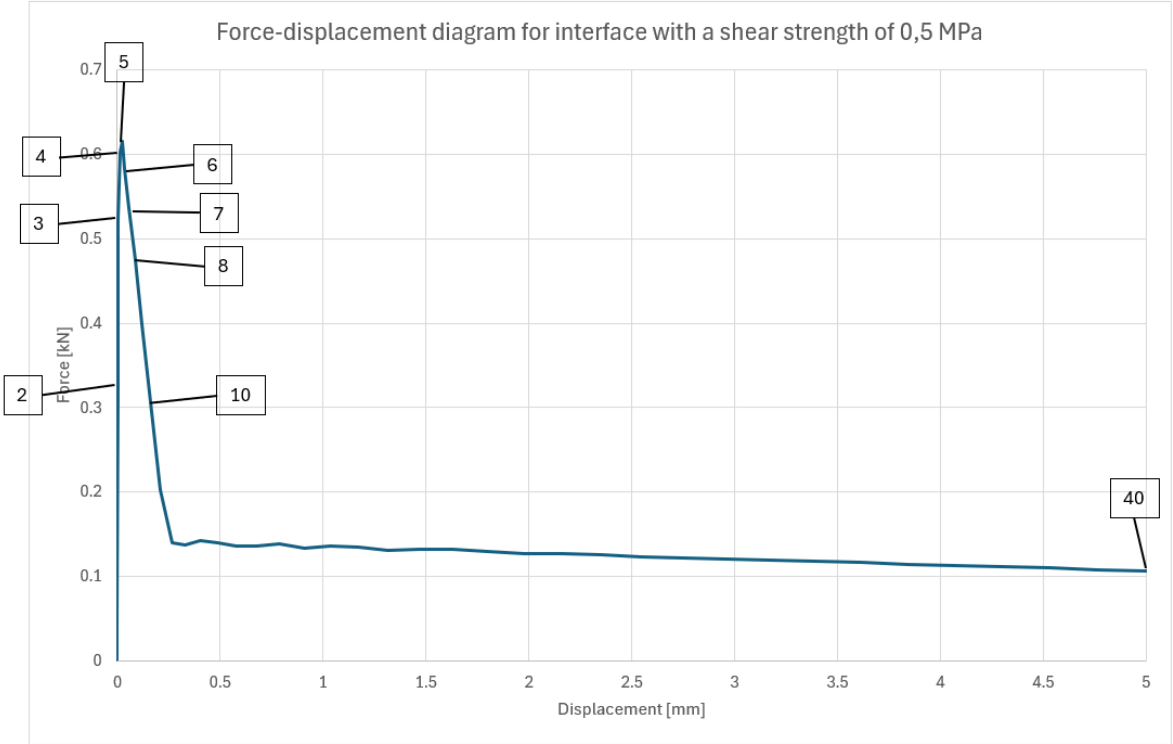

Figure A.53: Force displacement diagram of the analysis with an interface with a shear strength of 0.5 MPa, with important steps identified for further analysis.

In Figure A.54 the plastic strain in the specimen with an interfacial shear strength of 0.5 MPa is shown. It can be seen that in the entire specimen, no plastic strain above 0.0001 (0.01%) develops.

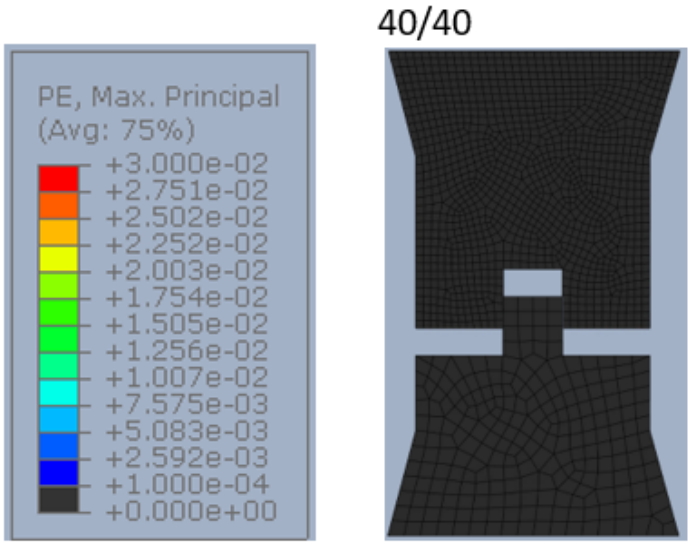

Figure A.54: Plastic strain values throughout the analysis with a color legend ranging from 0.0001 (0.01%) to 0.03 (3%).

The development of tensile interface damage for the case with a shear strength of 0.5 MPa shows no significant difference compared to the original interface behavior. However, the progression of damage in the vertical shear interface, as shown in Figure A.55, reveals key distinctions. Notably, the shear interface damage begins to significantly increase at step 5, which coincides with the point at which the

peak force is reached. This earlier onset, compared to both the original and lower shear strength cases, is followed by a much faster progression of shear interface damage.

In the force-displacement curve presented in Figure A.53, after the initial peak and subsequent drop in force, the force stabilizes around 0.15 kN and gradually declines. This residual force can primarily be attributed to the shallow post-peak behavior of the shear-sliding law governing the shear interface, which extends up to a displacement of 20 mm. The gradual slope of this curve implies that the shear interface is not fully damaged until the sliding displacement reaches 20 mm. As shown in Figure A.56, the shear interface is still not completely damaged by the end of the analysis.

It is unlikely that any remaining resistance is due to friction within the interface. This conclusion is supported by examining the x-direction deformation of the specimen at step 40/40, which is magnified by a factor of 1000 in Figure A.57. The figure shows that the surfaces of the interface are not in contact, indicating a small degree of separation in the x-direction. This separation prevents any compressive normal forces from developing across the interface, thereby eliminating the possibility of frictional stresses contributing to the remaining resistance.

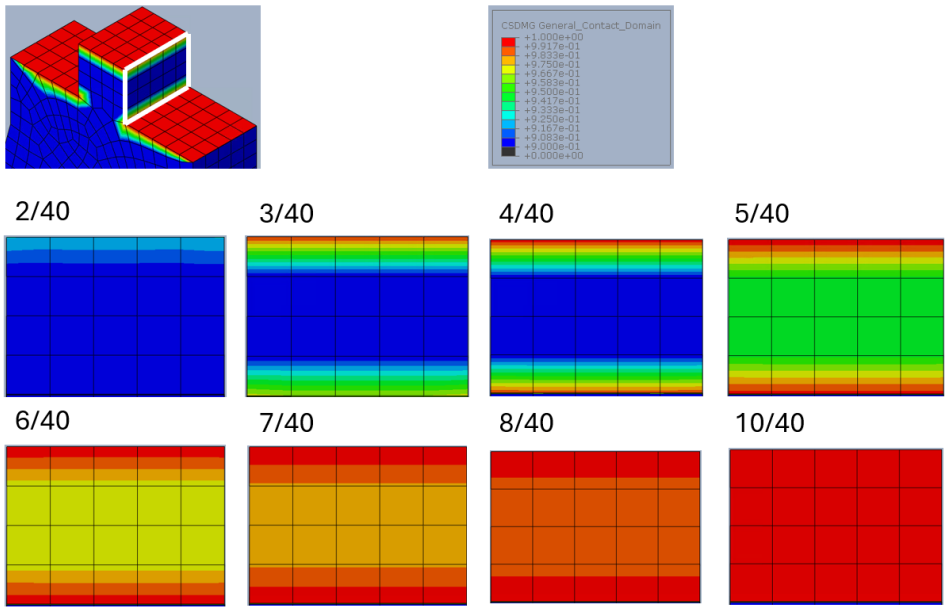

Figure A.55: Interface damage of the interface loaded in shear throughout the analysis of the specimen with a shear strength of 0.5 MPa. Color legend ranges from 0 (0%) to 1 (100%).

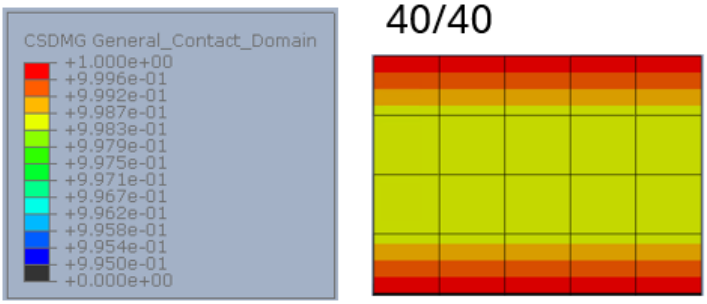

Figure A.56: Interface damage of the interface loaded in shear at step 40/40 of the analysis of the specimen with a shear strength of 0.5 MPa. Color legend ranges from 0.995 (99.5%) to 1 (100%).

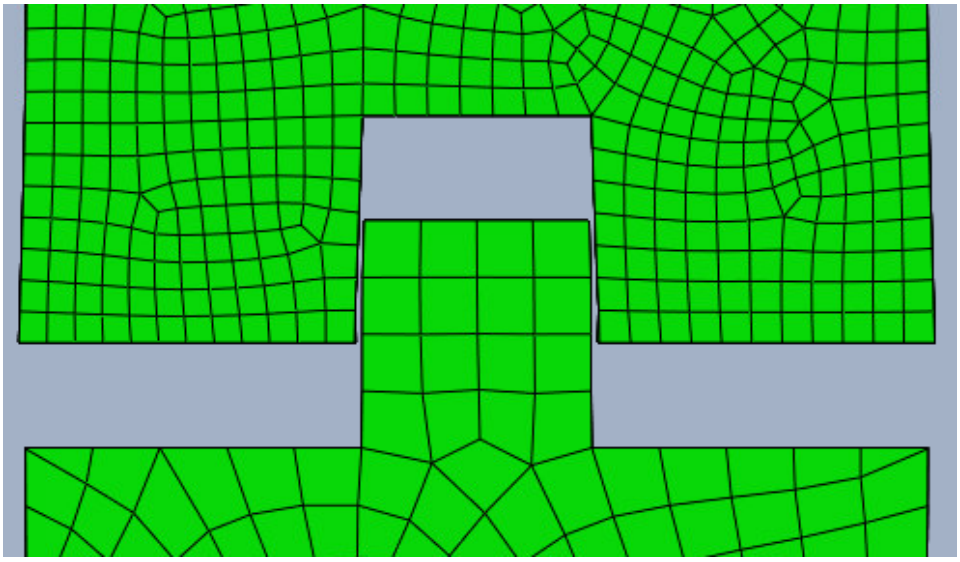

Figure A.57: Deformed shape of the SCG2 specimen with a interfacial shear strength of 0.5 MPa with the deformation in x-direction amplified by a factor 1000 at step 40/40.

A.5.2. / = 50 MPa

In Figure A.58, the force-displacement diagram for the analysis is shown, along with the locations of the key steps. After step 30, the force stabilizes around zero and starts to become numerically unstable towards the end. Consequently, the analysis has been limited to steps 1-30 to ensure accuracy and stability.

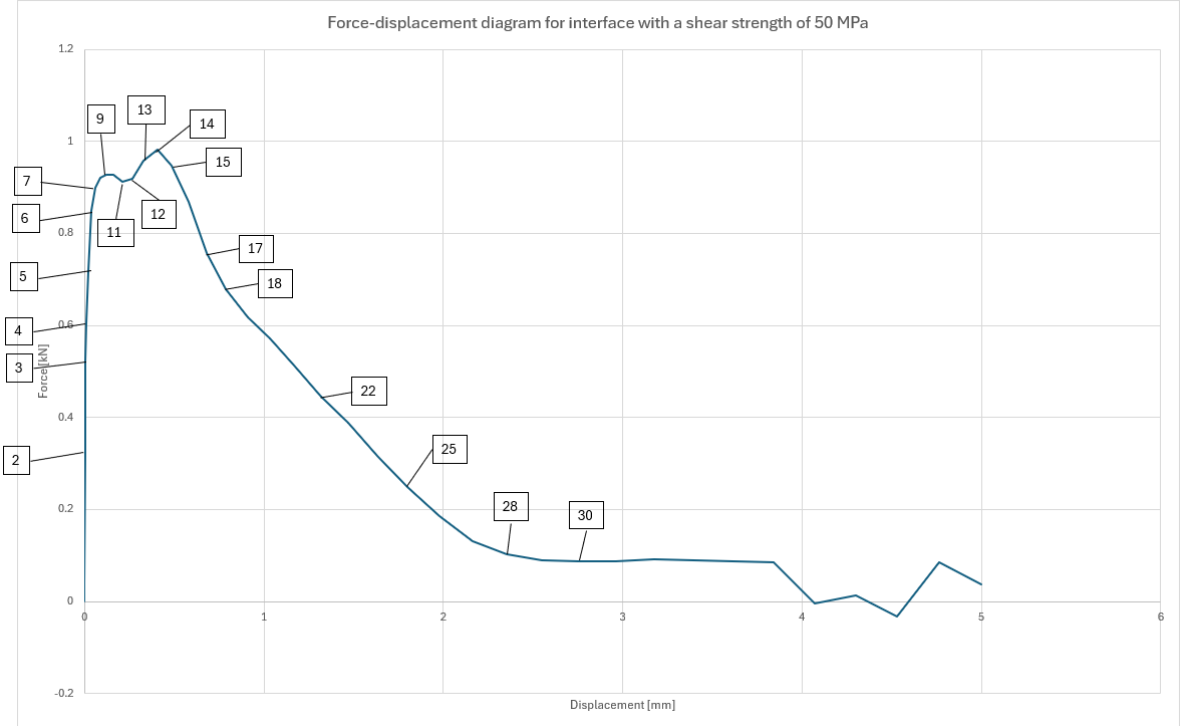

Figure A.58: Force displacement diagram of the analysis with an interface with a shear strength of 50 MPa, with important steps identified for further analysis.

The plastic strain development throughout the analysis, as shown in Figure A.59, reveals that up

until step 12, the strain evolution in the specimen with an interfacial shear strength of 50 MPa closely follows the behavior seen in the original case. However, after step 12, the plastic strain in the high shear strength specimen progresses more rapidly. Unlike in the original case, where plastic strain stabilizes after step 16, in this case, the strain continues to increase until the end of the analysis. From step 15 onwards, the plastic strain at the bottom of the tab exceeds the predefined color limit of 0.03 (3%), indicating significant material deformation.

To further understand the material behavior, the tensile damage parameter is presented in Figure A.60. This shows that tensile damage is primarily localized at the bottom of the tab, where material failure occurs, demonstrating a tab failure mechanism. It's important to note that tensile damage is derived from the material's single-crack behavior and remains zero until additional crack opening causes a reduction, rather than an increase, in stress values.

For a more comprehensive view of the damage distribution, the final step (30/40) is displayed with a lower limit of 0.0001, which highlights even the smallest damaged regions. These areas are mainly located around the top corners of the tab and in the material adjacent to the sides of the tab.

During the analysis, it is observed that the top part of the specimen moves to the right in the x-direction relative to the bottom part. This displacement behavior is consistent with findings later in the parametric study, particularly in specimens where the interface has a very high shear fracture energy. The occurrence of this phenomenon seems to be a defining characteristic in cases where the shear capacity of the vertical surfaces is exceptionally high. However, it remains unclear whether this behavior is a physically significant result or a consequence of numerical instabilities.

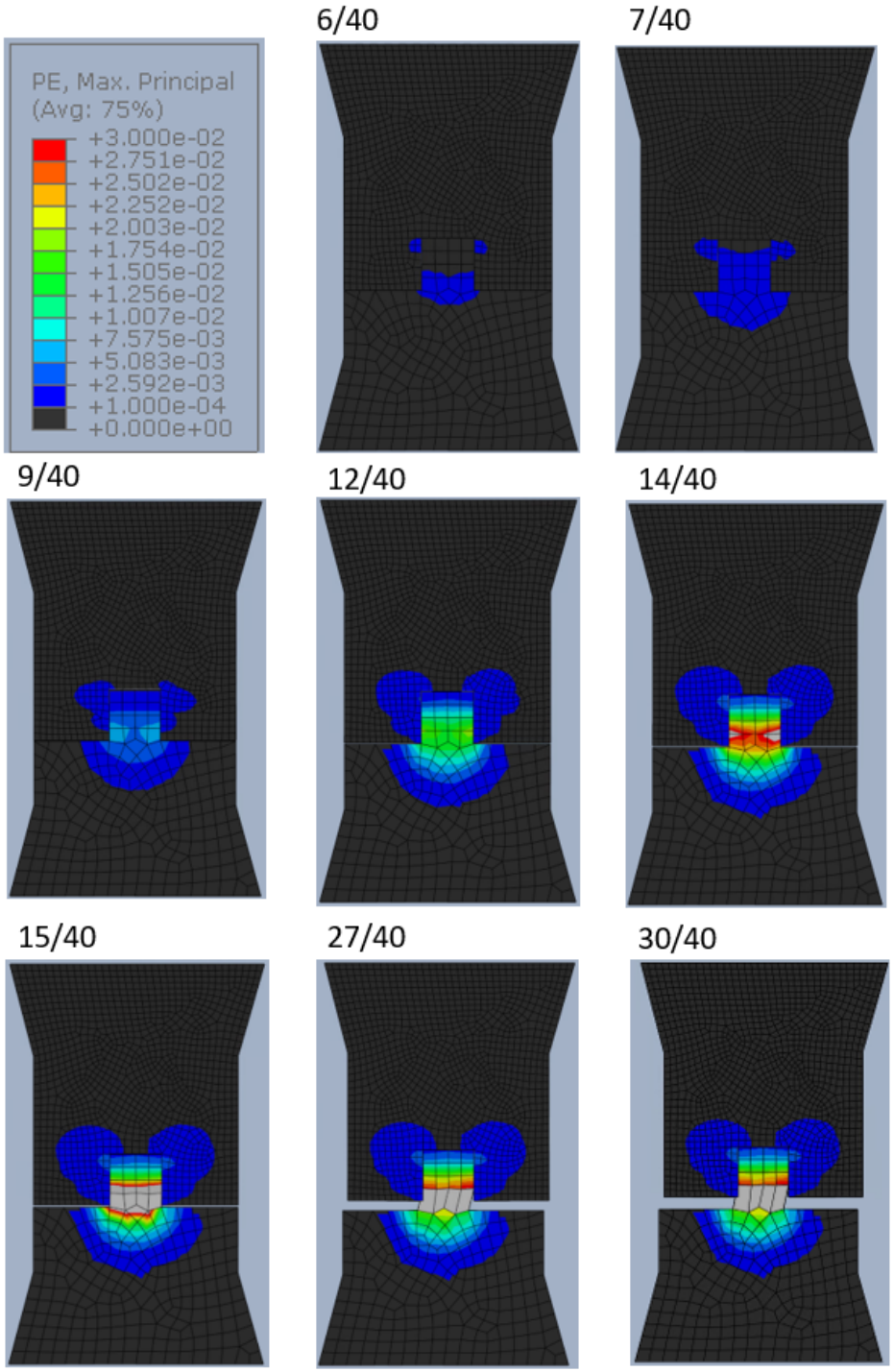

Figure A.59: Plastic strain values throughout the analysis with a color legend ranging from 0.0001 (0.01%) to 0.03 (3%).

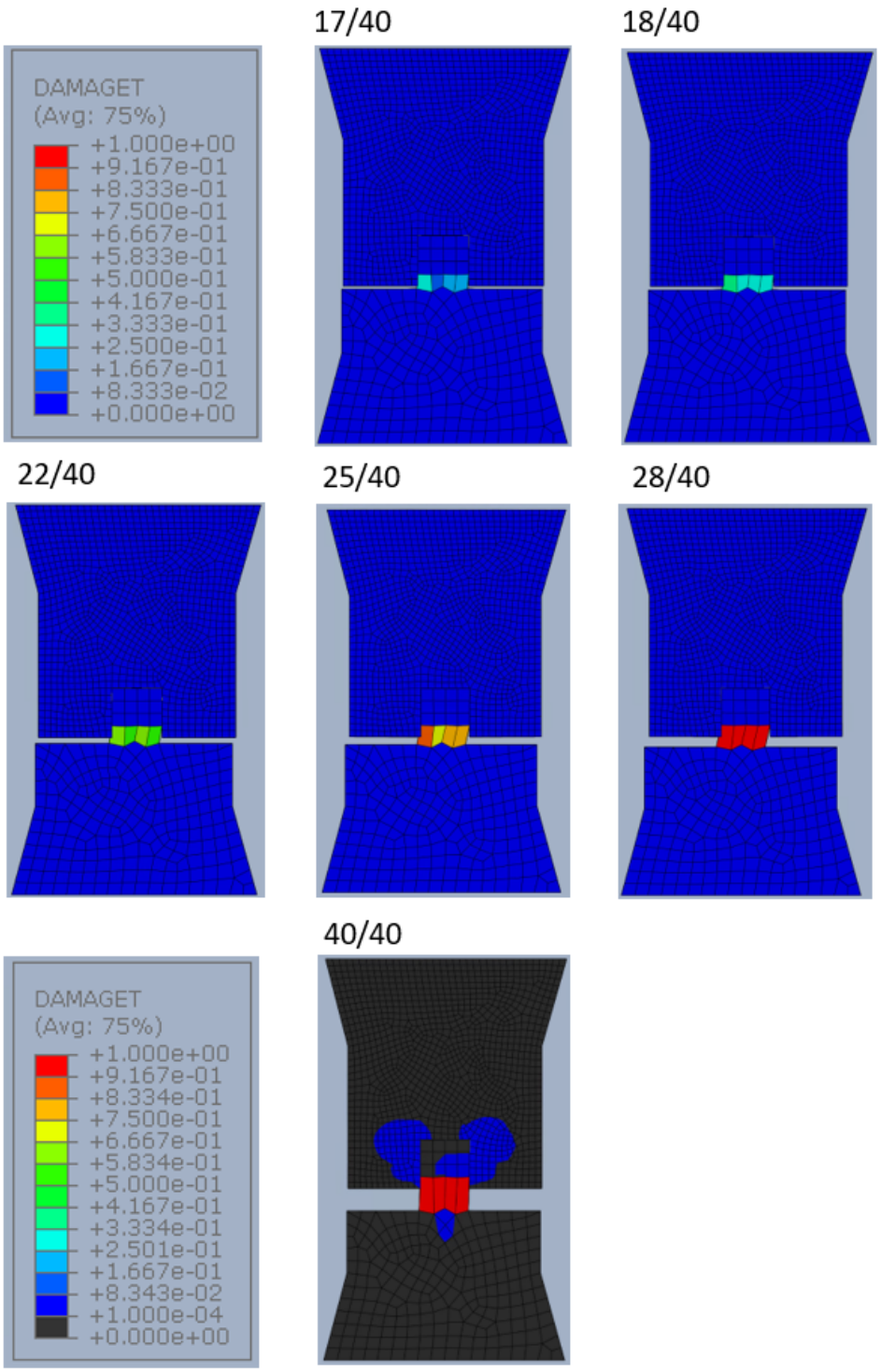

Figure A.60: Tensile damage values throughout the analysis with a color legend ranging from 0 (0%) to 1.0 (100%). Additionally for step 30 a color legend ranging from 0.0001 (0.01%) to 1.0 (100%) is used.

The development of tensile interface damage for the case with a shear strength of 50 MPa shows no significant deviation from the behavior observed in the original interface. However, the progression of damage in the vertical shear interface, as depicted in Figure A.61, reveals notable differences. Up to step 10, the shear interface damage evolves similarly to the original case. However, after step 10, the divergence becomes evident.

In the original case, the shear interface damage continues to increase steadily throughout the anal-

ysis, ultimately leading to a full pull-out failure mechanism. By contrast, in the case with an interfacial shear strength of 50 MPa, the shear interface damage progresses much more slowly after step 10. Beyond step 14, the damage ceases to increase, indicating that the failure mechanism shifts from pull-out to a tab failure. This slower progression and eventual stabilization of shear interface damage reflect the impact of the higher shear strength, which resists further damage and contributes to a different failure mode compared to the original interface.

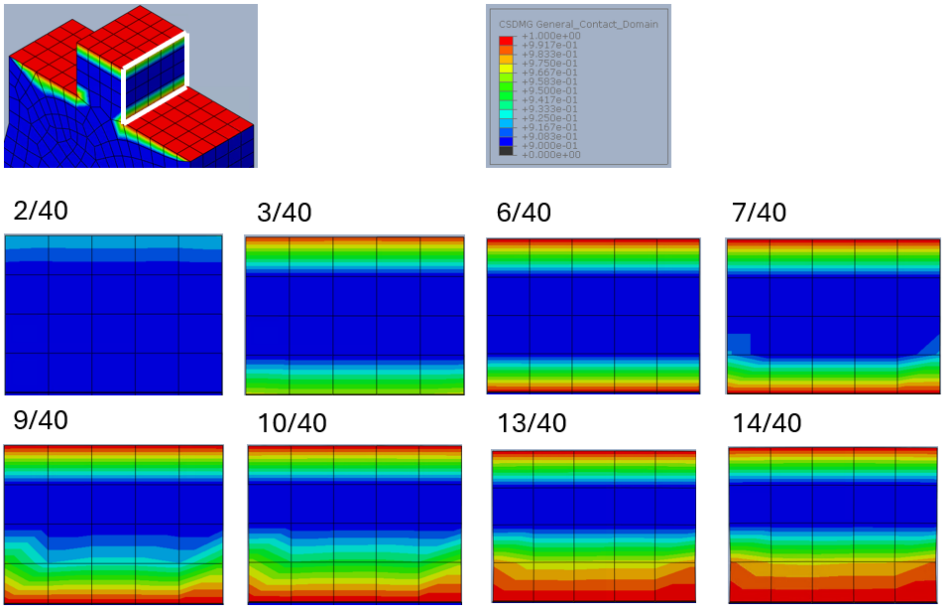

Figure A.61: Interface damage of the interface loaded in shear throughout the analysis of the specimen with a shear strength of 50 MPa. Color legend ranges from 0 (0%) to 1 (100%).

Lastly, the influence of the different values for the interfacial shear strength on the force-displacement behaviour is presented in Figure A.62. Additionally the same data is also presented as a stress-displacement diagram in Figure A.63.

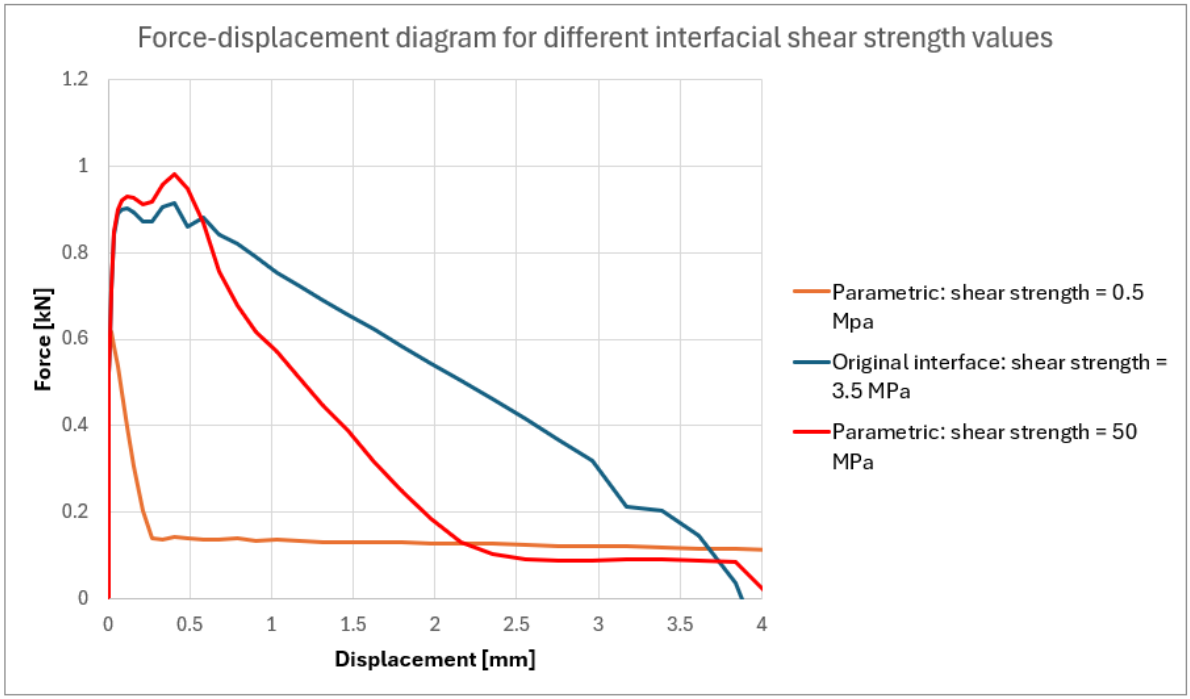

Figure A.62: Influence of the low and high values of interfacial shear strength on the force-displacement behaviour of the connection.

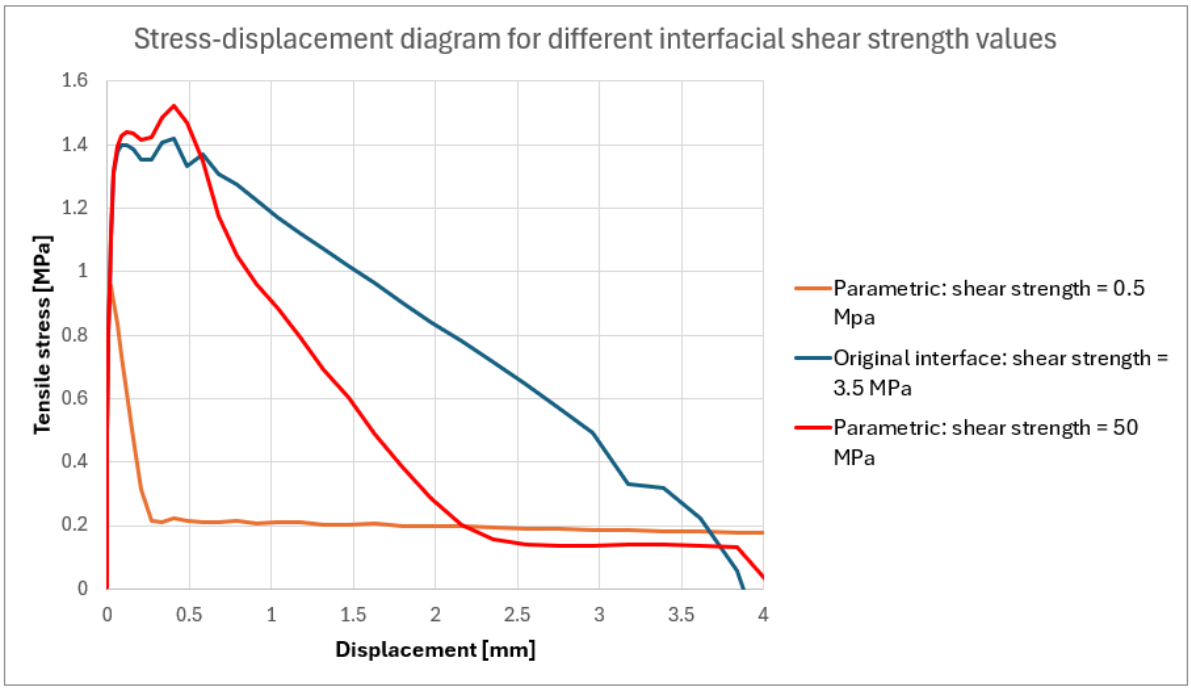

Figure A.63: Influence of the low and high values of interfacial shear strength on the tensile stress-displacement behaviour of the connection.

A.5.3. Discussion

Changes in shear strength do not significantly affect the tensile interface behavior of the specimen. Additionally it can be seen from the force-displacement diagrams, that variations in shear strength have little impact on the force-displacement behavior during the first four steps of the analysis. A zoomed-in

view of the force-displacement diagram for the first 0.2 mm of displacement, presented in Figure A.64, supports this observation.

It can be seen that, in the case of a shear strength of 0.5 MPa, the interface behavior is predominantly governed by the tensile interface capacity. Up until step 4, there is no shear interface damage, whether in the low, original, or high shear strength cases. This does not imply that shear strength is irrelevant in the initial interface behavior. Rather, in the case of a shear strength of 0.5 MPa, this value is just sufficient to contribute during the early stages of analysis. However, after step 4, the shear interface damages rapidly, making the influence of shear strength negligible as the analysis progresses.

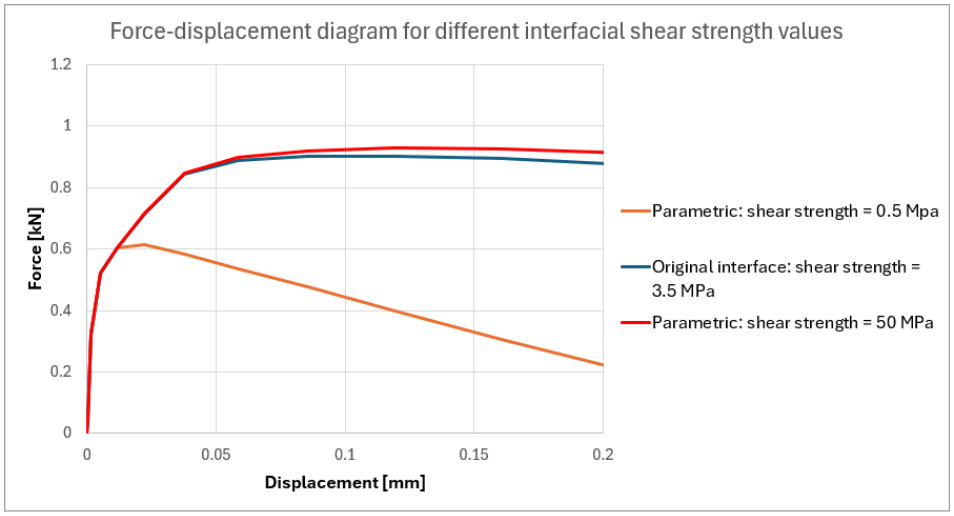

Figure A.64: Force-displacement diagram for different interfacial shear strengths, zoomed in on the first 0.2mm of displacement.

In the case of low shear strength, no plastic strain above 0.0001 (0.01%) is observed. This indicates that the tensile capacity of the interface, under these conditions, is insufficient to induce cracking in the tab without substantial shear contribution from the vertical surfaces. Additionally, for very low shear strength values, separation between the vertical surfaces occurs, eliminating any potential contribution from friction. This further reduces the interface's ability to transfer load effectively.

In contrast, when the interfacial shear strength is high, the progression of shear interface damage remains similar to the original case up to step 10, corresponding to the first peak in the force-displacement graph. Similarly, the plastic strain development mirrors that of the original case until step 12, just before the second peak begins to form. This, combined with the zoomed-in view of the force-displacement diagram in Figure A.64, suggests that during the initial stages of the analysis, up until the first peak, increasing the shear strength beyond the original value of 3.5 MPa does not significantly affect the connection's behavior.

However, after this initial peak, the results—interfacial damage behavior, plastic strain progression, and the force-displacement graph—indicate that a higher shear strength leads to a tab failure mechanism. The shear force developed within the vertical interface exceeds the force required to damage the material in the tab, resulting in a different failure mode.

In the case of the high shear strength value, it is observed that the top part of the specimen moves to the right in the x-direction relative to the bottom part. This displacement behavior is consistent with findings later in the parametric study, particularly in specimens where the interface has a very high shear fracture energy. This phenomenon appears to be characteristic of cases where the shear capacity of the vertical surfaces is significantly high, influencing the overall deformation pattern of the specimen.

A.6. Normal Fracture Energy

Description: The sixth variable in this parameter study is the value for the normal fracture energy, defined in Abaqus as the total area under the traction-separation curve of the interface's normal behaviour. The value of this energy is defined by the energy that is dissipated as a result of the damage process. Changing this value changes traction separation law by changing the maximum separation of the interface in tension. In this study only a higher value for the fracture energy has been studies, due to the already very low value for the normal fracture energy which is used in the original interface. This higher value for the fracture energy has a value of 10 N/mm. The effect of this change on the traction separation law is presented in Figure A.65.

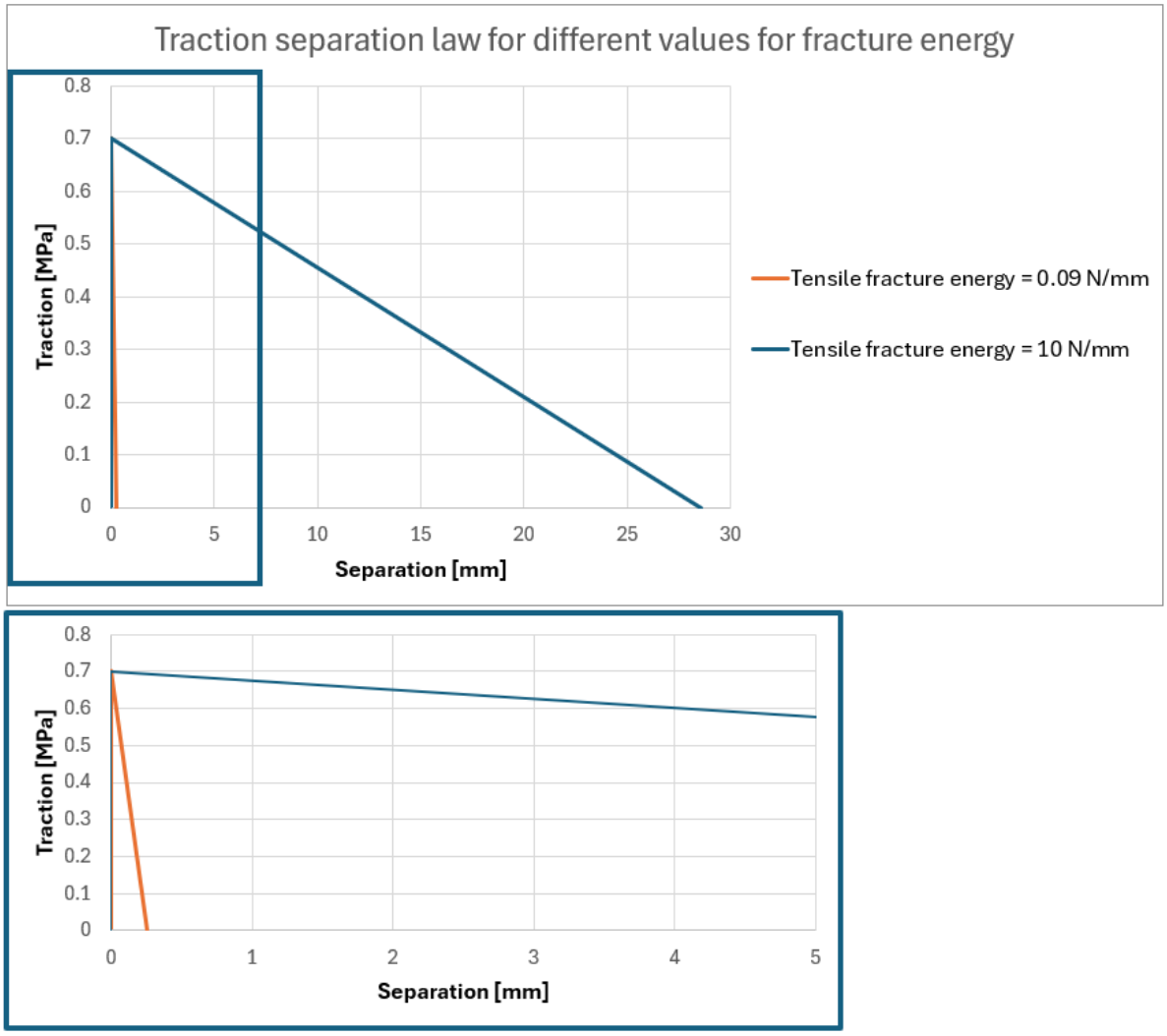

Figure A.65: Traction separation for a normal fracture energy of 10 N/mm versus the original interface with a normal fracture energy of 0.09 N/mm.

Results: For this parameter only a very high value for the normal fracture energy is chosen due to the already very low value of fracture energy in the original case.

In Figure A.66, the force-displacement diagram for the analysis is shown, along with the locations of the important steps. In the analysis all steps up until step 40 have been analysed.

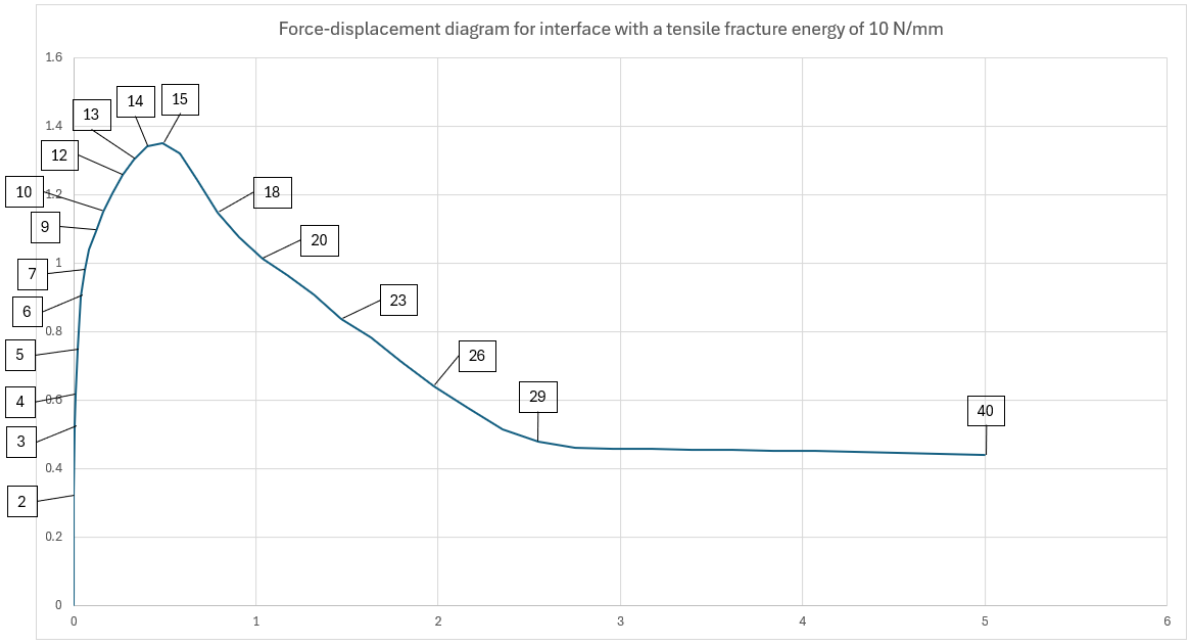

Figure A.66: Force displacement diagram of the analysis with an interface with a normal fracture energy of 10 N/mm, with important steps identified for further analysis.

The plastic strain development throughout the analysis is shown in Figure A.67. From the figure it can be seen that the plastic strain development in the case of a high normal fracture energy is roughly the same as in the original case up until step 12. After step 12 it can be seen that in the case of the high normal fracture energy the plastic strain in the tab increases significantly faster and that this continues increasing up until the end of the analysis, facilitating a tab failure mechanism. On the contrary, in the original case the plastic strain stops developing after step 16, facilitating a full pull-out failure mechanism.

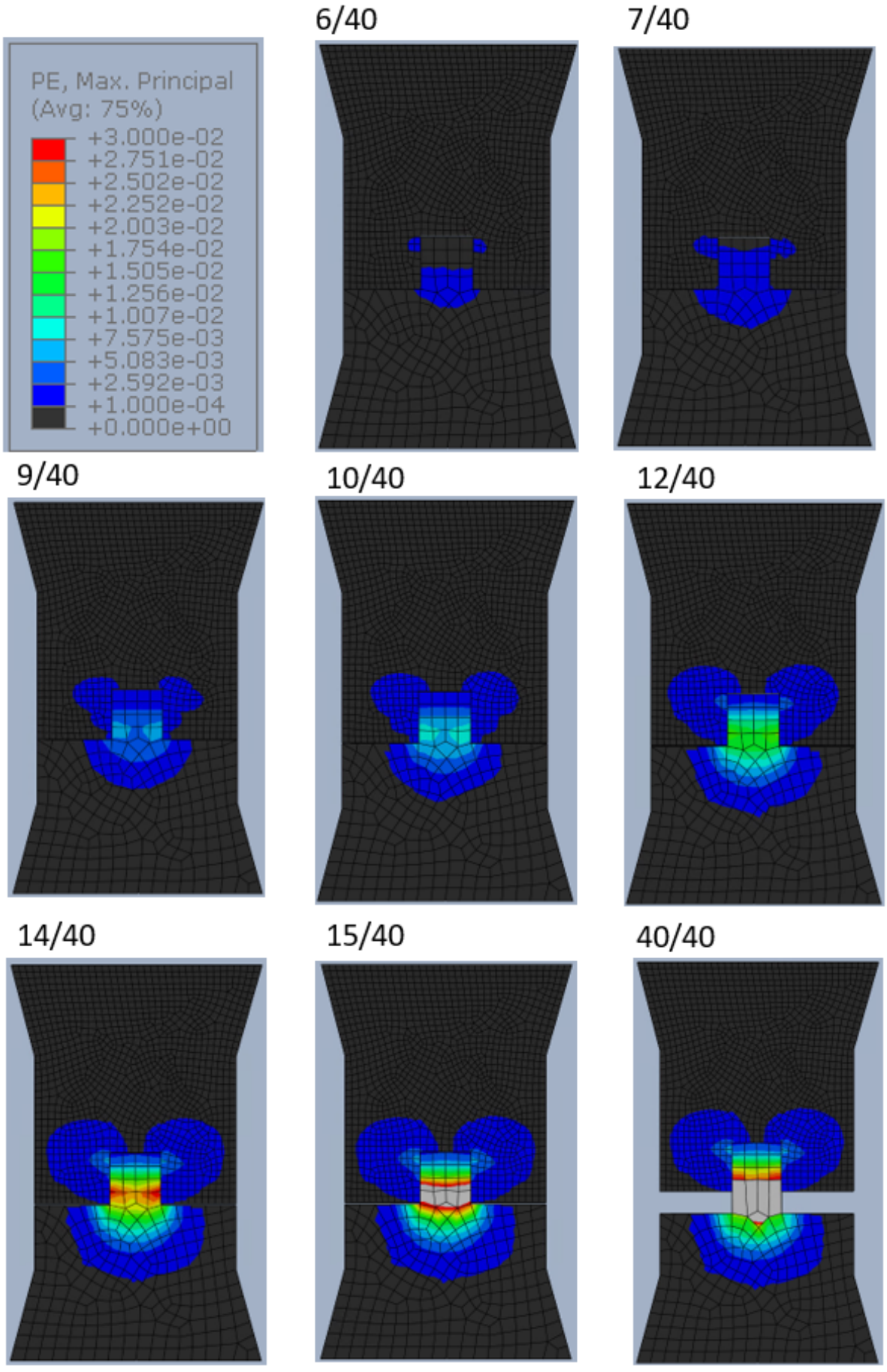

Figure A.67: Plastic strain values throughout the analysis with a color legend ranging from 0.0001 (0.01%) to 0.03 (3%).

When examining the tensile interface damage (see Figure A.68), only minor differences are noticeable. The interface deteriorates slightly more slowly than in the original case, but overall, no significant changes are observed in the tensile damage progression. However, when comparing the damage curves for the two different traction-separation laws, it becomes evident that even though the fracture energy—and thus the traction values at higher displacements—are considerably larger in the case of the standard fracture energy of 10 N/mm, the difference in tensile damage progression remains almost negligible. Similar to the scenario with very low shear strength, the maximum separation value beyond which the interface no longer transfers stresses is approximately 28 mm. Although this value is unrealistic, it prevents the force from dropping below 0.4 kN in the analysis. This plateau in force, following the initial decline, is attributed to the residual traction capacity of the tensile interface at high separation values.

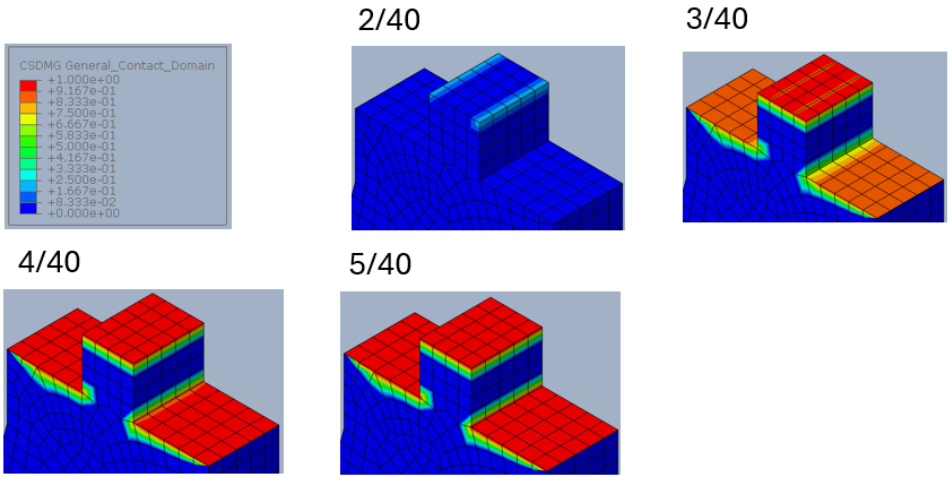

(a) Interface damage of the interface loaded in tension throughout the analysis with a color legend ranging from 0 (0%) to 1 (100%).

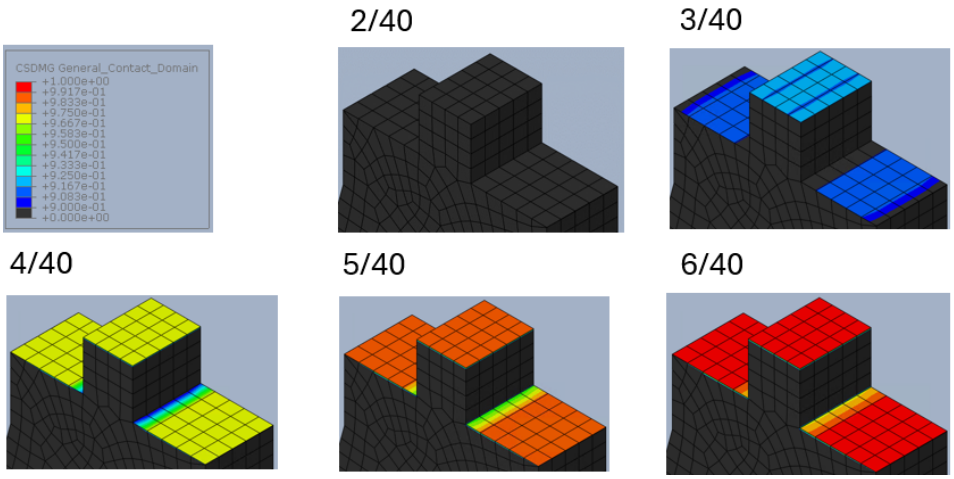

(b) Interface damage of the interface loaded in tension throughout the analysis with a color legend ranging from 0.9 (90%) to 1 (100%).

Figure A.68: Interface damage of the interface loaded in tension throughout the analysis of the specimen with a normal fracture energy of 10 N/mm.

In Figure A.69, the progression of shear interface damage throughout the analysis is depicted. Up to step 10, the development of shear interface damage is comparable to that in the original analysis. However, beyond step 10, a marked difference emerges: in the original case, the damage progresses rapidly and continues until the end of the analysis, resulting in a pull-out failure mechanism. In contrast,

for the case with high normal fracture energy, the damage progresses more slowly after step 10 and halts entirely by step 15, leading to a tab failure mechanism.

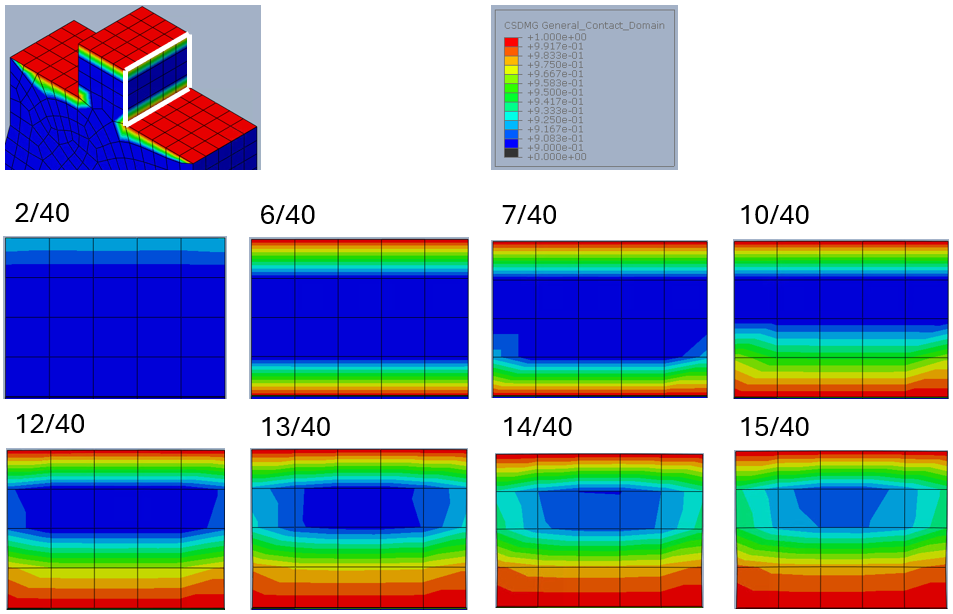

Figure A.69: Interface damage of the interface loaded in shear throughout the analysis of the specimen with a normal fracture energy of 10 N/mm. Color legend ranges from 0 (0%) to 1 (100%).

Lastly, the influence of the different values for the normal fracture energy on the force-displacement behaviour of the connection is presented Figure A.70. Additionally the same data is also presented as a stress-displacement diagram in Figure A.71.

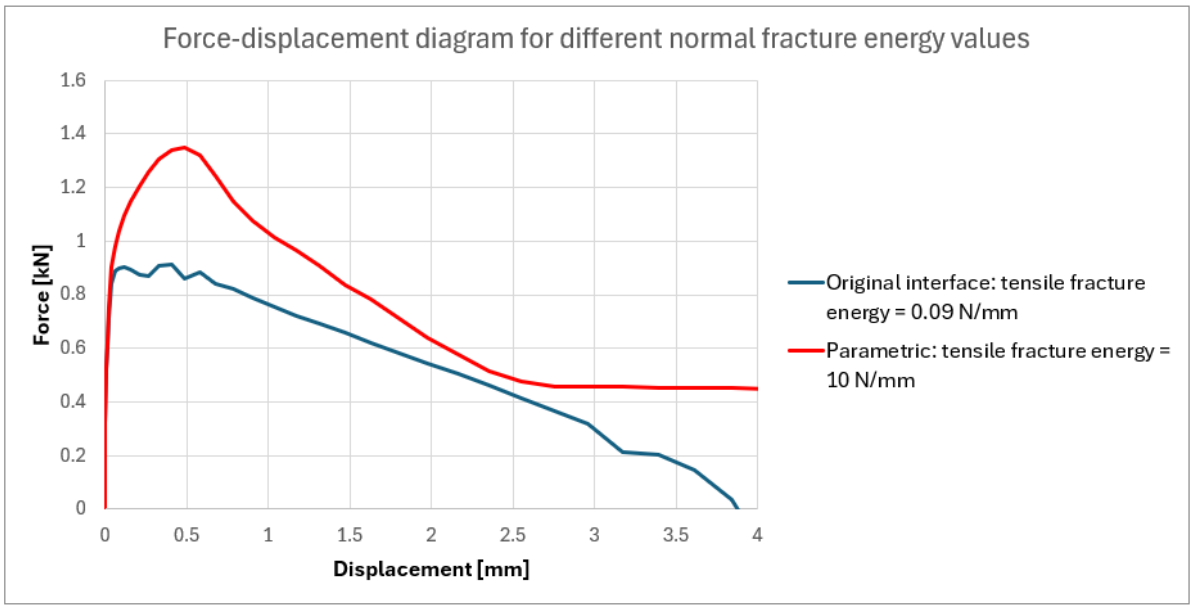

Figure A.70: Influence of the low and high values of normal fracture energy on the force-displacement behaviour of the connection.

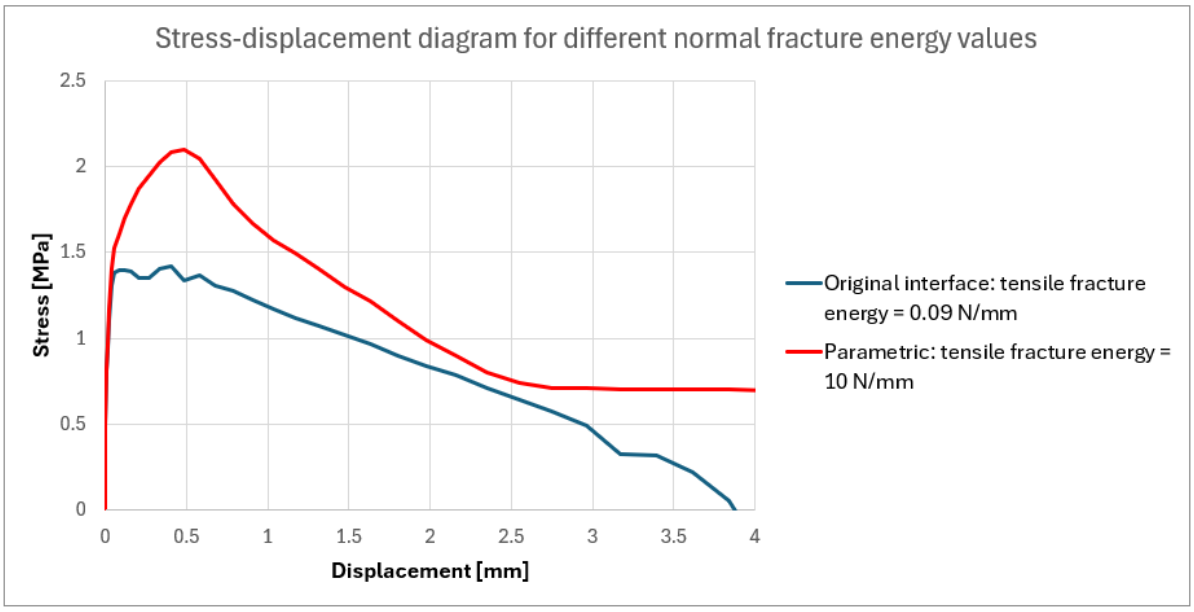

Figure A.71: Influence of the low and high values of normal fracture energy on the tensile stress-displacement behaviour of the connection.

A.6.1. Discussion

Changes in normal fracture energy do not significantly affect the tensile interface damage behavior, as noted earlier. However, due to the way the damage parameter is defined in Abaqus, this parameter serves as a reliable indicator of the onset of damage but not as a measure of how much stress can still be transferred through the interface. According to the traction-separation law, an interface with higher normal fracture energy can transmit larger stresses at greater separation values.

While no substantial difference is observed in the tensile interface damage progression, the force-displacement diagram (see Figure A.72) clearly indicates that increasing the normal fracture energy enhances stress transfer at lower displacements. This is evident from the higher stress transfer right after damage occurs in the tensile interface (step 3), compared to the original case.

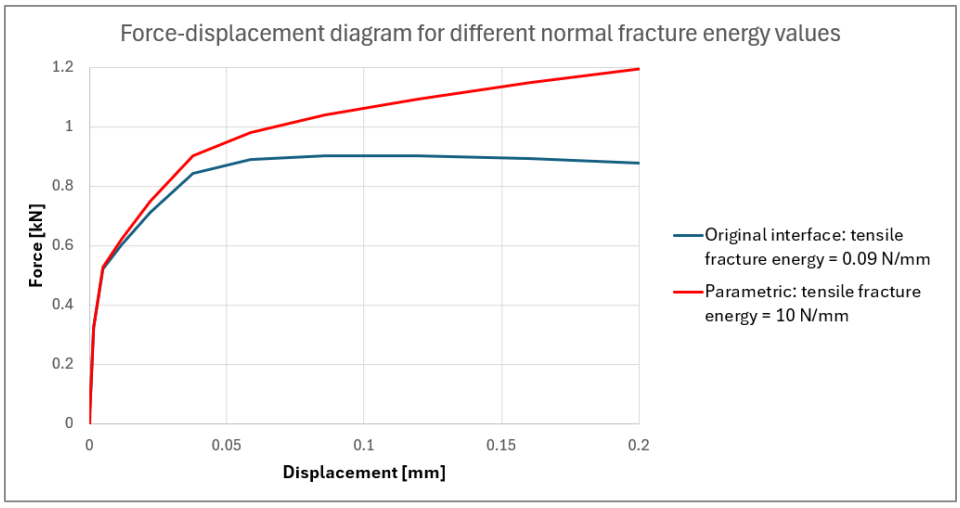

Figure A.72: Force-displacement diagram for different interfacial normal fracture energies, zoomed in on the first 0.2mm of displacement.

Moreover, after step 10, the increased normal fracture energy begins to significantly alter the shear

interface damage progression. Unlike the original case, where shear interface damage progresses rapidly after step 10 and continues up to the end of the analysis, the case with higher normal fracture energy exhibits a much slower progression of shear interface damage beyond this point. This delayed progression is primarily due to the tensile interface continuing to bear stress even at higher separations, which reduces the stress transfer demand on the vertical shear interfaces. As a result, the vertical shear interfaces remain relatively undamaged, and the shear damage progression halts after step 15, facilitating a transition from a pull-out failure mechanism to a tab failure mechanism.

This interaction between tensile and shear interface behavior is further reflected in the plastic strain development. Up until step 12, the plastic strain development is comparable between the original case and the case with higher normal fracture energy. However, after step 12, the higher normal fracture energy allows the interface to sustain greater stresses, which leads to a continuous increase in plastic strain. As the interface carries more load, the stresses eventually surpass the material's capacity in the tab, driving a localized failure and resulting in the development of a tab failure mechanism rather than the pull-out mechanism observed in the original case.

A.7. 1st and 2nd Shear Fracture Energy

Description: The seventh and last variable in this parameter study is the value for the shear fracture energy, where in this study no differentiation is made between the 1st and 2nd direction. This shear fracture energy is defined in Abaqus as the total area under the traction-separation curve of the interface shear behaviour. The value of this energy is defined by the energy that is dissipated as a result of the damage process. Changing this value changes traction separation law by changing the maximum separation of the interface in shear. In this study the values of 0.5 N/mm and 500 N/mm are used as a low and high values of the shear fracture energy respectively. Changing the shear fracture energy without changing the maximum shear contact stress also influences the maximum separation of the interface as can be seen in Figure A.73.

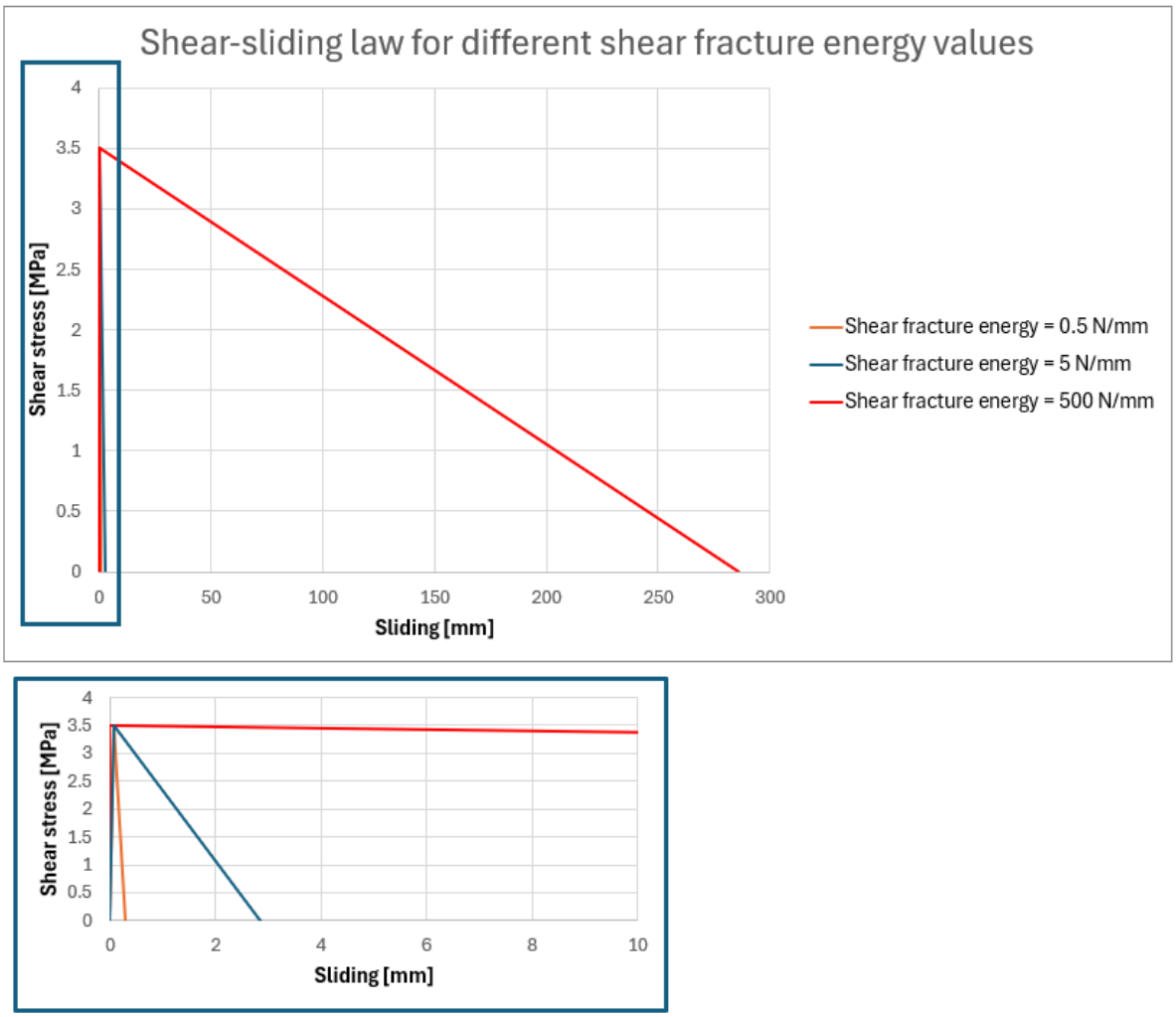

Figure A.73: Shear-sliding law for a shear fracture energy of 0.5 N/mm and 500 N/mm versus the original interface with a shear fracture energy of 5 N/mm.

Result: For both the shear fracture energy values of 0.5 N/mm and 500 N/mm the results are shown below. First the results for the shear fracture energy of 0.5 N/mm will be discussed and then afterwards the results for the interface with a shear fracture energy of 500 N/mm.

A.7.1. Shear fracture energy = 0.5 N/mm

In Figure A.74 the force-displacement diagram of the analysis is shown, together with the locations of the different relevant steps. In the analysis all steps up until step 40 have been analysed.

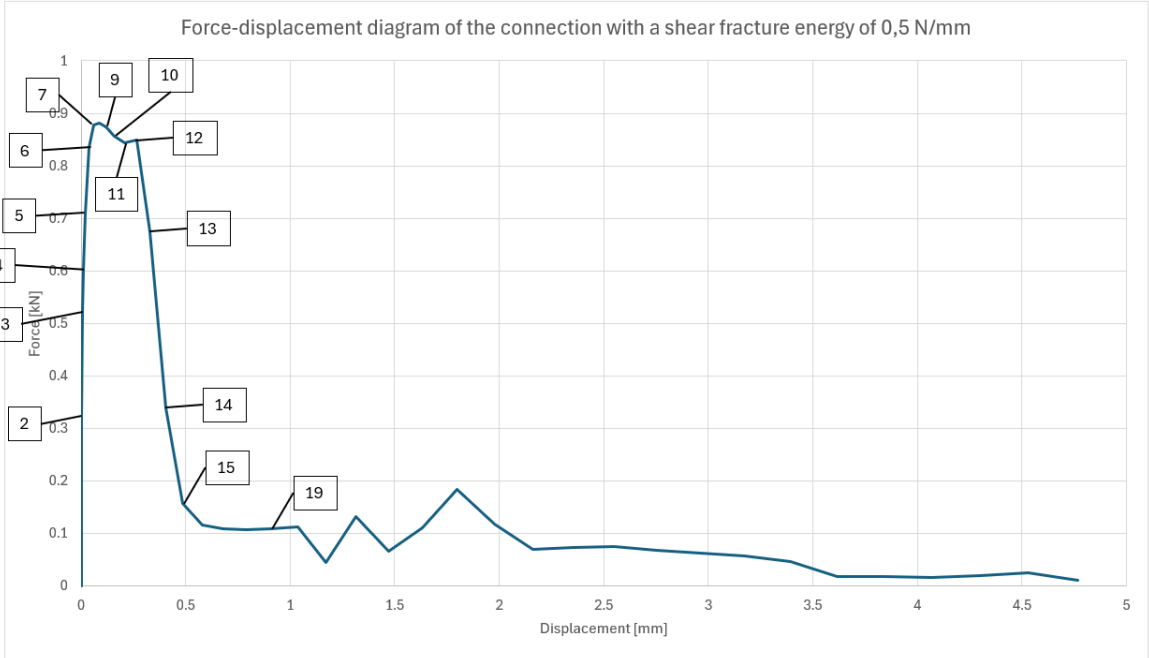

Figure A.74: Force displacement diagram of the analysis with an interface with a shear fracture energy of 0.5 N/mm, with important steps identified for further analysis.

The plastic strain development throughout the analysis is depicted in Figure A.75. Up until step 9, the plastic strain behavior in the case of low shear fracture energy closely mirrors that of the original case. However, from step 10 onward, notable differences emerge. In the low shear fracture energy case, the plastic strain, in the material surrounding the tab, is primarily concentrated next to the upper part of the tab, whereas in the original case, this strain extends further down the sides and nearly reaches the bottom of the tab. A significant divergence occurs after step 12, where plastic strain in the low shear fracture energy case remains relatively stagnant, while in the original case, it continues to increase considerably.

Despite these differences, both cases ultimately exhibit a plateau in plastic strain, leading to the development of a full pull-out failure mechanism. Additionally, from step 13 onward, some plastic strain begins to develop on the right side of the specimen, particularly around the bottom of the horizontal interface. This localized strain development is somewhat unexpected from a physical standpoint and may be attributed to numerical instabilities, which become more pronounced in the later stages of the analysis. These instabilities are also evident after step 19 in the force-displacement diagram (see Figure A.74), further supporting the idea that this behavior may not be physically significant.

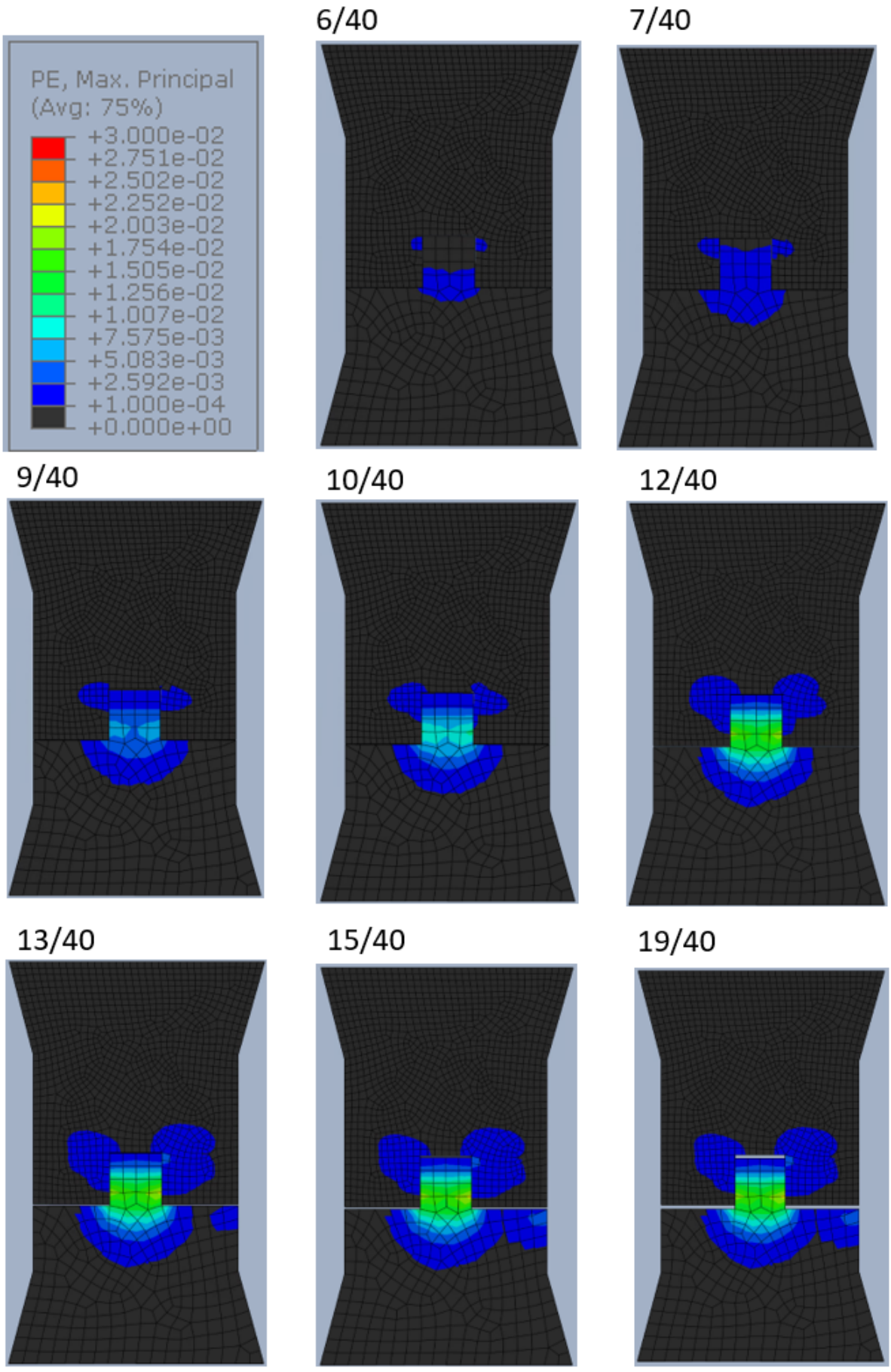

Figure A.75: Plastic strain values throughout the analysis with a color legend ranging from 0.0001 (0.01%) to 0.03 (3%).

The development of tensile interface damage in the case of a shear fracture energy of 0.5 N/mm shows no significant difference compared to the original interface behavior. However, the progression of damage in the vertical shear interface, as illustrated in Figure A.76, reveals notable distinctions. Up until step 10, the shear interface damage evolves similarly to the original case, which is expected since altering the fracture energy does not affect the initial part of the shear-sliding law, where stresses are sustained without damage. This is mostly the case for the shear interface up until step 10. Beyond step 10, however, the damage in the low shear fracture energy case accelerates rapidly. This swift progression occurs because the shear interface, with reduced fracture energy, becomes fully damaged at much lower sliding displacements, resulting in earlier degradation compared to the original case at equivalent sliding values.

This accelerated damage is also evident in the force-displacement diagram, where the force drops sharply after reaching the peak. The rapid decline in force is a result of fewer areas of the shear interface being capable of transferring stresses at the given displacement. Consequently, the overall load-bearing capacity of the interface diminishes significantly, leading to a much lower transferable force after the peak.

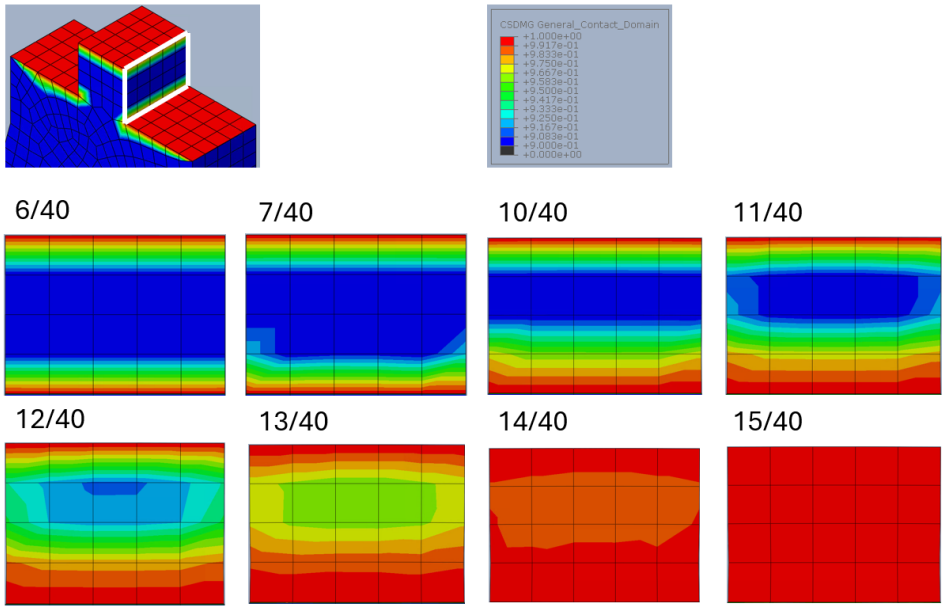

Figure A.76: Interface damage of the interface loaded in shear throughout the analysis of the specimen with a shear fracture energy of 0.5 N/mm. Color legend ranges from 0 (0%) to 1 (100%).

A.7.2. Shear fracture energy = 500 N/mm

In Figure A.77, the force-displacement diagram for the analysis is shown, along with the locations of the key steps. After step 30, the force stabilizes around zero and starts to become numerically unstable towards the end. Consequently, the analysis has been limited to steps 1-30 to ensure accuracy and stability.

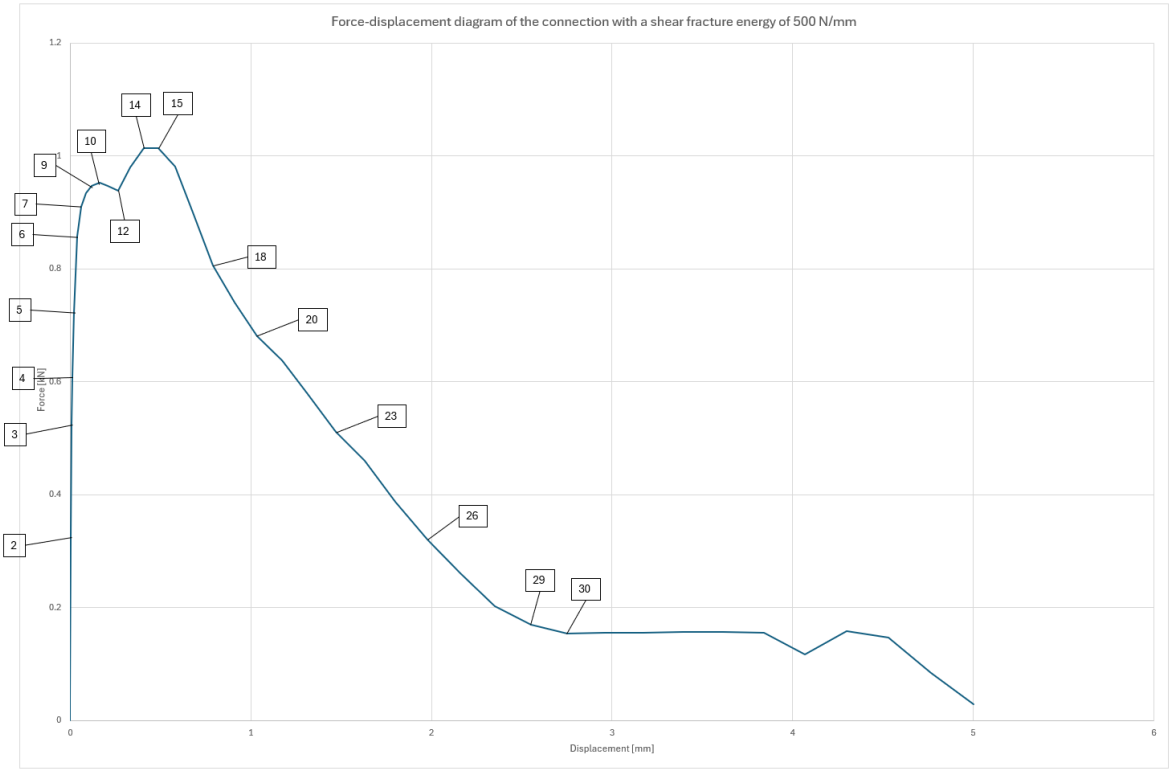

Figure A.77: Force displacement diagram of the analysis with an interface with a shear fracture energy of 500 N/mm, with important steps identified for further analysis.

The plastic strain development throughout the analysis, as shown in Figure A.78, reveals that up until step 12, the strain evolution in the specimen with an interfacial shear fracture energy of 500 N/mm closely follows the behavior seen in the original case. However, after step 12, the plastic strain in the high shear fracture energy specimen progresses more rapidly. Unlike in the original case, where plastic strain stabilizes after step 16, in this case, the strain continues to increase until the end of the analysis. From step 15 onwards, the plastic strain at the bottom of the tab exceeds the predefined color limit of 0.03 (3%), indicating significant material deformation.

To further understand the material behavior, the tensile damage parameter is presented in Figure A.79. This shows that tensile damage is primarily localized at the bottom of the tab, where material failure occurs, demonstrating a tab failure mechanism. It's important to note that tensile damage is derived from the material's single-crack behavior and remains zero until additional crack opening causes a reduction, rather than an increase, in stress values.

For a more comprehensive view of the damage distribution, the final step (30/40) is displayed with a lower limit of 0.0001, which highlights even the smallest damaged regions. These areas are mainly located around the top corners of the tab and in the material adjacent to the sides of the tab.

After step 30 of the analysis, the top part of the specimen shifts to the right in the x-direction relative to the bottom part. This displacement behavior is also evident in the parametric study involving high shear strength values. The occurrence of this phenomenon seems to be a defining characteristic in cases where the shear capacity of the vertical surfaces is exceptionally high. However, it remains unclear whether this behavior is a physically significant result or a consequence of numerical instabilities.

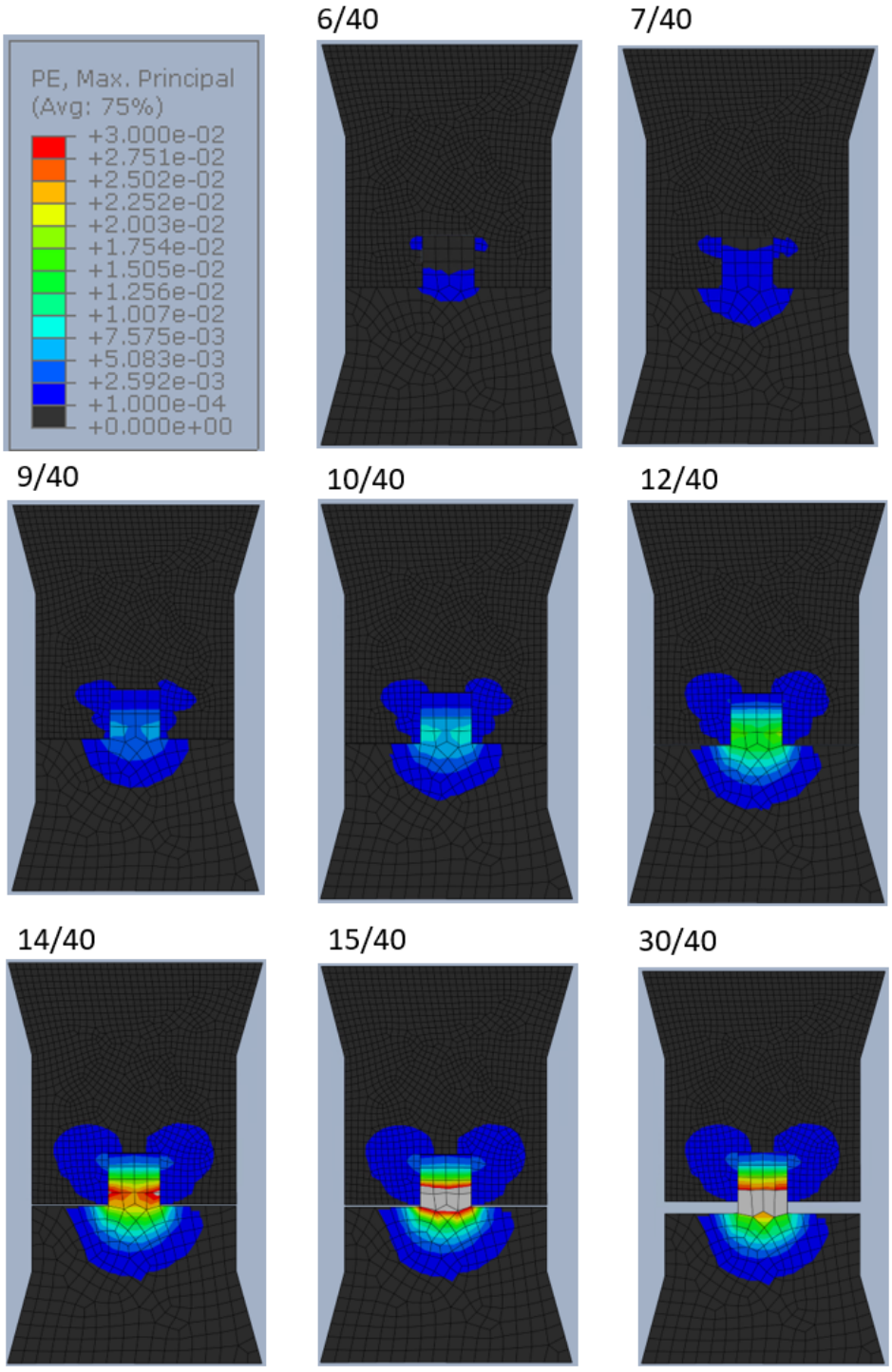

Figure A.78: Plastic strain values throughout the analysis with a color legend ranging from 0.0001 (0.01%) to 0.03 (3%).

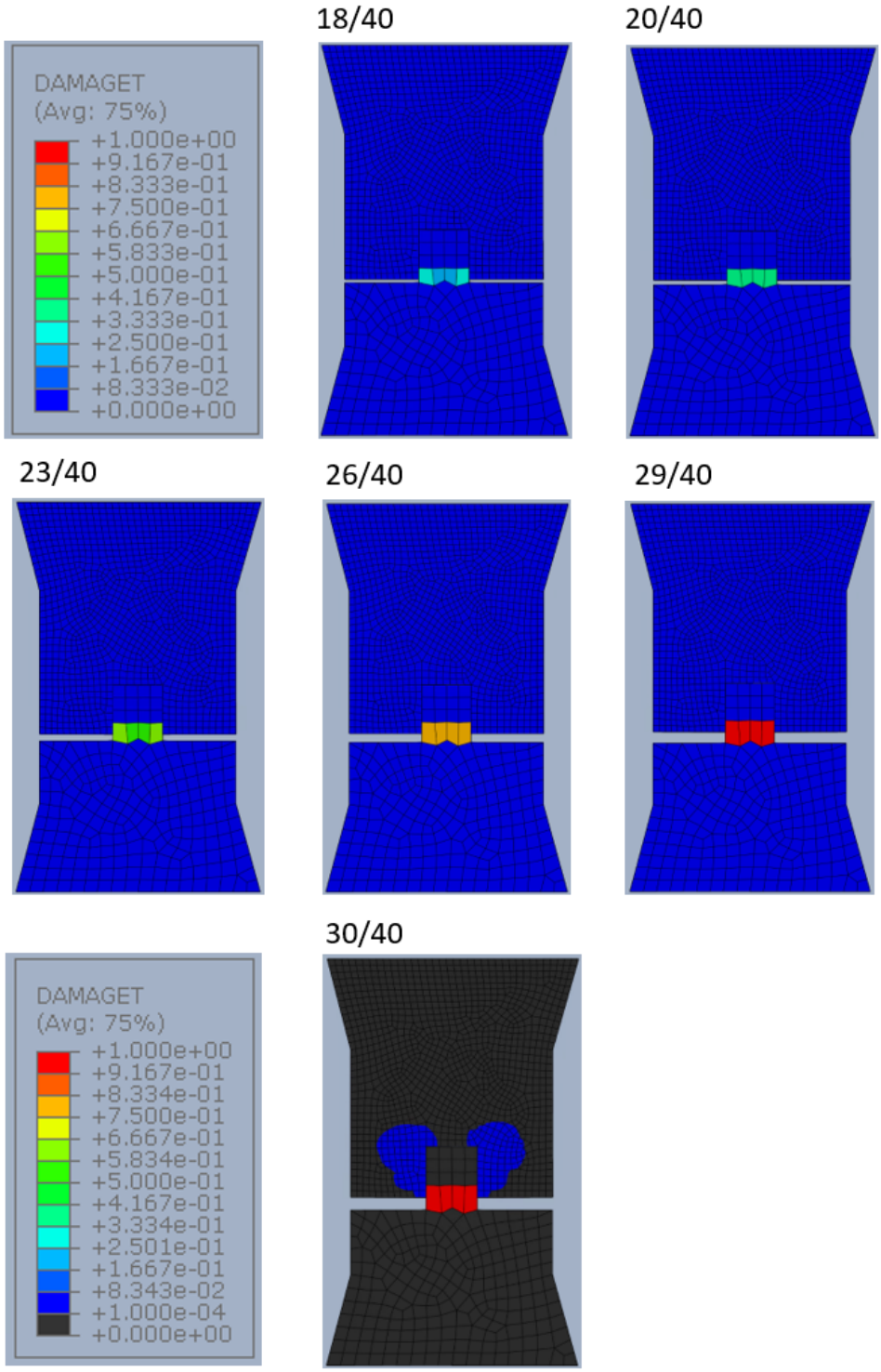

Figure A.79: Tensile damage values throughout the analysis with a color legend ranging from 0 (0%) to 1.0 (100%). Additionally for step 30 a color legend ranging from 0.0001 (0.01%) to 1.0 (100%) is used.

The development of tensile interface damage for the case with a shear fracture energy of 500 N/mm shows no significant deviation from the behavior observed in the original interface. However, the progression of damage in the vertical shear interface, as depicted in **??**, reveals notable differences. Up to step 10, the shear interface damage evolves similarly to the original case, which is expected since the early stages of damage are primarily governed by the initial stiffness and the tensile capacity rather than the fracture energy itself.

Beyond step 10, a clear divergence occurs. In the original case, the shear interface damage continues to increase steadily throughout the analysis, eventually leading to a full pull-out failure mechanism. In contrast, for the case with an interfacial shear fracture energy of 500 N/mm, the shear interface damage progresses at a much slower rate after step 10. By step 15, the damage effectively halts, suggesting that the interface has reached a stable state where additional shear displacement does not result in further damage. This cessation of damage progression indicates a shift in the failure mechanism from pull-out to a tab failure. The slower progression of damage in the higher shear fracture energy case reflects the enhanced ability of the interface to sustain higher shear stresses before degradation occurs. The higher fracture energy allows the interface to transfer more shear stress at greater sliding displacement values.

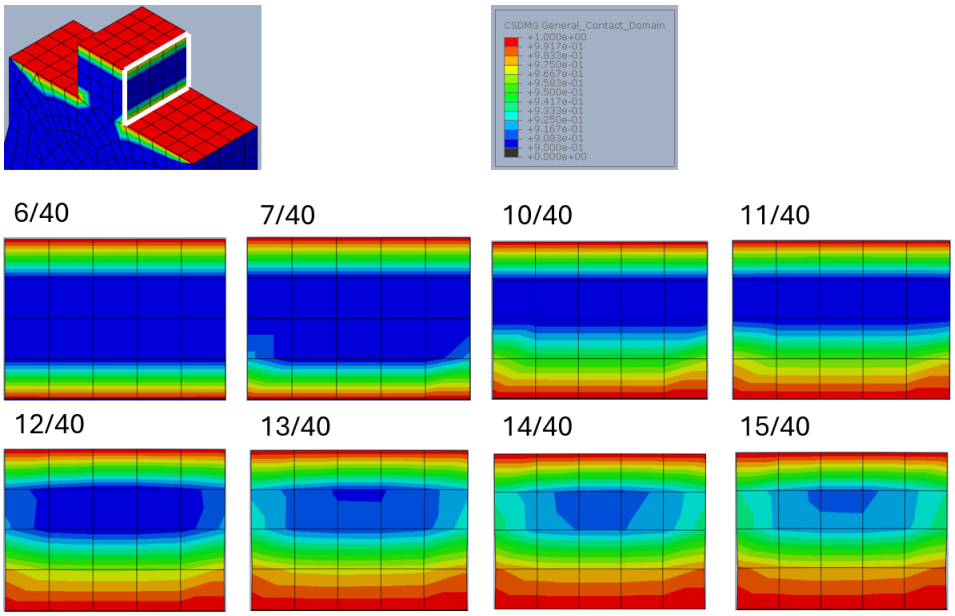

Figure A.80: Interface damage of the interface loaded in shear throughout the analysis of the specimen with a shear fracture energy of 500 N/mm. Color legend ranges from 0 (0%) to 1 (100%).

Lastly, the influence of the different values for the interfacial shear strength on the force-displacement behaviour is presented in Figure A.81. Additionally the same data is also presented as a stress-displacement diagram in Figure A.63.

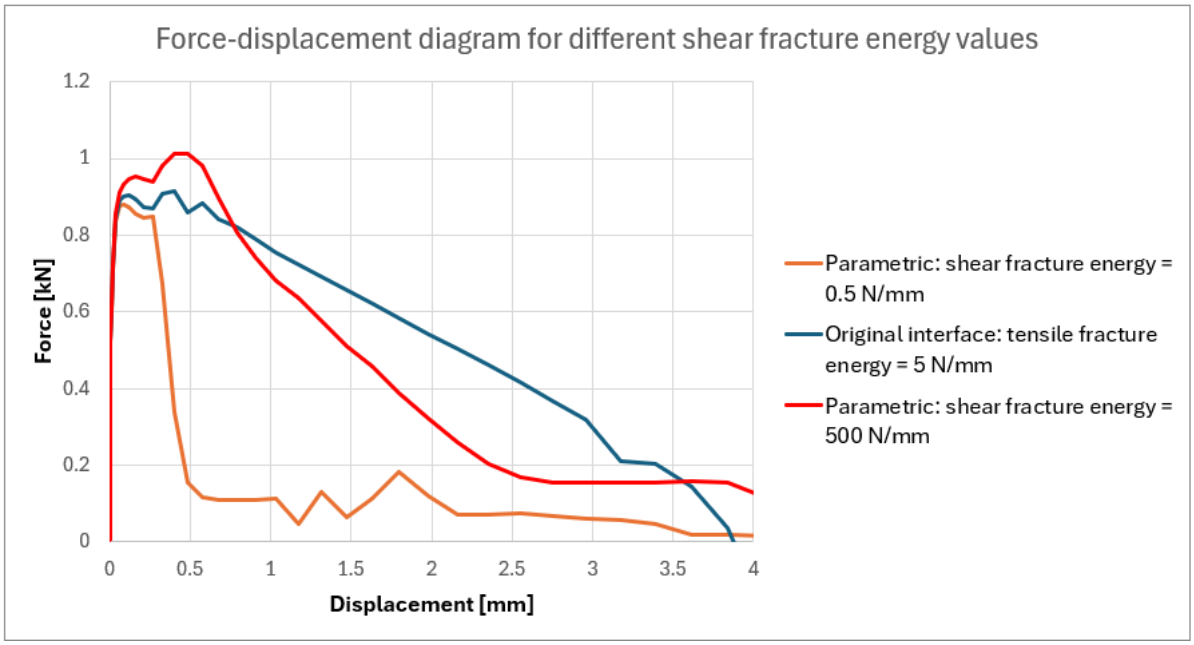

Figure A.81: Influence of the low and high values of interfacial shear fracture energy on the force-displacement behaviour of the connection.

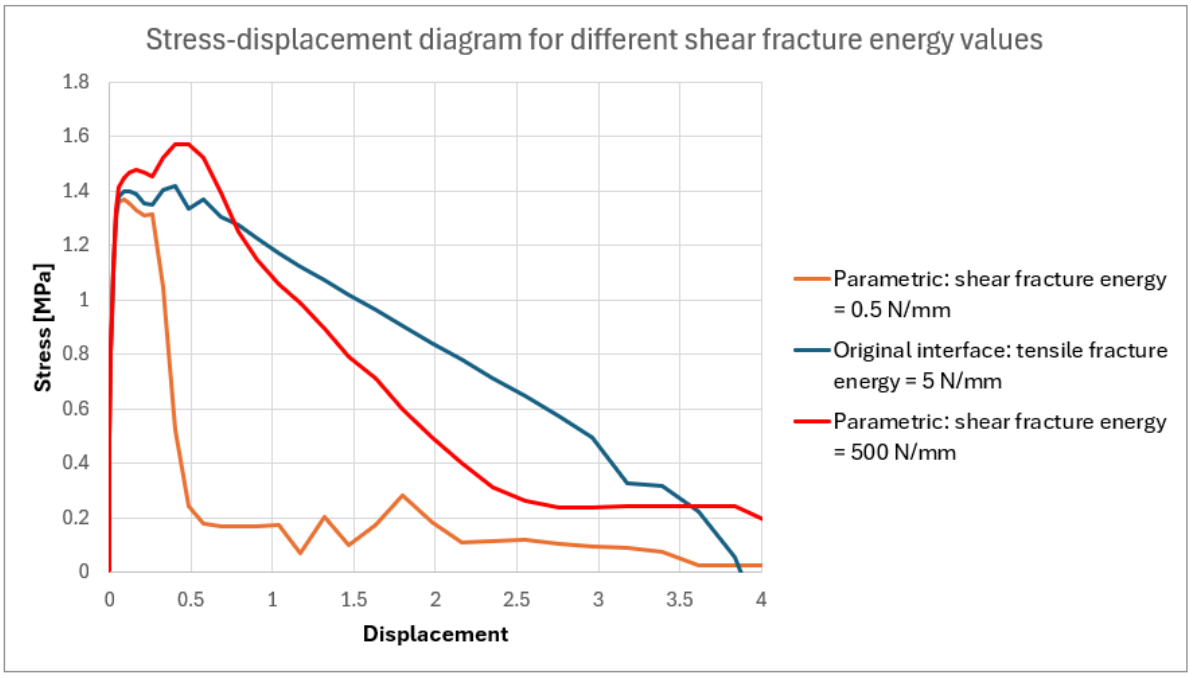

Figure A.82: Influence of the low and high values of interfacial shear fracture energy on the stress-displacement behaviour of the connection.

A.7.3. Discussion

Changes in the shear fracture energy do not show a significant effect on the plastic strain, tensile interface damage, or shear interface damage progression in the initial steps of the analysis. However, upon closer examination of the force-displacement diagram in the early stages (see Figure A.83), subtle discrepancies begin to emerge after step 3. Though these changes are small, they are indicative of how the shear fracture energy begins to influence the behavior of the system once minor damage

initiates in the shear interface.

This early-stage variation can be attributed to localized damage at the corners where the tensile and shear interfaces interact. At these points, the separation of the horizontal interface causes tensile interface damage to affect the shear interface in the same region. Consequently, the ability of the shear interface to sustain stress becomes increasingly dependent on the shear fracture energy, even at these early stages. For the case with the lowest shear fracture energy, the force is visibly lower compared to other cases, and vice versa for the higher shear fracture energy, reflecting the role of fracture energy in governing stress transfer capacity.

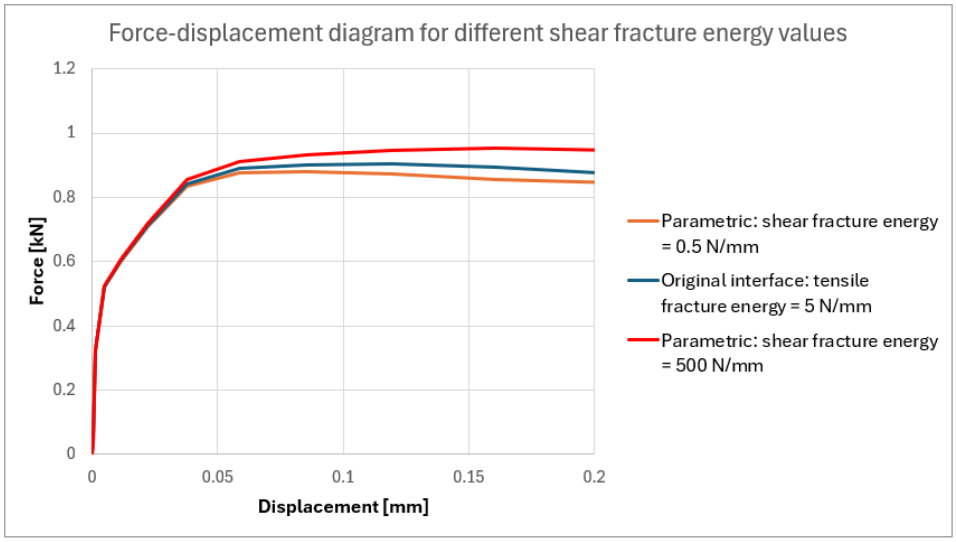

Figure A.83: Force-displacement diagram for different interfacial shear fracture energies, zoomed in on the first 0.2mm of displacement.

Beyond these initial discrepancies, more pronounced differences become evident after step 6, where the shear interface begins to undergo damage more visibly. Although the progression of shear interface damage appears to follow a similar pattern as in the original case, the influence of the shear fracture energy becomes more pronounced. The first significant divergence occurs after the first peak (around step 12), which aligns with observations from the plastic strain and shear interface damage progression. Here, the differences between low and high shear fracture energy cases become more evident.

In the case of high shear fracture energy, the plastic strain continues to increase after step 12, indicating that the interface is able to sustain higher shear stresses without rapid degradation. As a result, tensile material damage begins to occur in the surrounding material, signaling a shift toward a tab failure mechanism. This suggests that in high shear fracture energy scenarios, the interface is able to transfer larger stresses for a longer period before damage propagates through the material itself, ultimately causing failure in the tab rather than the interface.

On the other hand, in the case of low shear fracture energy, the shear interface rapidly accumulates damage after the first peak, leading to a full pull-out failure mechanism. The rate at which the force drops in this scenario is significantly faster than in the original case. This rapid drop in force, combined with findings from the parametric study on the friction coefficient, highlights the critical role of shear fracture energy in controlling the rate at which stress is reduced within the shear interface.

A.8. Summary

Friction

Friction plays a crucial role in resisting relative motion between surfaces at the interface. In the original case, the friction coefficient is 0.7, with low (frictionless) and high (10) friction values being considered for comparison.

The friction coefficient primarily influences the post-peak behavior of the interface, demonstrating minimal impact during the initial loading stages (up to step 10). In the early phases of loading, both tensile and shear interfaces remain intact, with damage occurring predominantly due to the inherent material and interface properties rather than frictional effects. As loading continues, the force-displacement behavior reveals that friction becomes significant only after the shear interface begins to sustain damage.

For a frictionless interface, the absence of friction allows shear damage to accumulate rapidly, culminating in a pull-out failure mechanism by step 12. This rapid degradation occurs because, without friction to resist sliding after cohesive failure occurs, the interface cannot maintain effective load transfer, leading to immediate separation and loss of structural integrity.

Conversely, a high friction coefficient enhances the interface's ability to resist sliding, resulting in slower shear interface damage. This delayed damage allows plastic strain to develop in the tab material, which contributes to the overall energy absorption of the system. The increase in plastic deformation before failure indicates that the material can dissipate more energy, ultimately leading to a tab failure mechanism. Interestingly, after the initial force peak, the rate of force reduction remains consistent across the original and frictionless cases, suggesting that the rate of stress transfer degradation in pull-out mechanisms is predominantly governed by cohesive interface damage rather than the frictional forces at play. This highlights the importance of cohesive properties in the interface under certain loading conditions, particularly when considering post-peak behavior.

In summary, higher friction coefficients enhance the interface's resistance to sliding, leading to delayed shear damage and a shift toward tab failure, while lower friction values result in rapid interface degradation and pull-out failure.

Normal Stiffness Coefficient

The normal stiffness coefficient determines the tensile stress required to deform the interface by a unit displacement. In the original case, the tensile stiffness coefficient is 3000 MPa/mm, with low (30 MPa/mm) and high (30000 MPa/mm) stiffness values used for comparison.

The normal stiffness coefficient plays a critical role in the interaction between the tensile and shear interfaces, significantly influencing their behavior under loading conditions. A low normal stiffness leads to an increased separation at the interface for a given applied normal stress. This greater separation allows the tensile interface to absorb more energy without immediate damage, resulting in delayed tensile interface failure. As a consequence, the shear interface becomes more actively engaged, sustaining shear stresses and preventing rapid damage. This synergy between the interfaces enables the system to support higher overall forces, culminating in a tab failure mechanism where the load is effectively transferred to the surrounding material.

In contrast, a high normal stiffness results in rapid stress transfer through the horizontal interface. The increased stiffness restricts separation, which can lead to quicker damage initiation in the tensile interface under tensile loads. Despite this early onset of damage, the initial peak force is significantly higher than in the original case. This high peak force reflects the combined effect of both shear and tensile interfaces. While this scenario might suggest superior load-carrying capacity initially, it ultimately leads to less effective stress distribution, resulting in a pull-out failure mechanism as the shear interface becomes overloaded and unable to sustain the accumulated stresses.

Despite the differences in tensile behavior, the post-peak responses in both high and original stiffness cases display similar characteristics. The shear interface fails to sustain the stresses effectively, leading to a transition to pull-out failure in both instances. This outcome emphasizes the intricate bal-

ance between normal stiffness and the interface's overall performance.

In summary, higher normal stiffness coefficients facilitate rapid stress transfer but can lead to premature tensile damage, resulting in pull-out failure. In contrast, lower normal stiffness values allow for delayed tensile damage, enabling a transition to tab failure as the combined interfaces effectively support higher loads.

Shear Stiffness Coefficient

The shear stiffness coefficient determines the shear stress required to deform the interface by a unit displacement. In the original case, the shear stiffness coefficient is 50 MPa/mm, with low (5 MPa/mm) and high (3000 MPa/mm) stiffness values used for comparison.

Variations in the shear stiffness coefficient significantly influence the dynamics between the tensile and shear interfaces. A low shear stiffness coefficient reduces the interface's resistance to deformation under shear loading. This leads to a lower initial peak force and quicker damage accumulation in the tensile interface, as the shear stresses are not efficiently transferred during loading. The delayed transfer of shear stress results in a greater reliance on the tensile interface to carry the load initially. Consequently, this scenario culminates in a pull-out failure mechanism, where the shear interface's contribution to stress transfer becomes negligible after significant sliding occurs.

In contrast, a high shear stiffness coefficient enhances the system's capacity to withstand shear deformation. The increased resistance delays the initiation of damage in the tensile interface, allowing for a more integrated interaction between the two interfaces. As the system can transfer higher stresses effectively, the overall performance improves, leading to a tab failure mechanism. This behavior is characterized by sustained load-bearing capacity, where the material can support significant shear stresses before damage propagates.

In summary, higher shear stiffness coefficients enhance the interface's ability to resist deformation, facilitating a tab failure mechanism through effective stress transfer, while lower shear stiffness leads to rapid tensile damage and pull-out failure due to delayed shear stress transfer.

Normal Contact Stress

Tensile strength defines the maximum stress the interface can withstand before damage begins. In the original case, the tensile strength is 0.7 MPa, with low (0.1 MPa) and high (10 MPa) tensile strength values used for comparison.

Variations in the shear stiffness coefficient significantly influence the dynamics between the tensile and shear interfaces. A low shear stiffness coefficient reduces the interface's resistance to deformation under shear loading. This leads to a lower initial peak force and quicker damage accumulation in the tensile interface, as the shear stresses are not efficiently transferred during loading. The delayed transfer of shear stress results in a greater reliance on the tensile interface to carry the load initially. Consequently, this scenario often culminates in a pull-out failure mechanism, where the shear interface's contribution to stress transfer becomes negligible after significant sliding occurs.

In contrast, a high shear stiffness coefficient enhances the system's capacity to withstand shear deformation. The increased resistance delays the initiation of damage in the tensile interface, allowing for a more integrated interaction between the two interfaces. As the system can transfer higher stresses effectively, the overall performance improves, leading to a tab failure mechanism. This behavior is characterized by sustained load-bearing capacity, where the material can support significant shear stresses before damage propagates.

The post-peak behavior in low and high shear stiffness cases shows alignment with the original specimen, indicating that while the failure mechanisms differ—pull-out in the low stiffness scenario and tab failure in the high stiffness case—the overall energy absorption capabilities of the system are affected by the shear stiffness. The distinct patterns of damage progression highlight the importance of this parameter in determining the overall failure mode.

In summary, higher shear stiffness coefficients enhance the interface's ability to resist deformation, facilitating a tab failure mechanism through effective stress transfer, while lower shear stiffness leads to rapid tensile damage and pull-out failure due to delayed shear stress transfer.

Shear Contact Stress

Shear strength defines the maximum shear stress the interface can withstand before damage begins. In the original case, the shear strength is 3.5 MPa, with low (0.5 MPa) and high (50 MPa) shear strength values used for comparison

Shear strength impacts the load-bearing behavior of the interface, though it primarily influences the shear interface rather than the tensile behavior. In the initial stages (up to step 4), variations in shear strength show little effect on the force-displacement behavior. This is because, during early loading, the tensile interface dominates the response, and no significant shear interface damage occurs, even with low or high shear strength values. In cases with very low shear strength, the tensile capacity of the interface is insufficient to induce significant cracking without support from shear contribution. There is no shear contribution from friction either, due to separation in the vertical surfaces of the interface.

In case of a low shear strength, the influence of the shear interface to capacity of the connection to transfer forces is only available in the initial stages of the analysis. Once the tensile interface starts to damage significantly the vertical interface cannot take up any significant stresses and thus the force take up by the connection drops rapidly. In high shear strength scenarios, the tensile behavior remains similar to the original case up until the first peak of the force-displacement curve. Beyond this point, however, higher shear strength causes a shift toward a tab failure mechanism, where shear forces accumulate enough to damage the tab material itself rather than just the interface. This transition happens because the vertical shear interface sustains higher forces, transferring load to the surrounding material, ultimately leading to localized tab failure instead of pull-out failure.

In summary, while shear strength has little impact in the early stages of analysis, lower values lead to rapid pull-out failure of the connection whereas higher values delay shear interface damage, transferring stress to the tab material and causing a shift from interface pull-out failure to tab failure.

Normal Fracture Energy

Normal fracture energy controls how much energy the interface can absorb before tensile failure occurs. In the original case, the normal fracture energy is 0.09 N/mm, with a high (10 N/mm) normal fracture energy value used for comparison.

Increasing the normal fracture energy strengthens the interface's ability to transfer stress even as separation increases. This is because normal fracture energy controls how much energy the interface can absorb before it fully fails. With higher normal fracture energy, the interface can endure greater separation while still bearing stress, which delays damage in the shear interface. This means the vertical (shear) interface experiences less stress early in the analysis, slowing the progression of shear damage.

In the later stages of the analysis (after step 10), this ability to maintain stress at larger separations leads to a noticeable shift in the failure mechanism. Rather than the typical pull-out failure, where the interface gradually loses its load-bearing ability, the specimen with higher normal fracture energy transitions towards a tab failure. This occurs because the tensile interface holds together longer, allowing higher stresses to accumulate, which are eventually transmitted to the tab itself. The result is not just slower interface damage but also a greater load transfer to the material of the specimen, causing localized failure in the tab rather than the interface.

In summary, higher normal fracture energy enhances stress transmission across the tensile interface, altering the failure mechanism from pull-out to tab failure. This occurs because the interface can sustain higher forces over a longer period, reducing stress on the shear interface and leading to a more distributed stress pattern that causes failure in the material rather than at the interface.

Shear Fracture Energy
Shear fracture energy controls how much energy the interface can absorb before shear failure occurs. In the original case, the shear fracture energy is 5 N/mm, with low (0.5 N/mm) and high (500 N/mm) shear fracture energy values used for comparison.

Higher shear fracture energy increases the interface's capacity to transfer shear stresses without breaking down quickly. In the early stages of the analysis (after step 3), small variations in force-displacement behavior suggest that shear fracture energy starts influencing stress transfer when minor shear damage initiates in areas where tensile and shear forces interact. The ability of the interface to sustain stress at these points depends directly on the amount of energy it can absorb before failure begins.

As the analysis progresses, larger differences in behavior become more noticeable, especially after step 12 when the shear interface damage becomes more severe. For specimens with high shear fracture energy, the interface absorbs more energy, allowing it to sustain higher shear stresses for higher sliding values. This slows the rate of shear damage progression, leading to tab failure. In this scenario, the material within the tab begins to fail due to the larger stresses being transmitted through the still-intact interface, reflecting a shift away from interface failure to material failure in the tab.

In contrast, with low shear fracture energy, the interface quickly reaches its capacity for absorbing shear energy, leading to rapid damage accumulation and a much faster force drop in the force-displacement diagram. This behavior leads to a pull-out failure mechanism, where the interface itself fails due to its inability to continue transferring shear stresses. In this case it is observed that the rate at which the force decreases in a full pull-out mechanism is mostly attributed to the amount of shear fracture energy in the interface.

Thus, higher shear fracture energy allows the interface to act as a more resilient barrier to shear forces, delaying failure and leading to a material-dominated failure (tab failure), while low shear fracture energy causes rapid shear damage and an interface-driven pull-out failure.

The presence of a wall effect around the interface, where fiber distribution and alignment are affected by the existing concrete, indicates that a larger region surrounding the interface is influenced than what is represented by the ITZ. To account for this effect while maintaining a realistic interface thickness, the thickness is set to 1 mm. This choice results in a normal stiffness coefficient of 32,000 MPa/mm and a shear stiffness coefficient of 13,333 MPa/mm, allowing for a more accurate representation of the interface behavior in the analysis. These values will be used in the next section for defining the optimal interface parameters to represent the experimental results from [21].

A.9. General Discussion

In the parametric study the behaviour of the connection has been investigated based on different configurations of interface parameters. This parametric study aimed to determine the effect of the different parameters on the behaviour of the connection. One of the important factors to look at is the failure mechanism in the different parameter configurations. The failure mechanisms are summarized in the table below.

Parameter	Value	Unit	Ultimate failure mechanism
Original case	-	-	pull-out failure
Friction coefficient	0	-	pull-out failure
	10	-	tab failure
Normal stiffness coefficient	30	MPa/mm	tab failure
	30000	MPa/mm	pull-out failure
Shear stiffness coefficient	5	MPa/mm	pull-out failure
	3000	MPa/mm	tab failure
Normal contact stress	0.1	MPa	pull-out failure
	10	MPa	SHCC material failure
Shear contact stress	0.5	MPa	pull-out failure
	50	MPa	tab failure
Normal fracture energy	10	N/mm	tab failure
Shear fracture energy	0.5	N/mm	pull-out failure
	500	N/mm	tab failure

Table A.2: The ultimate failure mechanisms for the different parameter values in the parametric study.

In examining the force-displacement behavior across failure mechanisms, delamination, pull-out and tab failure are represented. In Figure A.84, the force-displacement graphs for the delamination and pull-out failure mechanism illustrate that, except for the initial peak force observed with a high tensile stiffness coefficient of 30000 MPa/mm, the original connection and this high-stiffness connection display nearly identical post-peak behavior. The frictionless case behaves similarly as well; however, following its initial peak, the force briefly drops before continuing along a similar downward trend as the others, though slightly lower in magnitude.

In cases where a very low shear stiffness coefficient is applied, the large difference between shear and tensile stiffness leads to distinct behavior. Here, the tensile interface activates well before the shear interface, resulting in an early peak attributed almost solely to tensile interface behavior. After this peak, the force temporarily drops but rises again as the shear interface gradually engages and bears more load. Once the second peak is reached, the post-peak behavior mirrors that of the other configurations, maintaining a comparable downward trend in force-displacement.

The most pronounced differences emerge in cases with very low tensile strength, shear strength, and shear fracture energy. For the low shear fracture energy case, the initial force-displacement curve closely resembles the original and frictionless cases. However, after reaching the first peak, the force drops sharply due to the rapid decrease in allowable stresses at minimal sliding displacements, characteristic of low shear fracture energy. For the case with very low shear strength, the force-displacement graph closely follows the tensile traction-separation law shape, indicating that nearly all connection behavior is dominated by tensile properties.

Lastly, in the very low tensile strength case, although significant displacement capacity remains, the maximum force is substantially reduced compared to the other cases. Here, there is no initial peak, and the linear-elastic region displays a much lower stiffness, underscoring that the entire connection behavior is governed by the shear interface due to the minimal tensile resistance available.

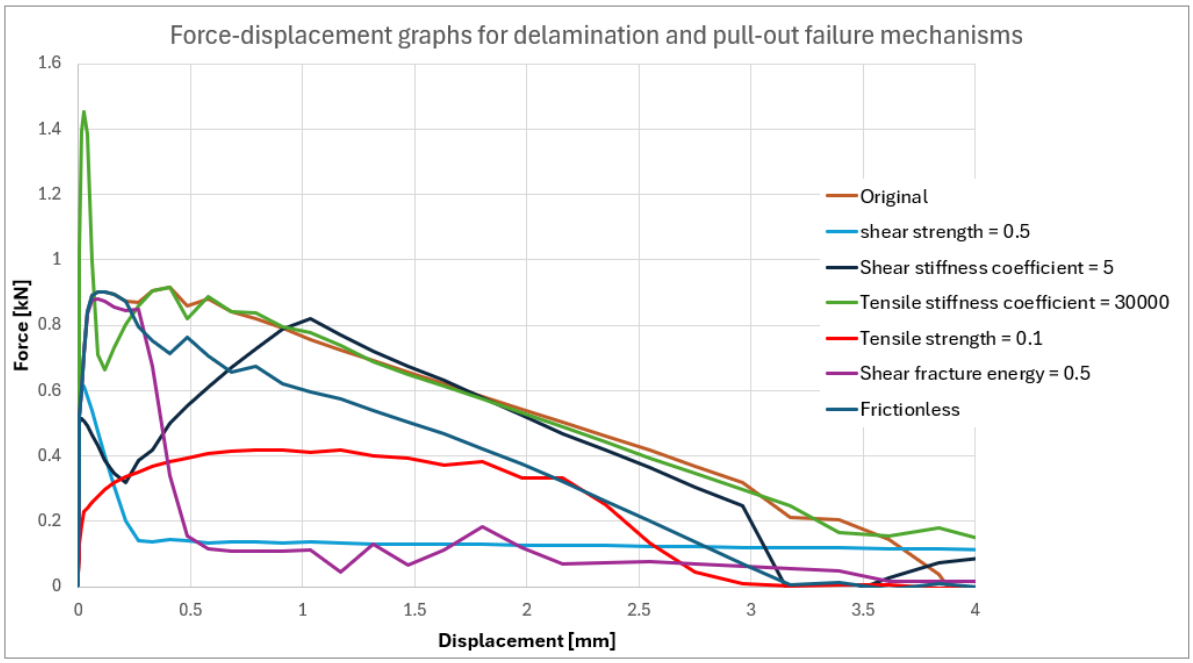

Figure A.84: Force-displacement graphs for the cases where a delamination or pull-out mechanism occurred.

When analyzing the force-displacement behavior for cases exhibiting a tab failure mechanism (see Figure A.85), it becomes apparent that all these cases display a similar post-peak trend in terms of the rate of force decline over displacement. For nearly all cases, except the one with high tensile fracture energy, the force-displacement curves are nearly identical, with only minor variations in the linear elastic stage and in the magnitude and timing of the first and second peaks.

In the high tensile fracture energy scenario, however, both the maximum force and the residual force at the end of the analysis are substantially greater. This increase arises from the high tensile fracture energy, where the allowable stress remains elevated even at larger separations. As a result, the interface continues to theoretically carry stresses despite significant separation, creating a non-physical residual load-bearing capacity. This behavior, though unrealistic for a physical interface, provides insights within the controlled scope of this parametric study.

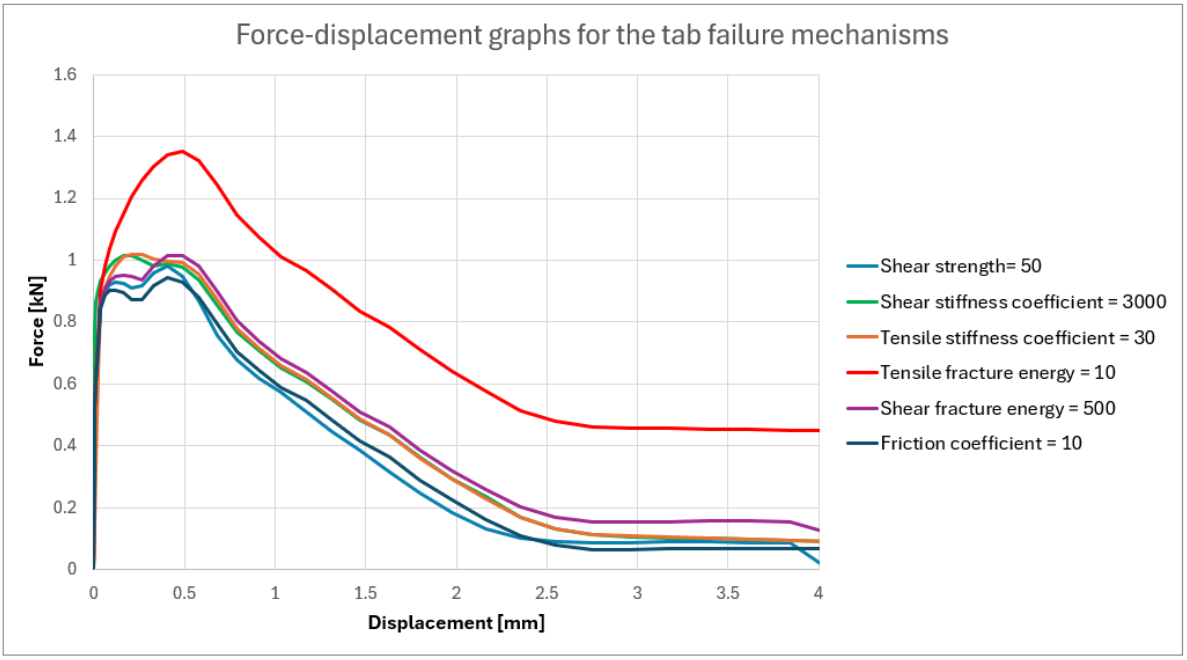

Figure A.85: Force-displacement graphs for the cases where a tab failure mechanism occurred.

In addition to discussing the ultimate failure mechanisms and their associated force-displacement behaviours, the energy absorption, defined as the area under the force-displacement curve up to a displacement of 2.75 mm, was calculated for all parametric study cases and is presented in Figure A.86. From this figure, it is clear that although the material within the tab is not fully activated in the original case, the absorbed energy for this case ranks among the highest, alongside the cases with high tensile strength and high tensile fracture energy. In the high tensile fracture energy case, much of the absorbed energy can be attributed to the plateau that forms after the initial force drop. This plateau is a result of the artificially high traction forces that continue to transfer stresses, even after the realistic failure point has been passed.

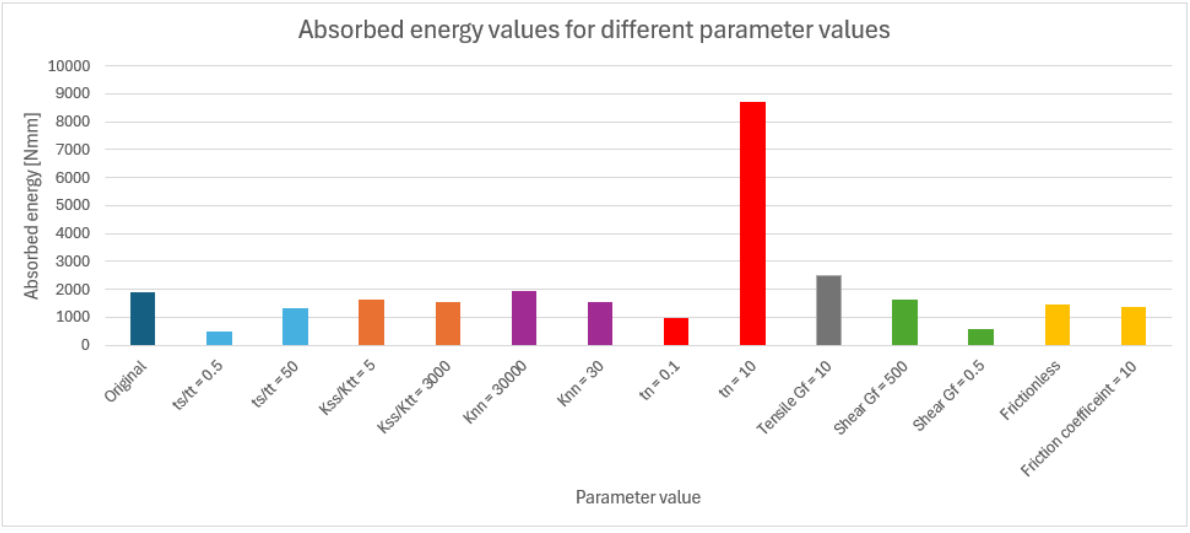

Figure A.86: Absorbed energy, defined as the area underneath the curve up until a displacement of 2.75mm, for all of the parametric analyses.

Significant differences in absorbed energy are observed across several cases, particularly those involving low shear strength, low tensile strength, high tensile strength, and low shear fracture energy.

The high tensile strength case results in the highest absorbed energy due to the extensive activation of material throughout the entire specimen, allowing for higher energy dissipation. On the other hand, the cases of low shear strength and low shear fracture energy exhibit the lowest absorbed energy. This is because, in these scenarios, most of the energy must be absorbed by the tensile interface, which has a very low fracture energy of just 0.09 N/mm, limiting its capacity to sustain significant stress before failure.

In the case of low shear fracture energy, the absorbed energy is slightly higher than that of low shear strength. This is because the full strength of the shear interface is reached, as shown in Figure A.87. For the very low shear strength scenario, the shear fracture energy is kept constant, leading to a high sliding displacement at which the interface fails. This phenomenon explains the plateau observed around a force of 0.2 MPa. If the force-displacement lines for both low shear strength and low shear fracture energy cases were extended to zero, the absorbed energy in the low shear strength case would be even lower than that of the low shear fracture energy case.

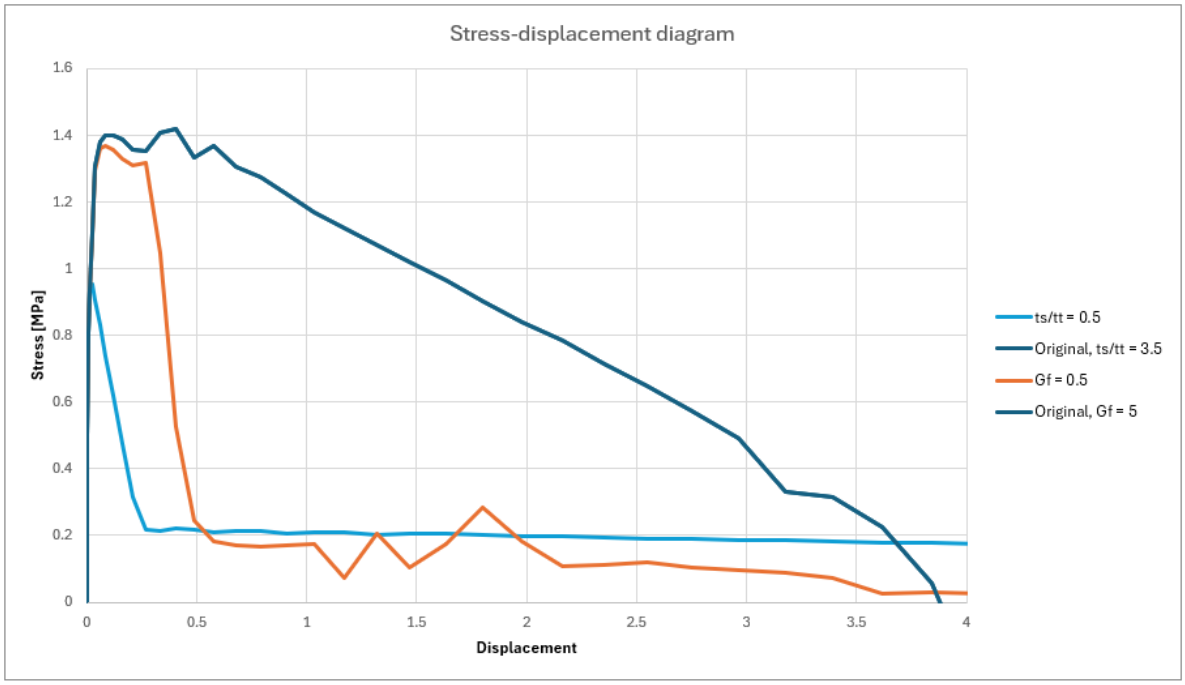

Figure A.87: Stress-displacement diagram for the original case and the low values for the shear strength and shear fracture energy of the interface.

From Table A.2 and Figure A.86, it can be concluded that although the SHCC material inside the tab is activated in cases with tab failure mechanisms, this activation does not significantly increase the amount of energy absorbed in the connection, according to the Abaqus analyses performed. This suggests that, despite the additional material engagement, the overall energy absorption remains relatively unaffected. However, it is important to verify whether the material behavior and ductility predicted by the Abaqus simulations during tab failure align with the ductility observed in experimental tests. Ensuring consistency between numerical and experimental results is crucial for validating the findings.

The shift from a pull-out failure mechanism to a tab failure mechanism helps explain the relatively minor changes observed in terms of displacement capacity and maximum stress in cases of significant changes in for example normal fracture energy, shear fracture energy etc.. This is because the displacement and stress values are quite similar between tab failure and the original case's pull-out failure mechanism. As a result, even though the failure mode changes, the overall structural behavior remains comparable, with only slight variations in performance metrics like displacement and peak stress.

Another set of influential parameters were the interface stiffness coefficients, both normal and shear. These coefficients primarily affect the initial behavior of the connection. When there is a significant dis-

parity between the normal and shear stiffness values, the tensile and shear responses of the interface become more distinct, with each mode operating relatively independently. However, when the stiffness coefficients are more closely aligned, the tensile and shear interfaces work together more effectively. This synergy between the two interfaces enhances the overall structural performance, often resulting in a tab failure mechanism. In this case, the combined tensile and shear capacity of the interface is utilized more efficiently, leading to a more cohesive and robust response under loading.

B

Failure mechanism identification parametric study

The parametric study investigated the effects of various interface parameters on connection behavior, aiming to understand how changes in friction, stiffness, contact stresses, and fracture energy influence the failure mechanisms.

The quantitative analytical analysis in section 3.2 identified five potential failure mechanisms. However, using the analytical model it was not possible to identify the fifth failure mode, side failure.

1. **Delamination Mechanism**: The interface separates with minimal activation of the SHCC material, resulting in reduced load capacity, primarily governed by the interface's traction-separation and shear slidign law in combination with friction. The failure occurs along the interface itself.
2. **Pull-Out Mechanism**: The tab is gradually extracted, with cracking occurring in the material both inside and around the tab. Rather than failing, the tab is pulled out intact.
3. **Tab Failure Mechanism**: Cracking develops inside and around the tab, ultimately causing failure within the tab material itself, driven by stress concentrations at its base.
4. **Material Failure Mechanism**: Multiple cracks form within the SHCC material, with no cracking along the interface, as though the interface were absent.
5. **Side Failure Mechanism**: Cracking develops along the sides of the tab, with dominant cracks forming at the top edges. This occurs due to non-homogeneous conditions or stress concentrations around the tab's top corners, while the bottom interface remains unaffected.

In the parametric study conducted using the continuum smeared cracking model (the Abaqus model), the observed failure mechanisms align with the classifications established in the analytical study. This parallel categorization allows for a consistent comparison of failure behaviors across both analytical and numerical analyses, providing further insights into the underlying mechanics of each failure mode.

It is important to note that, although the responses from the parametric study are compared to those from the analytical study, different constitutive laws for the shear and tensile interfaces were used in each case. Additionally, in the parametric study, parameters are altered one at a time, while in the analytical analysis, both the tensile and shear strengths were changed simultaneously, with other parameters held constant. This difference in approach indicates that as long as the interface governs the displacement response of the connection, making a direct, quantitative comparison between the two studies is challenging.

However, qualitative comparisons remain possible, particularly regarding the failure modes and the mechanisms by which they are induced. Despite the differing constitutive models, the peak forces reached in the various failure mechanisms should be of a similar order of magnitude in both studies,

as the material properties are assumed to be consistent across both analyses. These material properties play a significant role in determining the peak forces available in different failure mechanisms, as demonstrated by the analytical analysis.

Moreover, in failure mechanisms such as the pull-out and material failure modes, where the behavior of the SHCC material dominates the response, the force-displacement results from both the parametric and analytical studies should be quantitatively comparable. This is because, in these cases, the material properties exert the primary influence on the connection's behavior, rather than the specific interface properties.

Below, the various failure mechanisms are examined in detail. The results from the parametric study are discussed and compared to the analytical findings. Additionally, for each failure mechanism, a specific case from the parametric study is highlighted, focusing on the fracture response as indicated by the plastic strain. This response is analyzed, discussed and compared to experimental results from the same failure mechanism to provide deeper insights into each mechanism.

B.1. 1. Delamination

The delamination failure mechanism is characterized by the lack of significant cracking of the SHCC material within or around the tab. For the classification of failure mechanisms in this parametric study, minor and highly localized plastic strains, which represents cracking behaviour in the model, are permissible, provided they do not contribute meaningfully to material deformation.

There are two different cases from the parametric study in which a delamination mechanism is observed. The force-displacement behaviour of those two cases are shown in Figure B.1, where they are also compared to the analytical result from the delamination mechanism. Down below the two different cases are discussed.

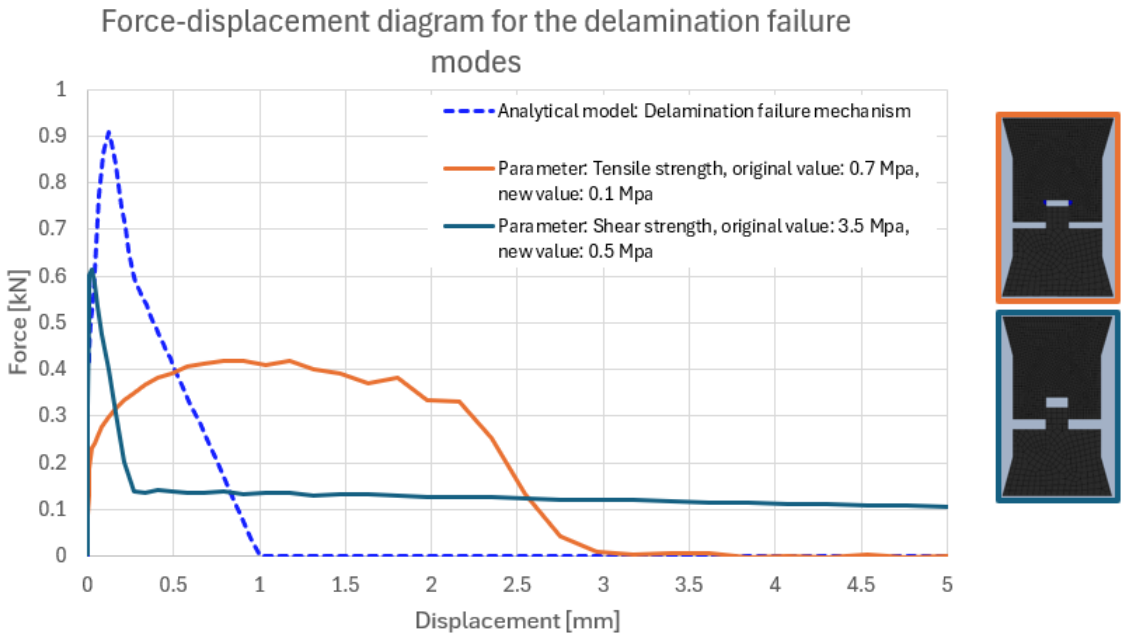

(a) Force-displacement behavior of the two parametric study cases in which a delamination failure mechanism occurred, including the analytical force-displacement behavior of a delamination failure mechanism.

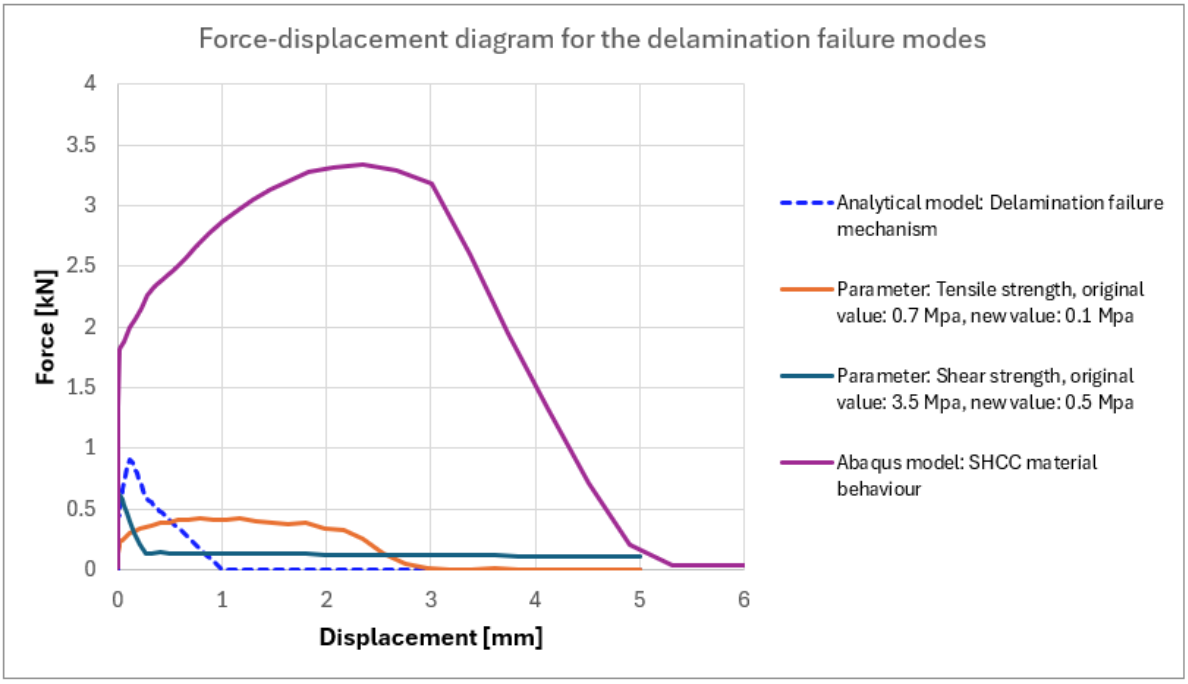

(b) Force-displacement behavior of the two parametric study cases in which a delamination failure mechanism occurred, including the analytical force-displacement behavior of a delamination failure mechanism and the force-displacement behavior of SHCC material.

Figure B.1: Force-displacement behavior of the two parametric study cases in which a delamination failure mechanism occurred.

1. **Low tensile strength:** In the first case of delamination, a very low tensile strength of 0.1 MPa is applied. This minimal tensile strength causes the connection's response to be dominated by the shear behavior along the vertical interfaces. The result is a substantial displacement capacity, primarily due to shear-sliding along these interfaces. However, the low tensile strength prevents the development of any significant peak force, leading to an overall reduced strength capacity in this scenario.

2. **Low Shear Strength:** In the second case, a very low shear strength of 0.5 MPa is applied. The force-displacement response closely aligns with the traction-separation law established for the tensile interface, indicating that the low shear strength renders the response nearly entirely dependent on the tensile interface behavior. It is important to note that the plateau observed following the steep drop in force represents a non-physical phenomenon stemming from the approach taken in the parametric study. Specifically, reducing the shear strength while maintaining the same fracture energy results in a low shear strength over an extensive sliding range, which leads to the emergence of this plateau.

As previously mentioned, while a direct quantitative comparison of the displacement behavior between the analytical results and the parametric study is difficult, it is possible to compare peak forces. As shown in Figure B.1a, the peak forces are similar across all three analyses, ranging from approximately 0.41 MPa to 0.62 MPa. The force-displacement responses indicate that the load-bearing capacity of the interface, when exhibiting a delamination failure mechanism, is notably low.

To illustrate the limited fracture response observed in the delamination failure mechanism, the parametric study case featuring low tensile strength is highlighted. In Figure B.2, the fracture response of the sample is depicted using plastic strain images. These images reveal that there is almost no plastic strain present in the specimen, with the only observable plastic deformation being highly localized and minimal, occurring in the material surrounding the top corners of the tab. This indicates that if a crack were to form, it would likely initiate at the top corners of the tab, albeit with minimal magnitude.

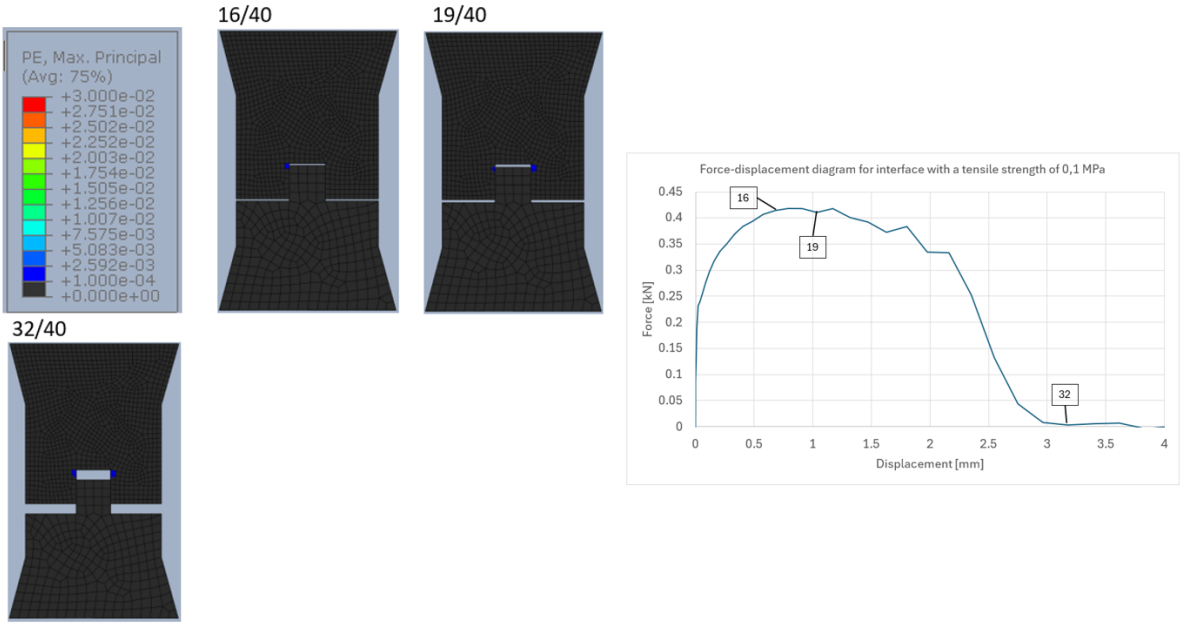

Figure B.2: Fracture response of the delamination failure mechanism for the low tensile strength parametric case, indicated by the plastic strain

In comparison, the literature reveals a similar delamination failure mechanism observed in one of the experimentally tested specimens reported in [21]. The fracture response depicted in Figure B.3 shows a clear absence of cracking within the tab and the surrounding material. The only visible cracks are located at the top corners of the tab, consistent with the predictions from the plastic strain analysis. This correlation between the numerical and experimental results reinforces the findings from the parametric study for the delamination failure mechanism.

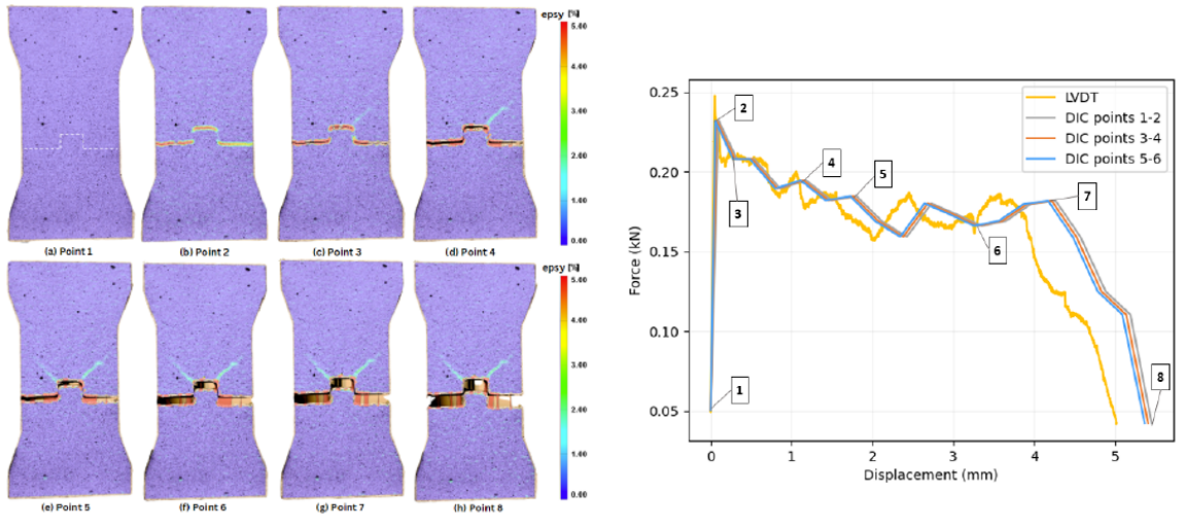

Figure B.3: Fracture response of the delamination failure mechanism as was presented in the experimental SLG12 specimen from [21].

B.2. 2. Pull-out

The pull-out mechanism is characterized by a combined interaction of sliding along the vertical shear interfaces and cracking within the SHCC material both inside and surrounding the tab.

In the original parametric study case, the observed failure mechanism was pull-out, where sliding along the shear interface occurred alongside cracking in the SHCC material within the tab, represented in Abaqus by plastic strain. Across the parametric study, five different variations of this pull-out mechanism are evident of which one is the original case, each showing distinct force-displacement responses. This variability arises not only from the extent of material activation, which ranges from moderate to extensive cracking within the tab, but also from the influence of the defined shear-sliding model on displacement behavior. Together, these factors shape both the deformation characteristics and the residual load-bearing capacity of the specimen, underscoring how both material activation and shear-sliding definitions contribute critically to the overall mechanical response.

The force-displacement behavior of the different cases in which a pull-out failure mechanism was observed, are shown in Figure B.4. Down below the four different cases of the parametric study are shortly discussed.

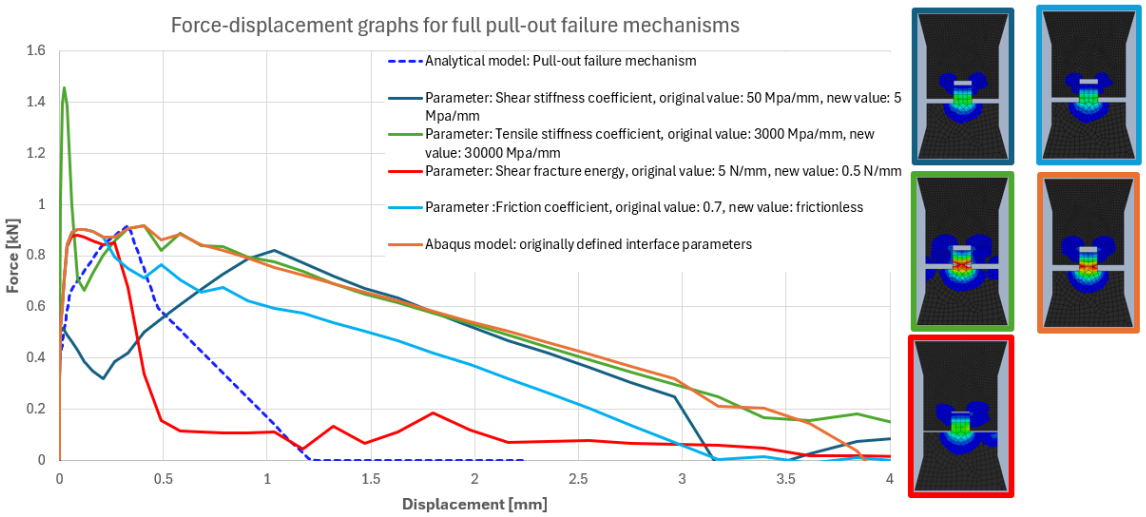

(a) Force-displacement behavior of the five parametric study cases in which a pull-out failure mechanism occurred, including the analytical force-displacement behavior of a pull-out failure mechanism.

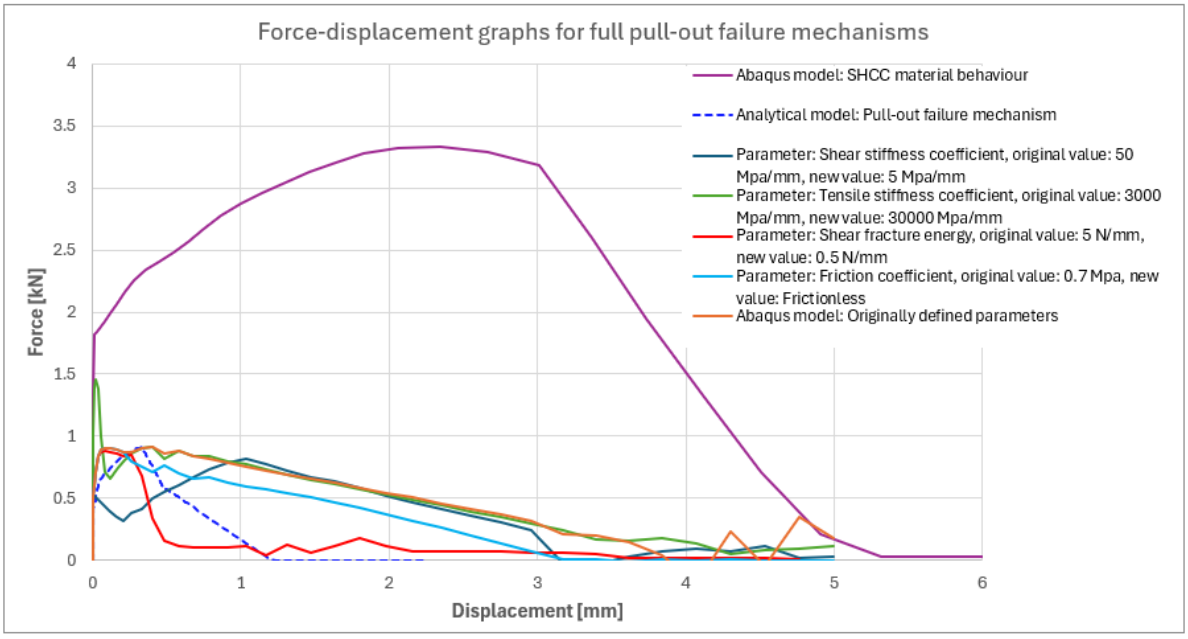

(b) Force-displacement behavior of the five parametric study cases in which a pull-out failure mechanism occurred, including the analytical force-displacement behavior of a pull-out failure mechanism and the force-displacement behavior of SHCC material.

Figure B.4: Force-displacement behavior of the five parametric study cases in which a pull-out failure mechanism occurred.

1. **Low shear stiffness coefficient:** In the first pull-out mechanism case, a very low shear stiffness coefficient is applied, creating a substantial difference between the tensile and shear stiffness values. This difference causes the tensile response of the horizontal interface to engage before the shear response of the vertical interface is activated. In the force-displacement graph, this is evident: an initial peak corresponds to the tensile response of the horizontal interface, after which the force declines following the tensile peak. Once this peak force is reached and the tensile response subsides, the force begins to increase again as the shear interface becomes active, taking over the load-bearing response.

2. **High tensile stiffness coefficient:**In the second pull-out mechanism case, a very high tensile stiffness coefficient is applied, again creating a substantial disparity between the tensile and shear stiffness values. This elevated tensile stiffness causes the force to reach a significantly high peak at the initial stage of the analysis. As detailed in Appendix A, this high peak force should not be interpreted as a prediction of physical response; instead, it reflects a numerical inconsistency within the model due to the combination of an excessively high stiffness coefficient with a comparatively low maximum stress capacity.

   Despite this numerical artifact, the results do suggest that, in cases where tensile stiffness is elevated, the initial tensile peak occurs earlier in the force-displacement response. This setup is likely to produce a separated response in the tensile and shear interface behaviors, similar to what was observed in the low shear stiffness coefficient case.

3. **Low shear fracture energy:** The third case in which a pull-out mechanism occurs involves a very low shear fracture energy. This reduction in shear fracture energy significantly limits the maximum displacement capacity in the shear-sliding law, leading to a notable effect on the force-displacement response of the connection. Initially, the response is similar to that of the original parametric study case, where the connection reaches a peak force. However, after reaching this peak, the force drops sharply. This rapid decline is attributed to the reduced sliding capacity of the vertical interfaces, which limits the extent of post-peak deformation.

4. **No friction:** The fourth case in which a pull-out mechanism occurs is when no friction is included in the model. As can be expected, friction influences the behavior after damage initiates in the

shear interface. This effect is visible in the force-displacement graph, where the response initially follows the same trend as in the original case. Once the peak force is reached, the force drops slightly before aligning precisely with the trend observed in the original interface configuration. This similarity indicates that friction mainly contributes to the load-bearing capacity post-peak, reinforcing the overall behavior but not altering the initial failure progression.

From these observations, it becomes evident that when the tensile and shear stiffness coefficients differ substantially in magnitude, the interfaces fail to interact cohesively, preventing the transfer of stresses needed to induce failure within the SHCC material itself. Instead, this imbalance leads to a predominant pull-out mechanism.

It is also notable that reducing friction alone does not significantly impact either the failure mode or the force-displacement response, particularly in cases where the friction coefficient is 0.7 or lower. This suggests that friction primarily acts as a secondary resistance force, rather than a primary mechanism influencing the overall connection behavior. The response with and without friction remains largely consistent until after the peak force, indicating that friction's role is more supplementary. However, as will be seen in the next failure mode, a significantly higher friction coefficient may alter the failure mode and behavior of the connection, potentially enhancing the load-bearing capacity and modifying the interaction between the interfaces.

In contrast, changes in shear fracture energy—impacting the maximum allowable sliding in the shear-sliding behavior—have a considerable effect on the force-displacement response. Reducing shear fracture energy directly limits the sliding capacity at the vertical interfaces, resulting in a sharply reduced displacement capacity of the connection. This reduction accelerates the force drop post-peak, diminishing the interface's ability to redistribute stress.

When comparing the behavior of the analytical pull-out mechanism to the parametric cases exhibiting a pull-out failure mechanism, it is evident that the peak force remains consistent across all scenarios, with a magnitude of approximately 0.9 MPa. This peak force is significantly higher than that observed in delamination failure mechanisms. As previously mentioned, while a direct quantitative comparison of displacement capacity between the two models is not feasible, trends can still be identified. In both the analytical case and the parametric study, displacement capacity tends to increase as cracking in the SHCC is incorporated into the pull-out mechanism. The notable exception occurs in the case with a low shear fracture energy, where the ultimate sliding value of the shear-sliding law is considerably reduced.

To illustrate the fracture response in the pull-out failure mechanism, the frictionless case from the parametric study is highlighted. In Figure B.5, the plastic strain images reveal the progression of deformation within the sample. Plastic deformation initiates at the bottom of the tab and in the material around the top corners of the tab. As loading increases, the magnitude of plastic strain intensifies, particularly within the tab itself, with the most notable concentration toward the lower region of the tab.

At the same time, the surrounding material shows an expansion of the affected area, though the plastic strain in these regions remains relatively low in magnitude. After reaching a certain point in the loading process (step 12), the plastic strain no longer increases. Instead, the tab is pulled out without additional cracking or further deformation of the surrounding material.

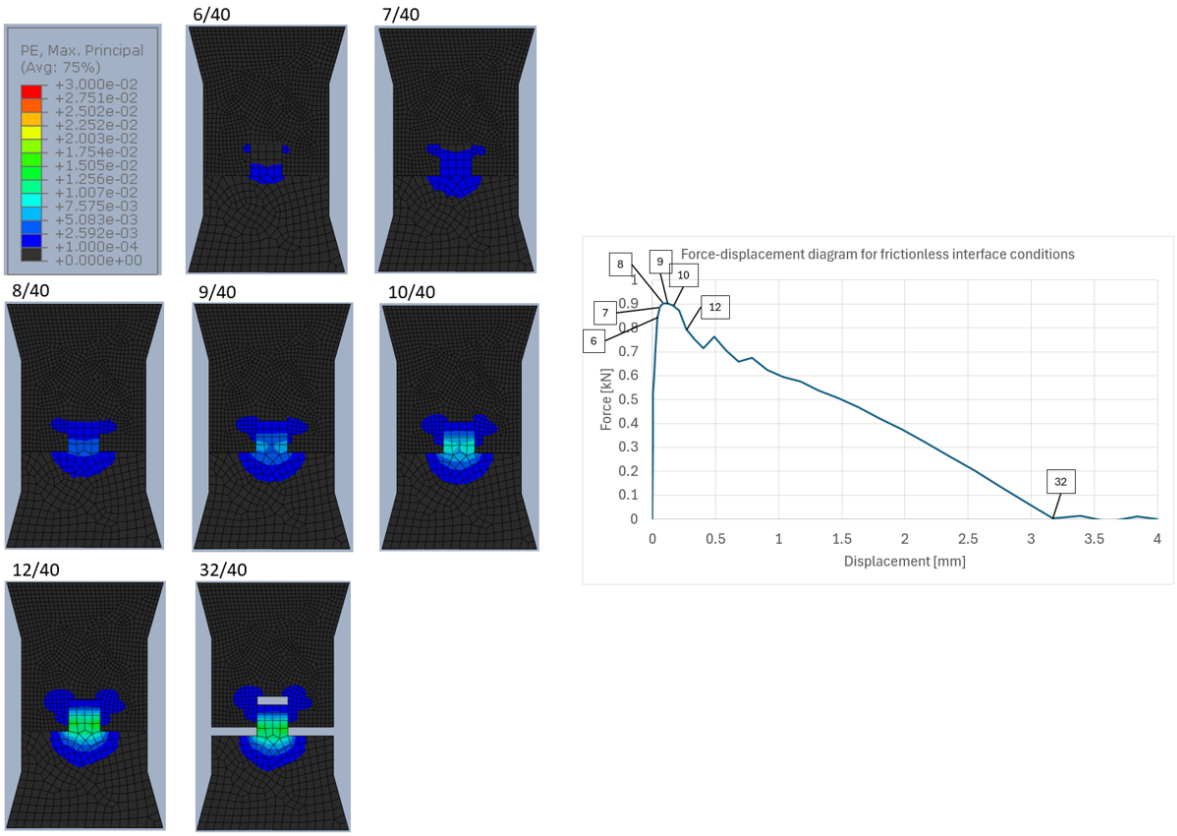

Figure B.5: Fracture response of the pull-out failure mechanism for the frictionless parametric case, indicated by the plastic strain

In comparison, the literature documents a similar pull-out failure mechanism in one of the experimentally tested specimens reported in [21]. The fracture response, shown in Figure B.6, reveals clear cracking both inside the tab and in the material surrounding it. This behavior aligns in principle with the fracture pattern predicted by the parametric model. However, a notable difference emerges: in the experimental specimen, there is extensive cracking at the top of the tab, and the cracks in the surrounding material are of similar magnitude to those within the tab. This contrasts with the parametric model, where cracking is more concentrated towards the bottom of the tab, and the surrounding material experiences less severe deformation.

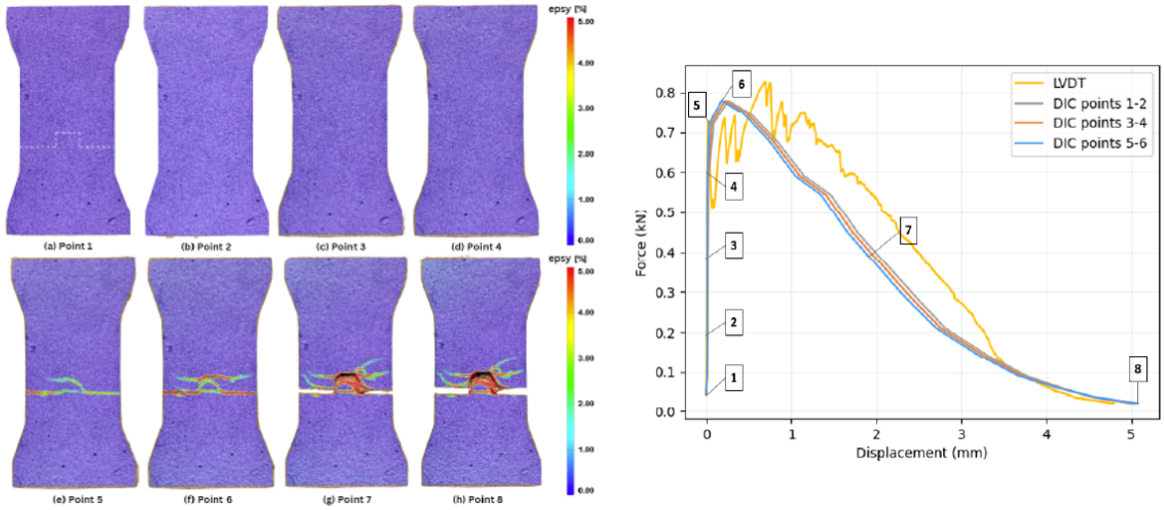

Figure B.6: Fracture response of the pull-out failure mechanism as was presented in the experimental SCG1 specimen from [21].

B.3. 3. Tab failure

In the tab failure mechanism the sliding in the shear interface is combined with cracking inside the tab. But rather than the interface failing in the end, the interface is stronger and the material inside the tab fails in the end. Across the parametric study, there were six different cases where a tab failure occurred. The force displacement behaviors of the various tab failure mechanisms which occurred are presented in Figure B.7. Down below the six different cases of the parametric study are shortly discussed.

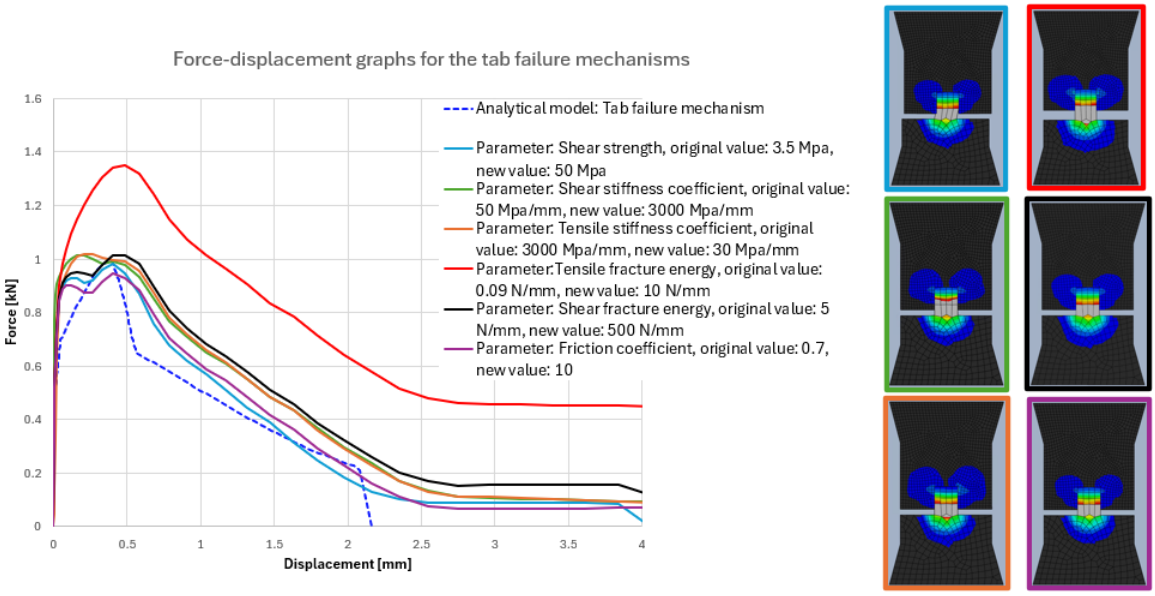

(a) Force-displacement behavior of the six parametric study cases in which a tab failure mechanism occurred, including the analytical force-displacement behavior of a tab failure mechanism.

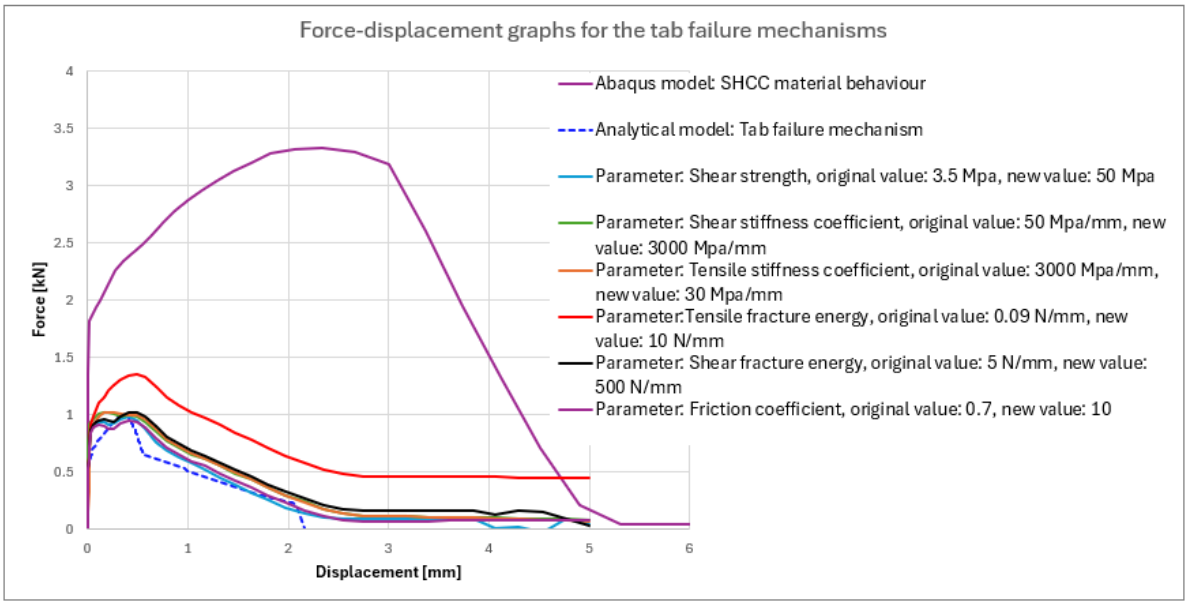

(b) Force-displacement behavior of the five parametric study cases in which a tab failure mechanism occurred, including the analytical force-displacement behavior of a tab failure mechanism and the force-displacement behavior of SHCC material.

Figure B.7: Force-displacement behavior of the six parametric study cases in which a tab failure mechanism occurred.

1. **High shear strength:** The first instance of the tab failure mechanism arises when the interface exhibits a very high shear strength. This elevated strength makes the interface stronger than the SHCC material within the tab, resulting in failure of the tab material, which subsequently dominates the force-displacement response.

2. **High Shear Stiffness Coefficient:** The second case occurs with a high shear stiffness coefficient, where both the shear and tensile stiffness coefficients are of similar magnitude. Unlike the pull-out mechanism, the tensile and shear interfaces effectively work together to support tensile forces on the connection. This synergy makes the interface stronger than the SHCC material inside the tab, causing the tab material to fail and thus dominate the force-displacement response.

3. **Low Tensile Stiffness Coefficient:** Similar to the previous case, a low tensile stiffness coefficient aligns the orders of magnitude of both stiffness coefficients. This configuration allows the interfaces to work effectively together in sustaining stresses on the connection, leading once again to a tab failure mechanism.

4. **High Tensile Fracture Energy:** In the fourth case, a high tensile fracture energy indicates that the ultimate separation at the tensile interface failure is significantly greater than in the original scenario. This capacity allows for substantial force transfer even at large separations of the interface. Consequently, the interface remains stronger than the material inside the tab, leading to the SHCC material dominating the force-displacement response. However, this situation is accompanied by an upward shift in the force-displacement behavior compared to other tab failure mechanisms, attributed to the ability of the horizontal interfaces to transfer significant stresses at large separations. It is important to note that this increase in capacity does not reflect a physical phenomenon but rather a non-physical consequence of the approach taken in the parametric study.

5. **High Shear Fracture Energy:** When high shear fracture energy is present, the sliding value at failure of the shear interface significantly increases, allowing shear stresses to be transferred even at substantial sliding values. This characteristic again makes the interface stronger than the material inside the tab, inducing a tab failure mechanism. In this case, there is no non-physical additional capacity since the failure of the SHCC material leads to a halt in sliding of the shear interfaces, allowing the material behavior to take precedence.

6. **High Friction Coefficient:** Finally, a very high friction coefficient can also induce a tab failure mechanism. Once the shear interface sustains damage, friction plays a crucial role in resisting sliding. With the high friction coefficient, the vertical interfaces can withstand significant stresses at larger sliding values, resulting in a stronger interface that causes the material inside the tab to fail rather than the interface itself.

In the tab failure mechanism, the force-displacement behavior is primarily governed by the material response, allowing for a quantitative comparison between the analytical and parametric models. While some discrepancies are evident between these two models, it is noteworthy that both reach a similar peak force and follow a similar trend.

After achieving the peak force, the analytical model demonstrates a steeper decline in force, followed by a distinct change in behavior associated with the dominant crack formation within the material. In contrast, the transition in the parametric model is much smoother. Despite these differences, the ultimate displacement capacities of both models are very similar, indicating a strong alignment in the predictions of the failure mode between the analytical and parametric approaches.

When comparing the behavior of the tab failure mode to the intrinsic material behavior of the SHCC, it is clear that the displacement capacity remains significantly lower. Even in comparison to the pull-out mechanism in the parametric model, which exhibited a larger displacement capacity, the tab failure mechanism in the parametric model is less capable. This phenomenon does not occur in the analytical model, where the displacement capacity is significantly increased going from a pull-out to tab failure mechanism. Notably, the peak force reached in the tab failure mechanism is slightly higher than that of the pull-out mechanism, this is expected, as a greater stress is transmitted through the tab material.

To illustrate the fracture response in the tab failure mechanism, the parametric study case with a high shear stiffness coefficient is highlighted. In Figure B.8, the plastic strain images display the progression of deformation within the sample. Plastic deformation initiates at the bottom of the tab and in the material around the top corners. As loading increases, the intensity of the plastic strain escalates, particularly within the tab, with the most significant concentration occurring near its lower region.

Simultaneously, the surrounding material shows a marked expansion in the affected area, though the magnitude of plastic strain in these regions remains relatively low. Unlike the pull-out case, where plastic strain plateaued after a certain point, here the plastic strain continues to rise, ultimately leading to material failure at the bottom of the tab.

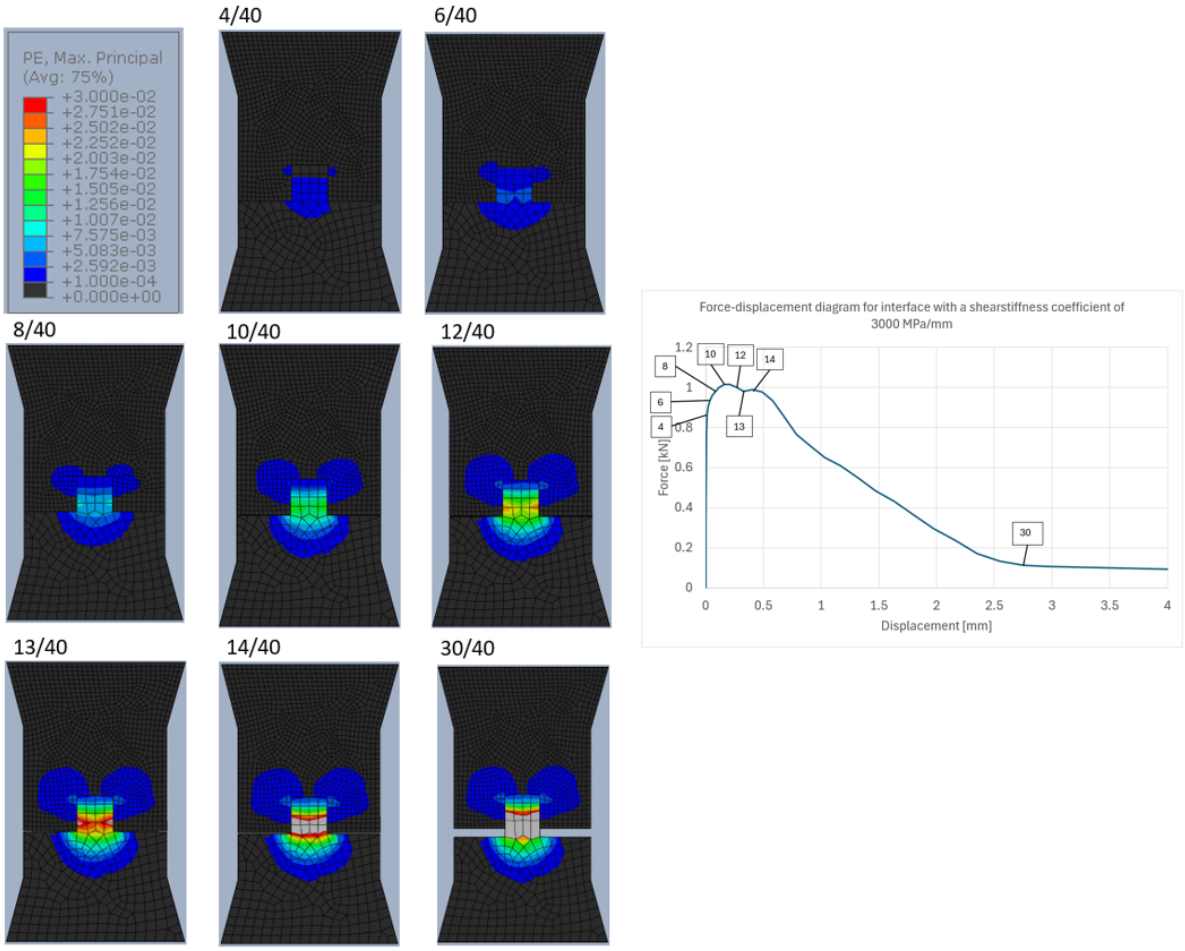

Figure B.8: Fracture response of the tab failure mechanism for the parametric case with a high shear stiffness coefficient, indicated by the plastic strain

In comparison, the literature documents a similar tab failure mechanism observed in one of the experimentally tested specimens reported by Papoulidou [21]. The fracture response, shown in Figure B.9, reveals significant cracking both within the tab and in the surrounding material. Cracks inside the tab extend into the surrounding material and propagate along the full height of the tab. Toward the end of the analysis, a dominant crack forms at the base of the tab, ultimately causing the connection to fail. This behavior generally aligns with the failure mechanism predicted by the parametric model.

However, two key differences stand out. First, the material surrounding the tab in the parametric model exhibits minimal deformation, whereas in the experimental specimen, it sustains significant damage. Second, in the parametric model, cracking is predominantly concentrated at the bottom of the tab, while in the experimental results, extensive cracking is distributed along the entire height of the tab, indicating a more widespread failure in the experimental specimen.

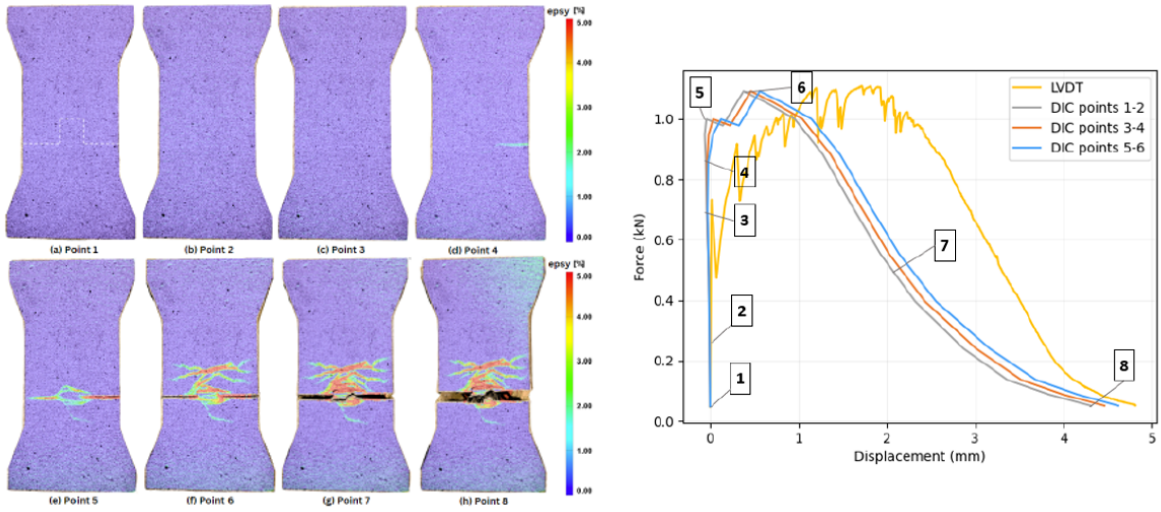

Figure B.9: Fracture response of the tab failure mechanism as was presented in the experimental SCG2 specimen from [21].

B.4. 4. Transitional failure

The fourth failure mechanism represents the failure mechanism where cracking occurs throughout the entire specimen, but at the end, the governing crack goes through both SHCC material and the interface. By utilizing homogeneous properties for both the SHCC material and the interfaces, it becomes feasible to activate this failure mechanism by increasing the interface strength. As observed in the previous failure mechanism, a tensile strength of 10 MPa is excessive, as it results in complete material failure. Therefore, a tensile interface strength equivalent to that of the SHCC material is selected. The force-displacement response associated with this failure mechanism, in comparison to the behavior of the SHCC material, is illustrated in Figure B.10.

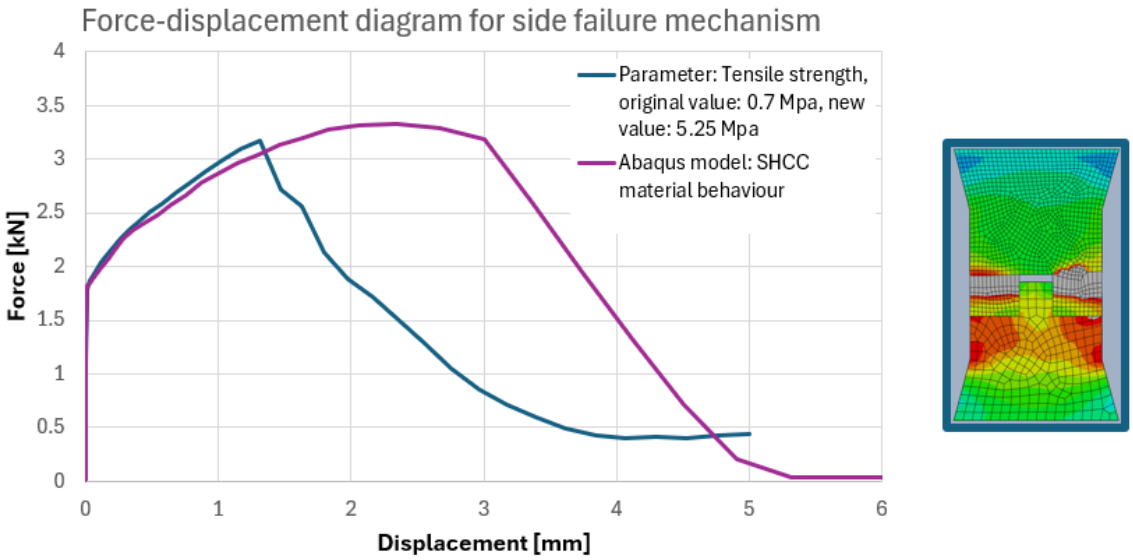

Figure B.10: Force-displacement behavior of the parametric study case in which a side failure mechanism occurred, including the SHCC material force-displacement behavior.

Additionally, the fracture response associated with this failure mechanism is illustrated in Figure B.11. These images reveal that plastic strain initiates around the interface, exhibiting high values particularly

in the bottom part of the specimen, similar to the material failure mechanism. However, in this case, concentrated plastic strain begins to develop around the top corners of the tab, leading to the formation of a dominant crack that subsequently extends toward the sides of the specimen. Continued displacement results in further widening of the crack.

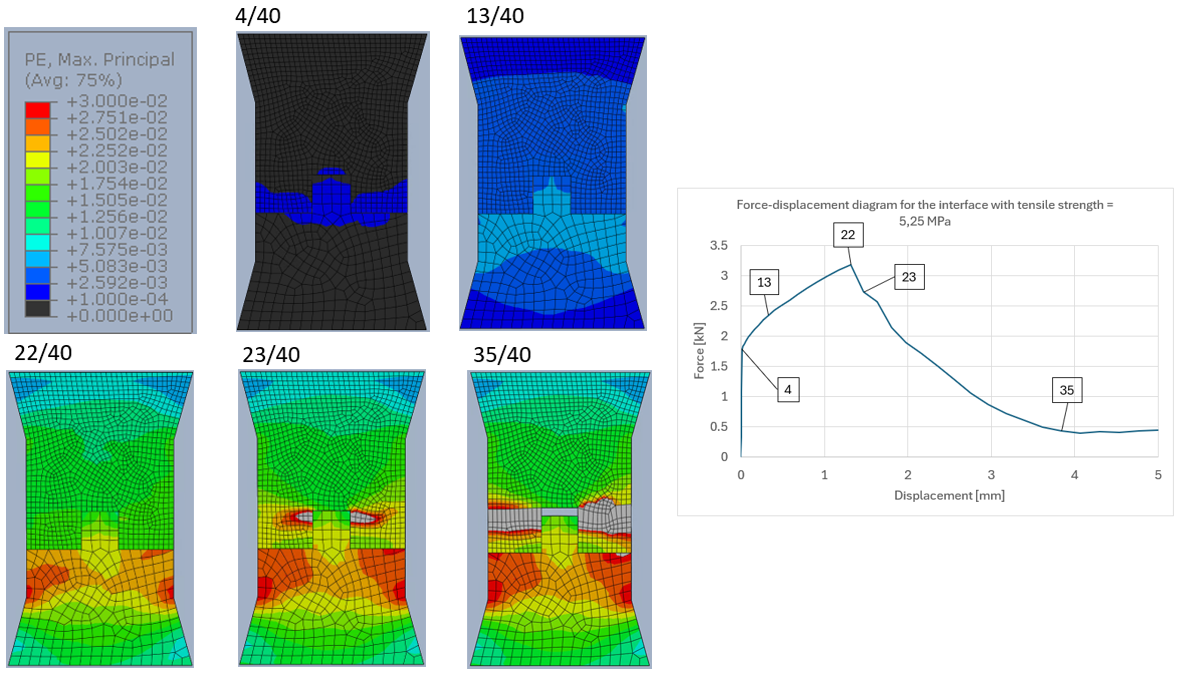

Figure B.11: Fracture response of the side failure mechanism for the Abaqus model with an interfacial tensile strength equal to the material tensile strength.

B.5. 5. Material failure

In material failure mechanism, the connection behaves as though no interface is present, leading to distributed cracking throughout the entire specimen rather than being localized around the interface. Across the parametric study, this failure mechanism was observed in a case with an exceptionally high tensile strength of 10 MPa. The force-displacement behavior for this material failure mechanism is shown in Figure B.12. Down below the parametric case is further discussed.

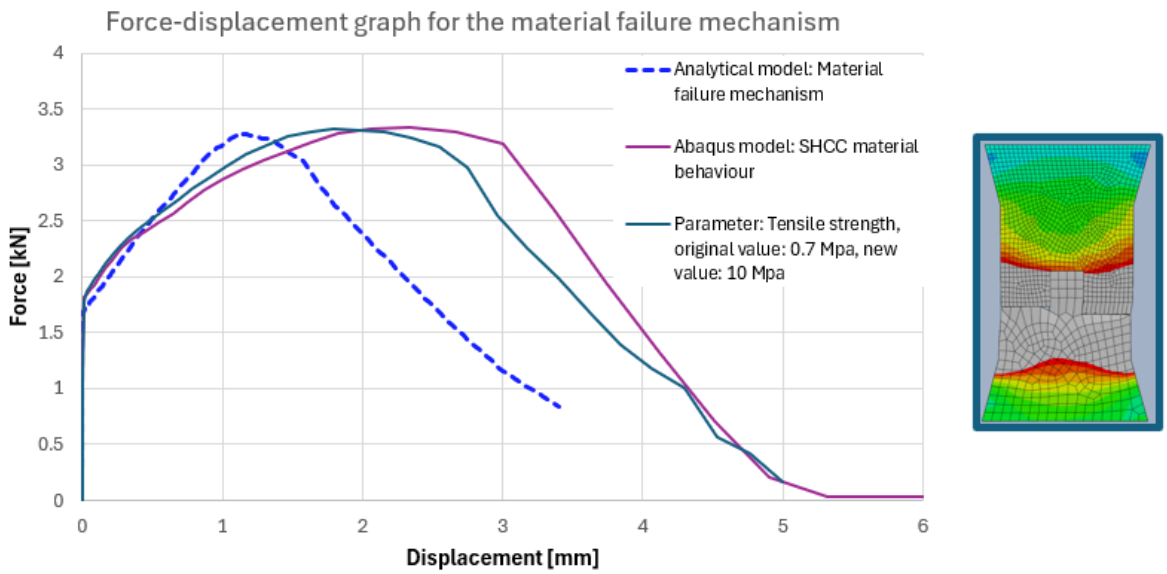

Figure B.12: Force-displacement behavior of the parametric study case in which a material failure mechanism occurred, including the analytical force-displacement behavior of the material failure mechanism and the force-displacement behavior of SHCC material.

1. **High tensile strength:** The only case in the parametric study where material failure occurred was when a significantly high tensile strength was applied. In this scenario, the interface was so strong that the material within the specimen failed before the interface itself could reach failure.

In the material failure mechanism, the force-displacement behavior of the specimen is governed entirely by the material response of the SHCC. However, a slight discrepancy can be observed between the force-displacement behavior of the SHCC material and that of the specimen experiencing material failure due to the high tensile strength of the interface. This difference in behavior can be attributed to two factors. First, the SHCC material response comes from a dogbone specimen with a different surface area and a uniform mesh size of 3mm. In contrast, the specimen uses a combination of 1.5mm and 3mm mesh to model different regions. Second, minor stress concentrations may still arise in the specimen due to variations in strength and stiffness at the interface, despite its high tensile strength.

Moreover, a significant difference is observed between the force-displacement behavior of the analytical model and the parametric model. However, this discrepancy can be explained by the difference in gauge length used to measure displacement. The parametric model uses a gauge length of 75mm, whereas the analytical model assumes a specimen height of 45mm. Consequently, the displacement behavior cannot be directly compared. A more accurate comparison would involve analyzing the strains, as shown in Figure B.13. Here, slight differences in behavior are visible, but these are due to the variation in how the SHCC material behavior is defined, rather than any fundamental difference in the failure mechanism itself.

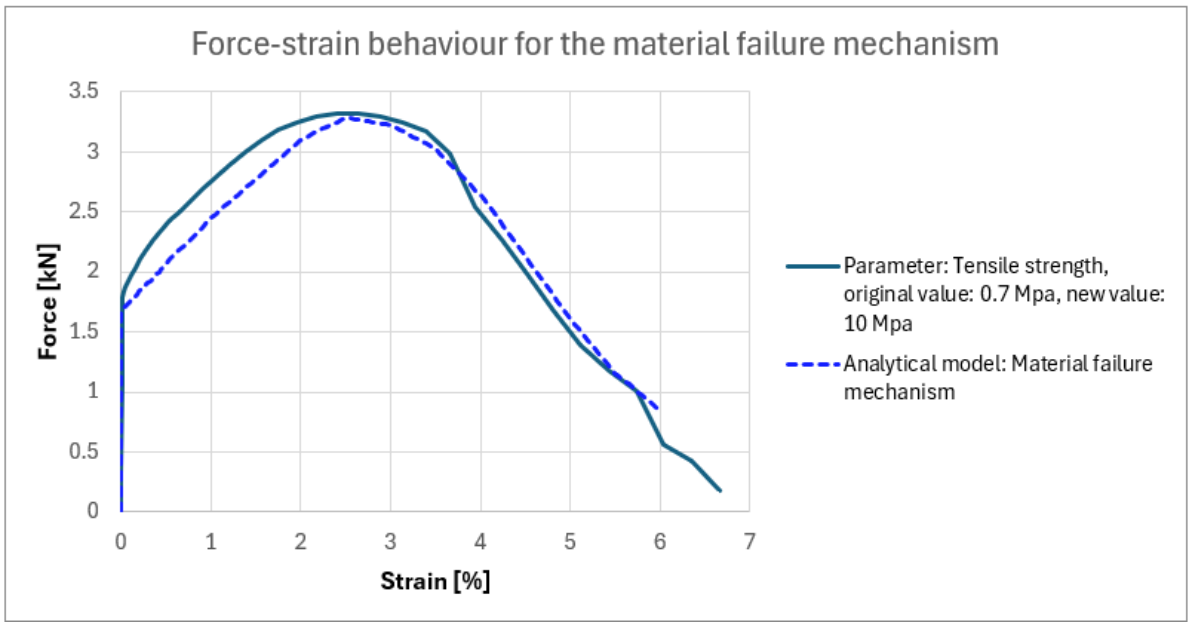

Figure B.13: Force-strain behavior of the parametric study case in which a material failure mechanism occurred, including the analytical force-strain behavior of the material failure mechanism.

To illustrate the fracture response associated with the material failure mechanism, the plastic strain distribution from the parametric study is presented in Figure B.14. Initial plastic strain is observed around the interface, subsequently propagating throughout the entire specimen. The majority of the plastic strain is concentrated in the bottom part of the specimen, followed by significant strain development in the upper region adjacent to the tab, where material failure occurs along the interface, but not within it. This behavior is more distinctly highlighted in Figure B.15, which utilizes a different color scale to depict plastic strain at the final step of the analysis. Here, it is evident that a dominant crack has formed in the material along the interface and through the material in the tab.

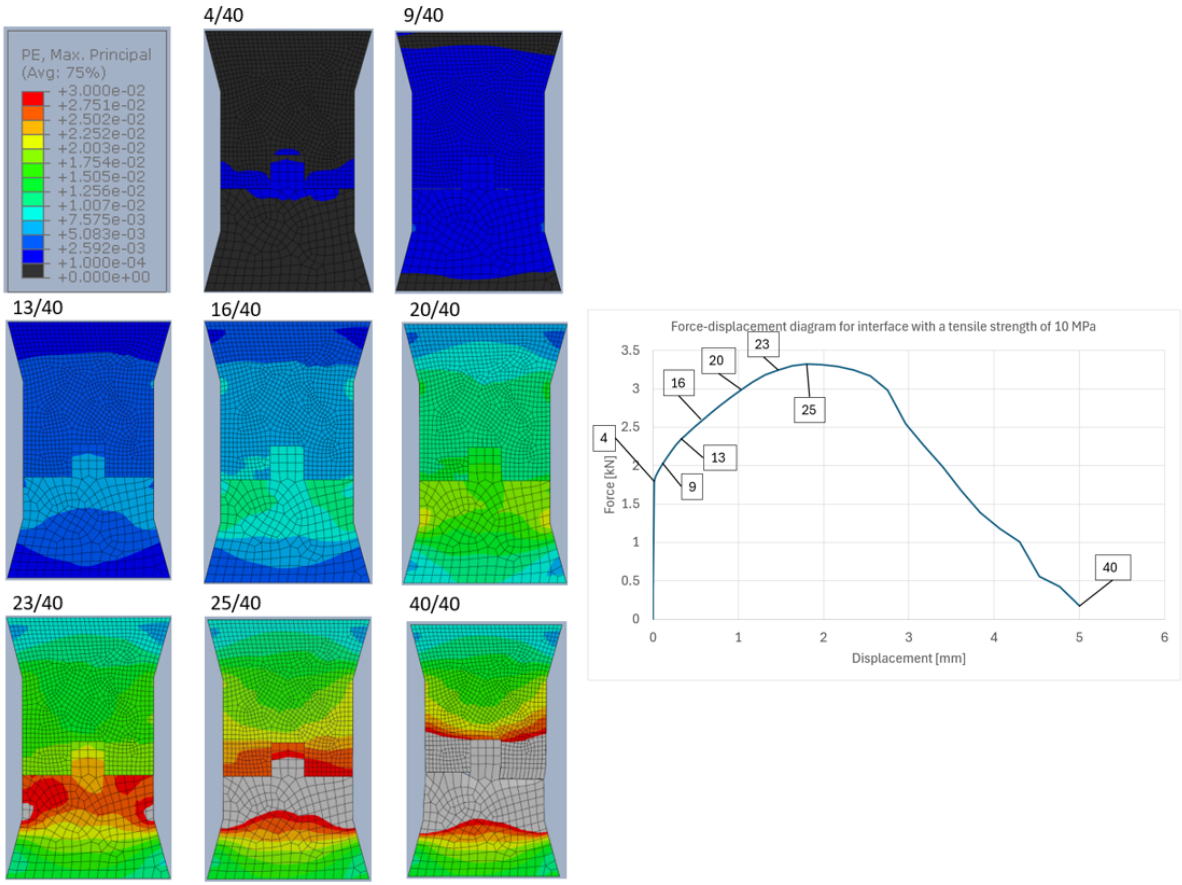

Figure B.14: Fracture response, indicated by plastic strain, of the material failure mechanism for the Abaqus model with an interfacial tensile strength of 10 MPa.

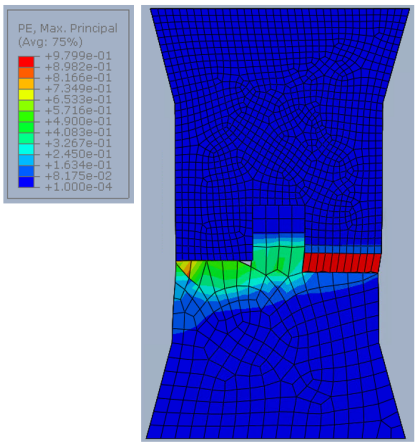

Figure B.15: Fracture response, indicated by the plastic strain, of the last step in the analysis of the Abaqus model with an interfacial tensile strength of 10 MPa, presenting a material failure mechanism

C

Lattice model results

C.1. Interface design with a width-to-height ratio of 1.5; different interface strengths

C.1.1. Interface strength 5%, w/h = 1.5

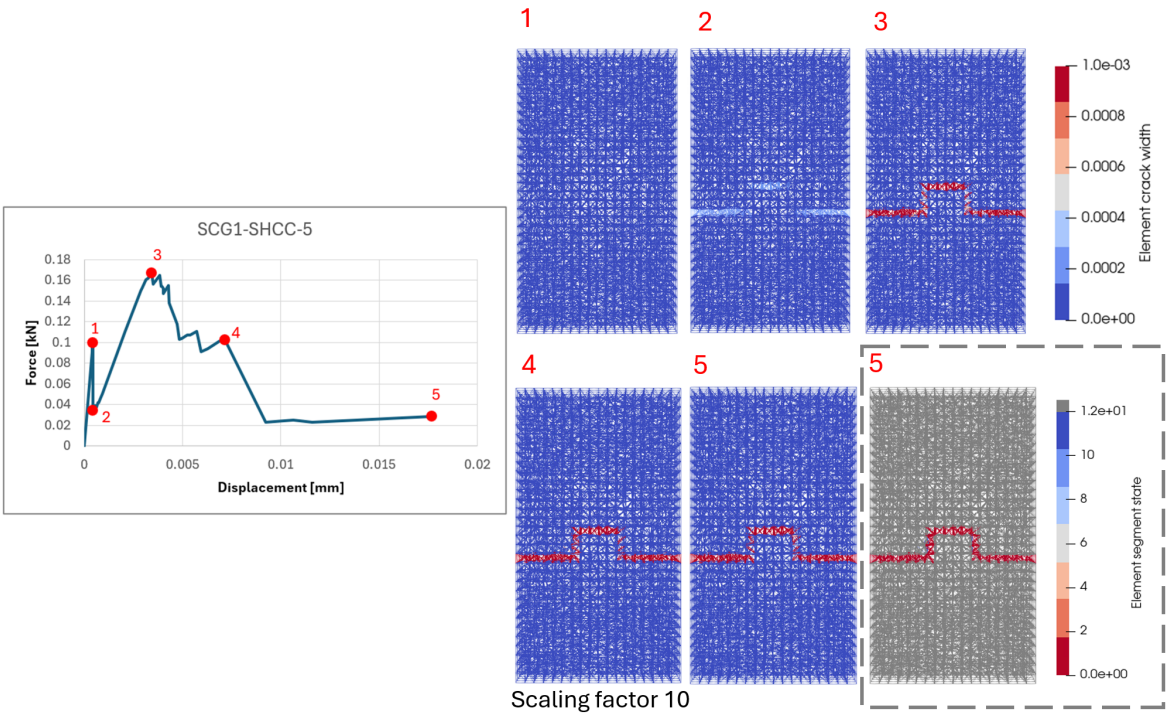

Figure C.1: Lattice model results for the SCG1-SHCC-5 specimen with 5% interface strength. The force-displacement curve is on the left, and the fracture response is on the right. In the grey box (final stage), grey represents undamaged elements, blue to red indicates increasing damage, and for the interface, pink denotes undamaged elements and red indicates damaged ones.

C.1.2. Interface strength 10%, w/h = 1.5

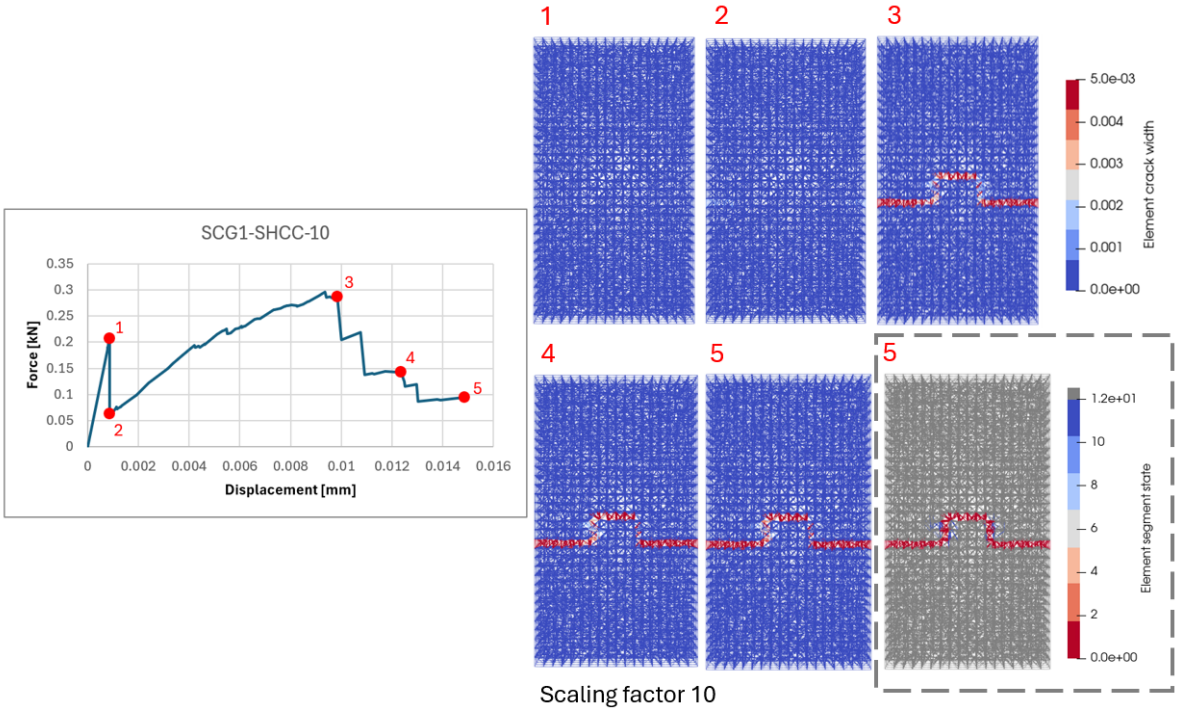

Figure C.2: Lattice model results for the SCG1-SHCC-10 specimen with 10% interface strength. The force-displacement curve is on the left, and the fracture response is on the right. In the grey box (final stage), grey represents undamaged elements, blue to red indicates increasing damage, and for the interface, pink denotes undamaged elements and red indicates damaged ones.

C.1.3. Interface strength 15%, w/h = 1.5

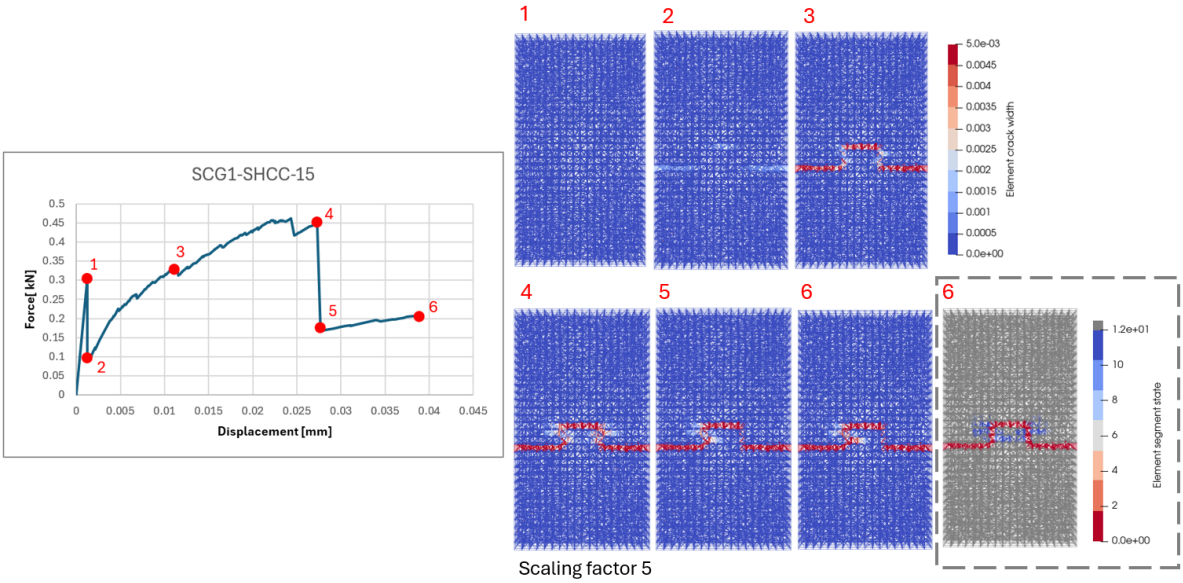

Figure C.3: Lattice model results for the SCG1-SHCC-15 specimen with 15% interface strength. The force-displacement curve is on the left, and the fracture response is on the right. In the grey box (final stage), grey represents undamaged elements, blue to red indicates increasing damage, and for the interface, pink denotes undamaged elements and red indicates damaged ones.

C.1.4. Interface strength 20%, w/h = 1.5

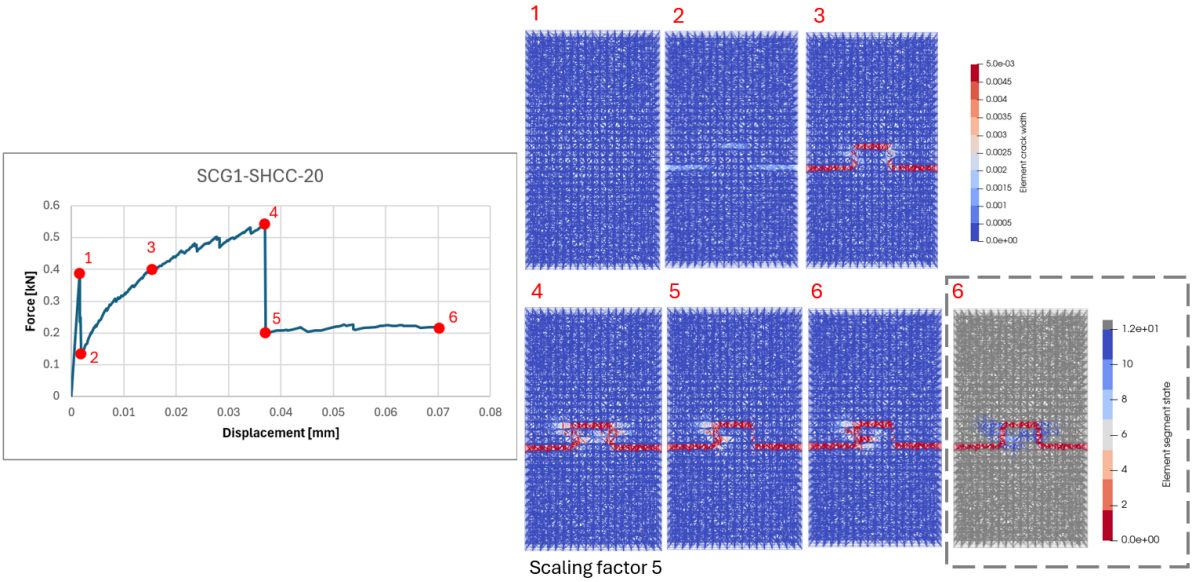

Figure C.4: Lattice model results for the SCG1-SHCC-20 specimen with 20% interface strength. The force-displacement curve is on the left, and the fracture response is on the right. In the grey box (final stage), grey represents undamaged elements, blue to red indicates increasing damage, and for the interface, pink denotes undamaged elements and red indicates damaged ones.

C.1.5. Interface strength 25%, w/h = 1.5

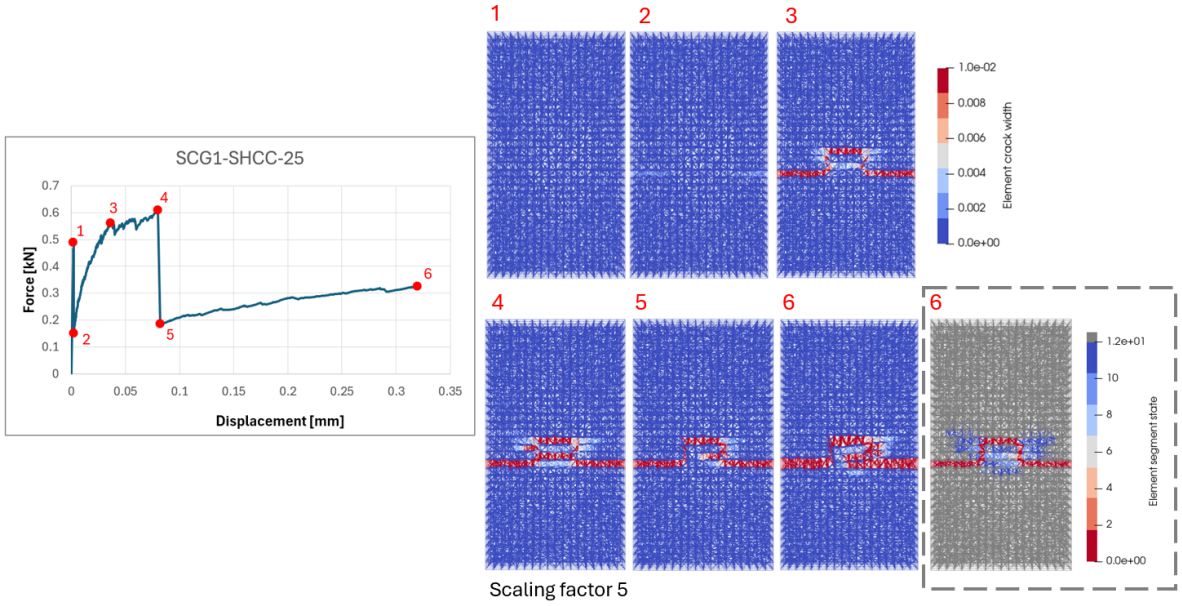

Figure C.5: Lattice model results for the SCG1-SHCC-25 specimen with 25% interface strength. The force-displacement curve is on the left, and the fracture response is on the right. In the grey box (final stage), grey represents undamaged elements, blue to red indicates increasing damage, and for the interface, pink denotes undamaged elements and red indicates damaged ones.

C.1.6. Interface strength 30%, w/h = 1.5

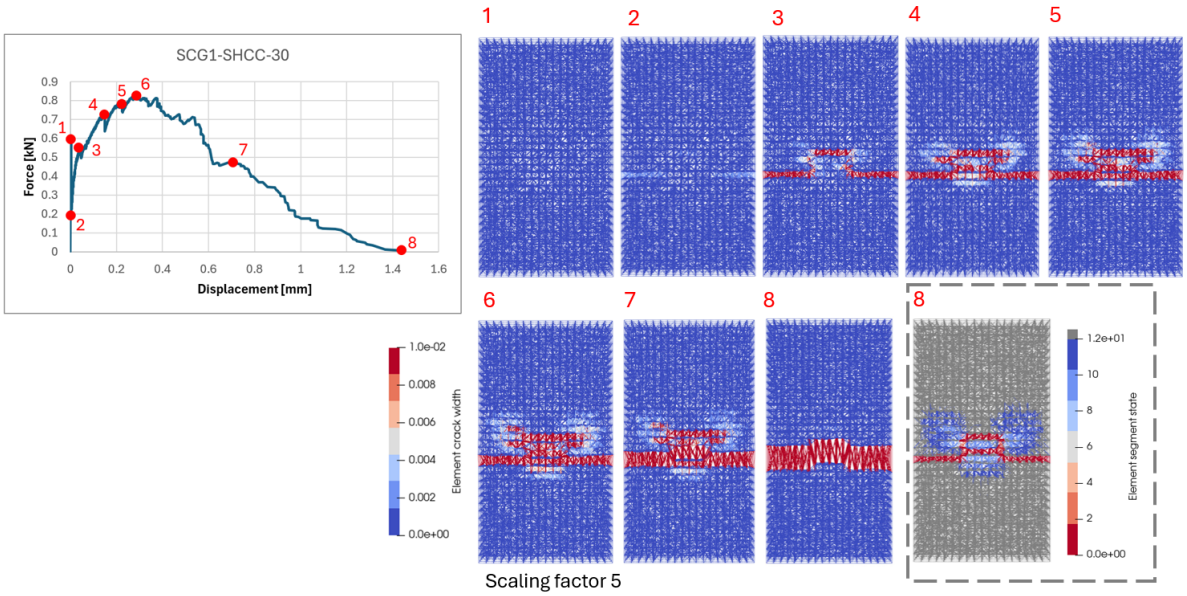

Figure C.6: Lattice model results for the SCG1-SHCC-30 specimen with 30% interface strength. The force-displacement curve is on the left, and the fracture response is on the right. In the grey box (final stage), grey represents undamaged elements, blue to red indicates increasing damage, and for the interface, pink denotes undamaged elements and red indicates damaged ones.

C.1.7. Interface strength 50%, w/h = 1.5

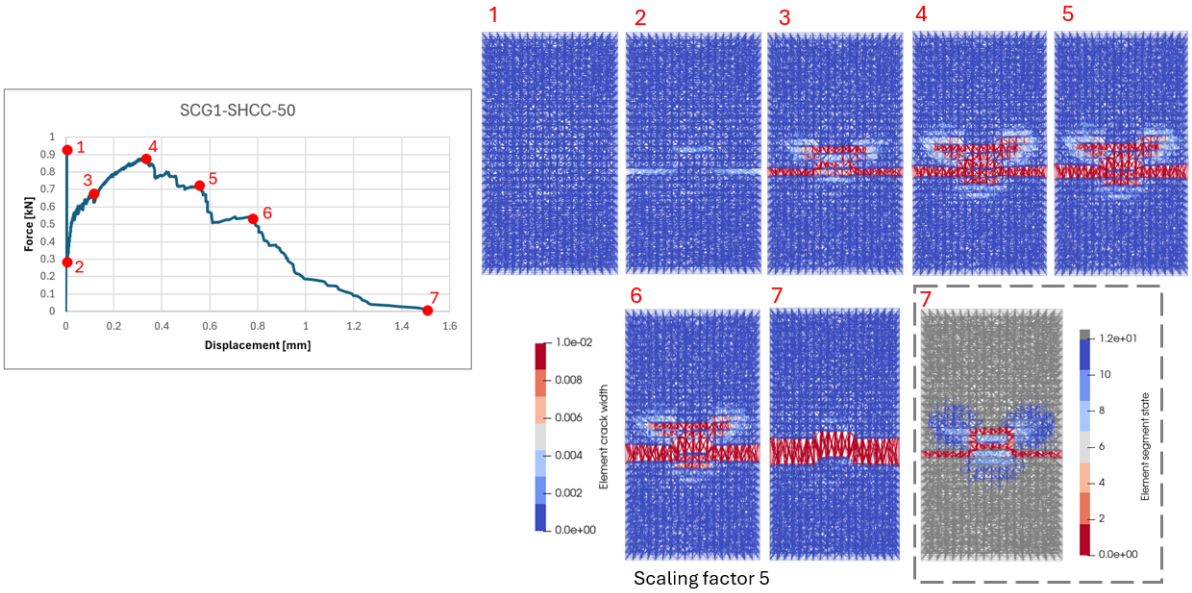

Figure C.7: Lattice model results for the SCG1-SHCC-50 specimen with 50% interface strength. The force-displacement curve is on the left, and the fracture response is on the right. In the grey box (final stage), grey represents undamaged elements, blue to red indicates increasing damage, and for the interface, pink denotes undamaged elements and red indicates damaged ones.

C.1.8. Interface strength 75%, w/h = 1.5

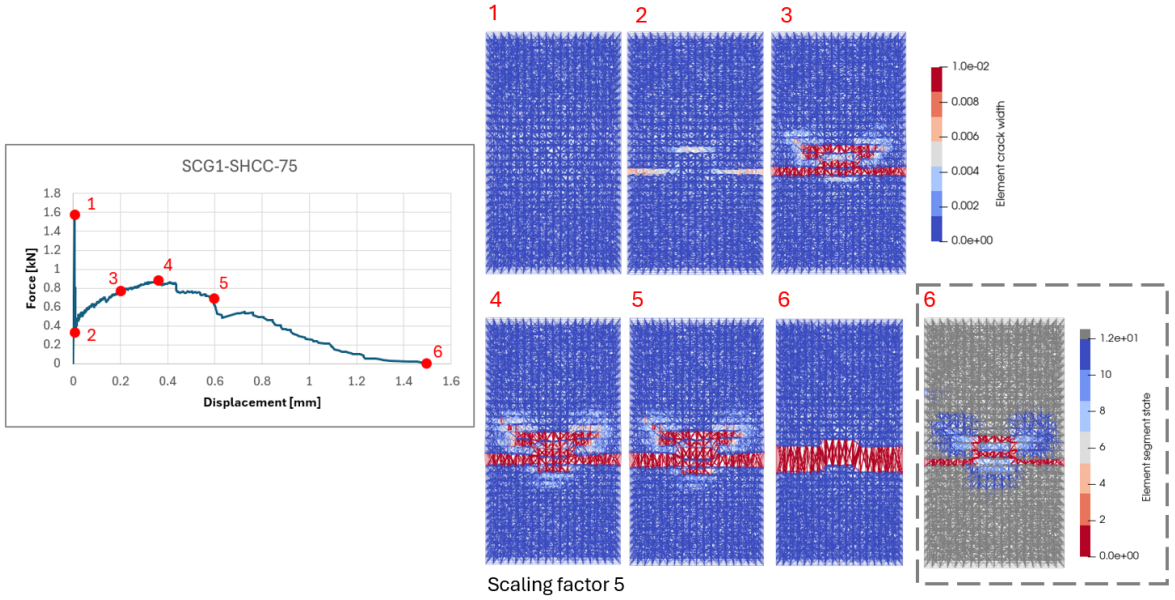

Figure C.8: Lattice model results for the SCG1-SHCC-75 specimen with 75% interface strength. The force-displacement curve is on the left, and the fracture response is on the right. In the grey box (final stage), grey represents undamaged elements, blue to red indicates increasing damage, and for the interface, pink denotes undamaged elements and red indicates damaged ones.

C.1.9. Interface strength 100%, w/h = 1.5

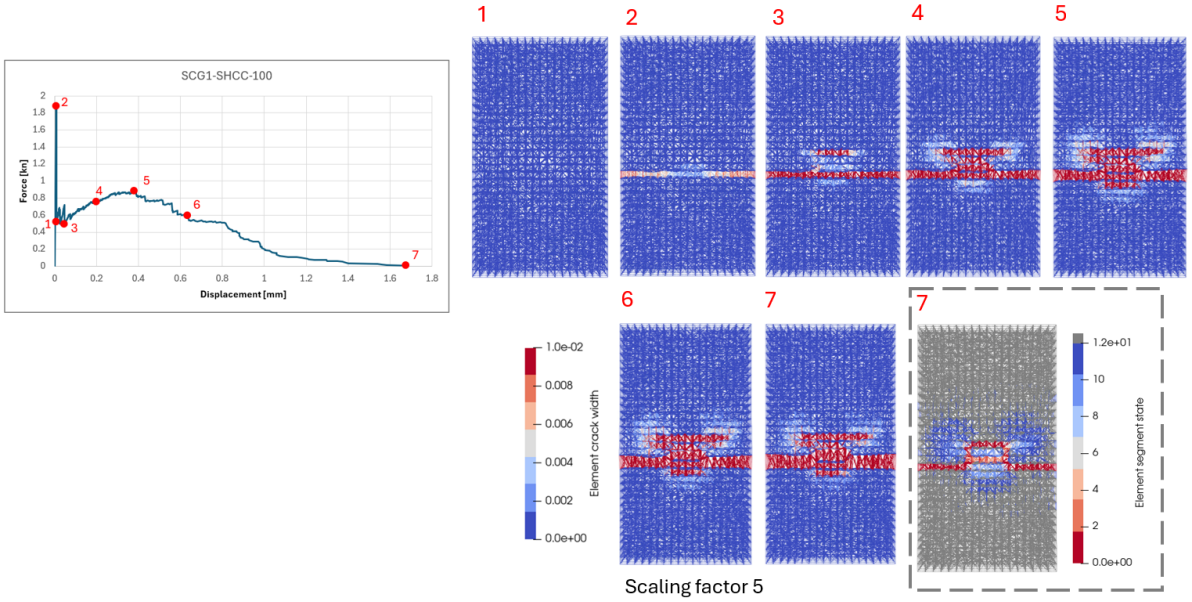

Figure C.9: Lattice model results for the SCG1-SHCC-100 specimen with 100% interface strength. The force-displacement curve is on the left, and the fracture response is on the right. In the grey box (final stage), grey represents undamaged elements, blue to red indicates increasing damage, and for the interface, pink denotes undamaged elements and red indicates damaged ones.

C.1.10. Interface strength 150%, w/h = 1.5

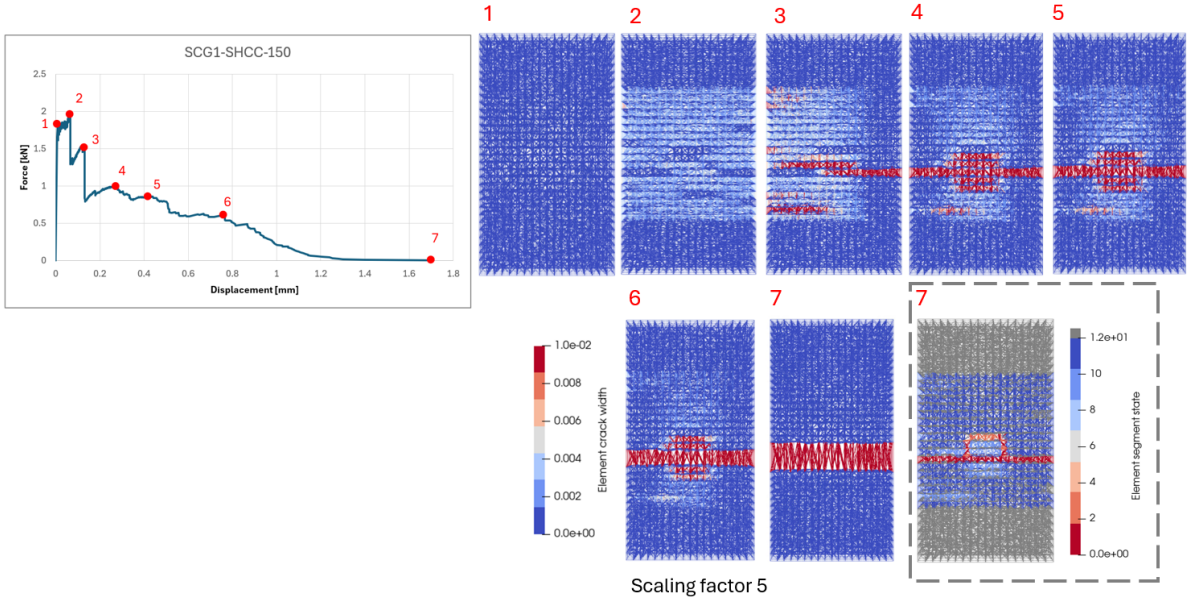

Figure C.10: Lattice model results for the SCG1-SHCC-150 specimen with 150% interface strength. The force-displacement curve is on the left, and the fracture response is on the right. In the grey box (final stage), grey represents undamaged elements, blue to red indicates increasing damage, and for the interface, pink denotes undamaged elements and red indicates damaged ones.

C.1.11. Interface strength 200%, w/h = 1.5

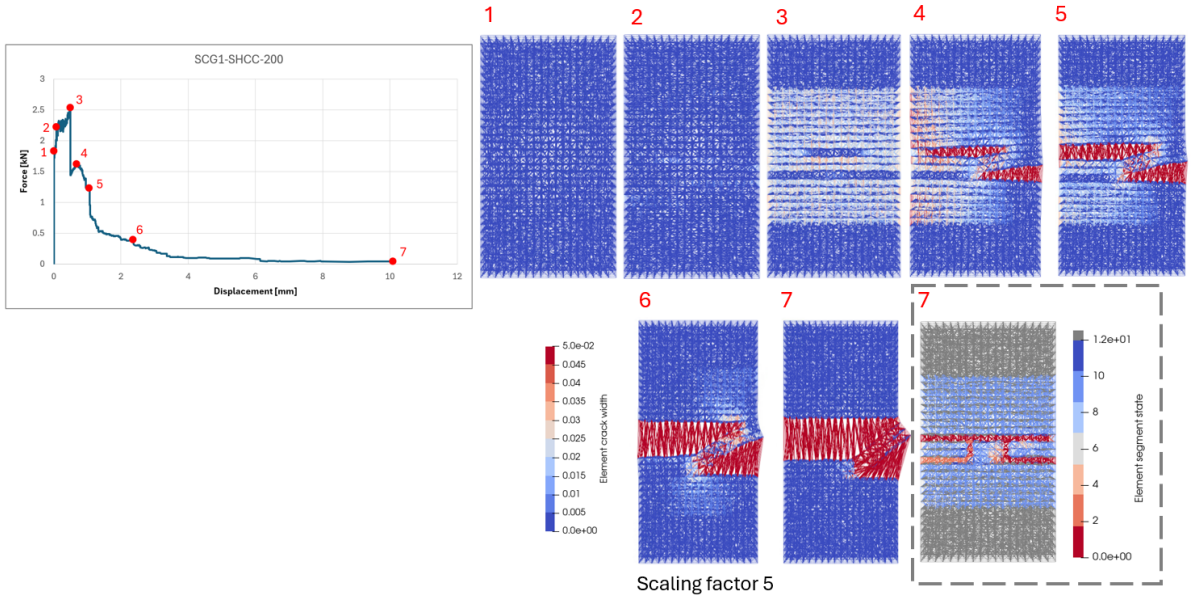

Figure C.11: Lattice model results for the SCG1-SHCC-200 specimen with 200% interface strength. The force-displacement curve is on the left, and the fracture response is on the right. In the grey box (final stage), grey represents undamaged elements, blue to red indicates increasing damage, and for the interface, pink denotes undamaged elements and red indicates damaged ones.

C.1.12. Interface strength 300%, w/h = 1.5

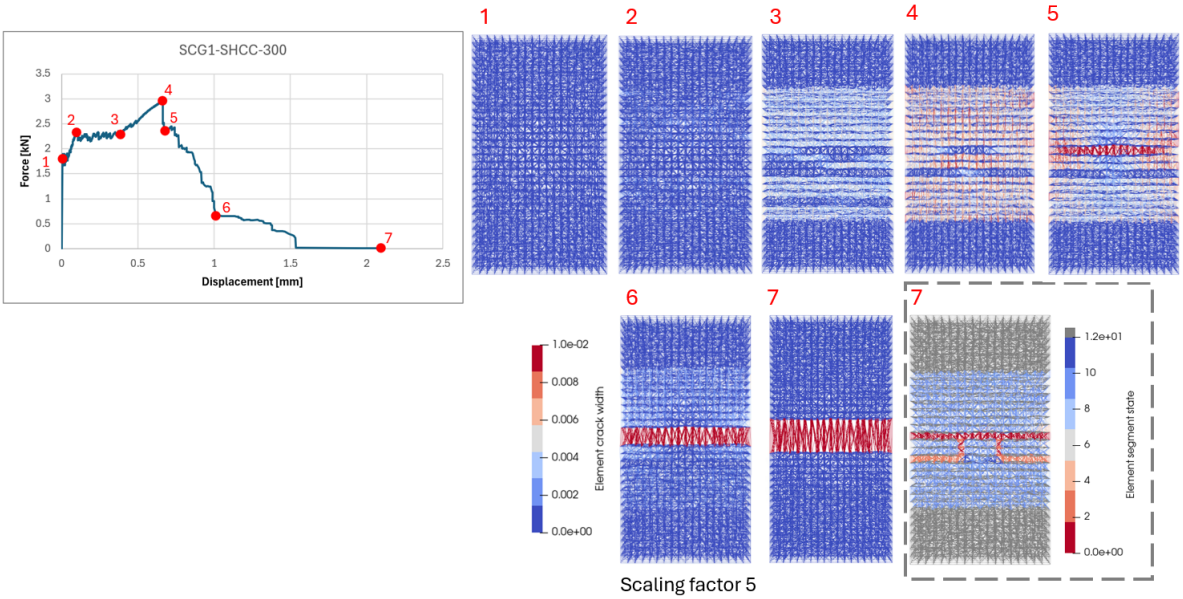

Figure C.12: Lattice model results for the SCG1-SHCC-300 specimen with 300% interface strength. The force-displacement curve is on the left, and the fracture response is on the right. In the grey box (final stage), grey represents undamaged elements, blue to red indicates increasing damage, and for the interface, pink denotes undamaged elements and red indicates damaged ones.

C.1.13. Interface strength 500%, w/h = 1.5

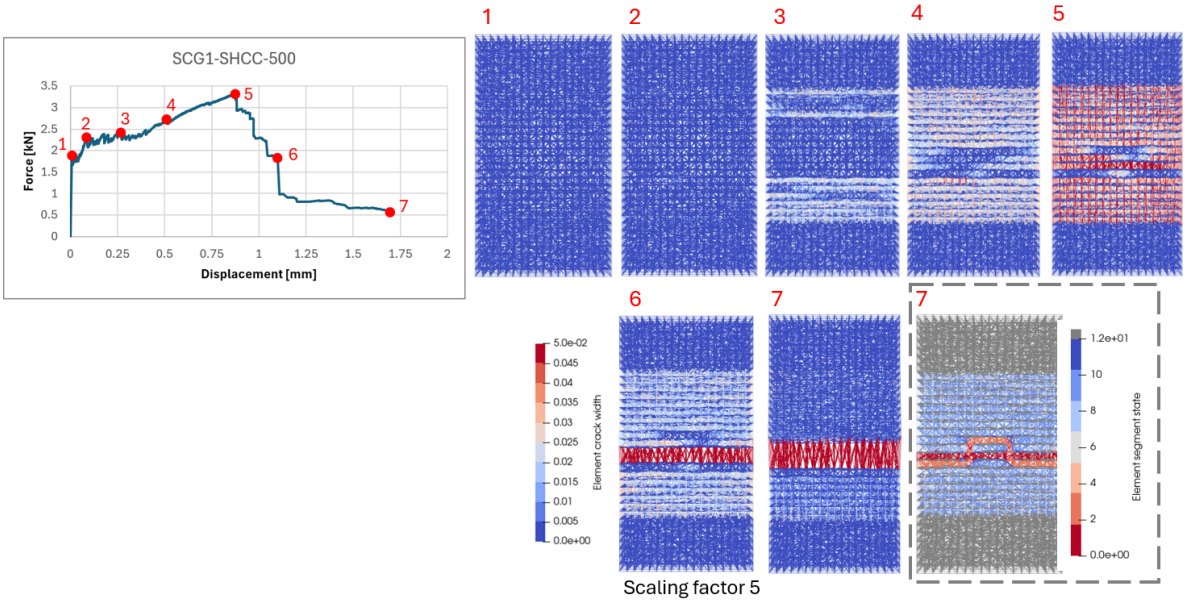

Figure C.13: Lattice model results for the SCG1-SHCC-500 specimen with 500% interface strength. The force-displacement curve is on the left, and the fracture response is on the right. In the grey box (final stage), grey represents undamaged elements, blue to red indicates increasing damage, and for the interface, pink denotes undamaged elements and red indicates damaged ones.

C.2. Interface design with a width-to-height ratio of 1.0; different interface strengths

C.2.1. Interface strength 5%, w/h = 1.0

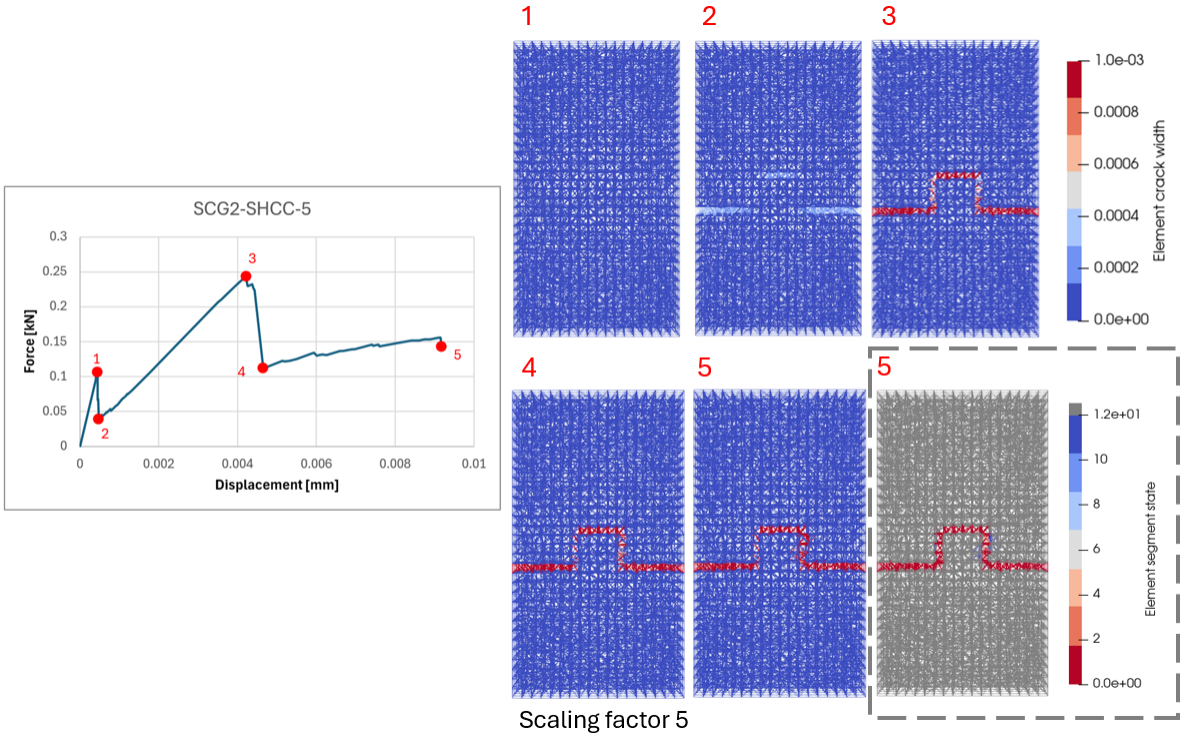

Figure C.14: Lattice model results for the SCG2-SHCC-5 specimen with 5% interface strength. The force-displacement curve is on the left, and the fracture response is on the right. In the grey box (final stage), grey represents undamaged elements, blue to red indicates increasing damage, and for the interface, pink denotes undamaged elements and red indicates damaged ones.

C.2.2. Interface strength 10%, w/h = 1.0

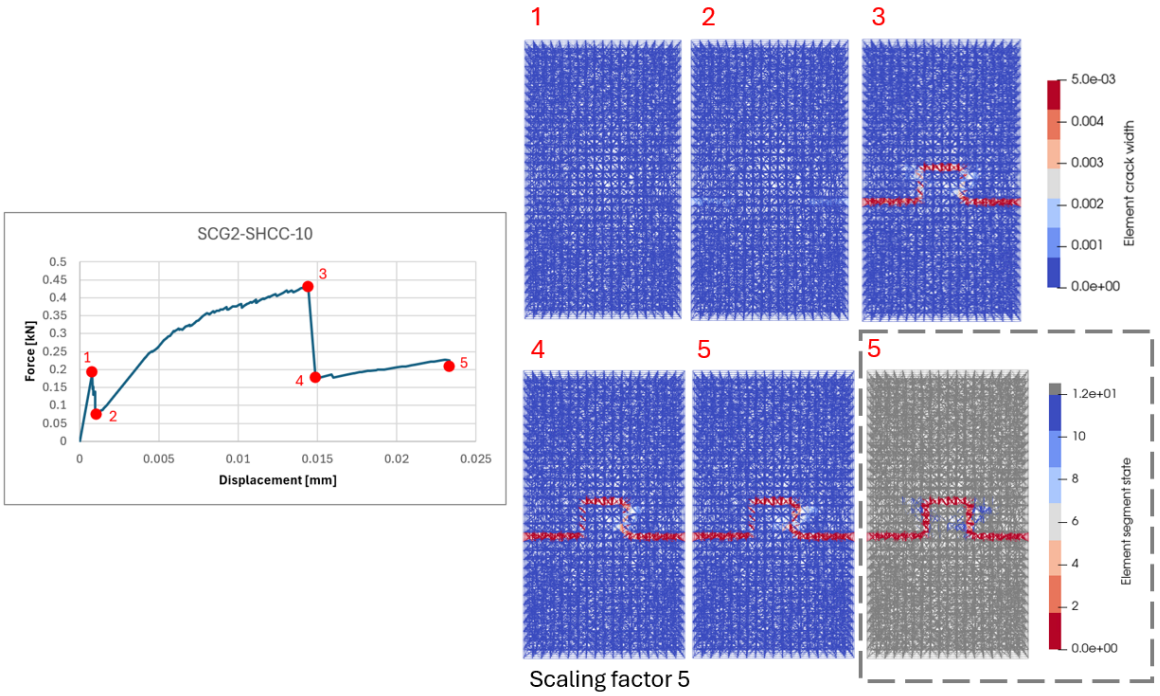

Figure C.15: Lattice model results for the SCG2-SHCC-10 specimen with 10% interface strength. The force-displacement curve is on the left, and the fracture response is on the right. In the grey box (final stage), grey represents undamaged elements, blue to red indicates increasing damage, and for the interface, pink denotes undamaged elements and red indicates damaged ones.

C.2.3. Interface strength 15%, w/h = 1.0

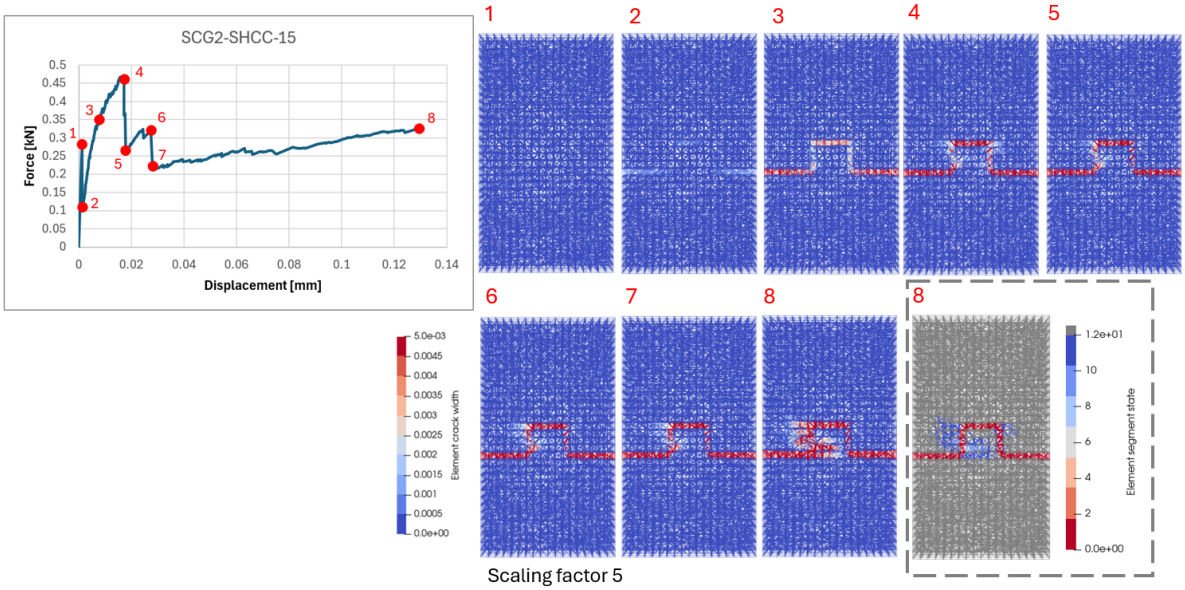

Figure C.16: Lattice model results for the SCG2-SHCC-15 specimen with 15% interface strength. The force-displacement curve is on the left, and the fracture response is on the right. In the grey box (final stage), grey represents undamaged elements, blue to red indicates increasing damage, and for the interface, pink denotes undamaged elements and red indicates damaged ones.

C.2.4. Interface strength 20%, w/h = 1.0

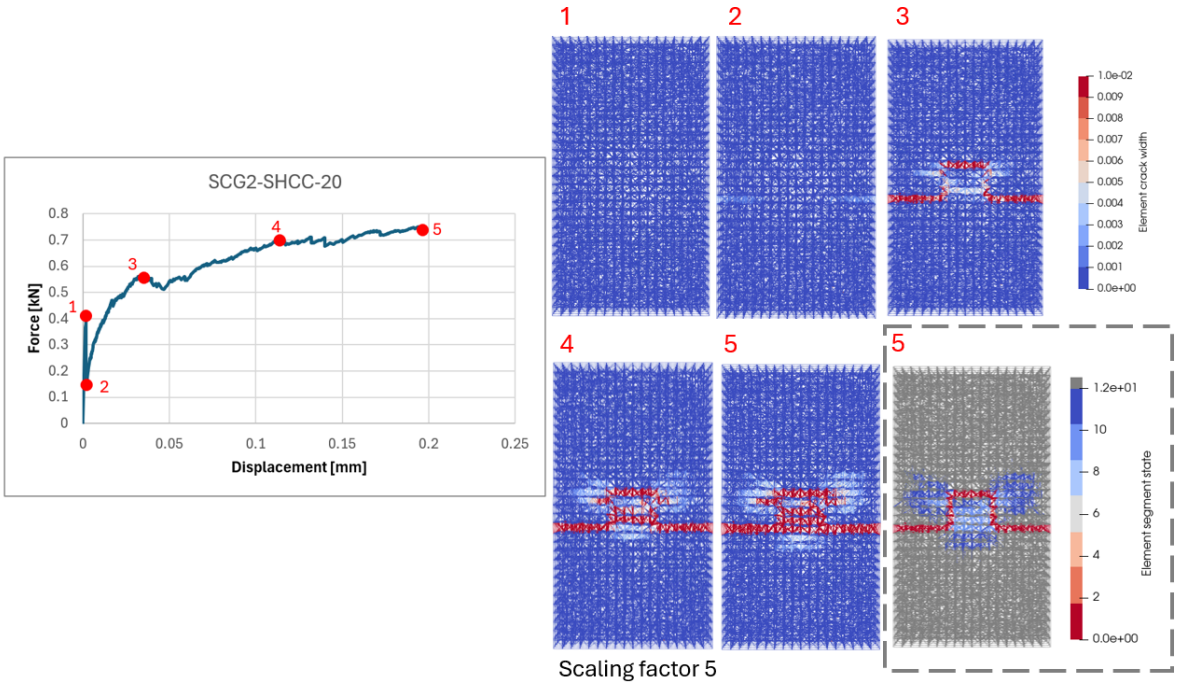

Figure C.17: Lattice model results for the SCG2-SHCC-20 specimen with 20% interface strength. The force-displacement curve is on the left, and the fracture response is on the right. In the grey box (final stage), grey represents undamaged elements, blue to red indicates increasing damage, and for the interface, pink denotes undamaged elements and red indicates damaged ones.

C.2.5. Interface strength 25%, w/h = 1.0

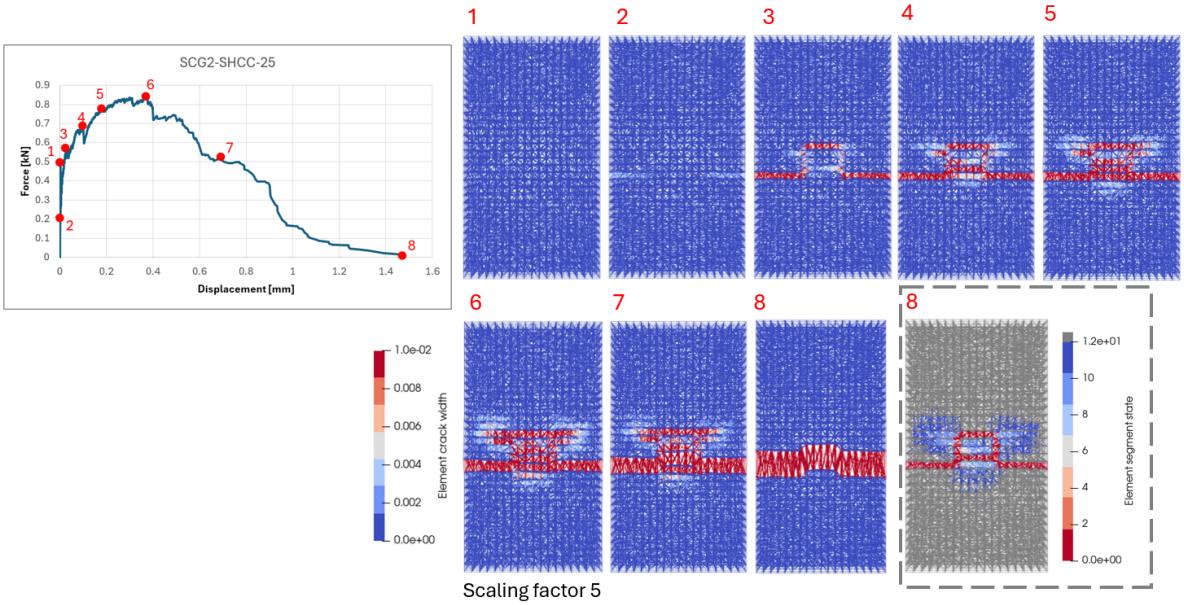

Figure C.18: Lattice model results for the SCG2-SHCC-25 specimen with 25% interface strength. The force-displacement curve is on the left, and the fracture response is on the right. In the grey box (final stage), grey represents undamaged elements, blue to red indicates increasing damage, and for the interface, pink denotes undamaged elements and red indicates damaged ones.

C.2.6. Interface strength 30%, w/h = 1.0

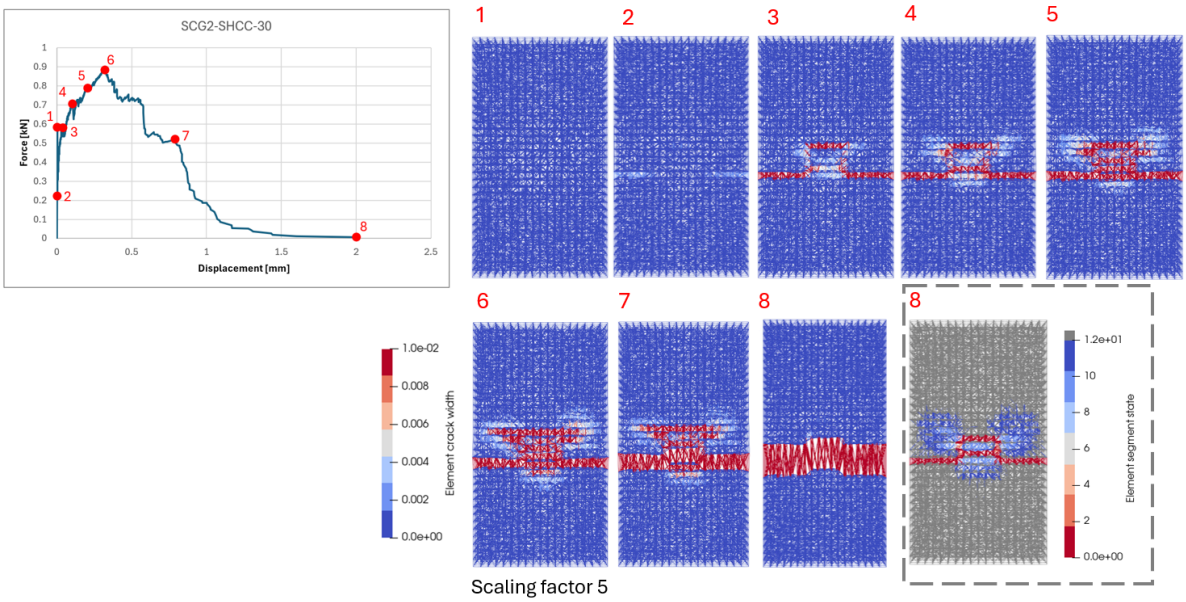

Figure C.19: Lattice model results for the SCG2-SHCC-30 specimen with 30% interface strength. The force-displacement curve is on the left, and the fracture response is on the right. In the grey box (final stage), grey represents undamaged elements, blue to red indicates increasing damage, and for the interface, pink denotes undamaged elements and red indicates damaged ones.

C.2.7. Interface strength 50%, w/h = 1.0

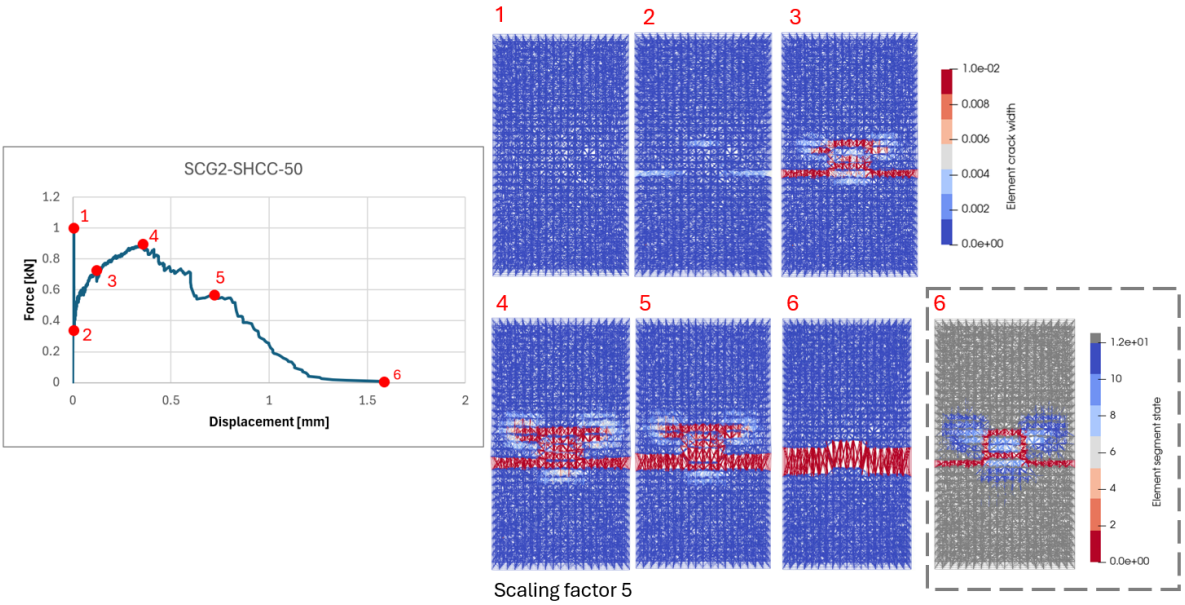

Figure C.20: Lattice model results for the SCG2-SHCC-50 specimen with 50% interface strength. The force-displacement curve is on the left, and the fracture response is on the right. In the grey box (final stage), grey represents undamaged elements, blue to red indicates increasing damage, and for the interface, pink denotes undamaged elements and red indicates damaged ones.

C.2.8. Interface strength 75%, w/h = 1.0

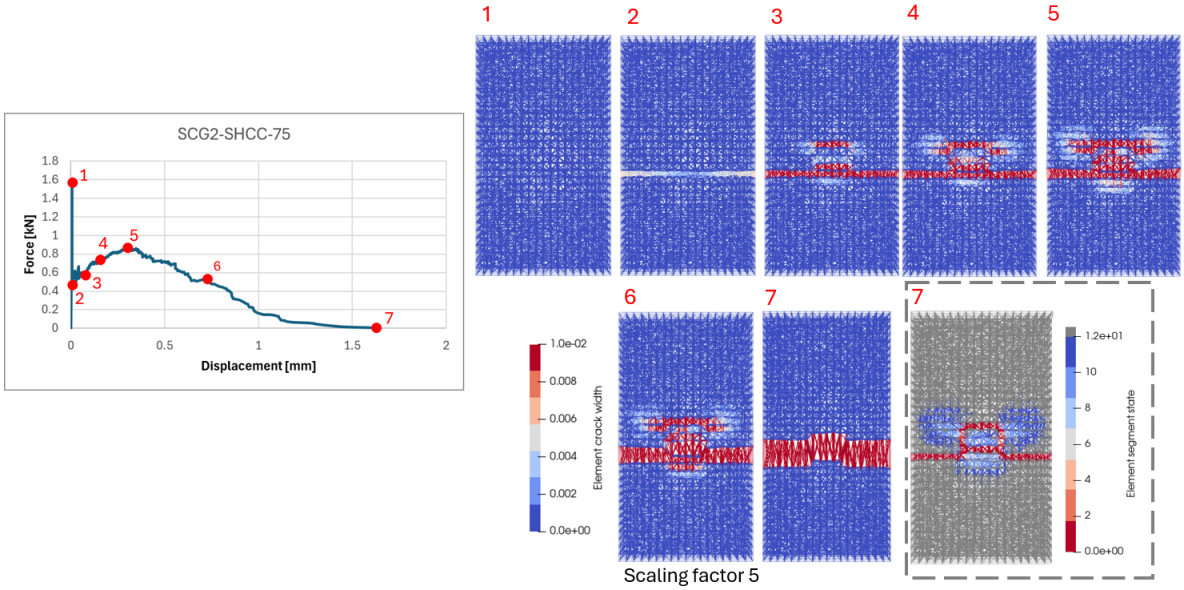

Figure C.21: Lattice model results for the SCG2-SHCC-75 specimen with 75% interface strength. The force-displacement curve is on the left, and the fracture response is on the right. In the grey box (final stage), grey represents undamaged elements, blue to red indicates increasing damage, and for the interface, pink denotes undamaged elements and red indicates damaged ones.

C.2.9. Interface strength 100%, w/h = 1.0

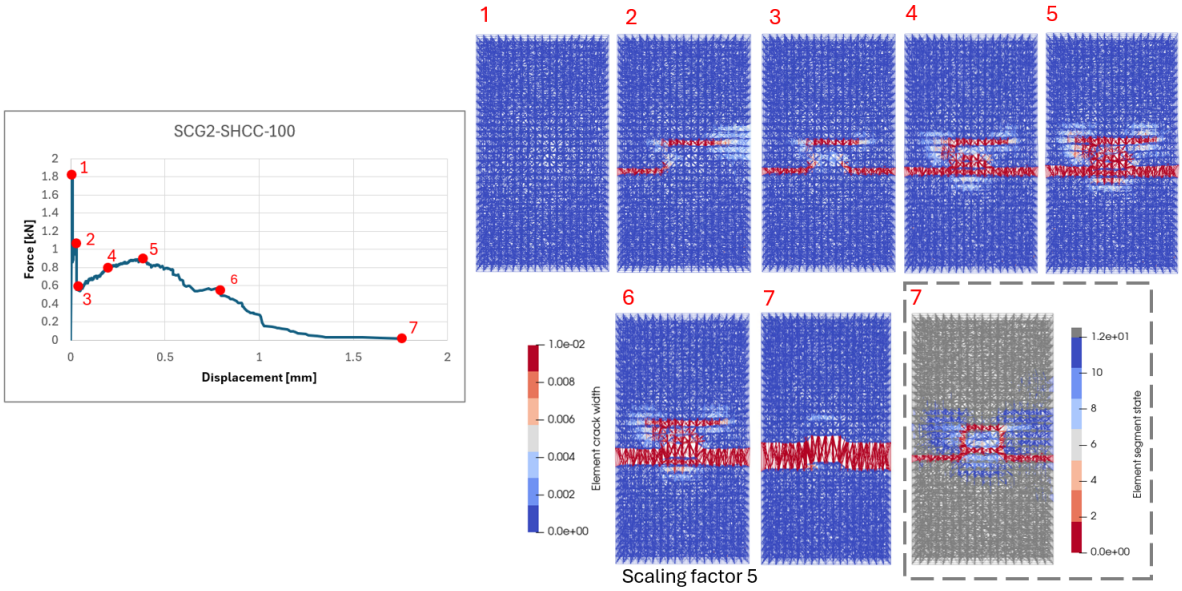

Figure C.22: Lattice model results for the SCG2-SHCC-100 specimen with 100% interface strength. The force-displacement curve is on the left, and the fracture response is on the right. In the grey box (final stage), grey represents undamaged elements, blue to red indicates increasing damage, and for the interface, pink denotes undamaged elements and red indicates damaged ones.

C.2.10. Interface strength 150%, w/h = 1.0

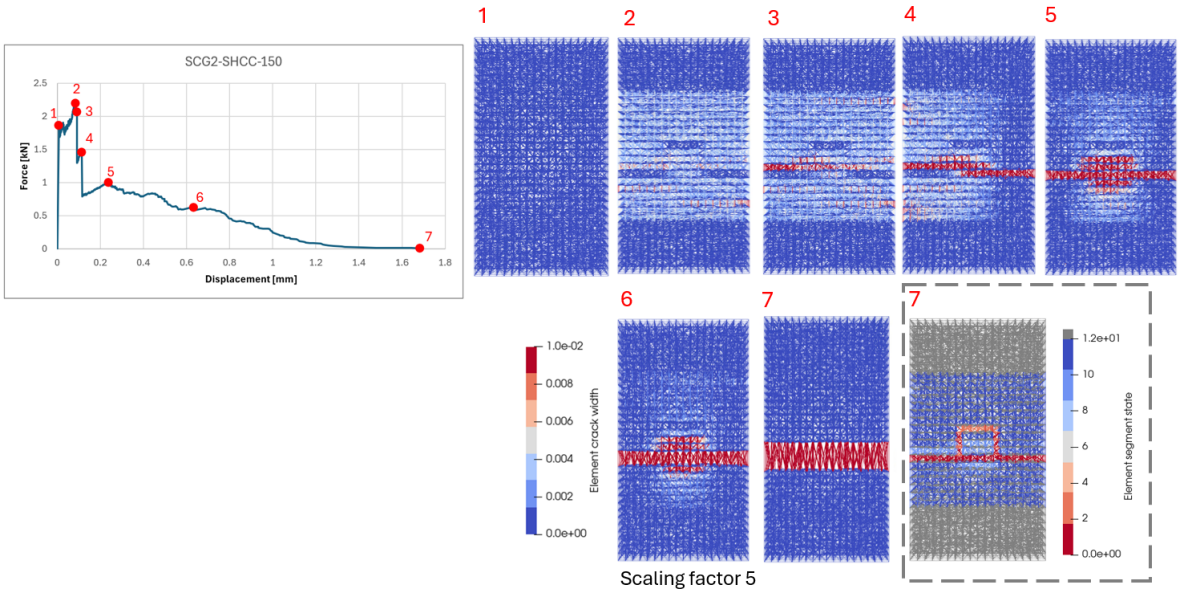

Figure C.23: Lattice model results for the SCG2-SHCC-150 specimen with 150% interface strength. The force-displacement curve is on the left, and the fracture response is on the right. In the grey box (final stage), grey represents undamaged elements, blue to red indicates increasing damage, and for the interface, pink denotes undamaged elements and red indicates damaged ones.

C.2.11. Interface strength 200%, w/h = 1.0

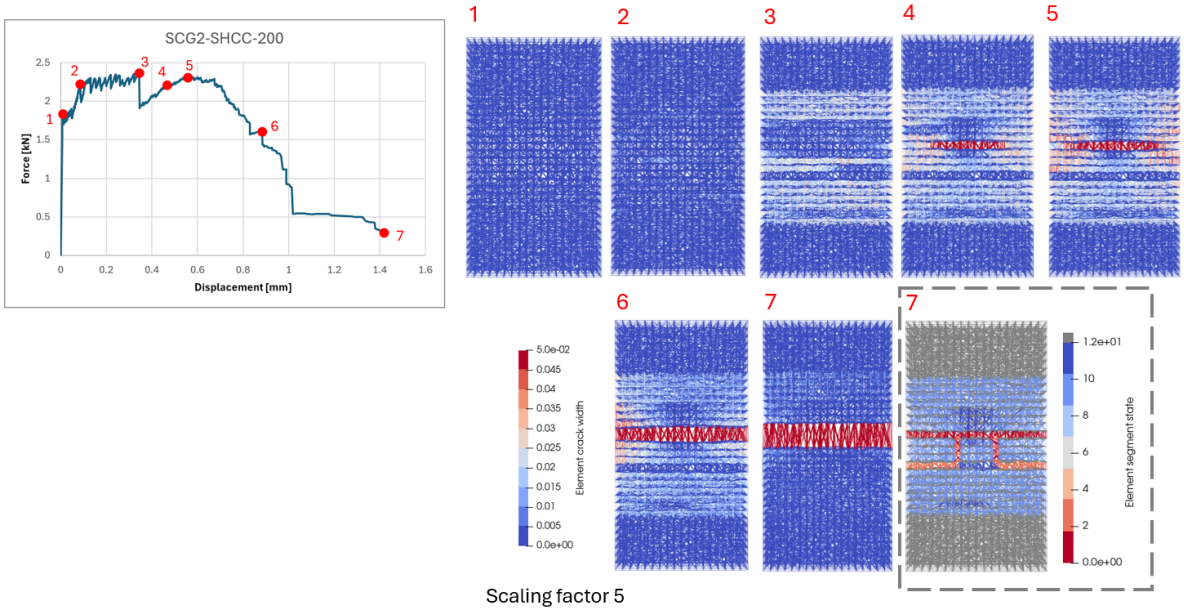

Figure C.24: Lattice model results for the SCG2-SHCC-200 specimen with 200% interface strength. The force-displacement curve is on the left, and the fracture response is on the right. In the grey box (final stage), grey represents undamaged elements, blue to red indicates increasing damage, and for the interface, pink denotes undamaged elements and red indicates damaged ones.

C.2.12. Interface strength 300%, w/h = 1.0

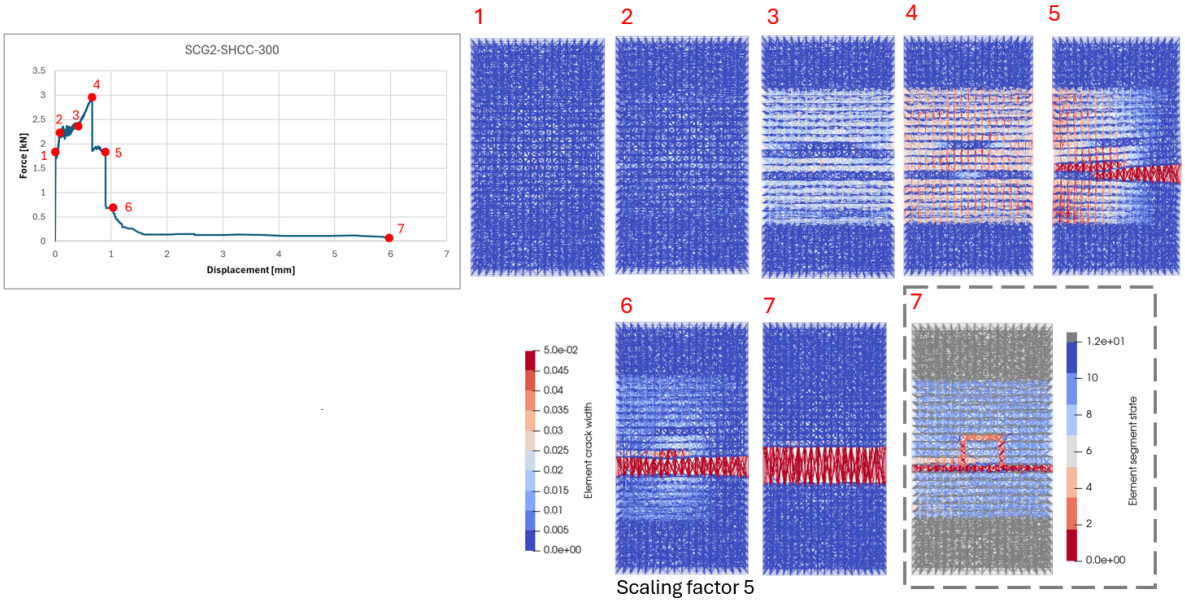

Figure C.25: Lattice model results for the SCG2-SHCC-300 specimen with 300% interface strength. The force-displacement curve is on the left, and the fracture response is on the right. In the grey box (final stage), grey represents undamaged elements, blue to red indicates increasing damage, and for the interface, pink denotes undamaged elements and red indicates damaged ones.

C.2.13. Interface strength 500%, w/h = 1.0

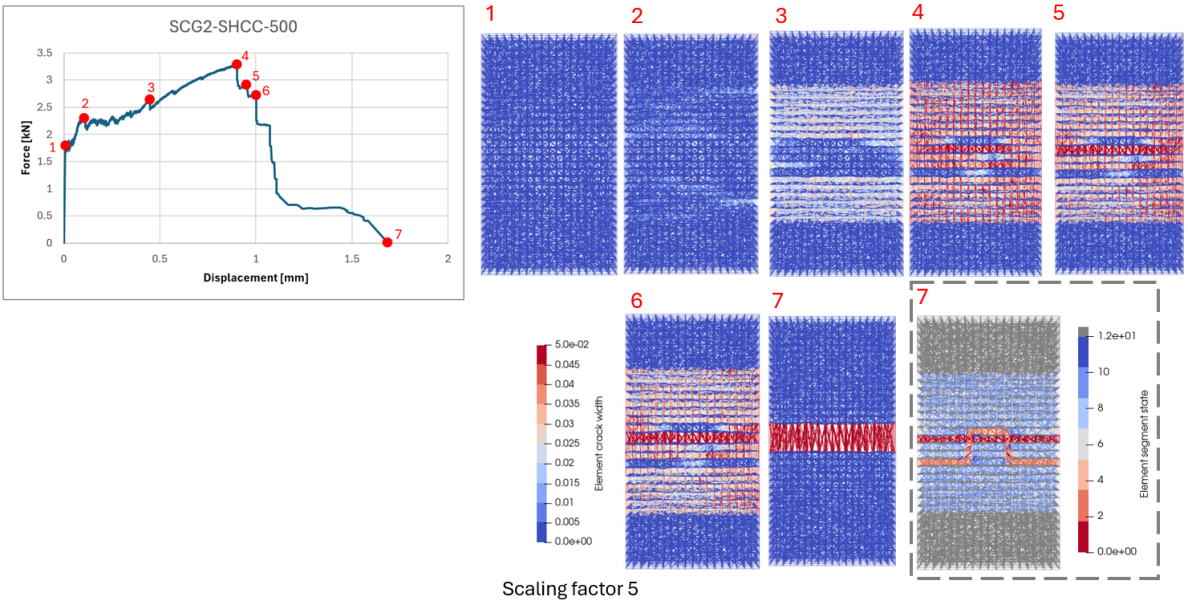

Figure C.26: Lattice model results for the SCG2-SHCC-500 specimen with 500% interface strength. The force-displacement curve is on the left, and the fracture response is on the right. In the grey box (final stage), grey represents undamaged elements, blue to red indicates increasing damage, and for the interface, pink denotes undamaged elements and red indicates damaged ones.